# Évolution spatio-temporelle de l'hydrothermalisme dans la plaque supérieure de l'arc des Petites Antilles en Guadeloupe : applications aux systèmes géothermaux

Alexiane Favier

▶ **To cite this version:**

Alexiane Favier. Évolution spatio-temporelle de l'hydrothermalisme dans la plaque supérieure de l'arc des Petites Antilles en Guadeloupe : applications aux systèmes géothermaux. Sciences de la Terre. Université des Antilles, 2019. Français. NNT : 2019ANTI0401 . tel-02798907v2

**HAL Id: tel-02798907**
**https://hal.science/tel-02798907v2**

Submitted on 7 Feb 2022

**HAL** is a multi-disciplinary open access archive for the deposit and dissemination of scientific research documents, whether they are published or not. The documents may come from teaching and research institutions in France or abroad, or from public or private research centers.

L'archive ouverte pluridisciplinaire **HAL**, est destinée au dépôt et à la diffusion de documents scientifiques de niveau recherche, publiés ou non, émanant des établissements d'enseignement et de recherche français ou étrangers, des laboratoires publics ou privés.

**THESE DE DOCTORAT DE L'UNIVERSITE DES ANTILLES**
**Ecole doctorale n°589 (Milieu insulaire tropical à risques)**

Présentée par :


# Alexiane FAVIER


Pour obtenir le titre de docteur en Sciences de l'Univers
Spécialité : Géosciences

# Evolution spatio-temporelle de l'hydrothermalisme dans la plaque supérieure de l'arc des Petites-Antilles en Guadeloupe. Applications aux systèmes géothermaux.

Thèse dirigée par Jean-Frédéric LEBRUN et Jean-Marc LARDEAUX

Préparée :

à l'Université des Antilles, au laboratoire Géosciences Montpellier UMR 5243 à Pointe-à-Pitre
et
à l'Université de Nice Sophia-Antipolis, au laboratoire Geoazur UMR 7329 à Valbonne

Soutenue le 30 octobre 2019 à Pointe-à-Pitre devant le jury :

| | | |
|---|---|---|
| Philippe MÜNCH | Pr à l'Université de Montpellier, GM | Président du jury |
| Béatrice LEDESERT | Pr à l'Université de Cergy-Pontoise, GEC | Rapporteure |
| Patrick LEDRU | Vice-Président Exploration, Orano Canada | Rapporteur |
| Mélody PHILIPPON | MCF à l'Université des Antilles, GM | Examinatrice |
| Philippe ROCHER | Responsable de la division géothermie, BRGM | Examinateur |
| Jean-Frédéric LEBRUN | Pr à l'Université des Antilles, GM | Directeur de thèse |
| Jean-Marc LARDEAUX | Pr à l'Université de Nice Sophia-Antipolis, Geoazur | Co-directeur de thèse |
| Chrystèle VERATI | MCF à l'Université de Nice Sophia-Antipolis, Geoazur | Co-encadrante de thèse |
| Michel CORSINI | Pr à l'Université de Nice Sophia-Antipolis, Geoazur | Invité |
| Céline DESSERT | Physicienne adjointe IPGP, OBSERA | Invitée |
| Simon VIARD | Coordinateur Géosciences, Teranov | Invité |

# Résumé

Cette thèse, effectuée dans le cadre du projet GEOTREF (plate-forme pluridisciplinaire d'innovation et de démonstration pour l'exploration et le développement de la GEOThermie haute énergie dans les REservoirs Fracturés), vise à préciser le fonctionnement des réservoirs géothermaux de haute-enthalpie. Le potentiel géothermal de l'arc insulaire des Petites Antilles est connu depuis les années 1980 au niveau de la province géothermale de Bouillante en Guadeloupe. Pour continuer à développer cette ressource il faut d'une part identifier de nouvelles zones potentielles et d'autre part mieux comprendre le fonctionnement des réservoirs géothermaux de haute-enthalpie.

Dans ce cadre, l'objectif de ces travaux est de caractériser l'évolution spatio-temporelle de l'hydrothermalisme au niveau de la plaque supérieure de l'arc. Pour cela nous proposons une analyse pluridisciplinaire (études structurales, géochimiques, minéralogiques, pétrologiques et géochronologiques) des complexes volcaniques les plus anciens de l'archipel de Guadeloupe. Ce sont les parties les plus érodées, qui permettent donc d'observer à l'affleurement les parties les plus profondes de la croûte de l'arc volcanique.

L'étude du Complexe Basal situé au nord de l'île de la Basse-Terre nous a permis d'identifier un métamorphisme hydrothermal (métamorphisme d'arc) dont les conditions P-T (faciès sub-Schistes Verts) sont compatibles avec le gradient géothermique conductif mesuré aujourd'hui. Ce métamorphisme, daté d'au plus 4 millions d'années, permet d'établir l'état thermique standard de la croûte de l'arc insulaire de Guadeloupe et démontre que la transition fragile-ductile est située à des profondeurs de l'ordre de 3 à 4 km.

Au niveau de l'île de Terre-de-Haut (Les Saintes), un paléo-réservoir exhumé a été identifié, servant de ce fait d'analogue de réservoir géothermal. Les transformations minéralogiques y ont été caractérisées : elles résultent d'un métamorphisme hydrothermal dans le faciès des Schistes-Verts (0,9 - 1,4 kbar, 360-375°C), synchrone du développement de couloirs de schistosité. Cette schistosité, de type pression–dissolution, révèle la présence d'horizons verticaux et latéraux de transfert de fluides hydrothermaux situés entre 2 et 3 km de profondeur. En comparant l'âge du volcanisme et la datation des phases hydrothermales de haute-température par la méthode $^{40}Ar$-$^{39}Ar$ à 2.59 ± 0.12 Ma, cela nous permet d'estimer une durée maximale de fonctionnement du paléo-réservoir à 650 ka.

Au cœur du système géothermal actif de l'île de la Basse-Terre, la découverte, l'analyse et la datation par la méthode K-Ar d'une nouvelle brèche hydrothermale à Vieux-Habitants révèle que l'activité géothermale actuelle correspond à un système épithermal distal relié à l'activité volcanique du Complexe Grande-Découverte-Soufrière, indiquant une neutralisation progressive des fluides en fonction de leur éloignement à la source de chaleur.

A partir de toutes ces données, un modèle conceptuel de fonctionnement d'un réservoir géothermal de haute-énergie en contexte d'arc actif est proposé qui intègre différents horizons latéraux, en particulier la transition fragile/ductile, et verticaux de transferts des fluides hydrothermaux.

**Mots clés :** Métamorphisme de bas degré - Schistosité de pression-dissolution - Géothermie de haute énergie - Méthodes $^{40}Ar/^{39}Ar$ et K-Ar – arc des Petites Antilles – Guadeloupe – GEOTREF

# Abstract

This thesis, as part of the GEOTREF project (a multidisciplinary innovative platform for exploration and development of high-enthalpy GEOThermal energy in Fractured REservoirs), aims to improve the thermo-mechanical evolution of high-energy geothermal reservoirs. The geothermal potential of Lesser Antilles arc is known since the 1980s in the geothermal field of Bouillante in Guadeloupe. In order to develop this resource, it is necessary to identify possible new key targets, and to better understand the modes of fluids and heat transfers in high-enthalpy geothermal reservoirs.

The objective of this work is thus to characterize the spatio-temporal evolution of hydrothermalism at the upper plate of the arc. For this purpose, we propose a multidisciplinary approach (combined structural, geochemical, mineralogical, petrological and geochronological analyses) focussed on the oldest volcanic complexes of the Guadeloupe archipelago. Being deeply eroded, these outcrops are key analogues of deep crustal parts of the volcanic arc.

The study of the Basal Complex located in the north of Basse-Terre Island reveals a hydrothermal metamorphism (arc metamorphism) developed under P-T conditions (sub-Greenschist facies) compatible with the conductive geothermal gradient measured today. This metamorphism, dated no more than 4 million years, establishes the standard thermal state of the crust of the island arc in Guadeloupe and shows that the brittle-ductile transition is located at depths of 3 to 4 km.

On the island of Terre-de-Haut (Les Saintes), an exhumed geothermal paleo-reservoir has been identified. Mineralogical and structural transformations have been characterized: they result from Greenschist facies a hydrothermal metamorphism (0.9 - 1.4 kbar, 360-375°C), synchronous with the development of pressure-solution controlled schistose corridors. The finite strain pattern of schistose corridors attests for both vertical and lateral hydrothermal fluid transfers at depths between 2 and 3 km. Comparison of the age of the volcanic activity and $^{40}Ar$-$^{39}Ar$ dating of the high-temperature hydrothermal phases at 2.59 ± 0.12 Ma allows us to estimate a maximum operating time of the paleo-reservoir at 650 ka.

Within the active geothermal system on Basse-Terre Island, the discovery, the analysis and the K-Ar dating of a new hydrothermal breccia at Vieux-Habitants reveals a link between current geothermal activity and volcanic activity of the Grande-Découverte-Soufrière complex, interpreted in the framework of a distal epithermal system involving a progressive neutralization of fluids with respect to their distance to the heat source.

On the basis of all these data, a conceptual model for the operation of a high-energy geothermal reservoir in the context of an active arc is proposed which integrates different horizons of lateral, in particular the brittle/ducile transition, and vertical transfers of hydrothermal fluids.



**Keywords:** Low-grade metamorphism – Pressure-solution schistosity – High-temperature geothermal energy – $^{40}Ar$-$^{39}Ar$ and K-Ar dating – Lesser Antilles arc – Guadeloupe – GEOTREF

# Remerciements

De nombreuses personnes sont intervenues au fil des mois, années… pour m'apporter leur aide, leur soutien, consciemment ou non, et m'ont permis de mener à bien ce travail de thèse. J'ai eu la chance d'avoir été très bien entourée et de faire de formidables rencontres qui m'ont permis d'en arriver là, alors par ces quelques lignes je vais tenter d'exprimer toute ma gratitude envers ces personnes.

Je tiens tout d'abord à remercier la personne qui m'a permis de m'insérer dans cette aventure antillaise en me présentant à une équipe formidable : Jean-Jacques Cornée. Merci Jean-Jacques d'avoir pensé à moi après ces mois passés dans ton bureau à GM et de m'avoir donné cette opportunité de poursuivre en thèse, bien que dans un tout autre domaine que mon stage de M2, je ne pouvais résister à la saisir. J'en profite pour remercier Aurélien Gay de m'avoir initiée au monde de la recherche.

Je remercie très sincèrement mes directeurs de thèse Jean-Frédéric Lebrun, Jean-Marc Lardeaux et Chrystele Verati pour leur présence et leur confiance. Merci Jean-Fred pour ta patience et ta persévérance dans les méandres de l'administration de l'UA, tu n'as jamais rien lâché et je sais que je t'ai donné du fil à retorde, heureusement tu as pu compter sur l'aide précieuse de Sandra Bausivoir. Merci Jean-Marc pour ta bienveillance, la transmission d'une infime partie de tes connaissances et de m'avoir toujours poussé à aller plus loin. Merci Chrystele de m'avoir fait découvrir le monde de la géochro (et du Schiste-Vert …), pour tes paroles toujours positives et encourageantes grâce auxquelles j'ai puisé ma motivation. Et je n'oublie pas de remercier un quatrième membre essentiel à cette équipe de direction de thèse : Michel Corsini, avec qui j'ai également pris plaisir à travailler, me rendre sur le terrain, braver les recommandations pour trouver de superbes échantillons là où soit disant il n'y avait rien à voir et faire parfois de drôles de rencontres sur notre route (iguanes, cabris, cochons, poules, crabes …).

Je tiens à remercier chaleureusement les membres de mon jury pour l'intérêt porté à mon travail et d'avoir tous fait le déplacement jusqu'en Guadeloupe pour la soutenance. Béatrice Ledésert et Patrick Ledru en leur charge de rapporteurs, je vous remercie d'avoir accepté de lire mon manuscrit et d'évaluer mon travail. Mélody Philippon, Philippe Rocher et Philippe Munch en leur qualité d'examinateurs, et Céline Dessert, Simon Viard et Michel Corsini en tant qu'invités, je vous remercie pour vos questions et vos remarques pertinentes à l'égard de mes recherches. Un grand merci à Philippe Munch, en sa qualité de président du Jury, d'avoir conduit la discussion de façon fluide et équitable entre les onze membres qui composaient ce jury.

Je remercie l'ADEME et le programme Investissement d'Avenir, au travers du projet GEOTREF, d'avoir financé mes travaux de recherche. Je remercie également Simon Viard, de

Teranov, en charge de la coordination du projet, d'avoir toujours suivi de près mes avancées et fait le lien entre les différents partenaires.

Bien qu'étudiante de l'Université des Antilles à Pointe-à-Pitre, en dehors des missions de terrain, j'ai passé la majeure partie de mon temps en métropole. Je remercie donc Marc Sosson et l'ensemble du laboratoire Geoazur pour son accueil et plus particulièrement à l'administration Véronique, Sandrine, Valérie et Fabienne sur qui j'ai toujours pu compter. Il m'est impossible d'oublier Jelena qui a toujours fait son possible pour m'aider à trouver des références bibliographiques. L'équipe du service informatique a fortement contribué à la bonne réalisation de cette thèse en me sauvant de situations complexes (du moins pour moi …) avec mon ordinateur : David, Jean-Baptiste, Lionel et Caroline. Si je me dirige à présent vers le sous-sol du bâtiment 1, là où la température est constante peu importe la saison, je remercie « chaudement » Sylvain et Christophe pour nos discussions enrichissantes, Matthieu puis Magali pour le temps considérable que vous m'avez fait gagner dans la préparation des échantillons.

Je n'oublie pas non plus ceux qui ont régulièrement fait irruption dans mon bureau ou que j'ai croisé dans les couloirs avec toujours des mots agréables (ou des gâteaux !) : Gueorgui, François, Jean-Xav, Laure S., Marie-O, Priscilla, Luc, Stefano, Cédric, Guillaume, Alexandre, Jean-Luc, Julien, Fabrice, Quentin, Lucie R., Frédérique, Damienne, Damien, Davide, Bernard …

Hors des murs de Geoazur j'ai également pu faire des rencontres importantes qu'il me tient de remercier. Jean-Luc Potdevin et Sandra Ventalon pour le temps que vous avez toujours su me dégager lors de mes venues à Lille. Gabriel Monge pour nos échanges techniques sur les DRX et cinématographiques. Et bien évidemment lors des missions de terrain où dès le début de ma thèse j'ai pu faire la connaissance des partenaires primordiaux du projet avec lesquels j'allais principalement pouvoir échanger pour mettre en relation nos résultats : Yves G., Marc D., Marc M., Mélody, il y a eu Emile aussi, mais surtout l'équipe des doctorants : Lucie, Vivien, Jeanne, Gildas et Claire, qu'il fut toujours plaisant de retrouver en Guadeloupe, en congrès ou encore aux Journées Scientifiques.

Pour veiller à la bonne réalisation d'une thèse, il est bon d'avoir un environnement apaisant pour souffler un peu et se soutenir les uns les autres grâce à des générations de doctorants qui se succèdent. Il y a ceux qui ont pris leur envol depuis quelques temps déjà : Alex, Stephen, Virginie, Maëlle, Laure D., Reine, Flore, Luc, Kévin, Laurent, Mathilde, Théa… Ceux qui sont encore là (mais plus pour très longtemps) : Emmanuelle, Asmae, Laurie, Pierre, Nico, Lionel, Zoé, Maria-José, Sara, Marco, Jean, Carlo, Milton, Flo, Hector, Caroline, Tiziano, Sébastien… Et les nouveaux qui viennent de commencer à qui je souhaite plein de courage pour aller jusqu'au bout. Il y a bien évidemment

ceux qui sont indispensables à ce juste équilibre et qui méritent un petit mot supplémentaire. Virginie, la première personne que j'ai eu la chance de rencontrer à mon arrivée et qui m'a tout de suite prévenue dans quoi j'avais mis les pieds. Alex et tes blagues, bien que celle des post-it était peut-être un peu prématurée. Maëlle et son don pour rapprocher les gens. Mathilde et ta bonne humeur communicative. Magali toujours à l'écoute. Nico mon camarade lyonnais. Flo et tes plaisanteries que je ne comprends pas toujours mais je note ton changement vestimentaire, on progresse ! Asmae merci pour ces moments de partage. Sara et Vincent pour ces agréables pauses déjeuner que vous nous offrez. Théa et tes péripéties, mais surtout ta terrible addiction aux potins avec Laurie, vous m'aurez bien fait rire ! Maria-José ma co-bureau en or, nos pauses thé/infusion et même café. Flore avec qui j'ai lié une belle amitié, à laquelle est venue s'associer Aurel pour former un super trio.

Enfin je remercie mes amis toujours présents malgré une certaine distance géographique : Nina, Séverine, Pierre, Camille, Jessica, Lise, Julie, Claire, Marieke... Hugo (et tes supers colocs) pour ton soutien ces derniers mois denses de fin de thèse (et ta relecture assidue !). A ma famille, mes parents … et mon petit Milo.

Merci à tous d'avoir su m'entourer, chacun à votre façon.

A présent place à la lecture de ce manuscrit, en espérant vous faire voyager comme si vous y étiez !

# Sommaire


Chapitre I : Introduction générale ..... 1

I.1. Contexte de l'étude ..... 2

I.2. Objectifs et problématique du sujet ..... 5

I.3. Démarche suivie et méthodes employées ..... 8

I.4. Organisation du manuscrit ..... 9

Chapitre II : Les géothermies ..... 11

II.1. Origine de la chaleur terrestre et des mécanismes de transfert ..... 12

II.2. Ressource géothermale : une anomalie de concentration ..... 15

II.3. Les différents types de géothermie ..... 17

II.4. Applications des ressources géothermales ..... 18

II.5. Avantages et inconvénients de la géothermie ..... 21

II.6. Méthodes exploratoires ..... 21

II.6.1. Investigations géologiques et hydrogéologiques ..... 22

II.6.2. Investigations géophysiques ..... 22

II.6.3. Investigations géochimiques ..... 23

II.7. La géothermie de haute-température ..... 23

II.7.1. Classification des systèmes géothermaux de haute-température ..... 23

II.7.2. Description des systèmes géothermaux de haute-température en contexte magmatique.. ..... 24

II.7.3. Fluides et altérations hydrothermales ..... 25

II.7.4. Géothermie de haute-température : quelques exemples emblématiques ..... 31

Chapitre III : Contexte géologique ..... 39

III.1. L'arc insulaire des Petites Antilles dans son contexte géodynamique ..... 40

III.2. L'archipel de Guadeloupe ..... 44

III.2.1. Le contexte tectonique ..... 44

III.2.2. Les complexes volcaniques de l'archipel ..... 46

III.2.3. L'érosion ..... 53

Chapitre IV : Evolution tectono-métamorphique de la croûte supérieure de l'arc volcanique en Guadeloupe : définition de l'état thermique de référence depuis 4 Ma ..... 57

IV.1. Préambule ..... 58

IV.2. Article 1 - Tectono-metamorphic evolution of shallow crustal levels within active volcanic arcs. Insights from the exhumed Basal Complex of Basse-Terre (Guadeloupe, French West Indies) ..... 60

IV.3. Article 2 - Arc-related metamorphism in the Guadeloupe archipelago (Lesser Antilles active island arc): First report and consequences ..... 84

Chapitre V : Evolution hydrothermale des parties profondes d'un paléo-réservoir géothermal dans l'arc de Guadeloupe : l'exemple de l'analogue exhumé de l'île de Terre-de-Haut (archipel des Saintes) ..... 93

# Sommaire

V.1. Préambule....94
V.2. Article 3 – Characterization of an exhumed high-energy geothermal paleo-reservoir: an example from Terre-de-Haut Island (Guadeloupe archipelago, Lesser Antilles arc)....95
V.2.1. Introduction....96
V.2.2. Regional setting....97
V.2.3. Material and methods....100
V.2.4. Diversity of Terre-de-Haut lithologies....103
V.2.5. Structural analysis....106
V.2.6. Petrography and mineralogy....110
V.2.7. Mineral equilibria modelling....115
V.2.8. Discussion....121
V.2.9. Conclusions....125
V.2.10. Supplementary data....125
V.2.11. Acknowledgment....126
Chapitre VI : Datation des systèmes hydrothermaux....129
VI.1. Préambule....130
VI.2. Article 4 – $^{40}Ar/^{39}Ar$ dating of high enthalpy geothermal systems: first attempt from meta-pyroxenes of Les Saintes archipelago (Lesser Antilles arc, Guadeloupe)....130
VI.2.1. Abstract....131
VI.2.2. Introduction....132
VI.2.3. Geological setting and previous mineralogical investigations....133
VI.2.4. Materials and Methods....134
VI.2.5. Results....138
VI.2.6. Discussion....143
VI.2.7. Conclusion....147
VI.2.8. Supplementary data....148
VI.2.9. Ackowledgments....148
VI.3. Perspectives afin de mieux contraindre la durée de vie des systèmes géothermaux....149
VI.4. Hydrothermalisme au niveau du système actif de la Basse-Terre – dans la zone du PER....150
VI.4.1. Etat des lieux des structures tectoniques et hydrothermales....150
VI.4.2. Protocole de séparation de l'alunite....156
VI.4.3. Datation K-Ar et analyses isotopiques....160
VI.4.4. Lien entre l'activité volcanique et géothermale du système actif de l'île de la Basse-Terre....165
Chapitre VII : Discussion des résultats obtenus....169
VII.1. Hydrothermalisme et rhéologie de la croute supérieure de l'arc volcanique des Petites Antilles en Guadeloupe....170

# Sommaire

VII.2. Apport de l'étude d'analogue exhumé au fonctionnement des systèmes géothermaux de l'arc volcanique de Guadeloupe ..... 174

VII.3. Le système géothermal de Guadeloupe : évolution spatio-temporelle de l'hydrothermalisme et comparaison avec les systèmes métallogéniques ..... 177

VII.3.1. Distribution spatiale des contraintes temporelles dans l'arc récent de Guadeloupe ..... 177

VII.3.2. Brèches hydrothermales et systèmes épithermaux ..... 178

VII.3.3. Réservoirs géothermaux et gîtes métallogéniques hydrothermaux ..... 180

Chapitre VIII : Conclusions générales et perspectives ..... 185

Chapitre IX : Bibliographie ..... 191

Chapitre X : Annexes ..... 215

X.1. Fiches de tâches du projet GEOTREF ..... 216

X.2. Article 1 - Supplementary data ..... 222

X.3. Article 2 - Supplementary data ..... 230

X.4. Article 3 - Supplementary data ..... 234

X.5. Article 4 – Supplementary data ..... 248

X.6. Article 5 – Petrophysical properties of volcanic rocks and impacts of hydrothermal alteration in the Guadeloupe Archipelago (West Indies) ..... 256

X.7. Article 6 – The characterisation of an exhumed high-temperature paleo-geothermal system on Terre-de-Haut Island (the Les Saintes archipelago, Guadeloupe) in terms of clay minerals and petrophysics ..... 278

# Chapitre I : Introduction générale

*Vue Sud sur l'île de Basse-Terre depuis l'île de Terre-de-Haut*
*Le volcan de la Soufrière au loin caché dans les nuages*

# Chapitre I

## I.1. Contexte de l'étude

Ce travail de recherche s'inscrit au sein du projet GEOTREF, soutenu par l'état français au travers des financements « Investissements d'Avenir » de l'ADEME (Agence De l'Environnement et de la Maîtrise de l'Energie).

Le projet GEOTREF (plateforme pluridisciplinaire d'innovation et de démonstration pour l'exploration et le développement de la GEOThermie haute énergie dans les REservoirs Fracturés) est un programme de recherche, d'expérimentation et d'innovation visant à :

- Améliorer la maîtrise du procédé d'exploration de la ressource géothermale dans l'arc des Petites Antilles,
- Optimiser les coûts d'exploration pour perfectionner les cibles de forages, afin de réduire le « risque géologique » lié aux investissements financiers importants pour leurs réalisations,
- Garantir une exploitation durable du réservoir lors de la phase de production.

Aujourd'hui, les processus contrôlant le fonctionnement des parties les plus profondes des réservoirs géothermaux de haute température associé aux systèmes volcaniques restent encore très mal connus alors qu'il s'agit d'une ressource durable et d'avenir. L'arc insulaire volcanique des Petites Antilles est favorable à l'existence de ce type de ressources géothermales. Cette énergie peut contribuer à diminuer la dépendance énergétique (vis-à-vis de l'importation de combustibles fossiles) des îles de l'arc caribéen pour la production d'électricité. Cela est déjà en partie le cas en Guadeloupe à Bouillante (Basse-Terre, Antilles Françaises), où des puits ont été forés dès les années 70, une centrale géothermique a été mise en service en 1985 et permet de fournir 6 à 8% de la production électrique de l'île (Laplaige *et al.*, **2013**) à partir de l'utilisation de la vapeur géothermale.

Un permis exclusif de recherche (PER) de gîtes géothermiques à haute-température de 120 km² (Figure I-1) a été attribué au niveau de Vieux-Habitants (Basse-Terre, Guadeloupe) dans le cadre du projet GEOTREF pour une durée de 5 ans à compter de la date de publication de l'arrêté du 10 mai 2016 au Journal officiel de la République Française. Il sert de site démonstrateur afin de valider les méthodologies et les outils de modélisation développés, dans le but de poursuivre le développement de la géothermie haute-énergie dans l'arc volcanique actif des Petites-Antilles.

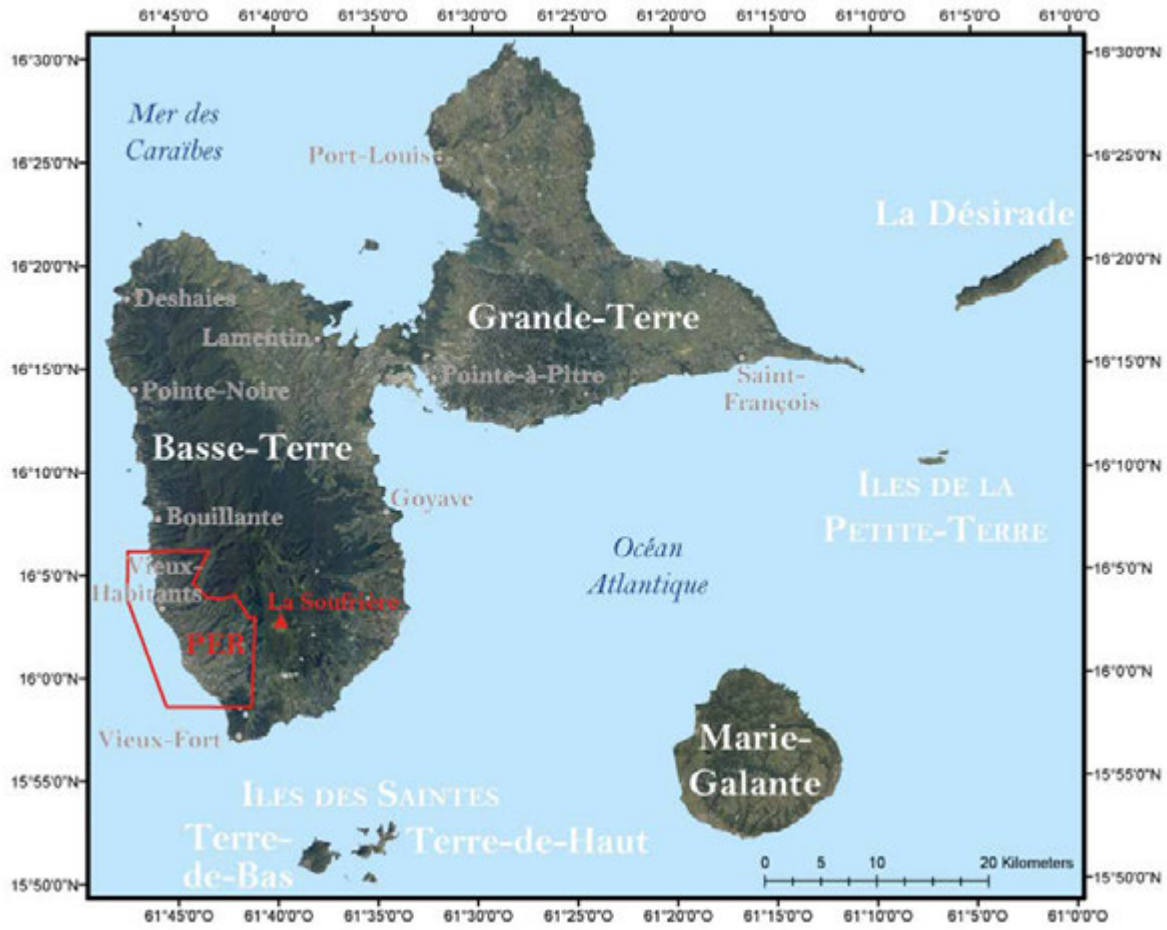


**Figure I-1 : Carte de l'archipel de Guadeloupe permettant de localiser le Permis Exclusif de Recherche (PER) de géothermie haute-température.**

Afin d'atteindre cet objectif, ce projet comprend :

- 16 thèses et des post-doctorats, répartis dans 9 laboratoires français issus d'organismes de recherche ou d'universités :
    - Le laboratoire Geoazur (UMR 7329), rattaché au CNRS et à l'Université de Nice-Sophia-Antipolis,
    - Le laboratoire GeoRessources (UMR 7359), rattaché au CNRS et à l'Université de Lorraine,
    - L'Institut Physique du Globe de Strasbourg (IPGS, UMR 7516) et le Laboratoire d'Hydrologie et de Géochimie de Strasbourg (LHyGeS, UMR 7517), rattachés au CNRS et à l'Université de Strasbourg,
    - L'Institut de Mécanique des Fluides de Toulouse (IFMT, UMR 5502), rattaché à l'Université de Toulouse et l'Institut Polytechnique de Toulouse,
    - Le pôle Guadeloupe de l'Université des Antilles (UA), dont l'unité de recherches en géologie est rattachée au laboratoire Géosciences Montpellier (UMR 5243),

    - Le laboratoire de géologie de l'Ecole Normale Supérieure de Paris (ENS, UMR 8538),
    - Le centre de recherche Armines, rattaché à l'école des Mines ParisTech,
    - Le Laboratoire Géosciences et Environnement de Cergy (GEC), rattaché à l'Université de Cergy-Pontoise.
- 2 entreprises privées françaises, en charge du pilotage du projet et de l'intégration et la valorisation des résultats, responsables respectivement de la coordination du projet et de la coordination scientifique :
    - Teranov : spécialisée dans la gestion de projets, l'ingénierie et les études pour la géothermie de haute-enthalpie,
    - KIDOVA : spécialisée en géostatistique, analyse de données spatiales et modélisation pour l'évaluation des ressources naturelles et des risques.

Actuellement, un accord est en cours de signature avec une troisième entreprise, comme partenaire financier extérieur, afin de poursuivre le développement industriel du projet.

Le projet s'articule en onze lots (Figure I-2), composé de 10 groupes de travail thématique (lots 2 à 8 et 10 à 12) et d'un coordinateur de projet (lot 1). Chaque groupe fait intervenir différents partenaires (laboratoires et entreprises) et est animé par un partenaire spécifique. Pour chaque groupe, des tâches ont été définies pour assurer la bonne conduite du projet. Pour chaque tâche, un ou plusieurs livrables en découlent et sont communiqués à l'ADEME pour être vérifiés en amont de chaque étape clé, servant au suivi du projet. Un douzième lot (lot 9) a été supprimé suite au retrait d'un partenaire industriel (Magnitude) qui était en charge d'un expérimentateur de microsismique.

Mes travaux de recherche correspondent à la thèse n°13 du projet GEOTREF, et s'insèrent dans le groupe travaillant sur l'acquisition des données géologiques de surface. Cette thèse s'est faite en collaboration entre l'Université des Antilles - Géosciences Montpellier (sous la direction de Jean-Frédéric LEBRUN) et l'Université de Nice-Sophia-Antipolis - Geoazur (sous la direction de Jean-Marc LARDEAUX et Chrystèle VERATI).

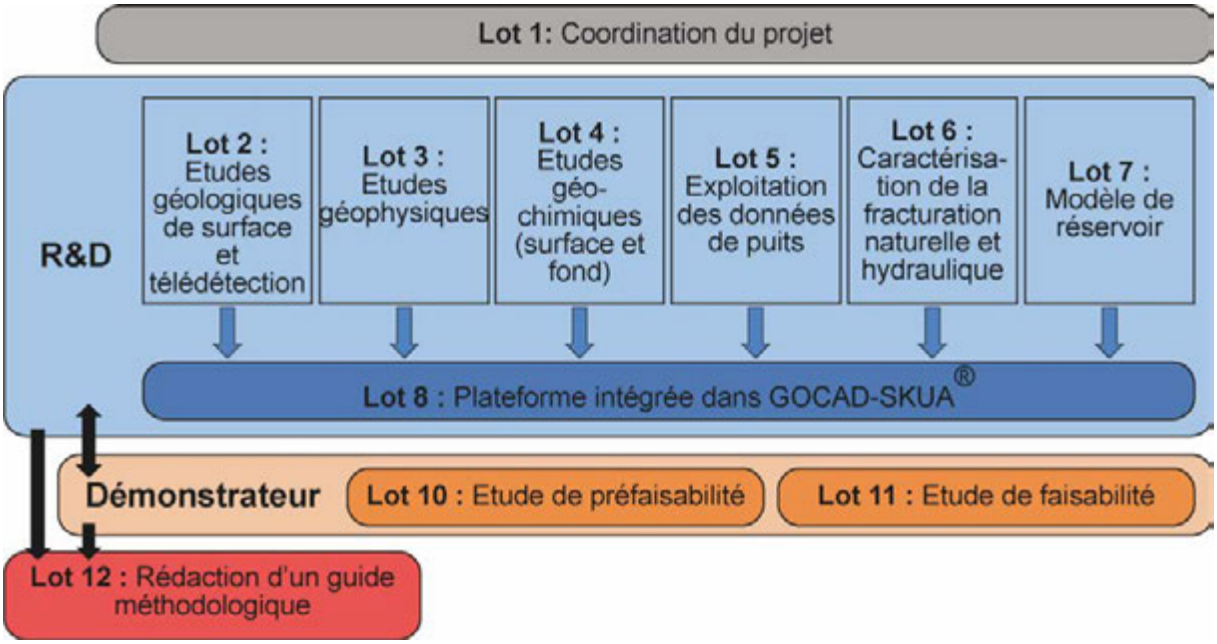


**Figure I-2 : Organisation générale du projet GEOTREF**

Les travaux de la thèse n°13 ont contribué à la réalisation de plusieurs tâches et livrables (en annexe **X.1**), présentés lors d'Etapes Clés (EC) passées ou à venir :

- Tâche n° 2.1 : Etude des affleurements, des analogues de terrains et des données régionales. Le livrable L2.1.1 sera présenté à l'EC5.
- Tâche n° 4.3 : Datation des systèmes hydrothermaux. Le livrable L4.3.1 a été présenté à l'EC3 en mai 2017 et sera rendu pour l'EC4 fin 2019.
- Tâche n° 10.3 : Etudes des manifestations géochimiques de surface. Le livrable 10.3.1 sera rendu pour l'EC4 fin 2019.
- Tâche n° 10.5 : Evaluation de la qualité de la ressource géothermique. Le livrable 10.5.1 a été présenté à l'EC3 de mai 2017 et sera rendu à l'EC4 fin 2019 accompagné d'un rapport de synthèse des études géologiques (GEOTREF, **2017**).
- Tâche n° 12.2 : Etude géologique de surface et télédétection. Le livrable 12.2.1 sera présenté à l'EC 6.

## I.2. Objectifs et problématique du sujet

L'enjeu de cette thèse est d'étudier l'évolution spatiale et temporelle de l'hydrothermalisme dans la plaque supérieure de l'arc des Petites Antilles, en lien avec le potentiel géothermique régional de l'arc volcanique actif.

Sur la côte ouest de la Guadeloupe, un programme de technologies durables pour la production d'électricité a été identifié dans les années 1970 à Bouillante. Dans le cas du champ géothermal de Bouillante, le réservoir sous la baie de Bouillante a été bien caractérisé en surface (Bouchot *et al.*,

**2010**), grâce à des investigations géologiques, géochimiques et géophysiques et plusieurs puits d'exploration et de production (Iundt & Ouzounian, **1984**; Abou-Akar *et al.*, **1992**; Sanjuan & Brach, **1997**; Guillou-Frottier, **2003**; Lachassagne *et al.*, **2009**; Thinon *et al.*, **2010**; Calcagno *et al.*, **2012**; Gailler *et al.*, **2013**). Mais son fonctionnement en profondeur est encore mal compris. Pour poursuivre le développement de la géothermie dans cette région propice, il est nécessaire de connaître la nature, la structure et les propriétés physiques des parties profondes des réservoirs. C'est pourquoi, il nous faut mieux caractériser le système géothermique de l'île de Basse-Terre en caractérisant ses parties profondes.

Dans le cadre du projet GEOTREF, il est envisagé de mettre en place une nouvelle usine pour la production d'électricité en Guadeloupe dans le secteur du PER (Figure I-1), situé plus au Sud du site actuel de Bouillante. Avec en premier lieu une étude géologique de surface couplée à d'autres méthodes développés par les différents partenaires du projet, qui conduiront par la suite à la mise en place d'un forage exploratoire qui pourra être transformé en forage d'exploitation de la ressource géothermale de haute-température.

Mes travaux de thèse ont pour but d'une part d'identifier les marqueurs d'une éventuelle ressource géothermale dans la zone d'étude de Vieux-Habitants et d'autre part de mieux comprendre le fonctionnement d'un système géothermal actif au niveau l'île de la Basse-Terre et par extension au niveau de l'arc des Petites-Antilles. L'identification et l'évaluation de la ressource géothermale passe au travers d'une démarche nouvelle : l'étude d'analogue des parties profondes d'un réservoir géothermal aujourd'hui exhumé. Ces systèmes fossiles sont une opportunité exceptionnelle pour caractériser :

- L'état thermique de l'arc en étudiant les processus et les vitesses des transferts des fluides hydrothermaux (et de chaleur) en contexte de subduction,
- Les structures tectoniques induites par les processus de dissolution-cristallisation et les paragenèses métamorphiques et hydrothermales associées, afin de pouvoir proposer des analogues, susceptibles d'être modélisés, aux systèmes géothermaux actifs actuels. Les paléo-systèmes hydrothermaux, aussi appelés fossiles, sont mis en évidence par l'identification des minéraux issus de l'altération hydrothermale, dont la répartition et la nature permettent de définir le volume où se concentrait l'activité (Chenevoy & Piboule, **2007**),
- La durée de vie des systèmes hydrothermaux en datant l'activité hydrothermale de haute et de plus basse températures, au niveau des systèmes fossiles et actifs, au regard des datations des complexes volcaniques. Cela reste une question fondamentale dans

l'exploitation des systèmes géothermaux. Des tentatives de datation sur des minéraux hydrothermaux montrent des résultats assez hétérogènes, d'un million à quelques milliers d'années seulement (Faure, **1986**; Deloule & Turcotte, **1989**; Nakai *et al.*, **1993**; Barnes, **1997**; Rowland & Sibson, **2004**), à l'image des périodes d'activité volcanique d'une région.

Un réservoir géothermal représente une anomalie de concentration en fluides et en chaleur, faisant de lui une ressource exploitable (White, **1965**), à condition de le comparer à l'évolution standard des roches en contexte similaire. Pour pouvoir mettre en évidence ce caractère spécifique, il est donc nécessaire de bien caractériser les roches volcaniques en contexte d'arc insulaire, dans lesquelles la ressource se met en place.

La seule façon de décrire et d'analyser les caractéristiques géologiques d'un réseau de migration de fluides dans les parties profondes d'un réservoir géothermal est de se tourner vers des analogues fossiles exhumés. Les analogues géologiques sont des objets ou des structures dont le contexte de formation et l'histoire géologique sont identiques à ceux de l'objet étudié, mais qui sont maintenant accessibles à l'observation. Soit plus anciens et affleurant à présent sous l'influence de l'érosion et/ou de l'exhumation, soit contemporains ou même plus récents mais dont l'histoire post-génétique les a rendus accessibles. Les sites exhumés permettent donc de visualiser les structures et les relations de l'ensemble du réseau de migration et d'échantillonner facilement ses éléments (i.e. les zones de circulation de fluides, les structures drainantes, les différents états de transformations et de déformations des roches) et de les analyser.

Dans l'industrie pétrolière l'utilisation d'analogue de terrain est une pratique courante afin d'évaluer la potentiel pétrolier d'une zone et donc de localiser la ressource à exploiter. Ils se basent sur les comparaisons analogiques entre les paramètres géologiques liés à des accumulations majeures de pétrole avec les données géophysiques et des forages (Beck & Lehner, **1974**). Il s'agit d'investigations préliminaires et superficielles d'analogues, puis d'une étude géologique approfondie des objets identifiés, afin de pouvoir déboucher sur l'exploitation de la ressource visée en profondeur. Ainsi depuis les travaux précurseurs de Bouma (**1962**), les turbidites des bassins sédimentaires exhumés dans les chaines de montagnes sont étudiées afin de caractériser les réservoirs pétroliers localisés en contexte de marge continentale passive (Middleton & Bouma, **1973**; Sinclair, **1997**; Mulder & Alexander, **2001**; Bouma & Ravenne, **2004**).
Les systèmes pétroliers sont clairement définis par leur roche mère, leur réservoir et les pièges. Les systèmes géothermaux ne se décrivent pas avec des éléments géologiques aussi univoques. Les

systèmes géothermaux apparaissent dans des environnements géologiques indivisibles et sont potentiellement présents partout dans le monde en considérant la répartition du flux de chaleur mondial (Moeck, **2014**). L'utilisation des ressources géothermales prend aussi en considération d'autres facteurs : la quantité de chaleur stockée à une profondeur donnée et si celle-ci est économiquement exploitable par forage. Au travers de cette thèse, nous proposons donc ici une nouvelle approche d'exploration géothermale avec le concept « d'analogue fossile » pour l'adapter et l'appliquer à la caractérisation des réservoirs géothermaux.

Une fois l'analogue d'un paléo-réservoir géothermal identifié, il est nécessaire de caractériser sa minéralogie, les structures présentes, de quantifier l'évolution thermodynamique des roches et d'évaluer la durée de vie de tels systèmes. De telles données sont essentielles afin de mieux contraindre les circulations de fluides en profondeur et ainsi de pouvoir les exploiter plus durablement au sein des réservoirs géothermaux.

## I.3. Démarche suivie et méthodes employées

Dans le périmètre du PER, la zone d'intérêt pour l'exploitation de la ressource géothermale, peu d'indices de surface affleurent. Nous n'avons accès qu'aux dépôts situés en surface et potentiellement à l'aplomb du système actif. Nous cherchons donc à avoir accès aux roches situées en profondeur. Les roches situées sur l'île de Basse-Terre sont soumises à des taux d'érosion mécaniques et chimiques de l'ordre de 1000 m/Ma (Sak *et al.*, **2010**; Lloret *et al.*, **2011**; Rad *et al.*, **2013**; Ricci *et al.*, **2015a**, **b**). Afin de décrire les paléo-systèmes exhumés en contexte d'arc magmatique, nous nous tournons donc vers les terrains les plus anciens de Basse-Terre (Samper *et al.*, **2007**). Cela va nous permettre d'identifier les potentiels analogues des parties profondes de l'île de Basse-Terre et de caractériser l'évolution des roches au cours du temps :

- Le complexe volcanique du Complexe Basal, situé dans la partie Nord de l'île de Basse-Terre,
- L'île de Terre-de-Haut (Les Saintes), située au Sud de l'île de Basse-Terre. Une zone fortement hydrothermalisée a été décrite dans la partie centrale de l'île (Jacques & Maury, **1988**; Verati *et al.*, **2016**).

Pour réaliser ce travail d'étude d'analogues des parties profondes d'un réservoir géothermal, différents types d'études ont été réalisés :

- Des campagnes de terrain :
    - Analyses structurale et micro-structurale (rhéologie), échantillonnage pour l'analyse de l'évolution du champ de déformation et des structures permettant la migration des fluides hydrothermaux,

- Des investigations minéralogiques, pétrographiques et pétrologiques pour l'étude des transformations des roches volcaniques au cours du temps :
    - Microscopie optique, électronique (MEB), Raman, DRX pour l'identification des paragenèses minérales,
    - Microsonde électronique, microscopie électronique pour définir la composition chimique des phases minérales,
    - Analyses isotopiques pour déterminer l'origine des fluides,
    - Thermo-barométrie, y compris la modélisation thermodynamique, afin de mettre en évidence l'évolution des conditions de pression et de température des roches volcaniques dans le temps.
- De la géochimie afin d'étudier la composition chimique des échantillons, à partir des éléments majeurs et traces.
- De la géochronologie $^{40}Ar$-$^{39}Ar$ et K-Ar dans le but de dater des phases volcaniques et hydrothermales.

Les résultats obtenus sont mis en relation avec les observations de surface (les analyses structurales, minéralogiques et la localisation des manifestations de surface) au niveau de la zone du PER et de Bouillante, afin de proposer un modèle conceptuel de fonctionnement d'un réservoir géothermal en profondeur.

## I.4. Organisation du manuscrit

Afin de présenter ce travail de thèse, le manuscrit sera organisé en cinq axes principaux.

Un premier axe s'attachera à rappeler l'état des connaissances en géothermie (Chapitre II :), puis un point sera fait sur le contexte géologique de la zone d'étude (Chapitre III :).

Un second axe visera à caractériser l'état thermique de référence de l'arc volcanique actif en Guadeloupe, par l'étude du métamorphisme au niveau du Complexe Basal (Chapitre IV :).

Le troisième axe s'attachera à l'identification et la caractérisation d'un paléo-réservoir géothermal sur l'île de Terre-de-Haut (Chapitre V :), proposant ainsi une nouvelle méthode d'exploration pour la ressource géothermale par l'étude d'analogue exhumé.

Un quatrième axe portera sur l'estimation de la durée de fonctionnement des réservoirs géothermaux de haute-température, au travers de la datation de phases hydrothermales issues de l'île de Terre-de-Haut et du secteur de Vieux-Habitants (Chapitre VI :).

Enfin un dernier axe (Chapitre VII :) proposera une synthèse générale de ce travail, à l'issu duquel un modèle conceptuel de fonctionnement des réservoirs géothermaux sera discuté pour mieux définir les parties profondes de l'arc volcanique des Petites-Antilles au niveau de l'archipel de Guadeloupe, avant de conclure (Chapitre VIII :).

## Chapitre II : Les géothermies

*Illustration : Jean-Jacques BELTRAMO, dessinateur de presse.*

*Journées Scientifiques de l'Observatoire de la Côte d'Azur à Sophia-Antipolis (06), le 15 novembre 2018.*

## II.1. Origine de la chaleur terrestre et des mécanismes de transfert

La température au centre de la Terre est estimée entre 5000 et 7000°C (Stacey, **1992**; Lowrie, **1997**; Lemale, **2015**). La chaleur terrestre provient de la formation de la planète (chaleur primitive d'accrétion et chaleur latente de cristallisation au sein du noyau), de la mise en place de mouvements convectifs au sein du manteau (Figure II-1) et majoritairement de la désintégration d'éléments radioactifs (K, U, Th) du noyau à la croûte (Turcotte & Schubert, **2002**).

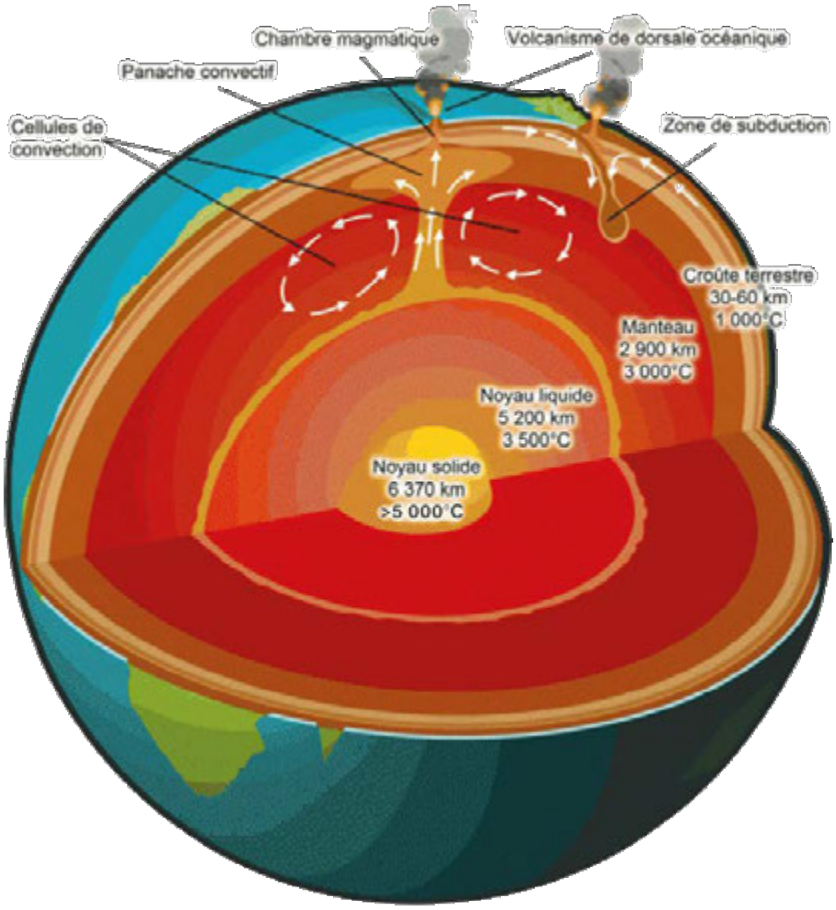


**Figure II-1 : Structure interne du globe terrestre (source : www.geothermie-perspectives.fr, 2019)**

Le transfert de la chaleur est régi par trois mécanismes : le **rayonnement** (propagation dans le vide d'ondes électromagnétiques entre la surface de la Terre, l'atmosphère et la biosphère), la diffusion ou **conduction** thermique (transfert de proche en proche par un différentiel de température, des zones chaudes vers les zones froides, sans déplacement de matière). Enfin, un écart positif au gradient géothermique standard conduit à un transfert de chaleur par **convection** thermique (contraste de densité avec une différence de température ou de salinité provoquant un déplacement de matière à l'état de fluide). Le fluide chauffé de densité plus faible a tendance à s'élever et à être remplacé par un fluide plus froid de densité plus élevée provenant des extrémités du système. La convection a tendance

à augmenter les températures dans la partie supérieure du système et à diminuer dans la partie inférieure (White, **1973**), entraînant une homogénéisation de la température.

La densité de **flux de chaleur** (q) est la quantité de chaleur (s'exprimant en Joule/seconde ou plus communément en Watt, aussi appelée puissance thermique), correspondant au taux de production d'énergie (Q) par unité de temps (t) dans un corps considéré, qui traverse une surface (S) et s'exprime en W/m² (*équation I.1*).

$$q = \frac{1}{S} . \frac{\partial Q}{\partial t} \quad (I.1)$$

Elle est proportionnelle au couplage entre le gradient géothermique et la conductivité thermique apparente (ci-dessous *équation I.2*).

Le **gradient géothermique** s'établit par la variation de température (T) de la Terre de la surface (en moyenne de 15°C) vers la profondeur (z), soit $\partial T/\partial z$ et s'exprime en °C/km (ou °K/m). Le gradient géothermique moyen dans la croûte terrestre est de l'ordre de 30°C/km (Thain *et al.*, **2006**), où la densité de flux de chaleur correspondant est de l'ordre de 50-60 mW/m². Ce gradient varie selon le contexte géodynamique. Il peut être plus élevé au niveau des dorsales (Islande), points chauds (Hawaï), arcs volcaniques actifs (Japon) ou cordillères liées à la subduction (les Andes), rift continental (Vallée du Rift est-africain), et enfin dans les bassins sédimentaires à croûte amincie (Fossé Rhénan).
La **conductivité thermique** ($\lambda$, s'exprimant en $W.m^{-1}.K^{-1}$) est l'aptitude du milieu (gaz, liquide, solide), d'une roche en ce qui concerne la géologie, à transférer la chaleur quand il existe un gradient de température (Eppelbaum *et al.*, **2014**). Il s'agit du cas particulier où la non-uniformité de la température entraîne un transfert d'énergie d'un point à un autre du système sans apport de matière. Quand les variations de températures ne sont pas trop importantes elle est régie par la loi de Fourier (1807) qui décrit la relation de la conduction de la chaleur dans un corps solide où la densité de flux de chaleur s'exprime sous forme vectorielle ($\vec{q}$, *équation I.2*) dans un champ de température tridimensionnel T(x,y,z) (où $\vec{\nabla}\ T = \partial T/\partial z$):

$$\vec{q} = -\lambda . \vec{\nabla}\ T \quad (I.2)$$

Le signe négatif traduit l'orientation du courant thermique vers les basses températures. Elle n'est valable qu'à un instant t de l'histoire de la conduction.
La deuxième loi de Fourier permet d'introduire la notion de conduction de la chaleur en prenant en compte la diffusivité thermique ($\alpha$, s'exprimant en $m^2.s^{-1}$) avec l'équation de la diffusion thermique

(*équation I.3*, avec ρ la masse volumique et Cp la capacité calorifique) à pression constante dans un milieu homogène pour le domaine de température étudié :

$$\alpha = \frac{\lambda}{\rho.Cp} \qquad (I.3)$$

Dans un modèle unidimensionnel où l'apport d'énergie se fait en conduction pure, la température T ne dépend que du temps t et de la profondeur z. D'après la loi de Fourier on obtient alors une seconde équation ou équation de la chaleur (1D) (*équation I.4*) :

$$\frac{\partial T}{\partial t} = \alpha . \frac{\partial^2 T}{\partial z^2} \quad (I.4)$$

Les transferts de chaleur se font principalement par conduction dans la lithosphère. Cette équation (*équation I.4*) permet de déterminer l'évolution de la température dans le temps et dans l'espace en fonction des distances parcourues. Ce sont donc des paramètres essentiels à estimer. Pour cela une solution généralisée (*équation I.5*) à cette équation (*équation I.4*) a été proposée par Carslaw et Jaeger (**1959**) :

$$z = \sqrt{\alpha . t} \quad soit \quad t = \frac{z^2}{\alpha} \quad (I.5)$$

On peut alors estimer que si la chaleur est transférée par simple conduction dans la lithosphère ($\alpha_{moyenne} = 10^{-6}$ m².s$^{-1}$) elle parcourt 5 à 6 km en 1 Ma (sachant que 1 Ma = 3,154 $10^{13}$ secondes).

La Terre évacue naturellement cette chaleur par conduction à une puissance thermique de 46 TW (Pollack *et al.*, **1993**; Ledru & Guillou-Frottier, **2010**), de l'ordre de 2/3 par les océans (30 TW, avec un flux de 101±2,2 mW/m²) et 1/3 par les continents (12TW, avec un flux de 65±1,6 mW/m²), et se régénère par la désintégration d'éléments radioactifs à un taux de 30 TW (Turcotte & Schubert, **2002**; Rybach, **2007**) depuis le noyau terrestre qui génère un flux de chaleur vers la surface. La Terre se refroidit donc progressivement depuis sa formation (Garibaldi, **2010**).

La perte de chaleur étant naturelle à la surface de la Terre, elle devient une ressource à partir du moment où la concentration de cette chaleur devient anormale dans certaines zones. La chaleur interne de la Terre peut alors être utilisée comme une source d'énergie, connue sous le nom d'énergie géothermique.

## II.2. Ressource géothermale : une anomalie de concentration

La géothermie est une source d'énergie locale exploitant la chaleur naturelle emmagasinée sous la surface de la Terre solide (directive 2009/28/CE du Parlement européen et du conseil du 23 avril 2009, relative à la promotion de l'utilisation de l'énergie produite à partir de sources renouvelables).

De nombreux termes sont utilisés pour parler d'aires géothermales, où le flux thermique diffère du flux normal (Chenevoy & Piboule, **2007**) générant une anomalie thermique. Grant et Bixley (**2011**) proposent une nomenclature et donnent la définition de quelques termes :

- Un **champ géothermal** : une aire géographique d'activité géothermale possédant un nom. Il s'agit d'une description purement géographique sans faire référence au système géothermal qui lui est plus vaste.
- Un **système géothermal** (Figure II-2) : un système hydrologique souterrain associé à un champ géothermique. Il se compose de trois éléments principaux : une source de chaleur, un réservoir et un fluide caloporteur. Il comprend tous les trajets des circulations de fluides de la source d'eau froide à la source de chaleur jusqu'à la remontée à la surface. Il permet de comprendre le fonctionnement des transferts de fluides (manifestations géothermales, chemins de circulations de fluides, transfert de chaleur et cellules de convection …).
- Un **réservoir géothermal** : la partie du champ géothermal la plus chaude et perméable, dont l'exploitation est économiquement rentable pour la production de chaleur ou d'électricité. Son existence dépend donc de la technologie utilisée pour accéder à la ressource et des prix de l'énergie (critères conjoncturels). Il est courant de forer plus profondément un champ existant afin d'augmenter le volume du réservoir à une plus grande profondeur.

L'utilisation des ressources géothermales se décompose donc en deux grandes familles (Figure II-3), en fonction de la température et des besoins :

- La production d'électricité (utilisation de la vapeur géothermale), appelée aussi géothermie de haute-énergie où les zones propices à son développement sont les régions tectoniques et volcaniques actives ;
- La production de chaleur (usage direct de la chaleur), appelée aussi géothermie de basse-énergie où les zones propices à son développement se situent dans les bassins sédimentaires.

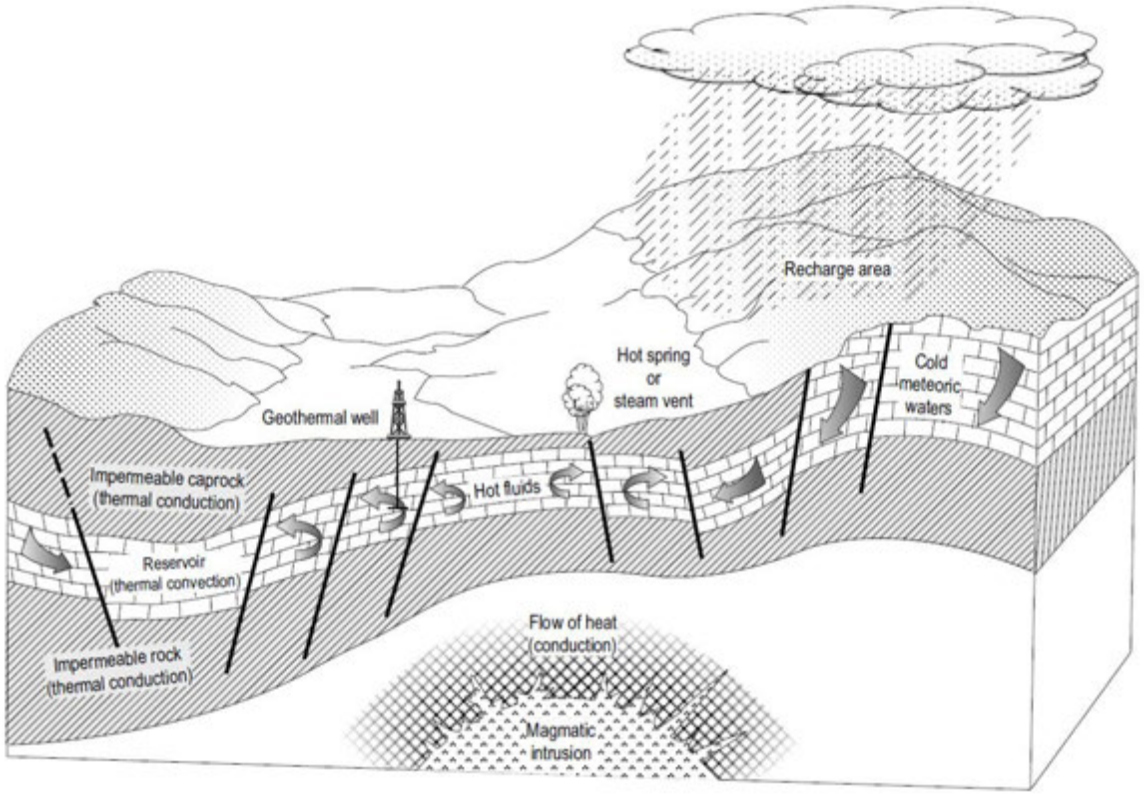


**Figure II-2: Modèle schématique d'un système géothermique (Dickson & Fanelli, 2013)**

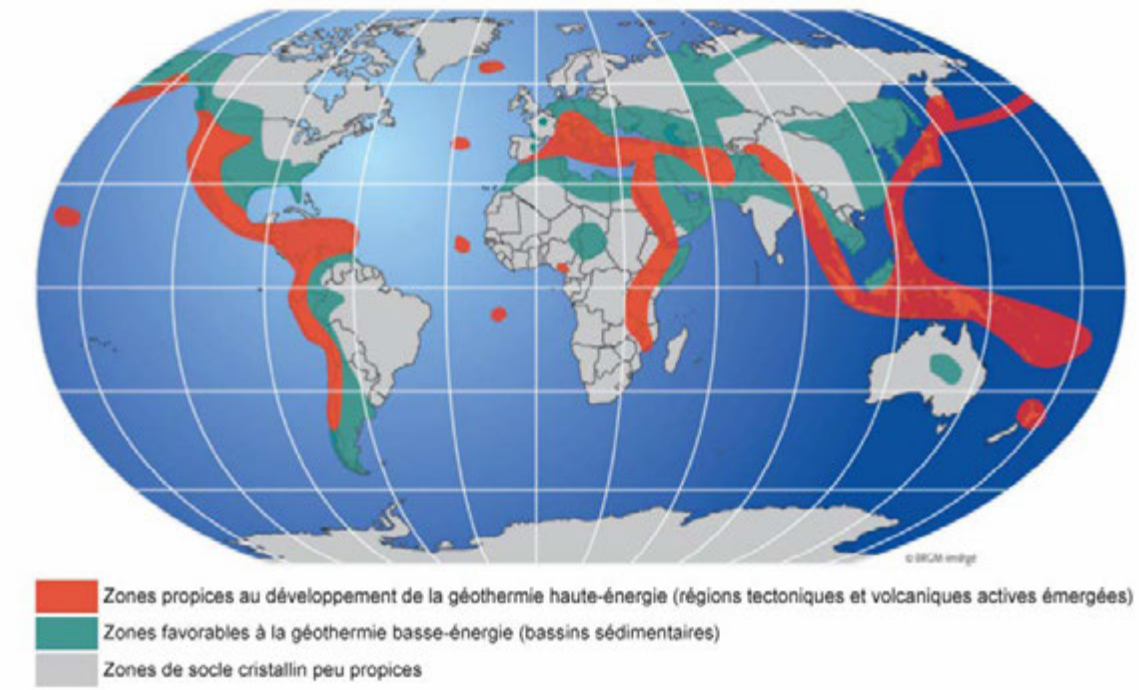


**Figure II-3: Ressources géothermiques mondiales (Varet, 2011)**

## II.3. Les différents types de géothermie

En fonction de la température (T) du sous-sol (ou du fluide exploité) et du contexte géologique (favorable ou non, Figure II-3), il existe différents types d'exploitation en géothermie (Figure II-4), dont voici quelques exemples en France (Figure II-5) :

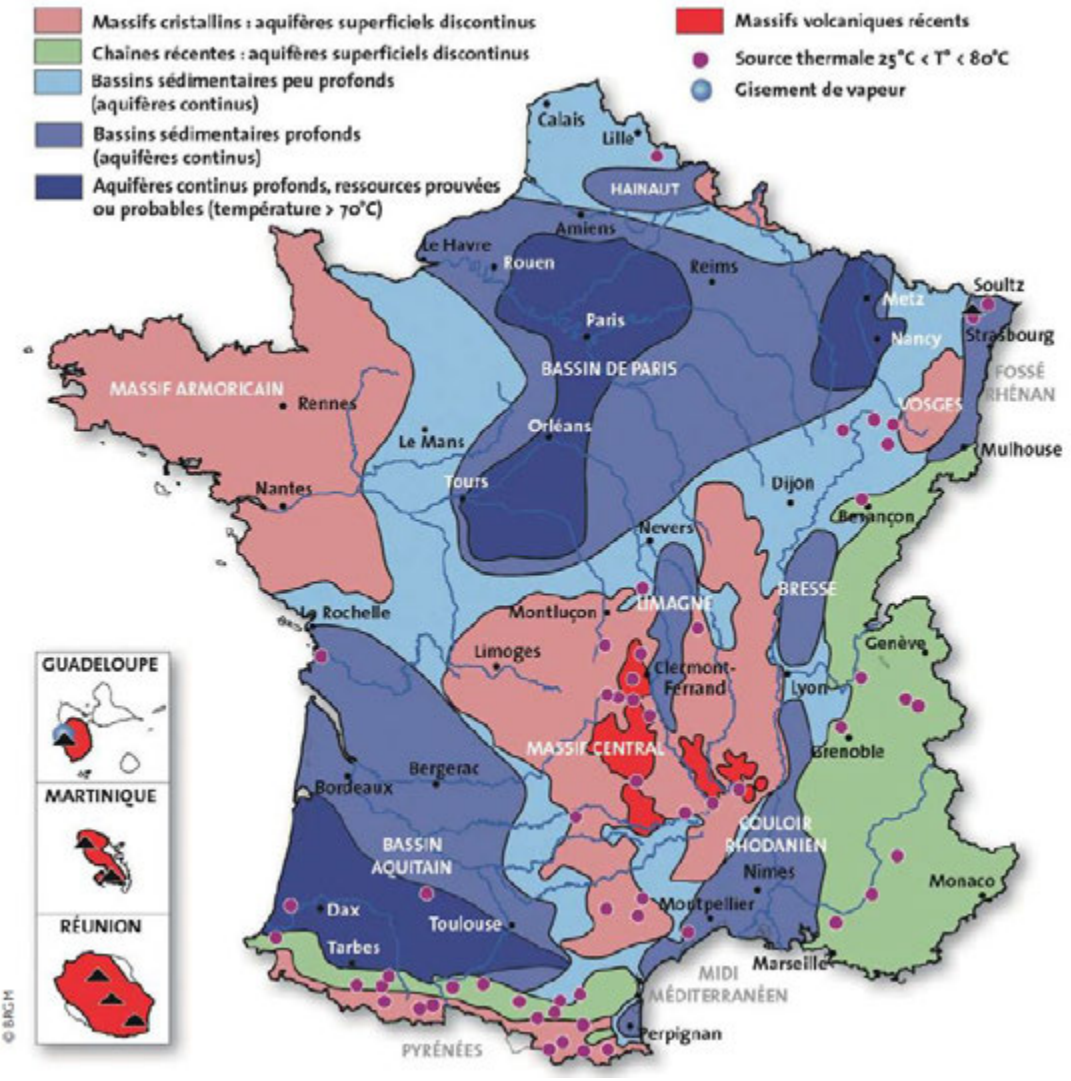


**Figure II-4: Carte des environnements géologiques favorables à l'exploitation de la géothermie en France (ADEME, 2012)**

- Dans les régions non volcaniques, on peut distinguer :
    - La géothermie de très-basse et basse-énergie (T < 120 °C) dans les bassins sédimentaires (c'est-à-dire les aquifères profonds et les formations superficielles) comme par exemple dans le Bassin de Paris ou le Bassin Aquitain.
    - La géothermie de haute-énergie (120 < T <160 °C) dans les régions tectoniques actives (c'est-à-dire les rifts continentaux ou bassins d'effondrement) comme par exemple dans la Limagne ou le Fossé Rhénan.

- Dans les régions volcaniques actives, on distingue :
    - La géothermie de très haute-énergie (T> 160 °C) dans des régions volcaniques émergées (c'est-à-dire au niveau des points chauds, des zones de subduction) comme aux Antilles ou à la Réunion.

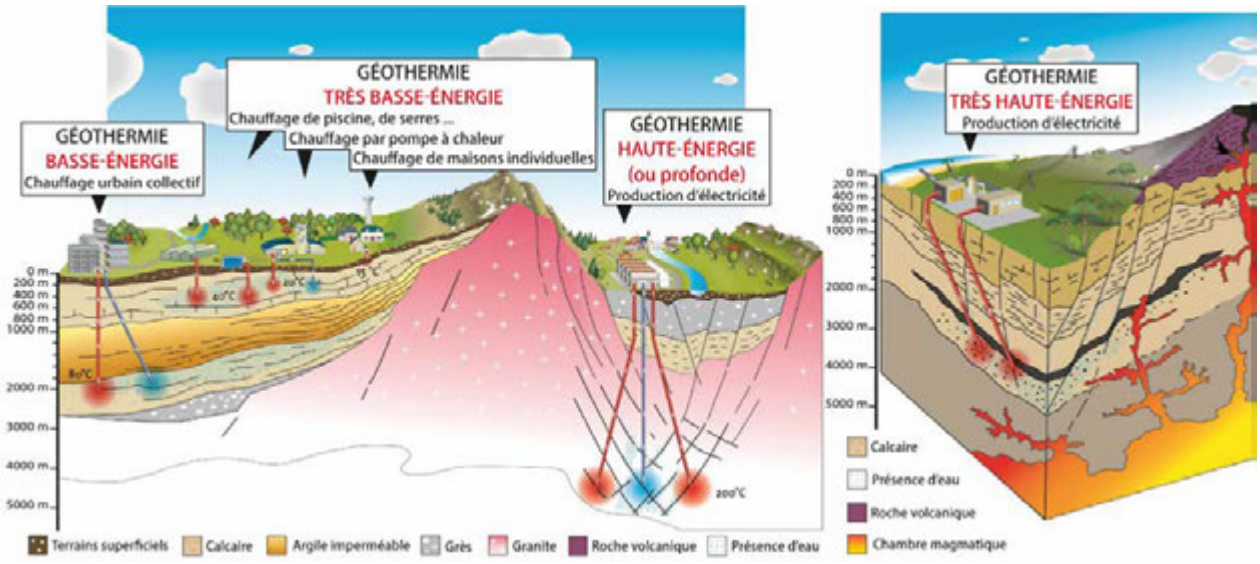


**Figure II-5 : Exemples des types d'exploitation de la géothermie (modifiée d'après source www.geothermie-perspectives.fr, 2019)**

Dans ce manuscrit les différents types de géothermie sont définis en fonction de la température du fluide géothermal, une autre classification se base sur la profondeur d'exploitation de la ressource géothermale en définissant une géothermie superficielle (< 2000 m) et une géothermie profonde (> 2000 m).

## II.4. Applications des ressources géothermales

Le critère qui sert de guide pour définir les usages de la géothermie est la température.

L'exploitation de la chaleur pour des usages individuels ou collectifs est permise par deux modes d'utilisation (Figure II-6) :

- La pompe à chaleur (PAC) géothermique (T < 30 °C) : utilisation de la température relativement constante du sous-sol comme source et réservoir de la chaleur pour le chauffage et le refroidissement, ainsi que la production d'eau chaude. La chaleur est captée à faible profondeur.
- L'usage direct par transfert de chaleur (30°C < T < 120°C) : utilisation directe de l'eau chaude provenant de la ressource géothermique. Elle se situe en profondeur et permet d'obtenir une puissance plus importante, le coût d'exploitation est cependant plus élevé du fait de la nécessité de forages.

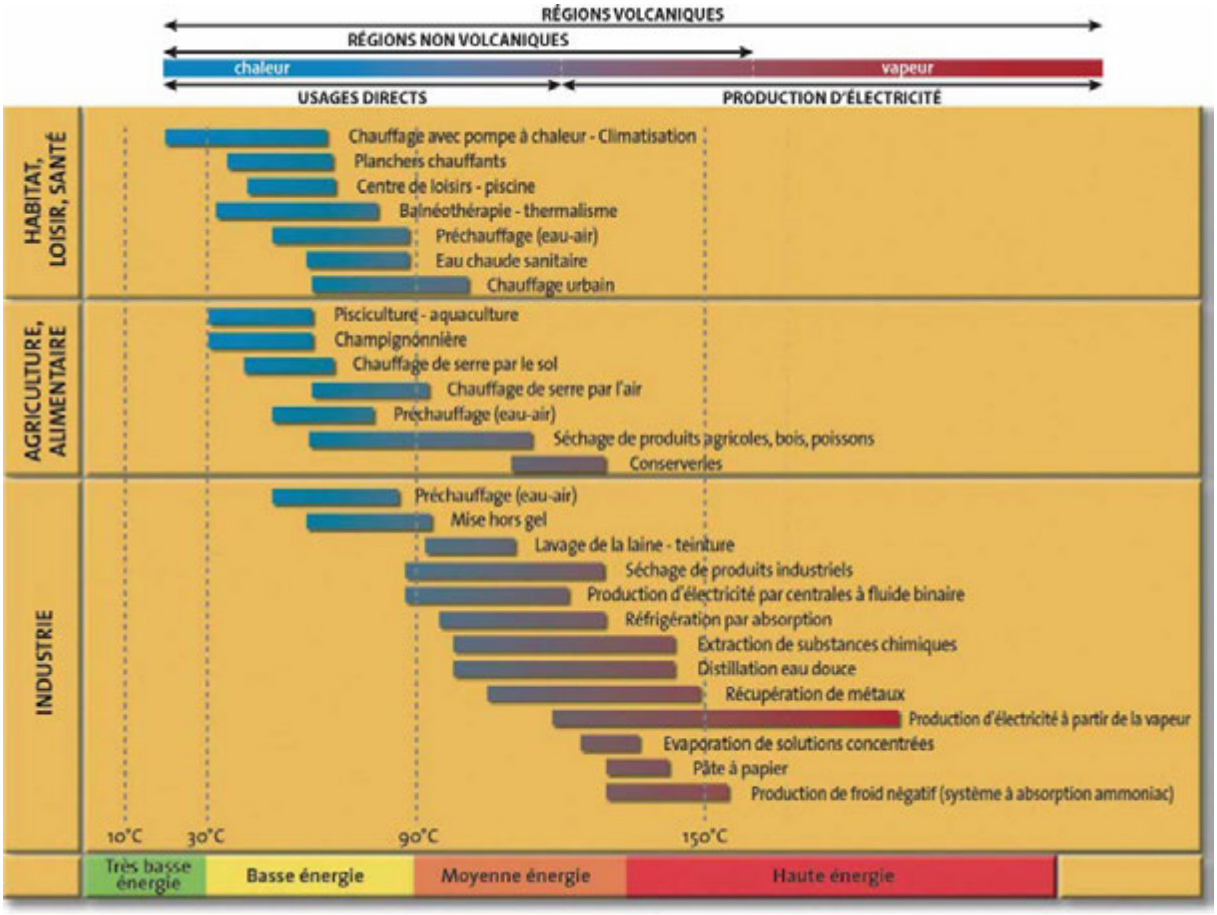


**Figure II-6: Principaux usages des ressources géothermales (modifiée d'après ADEME, 2012)**

La production d'électricité est permise pour des températures de la ressource géothermale plus élevées. Elle s'effectue par différents modes (Figure II-6) :

- Un système binaire ou cycle de Rankine (ORC) (90 °C < T < 160 °C) : le fluide géothermal est maintenu sous pression à l'état liquide au moyen d'une pompe placée dans le puits de production. En surface, il est conduit vers un échangeur de chaleur où il cède une partie de son énergie à un fluide volatile, appelé fluide de travail, lui permettant de se vaporiser à basse-température et de faire tourner une turbine et produire de l'électricité grace à un transformateur. Le fluide de travail évolue dans un circuit fermé (vaporisation, détente, condensation, pressurisation). Le fluide géothermal est réinjecté dans sa formation d'origine afin de se recharger en calories en profondeur.
- Un cycle de Rankine peut être couplé à un système EGS (Enhanced Geothermal System) (120 °C < T < 160 °C) : l'extraction de la chaleur se fait à partir d'un réseau de fractures préexistant ou stimulé par l'incorporation d'eau via un puits d'injection. Cette stimulation (hydraulique et/ou chimique) permet d'obtenir une forte perméabilité (Grant & Bixley, **2011**). Dans ce réseau de fractures, les fluides vont pouvoir circuler facilement dans le massif rocheux. L'eau

chauffée au contact de la roche est ensuite pompée à l'aide d'un puits de production. Elle est ensuite convertie en électricité.

- La production d'électricité conventionnelle dans des turbines à vapeur (T > 160°C) (Figure II-7) : l'extraction de fluide ou vapeur géothermale se fait par un puits de production. La vapeur géothermale est directement exploitée pour produire de l'électricité. Cette vapeur est ensuite convertie en électricité dans une centrale géothermique. L'eau de mer et les eaux de pluie infiltrées sont réchauffées en profondeur dans un réservoir fracturé. Une cellule convective naturelle est créée, les fluides chauds remontent tandis que les fluides froids descendent. Dans ce réservoir géothermique le fluide géothermal est composé d'eau et de vapeur à haute-température (200-250°C). Le fluide est ensuite récupéré par des puits de production (forages) d'où il sort à haute-pression (~6 bar) et est conduit vers un séparateur. La vapeur est ensuite dirigée vers une turbine à condensation qui produit de l'énergie cinétique. La turbine entraîne un alternateur qui transforme l'énergie cinétique en énergie électrique. La première centrale (d'une puissance de 20kW) ayant générée de l'électricité à partir de la ressource géothermale est l'installation de Larderello en Italie en 1904 (Lund, **2004**).

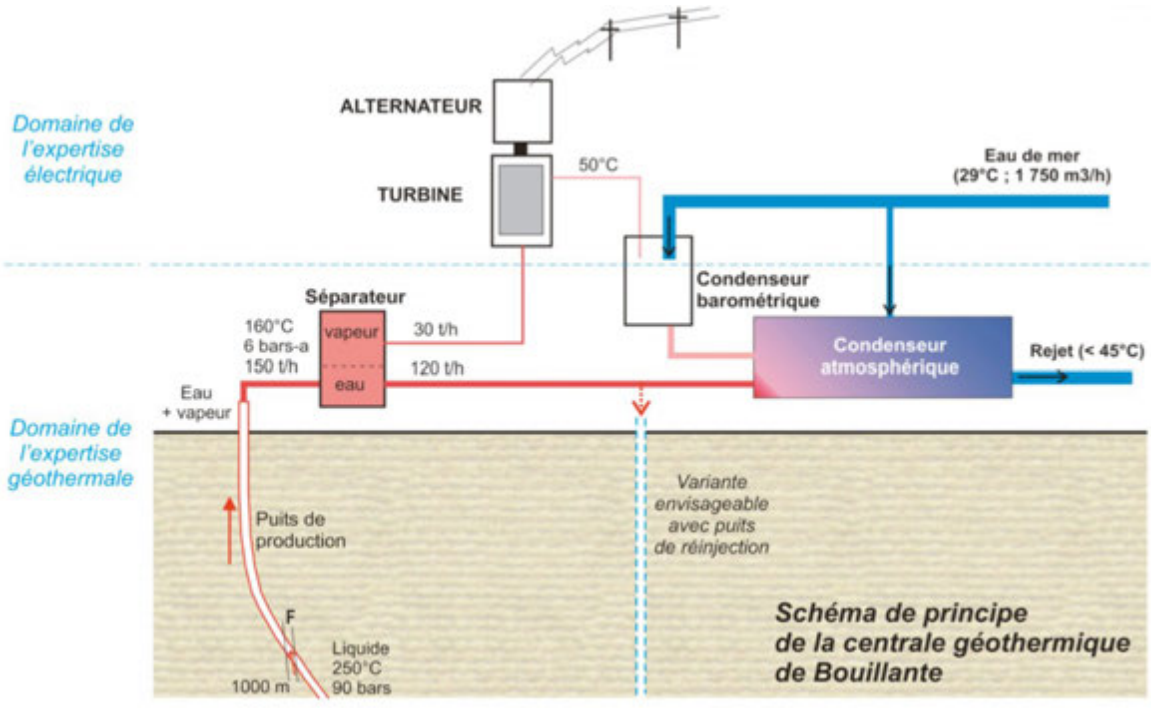


**Figure II-7 : Fonctionnement schématique d'une centrale géothermique, exemple de la centrale de Bouillante, Guadeloupe (Corsini, 2011)**

## II.5. Avantages et inconvénients de la géothermie

Les besoins énergétiques sont de plus en plus importants, avec une forte augmentation de la consommation des énergies fossiles (et donc une hausse permanente de leur prix, ainsi que les rejets en $CO_2$ que cela entraîne) jusqu'à leurs épuisements progressifs. Il est donc important d'avoir connaissance de l'impact de l'utilisation de la géothermie sur l'environnement et l'économie, par rapport à d'autres énergies dites renouvelables. C'est ce que montre la synthèse (Garibaldi, **2010**) suivante présentée dans le Tableau II-1.

**Tableau II-1: Récapitulatif des avantages et des inconvénients de l'utilisation de la géothermie**

| Avantages | Faiblesses |
|---|---|
| Ressource locale : indépendance vis-à-vis des pays exportateurs de pétrole | Ressource locale : contraintes de surface et intégration dans le paysage (nuisances sonores et visuelles) |
| Ressource renouvelable (dans le cas d'une utilisation raisonnée de la ressource, en évitant le refroidissement de la source en cas de réinjection de fluide froid), non carbonée, avec un impact environnemental faible (très peu de rejet de $CO_2$) | La mise en place d'une centrale géothermique pour la production d'électricité entraîne des rejets de gaz autre que le $CO_2$ : $H_2S$, $SO_2$, $H_2SO_4$ |
| Énergie indépendante des conditions climatiques, saisons ou heure, avec la recharge des terrains superficiels et la température constante du sous-sol profond grace au flux de chaleur terrestre | « Risque » géologique : résultats incertains des forages, microsismicité (lors des forages ou de la stimulation hydraulique), radioactivité naturelle (radioéléments pouvant être remontés en surface) |
| Capacités de production importantes | Délai important pour la valorisation |
| Coûts de fonctionnement faibles | Concept complexe et investissements initiaux très importants (qui augmentent avec la profondeur) : travaux d'exploration, réalisation de forages |

## II.6. Méthodes exploratoires

Avant le commencement de tout programme géothermique il est essentiel de recueillir les données géologiques, géophysiques et géochimiques régionales existantes. Cela permet également de mieux cibler la zone à explorer, afin de :

- Localiser un champ géothermique et évaluer sa nature,
- Définir de façon la plus précise possible son emplacement, sa superficie, sa profondeur, les gammes probables de température dans le but d'estimer son potentiel énergétique.

### II.6.1. Investigations géologiques et hydrogéologiques

Elles sont le point de départ de tout programme d'exploration afin d'établir un modèle géologique 3D d'une région cible présumée. Cela dans le but de définir des sites de forages potentiels (d'exploration et de production), après avoir identifié des zones perméables où des fluides chauds circulent.

- Les données à terre correspondent à : la carte géologique, l'analyse structurale, la carte des manifestations de surface, la carte des altérations hydrothermales,
- Les données avec un forage exploratoire permettent d'obtenir : la lithologie, le profil de température, le profil d'altération en profondeur et les zones de circulation.

La présence de manifestations superficielles d'activité thermique est un bon indicateur, en leur absence il est nécessaire d'étudier de façon plus détaillée l'environnement géologique, puis de compléter ces études avec des forages exploratoires. Les différentes informations obtenues peuvent également servir lors de la phase de production au niveau de la caractérisation du réservoir et de l'optimisation de son exploitation. Le forage de puits (d'exploration ou de production) étant extrêmement onéreux, il représente la dernière phase d'un programme d'exploration, et il reste le seul moyen de valider les différents modèles élaborés et d'évaluer les caractéristiques réelles et le potentiel d'un système géothermal (Combs & Muffler, **1973**).

### II.6.2. Investigations géophysiques

Elles ont pour but d'identifier et d'interpréter les anomalies (de nature diverses), à partir de la surface ou d'intervalles de profondeur, en les comparant aux normes environnantes. Une anomalie étant l'écart entre la valeur mesurée d'un certain paramètre et la valeur théorique de ce même paramètre en ce point. A partir des résultats, des modèles (directs ou inverses) sont proposés. Ces résultats sont comparés aux données géologiques, afin de définir les propriétés physiques des roches, et permettre de restreindre le nombre de modèles réalistes.

La complémentarité des méthodes permet d'identifier des variations d'anomalies similaires et donc les propriétés physiques des formations géologiques (latéralement et en profondeur) du milieu.

- Les méthodes potentielles : gravimétrie (densité), magnétisme (champ magnétique, susceptibilité magnétique, aimantation …), électrique (résistivité, conductivité, tomographie, champ électromagnétique naturel ou induit, magnétotellurie ou MT, polarisation spontanée …), relevé thermique (mesures de température, gradient géothermique, flux de chaleur …),
- Les méthodes de propagation des ondes sismiques (réflexion et réfraction), la microséismicité/sismologie, la bathymétrie/altimétrie (MNT).

Certaines de ces méthodes sont traditionnellement employées dans l'industrie pétrolière (sismique, magnétisme, gravimétrie), elles permettent d'obtenir des informations sur la géométrie, les structures

géologiques et la profondeur du réservoir (Dickson & Fanelli, **2013**). Mais elles ne permettent pas de définir le potentiel géothermal de la ressource, cette méthodologie intervient donc dans les dernières étapes de l'exploration pour définir la localisation des puits d'exploration. L'existence de fluides géothermaux dans les structures géologiques peuvent être obtenue par des prospections électrique et électromagnétique (MT), qui sont sensibles à la présence de fluides et à la température.
Les méthodes géophysiques sont coûteuses, elles doivent être employées en étroite collaboration avec les investigations géologiques (Meidav, **1998**).

#### II.6.3. Investigations géochimiques

Les analyses géochimiques (incluant les analyses isotopiques et élémentaires avec les majeurs et les traces) permettent de déterminer s'il s'agit d'un système géothermique dominé par l'eau ou la vapeur, d'estimer la température minimale du fluide en profondeur et de déduire les caractéristiques chimiques du fluide en profondeur afin d'en définir la source et la recharge possible (Dickson & Fanelli, **2013**). La connaissance de la composition chimique du fluide est également très importante pour le passage à la phase de forage de puits afin d'avoir des installations adaptées (éviter la corrosion du matériel utilisé, le choix du type de centrale, l'impact environnemental …). Ces analyses se font au niveau des sites d'expressions de surface ou dans les puits exploratoires.

## II.7. La géothermie de haute-température

L'objet de cette thèse étant focalisée sur les systèmes de haute-enthalpie, j'ai donc choisi de traiter plus en détail ce type de système géothermal. Ce sont donc les caractéristiques spécifiques aux systèmes de haute-température qui sont présentées dans les paragraphes suivants.

#### II.7.1. Classification des systèmes géothermaux de haute-température

La description d'un système géothermal de haute-température peut se faire en prenant différents types de référentiels (d'après Moeck, **2014**):

1. La source de chaleur, qui peut être de deux types : (1) issue d'un système magmatique actif dans la croûte supérieure ou (2) issue d'un système amagmatique. Dans le second cas, il n'est pas nécessaire d'avoir du magma dans la croûte supérieure, la chaleur provient alors de la lithosphère.
2. Le contexte tectonique qui peut être extensif, transtensif ou compressif. Cela va avoir une influence sur le régime thermique et le flux de chaleur, la dynamique des fluides et leur composition chimique, ainsi que sur le régime de contrainte et les séquences lithologiques.
3. Le contexte géodynamique (Pitcher, **1983**, **1993**; Barbarin, **1990**), qui influe sur le mode de transfert de chaleur :

a. Dans un système dominé par la convection (contrôlé par le volcanisme et/ou la tectonique active), les régimes tectoniques favorables sont :
    i. Les arcs magmatiques, au-dessus des zones de subduction en contexte de plaques convergentes,
    ii. Les marges en contexte de plaques divergentes situées au niveau des dorsales ou en contexte intracontinental,
    iii. Les marges en contexte de plaques transformantes avec des failles en décrochement,
    iv. En contexte d'intra-plaque océanique ou continental au niveau d'un point-chaud,
b. Dans un système dominé par la conduction (contrôlé par les failles et/ou la lithologie), principalement exploité par le développement de l'EGS où le rapport perméabilité/porosité et l'absence ou la présence de fluide sont des paramètres primordiaux. Les régimes tectoniques favorables sont :
    i. Un bassin intra-cratonique, en contexte de marge passive, avec la présence d'aquifère profond,
    ii. Un bassin d'avant-pays, avec la présence d'aquifère profond également,
    iii. Un socle cristallin, la chaleur venant d'une intrusion granitique très enrichie en éléments radioactifs.

Tous présentent une anomalie du gradient géothermique. La combinaison de ces typologies permet de décrire au mieux un champ géothermal, ce qui rend compte d'une grande diversité de champs géothermaux possibles.

### II.7.2. Description des systèmes géothermaux de haute-température en contexte magmatique

D'un point de vue géologique, le système géothermal de Haute-Température se compose de trois parties :

1. Une source de chaleur : une chambre magmatique récente, dans la croûte superficielle, située entre 3 et 10 km de profondeur. Elle permet la circulation de fluides et le développement de cellules de convection. Il peut s'agir d'une ou de plusieurs intrusions magmatiques, sans nécessairement un volcan actif à l'affleurement.
2. Un réservoir : perméable et chaud, où siège la convection des fluides géothermaux, alimenté par une recharge en fluides (météorique, marin, tardi-magmatique). Sa perméabilité peut être primaire, c'est-à-dire intra-formationnelle (suivant la nature de l'encaissant rocheux) ou inter-

formationnelle (c'est le cas d'un contact lithologique entre deux formations différentes), mais également secondaire avec la présence de fracturation post-dépôt.

3. Une couverture : imperméable, délimitant la cellule de convection. Cette couche peut être de type sédimentaire ou hydrothermale. Dans le second cas, la nature minéralogique de la couverture résulte de la mise en place du système géothermal. L'interaction fluide-roche entraîne en effet une altération hydrothermale, dont la nature du minéral argileux (illite, illite-smectite, smectite) varie en fonction de la température et de la profondeur (Mas *et al.*, **2006**; Bouchot *et al.*, **2010**). Des manifestations de surface d'eau peuvent exister comme les sources chaudes, les geysers ou des gaz (fumerolles). Des brèchifications hydrothermales peuvent aussi survenir, traduisant une ébullition subite dans le réservoir, provoquant la formation de vapeur et entraînant la remontée de clastes et leur éjection vers la surface (Elder, **1981**).

### II.7.3. Fluides et altérations hydrothermales

Les fluides jouent un rôle important dans les transferts de matière et de chaleur. Ces fluides peuvent être d'origine diverse : magmatique, métamorphique, dérivé des eaux de surface (météorique et marin) et issus des formations géologiques elles-mêmes. Ils peuvent interagir avec les roches magmatiques, métamorphiques ou sédimentaires. Une altération est le résultat de l'interaction entre le fluide et la roche. Cela entraîne un changement dans la composition minéralogique et chimique, de texture, de volume ou encore de perméabilité des roches. Le remplacement minéralogique dans le cas d'une altération hydrothermale est la combinaison entre la dissolution et la précipitation minéralogique en réponse à un environnement thermique et chimique. L'étude des minéralisations hydrothermales permet d'appréhender la nature des fluides purs qui ont circulé dans le système considéré.

L'altération hydrothermale est la conversion d'une association minérale originelle en une nouvelle association minérale qui est plus stable dans les nouvelles conditions de pression-température-pH et à l'équilibre avec le fluide qui percole dans la roche. Les textures et les structures originelles peuvent être en partie ou totalement transformées par ce type d'altération. Il est possible d'appliquer des méthodes thermodynamiques, sur le modèle des roches métamorphiques (Meyer & Hemley, **1967**), pour calculer les conditions de précipitations des minéraux néoformés identifiés.

On distingue traditionnellement l'altération hydrothermale et le métamorphisme. Dans le cadre du métamorphisme régional orogénique (ou de contact) les fluides riches en $CO_2$ et/ou $H_2O$ sont générés par la déstabilisation des minéraux initialement présents dans la roche et se trouvent généralement en petite quantité par rapport aux phases solides des roches. Le rapport fluide/roche est dans ce cas bas, et les fluides sont en équilibre thermique et chimique avec les phases solides. Les minéraux

hydrothermaux des systèmes géothermaux actifs sont similaires à ceux trouvés dans les roches métamorphiques de bas degré.

L'altération hydrothermale peut être de deux types suivant son intensité. Elle est dite « non pervasive » si elle affecte seulement une partie de la roche, en bordure de fractures sous forme d'un halo. Si l'altération affecte tout la roche elle est dite « pervasive », mais tous les minéraux ne sont pas obligatoirement remplacés, cela est fonction de l'équilibre chimique entre les minéraux et le fluide hydrothermal. Une distinction est également à faire en fonction de l'origine de l'altération. Elle est dite « supergène » si les processus qui en découlent sont d'origine superficielle, par opposition à « hypogène » s'ils sont d'origine profonde.

Les altérations hydrothermales et les fluides associés permettent d'estimer la température (Figure II-8), le pH, la perméabilité et le stade de l'évolution du système géothermal.

Les systèmes hydrothermaux sont un cas particulier des systèmes géothermaux. Ils sont qualifiés ainsi lorsqu'un fluide caloporteur (relié à une source de chaleur) circule dans un volume rocheux (White *et al.*, **1971**; Chenevoy & Piboule, **2007**). En exploration géothermale, la cartographie des assemblages minéralogiques néoformés, en surface ou en profondeur à l'aide des forages, permet de localiser les zones où les températures, les pressions ou les perméabilités sont les plus élevées. Des approches similaires sont utilisées en métallogénie pour cartographier les systèmes hydrothermaux fossiles associés aux corps minéralisés épithermaux.

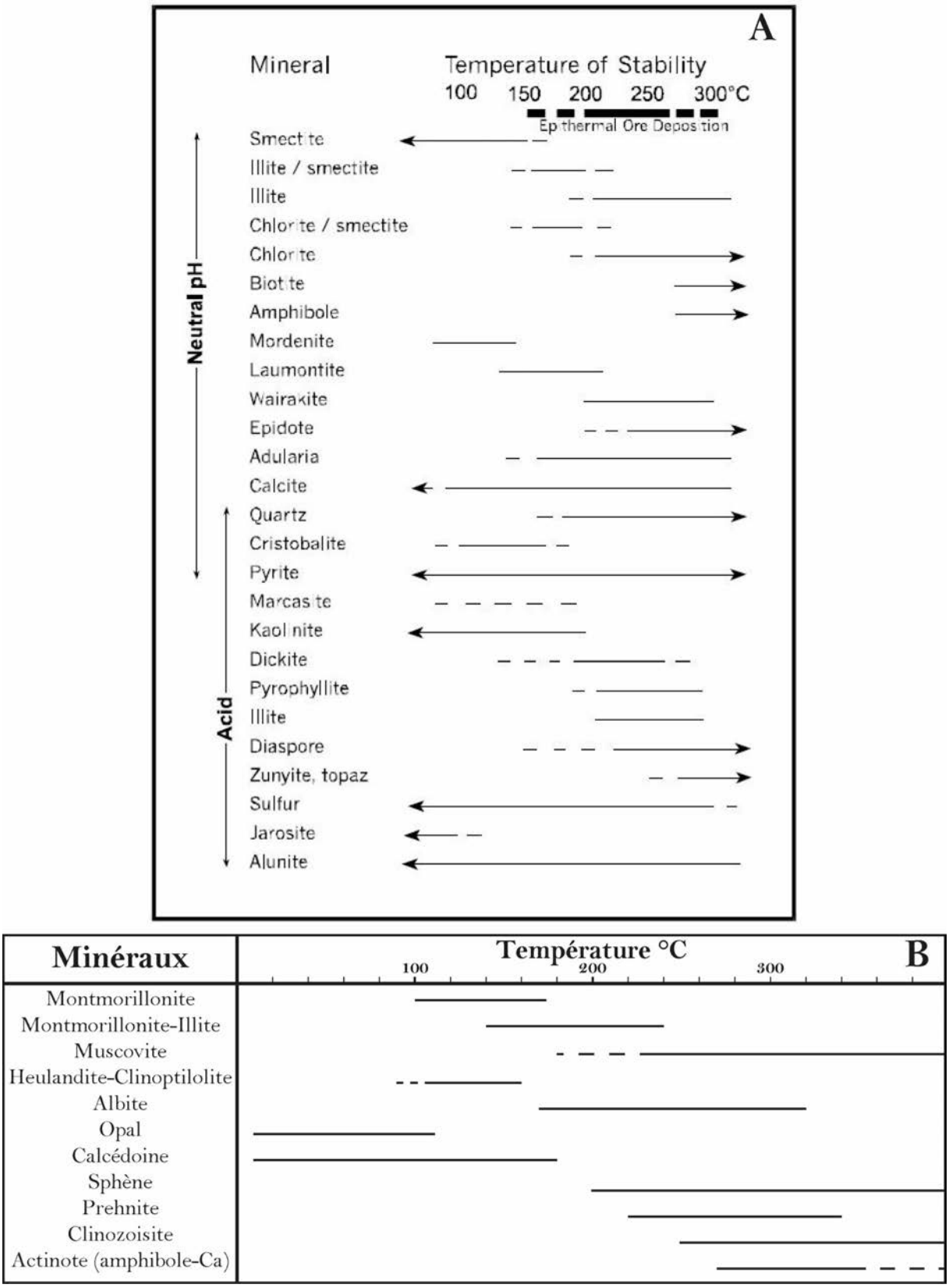


**Figure II-8 : Domaine de stabilité des minéraux hydrothermaux classiquement utilisés comme géothermomètres dans les systèmes géothermaux. A - White & Hedenquist, 1995. B – minéraux complémentaires d'après Henley & Ellis, 1983; Rancon, 1983; Reyes, 1990; Lagat, 2014.**

Un système épithermal est un terme minier désignant un gisement minéral formé à moins d'un kilomètre de profondeur à une température comprise entre 50 et 200°C (Lindgren, **1913**, **1933**; Pélissonnier, **1962**; Park & MacDiarmid, **1970**). Deux principaux types d'altération sont associés aux systèmes géothermaux volcaniques. On les retrouve sous forme de brèches hydrothermales, en fonction de leur degré de sulfidation (Heald *et al.*, **1987**, Figure II-9) :

- L'altération de type acide-sulfate, ou *high-sulfidation (HS)*, se compose d'une association d'alunite-kaolinite, où les dépôts sont riches en soufre. L'encaissant siliceux est lixivié par des fluides acides générés dans un environnement volcano-hydrothermal. Ce type de système indique une forte oxydation du milieu, classique des fluides hypogéniques acides. Ces fluides se forment lorsque les eaux souterraines se mélangent aux gaz magmatiques. Les fluides près de la surface peuvent atteindre des températures de 200 à 400°C (Rye *et al.*, **1992**), et sont enrichis en $SO_2$, HCl et NaCl.
- L'altération de type adulaire-calcite-séricite, ou *low-sulfidation (LS)*, où les dépôts sont pauvres en soufre. Ce type de système indique un milieu réducteur, les minéraux ainsi formés se font à partir de fluides à pH neutres. Ces fluides se forment au-dessus ou à proximité d'une source de chaleur. L'adulaire est caractéristique des températures et perméabilités élevées dans un système hydrothermal (Brown, **1977**).

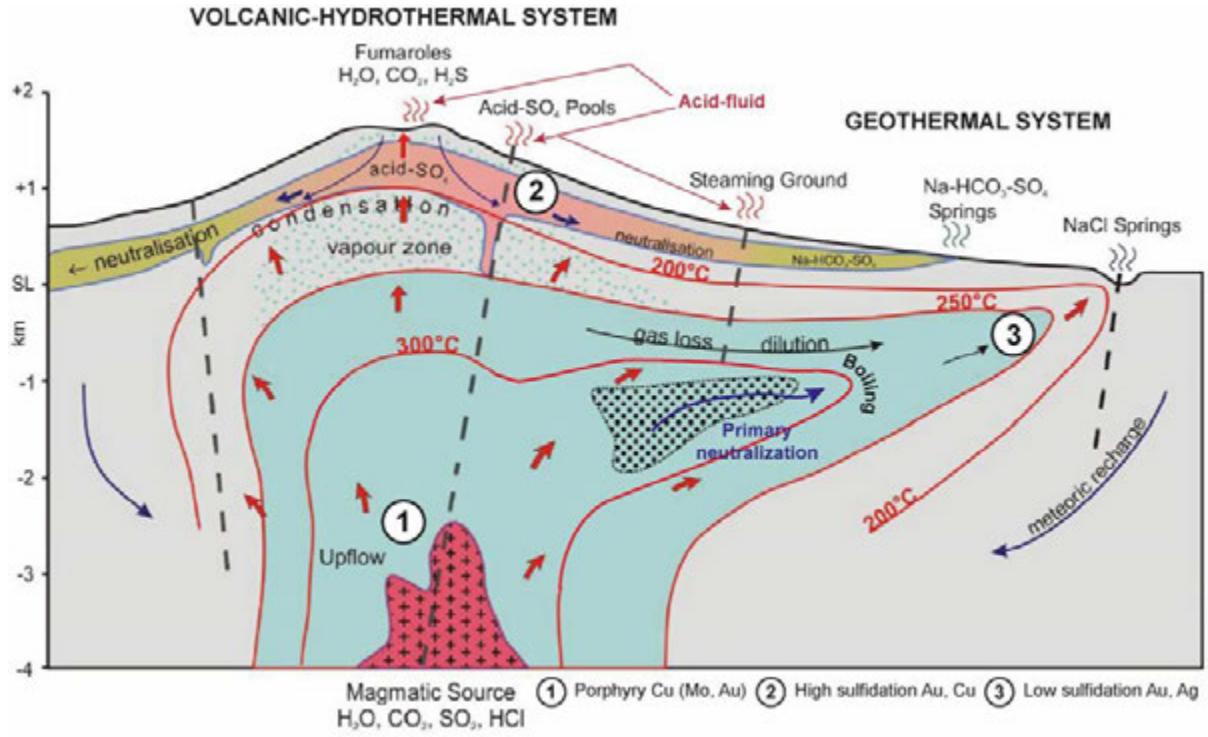


**Figure II-9 : Modèle schématique d'un système hydrothermal stratovolcanique mature (modifié d'après Hedenquist *et al.*, 2000; Bogie *et al.*, 2005)**

Les termes employés en exploration minière et géothermale ont évolué au cours du temps, une description commune des principaux types d'altération (Figure II-10) est proposée suivant une nomenclature à partir des assemblages minéralogiques (d'après Creasey, **1966**; Meyer & Hemley, **1967**; Rancon, **1983**; Heald *et al.*, **1987**; Bonnet *et al.*, **2007**; Shanks, **2012**), dont quelques exemples sont présentés ci-après.

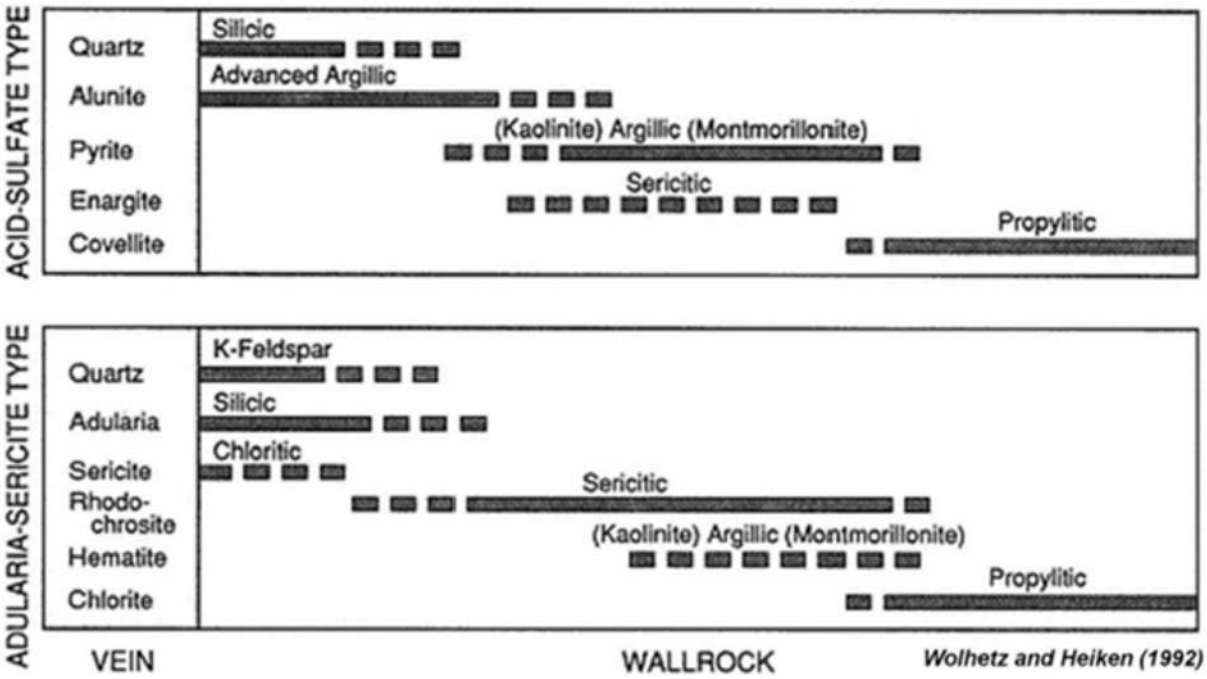


**Figure II-10 : Les minéraux d'altération présents en veine ou dans la roche encaissante correspondant aux types de dépôts acide-sulfate (HS) ou adulaire-séricite (LS) (Wohletz & Heiken, 1992)**

*II.7.3.a. L'altération propylitique*

Cette altération présente une paragenèse à quartz, épidote (zoisite, clinozoisite), albite, chlorite, carbonates (calcite), feldspath potassique et pyrite, avec parfois en association des zéolites (abondantes dans les sources chaudes, White, **1955**), elle se caractérise par l'addition d'$H_2O$, de $CO_2$ et localement de S. Suivant la prédominance d'une espèce minérale dans la paragenèse, il est possible de distinguer une sous-nomenclature : albitisation, chloritisation, zéolitisation, carbonatisation ou encore l'altération potassique. L'altération potassique est mise en évidence principalement par l'omniprésence de feldspaths potassiques et des micas (de type biotite et/ou muscovite) et révèle une teneur élevée en K et peut-être même de l'ajout de K au système, même si la quantité relative de minéraux potassiques peut être faible.

La présence d'épidote est un bon indicateur de la présence d'un réservoir géothermal de haute-température (>240°C). Concernant les carbonates, la formation de calcite est liée au mouvement de $CO_2$ contrôlé par les processus d'ébullition.

Ce type d'altération est liée à l'altération du feldspath. Le feldspath potassique ou sodique est un excellent indice de perméabilité. La phase primaire l'andésine est imperméable. Néanmoins sa perméabilité augmente au cours de son remplacement en phases secondaires, de façon croissante en albite, albite-adulaire, adulaire. L'adulaire (feldspath potassique) en plus d'être un indicateur de forte perméabilité, est également un indice d'ébullition dans le réservoir et se développe au détriment de l'illite. Il marque donc également la présence d'un réservoir géothermal actif. Cet assemblage à adulaire est généralement présent dans les zones de failles, en remplissage de veines ou de brèches, en association à de la calcite tabulaire et/ou du quartz lamellaire.

*II.7.3.b. L'altération séricitique (ou phyllique)*

Il s'agit de l'association de quartz, séricite (mica blanc de type muscovite ou paragonite, dont la taille est inférieure à 20 µm) et pyrite, suite à la déstabilisation des feldspaths en présence de fluides riches en $H^+$, $OH^-$, K et S (Pirajno, **2009**). Des argiles résiduelles peuvent être présentes (kaolinite), ainsi que les minéraux suivants : feldspath potassique, calcite, biotite, rutile, anhydrite et apatite. Cette altération est présente dans presque tous les systèmes hydrothermaux acides.

*II.7.3.c. L'altération argileuse*

L'assemblage minéralogique se compose classiquement de quartz, illite et pyrite, avec en association : kaolinite, smectite et calcite (Guilbert & Park, **1986**). Il s'agit de la formation de minéraux argileux due à un métasomatisme acide intense à des températures comprises entre 100 et 300°C (Pirajno, **2009**). Les argiles formées permettent d'obtenir la température du système hydrothermal et d'identifier la partie dans laquelle on se situe grâce au phénomène de zonation des phases argileuses dans le système hydrothermal.

La smectite est en surface dans la couche couverture (< 140°C). Les inter-stratifiés illite-smectite son présents au toit du réservoir géothermique (140-200°C), plus la part d'illite est importante plus la température est élevée et inversement. L'illite est au cœur du réservoir (> 210-220°C). La chlorite est présente de la couverture au réservoir (où elle est la plus abondante), sa simple présence ne permet pas de donner d'indication significative en terme de température. Il faut alors utiliser les méthodes géothermomètriques basées sur la chimie de la chlorite pour préciser ce paramètre intensif (Cathelineau, **1988**; De Caritat *et al.*, **1993**; Inoue *et al.*, **2009**; Lanari *et al.*, **2014**; Bourdelle & Cathelineau, **2015**).

*II.7.3.d. L'altération argileuse avancée*

Il s'agit d'une altération de sub-surface, induite par un fluide acide qui va lessiver la roche, elle est typique des systèmes « high-sulfidation ». Tous les feldspaths sont remplacés par des phases alumineuses. L'altération acide à l'affleurement est produite par la vapeur acide et se traduit par la

présence de : dickite, kaolinite, pyrophyllite, quartz, alunite à natro-alunite, barytine, soufre natif, tourmaline, hématite, silice (de type tridymite, cristobalite, opale ou quartz) (Guilbert & Park, **1986**).

*II.7.3.e. La silicification*

Cette altération témoigne d'une addition importante de silice dans la roche. Elle est généralement très importante dans les zones superficielles ou en surface d'un champ géothermique. Les dépôts siliceux (opale, calcédoine, quartz) sont issus de la précipitation de fluides chauds supérieurs à 175°C, dû à l'émergence de fluides chlorurés-sodiques issus du réservoir. La solubilité de la silice contenue dans les fluides géothermaux diminue conjointement avec la température.

Les minéraux siliceux prennent différentes formes :

- L'opale, la cristobalite et la tridymite sont présentes dans les zones inférieures à 100°C (avec la kaolinite ou la mordénite),
- Le quartz et la calcédoine sont présents seulement dans la zone à haute-température adulaire-quartz.

L'étude des altérations hydrothermales est donc un bon guide pour l'exploration géothermale, une aide précieuse pour identifier le caractère chimique des fluides hydrothermaux et leurs sources, et permet de caractériser l'évolution d'un système hydrothermal. Ces études peuvent être faites à l'affleurement ou en forage.

### II.7.4. Géothermie de haute-température : quelques exemples emblématiques

*II.7.4.a. Exemple du système de Larderello en Italie*

Le champ géothermal de Larderello est situé dans la partie Nord des Apennins en Italie, il s'étend sur une superficie de 250 km² et est caractérisé comme un système à vapeur dominante exploité par 200 puits de production répartis dans 21 centrales (Razzano & Cei, **2015**). Cette zone est affectée par une extension continentale post-collisionnelle depuis le début du Miocène (Carmignani *et al.*, **1994**; Rossetti *et al.*, **1999**; Bellani *et al.*, **2004**). Cette extension s'est accompagnée d'une phase magmatique à la fin du Miocène (Serri *et al.*, **1993**). Depuis le Pliocène un soulèvement rapide de la surface au Sud (Dallmeyer & Liotta, **1998**) contraste avec un subsidence thermique contemporaine au Nord (Bartole, **1995**; Bellani *et al.*, **2004**). Des bassins post-orogéniques se sont formés et localement le flux de chaleur y est très élevé (Baldi *et al.*, **1995**). Des couches perméables ont été identifiées à 3-4 km de profondeur où la température est de l'ordre de 350-400°C (Cameli *et al.*, **1993**, **2000**; Barelli *et al.*, **1995**, **2000**; Bertani & Cappetti, **1995**). C'est à cette même profondeur qu'un horizon (horizon K) a été identifié comme étant une zone de déformation localisée marquant la transition fragile-ductile (Liotta & Ranalli, **1999**; Brogi *et al.*, **2003**; Bellani *et al.*, **2004**; Ranalli & Rybach, **2005**), au sommet de l'intrusion granitique Quaternaire (Bertini *et al.*, **2006**). Les zones de cisaillement liées au contexte

extensif sont interprétées comme les principaux chemins de circulations des fluides géothermaux (Figure II-11).

Deux types de réservoirs sont connus et exploités industriellement (Bertini *et al.*, **1995**; Cappetti *et al.*, **2000**). Un premier réservoir superficiel est localisé au niveau de l'horizon cataclastique (correspondant aux évaporites triasiques) et est recouvert par les formations carbonatées (Jurassique) (Bertini *et al.*, **2006**). Un second plus profond situé entre 2 et 4,5km se localise au sein de roches métamorphiques fracturées (Batini *et al.*, **2003**; Bertini *et al.*, **2006**). Le fluide exploité est un mélange d'eau météorique et de fluides magmatiques et métamorphiques (Minissale, **1991**; Manzella *et al.*, **1998**).

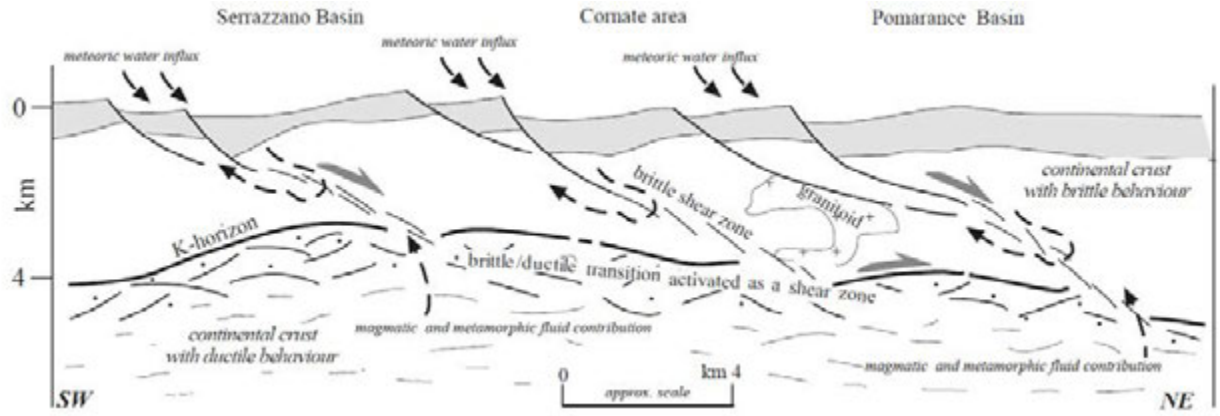


**Figure II-11 : Interprétation géologique du champ géothermal de Larderello (Ranalli & Rybach, 2005)**

Il s'agit d'un système géothermal de haute-température (260°C) avec une capacité de production d'électricité d'une puissance de 915 MWe installée en 2016 (Bertani & Romagnoli, **2017**), avec une production de 5 870 GWh qui permet de fournir 30 % des besoins en électricité de la Toscane (2,1 % des besoins de l'Italie) à partir de la vapeur géothermale.

*II.7.4.b. Exemple des systèmes de la Zone Volcanique de Taupo en Nouvelle-Zélande*

La Zone Volcanique de Taupo (TVZ), située au centre de l'île Nord de Nouvelle-Zélande en arrière de la zone de subduction de Hikurangi, correspond à un bassin d'arrière-arc en extension NW-SE (8 à 15 mm/an), orienté selon un segment NNE à SSW, présentant un flux thermique anormalement élevé (Wilson *et al.*, **1995**), avec une température supérieure à 350°C à des profondeurs inférieures à 5 km (Milicich *et al.*, **2013**). Elle est le siège d'une forte activité volcanique à laquelle est associée une altération hydrothermale depuis 1,8 Ma.

Une vingtaine de systèmes géothermaux actifs se concentrent dans cette zone (Figure II-12), sur une aire de 20 km² en moyenne. Ils sont associés à une structure de type graben à multiples blocs faillés, se composant d'un amas épais de roches volcaniques principalement rhyolitique avec des intercalations de sédiments lacustres (Chambefort *et al.*, **2014**). La majorité (60%) des champs

géothermaux de la TVZ suivent la zone d'accommodation NW-SE. Ils suggèrent une perméabilité verticale à la jonction entre le système de failles majeures NE-SW du rift et la zone d'accommodation. La seconde partie des champs (30%) se situent à l'extrémité des failles normales majeures. Par ailleurs, 36% de ces champs sont associés à une caldeira, présentant une perméabilité verticale à l'intersection de la faille NE-SW et la faille bordière de la caldeira.

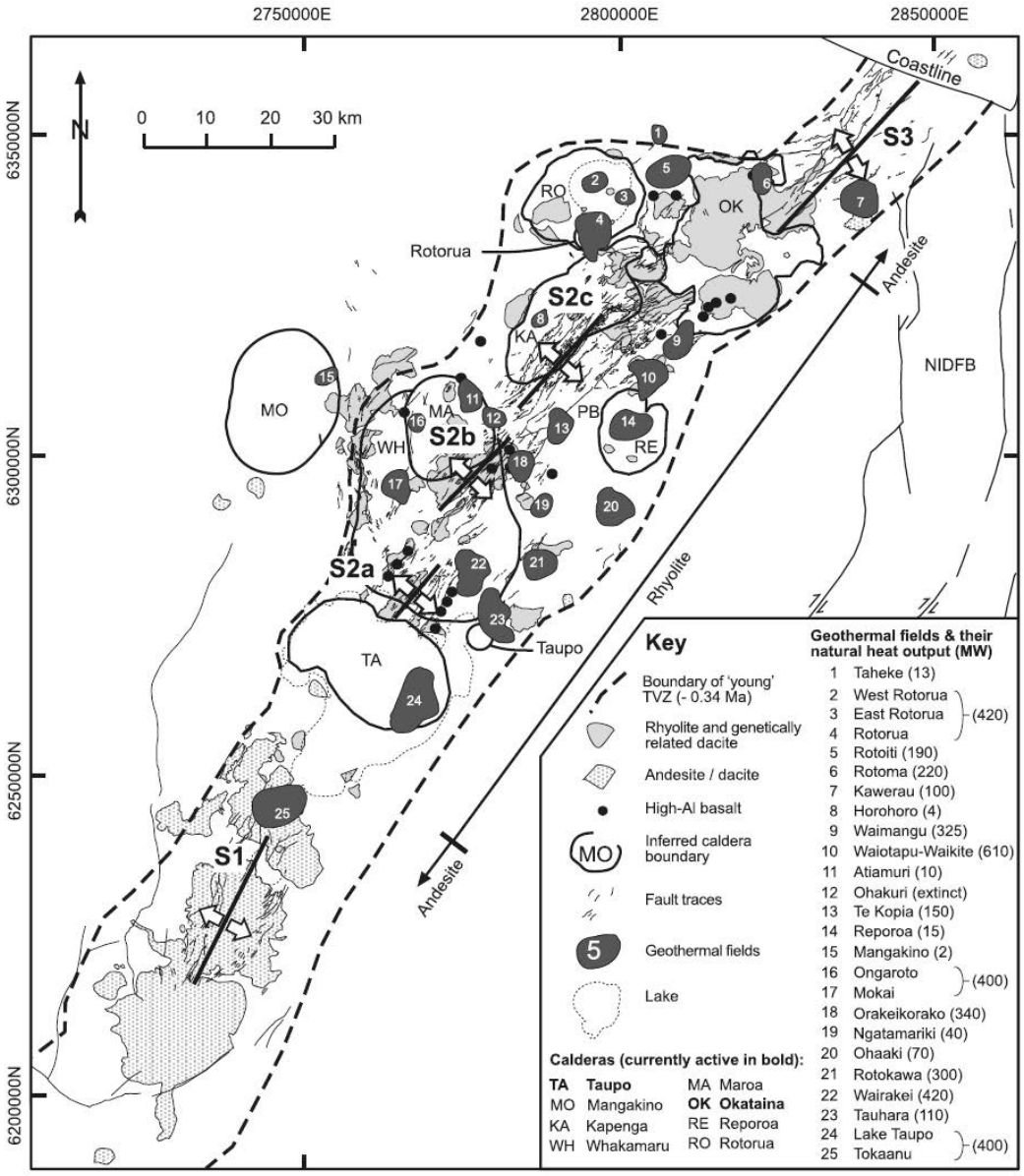


**Figure II-12 : Localisation des champs géothermaux de la Taupo Volcanic Zone (Rowland & Sibson, 2004)**

Il s'agit d'un système géothermal de haute-température (>250°C) avec une capacité de production d'électricité d'une puissance de 1068 MWe installée en 2016. La production d'électricité a démarré en 1958 à la centrale de Wairakei, puis s'est développée ensuite principalement dans la TVZ (90% des champs géothermaux de la Nouvelle-Zélande).

La production des centrales géothermales en 2014 fait état de 7 000 GWh (avec une augmentation de plus de 20% entre 2010 et 2014) soit 16,3% de la production totale d'électricité (Carey *et al.*, **2015**) à partir de la vapeur géothermale. Le fluide exploité est un mélange dû à l'interaction entre les eaux météoriques et les roches magmatiques en profondeur (Millot *et al.*, **2012**), et peut atteindre 250-320°C au cœur des réservoirs.

Des mesures de résistivité ont permis de localiser les champs actifs, à l'aplomb de panaches géothermaux (200-350°C) et des anomalies conductrices (30-50 ohm.m) délimitent les réservoirs (Heise *et al.*, **2008**). Au vu de la densité des panaches, la base des cellules de convection est estimée à 7-8 km de profondeur. Au toit du réservoir, la vapeur géothermale, due à l'ébullition au-dessus de l'aquifère, reste bloquée sous une couverture. Des expressions de surface se situent à l'aplomb du système, avec des fluides chlorurés sodiques neutres, entrainant des dépôts siliceux en surface, et de faible salinité.

Les systèmes géothermaux actifs sont stables depuis 20 (à Rotokawa, Krupp & Seward, **1987**) à 500 ka (à Ngatamariki, Arehart *et al.*, **2002**).

L'altération hydrothermale prograde s'intensifie avec la profondeur (Rosenberg *et al.*, **2009**). : (1) une altération argileuse (smectite, calcite +/- pyrite, +-/ illite-smectite) à une température inférieure à 140°C (Browne & Ellis, **1970**), (2) une altération propylitique (chlorite, quartz, épidote, +/- albite, +/- adulaire, +/- wairakite, +/- titanite) à une température supérieure à 210°C (Steiner, **1977**), marquant une zone de forte perméabilité et d'ébullition avec la présence d'adulaire en remplacement des feldspaths (> 230°C, White & Hedenquist, **1990**), (3) un niveau de plus forte altération hydrothermale (wairakite, épidote et prehnite) signant l'interaction de la roche avec un fluide neutre à légèrement acide à une température de 240-280°C.

*II.7.4.c. Exemple du système de Bouillante en Guadeloupe*

Le site géothermal de Bouillante se situe sur l'arc insulaire des Petites-Antilles, sur la face Ouest de l'île de Basse-Terre de l'archipel de Guadeloupe, correspondant à la région volcanique active et émergée. Le champ géothermal de Bouillante se situe à l'intersection entre deux grands systèmes de failles (Feuillet *et al.*, **2002**; Thinon *et al.*, **2010**; Calcagno *et al.*, **2012**) : (1) NNW-SSE de Montserrat-Bouillante-Les Saintes (MBLS, système transtensif décrochant, avec des failles senestres) associés à une orientation secondaire NE-SW et (2) E-W à ESE-WNW Bouillante-Capesterre (système en extension avec des failles normales). Les cibles de forages sont les failles, sachant qu'elles sont supposées être perméables, favorisant la circulation de fluides en profondeur, par l'infiltration d'eau météorique et d'eau de mer. La source de chaleur est supposée magmatique avec un volcanisme récent de type calco-alcalin. Des études ont montré que la ressource géothermale exploitée à Bouillante avait

un lien temporel avec le début du volcanisme du complexe volcanique Grande-Découverte-Soufrière (GDVC) (Patrier *et al.*, **2013**; Verati *et al.*, **2014**).

Il s'agit d'un système géothermal de haute-température (260°C) avec une capacité de production d'électricité d'une puissance de 15,5 MWe installée depuis 2005 (Sanjuan & Traineau, **2008**). Ce chiffre ne représente pas la capacité réelle de l'île car la géothermie est encore en cours de développement sur l'île.

La phase exploratoire a démarré en 1964, la production d'électricité a pu démarrer de 1986 à 1992 (EDF), puis a repris en 1996 (Géothermie Bouillante).

La production de la centrale en 2017 fait état de 112 197 MWh (une augmentation de 33% par rapport à 2016) soit 6,4% de la production totale d'électricité (OREC-Guadeloupe, **2018**) à partir de la vapeur géothermale. En moyenne elle permet de fournir 6 à 8% des besoins énergétique de l'archipel de Guadeloupe (soit plus de 7000 h d'électricité par an).

Le fluide exploité est composé à 58% d'eau de mer et à 42% d'eau douce météorique. Ce fluide est à une température d'environ 250°C entre 500 et 1000 m de profondeur (avec une stabilisation de la température due à la circulation des fluides), et 100°C en sub-surface (Figure II-13). De nombreuses sources chaudes (émergences et indices de surface liée à l'activité géothermale) sont identifiées sur la côte Ouest de l'île de Basse-Terre et en mer.

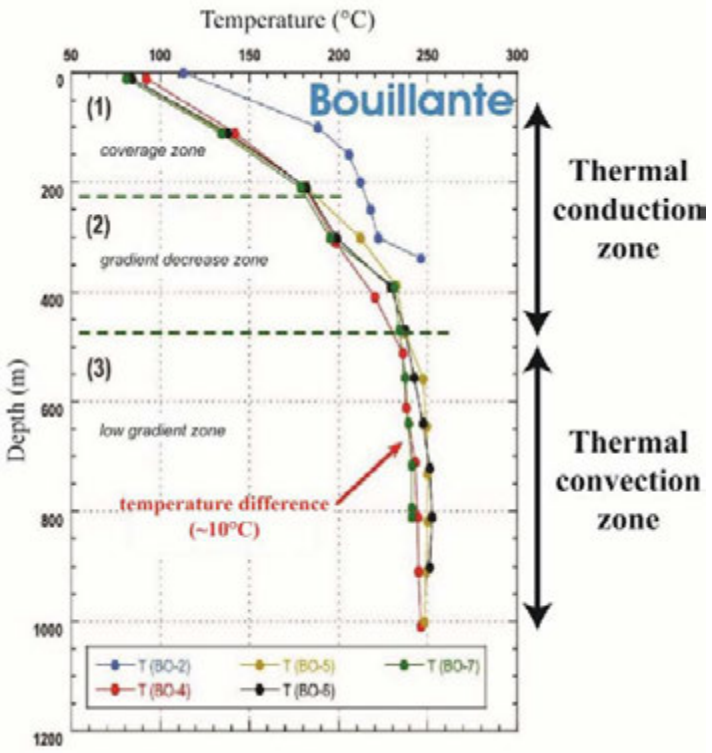


**Figure II-13 : Profils thermiques enregistrés en mars 2002 dans les puits du champs géothermal de Bouillante (modifiée d'après Guillou-Frottier, 2003)**

Un modèle conceptuel de réservoir géothermal (Johnston *et al.*, **1992**; Bouchot *et al.*, **2010**) a permis de définir le système géothermal de Bouillante en surface (Figure II-14) :

- Un réservoir avec la zone à illite et chlorite majoritaire (illite + chlorite +/- épidote + wairakite), se définissant par une altération propylitique, donnant une température comprise entre 240 et 260°C, avec une très forte résistivité (>20 ohm.m), une forte densité et une forte perméabilité ;
- Au toit du réservoir une couche mixte avec la zone à illite-smectites interstratifiées, une présence de chlorite inférieure à 50%, donnant une température comprise entre 200 et 240°C, avec une forte résistivité (< 20 ohm.m) et une faible densité ;
- Une couverture imperméable définie par la zone à smectite (smectite majoritaire de type beidellitique +/- heulandite) donnant une température comprise entre 110 et 200°C, avec une faible résistivité (< 2.5 ohm.m) et une faible densité ;
- Une couche superficielle résistante (50 premiers mètres) donnant une température inférieure à 150°C, de résistivité moyenne (2,5-10 ohm.m) et de forte densité ;
- Une brèche hydrothermale en surface liée à une éruption hydrothermale composée d'adulaires datés à 248,2 ka +/- 50,2 ka (Verati *et al.*, **2014**) et d'un ciment à quartz-calcédoine ;
- Plusieurs manifestations de surface existent : fumerolles, sources chaudes, anomalies thermiques du sous-sol.

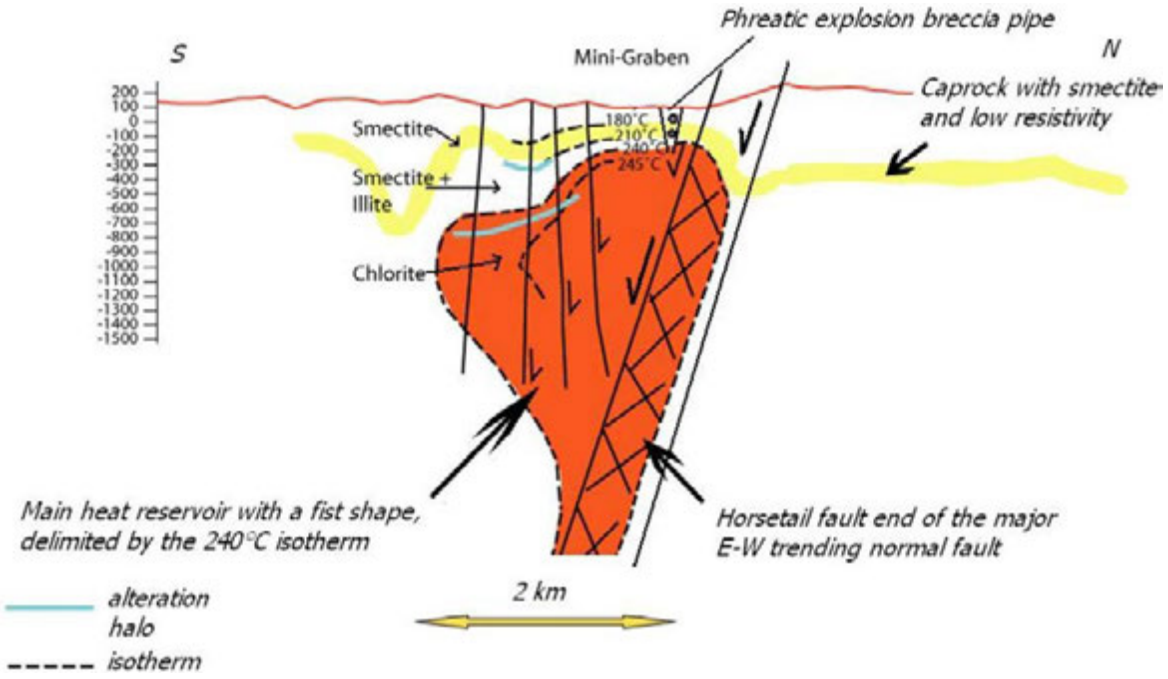


**Figure II-14 : Modèle conceptuel du système géothermal de Bouillante fait à partir de données de puits et de surface (Bouchot *et al.*, 2010)**

# Chapitre III : Contexte géologique

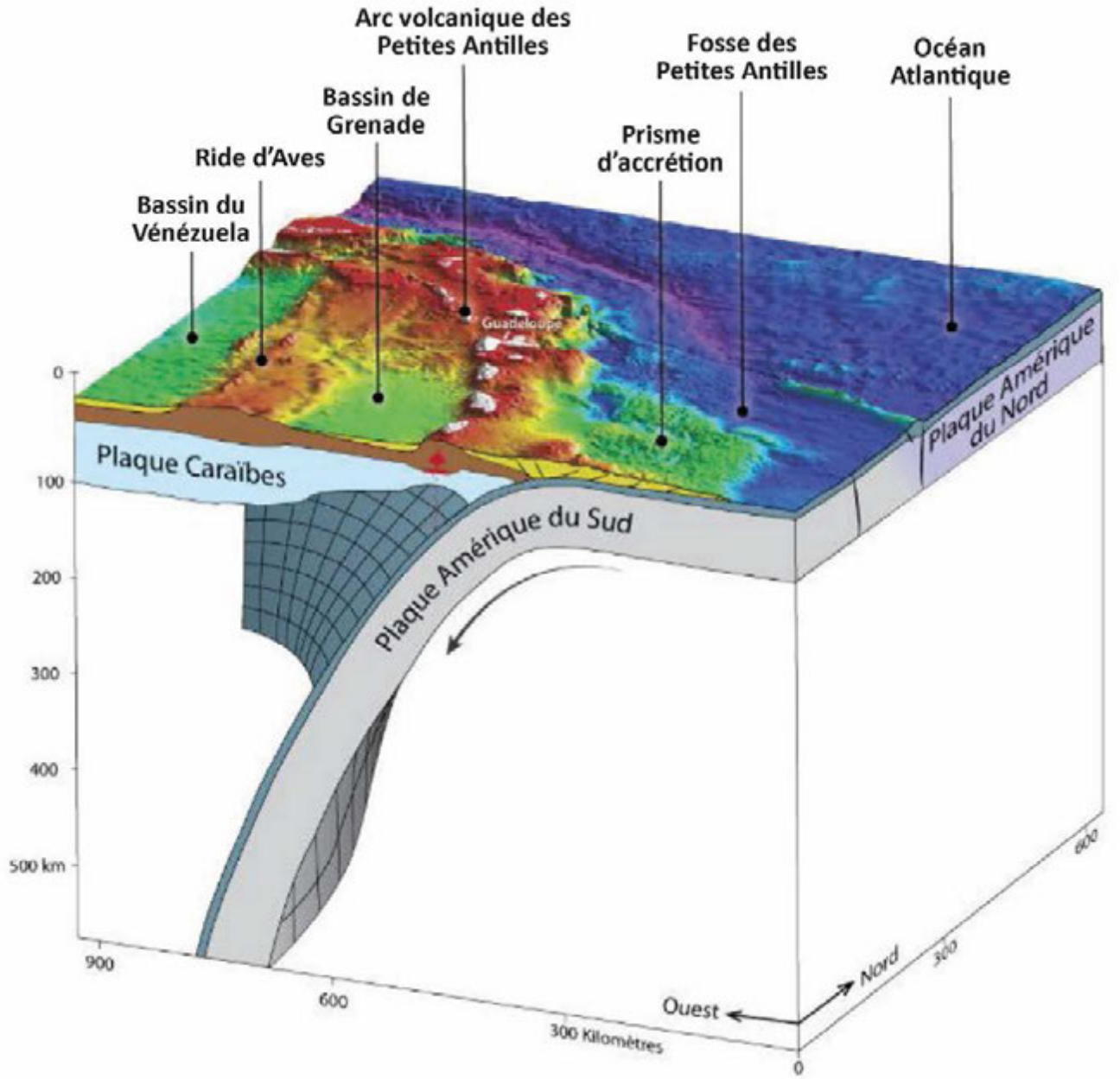


*Schéma montrant les plaques Amériques en subduction courbe et oblique sous la plaque Caraïbe.*

*Illustration issue de la campagne GARANTI © Géosciences Montpellier*

## III.1. L'arc insulaire des Petites Antilles dans son contexte géodynamique

L'arc volcanique des Petites Antilles est une des expressions de la subduction intra-océanique vers l'Ouest de la lithosphère océanique des plaques Amérique Nord et Sud (NAM ou NAP et SAM ou SAP respectivement) sous la bordure Est de la plaque Caraïbe, suivant une direction de convergence oblique (Ouest-Sud-Ouest) estimée à une vitesse moyenne de 2 cm/an pour les 30 derniers millions d'années (Bouysse, **1980**; Hawkesworth & Powell, **1980**; Dixon *et al.*, **1998**; DeMets *et al.*, **2000**; Macdonald *et al.*, **2000**; Feuillet *et al.*, **2001**, **2002**; López *et al.*, **2006**, Figure III-1). Cette convergence oblique, associée à de la compression, est accommodée par deux systèmes en décrochement majeurs en bordure Nord et Sud de la plaque Caraïbe, avec un mouvement senestre au niveau des Grandes Antilles et un mouvement dextre au Nord du Venezuela (Speed, **1985**; Burke, **1988**; Mann *et al.*, **1995**, **2002**; Pindell & Barrett, **1997**; Avé Lallemant & Sisson, **2005**; Calais *et al.*, **2006**, **2016**; Pindell & Kennan, **2009**). La bordure Ouest de la plaque Caraïbe accommode la subduction de l'Amérique Centrale avec les plaques Cocos et Nazca.

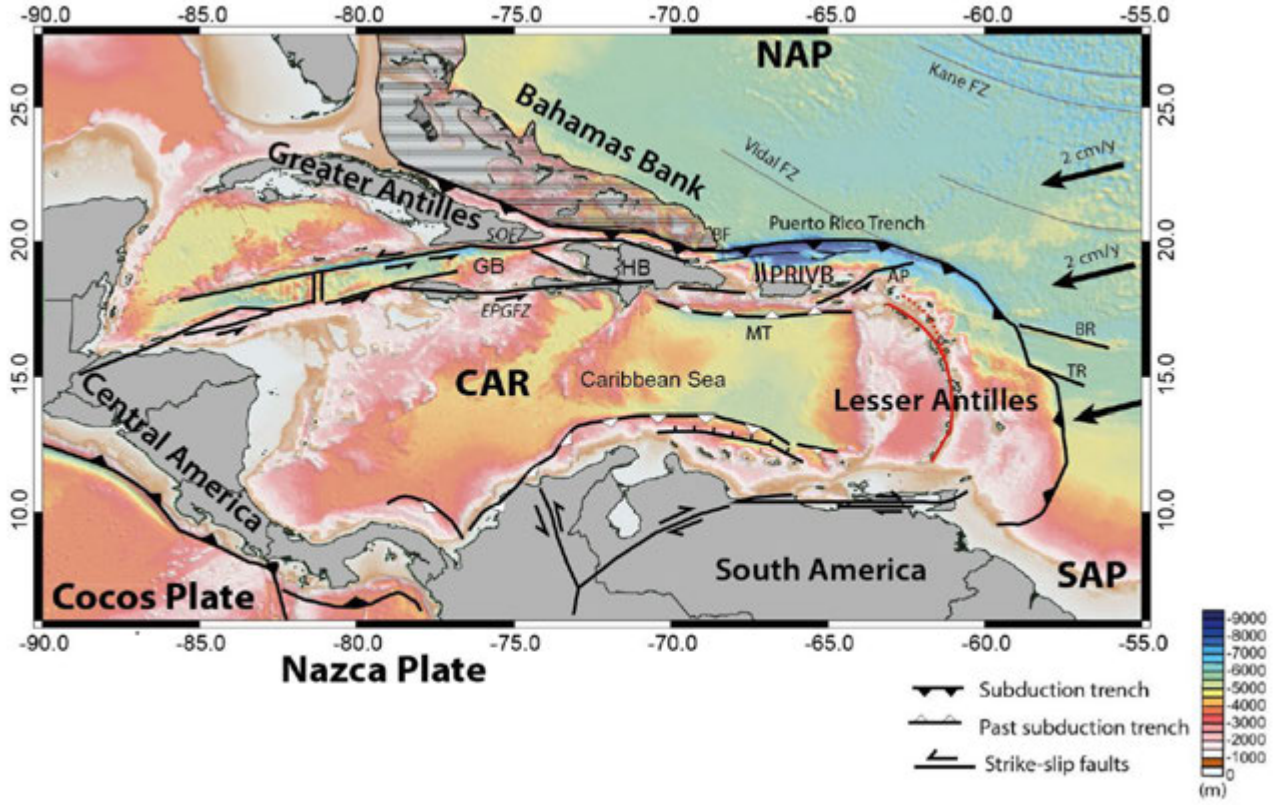


**Figure III-1 : Frontières tectoniques de la plaque Caraïbe (CAR). La frontière Nord se décompose en trois micro-blocs avec d'est en ouest, le bloc Puerto Rico-Îles Vierges (PRVIB), Hispaniola (HB) et Gonâve(GB). NAP : North American plate, SAP : South American plate, AP : Passage d'Anegada, MT : Fosse de Muertos, SOFZ : Septentrional Oriente Fault Zone, EPGPZ : Enriquillo-Plaintain Garden Fault Zone, BF : Faille de Bunce, BR : Ride de Barracuda, TR : Ride de Tiburon. (Laurencin, 2017)**

# Contexte géologique

La plaque chevauchante Caraïbe est en grande partie formée d'un large plateau océanique d'âge Crétacé supérieur, le « Caribbean-Colombian Oceanic Plateau » (CCOP) (Kerr *et al.*, **1997**, **1998**). L'épaisseur de la croûte a pu être estimée par différents auteurs, elle varie entre 8 et 24 km (Edgar *et al.*, **1971**; Case *et al.*, **1990**; Mauffret & Leroy, **1997**; Kerr *et al.*, **2003**) et peut aller jusqu'à 28 km dans la partie centrale des Petites Antilles (Kopp *et al.*, **2011**, Figure III-2-**A**). La plaque Caraïbe est donc considérée comme étant une croûte océanique épaissie, si on la compare à d'autres croûtes chevauchantes de subduction intra-océanique dont les épaisseurs maximales sont plutôt comprises entre 15 et 20 km (Kopp, **2013**).

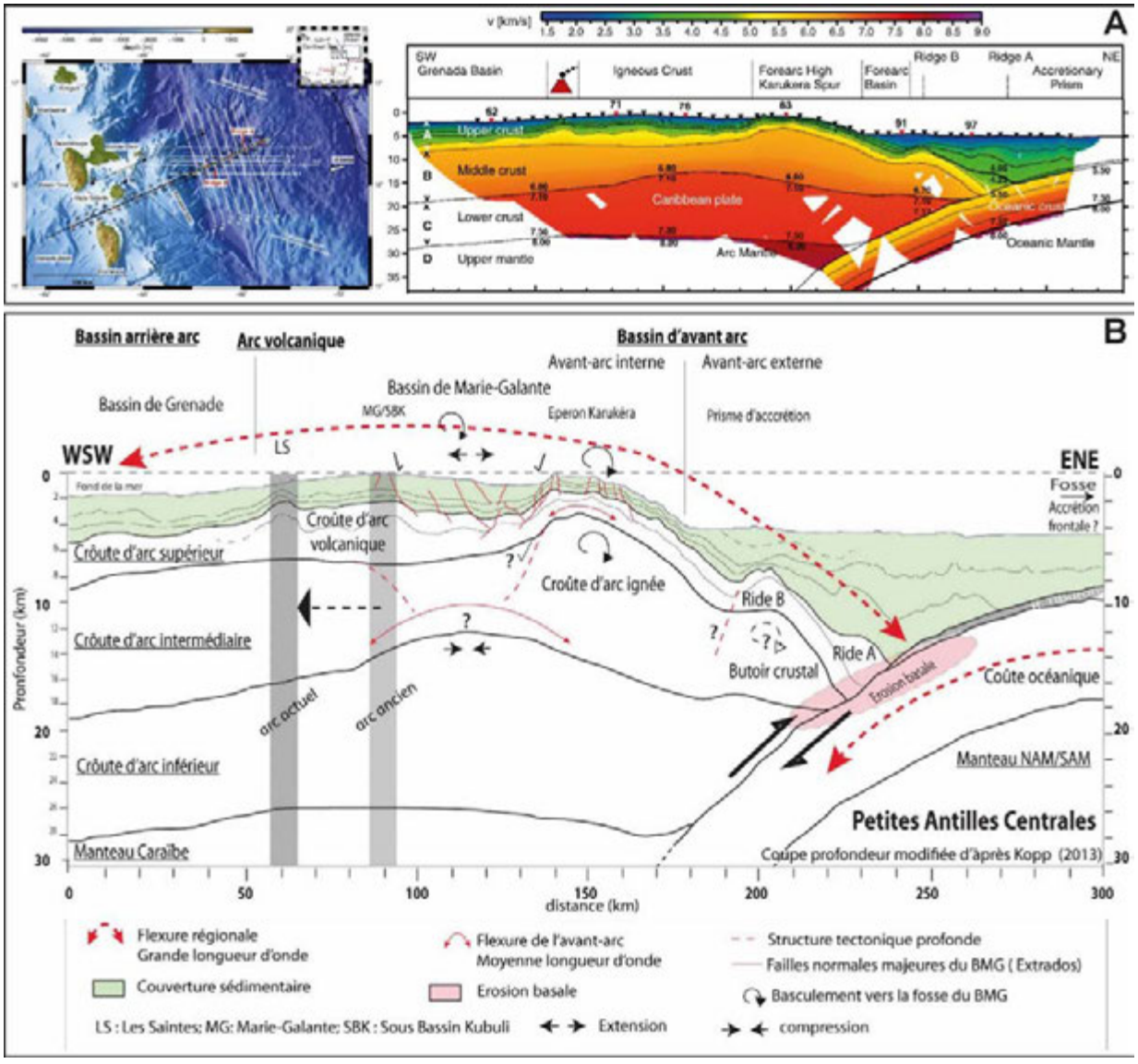


**Figure III-2 : A) Modèle de vitesse 2D par tomographie sismique de la zone de subduction des Petites Antilles (Kopp *et al.*, 2011). B) Interprétation de la coupe en A à partir de la coupe en profondeur modifiée de Kopp, 2013 pour obtenir un modèle de déformation flexurale à grande échelle et expliquer la mise en place de failles normales sur courbure de plis (de type extrados) dans le domaine avant-arc (De Min, 2014).**

De plus, la croûte supérieure de la plaque Caraïbe aurait pour origine un arc volcanique Jurassique plissé et déformé au Crétacé inférieur, comme cela a pu être observé au niveau du socle de l'île de la Désirade qui montre une signature géochimique d'arrière-arc (Bouysse *et al.*, **1983**; Gauchat, **2004**; Mattinson *et al.*, **2008**; Cordey & Cornee, **2009**; Neill *et al.*, **2010**; Corsini *et al.*, **2011**; Lardeaux *et al.*, **2013**). Si on tient compte de cette dernière observation, l'épaississement de la plaque Caraïbe est à la fois magmatique (plateau océanique) et tectonique (raccourcissement). Cependant l'origine de cette plaque est toujours débattue avec l'opposition de deux modèles. Un modèle défend une origine « Pacifique » (Kerr *et al.*, **1996**, **2003**; Spikings *et al.*, **2005**; Luzieux *et al.*, **2006**; Vallejo *et al.*, **2006**; Pindell & Kennan, **2009**), et un autre modèle s'oriente vers une origine « intra-Américaine » (James, **2003**, **2006**, **2009**; Giunta & Oliveri, **2009**; Giunta & Orioli, **2011**). Les investigations tomographiques pour étudier la structure du manteau n'ont pas permis de les départager (van Benthem *et al.*, **2013**). Néanmoins des travaux sur un assemblage de radiolaires d'âge Jurassique supérieur de l'île de la Désirade ont permis de mettre en évidence leur affinité Pacifique (Montgomery *et al.*, **1994**; Baumgartner *et al.*, **2004**; Cordey & Cornee, **2009**). Ces résultats tendent vers une formation de la croûte caribéenne dans la zone Pacifique avant sa migration vers l'Est et sa mise en place entre les deux Amériques (Kerr *et al.*, **1996**; Spikings *et al.*, **2005**; Luzieux *et al.*, **2006**; Vallejo *et al.*, **2006**; Corsini *et al.*, **2011**). Cette croûte est à présent recouverte de bassins sédimentaires volcano-détritiques et de plateformes carbonatées.

La zone de subduction des Petites Antilles est marquée par une fosse océanique délimitant le front de subduction NNW (Figure III-3) qui accommode du raccourcissement et des mouvements décrochants (Fitch, **1972**; Dickinson & Seely, **1979**; Jarrard, **1986**). La zone avant-arc est bien plus large au Sud (~450 km) qu'au Nord (~150 km), avec le développement du prisme d'accrétion de la Barbade, puis le bassin d'avant-arc de Tobago vers l'Ouest. En arrière-arc, le bassin de Grenade est limité à l'Ouest par la ride d'Avès qui est le vestige d'un arc insulaire (Bouysse *et al.*, **1985b**).
L'arc volcanique des Petites Antilles présente une forme convexe vers l'Est et s'étend sur 850 km de long, du passage d'Anegada au Nord jusqu'à la faille El Pilar au Sud. Il se compose d'une quinzaine d'îles, et se serait initié à partir du Paléocène (Andreieff *et al.*, **1981**; Maury *et al.*, **1990**).

Les Petites Antilles se sont formées à partir de deux arcs volcaniques successifs (Figure III-2-**B**), dont la morphologie actuelle en double arc est observable dans sa partie Nord à partir de l'île de la Martinique. Leur mise en place se serait faite dès le Miocène inférieur à moyen (Bouysse, **1979**; Bouysse & Guennoc, **1983**; Maury *et al.*, **1990**). Le changement du régime de convergence serait dû au changement de l'orientation de la lithosphère plongeante (NAM) suite à l'entrée en subduction de

rides asismiques : Barracuda, Tiburon ou St Lucia (Bouysse, **1979**; McCann & Sykes, **1986**; Bouysse & Westercamp, **1988**, **1990**; Bouysse *et al.*, **1990**; Maury *et al.*, **1990**; Gomez *et al.*, **2018**, Figure III-3). Ce changement est également marqué par une absence de dépôts volcaniques de 10 Ma, à l'exception de la Martinique où un arc intermédiaire a été identifié (Germa *et al.*, **2011**).

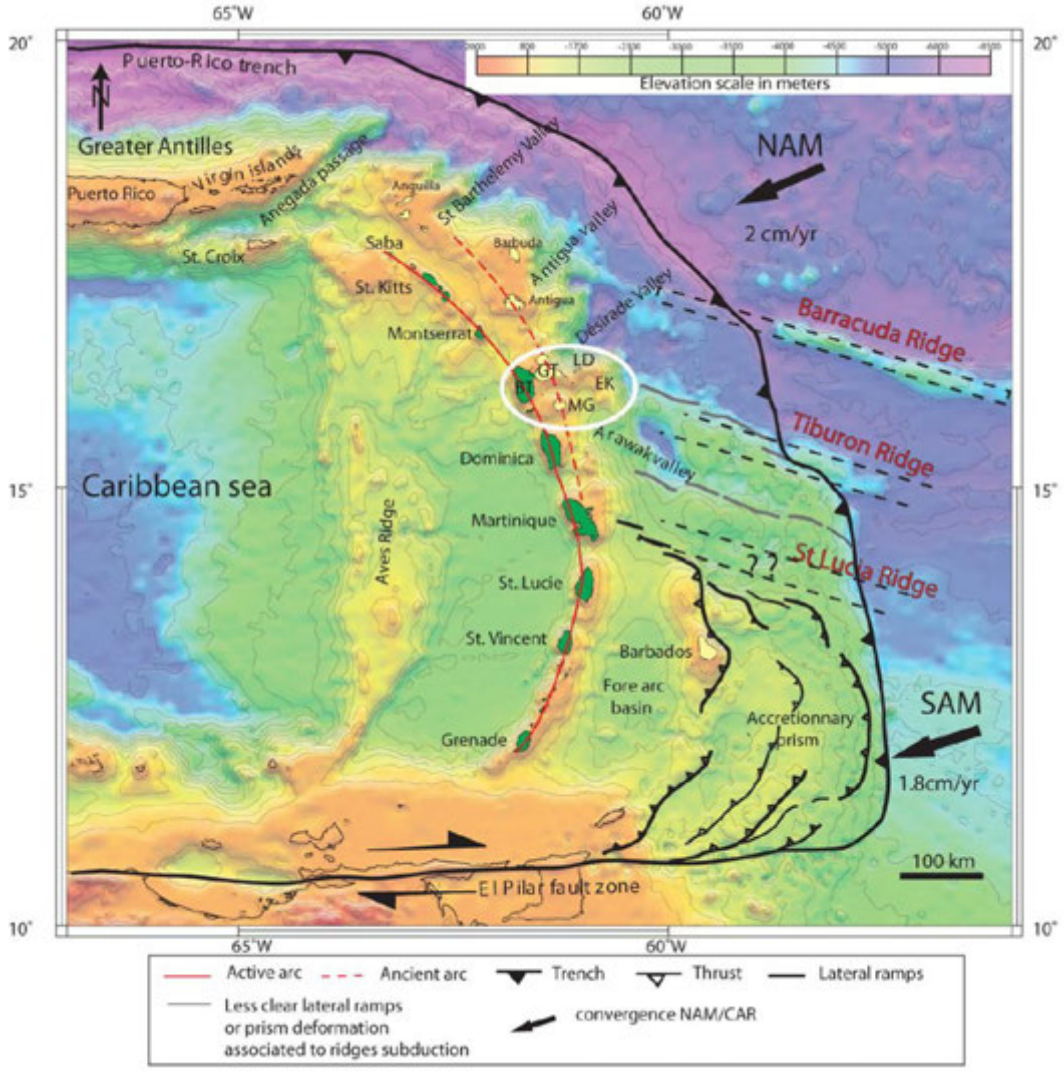


**Figure III-3 : Carte bathymétrique de la zone de subduction des Petites Antilles (De Min, 2014). Le cercle blanc localise l'archipel de Guadeloupe.**

Dans la partie Nord de l'arc, un régime tectonique en transtension s'exprime, le long de l'arc, d'une part par des failles décrochantes senestres et en échelon parallèles à la fosse et d'autre part par des grabens NE-SW et E-W perpendiculaires à la subduction en avant-arc (Feuillet, **2000**; Feuillet *et al.*, **2002**). Le partitionnement de la déformation disparaît vers le Sud à mesure que le front de subduction devient plus oblique.

A l'Est, l'arc externe a été actif de l'Eocène à l'Oligo-Miocène, puis a été recouvert d'un plateau calcaire d'âge Pliocène à Pleistocène moyen (Bouysse, **1983**; Bouysse & Garrabé, **1984**; Andreieff *et al.*, **1987**; Cornée *et al.*, **2012**; Münch *et al.*, **2014**).

A l'Ouest, l'arc interne concentre l'activité volcanique depuis le Miocène supérieur (Bouysse *et al.*, **1990**). Cependant, les îles volcaniques du Nord au Sud présentent une grande diversité pétrologique et géochimique (Brown *et al.*, **1977**; White & Dupré, **1986**; Turner *et al.*, **1996**; Macdonald *et al.*, **2000**; Labanieh, **2009**), et trois segments sont identifiés :

- la partie Nord de Saba à Montserrat, les laves sont d'affinité tholéiitique,
- la partie centrale de la Guadeloupe à la Martinique, les laves sont principalement calco-alcalines,
- enfin la partie Sud de Sainte-Lucie à Grenade, les laves appartiennent à la série alcaline.

La nature des laves des Petites Antilles varie principalement depuis des andésites à des dacites, cependant dans la partie Sud de l'arc des basaltes magnésiens ont été identifiés (Brown *et al.*, **1977**; Macdonald *et al.*, **2000**). Par ailleurs, le taux de production de magma varie également entre les différentes îles. Ce taux est supérieur dans les îles centrales (0,4 $km^3$/kyr) à celui des îles situées aux extrémités Nord et Sud (0,015 $km^3$/ky) (Wadge, **1984**).

## III.2. L'archipel de Guadeloupe

### III.2.1.Le contexte tectonique

L'archipel de Guadeloupe est très largement structuré par des réseaux de failles actives majoritairement normales, soit perpendiculaires soit parallèles au front de subduction, et identifiées à terre comme en mer (Feuillet, **2000**; Feuillet *et al.*, **2001**, **2002**, **2010**; Thinon *et al.*, **2010**; Corsini *et al.*, **2011**; Mathieu *et al.*, **2011**; Munch *et al.*, **2013**; Laigle *et al.*, **2013**; Lardeaux *et al.*, **2013**; De Min, **2014**; Leclerc *et al.*, **2014**; Legendre, **2018**). De nombreuses études ont montré l'importance de l'héritage structural, et de la réactivation tectonique (de failles à composante décrochantes passant à normales), dans le développement et le jeu des structures tectoniques actives (Bouysse, **1979**; Bouysse & Westercamp, **1990**; Feuillet *et al.*, **2002**, **2004**; Corsini *et al.*, **2011**; Lardeaux *et al.*, **2013**; De Min, **2014**; De Min *et al.*, **2015**; Legendre *et al.*, **2018**; Legendre, **2018**; Léticée *et al.*, **2019**; Leclerc & Feuillet, **2019**). Au vu du nombre important de failles actives, tant au niveau régional que local, certains auteurs proposent un contrôle tectonique de l'activité volcanique (Feuillet, **2000**; Feuillet *et al.*, **2001**, **2002**; Samper *et al.*, **2007**). A l'échelle de l'archipel quatre directions préférentielles de failles ont été mises en évidences (N30-N50, N80-N100, N120-N140 et N150-N180) et sont décrits ci-après (Figure III-4).

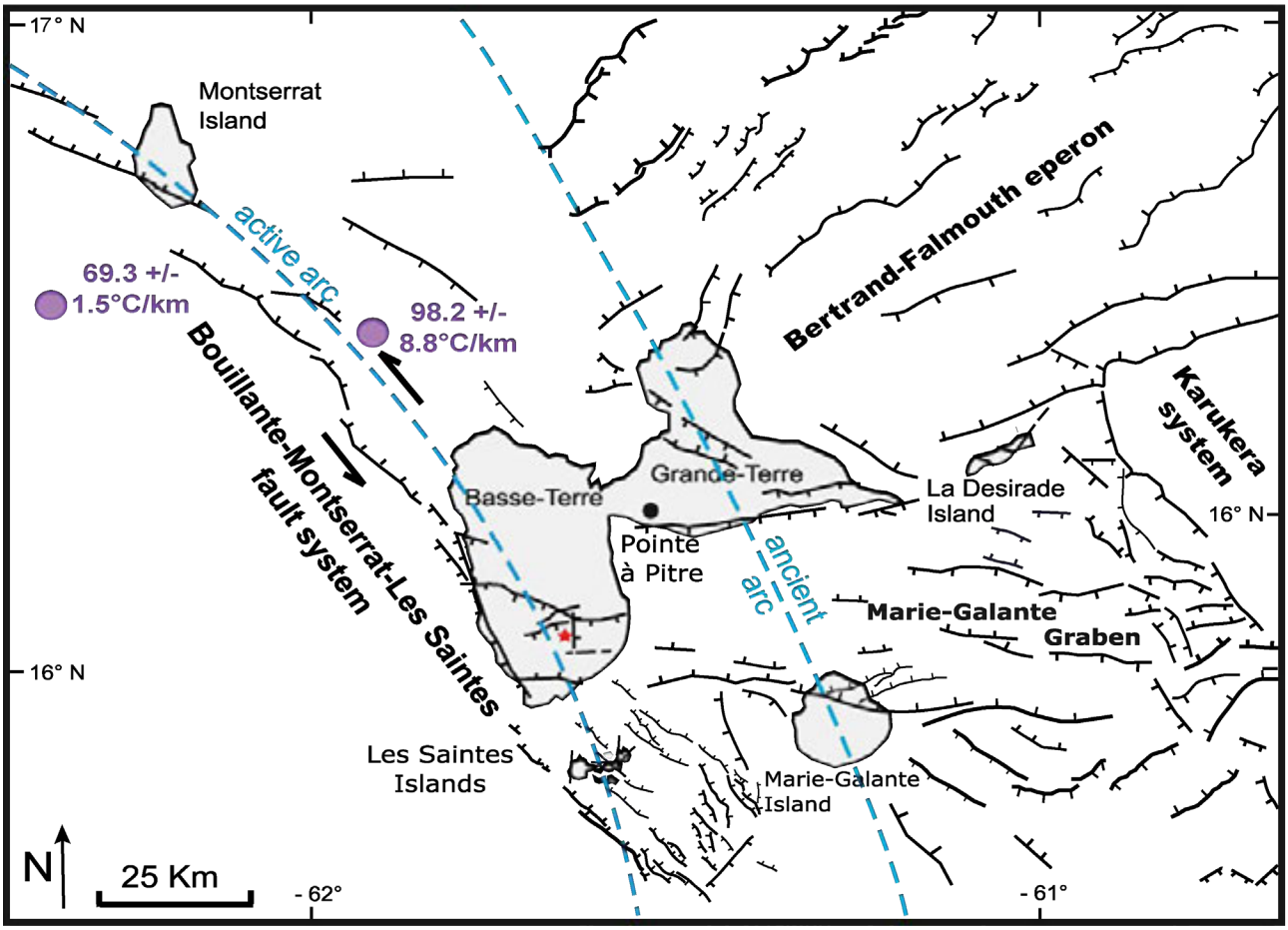


**Figure III-4 : Contexte structurale de l'archipel de Guadeloupe (modifiée d'après Feuillet et al., 2001, 2002, 2010; Corsini et al., 2011; Lardeaux et al., 2013; De Min, 2014; Leclerc et al., 2016; Verati et al., 2016). Les points violets correspondent aux mesures de flux de chaleur par Manga et al., 2012. L'étoile rouge localise le volcan actif de la Soufrière.**

*III.2.1.a. La direction N30-N50*

Cette direction de failles est perpendiculaire au front de subduction. Elle est principalement observable au niveau de l'éperon de Bertrand-Falmouth (aussi appelée vallée de la Désirade) (Figure III-4) formant des grabens et demi-grabens (Feuillet, **2000**; Feuillet *et al.*, **2001**). Au Nord de l'île de Grande-Terre ce système est interrompu par celui N120-N140. Elle passe à une direction N55-N60 au niveau de l'escarpement au Nord de la Désirade. Elle est visible également à la limite Sud-Est du plateau des Saintes et au Sud-Est du graben de Marie-Galante.

*III.2.1.b. La direction N80-N100*

Cette direction est perpendiculaire à l'arc. Elle est particulièrement visible au niveau du graben Est-Ouest de Marie-Galante. A l'Est, ce système recoupe l'éperon de Karukera pour se prolonger à l'Ouest jusqu'au Sud de l'île de Basse-Terre (Figure III-2-**B**), en lien avec le volcanisme actif (Feuillet *et al.*, **2002**). On peut également observer cette direction à terre sur l'île de Basse-Terre au niveau de la faille entre Bouillante et Capesterre d'orientation E-W à ESE-WNW.

*III.2.1.c. La direction N120-N140*

Cette direction est parallèle à l'arc. Ce système est marqué par le système Montserrat-Bouillante qui suit une orientation NW-SE à NNW-SSE de Saint-Kitts à la Dominique, bordant la côte Ouest de l'île de Basse-Terre. Il se compose d'un système de failles à composante décro-normales senestres organisées en échelon. Ce système montre une remarquable intersection avec la faille E-W de Bouillante-Capesterre (Calcagno *et al.*, **2012**). Au Sud de l'île de la Basse-Terre où se trouve le plateau insulaire des Saintes, le système Montserrat-Bouillante est interprété comme la prolongation jusqu'à la Dominique du système de failles du Roseau qui compose le système des Saintes (Feuillet *et al.*, **2010**, **2011**; Thinon *et al.*, **2010**). Elle forme un demi-graben entre l'île de Basse-Terre et la Dominique. On observe cette direction aussi du Nord-Ouest jusqu'à la pente Sud-Est de l'île de Grande-Terre. On retrouve également cette direction au Sud-Est de l'île de Marie-Galante.

*III.2.1.d. La direction N150-N180*

Cette direction est parallèle au front de subduction. Ce système marque particulièrement l'éperon de Karukera coupé à l'Ouest par les failles du système du graben de Marie-Galante et marqué à l'Est par la présence du prisme d'accrétion (Figure III-2-**B**, De Min, **2014**). Au niveau de l'île de Basse-Terre on observe cette direction structurale au niveau de la faille de Ty qui recoupe le volcan actif de la Soufrière. Enfin on retrouve également ce système au cœur du graben des Saintes dans sa partie Sud-Est.

On retrouve également ces quatre directions de failles majeures à terre au niveau des îles de l'archipel des Saintes, principalement à composante normales (Verati *et al.*, **2016**; Navelot *et al.*, **2018**).
Au niveau de l'île de la Désirade seul trois de ces systèmes de failles sont identifiés : N120-N140, N30-N50 et N80-N100 (Corsini *et al.*, **2011**; Lardeaux *et al.*, **2013**).

### III.2.2.Les complexes volcaniques de l'archipel

Dans l'archipel de Guadeloupe, l'activité volcanique la plus récente est concentrée dans l'arc interne, et se situe au niveau de l'île de Basse-Terre et de l'archipel des Saintes (Figure III-4). Ces îles volcaniques à l'Ouest se distinguent par leur relief important (altitude de 1467 m maximum à la Soufrière), qui contraste avec celui des îles de l'archipel à l'Est (altitude de 276 m à la Grande-Montagne de l'île de la Désirade, 30 à 50 m en moyenne) : Grande-Terre, Marie-Galante et la Désirade. Des mesures de gradients de température ont été faites dans les Petites Antilles, au niveau de l'arc actif aux abords de la Guadeloupe les données obtenues sont comprises entre 69,3 ± 1,5°C/km et 98,2 ± 8,8°C/km (Manga et al., 2012, Figure III-4), et illustrent un flux de chaleur régional élevé en lien avec l'activité magmatique.

# Contexte géologique

En parallèle d'une activité tectonique complexe, l'île de la Basse-Terre se distingue par un alignement de volcans d'orientation NNW-SSE, qui aurait progressivement migré vers le Sud. Cette migration a été attribuée par Bouysse et Westercamp (**1990**) à l'entrée en subduction de la ride Tiburon il y a 2 Ma (Figure III-3).

Une première carte géologique de l'ensemble de l'île de la Basse-Terre a été établie dans les années 1960 (De Reynal de Saint-Michel, **1966**), elle se basait sur une étude pétrographique des laves et a permis de définir différentes unités volcaniques. Dans les années 1980 des études géochimiques et géochronologiques ont permis d'améliorer grandement cette carte dans la partie Sud de la Basse-Terre (Briden *et al.*, **1979**; Blanc, **1983**; Bouysse *et al.*, **1985a**, **c**, **1988**; Boudon *et al.*, **1988**; Gadalia *et al.*, **1988**) et au niveau de l'archipel des Saintes (Jacques *et al.*, **1984**; Jacques & Maury, **1988**). Plus récemment des études structurales et une nouvelle base de données géochronologiques ont permis de mettre en évidence la présence de cinq principaux complexes volcaniques sur l'île de la Basse-Terre et de deux phases volcaniques principales dans l'archipel des Saintes (Carlut *et al.*, **2000**; Samper *et al.*, **2007**, **2009**; Mathieu, **2010**; Mathieu *et al.*, **2013**; Zami *et al.*, **2014**; Ricci *et al.*, **2015a**, **b**, **2017**, **2018**; Verati *et al.*, **2016**).

Suite à l'évolution significative des méthodes de datations géochronologiques sur les roches volcaniques, de nouvelles études (Samper *et al.*, **2007**, **2009**; Zami *et al.*, **2014**; Ricci *et al.*, **2015a**, **b**, **2017**) ont remis en cause les précédentes données géochronologiques (Briden *et al.*, **1979**; Blanc, **1983**; Bouysse *et al.*, **1985a**, **c**; Gadalia *et al.*, **1988**; Carlut *et al.*, **2000**). Les premiers résultats de datations avaient été acquis, dans les années 1980-90, sur la roche totale ou la mésostase, sans tenir compte de la probable altération du matériel utilisé, pouvant avoir pour conséquence un lessivage du potassium et/ou une incorporation et/ou une perte d'argon (Samper, **2007**; Ricci, **2014**). Bouysse et al. (**1985c**) avaient eux-mêmes souligné que les données radiochronologiques obtenues en Guadeloupe étaient sujettes à révision et que le nombre de mesures n'était pas suffisant. C'est pourquoi seules les données de datations K-Ar effectuées sur une mésostase séparée et liées à des mesures de paléomagnétisme cohérentes, mais aussi dont la perte au feu est inférieure à 2%, sont aujourd'hui prises en compte, afin de contraindre l'évolution volcanique de l'île de la Basse-Terre (Blanc, **1983**; Carlut *et al.*, **2000**; Samper *et al.*, **2007**, **2009**; Ricci *et al.*, **2015a**, **b**, **2017**, **2018** ; Figure III-5). Ce même travail de tri doit être appliqué au niveau des âges obtenus sur l'archipel des Saintes afin de ne conserver que les datations les plus récentes (Zami *et al.*, **2014**) faites sur la mésostase séparée contrairement aux précédentes mesures (Jacques *et al.*, **1984**) faites sur la roche totale (Figure III-5).

Du volcanisme sous-marin a également été identifié en mer au niveau de la zone Ouest de l'île de la Basse-Terre, mais les corrélations avec les complexes volcaniques à terre sont délicates du fait du fort impact de l'altération hydrothermale sur les roches et les résultats de datation obtenus (Samper, **2007**).

La majorité des études se sont concentrées sur la partie Sud de l'île de la Basse-Terre en raison de la présence du volcanisme actif et des risques induits par celui-ci. Les coulées de laves occupent un tiers de l'île de la Basse-Terre (Samper, **2007**). Les conditions d'affleurement sont restreintes du fait des conditions climatiques tropicales induisant le développement d'une couverture végétale dense accompagnée d'un sol épais (jusqu'à 70 m), de la présence de reliefs escarpés et d'une érosion différentielle des massifs volcaniques (Samper, **2007**; Mathieu, **2010**; Ricci, **2014**).

Dans les parties suivantes, seuls les édifices volcaniques à terre sont présentés, dont la synthèse des données chronologiques est présentée en Figure III-5.
Une synthèse des données géochimiques disponibles de ce secteur a été récemment réalisée par Navelot (**2018** ; Figure III-6). Elle confirme l'appartenance du volcanisme de la Guadeloupe majoritairement à la série calco-alcaline avec une différenciation depuis des basaltes jusqu'à des dacites (Jacques *et al.*, **1984**; Boudon *et al.*, **1988**; Samper *et al.*, **2007**, **2009**; Ricci, **2014**; Zami *et al.*, **2014**; Ricci *et al.*, **2017**).

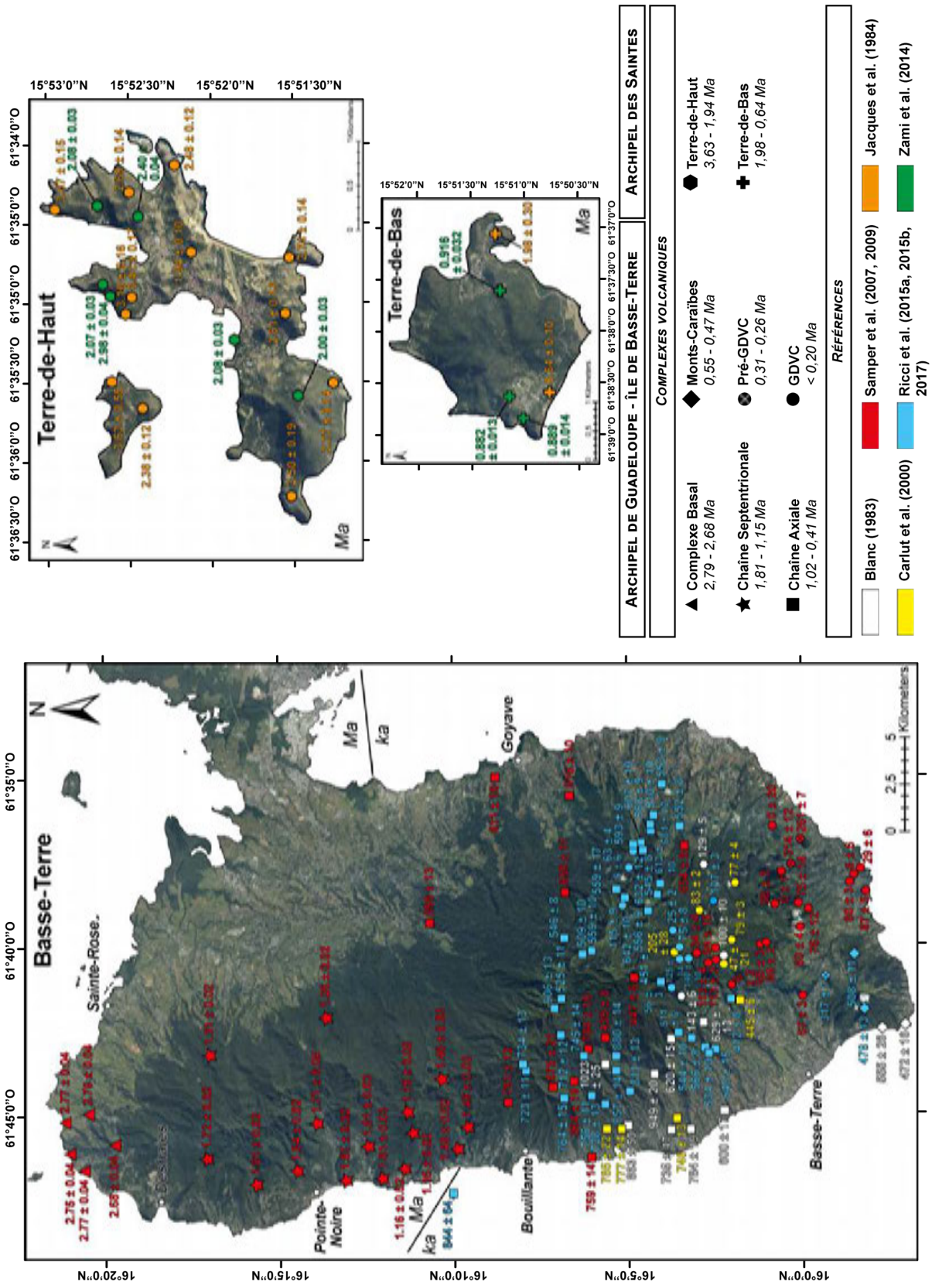


**Figure III-5 : Synthèse des données chronologiques K-Ar obtenues sur mésostase séparée disponibles sur les îles de la Basse-Terre, de Terre-de-Haut et de Terre-de-Bas, illustrant la répartition des mesures et la localisation des différents complexes volcaniques identifiables.**

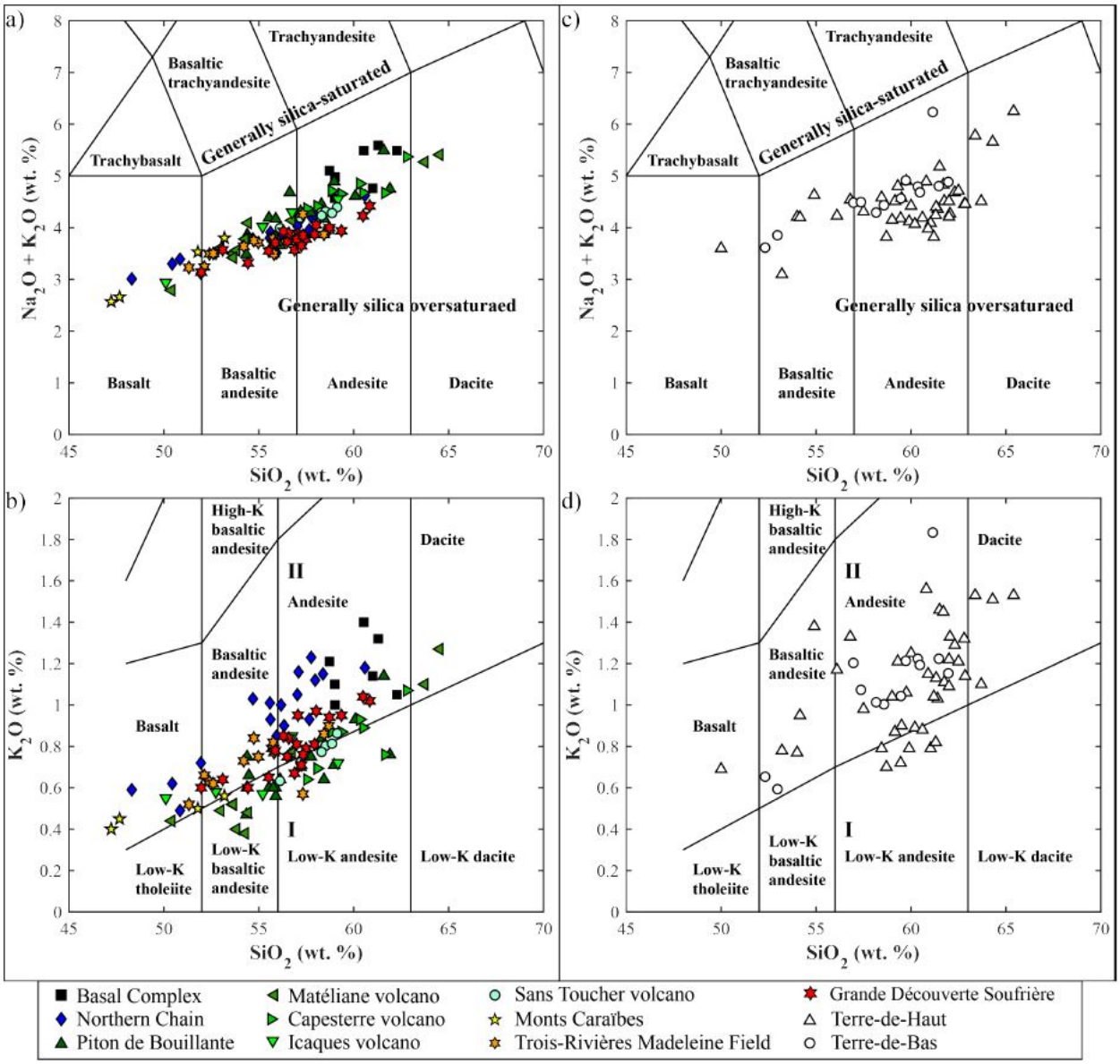


**Figure III-6 : Synthèse des données géochimiques des coulées de laves du volcanisme récent de la Guadeloupe (Navelot, 2018). a) et b) échantillons issus de l'île de Basse-Terre (Samper *et al.*, 2009; Ricci, 2014; Ricci *et al.*, 2017) ; c) et d) échantillons issus de l'archipel des Saintes (Jacques *et al.*, 1984; Zami *et al.*, 2014), I: calc-alkaline series, II: high-K calc-alkaline series, II : . a) et c) présentent le diagramme silice-alcalins d'après Bas et al. (1986) ; b) et d) présentent le diagramme silicium-potassium d'après Peccerillo and Taylor (1976).**

*III.2.2.a. Le Complexe Basal*

Le Complexe Basal est le complexe volcanique situé le plus au Nord, il s'étend de Sainte-Rose à Deshaies. Ce complexe est le moins étudié car souvent décrit comme une zone intensément altérée et érodée, dont les structures volcaniques sont peu reconnaissables rendant difficile sa datation (Mathieu, **2010**; Ricci, **2014**). Son âge a malgré tout été estimé entre 2,79 ± 0,04 et 2,68 ± 0,04 Ma

(Samper *et al.*, **2007**). Il se compose de laves massives andésitiques sub-aériennes très érodéees et de quelques dômes volcaniques à peine mieux préservés.

De nouvelles données ont été acquises sur ce complexe au cours de ce travail de thèse et seront présentées dans le chapitre IV.

*III.2.2.b. La Chaîne Septentrionale*

Ce complexe se situe au Sud du Complexe Basal et s'étend sur le tiers de l'île de la Basse-Terre, dont l'âge est estimé entre 1,81 ± 0,03 et 1,15 ± 0,02 Ma (Samper et al., 2007). L'activité volcanique a été dominante au Nord avant de migrer vers le Sud. Il se compose de coulées de lave andésitique à basaltique, les plus riches en K avec le Complexe Basal qui les distingue des autres complexes (Dagain, **1981**, Figure III-6). La présence d'un dôme volcanique au niveau des Mamelles ainsi que des dépôts de nuées ardentes est également à souligner. L'âge du dôme des Mamelles reste encore inconnu aujourd'hui.

*III.2.2.c. La Chaîne Axiale*

L'activité volcanique poursuit sa migration vers le Sud au niveau de la Chaîne Axiale, datée entre 1023 ± 25 et 435 ± 8 ka (Blanc, **1983**; Carlut *et al.*, **2000**; Samper *et al.*, **2007**; Ricci *et al.*, **2015a**, **b**, **2017**). L'alignement des édifices volcaniques se trouve à présent être orienté selon la direction WNW-ESE, semblable à la direction du système de failles Bouillante-Montserrat (Feuillet *et al.*, **2002**; Komorowski *et al.*, **2005**; Mathieu *et al.*, **2013**). Ce système se compose principalement de coulées de lave et de hyaloclastites, bien que des dépôts pyroclastiques et d'avalanches de débris aient également pu être identifiés en dépit de l'érosion.

Certains auteurs différencient dans la partie Nord-Ouest de cette chaîne la province volcanique de Bouillante active entre 1023 ± 25 et 746 ± 13 ka et l'interprètent comme la succession d'évènements sous-marin et sub-aérien, dont les laves sont très différenciées (Blanc, **1983**; Gadalia *et al.*, **1988**; Carlut *et al.*, **2000**; Samper *et al.*, **2007**; Bouchot *et al.*, **2010**; Ricci *et al.*, **2015a**). Cette distinction a surtout été faite suite à l'identification d'un potentiel géothermal au niveau de Bouillante dans les années 1980 et donc le piton de Bouillante a été étudié en détail. Pour la suite du manuscrit cette province sera inclue dans la Chaîne Axiale, comme le propose les synthèses géochronologiques les plus récentes (Samper *et al.*, **2007**).

*III.2.2.d. Le Complexe de la Grande-Découverte et de Trois-Rivière-Madeleine*

Le Complexe de la Grande-Découverte (GDVC) témoigne du volcanisme actif aujourd'hui, qui a débuté il y a 205 ± 28 ka (Blanc, **1983**; Carlut *et al.*, **2000**; Samper *et al.*, **2007**, **2009**; Ricci *et al.*, **2017**). Il se compose de coulées de laves andésitiques et de coulées pyroclastiques, et plus récemment des dépôts de ponces (Boudon *et al.*, **1988**; Komorowski *et al.*, **2002**, **2005**). Trois phases volcaniques principales y ont été identifiées :

La première phase définit le complexe de Grande Découverte actif entre 200 et 42 ka. Son axe volcanique est orienté selon la direction Est-Ouest, semblable à celle du graben de Marie-Galante, et leur activité pourrait être reliée (Feuillet *et al.*, **2001**). La seconde phase témoigne de l'activité du volcan Carmichaël entre 42 et 11,5 ka, qui s'estompe suite à deux évènements majeurs d'effondrement de son flanc ouest datés à 13,5 et 11,5 ka respectivement et produisant une importante avalanche de débris (Boudon *et al.*, **1988**, **1992**; Komorowski *et al.*, **2002**). La troisième phase a débuté il y a 8500 ans (Blanc, **1983**) au cœur de la dépression post-effondrement et accueille à présent le dôme actif de la Soufrière dont la mise en place a été datée à 1535 AD (Feuillet *et al.*, **2002**; Komorowski *et al.*, **2002**; Semet *et al.*, **2002**; Boudon *et al.*, **2003**).

Cependant des échantillons localisés au Sud de ce complexe montrent un âge bien plus ancien, d'où l'appellation « pré-GDVC » (Figure III-5). Leur origine est incertaine, ils pourraient très bien appartenir à la Chaîne Axiale et auraient pu avoir été recouverts postérieurement par les formations GDVC.

Au cœur de GDVC une distinction est régulièrement faite avec un second volcanisme très récent plus au Sud nommé Trois-Rivière-Madeleine (TRMF). Il se situe entre GDVC et les Monts-Caraïbes, son activité aurait débuté il y a 100 ka (Samper *et al.*, **2009**). Il présente le second risque volcanique du secteur. Il se compose de coulées de lave et de dôme associés à de rares dépôts pyroclastiques et de scories. Pour la suite de ce manuscrit TRMF sera associé à GDVC.

*III.2.2.e. Le Monts-Caraïbes*

Il s'agit d'un complexe situé à l'extrémité Sud de l'île de la Basse-Terre, et daté entre 555 ± 26 et 472 ± 16 ka (Blanc, **1983**; Ricci *et al.*, **2017**). Il est interprété par certains auteurs comme étant d'origine sous-marine et phréatomagmatique, avec des stades finaux composés d'éruptions aériennes (Westercamp & Tazieff, **1980**; Boudon *et al.*, **1989**; Mathieu, **2010**; Ricci *et al.*, **2017**, **2018**). Son fonctionnement est contemporain de celui de la Chaîne Axiale.

*III.2.2.f. L'archipel des Saintes*

L'archipel se situe entre l'île de la Basse-Terre et la Dominique. Il est constitué de neuf îlots dont seulement deux sont habités : Terre-de-Haut et Terre-de-Bas.

Les études les plus récentes ont mis en évidence deux phases volcaniques principales : une phase majeure au sein de Terre-de-Haut datée entre 2,98 ± 0.04 et 2,00 ± 0.03 Ma et une phase de construction de Terre-de-Bas, rapide et datée entre 0,916 ± 0,032 et 0,882 ± 0,013 Ma. La migration de l'activité volcanique à l'Ouest est probablement contrôlée par le graben des Saintes (Zami *et al.*, **2014**). Le volcanisme de Terre-de-Haut est contemporain de celui émis dans le Complexe Basal, alors que celui de Terre-de-Bas est relié temporellement à la Chaîne Axiale.

### III.2.3.L'érosion

Si les processus volcaniques et sédimentaires sont à l'origine de la construction de l'arc insulaire des Petites-Antilles, les processus érosifs sont responsables de la destruction de cet arc. Ils sont donc un élément important dans l'évolution géologique de cette région.

L'érosion est un phénomène majeur responsable de l'évolution morphologique de la surface de la Terre, sous l'action des agents de la géodynamique externe. Deux grands types de processus complémentaires sont en interaction permanente : l'altération chimique (fonction de la nature des matériaux) et l'érosion mécanique (corrélable avec la topographie ou la tectonique). Ils conduisent à la destruction du matériel rocheux, à son transport puis à l'accumulation de débris.
Les principaux types d'érosions identifiés en Guadeloupe sont (Ricci, **2014**) : 1) l'érosion par l'eau (chimique et mécanique) qui est fonction du débit hydrique, des pentes et de la composition des eaux supergènes, 2) l'érosion éolienne (mécanique) qui est dépendante de la nature du sol, de la topographie et de la couverture végétale, 3) l'érosion hydrothermale (chimique) qui est généralement fréquente en contexte volcanique sous l'effet de la circulation souterraine de fluides chauds chargés en minéraux dissous, dont l'efficacité est également fonction du type de lithologies traversées.
Il faut également souligner le rôle d'évènements « catastrophiques » (à très courte échelle de temps mais avec d'importants volumes déplacés) qui contribuent à l'évolution régionale du relief : effondrement de flancs de volcans, avalanches de débris, glissements de terrain, cyclones, tempêtes tropicales (Deplus *et al.*, **2001**; Boudon *et al.*, **2007**; Allemand *et al.*, **2014**). A de longues échelles de temps, le contexte géodynamique (i.e. subduction) et le contexte climatique (i.e. tropical) restent les facteurs dominants (White & Blum, **1995**).

Des études récentes (Rad *et al.*, **2006**, **2007**, **2011**, **2013**; Samper *et al.*, **2007**; Dessert *et al.*, **2015**; Ricci *et al.*, **2015a**) ont cherché à estimer les taux d'érosion, qui affectent l'île de Basse-Terre en Guadeloupe, afin de comprendre l'évolution des reliefs.
Ils couplent différentes méthodes de quantification de l'érosion : évaluation des taux de dénudation par l'étude de la teneur en sédiments, du granoclassement et des analyses chimiques et isotopiques des sédiments dans les rivières ; estimation du bilan de masse entre les phases solides et les phases dissoutes à partir de la composition des particules dissoutes dans l'eau et du débit des rivières ; des mesures de température, pH, conductivités et d'isotopes sur la collecte des eaux de pluie, de sources thermales, de rivières, de roches et de sols ; mesures de l'épaisseur des sols et de l'âge du bassin versant ; élaboration de modèles numériques couplant des données géomorphologiques et des données géochronologiques à l'échelle de chaque édifice volcanique.

Les mesures ponctuelles ne permettent pas de rendre compte de l'évolution du comportement de l'érosion sur le long terme, mais on obtient ainsi un taux d'érosion minimal. Par ailleurs, les études géomorphologiques et les reconstructions de l'évolution des reliefs s'appuient sur la topographie actuelle mais elles doivent aussi intégrer la connaissance des conditions initiales de surface (pré-érosionnelles). Or celles-ci sont rarement bien préservées au sein des complexes volcaniques les plus anciens, l'estimation du taux d'érosion est alors également minimisée.

L'île de la Basse-Terre, du fait de son relief et des conditions climatiques tropicales, est sujette à une pluviométrie importante (Ricci, **2014**):

- Du côté Ouest, appelée aussi côte-sous-le-vent : 2500 mm/an
- Du côté Est, appelée aussi côte-au-vent (ou Capesterre) : 4600 mm/an

La pluviométrie couplée aux données géochronologiques (Blanc, **1983**; Carlut *et al.*, **2000**; Samper *et al.*, **2007**, **2009**; Ricci *et al.*, **2015a**, **b**, **2017**) permet d'estimer l'érosion au cours des derniers 3 Ma, et différentes approches ont été proposées :

- Samper et al. (**2007**) ont proposé une reconstruction numérique des massifs volcaniques, suite aux effondrements de flancs de volcans, qui permet d'estimer le taux d'érosion dans la partie centrale de la Basse-Terre compris entre 1250 t/km²/an pour les derniers 600 ka (au niveau de la Chaîne Axiale) et 5250 t/km²/an au cours des derniers 200 ka (au niveau de GDVC).
- Rad et al. (**2006, 2007, 2011a, 2013**) estiment une altération mécanique comprise entre 800 et 4000 t/km²/an et une érosion chimique comprise entre 200 et 1080 t/km²/an, soit un taux d'érosion total compris entre 900 et 4120 t/km²/an. Plus localement le taux d'érosion moyen au niveau de la côte Est (Capesterre-Carbet) est estimée entre 430 et 2000 t/km²/an et sur la côte Ouest (Vieux-Habitants) entre 100 et 200 t/km²/an. Les deux paramètres principaux qui contrôlent le taux d'érosion sont l'hydrothermalisme et l'âge des édifices volcaniques. Les valeurs proposées s'expliquent par l'impact de l'hydrothermalisme sur les roches, qui combine une interaction fluide-roche à haute-température, la circulation de fluides acides dérivés de fluides magmatiques et l'infiltration de ses fluides à travers des formations poreuses. Cependant ce bilan reste sous-estimé dans les zones volcaniques les plus anciennes.
- Enfin Ricci et al. (**2015a**), en se basant sur les données géochronologiques et sur un modèle de reconstruction de la topographie, proposent un nouveau taux d'érosion moyen compris entre 610 et 1350 ± 550 t/km²/an pour la partie Sud de la Basse-Terre. La morphologie et les lithologies volcaniques ont un impact significatif sur les taux d'érosion observés, comparé à l'effet de barrière induit par les reliefs qui serait négligeable. Cette méthode est difficilement applicable pour les édifices volcaniques dont la morphologie initiale est peu préservée et présentant une histoire volcanique complexe (Ricci, **2014**).

# Chapitre IV : Evolution tectono-métamorphique de la croûte supérieure de l'arc volcanique en Guadeloupe : définition de l'état thermique de référence depuis 4 Ma

*Face Sud du Gros Morne à Deshaies, Basse-Terre*

# Chapitre IV

## IV.1. Préambule

Depuis les travaux fondamentaux de Miyashiro (**1961**), Oxburgh et Turcotte (**1970**) et Ernst (**1973**, **1976**), les zones de subduction sont reconnues comme des lieux privilégiés pour le développement des processus métamorphiques et des transformations structurales associées :

- dans la plaque plongeante, les conditions de haute-pression et basse-température sont atteintes et s'expriment par la succession des faciès des Schistes Bleus et des Eclogites en fonction de la profondeur (Figure IV-1) ;
- à l'inverse dans la plaque supérieure, le développement d'un arc magmatique est à l'origine d'importants transferts de fluides et de chaleur (« hydrothermalisme *sensu-lato* ») conduisant à la mise en place de conditions de moyenne à basse-pression et haute-température, depuis la base jusqu'au sommet de la croûte d'arc, se succèdent les faciès des Granulites, des Amphibolites, des Amphibolites à épidote, des Schistes-Verts, de Prehnite-Pumpellyite (appelé aussi « *sub-Greenschist* ») et des Zéolites (Figure IV-1).

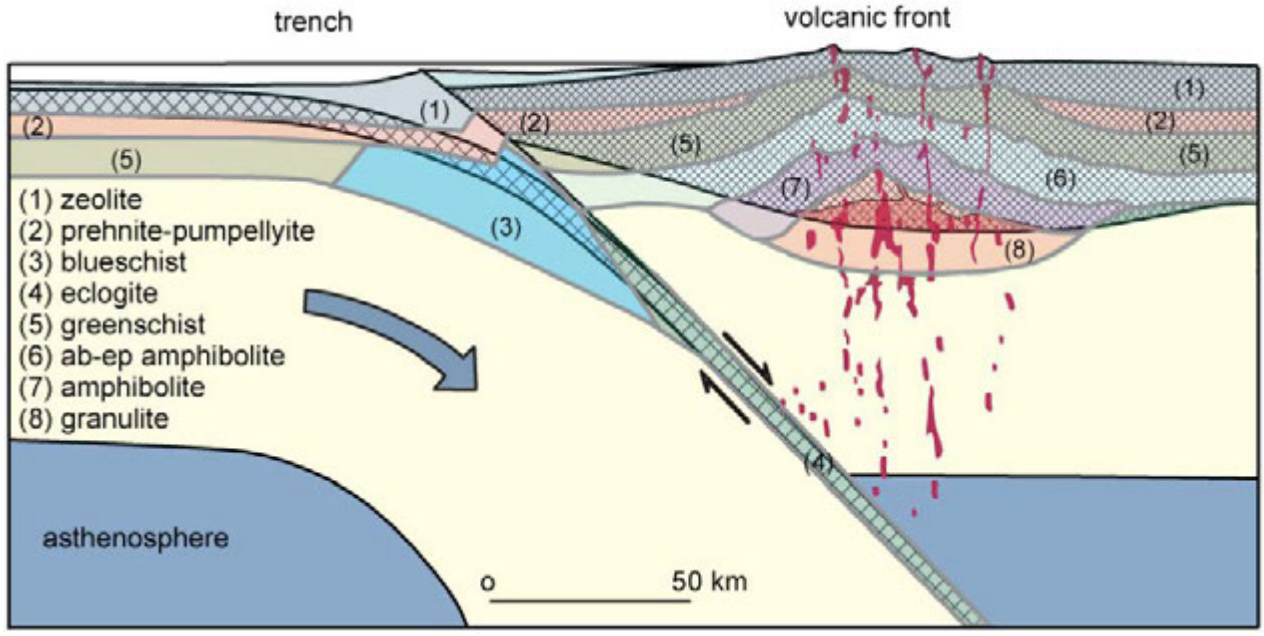


**Figure IV-1 : Coupe transversale schématique d'un arc insulaire comprenant la plaque plongeante et la plaque supérieure avec l'arc volcanique. Les différents faciès métamorphiques se développent et se localisent ainsi selon le taux de convergence, l'âge de l'arc et la nature de la lithosphère subduite. D'après Ernst, 1976.**

Cette dualité des conditions métamorphiques entre plaque inférieure et plaque supérieure d'une zone de subduction est décrite sous le terme de « *paired metamorphic belts* » (Miyashiro, **1961**; Brown, **2010**). Comme présenté dans la synthèse du contexte géologique de notre étude (en chapitre III), l'arc récent des Petites Antilles a fait l'objet de nombreuses investigations géophysiques, sismo-tectoniques, magmatiques (géochimie, volcanologie), géochronologiques, sédimentologiques et

géomorphologiques. Jusqu'à présent aucune trace d'un métamorphisme régional et d'une déformation ductile associée n'y a été identifiée. C'est pour tenter de mettre en évidence ce type de métamorphisme d'arc en Guadeloupe que nous avons choisi de travailler sur le Complexe Basal, localisé au nord de la Basse-Terre. C'est en effet dans ce complexe que sont décrits les terrains les plus anciens (Samper *et al.*, **2007**) et, vu d'une part des taux d'érosion calculés (Samper *et al.*, **2007**; Rad *et al.*, **2013b**; Ricci *et al.*, **2015a**) et d'autre part de l'importante tectonique active en extension qui affecte l'île de la Basse-Terre (Feuillet *et al.*, **2001**; De Min, **2014**), ce Complexe Basal permet d'observer les parties les plus érodées et potentiellement les plus "exhumées" de l'arc récent. Ce qui revient à dire que le Complexe Basal permet d'étudier une partie plus "profonde" de la croûte supérieure de l'arc de la Guadeloupe. Cette partie de l'île a été peu étudiée jusque-là, et est décrite comme fortement altérée, avec des structures volcaniques difficilement identifiables (Mathieu, **2010**; Ricci, **2014**). Pour cette étude, il a été nécessaire d'établir une carte géologique à haute-résolution, en différenciant les lithologies observées sur la base de critères géochimiques (majeurs et traces) et pétrographiques. Nous avons également produit une carte structurale détaillée et une carte des minéralisations secondaires, c'est-à-dire post-volcaniques, affectant les différentes lithologies. L'ensemble de nos résultats est présenté sous la forme de deux publications, l'une acceptée (sous presse, https://doi.org/10.1051/bsgf/2019011) au *Bulletin de la Société géologique de France* et l'autre publiée dans la revue *Lithos* en 2018 (https://doi.org/10.1016/J.LITHOS.2018.08.005).

Les principaux résultats de nos études sont les suivants :

- Découverte d'un métamorphisme d'arc dans la plaque supérieure de la zone de subduction des Petites Antilles avec trois stades de transformations indiquant le refroidissement progressif de la croûte de l'arc : haute-température (*greenschist to sub-greenschist facies*), moyenne température (*zeolite facies*), basse-température (altération de sub-surface). Les conditions P-T calculées du pic métamorphique correspondent à la transition entre les faciès à Prehnite-Actinote (sans pumpellyite) et Schistes Verts (0,6-2 kbar et 250-300°C) ;
- Découverte de structures tectoniques ductiles (schistosité de type pression-dissolution), à des niveaux crustaux peu profonds dans le système d'arc volcanique de Guadeloupe ;
- Production d'une carte géologique réactualisée de la partie Nord de l'île de la Basse-Terre ;
- Nouvelle définition de la limite tectonique entre les complexes volcaniques du Complexe Basal et de la Chaîne Septentrionale, par la datation du Gros Morne de Deshaies par la méthode $^{40}Ar/^{39}Ar$ (4.28 ± 0.68 Ma) ;
- Proposition d'un modèle de transfert de la chaleur et des fluides à l'intérieur des niveaux crustaux peu profonds de l'arc volcanique actif de Guadeloupe, impliquant des transferts verticaux et latéraux et une transition "fragile-ductile" estimée à 3-4 km de profondeur.

Il est important de souligner que :

- Les fluides hydrothermaux contrôlent la nature des réactions minéralogiques (ce sont principalement les pyroxènes et les amphiboles des laves qui sont pseudomorphosés), la cinétique de ces transformations et la formation des couloirs de schistosité par le mécanisme de dissolution-recristallisation ;
- Les paramètres intensifs du métamorphisme d'arc calculés définissent un paléo-gradient compatible avec le gradient conductif actuel mesuré et qui est compris entre 70 et 100°C/km (Manga *et al.*, **2012**).

En ce qui concerne les applications à la géothermie, nous montrons ainsi que le gradient géothermique est constant depuis 4 Ma et qu'il constitue ainsi l'état de référence, c'est à dire l'état « standard », qui devra être perturbé afin de conduire à la constitution d'une « ressource géothermale ».

## IV.2. Article 1 - Tectono-metamorphic evolution of shallow crustal levels within active volcanic arcs. Insights from the exhumed Basal Complex of Basse-Terre (Guadeloupe, French West Indies)

Alexiane Favier[1-2], Jean-Marc Lardeaux[2-3], Lucie Legendre[1], Chrystele Verati[2], Melody Philippon[1], Michel Corsini[2], Philippe Münch[4], Sandra Ventalon[5]

1: UMR 5243 Géosciences Montpellier, Université des Antilles-CNRS-Université de Montpellier

2: UMR 7329 Geoazur, Université de Nice Sophia Antipolis-CNRS

3: Czech Geological Survey, Centre for Lithospheric Research

4: UMR 5243 Géosciences Montpellier, Université de Montpellier-CNRS-Université des Antilles

5 : UMR 8187 Laboratoire d'Océanologie et de Géosciences, Université de Lille

Cet article a été accepté pour publication en aout 2019 au journal *Bulletin de la Société Géologique de France* (https://doi.org/10.1051/bsgf/2019011).

BSGF - Earth Sciences Bulletin 2019, 190, 10
© A. Favier *et al.*, Published by EDP Sciences 2019
https://doi.org/10.1051/bsgf/2019011

BSGF
Earth Sciences Bulletin
Available online at:
www.bsgf.fr

OPEN ACCESS

# Tectono-metamorphic evolution of shallow crustal levels within active volcanic arcs. Insights from the exhumed Basal Complex of Basse-Terre (Guadeloupe, French West Indies)

Alexiane Favier[1,2,*], Jean-Marc Lardeaux[2,3], Lucie Legendre[1], Chrystele Verati[2], Melody Philippon[1], Michel Corsini[2], Philippe Münch[4] and Sandra Ventalon[5]

[1] UMR 5243 Géosciences Montpellier, Université des Antilles-CNRS-Université de Montpellier, Campus de Fouillole, 97159 Pointe à Pitre Cedex, Guadeloupe, France
[2] UMR 7329 Geoazur, Université de Nice Sophia Antipolis, Observatoire de la Côte d'Azur, 250, rue Albert Einstein, Sophia Antipolis, 06560 Valbonne, France
[3] Czech Geological Survey, Centre for Lithospheric Research, Klárov 3, 118 21 Prague 1, Czech Republic
[4] UMR 5243 Géosciences Montpellier, Université de Montpellier-CNRS-Université des Antilles, Place Eugène Bataillon, 34095 Montpellier, France
[5] UMR 8187 Laboratoire d'Océanologie et de Géosciences, Université de Lille, Avenue Paul Langevin, 59655 Villeneuve d'Ascq, France

Received: 7 March 2019 / Accepted: 18 August 2019

**Abstract** – In order to decipher the tectono-metamorphic evolution of shallow crustal levels of the active volcanic arc of the Guadeloupe archipelago (Lesser Antilles) we present new geochemical, geochronological, mineralogical and structural investigations of the so-called Basal Complex, the oldest and most eroded volcanic complex of Basse-Terre in Guadeloupe. Based on geochemical and mineralogical criteria we propose an updated geological map of this northern area of Basse-Terre. Using $^{40}Ar$–$^{39}Ar$ geochronology we demonstrate first that the eroded "Gros Morne" of Deshaies belong to the Basal Complex, and second that this complex is characterized by 4.3 to 2 Ma old volcanism. Structural analysis reveals a long-lived deformation history with the development through time of N80-N100 schistose zones; N110-N140 and N160-N10 oriented hydrothermal breccias and N140-N150 brittle normal faults. The boundary between the Basal Complex and the southernmost Septentrional Chain corresponds to a series of faults with N 150° and N 50° main directions. Detailed mineralogical and petrological investigations, including thermodynamic modeling, allow the identification of three phases of post-magmatic mineralogical transformations with first a high-temperature stage under Greenschist to sub-Greenschist facies conditions (0.6–2 kbar for 250–300 °C), a re-equilibration under Zeolite facies conditions and finally a sub-surface alteration. The consistency between P–T conditions of metamorphism and the present day measured geothermal gradient demonstrates that the metamorphic pattern is the record of hydrothermal fluids circulation during building and cooling of the Lesser Antilles magmatic arc. The tectono-metamorphic evolution recognized in the Basal Complex enables us to propose a conceptual model for heat and fluid transport within shallow crustal levels of the Guadeloupe active volcanic arc.

**Keywords:** arc-related metamorphism / Lesser Antilles / Guadeloupe / Basal Complex / tectono-metamorphic evolution / hydrothermal fluids

**Résumé – Évolution tectono-métamorphique des niveaux superficiels de la croûte dans les arcs volcaniques actifs. Exemple du Complexe Basal exhumé de Basse-Terre (Guadeloupe, Antilles françaises).** Afin de décrypter l'évolution tectono-métamorphique des niveaux crustaux peu profonds de l'arc volcanique actif de l'archipel de la Guadeloupe (Petites Antilles), nous présentons de nouvelles investigations géochimiques, géochronologiques, minéralogiques et structurales du Complexe Basal, le plus ancien et le plus érodé des complexes volcaniques de Basse-Terre en Guadeloupe. Sur la base de critères géochimiques et minéralogiques, nous proposons une carte géologique actualisée de cette zone nord de la Basse-Terre. En utilisant la géochronologie $^{40}Ar$–$^{39}Ar$ nous démontrons d'abord que le « Gros Morne »

*Corresponding author: favier@geoazur.unice.fr

This is an Open Access article distributed under the terms of the Creative Commons Attribution License (http://creativecommons.org/licenses/by/4.0), which permits unrestricted use, distribution, and reproduction in any medium, provided the original work is properly cited.

érodé de Deshaies appartient au Complexe Basal, ensuite que ce complexe est caractérisé par un épisode volcanique actif entre 4,3 et 2 Ma. L'analyse structurale révèle une histoire de déformation significative avec le développement dans le temps de zones schisteuses N80-N100, de brèches hydrothermales orientées N110-N140 et N160-N10 et de failles normales N140-N150 majoritairement. La limite entre le Complexe Basal et la Chaîne Septentrionale correspond à une série de failles dont les directions principales sont N 150° et N 50°. Des études minéralogiques et pétrologiques détaillées, incluant la modélisation thermodynamique, permettent d'identifier trois phases de transformations minéralogiques post-magmatiques avec d'abord un épisode de haute-température dans des conditions de faciès de Schistes-Verts à sub-Schistes-Verts (0,6–2 kbar pour 250–300 °C), un rééquilibrage sous conditions de faciès à Zéolites et finalement une altération de sub-surface. La cohérence entre les conditions P–T du métamorphisme et le gradient géothermique mesuré aujourd'hui démontre que ce métamorphisme témoigne de la circulation des fluides hydrothermaux pendant la construction et le refroidissement de l'arc magmatique des Petites Antilles. L'évolution tectono-métamorphique reconnue dans le Complexe Basal nous permet de proposer un modèle conceptuel de transport de la chaleur et des fluides à l'intérieur des niveaux crustaux peu profonds de l'arc volcanique actif de la Guadeloupe.

**Mots clés :** métamorphisme d'arc / Petites Antilles / Guadeloupe / Complexe Basal / évolution tectono-métamorphique / fluides hydrothermaux

## 1 Introduction

Elucidating the structural and mineralogical transformations driven by heat and fluid transfers within the crust of magmatic arcs is an important yet tricky problem. It controls the formation of metal ores, particularly porphyry and epithermal ore deposits, and as well is vital for enabling the exploitation of geothermal resources (Sillitoe and Perelló, 2005; Rowland and Simmons, 2012; Chambefort *et al.*, 2017). Such tectono-metamorphic evolutions have been frequently deciphered within ancient, inactive, magmatic arcs, whereas similar data from present-day active oceanic island volcanic arcs remain scarce, mainly because of bad outcrop conditions (Coombs, 1960; Miyashiro, 1967; Oxburgh and Turcotte, 1970; Ernst, 1973; Brown, 2010; Ducea *et al.*, 2015). In the Lesser Antilles active arc, the Guadeloupe archipelago provides a natural laboratory for studying arc-related tectonic and metamorphic processes, first because Basse-Terre, *i.e.* the volcanic part of Guadeloupe Island, is entirely volcanic showing a north-south decreasing age gradient of its volcanic phases (Samper *et al.*, 2007, 2009) where the northern part, so-called Basal Complex, consists of the oldest – Pleistocene – eruptive rocks (lava, block & ash flow tuffites) exposed on the island. Second, located at tropical latitudes, Basse-Terre of Guadeloupe is prone to significant weathering and erosion processes (Dessert *et al.*, 2015) where mechanical and chemical erosion rates of around 1–2 mm/yr are effective (Sak *et al.*, 2010, Lloret *et al.*, 2011; Rad *et al.*, 2013; Ricci *et al.*, 2015a, b). In this context, the Basal Complex is a key target for deciphering the evolution of shallow crustal levels of the Lesser Antilles arc as it exposes the most eroded part of the Basse-Terre volcanic chain, consisting of the basement of the volcanic chain. Within this frame, we investigate the tectono-metamorphic evolution of this exhumed piece of the upper crustal level of the Lesser Antilles volcanic arc. We mapped and characterized the lithologies (geochemistry, geochronology) and the structures (structural and kinematic analysis) of the Basal Complex and propose an updated geological map of this northern area of Basse-Terre. Furthermore, we accurately document its metamorphic evolution by the means of a detailed study of the metamorphic reactions preserved in the exposed lava flows and thermodynamic modeling of the mineralogical equilibrium. This dataset allows us to discuss the heat and fluid transfers in the Lesser Antilles magmatic arc, so as to propose a conceptual scheme of these transfers and their influence on the strain accommodation and metamorphic evolution, in the framework of the shallow crustal level of an active volcanic arc.

## 2 Guadeloupe in the Lesser Antilles geological context

The Lesser Antilles volcanic arc is the consequence of the southwest-directed subduction of the North American plate beneath the Caribbean plate (Hawkesworth and Powell, 1980; Demets *et al.*, 2000, Fig. 1A). Since Eo–Oligocene times, two main magmatic arcs were produced through time with a progressive westward migration from an external to an internal volcanic arc, which is still active today (Briden *et al.*, 1979; Westercamp, 1979; Bouysse *et al.*, 1990; Maury *et al.*, 1990; Dixon *et al.*, 1998; Feuillet *et al.*, 2002; Germa *et al.*, 2011).

The Guadeloupe archipelago is formed by the juxtaposition of two geological systems. To the east, Guadeloupe consists of Grande-Terre, La Désirade, Petite-Terre and Marie-Galante Islands, on which early Pliocene-middle Pleistocene limestones were deposited upon volcanic and/or sedimentary crust (Bouysse and Garrabé, 1984; Andreieff *et al.*, 1987; Bouysse *et al.*, 1993; Cornée *et al.*, 2012; Lardeaux *et al.*, 2013; Münch *et al.*, 2013, 2014). To the west, Guadeloupe is composed of Basse-Terre and Les Saintes Islands, which correspond to the inner active arc (Andreieff *et al.*, 1987; Westercamp, 1988; Carlut *et al.*, 2000; Mathieu *et al.*, 2013; Zami *et al.*, 2014; Verati *et al.*, 2016). Basse-Terre consists of a cluster of volcanic complexes, frequently called "volcanic chains", with from north to south (Samper *et al.*, 2007): the oldest Basal Complex characterized by a 3 to 2 Ma aged volcanism, the Septentrional Chain between 1.8 to 1.1 Ma, the Axial Chain active from 1 to 0.4 Ma, the Grande Découverte – Trois

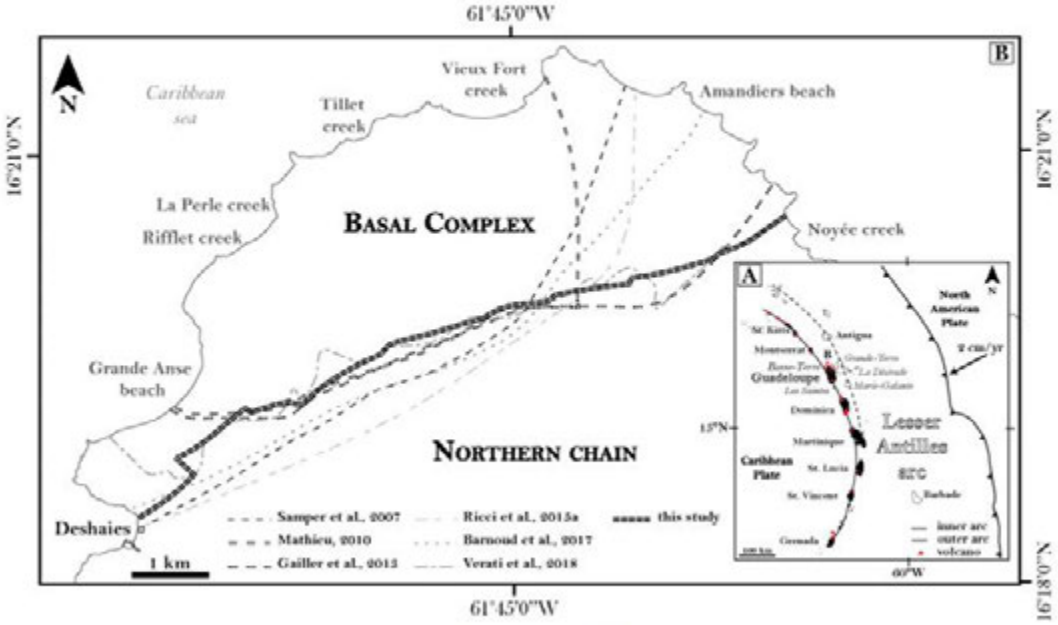


**Fig. 1.** A: Geodynamic setting of the Lesser Antilles arc (after Feuillet *et al.*, 2001); B: Map of the North of Basse-Terre Island (Guadeloupe) with a review of the several boundaries between the Basal Complex and the Northern Chain proposed in previous studies (Samper *et al.*, 2007; Mathieu, 2010; Gailler *et al.*, 2013; Ricci *et al.*, 2015a; Barnoud *et al.*, 2017; Verati *et al.*, 2018).

Rivières Complex (0.2 Ma-recent) including the present-day active La Soufrière volcano (Boudon *et al.*, 1987, 2008), and the Monts Caraïbes Chain built at around 0.6–0.4 Ma (Blanc, 1983; Ricci *et al.*, 2017).

Several authors have focused their petrographic and geochemical studies on fresh volcanic rocks of the southern active volcanic part of the archipelago, and most of the studies have concentrated further south or near La Soufrière volcano or Bouillante geothermal field providing a revision of the ages of the volcanic formations and the lithological contours (Brown *et al.*, 1977; Dagain, 1981; Blanc, 1983; Boudon *et al.*, 1989; Samper *et al.*, 2007, 2009; Patrier *et al.*, 2013; Verati *et al.*, 2014; Ricci *et al.*, 2017). A recent study has shown the evolution of petrophysical properties from fresh to hydrothermalized volcanic rocks in the volcanic island of Guadeloupe archipelago (Navelot *et al.*, 2018).

However, in the northern part of Basse-Terre, the Basal Complex is exposed and consists of strongly weathered volcanic formations (Mathieu *et al.*, 2013). It has not been remapped since the late sixties (De Reynal de Saint-Michel, 1966), as mapping such area, where exposures are scarce and the vegetal coverage is dense, is challenging. Geophysical investigations provide a regional image of the Basal Complex appearing as the volcanic basement on which the younger volcanic systems have been emplaced (Gailler *et al.*, 2013). Moreover, regional low-grade metamorphism and associated deformation has recently been evidenced in this complex (Verati *et al.*, 2018). Although there is a general agreement to consider Basse-Terre as a cluster of volcanic complexes that become progressively younger southward, the identified boundary between the Basal Complex and the Northern Chain varies depending on previous studies and their interpretation of mapping (Westercamp and Tazieff, 1980; Blanc, 1983; Bouysse *et al.*, 1990; Maury *et al.*, 1990; Samper *et al.*, 2007; Gailler *et al.*, 2013). This limit is difficult to determine because exposure of outcrops is limited in northern Basse-Terre. Moreover, near the coastline, the attribution of the Deshaies eroded dome (so called "Gros Morne") either to the Basal Complex or to the Northern Chain remains a topic of debate (Samper *et al.*, 2007; Mathieu, 2010; Gailler *et al.*, 2013; Ricci *et al.*, 2015a; Barnoud *et al.*, 2017; Verati *et al.*, 2018; Fig. 1B). Thus, in order to overcome this ambiguity, we have investigated the age of this dome by the use of $^{40}Ar/^{39}Ar$ geochronology.

## 3 Material and methods

### 3.1 Mapping lithologies and structures

With this study, we improve the geological knowledge of the Basal Complex by mapping accurately this volcanic unit, we have distinguished the following formations (see Sect. 3.1 for a detailed description of the lithology):

- often very thick soils, which occupy a significant part (more than 50%) of the mapping area;
- superficial quaternary sedimentary formations;
- debris flows;
- lava flows.

This study presents a structural data set consisting of about 230 measurements of bedding, fractures, faults, schistosity, and kinematic criteria acquired over 12 sites across the North of Basse-Terre Island.

These data have allowed us to refine the map of this area, based on previous authors (De Reynal de Saint-Michel, 1966; Dagain *et al.*, 1981).

### 3.2 Paleo stress tensors

We have inversed fault kinematics with the right dihedron method to obtain the paleo-stress tensor using WinTensor software (Angelier and Mechler, 1977; Angelier, 1979; Delvaux and Sperner, 2003). WinTensor allows rotational optimization of the obtained tensor by performing iterative tests of tensors in order to minimize a misfit function (Delvaux and Sperner, 2003). We have performed these inversions with a dataset consisting of fault strikes, dips, plunges of the striae and kinematic criteria. For consistency, a minimum of four structural measurements (faults direction and dip, pitch and kinematics) is needed to obtain a robust paleotensor. The quality of inversion is given by QRw (world stress map quality criteria) ranging from A (very good) to E (poor quality) depending of the amount of data use for the inversion ($n$), the ratio between the amount of data used for the inversion over the amount of input data ($n/nt$), deviation between observed and theoretical slip direction ($\alpha_m$), the sense of slip confidence level ($Cl_m$) and the type of structure (fault, fracture, shear zone). The tensor quality is given by QRt, ranging from A (very good) to E (poor quality) and depending on QRw and the dispersion of the measured structures: more dispersed are the data, better is the quality Delvaux and Sperner (2003) (reported in the supplementary data in Appendix Tab. A1).

### 3.3 Geochronology

Grains of plagioclase were extracted from one fresh dacite lava flow sampled north of Deshaies. After magnetic separation (Frantz separator), approximately 200 grains aliquots of limpid plagioclase crystals (160–500 µm) were handpicked under a binocular microscope and were repeatedly ultrasonically cleaned in 2N $HNO_3$ and then in distilled water and methanol for a few minutes.

The samples were packed in aluminum foil for irradiation in the core of the Triga Mark II nuclear reactor of Pavia (Italy) with several aliquots of sanidine from Taylor Creek Rhyolite (TCR standard, 28.619 ± 0.034 Ma in Renne *et al.*, 2010) as a flux monitor. The argon isotopic interferences on K and Ca were determined by the irradiation of KF and $CaF_2$ pure salts from which the following correction factors were obtained: $(^{40}Ar/^{39}Ar)_K = 969 \times 10^{-3} \pm 3.6 \times 10^{-5}$ at 1σ, $(^{38}Ar/^{39}Ar)$ $K = 1297 \times 10^{-2} \pm 4.5 \times 10^{-4}$ at 1σ, $(^{39}Ar/^{37}Ar)$ $Ca = 7.27 \times 10^{-4} \pm 4.0 \times 10^{-5}$ at 1σ, and $(^{36}Ar/^{37}Ar)$ $Ca = 2.88 \times 10^{-4} \pm 1.6 \times 10^{-5}$ at 1σ. $^{40}Ar/^{39}Ar$ step heating analyses were performed at Geosciences Montpellier (France). The gas extraction and purification lines consist of (a) an $IRCO_2$ laser of 100 kHz used at 3–20% power to heat the samples during 180 s, (b) a lens system for beam focusing, (c) a steel chamber, maintained at $10^{-8}$–$10^{-9}$ bar, and (d) two Zr–Al getters for the purification of the gases. The argon isotopes were analyzed with ARGUS VI multicollector mass spectrometer. The mass discrimination was monitored daily using an automated air pipette and provided a mean value of 0.996817 ± 0.0013 (1σ) per dalton. Blank analyses were performed every three sample step. The raw data of each step and blank were processed, and the ages were calculated using the ArArCALC software (Koppers, 2002). Dating parameters (typical blank values, irradiation parameters and Ar–Ar analytical details) are reported in the supplementary data in Appendix (Tab. A2). The criteria for defining plateau ages are as follows: (1) Plateau steps should contain at least 50% of released $^{39}Ar$, (2) there should be at least three successive steps in the plateau, and (3) the integrated age of the plateau should be in agreement with each apparent age of the plateau within a 2σ confidence interval.

### 3.4 Geochemistry and petrology

In order to improve the definition of the lithotypes proposed on the geological map, the magmatic characters of the lavas flows were established. Whole rock major and trace element analyses were thus realized on several samples (analytical results are provided in the supplementary data in Appendix Tabs. A3 and A4). We carefully selected the rock exposure to ensure that the main types of lava flows were sampled. We analysed rock powders by Inductively Coupled Plasma Atomic Emission Spectrometry (ICP-AES) and Inductively Coupled Mass Spectrometry (ICP-MS), for major and trace elements respectively, at the Geochemical and Petrographical Research Center in Nancy (SARM laboratory, CNRS-CRPG, with the procedure proposed by Carignan *et al.*, 2001).

In order to constrain and quantify the petrological evolution of the Basal Complex, we investigated 80 thin sections. Mineral chemistry data were achieved by both electron microprobe analyses and diffractometry (system XPert-Pro MPD, Bragg Brentano geometry, Cu anticathode, KAlpha1 and KAlpha2 rays, PIXcel detector at the CEMEF in Sophia-Antipolis Scientific Center). Major elements analyses were performed at the "Service Commun de Microsonde" at Montpellier University on a Cameca-SX100 electron microprobe. The operating conditions were a 20 kV accelerating voltage and 10 nA beam current. The chemical analyses of the metamorphic phases are presented in the supplementary data in Appendix Table A5 (Schumacher, 1997).

We also used Raman spectrometry to complete mineral determination (in the supplementary data, Appendix A). The spectra were recorded with a LabRam HR800UV Jobin-Yvon™ microspectrometer equipped with 1800 g/mm gratings and using 532 nm green laser excitation; acquisition time-span varied from 20 to 70 s during three accumulating cycles.

## 4 Revisiting the geology of the Basal Complex: Towards an updated geological map

### 4.1 Geological formations

#### 4.1.1 Superficial formations

The Basal Complex is only found in the northern Basse-Terre, where the soils consist of vertisols, *i.e.* typical of old weathered volcanic rocks, with high kaolinite and

**Fig. 2.** Volcanic prismation in a rhyodacites lava flow East of Tillet creek, which progressively evolves into a schistosity plane.

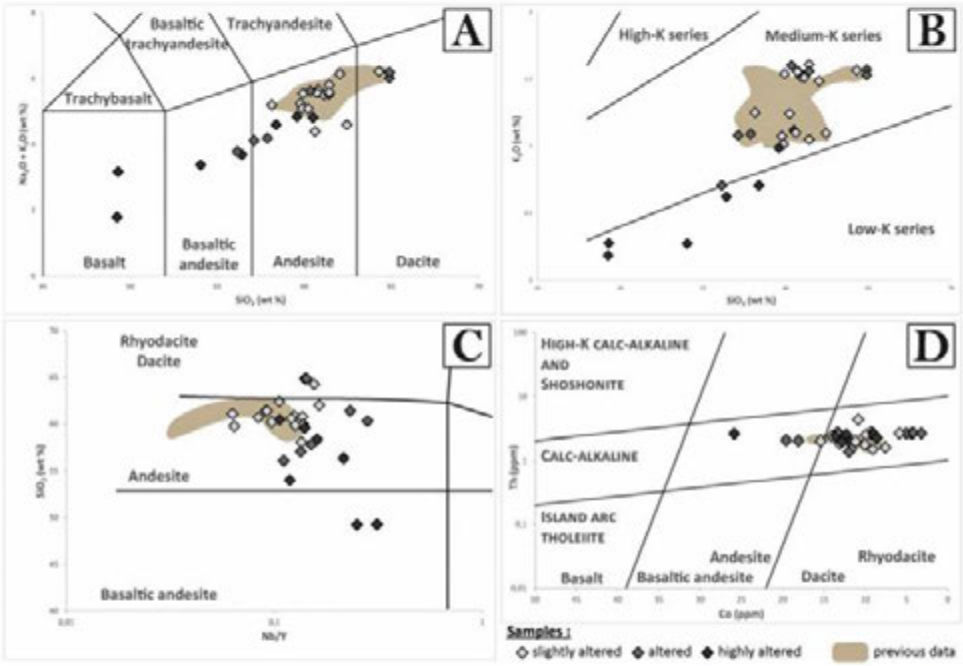


**Fig. 3.** Geochemical characterization of lava flows. A: Total alkali *vs.* silica diagram after Bas *et al.* (1986), previous data from: Samper *et al.* (2007), Ricci *et al.* (2017) and Navelot *et al.* (2018); B: $SiO_2$ *vs.* $K_2O$ plot after Peccerillo and Taylor (1976), previous data from Samper *et al.* (2007, 2009), Ricci *et al.* (2017) and Navelot *et al.* (2018); C: $SiO_2$ *vs.* Nb/Y diagram after Winchester and Floyd (1977), previous data from Ricci *et al.* (2017); D: Co *vs.* Th plot after Hastie *et al.* (2007), previous data from Ricci *et al.* (2017).

montmorillonite contents (see Dessert *et al.*, 2015 for a review). The superficial sedimentary formations consist of detrital deposits and alluviums. The debris flow deposits, interbedded with lava flows, contain blocks of contrasted sizes varying ranging between centimeter to meter of andesites and dacites as well as varicolored clay aggregates. In a restricted number of places, volcano-clastic deposits are interlayered within debris flows.

### 4.1.2 Lavas flows

Lavas flows are easily observable along the coastline, and they extend inland up to 100 to 150 m above sea level, while eroded volcanic pitons and domes of 200 to 300 m high are still recognizable in the landscape. Along the coastal exposures, rocks show porphyric textures with different abundances (30–60%), of plagioclases, pyroxenes and/or oxydes phenocrysts. Columnar jointing of andesite and dacite lavas flows is a common volcanic structure that can be recognized at the regional scale. Lithological interfaces, stratigraphy or $S_0$, are easily observable within sequences of alternating lava flows and pyroclastic deposits. Lava flows fabrics, particularly well expressed in dacites and rhyodacites, precisely prismation (Fig. 2) and magmatic fluidality are also typical examples of primary volcanic structures.

In the Total Alkali *versus* Silica (TAS) diagram (Bas *et al.*, 1986; Fig. 3A) $SiO_2$ contents range from 49 to 65 wt.% for lava flows and our sample's compositions evolve from basalt to dacite. In the $K_2O$ *versus* $SiO_2$ diagram (Peccerillo and Taylor,

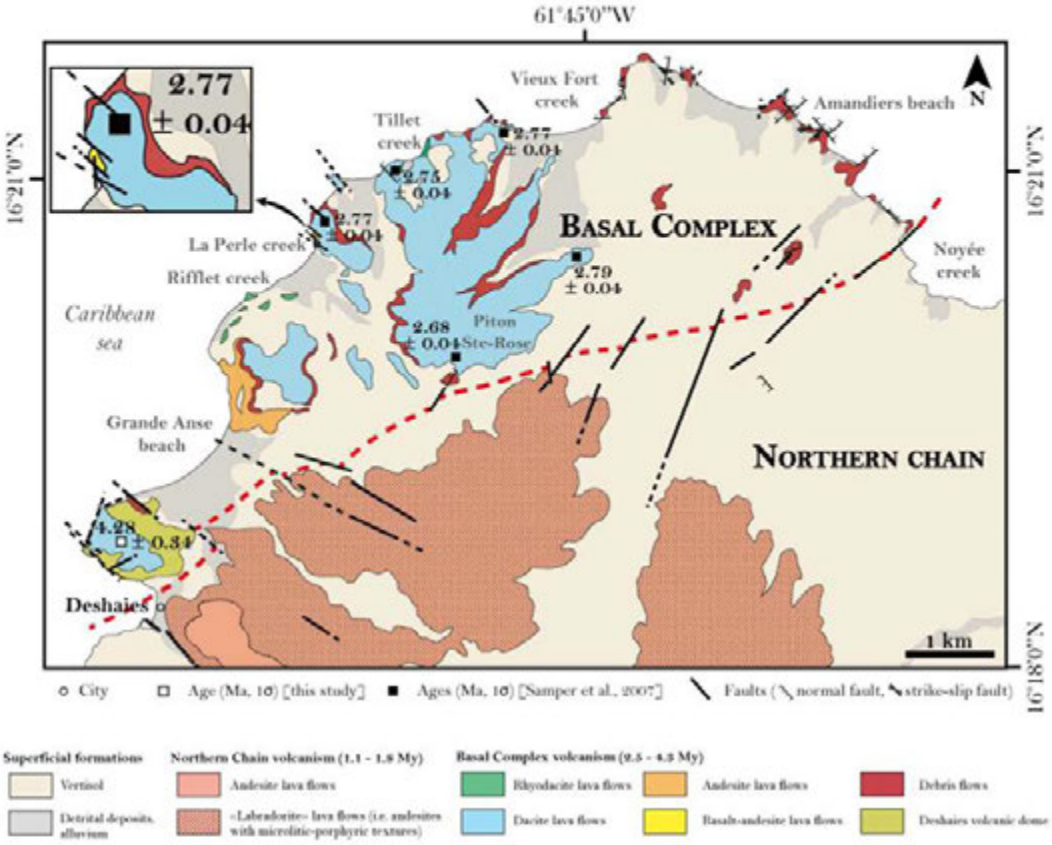


**Fig. 4.** Geological map of the North of Basse-Terre Island (modified after De Reynal de Saint-Michel, 1966), showing the main lithologies and geochemical affinities of volcanic rocks.

1976 for arc volcanic lavas; Fig. 3B), the studied lavas fall within the fields of Median-K to Low-K series. In the $SiO_2$ *versus* Nb/Y diagram (Winchester and Floyd, 1977; Fig. 3C), the studied samples belong to the calc-alkaline serie of basaltic-andesite to dacite. All together, these diagrams, classically used to define the chemical composition of volcanic rocks, show that the majority of the samples are andesites.

However, major and some trace elements, mainly Large Ion Lithophile Element (LILE) and Light Rare Earth Element (LREE), are severely mobile in weathered and/or hydrothermally altered lavas. Therefore, to improve the geochemical characterization of our samples, we selected diagrams based only on minor and trace elements considered as being the most immobile. Samples where LOI (loss on ignition) is below 1–2%, demonstrating that weathering is insignificant, are named "slightly altered" while samples with LOI above 3%, evidencing alteration, are named "altered" to "highly altered". The Zr/Ti–Nb/Y diagram is classically employed for recognizing rock types even in altered rocks (Winchester and Floyd, 1977; Pearce, 1996), but in tropical regions due to extreme chemical weathering conditions, even Ti and Zr are mobile (Braun *et al.*, 1993, 2005; Melfi *et al.*, 1996; Nahon and Merino, 1996; Cornu *et al.*, 1999; Ma *et al.*, 2007). We therefore used the Th–Co diagram proposed by Hastie *et al.* (2007) for altered arc volcanic rocks, and in this diagram the studied rocks show typical characters of calc-alkaline volcanic series (Fig. 3D). Our samples, basaltic andesite to rhyodacite, thus followed a differentiated serie. All together, these geochemical data indicate that the Basal Complex lavas belong to the Medium K calc-alkaline series with the following more or less differentiated types: basaltic-andesites, andesites, dacites and rhyodacites. We used therefore this nomenclature in the proposed updated geological map (Fig. 4).

Moreover, we also used trace elements diagrams to compare our results to data from other volcanic rocks in Basse-Terre, as well as results obtained on the fresh rocks of the Basal Complex (Samper *et al.*, 2007). The Rare-Earth-Element (REE) diagrams normalized to chondrite values (after Sun and McDonough, 1989; Fig. 5A) display relatively constant slopes, with small enrichment in Light REE (LREE) for most samples, typical for subduction related calc-alkaline REE chondrite-normalized patterns. The multi-element diagrams of

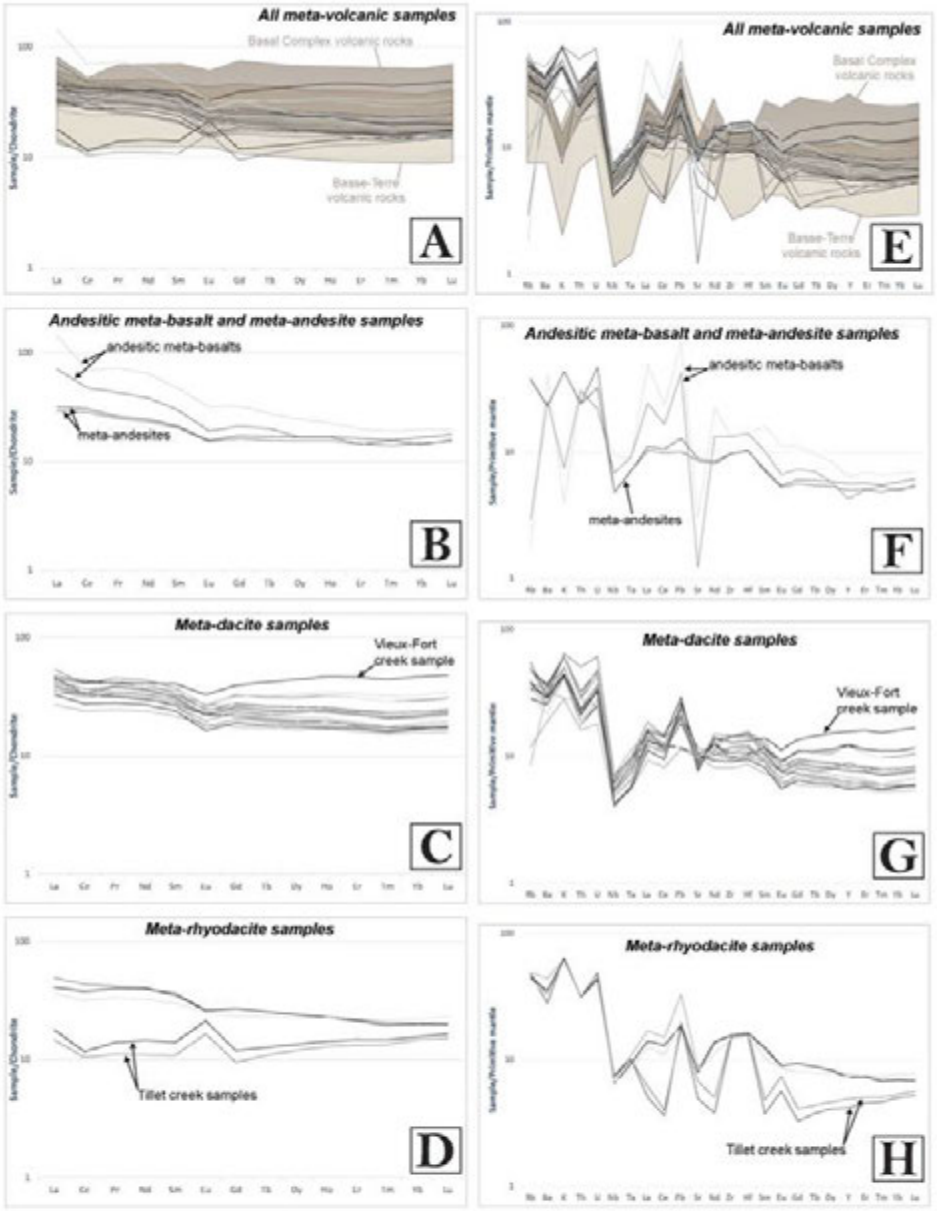


**Fig. 5.** A–D: Rare Earth Element (REE) patterns normalized to chondrite values (after Sun and McDonough, 1989) of the samples used in this study; E–H: Multi-element patterns normalized to primitive-mantle (after Sun and McDonough, 1989) for the same samples as in Figures 4A–4D. The shaded bands correspond to the range determined for volcanic rocks of the whole Basse-Terre and the Basal Complex (from Blanc, 1983; Samper *et al.*, 2007; Ricci *et al.*, 2017).

incompatible elements normalized to primitive mantle (Sun and McDonough, 1989; Fig. 5E) display patterns typical of arc lavas, with Pb, U and Large Ion Lithophile Element (LILE) enrichments, and also Nb and Ta depletions (Labanieh, 2009).

In andesitic meta-basalts (Fig. 5B), samples display first significant HREE depleted patterns (with 80 to 110 times chondritic abundances for LREE and 20 times chondritic abundances for HREE), typically described after extensive

weathering (Ma *et al.*, 2007) and second slightly negative Eu anomaly which may be interpreted as plagioclase fractionation (Taylor and McLennan, 1995) or as hydrothermal alteration under mildly acidic low-temperature solutions. Finally, the multi-elements diagrams (Fig. 5F) show a strong Rb, Sr and K depletion, indicating the influence of surface alteration processes (Patino *et al.*, 2003).

In meta-andesites (Fig. 5B), the observed patterns displays slightly LREE enrichment, and positives Eu, Ce and Gd anomalies attest for intense weathering (Ma *et al.*, 2007). However, it has also been demonstrated that strong hydrothermal alteration may also lead to positive anomaly of Ce.

In meta-dacites (Fig. 5C), the observed trends display a flat-type or a very slight LREE enrichment with negative Ce anomaly for a few samples. This feature is interpreted as a post-magmatic process due to surface alteration processes under tropical weathering conditions (Cotten *et al.*, 1995; Samper *et al.*, 2009; Ricci *et al.*, 2017). A sample from Vieux-Fort creek (BT5_01) shows LREE depletion and negative Eu anomaly reflecting high-temperature alteration under mildly acidic conditions (Bau, 1991). In multi-elements diagrams (Fig. 5G), our patterns are comparable to those previously described for the Basal Complex. Several samples show positive Y anomaly, in relation with surface alteration processes, specifically under tropical climates (Cotten *et al.*, 1995; Labanieh, 2009).

In meta-rhyodacites (Fig. 5D), two types of trends can be highlighted. A first one, similar to the patterns previously recognized for the same lavas within the Basal Complex patterns. A second pattern, observed for Tillet creek samples (BT9_01-02), displays a flat-type trend with negative Ce and large positive Eu anomalies. This likely result from rock interaction with acidic high-temperature hydrothermal fluids (Michard *et al.*, 1983; Michard, 1989; Cotten *et al.*, 1995). Multi-elements diagrams also show two different patterns (Fig. 5H), both with Zr–Hf positive anomalies. If the first one is similar to the trends depicted in the Basal Complex volcanic rocks, another one characterizes the samples with strong negative La–Ce anomalies, negative Sr–Nd anomalies and always a large Eu anomaly.

All together, these data demonstrate that the volcanic rocks of the Basal Complex were severely transformed after their crystallization in relation with hydrothermal fluid circulations and supergene alterations.

Fortunately, even in significantly altered volcanic rocks, the primary volcanic mineralogy is, at least partly preserved, allowing the mineralogy of the mapped formations to be characterized. From a mineralogical point of view, the basaltic andesites and andesites display a volcanic primary association with phenocrysts of mafic plagioclase, clinopyroxene and ilmenite and/or titanomagnetite, in a decreasing order of abundance. Groundmass is typically microlitic and oxide-rich. In the andesites, the primary volcanic mineralogy is an association of phenocrysts of plagioclase, clinopyroxene, orthopyroxene and ilmenite, with rare amphiboles. The groundmass is characterized by the great quantity of microlites of plagioclase and oxides. Dacites and rhyodacites are composed of phenocrysts of plagioclase, orthopyroxene, clinopyroxene, ilmenite and quartz, while the groundmass is rich in quartz, plagioclase, oxides and anorthoclase microlites.

### 4.2 Structure and strain pattern

At a regional scale, lithological interfaces and lava flows fabrics are oriented in two main directions N 160°–170° and N 20°–30°, moderately dipping between 4° and 44°, with a mean dip of 20° towards West (Legendre, 2018)(Fig. 6B). Primary magmatic structures are overprinted by secondary tectonic structures. We identify three types of tectonic structures that developed during the progressive cooling of this volcanic complex through time and classify these as ductile structures, structures developed at the brittle-ductile transition and brittle structures.

#### 4.2.1 Ductile strain

At a mesoscopic scale the tectonic fabric is defined by smooth parallel cleavage areas separated by centimeter-scale undeformed zones (*i.e.* microlithons). Because cleavages are frequently interrupted at the scale of the outcrop (Fig. 7A), this tectonic fabric corresponds to pervasive disjunctive spaced cleavages (Powell, 1979; Passchier and Trouw, 2005). Spaced cleavage stripes (in the sense of Beach, 1982) are common and appear yellow-greenish to pink, with respect to the volcanic matrix, because of the crystallization of secondary minerals (Fig. 7). In some cases, the cleavage stripes turn into stylolithic joints (Fig. 7B). Moreover, seams are underlined by insoluble residues as well as volcanic enclaves (Fig. 7C) truncated by disjunctive schistosity planes (Fig. 7D), representing evidences for a pressure-solution processes driven strain (Fig. 7E; Rutter, 1976; Beach, 1979). Networks of quartz, albite, pyrite or calcite bearing veins frequently interconnect the schistosity planes. This geometry is comparable to the one described when dilatant micro-faults occur in jointed cohesive rocks (Ketterman *et al.*, 2016). Thin sections also show that dissolution of phenocrysts is underlined by the development of dark and pink seams of insoluble minerals (Fig. 7F), mainly fine-grained Fe-oxides, at the grain boundaries. Regional finite strain pattern displays localized schistose domains surrounding lenses of undeformed country rocks (Fig. 2), preserving primary magmatic structures. Structural mapping evidences moderately dipping schistosity planes with a N 80°–100° main direction (Fig. 6A).

#### 4.2.2 Brittle-ductile strain

In a specific area, north of La Perle creek, we have identified "hydrothermal tectonic breccias" (Sibson, 1977; Jébrak, 1997; Woodcock and Mort, 2008). Along steeply dipping fault planes we observed textures of fragmentation containing large fragments of volcanic rocks. More than 60% of the fragments are larger than 2 cm in diameter giving rise to "mosaic breccias" according to the classifications of Jébrak (1997) or Woodcock and Mort (2008). These volcanic rocks fragments are cemented in a fine-grained matrix entirely composed of hydrothermal and strongly altered minerals. Thus these breccias are cohesive following Sibson's (1977) textural classification. Most of the fragments are angular (Fig. 8B), a common feature for fluid assisted brecciation. However, some fragments, generally small-sized, are more rounded due to local dissolution processes (Fig. 8A). In a few cases, the spaced volcanic fragments are oriented parallel to the observed fault planes. All together, these features are compatible with

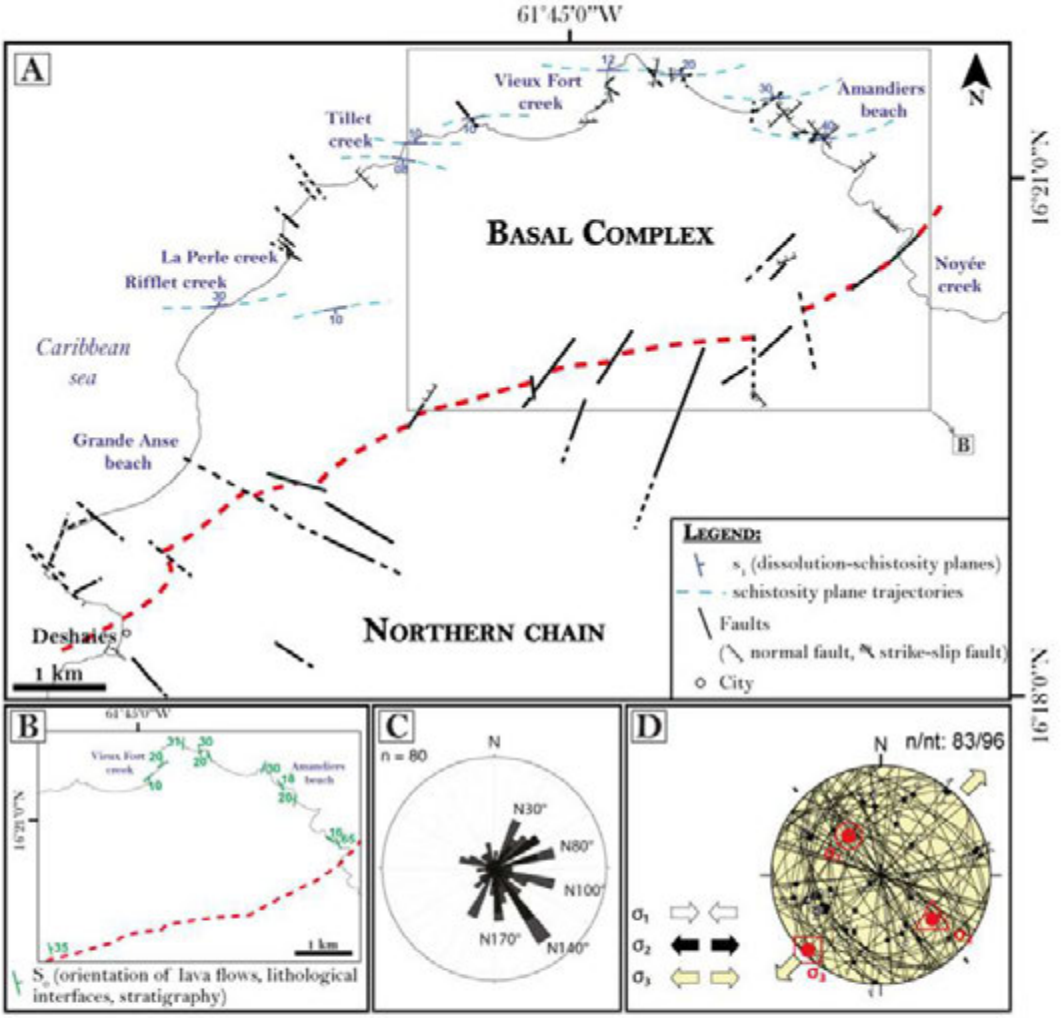


**Fig. 6.** A: Tectonic sketch map of the North of Basse-Terre where the main faults observed are reported with measures of the dissolution-schistosity planes and the extension of their trajectories. The red dotted line indicates the boundary between the volcanic complexes of the Basal Complex and the Northern Chain; B: Simplified map of the orientations of lava flows and horizons surface ($S_0$); C: Rose diagram displaying the faults measured in the Basal Complex; D: Paleotensor obtained by inversion of field data (faults with kinematics criteria, fractures).

deformation processes developed at the brittle to ductile transition. These hydrothermal tectonic breccias occur under two aspects that are easy to identify in the field by their colour: (1) red, within which some volcanic clasts are partly preserved in the core of hydrothermal secondary minerals (Figs. 8A, 8C and 8D), (2) yellow-green within which volcanic clasts are only phantoms replaced by clay minerals indicating an almost complete supergene alteration of the whole hydrothermal mineralogy (Figs. 8A–8C). Besides this difference in the degree of supergene alteration, these breccias show differences of orientation and two major directions were highlighted (Fig. 8E): N110-N140 and N160-N10.

#### 4.2.3 Brittle strain

The Basal Complex is also affected by brittle structures. The four families of regional directions are represented on the mapped area (Fig. 6A), with a main dominant fault family of N140-N150 (Fig. 6C) and with centimetrical offsets. Tectoglyphs along fault planes show normal dip-slip to oblique slip kinematics at all measurements sites, except at one locality where the offset of an andesitic pebble shows an apparent inverse kinematics, although the fault plane does not display any kinematic indications. At each site and although kinematics indicators were scarce, giving weak inversion data

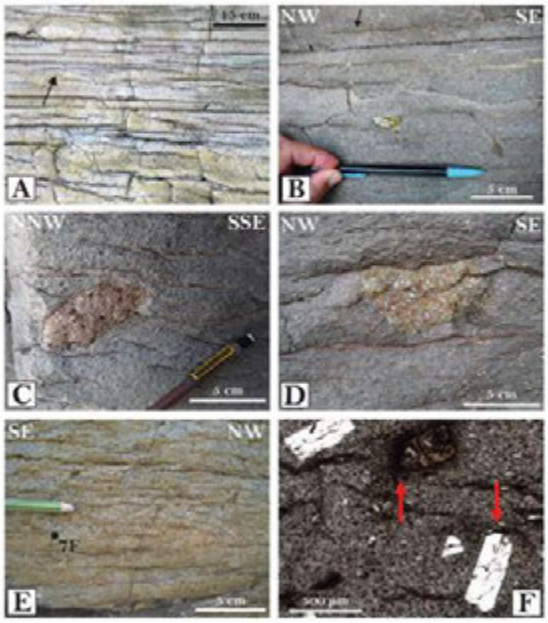


**Fig. 7.** A: Discrete and spaced cleavages, frequently interrupted at the outcrop scale, underlined by pink and dark seams of insoluble minerals in a meta-rhyodacite lava flow (western part of Tillet creek); B: Dissolution-schistosity plane underlined by insoluble minerals where cleavage becomes a stylolithic joints in a meta-rhyodacite lava flow from Tillet creek; C: Volcanic enclave in the core of pervasive disjunctive spaced cleavages in a meta-rhyodacite deposit from Tillet creek; D: Dissolution-schistosity planes and truncated volcanic enclave in a meta-rhyodacite deposit from Tillet creek; E: Disjunctive schistosity planes highlighting pressure-solution seams in a meta-rhyodacite lava flow from Rifflet creek. The black square indicates the location of the sample in Figure 7E; F: Photomicrographs of microstructures from schistose zones observed in thin sections using polarized and cross-polarized microscopy. Schistosity is underlined by oxides in a meta-rhyodacite lava flow from Rifflet creek. Red arrows highlight microstructures of dissolution at the grain boundary of a meta-pyroxene and a plagioclase volcanic phenocryst.

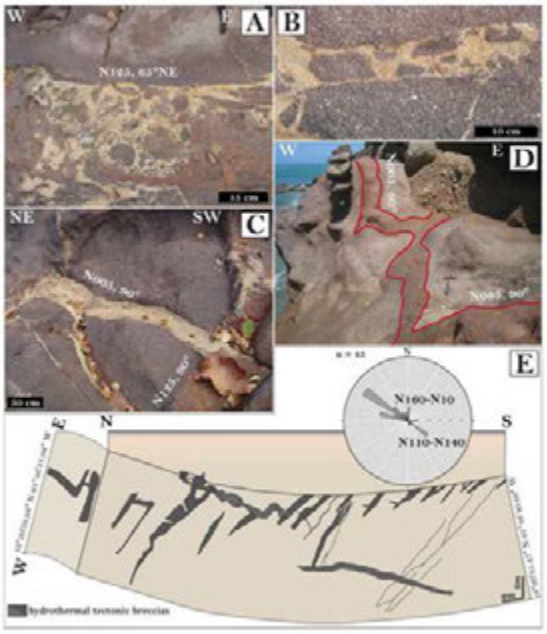


**Fig. 8.** Several structures of hydrothermal tectonic breccias from La Perle creek. A: Hydrothermal tectonic breccia with more rounded fragments due to local dissolution processes; B: Hydrothermal tectonic breccia where fragments are angular; C: Yellow-green hydrothermal tectonic breccia cutting a red hydrothermal tectonic breccia, both breccias are meta-dacite; D: Red hydrothermal tectonic breccia of meta-basalt-andesite; E: Schematic representation highlighting two major directions at the scale of the outcrop.

at individual sites, paleostress inversion shows a $\sigma_3$ trending NE-SW and NW-SE along N 50° and N 150° trending faults, respectively. Inversion of the whole dataset provides a pure-extensional stress regime with $\sigma_3$ trending NE-SW (Fig. 6D).

The trend of the southern boundary of the Basal Complex is a lineament at N 50° defined by a series of N 150° and N 50° faults, showing the same relationship with N 150° crosscutting N 50° faults.

### 4.3 Southern boundary of the Basal Complex

The two plagioclase aliquots from the sampled dacite (aliquots A and B, Fig. 9, Tab. 1, Tab. A2) yield two concordant plateau ages of 4.10 ± 1.03 Ma (91.36% of $^{39}$Ar released, MSWD = 0.49) and 4.42 ± 0.91 Ma (86.67% of $^{39}$Ar released, MSWD = 0.51) respectively. The inverse isochron calculations yield ages at 4.05 ± 1.39 Ma (MSWD = 0.61; initial $^{40}$Ar/$^{36}$Ar ratio at 301.09 ± 53.47) and 3.46 ± 1.92 Ma (MSWD = 0.20; initial $^{40}$Ar/$^{36}$Ar ratio at 360.2 ± 111.0) respectively. The combination of aliquot analyses yields a plateau age at 4.28 ± 0.68 Ma (87.89% of $^{39}$Ar released, MSWD = 0.48) and an inverse isochron age of 3.97 ± 1.03 Ma (MSWD = 0.46) with an initial $^{40}$Ar/$^{36}$Ar ratio at 316.4 ± 48.4 indicating that the trapped $^{40}$Ar/$^{36}$Ar is indistinguishable from atmospheric $^{40}$Ar/$^{36}$Ar (Lee *et al.*, 2006). However, the uncertainty of the plateau age is relatively high because of important atmospheric $^{40}$Ar contribution with respect to radiogenic $^{40}$Ar (16 to 81%, see in supplementary data). All single ages are concordant at the 2$\sigma$ level and we retain the combined plateau age of 4.28 ± 0.68 Ma as the best estimate of the age of the dacite lava flow. This new $^{40}$Ar–$^{39}$Ar dating demonstrates that the "Gros Morne" dacite dome belongs to the Basal Complex. This Ar–Ar age is older than recent previous obtained K–Ar ages for the Basal Complex (Samper *et al.*, 2007). We sampled the Gros Morne volcanic dome located further west than the sampled lava flows dated in Samper *et al.* (2007) (Fig. 2). Similarly to these authors, we have selected only the rocks that seemed fresh enough in order to minimize the potential impacts of hydrothermalism and

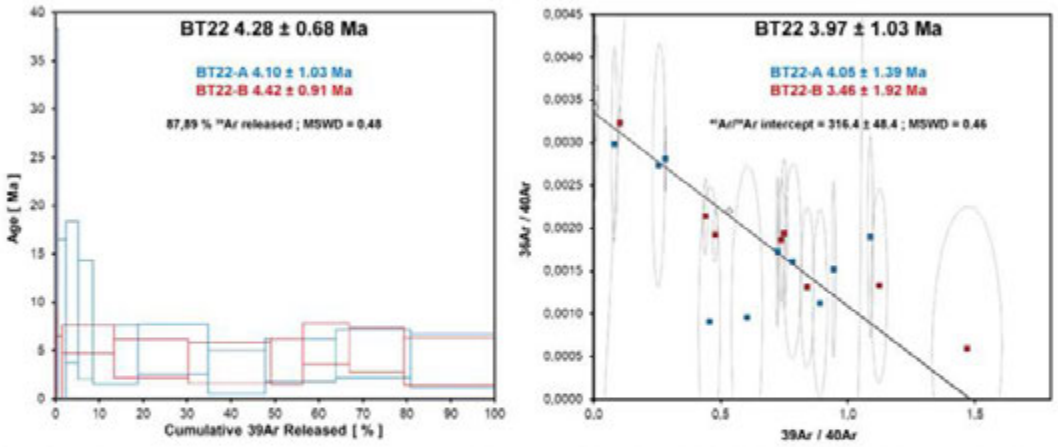


**Fig. 9.** Uncertainties herein are given at the 2$\sigma$ level. A: $^{40}Ar/^{39}Ar$ spectra for BT22-sample from "Gros Morne" dacite dome of Deshaies; B: Inverse isochron for BT22-sample from "Gros Morne" dacite dome of Deshaies. MSWD = Mean Square Weighted Deviation.

**Table 1.** $^{40}Ar/^{39}Ar$ analyses results.

| Sample | Latitude | Longitude | Lithology | Metarial dated | Analyse | Plateau age (Ma) | ±2$\sigma$ | % $^{39}Ar$ released | MSWD | Inverse isochrone age (Ma) | ±2$\sigma$ | $^{40}Ar/^{36}Ar$ intercept | ±2$\sigma$ | MSWD | Total fusion age (Ma) | ±2$\sigma$ |
|---|---|---|---|---|---|---|---|---|---|---|---|---|---|---|---|---|
| BT22 | 16°18' 49.59" N | 61°47' 47.73" W | Dacite lava flow | Plagioclase | A | 4.10 | 1.03 | 91.36 | 0.49 | 4.05 | 1.39 | 301.09 | 53.47 | 0.61 | 4.46 | 1.11 |
| | | | | | B | 4.42 | 0.91 | 86.67 | 0.51 | 3.46 | 1.92 | 360.2 | 111.0 | 0.20 | 4.46 | 0.85 |
| | | | | | A + B combined | 4.28 | 0.68 | 87.89 | 0.48 | 3.97 | 1.03 | 316.40 | 24.20 | 0.46 | 4.46 | 0.70 |

alteration on geochronological results in relation with K losses and Ar enrichments. Given that we considered previous K–Ar ages as significant, two different volcanic events may have occurred. Taking into account this new chronological constraint, south of the Deshaies dome, the Basal Complex is therefore clearly limited by a series of faults with N 150° and N 50° main directions. Its northeastern limit is also tectonic marked by mainly N 50° oriented faults. Far for the coastline, in areas where outcrops are of bad quality and thus in absence of field observations, a morphological limit, with Basal Complex formations covered by lava flows from the Northern Chain, is not excluded.

## 5 Metamorphic evolution of the Basal Complex

Mineralogical evidences for low-grade metamorphism have been recently discovered in the Basal Complex (Verati *et al.*, 2018), however detailed investigations of the diversity of the mineralogical evolutions observable in the various volcanic lithologies still lack.

Under low-temperature conditions, metamorphic recrystallizations are incomplete and metamorphic phases coexist with metastable magmatic minerals (Frey and Robinson, 1999). It is the case in the studied rocks, which present systematic textural evidences of such chemical disequilibrium, particularly partial replacement of volcanic phases.

This peculiar metamorphism affects the whole Basal Complex and is identified by the systematic occurrence of post-magmatic reaction phases (Fig. 10).

### 5.1 Mineralogical characterization of metamorphic assemblages

In andesitic meta-basalts (Fig. 11A), secondary minerals are: quartz, albite, chlorite, actinolite, titanite, scarce white micas, prehnite, epidote and calcite. Chlorite occurs as millimeter patches within the groundmass or relicts of magmatic pyroxenes. Actinolite is present as acicular crystals around volcanic clinopyroxenes or in association with chlorites in the groundmass. Titanite is recognized as fine-grained brownish aggregates within relicts of plagioclase phenocrysts, while white mica occurs, in association with epidote and quartz, as replacement patches in volcanic phenocrysts. Prehnite occurs as colourless pseudomorphic patches or radially developed aggregates of low relief. These rocks are severely altered resulting in an argilic overprint (significant development of clay minerals) typical of alteration under tropical conditions.

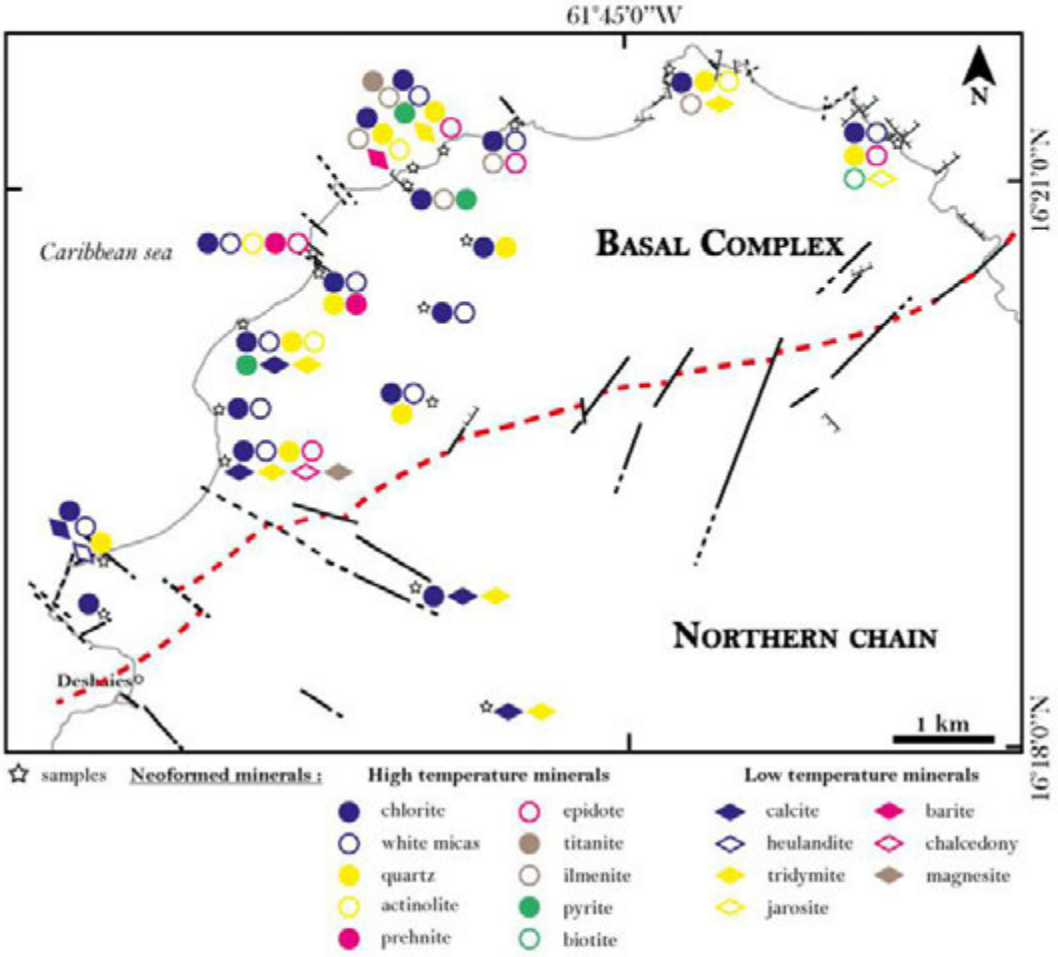


**Fig. 10.** Distribution of metamorphic phases (high and low temperatures) within the Basal Complex (modified after Verati *et al.*, 2018). Locations of sampling sites are reported with stars.

In meta-andesites, chlorite, actinolite, albite, quartz, white mica, titanite are the ubiquitous metamorphic assemblage accompanied by variably developed epidote and oxides minerals. Chlorite colors range from pale green to various shades of yellow and brown. Actinolite commonly occurs as colorless crystals, sometimes in association with chlorite, at the rims of volcanic clinopyroxenes. Magmatic amphiboles are progressively transformed into a fringe of epitaxial acicular actinolites. Small sized titanite grains are associated with actinolite within reaction rims around pyroxenes. In some samples, coronas of metamorphic albite occur surrounding volcanic plagioclases, while in other rocks plagioclase phenocrysts are partially replaced by albite, white micas and calcite. Millimeter-sized grains of epidote are observable in the volcanic groundmass. Numerous cracks and veinlets are filled by calcite and tridymite (Fig. 12A) ± quartz ± albite ± chlorite. This assemblage must be interpreted as lower temperature assemblage developed during progressing cooling of the meta-andesite. These meta-andesites are also deeply altered giving rise to a typical assemblage of quartz, pyrite, calcite, magnesite, chalcedony (Fig. 12B), gypsum and clays minerals (kaolinite, illite, montmorillonite, smectite).

Comparable to what has been recently proposed by Verati *et al.* (2018), for meta-dacites (Fig. 11B) and meta-rhyodacites (Fig. 11C), the secondary metamorphic association is: albite, muscovite, chlorite, titanite, quartz, clinozoisite/epidote and ilmenite. White mica appears as irregular pseudomorphic patches, mainly rectangular, and close to quartz veins. We also observed sulphate, like barite, typical for low- temperature conditions and supergene alteration products with clays minerals (smectite and montmorillonite).

In some debris flow, metamorphic assemblages can also be identified (Fig. 11D): chlorite, white micas, quartz, actinolite, epidote, biotite and ilmenite. The meta-debris flows are also

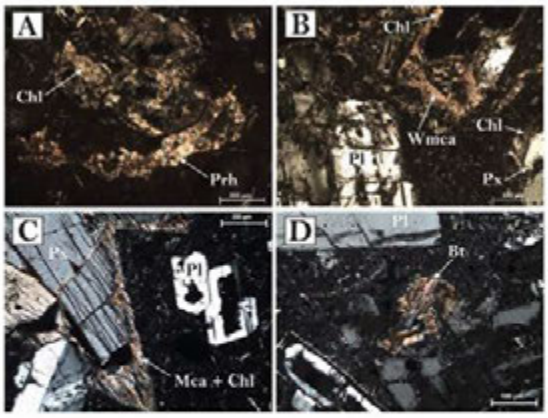


**Fig. 11.** Photomicrographs of highly metamorphic transformations in PPL. Bt: biotite; Chl: chlorite; Mca: micas; Wmca: white micas; Pl: plagioclase; Prh: prehnite; Px: pyroxene. A: Basalt-andesitic lava flow from La Perle creek (BT13); B: Dacitic lava flow from a dome south of Rifflet (BT17); C: Rhyodacitic lava flow from Rifflet creek (BT16); D: Debris flow from Amandiers beach (BT1).

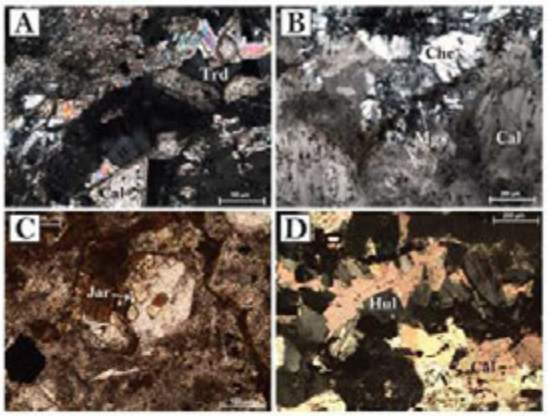


**Fig. 12.** Photomicrographs of hydrothermal alteration in PPL. Cal: calcite; Chc: chalcedony; Hul: heulandite; Jar: jarosite; Mgs: magnesite; Trd: tridymite. A: Andesitic lava flow from north of Grande-Anse beach (BT19); B: Vein in andesitic lava flow from north of Grande-Anse beach (BT19); C: Debris flow from Amandiers beach (BT1); D: Vein in debris flow from south of Grande-Anse beach, at the bottom of Gros-Morne near Deshaies (BT21).

hydrothermally altered giving rise to a typical assemblage of pyrite, calcite, $SiO_2$ polymorphs (tridymite, chalcedony) and sulphate (jarosite) (Fig. 12C). In the southern part of Grande Anse beach, veins and fractures that cut the debris flows are filled by calcite and heulandite (Fig. 12D).

Together with their geochemical evolution (see trace elements evolutions presented in previous paragraphs), the observed mineralogical evolution reveals that the Basal Complex offers a spectacular example of allochemical metamorphism in relation with hydrothermal fluid circulation during cooling of the magmatic arc, ending with supergene alterations.

### 5.2 Metamorphic P–T conditions

The mineral assemblages recognized within the meta-volcanites from the Basal Complex are a diagnostic for sub-greenschist facies conditions, close to the onset of the greenschist facies (Liou *et al.*, 1985; Schiffman and Day, 1999; Robinson *et al.*, 2005).

A first approach for a qualitative estimation of P–T conditions is the use of available petrogenetic grids. Such grids have been determined for metabasites and can thus be used only for the studied andesitic meta-basalts (Liou *et al.*, 1985; Frey and Robinson, 1999). At the transition between sub-greenschist and greenschist facies, in the simplified basaltic system (*i.e.* NCMASH, $Na_2O$–CaO–MgO–$Al_2O_3$) system, an invariant point (so-called CHEPPAQ) is identified, which separates a higher-pressure mineral association (actinolite + chlorite + epidote + pumpellyite + quartz) from a lower-pressure assemblage (prehnite + epidote + chlorite + quartz). Depending on the selected activity models for thermodynamic modeling, the P–T position of the invariant point between prehnite bearing assemblages, pumpellyite bearing assemblages and greenschist facies assemblages varies between 3 and 4 kbar and between 300 and 380 °C (Liou *et al.*, 1987; Frey *et al.*, 1991; Powell *et al.*, 1993; Beiersdorfer and Day, 1995; Day and Springer, 2005). Whatever the selected model, the metamorphic temperature for the mineralogical assemblages depicted in the studied samples is well constrained between 220 and 380 °C. For such a temperature range, the absence of clear pumpellyite + actinolite + chlorite + epidote assemblage suggests that metamorphic pressures did not exceed 2.5–3 kbar.

Thermobarometry is a second approach available and chlorite thermometry is particularly well adapted for low-grade metamorphic rocks, particularly using recent thermodynamic calibrations (Lanari *et al.*, 2014; Bourdelle and Cathelineau, 2015). The application of these geothermometer to all the analyzed chlorites in both andesitic meta-basalts and meta-rhyodacites, with the assumption that Total Fe = $Fe^{2+}$, indicates a temperature range of 230–320 °C, thus consistent with the previous temperature estimation. Pressure values can be roughly estimated by the application of the geobarometer of Brown (1977), to amphibole composition within andesitic meta-basalts, when this mineral is associated with albite, chlorite and iron oxide. With Na M4 values lower than 0.05 and $Al^{iv}$ below 0.5 the estimated pressure is less than 2 kbar. Furthermore, the values of the $K_D^{Mg-Fe}$ for coexisting actinolite and chlorite range between 1.1 and 1.3, typical of metamorphic amphiboles under low-grade conditions (Robinson *et al.*, 2004).

Furthermore, thermodynamic calculations were performed with the free energy minimization programs THERIAK and DOMINO (De Capitani and Petrakakis, 2010; updated software v. 4 February 2017) and the internally consistent thermodynamic "tcdb55c2d" database (Holland and Powell, 1998; updated Nov. 2003). However, thermodynamic modeling requires a strict definition of the chemical system to ensure

it corresponds to the effective bulk chemistry equilibrated during the metamorphic peak event. The previously presented geochemical data demonstrate that a significant number of the studied samples were subject to severe chemical modifications during cooling and supergene alterations. REE patterns normalized to chondrite values (Fig. 5) allowed the identification of the samples that were not affected by late alterations and thus that best preserved the chemical system effective during metamorphic peak conditions.

Theses two samples (BT9_01-02) are meta-rhyodacites from Tillet creek (Fig. 5D). We calculated P–T pseudosections, at the whole rock scale with the metamorphic assemblage: albite + muscovite + chlorite + titanite + quartz + clinozoisite + ilmenite.

As a consequence of weathering under tropical conditions, the estimation of $Fe^{3+}$ content in the studied samples is always questionable. We therefore used the values proposed for the Fe-oxidation state of sub-arc magmatism, proposed by Lee *et al.* (2010), and recently discussed and applied to meta-volcanites by Verati *et al.* (2018). Following these previous studies, a maximum of 5% of $Fe^{3+}$ for the composition of the metamorphic equilibrium has to be envisaged and thus two chemical systems, with 0 and 5% of $Fe^{3+}$ were simulated.

The two pseudosections were calculated in the system $SiO_2$–$Al_2O_3$–$TiO_2$–FeO–MgO–$Na_2O$–CaO–$K_2O$–$H_2O$, and assuming $H_2O$ in excess (Fig. 13). In the system calculated with O ($Fe_2O_3$) = 0.29 corresponding to a 5% conversion of all Fe as FeO to $Fe_2O_3$ (Fig. 13A), minerals accommodating $Fe^{3+}$, like epidote or riebeckite are largely stabilized. Whatever the $Fe^{3+}$ content, with $H_2O$ in excess in the system zeolites are particularly well developed, even under temperatures higher than 300 °C and pressures higher than 1.5 kbar (Figs. 13A and 13B). Moreover, there is no stability field that corresponds exactly to the observed mineralogical composition, as paragonite is systematically associated with muscovite. It is in the temperature range of 300–320 °C for pressure higher than 1.4 kbar for 5% of $Fe_2O_3$ and in the temperature range of 280–320 °C for pressure higher than 1.7 kbar for 0% of $Fe_2O_3$, that we can find the mineralogical association which is the closest to the one really observed, although two white micas are always present in the modeled pseudosections.

Therefore, it appears critical to test the $H_2O$ impact on the stability field of the mineral assemblages. Using the Theriak-domino program, it is possible to generate a P-X($H_2O$) equilibrium phase diagram at a fixed temperature. We choose a temperature of 280 °C in agreement with chlorite thermometry results and two equilibrium diagrams were calculated respectively with 5 and 0% $Fe_2O_3$ (Figs. 13C and 13D). With 5% of $Fe_2O_3$ in the system, riebeckite is still well developed and two white micas are always stable together (Fig. 13A). It is only when we consider a phase diagram with all Fe as FeO (0% $Fe_2O_3$) (Fig. 13D), that we obtain the expected mineralogy. The association albite + ilmenite + chlorite + muscovite + clinozoisite + titanite + quartz is indeed for $0.60 < X(H_2O) < 0.75$ in the pressure range of 0.6–2.0 kbar. As demonstrated in Verati *et al.* (2018), in a totally different chemical system, the amount of $H_2O$ available within the metamorphic fluids appears to be a key parameter for the stability of the observed metamorphic assemblage of Basse-Terre.

All together, available petrogenetic grids, thermobarometry and pseudosection modeling provide coherent estimation of the metamorphic P–T conditions suffered by the volcanic rocks of the Basal Complex in the range of 250–300 °C and 0.6–2.0 kbar. This metamorphic evolution is the result of a high-temperature and low-pressure regime typically developed within magmatic arcs setting.

## 6 Discussion

### 6.1 Finite strain pattern and deformation history

Structural analysis allows the determination of the different directions of deformation through time during progressive cooling:

- N80-N100 for tectonic ductile structures;
- N110-N140 and N160-N10 for tectonic structures at the brittle-ductile transition;
- mainly N140-N150, and in a few cases N30-N50, N80-N100 and N160-N10, for tectonic brittle structures.

Dissolution-schistosity planes highlight ductile deformation. Pressure solution is now widely regarded as a mechanism accomplishing fluid-assisted ductile deformation under low-temperature conditions within the upper crust (Rutter, 1976; Gundersen *et al.*, 2002; Gratier *et al.*, 2013). However, strain is heterogeneous at all scales in the Basal Complex. Indeed, the regional finite strain pattern displays localized schistose domains surrounding lenses of undeformed country rocks, preserving primary magmatic structures. Structural mapping evidenced moderately dipping schistosity planes with a N 80°–100° main and exclusive direction (Fig. 6A). This structural pattern with sub-horizontal undeformed lenses strongly suggests a regional flattening stress regime, characterized by a component of vertical shortening.

During progressive cooling of the Basal Complex formations, brittle-ductile (hydrothermal tectonic breccias) and brittle structures (fractures, faults) develop with several observable directions. The change in stress regime remains unknown.

We did not observe systematic relations between the orientation of the breccias and their colours. Furthermore, we did not decipher relative chronological criteria of crosscutting relationships between both directions of breccias, as the stepping criteria are repeatedly reversed at the outcrop scale. If we take into account these various observations, it seems preferable to interpret these two structural directions as being synchronous rather than the result of two superimposed extensive events in time.

It is also difficult to define a strict chronology between the different brittle structures. This is explained by the limited observation of outcrops displaying kinematics or intersections at the scale of the Basal Complex. For this reason, we propose two hypotheses. Although we cannot rule out that the activation of theses faults may be synchronous, similarly to what we observed along semi-brittle structures, scarce outcrop-scale evidences suggest that the N140-N150 trending faults are crosscutting the N30-N50 trending faults. At the regional scale this observation is corroborated by the N 50° trending paleovalleys in which the St Rose Piton lavas have flowed and by the sharp N 150° boundary west of La Perle lava flows that may result from faulting along the directions N140-

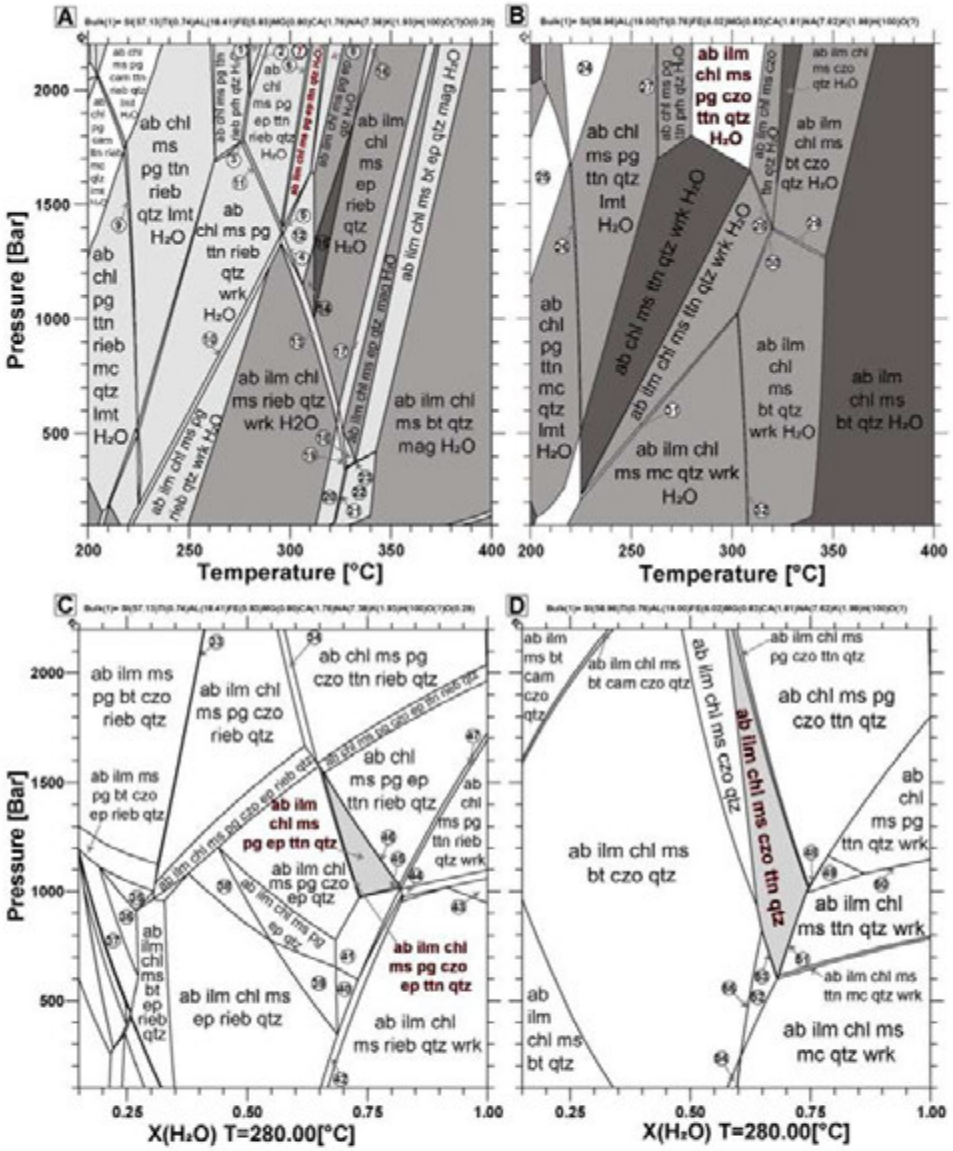


**Fig. 13.** Mineral abbreviations are from Kretz (1983). The main stable mineralogical assemblages are given, the others are listed in the Appendix Table A6. A: Calculated P–T pseudosection for a meta-rhyodacite sample (BT9-01) with $H_2O$ saturation and 5% $Fe^{3+}$ (of total iron). The rock composition, given as mol.% oxide. Fields are colored with respect to their variances, darker colours indicate lower-variance assemblages. The stability fields written in red and bold correspond to the closest observed assemblage. 4 = ab ilm chl ms pg ep rieb qtz wrk $H_2O$; 5 = ab ilm chl ms pg ep ttn qtz wrk $H_2O$; 6 = ab ilm chl ms pg ep ttn rieb qtz $H_2O$; 7 = ab ilm chl ms pg czo ep ttn qtz $H_2O$; 8 = ab ilm chl ms pg czo ep qtz $H_2O$ and 12 = ab ilm chl ms pg ep qtz wrk $H_2O$; B: Calculated P–T pseudosection for a meta-rhyodacite sample (BT9-01) with $H_2O$ saturation and total iron as $Fe^{2+}$. Rock composition is given as mol.% oxide. Fields are colored with respect to their variances, darker colours indicate lower-variance assemblages. The stability field written in red and bold correspond to the closest observed assemblage. 28 = ab ilm chl ms czo ttn qtz wrk $H_2O$; C: P-X($H_2O$) equilibrium phase diagram calculated at 280 °C, using the same base composition of Figure 13A. The stability fields colored in grey correspond to the closest observed assemblage. 41 = ab ilm chl ms pg ep qtz wrk; 45 = ab ilm chl ms pg ep ttn qtz wrk; 46 = ab ilm chl ms pg ep ttn rieb qtz; D: P-X($H_2O$) equilibrium phase diagram calculated at 280 °C, using the same base composition of Figure 13B. The stability field colored in grey corresponds to the observed assemblage. 51 = ab ilm chl ms czo ttn qtz wrk; 52 = ab ilm chl ms czo mc qtz; 53 = ab ilm chl ms czo ttn mc qtz.

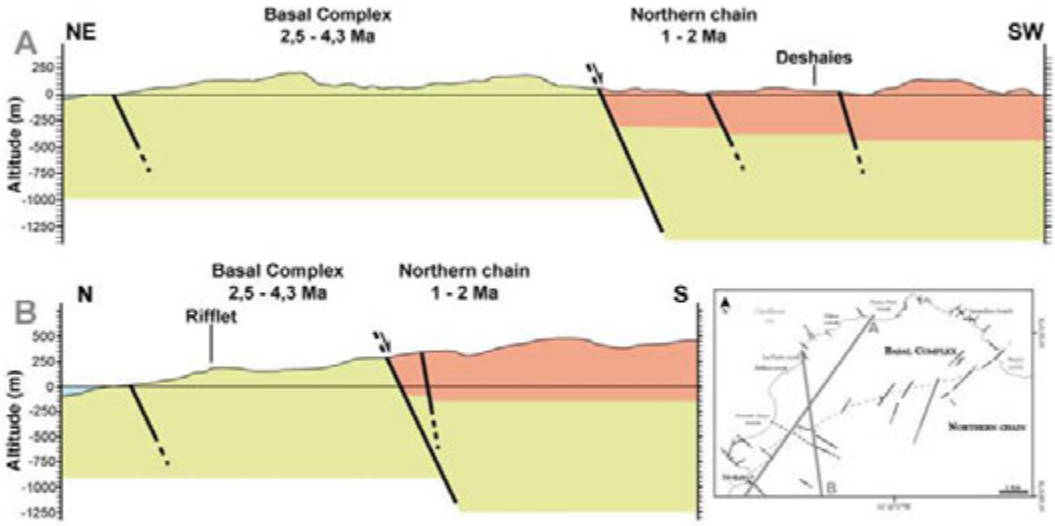


**Fig. 14.** Cross-sections showing the geometric relation between the two volcanic complexes (Basal Complex and Northern Chain).

N150 (see Fig. 6A). The N140-N150 faulting event seems to postdate the N30-N50 one. However, many studies (Bouysse, 1979; Bouysse and Westercamp, 1990; Feuillet *et al.*, 2002, 2004; Corsini *et al.*, 2011; Lardeaux *et al.*, 2013; De Min, 2014; Legendre, 2018) have shown that the deformed areas of the Guadeloupe archipelago have a long history and that active deformation is largely conditioned by the reactivation of structures, emphasising structural heritage. Following this hypothesis, structures with different orientations can be reactivated at the same time. Moreover, our paleostress inversion of the whole dataset of kinematics measurements gives a pure-extensional stress regime $\sigma_3$ trending NE-SW (Fig. 6D).

On the scale of the Guadeloupe archipelago with onshore and offshore investigations (Feuillet *et al.*, 2002, 2010, 2011; Thinon *et al.*, 2010; Mathieu *et al.*, 2011; Corsini *et al.*, 2011; Laigle *et al.*, 2013; Lardeaux *et al.*, 2013; Münch *et al.*, 2013; Leclerc *et al.*, 2014), statistically, the N150-N10 structures are presented as the most recent ones, while the N40-N50 structures are the oldest in the proposed relative chronology. According to many authors, the N120-N140 structures have been synchronously activated by transtension.

Finally, similar trends, observed in brittle, semi-brittle and ductile tectonic structures suggest strong inheritances within the crust of the volcanic arc of the Lesser Antilles and corroborates observations from previous workers along the Lesser Antilles volcanic arc (Corsini *et al.*, 2011; Lardeaux *et al.*, 2013; De Min *et al.*, 2015; Legendre *et al.*, 2018). In such a framework, the boundaries between volcanic complexes are possibly controlled by brittle normal faults, developed under recent to active extensional tectonic regimes, as it is the case for the geometric relation between the Basal Complex and the Northern Chain (Fig. 14).

### 6.2 Petrological evolution of the Basal Complex

The proposed new geological map shows a diversity of volcanic lithologies consistent with the magmatic differentiation of calc-alkaline series. Geochemical investigations allow the identification of a complete serie from basaltic-andesites to rhyodacites that has never been identified before. Even in the most altered parts of the Basal Complex, REE and multi-elements diagrams (Fig. 5) provide evidence of a triple geochemical signature: calc-alkaline magmatic differentiation, high-temperature transformation (metamorphism) and low-temperature sub-surface alteration.

These post-magmatic mineralogical transformations are the record of a progressive cooling of the Basal Complex through time and three main stages can be recognized:

- a high-temperature stage with albite, chlorite, white-micas, actinolite, biotite, prehnite, epidote, quartz, titanite, typical for sub-greenschist to greenschist facies conditions;
- a low-temperature re-equilibration stage under zeolite facies conditions with tridymite, chalcedony, calcite, quartz, chlorite, jarosite, heulandite and barite;
- and a sub-surface stage with development of clays minerals and gypsum typical for supergene alteration.

If we compare the calculated P–T conditions with the values of 70.0 to 98.2 ± 8.8 °C/km (conductive geotherm, Manga *et al.*, 2012) measured for the present day geotherm near Basse-Terre, our data supports the idea that the development of this metamorphic pattern and the building of the active magmatic arc are synchronous. The temperatures reached during the Greenschist to sub-Greenschist facies metamorphic stage are high enough to lead significant chemical exchanges between contrasted rock types. In such a case potential K and Ar losses/enrichments, are still possible

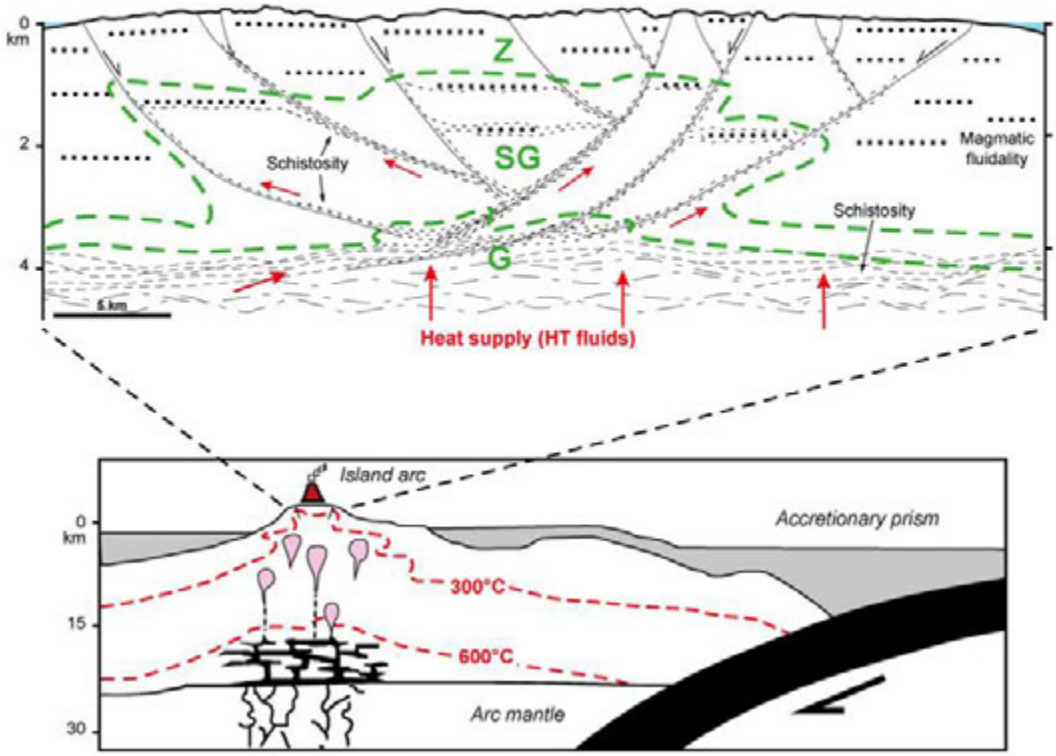


**Fig. 15.** Conceptual model for arc related metamorphism and deformation in the Lesser Antilles volcanic arc in Guadeloupe. The crustal thickness of the island arc is drawn after Kopp *et al.* (2011). The brittle/ductile transition is represented as a sub-horizontal horizon acting as a shear zone. The geometry of faults and the schistose zone pattern are purely indicative. Z = Zeolite facies zone; SG = Sub-Greenschist facies zone; G = Greenschist facies zone. Red arrows = Magmatic and hydrothermal fluid contribution.

in dacite lavas. Consequently, the new age of 4.3 Ma obtained on the Deshaies eroded dome must be considered as a "maximal" age for the Basal Complex.

The mineralogical evolution, which reflects cooling (or exhumation), is consistent with the structural evolution, showing an evolution from ductile structures (controlled by dissolution-recrystallization process), to brittle-ductile (hydrothermal breccias) and brittle structures (fractures, faults). The Basal Complex is thus a key area to understand the thermo-mechanical evolution of the shallow crustal levels of active volcanic arcs. As a working hypothesis, we suggest that similar "arc-related metamorphism", although recognized on a small area of northern Basse-Terre of Guadeloupe, is a common feature at the scale of the whole Lesser Antilles arc, and could now be recognized in other eroded zones of the recent or ancient volcanic arcs as in St. Kitts or Martinique for example.

### 6.3 Regional model for heat and fluid transfers within the upper crust of Lesser Antilles active arc

Relationships between metamorphism and tectonics enable a conceptual model (Fig. 15) to be proposed including the depth of the brittle-ductile transition. If the conductive geothermal gradient is uniform (Manga *et al.*, 2012; Verati *et al.*, 2018), our observations can be extended to the whole island, and thus temperatures in the range of 250–300 °C possibly occur at a depth of 3–4 km. Consequently, the faults observed at the surface, more often strongly dipping, must be rooted on the brittle-ductile transition, and potentially tend to be more horizontal at that transition depth. This rheological interface is then potentially a preferential pathway for regional heat and fluid transfers, and in connection to the already known fault network and/or to volcanic structures (interfaces between lava flows, volcanic fabrics,...), offering a system of connected physical vertical and more horizontal discontinuities able to drive the hydrothermal fluids circulation at the whole scale of Basse-Terre arc crust. This result opens new exciting perspectives first for the exploration of geothermal resources, only known and already exploited in the Bouillante bay (Bouchot *et al.*, 2010; Calcagno *et al.*, 2012; Verati *et al.*, 2014), and second in a more general way for the understanding of genesis of metallic ore deposits in volcanic arcs, following the idea that epithermal systems are comparable to geothermal systems (White & Hedenquist, 1995).

## 7 Conclusions

In the northern part of the island of Basse-Terre of Guadeloupe, the Basal Complex, including the Deshaies eroded dome, is composed of a well-differentiated calc-alkaline volcanic serie, with basaltic-andesites, andesites, dacites and rhyodacites. Its southern boundary corresponds to a series of faults of N 150° and N 50° main directions.

New $^{40}Ar$–$^{39}Ar$ dating on magmatic plagioclases demonstrates a magmatic activity with a significant time span, in the range of 4.3 to 2 Ma.

The Basal Complex offers a spectacular example of arc-related metamorphism in relation with a hydrothermal fluid circulation during the building and the cooling of the Lesser Antilles magmatic arc. Three main stages of post-magmatic mineralogical transformations record this evolution with: first a high-temperature stage under Greenschist to sub-Greenschist facies conditions (0.6–2 kbar for 250–300 °C), a re-equilibration stage under Zeolite facies conditions and finally a sub-surface alteration stage. This metamorphism is consistent with the present day geothermal gradient measured near the northwestern coast of Basse-Terre Island (Manga *et al.*, 2012).

In parallel with this metamorphic evolution, a significant deformation history has been characterized. The finite strain pattern consists in the development and superposition through time of N80-N100 oriented schistose domains, driven by pressure-solution processes, of hydrothermal breccias associated to N110-N140 and N160-N10 faults, and finally of brittle normal faults, with dominant trends N140-N150.

The Basal Complex is an exhumed and eroded piece of the shallow crustal levels of the Lesser Antilles volcanic arc and thus represents a key-target for understanding its whole thermo-mechanical evolution.

The depicted tectono-metamorphic evolution is compatible with brittle-ductile transition located at around 3–4 km deep at the scale of the Basse-Terre Island. In such a framework, steeply dipping normal faults are probably rooted on this rheological interface. The connection of brittle faults to schistose domains provides connected vertical and horizontal physical discontinuities allowing heat and hydrothermal fluid transfers at shallow depth within the Guadeloupe archipelago.

## Supplementary Material

**Appendix A:** Raman spectrometry spectra used to complete mineral determination.
**Table A1:** Results of paleotensors obtained by field data inversion in the Basal Complex of the Basse-Terre de Guadeloupe.
**Table A2:** $^{40}Ar/^{39}Ar$ analyses results, ArArCalc files.
**Table A3:** New major element data set of whole-rock samples analysed for this study.
**Table A4:** New trace element data set of whole-rock samples analysed for this study.
**Table A5:** Microprobe analysis of metamorphic phases. Ox = oxygen number.
**Table A6:** All stable mineralogical assemblages listed in Figure 13. Mineral abbreviations are from Kretz (1983).

The Supplementary Material is available at http://www.bsgf.fr/10.1051/bsgf/2019011/olm.

*Acknowledgment.* This paper is a contribution to the GEOTREF program, funded by the French government with the program of "Investissements d'Avenir" and tutored by ADEME. We thank the researchers from the GEOTREF consortium for greatful discussions during the fieldwork campaigns in Guadeloupe and during scientific meetings. We sincerely would like to thank the reviews, the comments and the suggestions of Agnès Samper and Christoph von Hagke that significantly improved the manuscript. The authors thank Vivien Navelot for his donation of some samples and geochemical data, Matthieu Zanti for sampling preparation, Arthur Iemmolo for his technical support during $^{40}Ar/^{39}Ar$ analysis and Gabriel Monge for his welcome to CEMEF for the use of the X-ray Diffraction device.

## References

Andreieff P, Bouysse P, Westercamp D. 1987. Géologie de l'arc insulaire des Petites Antilles, et évolution géodynamique de l'Est-Caraïbes. Université de Bordeaux I, Bordeaux (France).

Angelier J. 1979. Determination of the mean principal directions of stresses for a given fault population. *Tectonophysics* 56: T17 T26. DOI: 10.1016/0040-1951(79)90081-7.

Angelier J, Mechler P. 1977. Sur une méthode graphique de recherche des contraintes principales également utilisables en tectonique et en séismologie : la méthode des dièdres droits. *Bulletin de la Société géologique de France* S7-XIX: 1309 1318. DOI: 10.2113/gssgfbull.S7-XIX.6.1309.

Barnoud A, Bouligand C, Coutant O, Carlut J. 2017. Magnetic structure of Basse-Terre volcanic island (Guadeloupe, Lesser Antilles) inferred from 3D inversion of aeromagnetic data. *Journal of Volcanology and Geothermal Research* 348: 1 11. DOI: 10.1016/j.jvolgeores.2017.10.005.

Bas MJL, Maitre RWL, Streckeisen A, Zanettin B. 1986. A chemical classification of volcanic rocks based on the total alkali-silica diagram. *Journal of Petrology* 27: 745 750. DOI: 10.1093/petrology/27.3.745.

Bau M. 1991. Rare-earth element mobility during hydrothermal and metamorphic fluid-rock interaction and significance of the oxidation state of europium. *Chemical Geology* 93: 219 230. DOI: 10.1016/0009-2541(91)90115-8.

Beach A. 1979. Pressure solution as a metamorphic process in deformed terrigenous sedimentary rocks. *Lithos* 12: 51 58. DOI: 10.1016/0024-4937(79)90062-8.

Beach A. 1982. Chemical processes in deformation at low metamorphic grades: Pressure solution and hydraulic fracturing. *Episodes* 4: 22 25.

Beiersdorfer RE, Day HW. 1995. Mineral paragenesis of pumpellyite in low-grade mafic rocks. In: Schiffman P, Day HW, eds. *Low-grade metamorphism of mafic rocks*. Boulder, Colorado: Geological Society of America, Special Paper, pp. 5 28.

Blanc F. 1983. Corrélations chronologiques et géochimiques des formations volcaniques du Sud de La Basse-Terre de Guadeloupe (Petites Antilles) : début du cycle récent. Université Scientifique et Médicale de Grenoble, Grenoble (France).

Bouchot V, Traineau H, Guillou-Frottier L, Thinon I, Baltassat J-M, Fabriol H, *et al.* 2010. Assessment of the Bouillante Geothermal Field (Guadeloupe, French West Indies): Toward a conceptual model of the high temperature geothermal system. In: *Proceedings*

*of the World Geothermal Congress 2010, Bali, Indonesia, 25 29 April 2010*, (International Geothermal Association).

Boudon G, Semet MP, Vincent PM. 1987. Magma and hydrothermally driven sector collapses: The 3100 and 11 500 y. B.P. eruptions of la Grande Découverte (la Soufrière) volcano, Guadeloupe, French West Indies. *Journal of Volcanology and Geothermal Research* 33: 317 323. DOI: 10.1016/0377-0273(87)90021-7.

Boudon G, Semet MP, Vincent PM. 1989. The evolution of La Grande Découverte (La Soufrière) volcano, Guadeloupe (F.W.I.). In: Latter J, ed. *Volcanic hazards: Assessment monitoring. IAVCEI Proceedings in Volcanology; Berlin*, (Springer, Heidelberg, Berlin), pp. 86 109. DOI: 10.1007/978-3-642-73759-6_5.

Boudon G, Komorowski JC, Villemant B, Semet MP. 2008. A new scenario for the last magmatic eruption of La Soufrière of Guadeloupe (Lesser Antilles) in 1530 A.D. Evidence from stratigraphy radiocarbon dating and magmatic evolution of erupted products. *Journal of Volcanology and Geothermal Research* 178: 474 490. DOI: 10.1016/j.jvolgeores.2008.03.006.

Bourdelle F, Cathelineau M. 2015. Low-temperature chlorite geothermometry: A graphical representation based on a T-R2+-Si diagram. *European Journal of Mineralogy* 27: 617 626. DOI: 10.1127/ejm/2015/0027-2467.

Bouysse P. 1979. Caractères morphostructuraux et évolution géodynamique de l'arc insulaire des Petites Antilles (campagne ARCANTE 1). *Bulletin du Bureau de Recherches géologiques et Minières* 2: 185 210.

Bouysse P, Garrabé F. 1984. Évolution tectonique néogène des îles calcaires de l'archipel de Guadeloupe. *Comptes Rendus de l'Académie des Sciences de Paris* II: 763 766.

Bouysse P, Westercamp D. 1990. Subduction of Atlantic aseismic ridges and Late Cenozoic evolution of the Lesser Antilles island arc. *Tectonophysics* 175: 349 380. DOI: 10.1016/0040-1951(90)90180-G.

Bouysse P, Westercamp D, Andreieff P. 1990. The Lesser Antilles island arc. In: Moore JC, Mascle A, eds. *Proceedings of the Ocean Drilling Program Scientific Results*, pp. 29 44.

Bouysse P, Garrabé F, Mauboussin T, Andreieff P, Battistini R, Carlier P, *et al.* 1993. Carte géologique du département de La Guadeloupe, notice explicative: Marie-Galante et Îlets de La Petite-Terre, Scale 1:50.000. Orléans, France.

Braun J-J, Pagel M, Herbillo A, Rosin C. 1993. Mobilization and redistribution of REEs and thorium in a syenitic lateritic profile: A mass balance study. *Geochimica et Cosmochimica Acta* 57: 4419 4434. DOI: 10.1016/0016-7037(93)90492-F.

Braun J-J, Ngoupayou JRN, Viers J, Dupre B, Bedimo Bedimo J-P, Boeglin J-L, *et al.* 2005. Present weathering rates in a humid tropical watershed: Nsimi, South Cameroon. *Geochimica et Cosmochimica Acta* 69: 357 387. DOI: 10.1016/j.gca.2004.06.022.

Briden JC, Rex DC, Faller AM, Tomblin JF. 1979. K Ar geochronology and palaeomagnetism of volcanic rocks in the Lesser Antilles island arc. *Philosophical Transactions of the Royal Society A: Mathematical, Physical and Engineering Sciences* 291: 485 528. DOI: 10.1098/rsta.1979.0040.

Brown EH. 1977. Phase equilibria among pumpellyite, lawsonite, epidote and associated minerals in low-grade metamorphic rocks. *Contributions to Mineralogy and Petrology* 64: 123 136. DOI: 10.1007/BF00371507.

Brown M. 2010. Paired metamorphic belts revisited. *Gondwana Research* 18: 46 59. DOI: 10.1016/j.gr.2009.11.004.

Brown GM, Holland JG, Sigurdsson H, Tomblin JF, Arculus RJ. 1977. Geochemistry of the Lesser Antilles volcanic island arc. *Geochimica et Cosmochimica Acta* 41: 785 801. DOI: 10.1016/0016-7037(77)90049-7.

Calcagno P, Bouchot V, Thinon I, Bourgine B. 2012. A new 3D fault model of the Bouillante geothermal province combining onshore and offshore structural knowledge (French West Indies). *Tectonophysics* 526-529: 185 195. DOI: 10.1016/j.tecto.2011.08.012.

Carignan J, Hild P, Mevelle G, Morel J, Yeghicheyan D. 2001. Routine analyses of trace elements in geological samples using flow injection and low pressure on-line liquid chromatography coupled to ICP-MS: A study of geochemical reference materials BR, DR-N, UB-N, AN-G and GH. *Geostandards and Geoanalytical Research* 25: 187 198. DOI: 10.1111/j.1751-908X.2001.tb00595.x.

Carlut J, Quidelleur X, Courtillot V, Boudon G. 2000. Paleomagnetic directions and K/Ar dating of 0 to 1 Ma lava flows from La Guadeloupe Island (French West Indies): Implications for time-averaged field models. *Journal of Geophysical Research: Solid Earth* 105: 835 849. DOI: 10.1029/1999JB900238.

Chambefort I, Lewis B, Simpson MP, Bignall G, Rae AJ, Ganefianto N. 2017. Ngatamariki geothermal system: Magmatic to epithermal transition in the Taupo volcanic zone, New Zealand. *Economic Geology* 112: 319 346. DOI: 10.2113/econgeo.112.2.319.

Coombs DS. 1960. Lower-grade mineral facies in New Zealand. In: *Proceedings of the 21st International Geological Congress, Copenhagen*, pp. 339 351.

Cornée J-J, Léticée J-L, Münch P, Quillévéré F, Lebrun J-F, Moissette P, *et al.* 2012. Sedimentology, palaeoenvironments and biostratigraphy of the Pliocene-Pleistocene carbonate platform of Grande-Terre (Guadeloupe, Lesser Antilles forearc). *Sedimentology* 59: 1426 1451. DOI: 10.1111/j.1365-3091.2011.01311.x.

Cornu S, Lucas Y, Lebon E, Ambrosi J-P, Luizão F, Rouiller J, *et al.* 1999. Evidence of titanium mobility in soil profiles, Manaus, central Amazonia. *Geoderma* 91: 281 295. DOI: 10.1016/S0016-7061(99)00007-5.

Corsini M, Lardeaux JM, Verati C, Voitus E, Balagne M. 2011. Discovery of lower cretaceous symmetamorphic thrust tectonics in French Lesser Antilles (La Désirade Island, Guadeloupe): Implications for Caribbean geodynamics. *Tectonics* 30: 1 15. DOI: 10.1029/2011TC002875.

Cotten J, Le Dez A, Bau M, Caroff M, Maury RC, Dulski P, *et al.* 1995. Origin of anomalous rare-earth element and yttrium enrichments in subaerially exposed basalts: Evidence from French Polynesia. *Chemical Geology* 119: 115 138. DOI: 10.1016/0009-2541(94)00102-E.

Dagain J. 1981. La mise en place du massif volcanique Madeleine-Soufrière, Basse-Terre de Guadeloupe, Antilles. Université Paris Sud, Orsay.

Dagain J, Paterne M, Westercamp D. 1981. La mise en place du massif volcanique Madeleine-Soufrière, Basse-Terre de Guadeloupe, Antilles. *Comptes Rendus de l'Académie des Sciences de Paris* 292: 921 926.

Day HW, Springer RK. 2005. The first appearance of actinolite in the prehnite pumpellyite facies, Sierra Nevada, California. *The Canadian Mineralogist* 43: 89 104. DOI: 10.2113/gscanmin.43.1.89.

De Capitani C, Petrakakis K. 2010. The computation of equilibrium assemblage diagrams with Theriak/Domino software. *American Mineralogist* 95: 1006 1016. DOI: 10.2138/am.2010.3354.

De Min L. 2014. Sismo-stratigraphie multi-échelles d'un Bassin d'avant-arc: le Bassin de Marie-Galante, Petites Antilles. Université des Antilles et de la Guyane, Pointe-à-Pitre (Guadeloupe).

De Min L, Lebrun J-F, Cornee J-J, Münch P, Léticée J-L, Quillévéré F, *et al.* 2015. Tectonic and sedimentary architecture of the Karukéra spur: A record of the Lesser Antilles fore-arc deformations since the Neogene. *Marine Geology* 363: 15 37. DOI: 10.1016/j.margeo.2015.02.007.

De Reynal de Saint-Michel A. 1966. Carte géologique à l'échelle 1:50 000 du département de La Guadeloupe Feuilles de Basse-Terre et des Saintes. Paris.

Delvaux D, Sperner B. 2003. New aspects of tectonic stress inversion with reference to the TENSOR program. *Geological Society, London, Special Publications* 212: 75 100. DOI: 10.1144/GSL.SP.2003.212.01.06.

Demets C, Jansma PE, Mattioli G, Dixon TH, Farina F, Bilham R, *et al.* 2000. GPS geodetic constraints on Caribbean-North America plate motion. *Geophysical Research Letters* 27: 437 440.

Dessert C, Lajeunesse E, Lloret E, Clergue C, Crispi O, Gorge C, *et al.* 2015. Controls on chemical weathering on a mountainous volcanic tropical island: Guadeloupe (French West Indies). *Geochimica et Cosmochimica Acta* 171: 216 237. DOI: 10.1016/j.gca.2015.09.009.

Dixon TH, Farina F, Demets C, Jansma P, Mann P, Calais E. 1998. Relative motion between the Caribbean and North American plates and related boundary zone deformation from a decade of GPS observations. *Journal of Geophysical Research: Solid Earth* 103: 15157 15182. DOI: 10.1029/97JB03575.

Ducea MN, Saleeby JB, Bergantz G. 2015. The architecture, chemistry, and evolution of continental magmatic arcs. *Annual Review of Earth and Planetary Sciences* 43: 299 331. DOI: 10.1146/annurev-earth-060614-105049.

Ernst WG. 1973. Blueschist metamorphism and P T regimes in active subduction zones. *Tectonophysics* 17: 255 272. DOI: 10.1016/0040-1951(73)90006-1.

Feuillet N, Manighetti I, Tapponnier P. 2001. Extension active perpendiculaire à la subduction dans l'arc des Petites Antilles (Guadeloupe, Antilles françaises). *Comptes Rendus de l'Académie de Sciences Série IIa : Sciences de la Terre et des Planètes* 333: 583 590. DOI: 10.1016/S1251-8050(01)01543-9.

Feuillet N, Manighetti I, Tapponnier P, Jacques E. 2002. Arc parallel extension and localization of volcanic complexes in Guadeloupe, Lesser Antilles. *Journal of Geophysical Research* 107(B12): ETG 3 1 29. DOI: 10.1029/2001JB000308.

Feuillet N, Tapponnier P, Manighetti I, Villemant B, King GCP. 2004. Differential uplift and tilt of Pleistocene reef platforms and Quaternary slip rate on the Morne-Piton normal fault (Guadeloupe, French West Indies). *Journal of Geophysical Research: Solid Earth* 109: 1 18. DOI: 10.1029/2003JB002496.

Feuillet N, Leclerc F, Tapponnier P, Beauducel F, Boudon G, Le Friant A, *et al.* 2010. Active faulting induced by slip partitioning in Montserrat and link with volcanic activity: New insights from the 2009 GWADASEIS marine cruise data. *Geophysical Research Letters* 37: 1 6. DOI: 10.1029/2010GL042556.

Feuillet N, Beauducel F, Tapponnier P. 2011. Tectonic context of moderate to large historical earthquakes in the Lesser Antilles and mechanical coupling with volcanoes. *Journal of Geophysical Research: Solid Earth* 116: 1 26. DOI: 10.1029/2011JB008443.

Frey M, Robinson D. 1999. Low-grade metamorphism. Oxford: Blackwell, John Wiley & Sons (Ed.).

Frey M, De Capitani C, Liou JG. 1991. A new petrogenetic grid for low-grade metabasites. *Journal of Metamorphic Geology* 9: 497 509. DOI: 10.1111/j.1525-1314.1991.tb00542.x.

Gailler LS, Martelet G, Thinon I, Bouchot V, Lebrun JF, Münch P. 2013. Crustal structure of Guadeloupe Islands and the Lesser Antilles arc from a new gravity and magnetic synthesis. *Bulletin de la Société géologique de France* 184: 77 97. DOI: 10.2113/gssgfbull.184.1-2.77.

Germa A, Quidelleur X, Labanieh S, Chauvel C, Lahitte P. 2011. The volcanic evolution of Martinique Island: Insights from K Ar dating into the Lesser Antilles arc migration since the Oligocene. *Journal of Volcanology and Geothermal Research* 208: 122 135. DOI: 10.1016/j.jvolgeores.2011.09.007.

Gratier J-P, Dysthe DK, Renard F. 2013. *The role of pressure solution creep in the ductility of the Earth's upper crust*, Ed. Advances in Geophysics. DOI: 10.1016/B978-0-12-380940-7.00002-0.

Gundersen E, Renard F, Dysthe DK, Bjørlykke K, Jamtveit B. 2002. Coupling between pressure solution creep and diffusive mass transport in porous rocks. *Journal of Geophysical Research: Solid Earth* 107: ECV 19-1-ECV 19 19. DOI: 10.1029/2001JB000287.

Hastie AR, Kerr AC, Pearce JA, Mitchell SF. 2007. Classification of altered volcanic island arc rocks using immobile trace elements: Development of the Th Co discrimination diagram. *Journal of Petrology* 48: 2341 2357. DOI: 10.1093/petrology/egm062.

Hawkesworth CJ, Powell M. 1980. Magma genesis in the Lesser Antilles island arc. *Earth and Planetary Science Letters* 51: 297 308. DOI: 10.1016/0012-821X(80)90212-5.

Holland TJB, Powell R. 1998. An internally consistent thermodynamic data set for phases of petrological interest. *Journal of Metamorphic Geology* 16: 309 343.

Jébrak M. 1997. Hydrothermal breccias in vein-type ore deposits: A review of mechanisms, morphology and size distribution. *Ore Geology Reviews* 12: 111 134. DOI: 10.1016/S0169-1368(97)00009-7.

Kettermann M, Von Hagke C, Van Gent HW, Grutzner C, Urai JL. 2016. Dilatant normal faulting in jointed cohesive rocks: A physical model study. *Solid Earth* 7: 843 856. DOI: 10.5194/se-7-843-2016.

Kopp H, Weinzierl W, Becel A, Charvis P, Evain M, Flueh ER, *et al.* 2011. Deep structure of the central Lesser Antilles island arc: Relevance for the formation of continental crust. *Earth and Planetary Science Letters* 304: 121 134. DOI: 10.1016/j.epsl.2011.01.024.

Koppers AAP. 2002. ArArCALC Software for 40Ar/39Ar age calculations. *Computers & Geosciences* 28: 605 619. DOI: 10.1016/S0098-3004(01)00095-4.

Kretz R. 1983. Symbols for rock-forming minerals. *American Mineralogist* 68: 277 279.

Labanieh S. 2009. Géochimie de l'île de La Martinique aux Petites Antilles. Université Joseph-Fourier Grenoble I, Grenoble (France).

Laigle M, Becel A, De Voogd B, Sachpazi M, Bayrakci G, Lebrun J-F, Evain M. 2013. Along-arc segmentation and interaction of subducting ridges with the Lesser Antilles Subduction forearc crust revealed by MCS imaging. *Tectonophysics* 603: 32 54. DOI: 10.1016/j.tecto.2013.05.028.

Lanari P, Wagner T, Vidal O. 2014. A thermodynamic model for di-trioctahedral chlorite from experimental and natural data in the system MgO FeO $Al_2O_3$ $SiO_2$ $H_2O$: Applications to P T sections and geothermometry. *Contributions to Mineralogy and Petrology* 167: 1 19. DOI: 10.1007/s00410-014-0968-8.

Lardeaux JM, Münch P, Corsini M, Cornée J-J, Verati C, Lebrun J-F, *et al.* 2013. La Désirade Island (Guadeloupe, French West Indies): A key target for deciphering the role of reactivated tectonic structures in Lesser Antilles arc building. *Bulletin de la Société géologique de France* 184: 21 34. DOI: 10.2113/gssgfbull.184.1-2.21.

Leclerc F, Feuillet N, Cabioch G, Deplus C, Lebrun J-F, Bazin S, *et al.* 2014. The Holocene drowned reef of Les Saintes plateau as witness

of a long-term tectonic subsidence along the Lesser Antilles volcanic arc in Guadeloupe. *Marine Geology* 355: 115 135. DOI: 10.1016/j.margeo.2014.05.017.

Lee J-Y, Marti K, Severinghaus JP, Kawamura K, Yoo H-S, Lee JB, *et al.* 2006. A redetermination of the isotopic abundances of atmospheric Ar. *Geochimica et Cosmochimica Acta*, 4507 4512.

Lee C-TA, Luffi P, Le Roux V, Dasgupta R, Albaréde F, Leeman WP. 2010. The redox state of arc mantle using Zn/Fe systematics. *Nature* 468: 681 685. DOI: 10.1038/nature09617.

Legendre L. 2018. Évolution tectonique du Nord de l'arc des Petites Antilles. Université des Antilles, Pointe-à-Pitre (Guadeloupe).

Legendre L, Philippon M, Münch P, Leticée J-L, Noury M, Maincent G, *et al.* 2018. Trench bending initiation: Upper plate strain pattern and volcanism. Insights from the Lesser Antilles arc, St. Barthelemy Island, French West Indies. *Tectonics* 37: 2777 2797. DOI: 10.1029/2017TC004921.

Liou JG, Maruyama S, Cho M. 1985. Phase equilibria and mixed parageneses of metabasites in low-grade metamorphism. *Mineralogical Magazine* 49: 321 333. DOI: 10.1180/minmag.1985.049.352.03.

Liou JG, Mauyama S, Cho M. 1987. Very low-grade metamorphism of volcanic and volcaniclastic rocks-mineral assemblages and mineral facies. In: Frey M, ed. *Low temperature metamorphism*. Blackie, Glasgow, pp. 59 113.

Lloret E, Dessert C, Gaillardet J, Albéric P, Crispi O, Chaduteau C, *et al.* 2011. Comparison of dissolved inorganic and organic carbon yields and fluxes in the watersheds of tropical volcanic islands, examples from Guadeloupe (French West Indies). *Chemical Geology* 280: 65 78. DOI: 10.1016/j.chemgeo.2010.10.016.

Ma J-L, Wei G-J, Xu Y-G, Long W-G, Sun W-D. 2007. Mobilization and re-distribution of major and trace elements during extreme weathering of basalt in Hainan Island, South China. *Geochimica et Cosmochimica Acta* 71: 3223 3237. DOI: 10.1016/j.gca.2007.03.035.

Manga M, Hornbach MJ, Le Friant A, Ishizuka O, Stroncik N, Adachi T, *et al.* 2012. Heat flow in the Lesser Antilles island arc and adjacent back arc Grenada basin. *Geochemistry, Geophysics, Geosystems* 13: 1 19. DOI: 10.1029/2012GC004260.

Mathieu L. 2010. The structure of Guadeloupe, Maderas and Mt Cameroon volcanoes and the impact of strike-slip movements. Université Blaise Pascal Clermont-Ferrand II, Trinity College Dublin, Clermont-Ferrand (France) and Dublin (Ireland).

Mathieu L, Van Wyk de Vries B, Pilato M, Troll VR. 2011. The interaction between volcanoes and strike-slip, transtensional and transpressional fault zones: Analogue models and natural examples. *Journal of Structural Geology* 33: 898 906. DOI: 10.1016/j.jsg.2011.03.003.

Mathieu L, Van Wyk de Vries B, Mannessiez C, Mazzoni N, Savry C, Troll VR. 2013. The structure and morphology of the Basse-Terre Island, Lesser Antilles volcanic arc. *Bulletin of Volcanology* 75: 1 15. DOI: 10.1007/s00445-013-0700-y.

Maury RC, Westbrook GK, Baker PE, Bouysse P, Westercamp D. 1990. Chapter 5: Geology of the Lesser Antilles. In: Dengo G, Case JE, eds. *The geology of North America*, Vol. H. Boulder, Colorado, pp. 141 166.

Melfi AJ, Subies F, Nahon D, Formoso MLL. 1996. Zirconium mobility in bauxites of Southern Brazil. *Journal of South American Earth Sciences* 9: 161 170. DOI: 10.1016/0895-9811(96)00003-X.

Michard A. 1989. Rare earth element systematics in hydrothermal fluids. *Geochimica et Cosmochimica Acta* 53: 745 750. DOI: 10.1016/0016-7037(89)90017-3.

Michard A, Albarède F, Michard G, Minster JF, Charlou JL. 1983. Rare-earth elements and uranium in high-temperature solutions from East Pacific Rise hydrothermal vent field (N° 13). *Nature* 303: 795 797. DOI: 10.1038/303795a0.

Miyashiro A. 1967. Orogeny regional metamorphism and magmatism in the Japanese Islands. *Geological Society of Denmark* 17: 390 446.

Münch P, Lebrun JF, Cornee JJ, Thinon I, Guennoc P, Marcaillou BJ, *et al.* 2013. Pliocene to Pleistocene carbonate systems of the Guadeloupe archipelago, French Lesser Antilles: A land and sea study (the KaShallow project). *Bulletin de la Société géologique de France* 184: 99 110. DOI: 10.2113/gssgfbull.184.1-2.99.

Münch P, Cornee J-J, Lebrun JF, Quillevere F, Verati C, Melinte-Dobrinescu M, *et al.* 2014. Pliocene to Pleistocene vertical movements in the forearc of the Lesser Antilles subduction: Insights from chronostratigraphy of shallow-water carbonate platforms (Guadeloupe archipelago). *Journal of the Geological Society* 171: 329 341. DOI: 10.1144/jgs2013-005.

Nahon D, Merino E. 1996. Pseudomorphic replacement *versus* dilation in laterites: Petrographic evidence, mechanisms, and consequences for modelling. *Journal of Geochemical Exploration* 57: 217 225. DOI: 10.1016/S0375-6742(96)00038-6.

Navelot V, Géraud Y, Favier A, Diraison M, Corsini M, Lardeaux J-M, *et al.* 2018. Petrophysical properties of volcanic rocks and impacts of hydrothermal alteration in the Guadeloupe Archipelago (West Indies). *Journal of Volcanology and Geothermal Research* 360: 1 21. DOI: 10.1016/j.jvolgeores.2018.07.004.

Oxburgh ER, Turcotte DL. 1970. Thermal structure of island arcs. *GSA bulletin* 81: 1665 1688. DOI: 10.1130/0016-7606(1970)81[1665:TSOIA]2.0.CO;2.

Passchier CW, Trouw RAJ. 2005. Microtectonics, 2nd ed. Berlin, Heidelberg: Springer.

Patino LC, Velbel MA, Price JR, Wade JA. 2003. Trace element mobility during spheroidal weathering of basalts and andesites in Hawaii and Guatemala. *Chemical Geology* 202: 343 364. DOI: 10.1016/j.chemgeo.2003.01.002.

Patrier P, Bruzac S, Pays R, Beaufort D, Bouchot V, Verati C, Gadalia A. 2013. Occurrence of K-feldspar-bearing hydrothermal breccias in the Bouillante geothermal field (Basse-Terre Guadeloupe). *Bulletin de la Société géologique de France* 184: 119 128. DOI: 10.2113/gssgfbull.184.1-2.119.

Pearce JA. 1996. A user's guide to basalt discrimination diagrams. In: Wyman DA, ed. *Trace element geochemistry of volcanic rocks: Application to massive sulphide exploration*. Geological Association of Canada, Short Course Notes, pp. 79 113.

Peccerillo A, Taylor SR. 1976. Geochemistry of Eocene calc-alkaline volcanic rocks from the Kastamonu area, Northern Turkey. *Contributions to Mineralogy and Petrology* 58: 63 81. DOI: 10.1007/BF00384745.

Powell CM. 1979. A morphological classification of rock cleavage. *Tectonophysics* 58: 21 34. DOI: 10.1016/0040-1951(79)90320-2.

Powell WG, Carmichael DM, Hodgson CJ. 1993. Thermobarometry in a subgreenschist to greenschist transition in metabasites of the Abitibi greenstone belt, Superior Province, Canada. *Journal of Metamorphic Geology* 11: 165 178. DOI: 10.1111/j.1525-1314.1993.tb00138.x.

Rad S, Rivé K, Vittecoq B, Cerdan O, Allègre CJ. 2013. Chemical weathering and erosion rates in the Lesser Antilles: An overview in Guadeloupe, Martinique and Dominica. *Journal of South American Earth Sciences* 45: 331 344. DOI: 10.1016/j.jsames.2013.03.004.

Renne PR, Mundil R, Balco G, Min K, Ludwig KR. 2010. Joint determination of 40K decay constants and 40Ar*/40K for the Fish Canyon sanidine standard, and improved accuracy for 40Ar/39Ar geochronology. *Geochimica et Cosmochimica Acta* 74: 5349 5367. DOI: 10.1016/j.gca.2010.06.017.

Ricci J, Lahitte P, Quidelleur X. 2015a. Construction and destruction rates of volcanoes within tropical environment: Examples from the Basse-Terre Island (Guadeloupe, Lesser Antilles). *Geomorphology* 228: 597 607. DOI: 10.1016/j.geomorph.2014.10.002.

Ricci J, Quidelleur X, Lahitte P. 2015b. Volcanic evolution of central Basse-Terre Island revisited on the basis of new geochronology and geomorphology data. *Bulletin of Volcanology* 77: 84. DOI: 10.1007/s00445-015-0970-7.

Ricci J, Quidelleur X, Pallares C, Lahitte P. 2017. High-resolution K Ar dating of a complex magmatic system: The example of Basse-Terre Island (French West Indies). *Journal of Volcanology and Geothermal Research* 345: 142 160. DOI: 10.1016/j.jvolgeores.2017.07.013.

Robinson D, Bevins RE, Aguirre L, Vergara M. 2004. A reappraisal of episodic burial metamorphism in the Andes of central Chile. *Contributions to Mineralogy and Petrology* 146: 513 528. DOI: 10.1007/s00410-003-0516-4.

Robinson D, Bevins RE, Rubinstein N. 2005. Subgreenschist facies metamorphism of metabasites from the Precordillera terrane of western Argentina; constraints on the later stages of accretion onto Gondwana. *European Journal of Mineralogy* 17: 441 452. DOI: 10.1127/0935-1221/2005/0017-0441.

Rowland JV, Simmons SF. 2012. Hydrologic, magmatic, and tectonic controls on hydrothermal flow, Taupo volcanic zone, New Zealand: Implications for the formation of epithermal vein deposits. *Economic Geology* 107: 427 457. DOI: 10.2113/econgeo.107.3.427.

Rutter EH. 1976. The kinetics of rock deformation by pressure solution. *Philosophical Transactions of the Royal Society London* 283: 203 219. DOI: 10.1098/rsta.1976.0079.

Sak PB, Navarre-Sitchler AK, Miller C, Daniel CC, Gaillardet J, Buss HL, *et al.* 2010. Controls on rind thickness on basaltic andesite clasts weathering in Guadeloupe. *Chemical Geology* 276: 129 143. DOI: 10.1016/j.chemgeo.2010.05.002.

Samper A, Quidelleur X, Lahitte P, Mollex D. 2007. Timing of effusive volcanism and collapse events within an oceanic arc island: Basse-Terre, Guadeloupe archipelago (Lesser Antilles Arc). *Earth and Planetary Science Letters* 258: 175 191. DOI: 10.1016/j.epsl.2007.03.030.

Samper A, Quidelleur X, Komorowski J-C, Lahitte P, Boudon G. 2009. Effusive history of the Grande Découverte Volcanic Complex, southern Basse-Terre (Guadeloupe, French West Indies) from new K Ar Cassignol Gillot ages. *Journal of Volcanology and Geothermal Research* 187: 117 130. DOI: 10.1016/j.jvolgeores.2009.08.016.

Schiffman P, Day HW. 1999. Petrological methods for the study of very low-grade metabasites. In: Frey M, Robinson D, eds. *Very low-grade metamorphism*. Oxford, UK: Blackwell Publishing Ltd., pp. 108 142. DOI: 10.1002/9781444313345.ch4.

Schumacher JC. 1997. The estimation of ferric iron in electron microprobe analysis of amphiboles. *Mineralogical Magazine* 61: 312 321. DOI: 10.1017/S0026461X00011397.

Sibson RH. 1977. Fault rocks and fault mechanisms. *Journal of the Geological Society* 133: 191 213. DOI: 10.1144/gsjgs.133.3.0191.

Sillitoe RH, Perelló J. 2005. Andean copper province Tectonomagmatic settings, deposit types, metallogeny, exploration, and discovery. *Society of Economic Geologists, Economic Geology 100th Anniversary Volume*, 845 890.

Sun S-S, McDonough WF. 1989. Chemical and isotopic systematics of oceanic basalts: Implications for mantle composition and processes. *Geological Society, London, Special Publications* 42: 313 345. DOI: 10.1144/GSL.SP.1989.042.01.19.

Taylor SR, McLennan SM. 1995. The geochemical evolution of the continental crust. *Reviews of Geophysics* 33: 241. DOI: 10.1029/95RG00262.

Thinon I, Guennoc P, Bitri A, Truffert C. 2010. Study of the Bouillante Bay (West Basse-Terre Island shelf): Contribution of geophysical surveys to the understanding of the structural context of Guadeloupe (French West Indies Lesser Antilles). *Bulletin de la Société géologique de France* 181: 51 65. DOI: 10.2113/gssgfbull.181.1.51.

Verati C, Patrier-Mas P, Lardeaux J-M, Bouchot V. 2014. Timing of geothermal activity in an active island-arc volcanic setting: First 40Ar/39Ar dating from Bouillante geothermal field (Guadeloupe, French West Indies). *Geological Society, London, Special Publications* 378: 285 295. DOI: 10.1144/SP378.19.

Verati C, Mazabraud Y, Lardeaux J-M, Corsini M, Schneider D, Voitus E, *et al.* 2016. Tectonic evolution of Les Saintes archipelago (Guadeloupe, French West Indies): Relation with the Lesser Antilles arc system. *Bulletin de la Société géologique de France* 187: 3 10. DOI: 10.2113/gssgfbull.187.1.3.

Verati C, Lardeaux J-M, Favier A, Corsini M, Philippon M, Legendre L. 2018. Arc-related metamorphism in the Guadeloupe archipelago (Lesser Antilles active island arc): First report and consequences. *Lithos* 320-321: 592 598. DOI: 10.1016/j.lithos.2018.08.005.

Westercamp D. 1979. Diversity, structural control and origin of recent volcanism in the Lesser Antilles island arc. *Bulletin du Bureau de Recherches géologiques et Minières* Section IV: 211 226.

Westercamp D. 1988. Magma generation in the Lesser Antilles: Geological constraints. *Tectonophysics* 149: 145 163. DOI: 10.1016/0040-1951(88)90123-0.

Westercamp D, Tazieff H. 1980. Guide géologiques régionaux, Martinique, Guadeloupe, Saint-Martin, La Désirade. Paris: Elsevier M.

White NC, Hedenquist JW. 1995. Epithermal gold deposits: Styles, characteristics and exploration. *SEG Newsl* 23: 1 9.

Winchester JA, Floyd PA. 1977. Geochemical discrimination of different magma series and their differentiation products using immobile elements. *Chemical Geology* 20: 325 343. DOI: 10.1016/0009-2541(77)90057-2.

Woodcock NH, Mort K. 2008. Classification of fault breccias and related fault rocks. *Geological Magazine* 145: 435 440. DOI: 10.1017/S0016756808004883.

Zami F, Quidelleur X, Ricci J, Lebrun J-F, Samper A. 2014. Initial sub-aerial volcanic activity along the central Lesser Antilles inner arc: New K Ar ages from Les Saintes volcanoes. *Journal of Volcanology and Geothermal Research* 287: 12 21. DOI: 10.1016/j.jvolgeores.2014.09.011.

**Cite this article as:** Favier A, Lardeaux J-M, Legendre L, Verati C, Philippon M, Corsini M, Münch P, Ventalon S. 2019. Tectono-metamorphic evolution of shallow crustal levels within active volcanic arcs. Insights from the exhumed Basal Complex of Basse-Terre (Guadeloupe, French West Indies), *BSGF - Earth Sciences Bulletin* 190: 10.

# Etat thermique de référence

*Supplementary Material*: Documents disponibles dans le chapitre Annexe de ce manuscrit (Article 1 - Supplementary data)

## IV.3. Article 2 - Arc-related metamorphism in the Guadeloupe archipelago (Lesser Antilles active island arc): First report and consequences

Cet article a fait l'objet d'une publication *Letter* dans le journal *Lithos* en 2018 (https://doi.org/10.1016/J.LITHOS.2018.08.005).

Lithos 320–321 (2018) 592–598

Contents lists available at ScienceDirect

Lithos

journal homepage: www.elsevier.com/locate/lithos

Letter

# Arc-related metamorphism in the Guadeloupe archipelago (Lesser Antilles active island arc): First report and consequences

Chrystèle Verati [a,*], Jean-Marc Lardeaux [a,b], Alexiane Favier [a,c], Michel Corsini [a], Melodie Philippon [c], Lucie Legendre [c]

[a] UMR Geoazur, Université de Nice Sophia Antipolis, Observatoire de la Côte d'Azur, 250 rue Albert Einstein, Sophia Antipolis, 06560, Valbonne, France
[b] Czech Geological Survey, Centre for Lithospheric Research, Klárov 3, 118 21 Prague 1, Czech Republic
[c] UMR Géosciences Montpellier, Université des Antilles, Campus de Fouillole, 97159 Pointe à Pitre Cedex, Guadeloupe, France

ARTICLE INFO

*Article history:*
Received 26 January 2018
Accepted 2 August 2018
Available online 7 August 2018

*Keywords:*
Low-grade metamorphism
pressure-solution
Lesser Antilles active arc
Basse-Terre of Guadeloupe

ABSTRACT

We unravel for the first time the expression of a low-grade metamorphic event affecting the deepest exposures of the Guadeloupe Island, central Lesser Antilles, Caribbean plate. The work offers a novel insight for the presence of young (<3 Ma) sub-greenschist facies metamorphism in the Lesser Antilles active arc and is consistent with the elevated geothermal gradients measured for the arc axis regionally. Quantitative pressure-temperature constraint (i.e. pseudosection) for this metamorphism as well as fluid/rock ratios are discussed. This paper offers the first report of "ductile" deformation mechanisms (i.e. pressure-solution) operating at shallow crustal levels of the Antilles volcanic arc system.

© 2018 Elsevier B.V. All rights reserved.

## 1. Introduction

Since pioneering works of Miyashiro (1961), Oxburgh and Turcotte (1970) and Ernst (1973), island arcs and back-arcs regions are recognized as a suitable tectonic setting for development of regional high-temperature/low-pressure metamorphism. This arc related metamorphism, expressed within the upper plate of the subduction zone, is interpreted as the merging of magmatic sub-systems producing regional high heat flow and fluid-driven recrystallizations (Brown, 2010).

The Lesser Antilles subduction zone is a widely known intra-oceanic subduction system where oceanic crust of the North and South America subducts beneath the eastern margin of the Caribbean plate (Bouysse and Westercamp, 1990; Fig. 1). However, even if the Lesser Antilles volcanic arc is regarded as an emblematic example for heat and fluids transfers during intra-oceanic subduction, and in spite of a significant number of detailed petrological (Boudon et al., 1987, 1998; Davidson, 1987; MacDonald et al., 2000; Maury et al., 1990) and structural (Calcagno et al., 2012; Feuillet et al., 2002; Mathieu et al., 2013) investigations, the metamorphic evolution related to its development has never been described so far.

In this paper we document the discovery of regional low-grade metamorphism and associated deformation at the brittle/ductile transition in the volcanic island of Guadeloupe archipelago (i.e. Basse Terre and Les Saintes), which is one of the meridian island of the volcanic arc, standing the upper plate of the Lesser Antilles subduction zone.

## 2. Basse- Terre of Guadeloupe: key areas for identifying arc-related metamorphism

The convergent plate boundary between the Caribbean and the North and South American plates is marked by the subduction in a WSW direction of the Atlantic oceanic crust beneath the Caribbean plate at a rate of 2 cm yr-1 (Demets et al., 2000) (Fig. 1). The thickness of the Caribbean plate, ca. 24 km, is intermediate between typical continental and oceanic values (Kopp et al., 2011). Two volcanic arcs successively emplaced since Mid-Eocene, with a westward migration through time from the outer to the inner arc, which is still active nowadays (Bouysse and Westercamp, 1990; Germa et al., 2011).

In Guadeloupe Archipelago, the island arc is divided in two ridges: the eastern one corresponds to the ancient arc covered by a carbonate platform of Grande Terre while the western one, composed of Basse Terre and Les Saintes islands, corresponds to the inner active arc (Fig. 1). The tectonic evolution of Guadeloupe (Fig. 1B) is the result of a transtensive regime leading to the development of both normal and strike-slip faults (Feuillet et al., 2002; Mathieu et al., 2013).

* Corresponding author.
*URL's:* verati@unice.fr (C. Verati), lardeaux@unice.fr (J.-M. Lardeaux), Alexiane.FAVIER@unice.fr (A. Favier), corsini@unice.fr (M. Corsini), Melodie.Philippon@gm.univ-montp2.fr (M. Philippon).

https://doi.org/10.1016/j.lithos.2018.08.005
0024-4937/© 2018 Elsevier B.V. All rights reserved.

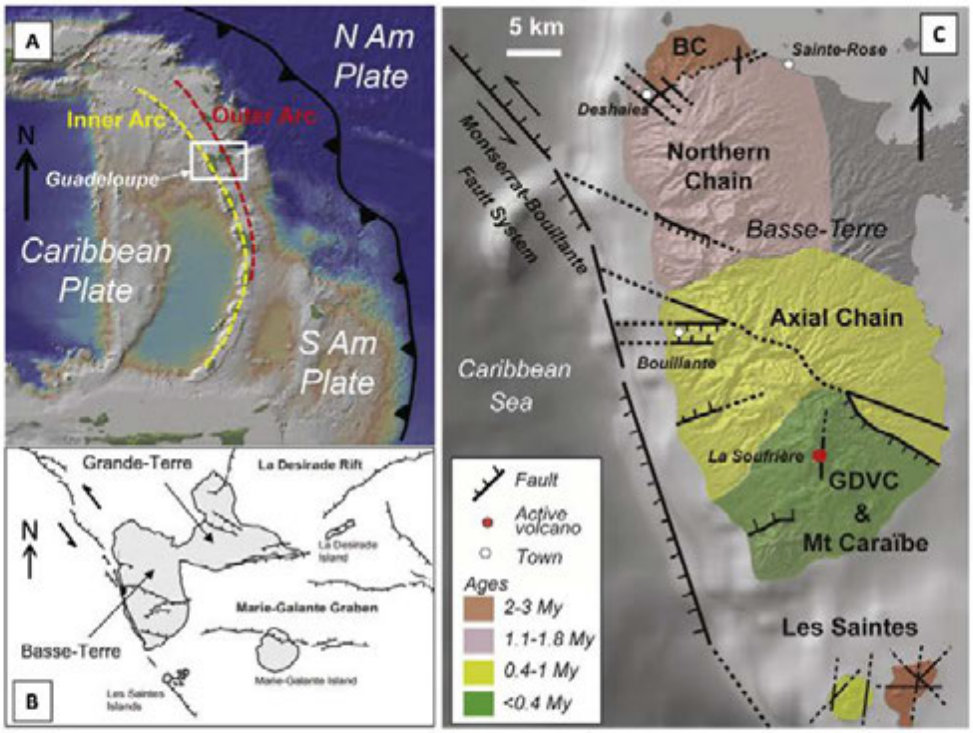


**Fig. 1.** A - Location of the Lesser Antilles arc system. Inner and Outer arc are reported (after Bouysse and Westercamp, 1990). B - Main active faults in the Guadeloupe archipelago (after Feuillet et al., 2002). C - Map of the active volcanic arc in Guadeloupe archipelago (i.e. Basse-Terre and Les Saintes) displaying the different volcanic complexes and the main tectonic structures after Boudon et al. (1987), Feuillet et al. (2002), Samper et al. (2007), Mathieu et al. (2013), Zami et al. (2014) and Verati et al. (2016). GDVC = Grande Decouverte Volcanic Complex; BC = Basal Complex.

Basse-Terre is made of late Pliocene to Quaternary volcanoes that are progressively younger southward, ending with the active La Soufrière dome (Ricci et al., 2015a; Samper et al., 2007) (Fig. 1). The northern half of Basse Terre is made of weathered rocks referred to as the Basal Complex and of the eroded Northern Chain built on N.160-oriented faults interpreted as a "volcanic axis" and parallel to the subduction front (Mathieu et al., 2013). The oldest volcanic rocks, dated at 2.8 to 2.7 Ma (Samper et al., 2007) belong to the Basal Complex cropping out north of Deshaies and Sainte-Rose towns (Fig. 1). It consists of calc-alkaline lava flows including some intercalations of debris flows. Available geomorphological studies indicate that this Basal Complex corresponds to strongly eroded volcanic formations (Mathieu et al., 2013) (Fig. 1). The Basal Complex is the volcanic basement on which the younger volcanic edifices emplaced through time (Gailler et al., 2013). The lavas of this Basal Complex are partly covered by the volcanic formations of the Northern Chain, within which more than twenty 600 to 700 m high volcanic complexes are observed. Because mean erosion rates (i.e. mechanical and chemical rates) within this volcanic arc have been constrained by geochemical and geomorphological investigations in the range of 0.5 +/− 0.2 mm/yr. (Ricci et al., 2015b) to 1 mm/yr. (Rad et al., 2013; Samper et al., 2007), the overburden suffered by these volcanic rocks can be estimated between 1.5 and to 3 km. Consequently, the Guadeloupe archipelago offers a unique opportunity to investigate a deeply eroded segment of the Lesser Antilles active arc.

### 3. Evidences for spaced disjunctive cleavage development

In the Basal Complex of Basse Terre spaced disjunctive cleavage planes (Powell, 1979) are developed at the outcrop scale (Fig. 2A). Discrete, dissolution-schistosity planes are also developed and are clearly evidenced by dark seams of insoluble dark minerals (Fig. 2B and C). Truncated volcanic enclaves and/or phenocrysts are reliable evidences for the development of pressure-solution cleavage (Fig. 2B and C). These spaced schistose zones are developed at the expense of primary volcanic structures like lava flow-fabric or lithological interfaces. Networks of quartz, albite or calcite- bearing veins and fractures frequently interconnect the cleavage planes (Fig. 2D).

The association of these structures is compatible with an evolution of deformation conditions at the brittle/ductile transition. Both structures (Fig. 2D) are consistent with a finite strain ellipsoid with a horizontal maximum stretch, and thus with an extensional regime.

All together, these structures suggest that these rocks underwent localized fluid-assisted deformation under low-grade metamorphic conditions (e.g. Gratier et al., 2013).

### 4. Evidences for low-grade hydrothermal metamorphism

Because the lavas from the Basal Complex are weathered and partly metamorphosed, in order to characterize their magmatic signature, we use the Th—Co diagram proposed by Hastie et al., 2007 (see Fig. A1 and Table A1 in the supplementary data). All the sampled rocks reveal a calc-alkaline affinity, and compositions range between andesite, dacite and rhyodacite. In all the studied samples, igneous textures are extensively well-preserved and relict igneous feldspar, pyroxene, amphibole and oxides are widespread (Fig. 3).

Metamorphic phases are only locally developed and recrystallizations are characterized by (i) partial replacement of volcanic phenocrysts (pseudomorphs) and/or interstitial domains, (ii) neo formation of metamorphic phases in scattered patches, amygdules, cracks and veinlets or in voids in the volcanic groundmass. These observations demonstrate that chemical equilibrium was not achieved at the mesoscale because of low temperatures of metamorphism, low rocks permeability/porosity and/or low fluid/rock ratios. Such incomplete reactions and disequilibrium textures are typical for low-grade metamorphism

**Fig. 2.** Mesoscopic tectonic structures in the Basal Complex. A - Spaced disjunctive cleavage planes in a meta-andesite (Breton Pointe). B - Dissolution-schistosity planes underlined by dark seams of insoluble minerals. Volcanic enclaves are truncated by dissolution-schistosity plane (Tillet Creek). Arrows indicate some dissolution cleavage. C - Discrete and spaced dissolution planes underlined by dark (insoluble minerals) or white to yellow (calcite +/− albite, chlorite) seams in a meta-rhyodacite lava flow (Tillet Creek). D - Fractures interconnecting the cleavage planes. The axes of the finite strain ellipsoid, are reported.

affecting meta-volcanic rocks (Frey and Robinson, 1999; Robinson et al., 2005).

Chlorite, white mica, albite, quartz, titanite define the ubiquitous metamorphic assemblage, and in most rocks they are accompanied by variably developed epidote, calcite, actinolite, sulphides and oxides (Fig. 3). In many samples, significant amounts of calcite and quartz +/− albite occur within cracks and veinlets. The metamorphic phases are difficult to decipher because exposure is often limited and metamorphism is of very-low grade in the upper crust of an island arc. However, the regional extent of this metamorphism is demonstrated by the systematic occurrence of post-magmatic reaction phases at the scale of the whole Basal Complex (Fig. 3D).

45 samples were observed in thin sections, chlorite occurs in close association with white mica as irregular patches disseminated or interconnected within groundmass domains and relict volcanic phenocrysts of pyroxene and plagioclase (Fig. 3A and C). Although igneous compositions and zoning of primary feldspars are retained in most instances, plagioclase grains show varying degrees of transformation in albite. The latter occurs as irregular patches or at the rims of magmatic plagioclase. Titanite is recognized as fine-grained brownish aggregates disseminated within the groundmass. Epidote is locally recognized as aggregates of xenoblastic millimeter-sized grains in volcanic plagioclase and volcanic groundmass. In the less differentiated samples (i.e. meta-andesites) actinolite occurs as pale-green acicular crystals, locally in association with chlorite and/or prehnite, at the rims of volcanic clinopyroxene (Fig. 3B). Some samples are also deeply altered giving rise to an argilic overprint with clay minerals, pyrite, chalcedony and gypsum typical for advanced alteration under tropical conditions.

To constrain P-T conditions, we selected the least altered samples from which we chose the samples with the largest number of new metamorphic phases. The mineralogy of these samples, two meta-rhyodacites sampled in Tillet Creek (samples BT6 and BT14 Fig. 3D), was investigated in detail. Under the microscope, together with plagioclase phenocrysts, we observed chlorite, white micas, titanite, oxides and a restricted number of small-sized epidotes. White mica occurs as irregular, mostly rectangular, pseudomorphic patches and in radial aggregates in association with quartz in veinlets.

Powder, obtained from these samples, was analyzed at the CEMEF in Sophia-Antipolis Scientific Center using a Diffractometer system XPert-Pro MPD (Bragg Brentano geometry, Cu anticathode, KAlpha1 and KAlpha2 rays, PIXcel detector). Corresponding spectra have been interpreted using MATCH! Software (v. 3.5.0.99, "COD 20170703 database, see Fig. A2 in the supplementary data). XRD whole analyses on powder identify magmatic plagioclases (andesine-bytownite), oxide (magnetite) and K-feldspar (anorthoclase) as well as quartz, albite, muscovite, chlorite, smectite and montmorillonite. These last two minerals are supergene alteration products.

Microprobe analyses of metamorphic minerals were performed on a Cameca SX100 electron microprobe at the University of Montpellier, operating with a 20 kV accelerating voltage and 10 nA beam current. Representative compositions of phases are presented in Table A2 in supplementary data. The occurrence of anorthoclase in the volcanic groundmass, depicted by XRD analyses, is confirmed by microprobe analyses. Two types of white micas were identified, muscovite in pseudomorphs and pyrophyllite in veinlets. For chlorite electron microprobe analyses, total iron was analyzed as FeO, and the Fe/Fe + Mg ratio is in the range 0.4–0.5. Chlorite has $Al^{IV}$ contents higher than 1.1, which is characteristic of metamorphic chlorite (Robinson et al., 2005).

To quantify the temperature of metamorphism, we first used the "chlorite geothermometers". Chlorite compositions can be used for thermobarometric estimates in various geological contexts (see Lanari et al., 2014 with references therein), and during the three last decades empirical (Cathelineau and Nieva, 1985) and semi-empirical calibrations (Inoue et al., 2010) of this thermometer have been developed.

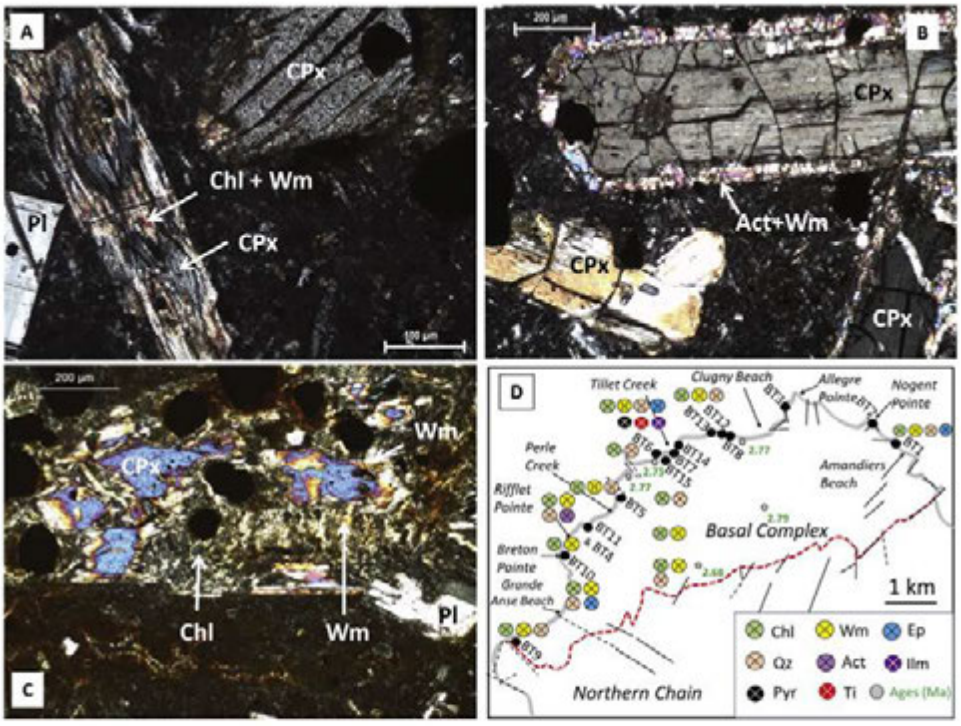


**Fig. 3.** A, B, C: Metamorphic transformations in meta-volcanic rocks (thin sections under cross-polarized light). A: Chlorite (Chl) with white mica (Wm) as irregular patches disseminated within a phenocryst of pyroxene (Rifflet Pointe); B: Actinolite (Act) and white mica (Wm) at the rims of volcanic clinopyroxenes (CPx) (Rifflet Pointe), C: Clinopyroxene replaced by patches of chlorite (Chl) and white mica (Wm) (Grande Anse Beach). D: Distribution of metamorphic phases within the Basal Complex. Locations of sampling sites (sites BT1 to BT15) are reported. Ilm = ilmenite, Chl = chlorite, Wm = white mica, Ep = epidote, Qz = quartz, Act = actinolite, Pyr = pyrite, Ti = titanite. Dotted red line represents the boundary between the Basal Complex and the Northern Chain (modified after Samper et al., 2007 and Gailler et al., 2013). The observed faults are also reported (black lines) while K–Ar ages in Ma (Samper et al., 2007) are reported in grey.

However, recent thermodynamic investigations underline that these calibrations cannot be used in the framework of internally consistent thermodynamic data sets. In order to overcome this problem, Lanari et al. (2014) have proposed an activity-composition model in the system $FeO–MgO–Al_2O_3–SiO_2–H_2O$, compatible with the Holland and Powell (1998) internally consistent thermodynamic data set and thus with phase equilibrium computation programs. This new calibration is particularly adapted for low-temperature (<400 °C) metamorphic and hydrothermal conditions. Lanari et al. (2014) proposed two calibrations for chlorite thermometry, among which one is useful even when the amount of $Fe^{3+}$ in chlorite is unknown (i.e. with the assumption that Fe Tot. = $Fe^{2+}$). Using this calibration, a temperature range between 268 and 280 °C, with uncertainties of +/− 50 °C, is obtained. Moreover, for low-temperature chlorites, a new T-R2 + -Si diagram is also available for thermometry (Bourdelle and Cathelineau, 2015). This new thermometer neglects the non-ideal contribution of site mixing in chlorites as well as the impact of the $Fe^{3+}$ content. Despite these simplifications, the Bourdelle and Cathelineau (2015) calibration provides an efficient tool for thermometric purposes in the 100–400 °C range. Using this calibration, temperature values between 220 and 260 °C are obtained. Summing up, under low-pressure conditions, chlorite thermometry applied to the studied meta-rhyodacites provides temperature values in the range 215–330 °C, thus typical of sub-greenschist facies conditions (Frey and Robinson, 1999).

Furthermore, in the studied meta-rhyodacites the distinctive assemblage is: albite + muscovite + chlorite + titanite + quartz + clinozoisite + ilmenite. In order to interpret such an assemblage, we also calculated P-T pseudosections (isochemical phase diagrams) for the considered samples. Thermodynamic calculations were performed with the free energy minimization program THERIAK and DOMINO (De Capitani and Petrakakis, 2010, updated software v. 4 February 2017) and the internally consistent thermodynamic "tcdb55c2d" database (Holland and Powell, 1998; updated Nov. 2003). Mixing models used for solid solutions are presented in supplementary data (Table A3). However, such an approach requires an equilibrated metamorphic assemblage. In our case we observed numerous textural evidences of chemical disequilibrium. Equilibrium was not achieved at the whole rock scale and only local domains record the metamorphic evolution. Under low temperature conditions, the metamorphic phases compositions may not be in complete equilibrium with the effective bulk composition under which they develop (Frey and Robinson, 1999). To overcome this problem, we decided to explore the metamorphic conditions leading, at a local scale, to pseudomorphs development, particularly at the expense of magmatic plagioclase. Pseudomorphic clusters of albite-quartz-muscovite-chlorite-titanite-clinozoisite-ilmenite are developed after andesine. Phase diagrams were thus calculated using the local chemical composition of the pseudomorph (principle of local equilibrium and reactive bulk composition, see Lanari and Engi, 2017 for discussion) established from microprobe mineral compositions and modal amounts obtained from optical analysis (Table A4 in supplementary data). Whatever the size is, the selected reactive bulk composition has to include water content and oxidation state and these specific parameters are unknown or poorly known (see discussions in Diener and Powell, 2010 and Rebay et al., 2010, with references therein).

Because, our rocks are significantly affected by surface weathering processes including oxidation under tropical conditions, a direct measure of the amount of $Fe^{3+}$ in the rock is not significant. To investigate the effect of variable $Fe^{3+}$ content on the phase relations, we used the values for the Fe-oxidation state of sub-arc magmatism proposed by

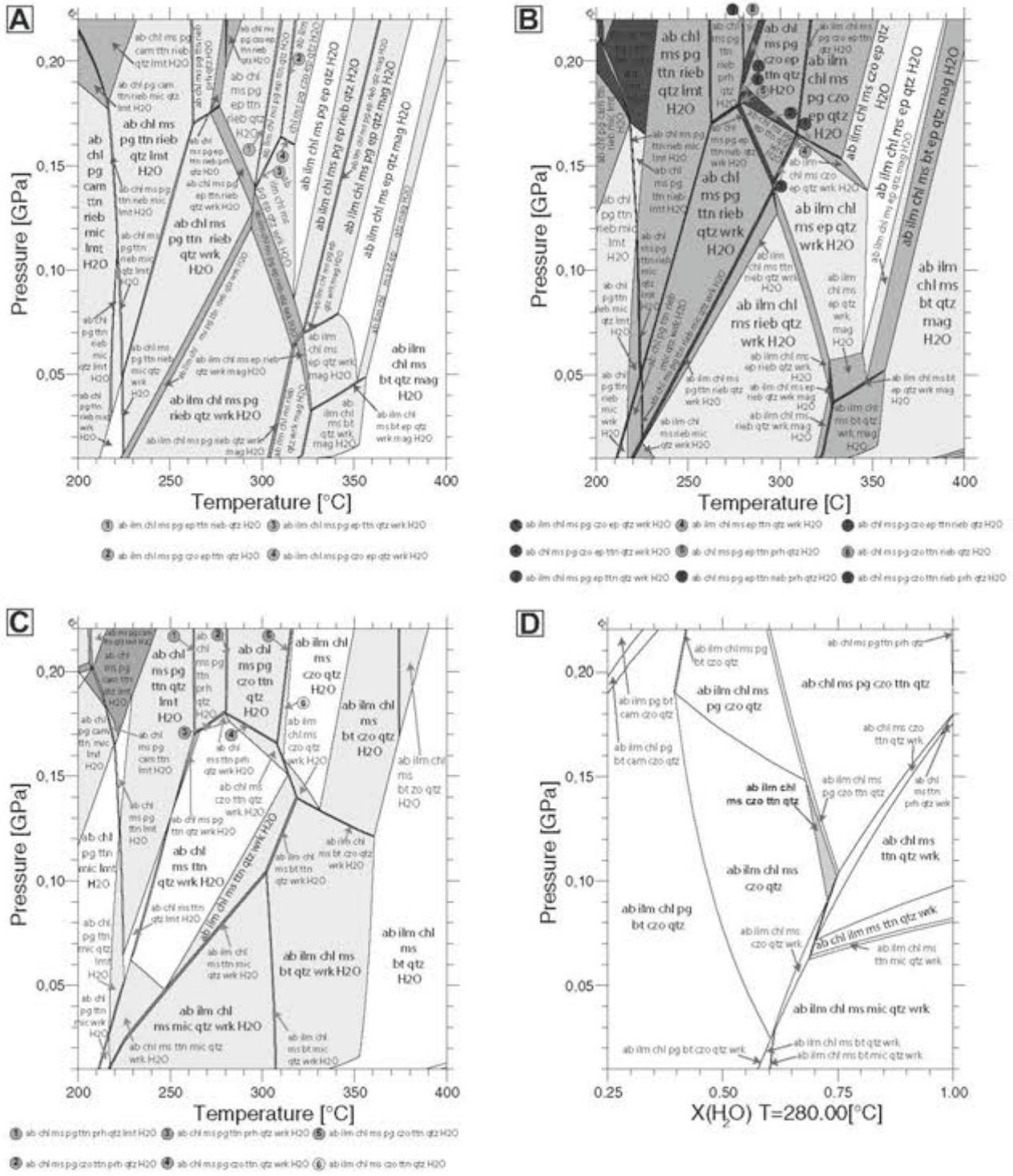


**Fig. 4.** Mineral abbreviations are from Kretz, 1983. A - Calculated P-T pseudosection with $H_2O$ saturation and 10% $Fe^{3+}$ (of total iron). The rock composition, given as mol.% oxide, is $SiO_2$ (69.64) - $TiO_2$ (0.75) - $Al_2O_3$ (23.85) - $Fe_2O_3$ (0.70) - FeO (6.98) - MgO (0.87) - CaO (3.62) - $Na_2O$ (9.19) - $K_2O$ (1.90). Fields are colored with respect to their variances, darker colours indicate higher-variance assemblages. B - Calculated P-T pseudosection with $H_2O$ saturation and 5% $Fe^{3+}$ (of total iron). The rock composition, given as mol.% oxide, is $SiO_2$ (70.06) - $TiO_2$ (0.76) - $Al_2O_3$ (23.89) - $Fe_2O_3$ (0.35) - FeO (7.00) - MgO (0.87) - CaO (3.63) - $Na_2O$ (9.21) - $K_2O$ (1.91). Fields are colored with respect to their variances, darker colours indicate higher-variance assemblages. C - Calculated P-T pseudosection for andesine pseudomorph with $H_2O$ saturation and total iron as $Fe^{2+}$. The rock composition, given as mol.% oxide, is $SiO_2$ (70.18) - $TiO_2$ (0.76) - $Al_2O_3$ (23.94) - FeO (7.01) - MgO (0.87) - CaO (3.63) - $Na_2O$ (9.22) - $K_2O$ (1.91). Fields are colored with respect to their variances, darker colours indicate higher-variance assemblages. D - P-X($H_2O$) equilibrium phase diagram calculated at 280 °C, using the same base composition of Fig. 4C. The stability field colored in grey corresponds to the observed assemblage.

Lee et al. (2010). Following this recent review, even if arc magmatism is widely believed to be oxidized, the primary $Fe^{3+}/Fe_{tot}$ ratios are around 0,1 and 0,15. However these values reflect the whole rock chemical composition. Because we work on the local chemical composition of a plagioclase pseudomorph, the $Fe^{3+}$ value can be much lower. Thus, three chemical systems, with respectively 10%, 5% and 0%, for the local effective composition, were simulated in order to cover the entire compositional spectrum.

The three pseudosections were calculated in the system $SiO_2$-$Al_2O_3$-$TiO_2$-FeO-MgO-$Na_2O$-CaO-$K_2O$-$H_2O$ and assuming $H_2O$ in excess (Fig. 4A, B and C). They show specific differences and remarkable similarities. In the first one, calculated with O ($Fe_2O_3$) = 0,70 corresponding to 10% conversion of all Fe as FeO to $Fe_2O_3$ (Fig. 4A), minerals accommodating $Fe^{3+}$, like epidote or riebeckite are stabilized. Particularly, riebeckite is a common phase in the considered P-T range and, with 20% of $Fe^{3+}$, riebeckite becomes stable at all P-T conditions. In the second P-T pseudosection, calculated with O ($Fe_2O_3$) = 0.35 corresponding to 5% conversion of all Fe as FeO to $Fe_2O_3$ (Fig. 4B), riebeckite is less developed than in the previous system. A third P-T pseudosection presents the chemical system with all Fe as FeO (Fig. 4C), and there is thus no riebeckite in the studied P-T range.

In all cases, as a consequence of $H_2O$ in excess in the system, the stability fields of zeolites are particularly well developed, even under temperatures higher than 300 °C and pressures higher than 0,15 GPa.

Furthermore, in the three systems, even in P-T domains without zeolite and/or riebeckite, there is no stability field that corresponds exactly to the observed mineralogical composition as paragonite is systematically associated with muscovite. It is in the temperature range of 280–320 °C for P higher than 0,14 GPa that we can find the mineralogical association which is the closest to that really observed, although two white micas are always present.

Consequently, it is critical to test the $H_2O$ influence on the stability field of the mineral assemblages. Using Theriak-domino suite it is possible to build P-X($H_2O$) equilibrium phase diagram at a fixed temperature. The latter was fixed at 280 °C based on the results of chlorite thermometry and three equilibrium diagrams were calculated respectively with 10%, 5% and 0% of $Fe_2O_3$ in the chemical system. Only the phase diagram with $Fe_2O_3$ = 0%, which is consistent with the depicted mineralogy, is here presented (Fig. 4D). The amount of $H_2O$ available within the metamorphic fluid appears to be a key parameter for the stability of the observed assemblage. With 0,70 < X($H_2O$) < 0,75 the observed albite-muscovite-chlorite-titanite-quartz-clinozoisite-ilmenite assemblage is stable in the pressure range of 0,09–0,15 GPa.

Combining geothermometry and P-T modeling a pressure range of 0,09 to 0,15 GPa, for a temperature of about 280 +/− 30 °C, with an amount of $H_2O$ in the range 70–75% within the metamorphic fluids and with $XFe_{3+}$ < 0,05 is required to develop the observed metamorphic assemblage.

Because the development of this metamorphic imprint is synchronous with Guadeloupe active arc building, we need to test the consistency of the calculated P-T conditions with the values of 70–120 °C/km measured for the present day geotherm near Basse-Terre (Manga et al., 2012). For temperatures between 260 and 300 °C, a pressure range between 0,09 and 0,15 GPa is in agreement with a minimal value of 70 °C/km (conductive geotherm).

## 5. Consequences for the thermo-mechanical behavior at shallow crustal level of volcanic arcs

In the most eroded volcanic formations of the Guadeloupe archipelago, we discover the occurrence of pervasive low-grade metamorphism (i.e. arc "auto-metamorphism"). Our observations are consistent with the thermal behavior of many island arcs within which calc-alkaline volcanic rocks are subjected to hydrothermal recrystallizations leading the development of greenschist, sub-greenschist and zeolite facies series in the upper part of the arc crust (Bird and Spieler, 2004; Miyashiro, 1961; Schiffman et al., 1984). In numerous examples, regional hydrothermal metamorphism is coeval with arc building and heat input is related to continuous or episodic emplacement of magmatic intrusions (Giggenbach, 1992; Vry et al., 2010). In the studied case, the calc alkaline volcanic rocks metamorphosed under subgreenschist facies conditions are dated at <3 Ma, consequently the Guadeloupe archipelago exhibits an extremely young example of exposed metamorphic terrain.

Until now, brittle deformation was the only mechanism proposed to accommodate strain in the upper crust of the Guadeloupe island arc (Calcagno et al., 2012; Feuillet et al., 2002; Lardeaux et al., 2013; Verati et al., 2016). The discovery of spaced cleavage development and associated dissolution schistosity demonstrates that fluids-assisted deformation is also an active mechanism in this upper crust. In the last fourty years, it has been demonstrated that brittle and ductile mechanisms (i.e. pressure solution creep) are very often spatially associated in the upper crust (Gratier et al., 2013; Renard et al., 2000; Rutter, 1983). In zones where geological fluids circulate from depth, pressure solution creep interacts with brittle deformation at upper crustal levels (Gratier et al., 2013; Sibson and Rowland, 2003). These natural data have implications for the crustal rheology of the Lesser Antilles island arc. As suggested by evidence for pressure solution at all depths along the active and seismogenic San Andreas fault (Gratier et al., 2003), interactions between brittle deformation and fluids flow can control the mechanical behavior of active faults and the duration of seismic cycles in a region submitted to significant geological hazards.

The fact that temperatures close to 300 °C are reached at depths of about 3–4 km in the volcanic arc basement is consistent with a shallow depth for the frictional-viscous ("brittle-ductile") transition in fault zones. In this upper crust, brittle faults can be connected and/or relayed by gently dipping schistose zones facilitating lateral magmatic and hydrothermal fluids and heat transfers as described in other active arc systems (Ranalli and Rybach, 2005). Consequently, the metamorphic zonation is not only the result of vertical transfers but may be also controlled by lateral heat and fluids transfers and thus controlled by the geometry of the finite deformation pattern.

## Appendix A. Supplementary data

Supplementary data to this article can be found online at https://doi.org/10.1016/j.lithos.2018.08.005.

## References


Bird, D.K., Spieler, A.R., 2004. Epidote in geothermal systems. Rev. Mineral. Geochem. 56, 235–300.

Boudon, G., Semet, M.P., Vincent, P.M., 1987. Magma and hydrothermally driven sector collapses: the 3100 and 11,500 y. B.P. eruptions of La Grande Decouverte (La Soufriere) Volcano, Guadeloupe, French West Indies. J. Volcanol. Geotherm. Res. 33, 317–323.

Boudon, G., Villemant, B., Komorowski, J.-C., Ildefonse, P., Semet, M., 1998. The hydrothermal system at Soufriere Hills Volcano Montserrat (West Indies): Characterization and role in the ongoing eruption. Geophys. Res. Lett. 25, 3693–3696.

Bourdelle, F., Cathelineau, M., 2015. Low-temperature chlorite geothermometry: a graphical representation based on a T-R2+-Si diagram. Eur. J. Mineral. 27, 617–626.

Bouysse, P., Westercamp, D., 1990. Subduction of Atlantic aseismic ridges and Late Cenozoic evolution of the Lesser Antilles island arc. Tectonophysics 175, 349–380.

Brown, M., 2010. Paired metamorphic belts revisited. Gondwana Res. 18, 46–59.

Calcagno, P., Bouchot, V., Thinon, I., Bourgine, B., 2012. A new 3D fault model of the Bouillante geothermal province combining onshore and offshore structural knowledge (French West Indies). Tectonophysics 526–529, 185–195.

Cathelineau, M., Nieva, D., 1985. A chlorite solid solution geothermometer the Los Azufres (Mexico) geothermal system. Contrib. Mineral. Petrol. 91 (3), 235–244.

Davidson, J.P., 1987. Crustal contamination versus subduction zone enrichment: examples from the Lesser Antilles and implications for mantle source compositions of island arc volcanic rocks. Geochim. Cosmochim. Acta 51, 2185–2198.

De Capitani, C., Petrakakis, K., 2010. The computation of equilibrium assemblage diagrams with Theriak/Domino software. Am. Mineral. 95, 1006–1016.

Demets, C., Jansma, P.E., Mattioli, G.S., Dixon, T.H., Farina, F., Bilham, R., Calais, E., Mann, P., 2000. GPS geodetic constraints on Caribbean-North America plate motion. Geophys. Res. Lett. 27, 437–440.

Diener, J.F.A., Powell, R., 2010. Influence of ferric iron on the stability of mineral assemblages. J. Metamorph. Geol. 28, 599–613.
Ernst, W.G., 1973. Blueschist metamorphism and P-T regimes in active subduction zones. Tectonophysics 17, 255–272.
Feuillet, N., Manighetti, I., Tapponnier, P., Jacques, E., 2002. Arc parallel extension and localization of volcanic complexes in Guadeloupe, Lesser Antilles. J. Geophys. Res. 107 (B12), 2331.
Frey, M., Robinson, D., 1999. Low-Grade Metamorphism. Blackwell Science, Oxford (313 pp).
Gailler, L.S., Martelet, G., Thinon, I., Bouchot, V., Lebrun, J.F., Münch, P., 2013. Crustal structure of Guadeloupe islands and the Lesser Antilles arc from a new gravity and magnetic synthesis. Bull. Soc. Géol. France 184, 77–97.
Germa, A., Quidelleur, X., Labanieh, S., Chauvel, C., Lahitte, P., 2011. The volcanic evolution of Martinique Island: insights for the Lesser Antilles arc migration since the Oligocene. J. Volcanol. Geotherm. Res. 208, 122–135.
Giggenbach, W., 1992. Magma degassing and mineral deposition in hydrothermal systems along convergent plate boundaries. Econ. Geol. 87, 1927–1944.
Gratier, J.P., Favreau, P., Renard, F., 2003. Modeling fluid transfer along California faults when integrating pressure solution crack sealing and compaction processes. J. Geophys. Res. 108 (B2), 28–52.
Gratier, J.P., Dysthe, D.K., Renard, F., 2013. The role of pressure solution creep in the ductility of the Earth's upper crust. Adv. Geophys. 54, 47–179.
Hastie, A.R., Kerr, A.C., Pearce, J.A., Mitchell, S.F., 2007. Classification of Altered Volcanic Island Arc Rocks using Immobile Trace Elements: Development of the Th-Co Discrimination Diagram. J. Petrol. 48, 2341–2357.
Holland, T.J.B., Powell, R., 1998. An internally consistent thermodynamic data set for phases of petrological interest. J. Metamorph. Geol. 16, 309–343.
Inoue, A., Kurokawa, K., Hatta, T., 2010. Application of chlorite geothermometry to hydrothermal alteration in Toyoha geothermal system, Southwestern Hokkaido, Japan. Resour. Geol. 60, 52–70.
Kopp, H., Weinzierl, W., Becel, A., Charvis, P., Evain, M., Flueh, E.R., Gailler, A., Galve, A., Hirn, A., Kandilarov, A., Klaeschen, D., Laigle, M., Papenberg, C., Planert, L., Roux, E., 2011. Deep structure of the central Lesser Antilles Island Arc: Relevance for the formation of continental crust. Earth Planet. Sci. Lett. 304, 121–134.
Kretz, R., 1983. Symbols for rock-forming minerals. Am. Mineral. 68, 277–279.
Lanari, P., Engi, M., 2017. Local bulk composition effects on metamorphic mineral assemblages. Rev. Mineral. Geochem. 83, 55–102.
Lanari, P., Wagner, T., Vidal, O., 2014. A thermodynamic model for di-trioctahedral chlorite from experimental and natural data in the system MgO-FeO-Al2O3-SiO2-H2O: applications to P-T sections and geothermometry. Contrib. Mineral. Petrol. 167, 968.
Lardeaux, J.M., Münch, P., Corsini, M., Cornée, J.J., Vérati, C., Lebrun, J.F., Quilléveré, F., Melinte-Dobrinescu, M., Léticée, J.-L., Fietzke, J., Mazabraud, Y., Cordey, F., Randrianasolo, A., 2013. La Désirade island (Guadeloupe, French West Indies): a key target for deciphering the role of reactivated tectonic structures in Lesser Antilles arc building. Bull. Soc. Géol. France 184, 21–34.
Lee, C.T.A., Luffi, P., Le Roux, V., Dasgupta, R., Albarede, F., Leeman, W.P., 2010. The redox state of arc mantle using Zn/Fe systematics. Nature 468, 681–685.
MacDonald, R., Hawkesworth, C.J., Heath, E., 2000. The Lesser Antilles volcanic chain: a study in arc magmatism. Earth Sci. Rev. 49, 1–76.
Manga, M., Hornbach, M.J., Le Friant, A., Ishizuka, O., Stroncik, N., Adachi, T., Aljahdali, M., Boudon, G., Breitkreuz, C., Fraass, A., Fujinawa, A., Hatfield, R., Jutzeler, M., Kataoka, K., Lafuerza, S., Maeno, F., Martinez-Colon, M., McCanta, M., Morgan, S., Palmer, M.R., Saito, T., Slagle, A., Stinton, A.J., Subramanyam, K.S.V., Tamura, Y., Talling, P.J., Villemant, B., Wall-Palmer, D., Wang, F., 2012. Heat flow in the Lesser Antilles island arc and adjacent back arc Grenada basin. Geochem. Geophys. Geosyst. 13, Q08007.
Mathieu, L., Van Wyk De Vries, B., Mannessiez, N., Mazzoni, N., Savry, C., Troll, V.R., 2013. The structure and morphology of the Basse Terre Island, Lesser Antilles volcanic arc. Bull. Volcanol. 75, 700.
Maury, R.C., Westbrook, G.K., Baker, P.E., Bouysse, P., Westercamp, D., 1990. Geology of the Lesser Antilles. In: Dengo, G., Case, J.E. (Eds.), The Geology of North America. Vol. H., The Caribbean Region. Geological Society of America Bulletin, pp. 141–200.
Miyashiro, A., 1961. Evolution of metamorphic belts. J. Petrol. 2, 277–311.
Oxburgh, E.R., Turcotte, D.L., 1970. Thermal Structure of Island Arcs. Geol. Soc. Am. Bull. 81, 1665–1688.
Powell, C.M., 1979. A morphological classification of rock cleavage. Tectonophysics 58, 21–34.
Rad, S., Rivé, K., Vittecoq, B., Cerdan, O., Allègre, C.J., 2013. Chemical weathering and erosion rates in the Lesser Antilles: An overview in Guadeloupe, Martinique and Dominica. J. S. Am. Earth Sci. 45, 331–344.
Ranalli, G., Rybach, L., 2005. Heat flow, heat transfer and lithosphere rheology in geothermal areas: features and examples. J. Volcanol. Geotherm. Res. 148, 3–19.
Rebay, G., Powell, R., Diener, J.F.A., 2010. Calculated phase equilibria for a MORB composition in a P-T range, 450–650 °C and 18–28 kbar: the stability of eclogite. J. Metamorph. Geol. 28, 635–645.
Renard, F., Gratier, J.P., Jamtveit, B., 2000. Kinetics of crack-sealing, intergranular pressure solution, and compaction around active faults. J. Struct. Geol. 22, 1395–1407.
Ricci, J., Quidelleur, X., Lahitte, P., 2015a. Volcanic evolution of central Basse-Terre island revisited on the basis of new geochronology and geomorphology data. Bull. Volcanol. 77, 84.
Ricci, J., Lahitte, P., Quidelleur, X., 2015b. Construction and destruction rates of volcanoes within tropical environment: examples from the Basse-Terre Island (Guadeloupe, Lesser Antilles). Geomorphology 228, 597–607.
Robinson, D., Bevins, R.E., Rubinstein, N., 2005. Subgreenschist facies metamorphism of metabasites from the Precordillera terrane of western Argentina; constraints on the later stages of accretion onto Gondwana. Eur. J. Mineral. 17, 441–452.
Rutter, E.H., 1983. Pressure solution in nature, theory, and experiment. J. Geol. Soc. Lond. 140, 725–740.
Samper, A., Quidelleur, X., Lahitte, P., Mollex, D., 2007. Timing of effusive volcanism and collapse events within an oceanic arc island: Basse-Terre, Guadeloupe archipelago (Lesser Antilles Arc). Earth Planet. Sci. Lett. 258, 175–191.
Schiffman, P., Elders, W.A., Williams, A.E., McDowell, S.D., Bird, D.K., 1984. Active metasomatism in the Cerro Prieto geothermal system, Baja California, Mexico: A telescoped low-pressure, low-temperature metamorphic facies series. Geology 12, 12–15.
Sibson, R.H., Rowland, J.V., 2003. Stress, fluid pressure, and structural permeability in seismogenic crust, North Island, New Zealand. Geophys. J. Int. 154, 584–594.
Verati, C., Mazabraud, Y., Lardeaux, J.-M., Corsini, M., Schneider, D., Voitus, E., Zami, F., 2016. Tectonic evolution of les Saintes archipelago (Guadeloupe, French West Indies): Relation with the Lesser Antilles arc system. Bull. Soc. Géol. France 187, 3–10.
Vry, V.H., Wilkinson, J.J., Seguel, J., Millan, J., 2010. Multistage intrusion, brecciation, and veining at El Teniente, Chile: evolution of a nested porphyry system. Econ. Geol. 105, 119–153.
Zami, F., Quidelleur, X., Ricci, J., Lebrun, J.-F., Samper, A., 2014. Initial sub-aerial volcanic activity along the central Lesser Antilles inner arc: New K–Ar ages from Les Saintes volcanoes. J. Volcanol. Geotherm. Res. 287, 12–21.

*Supplementary data*: Documents disponibles dans le chapitre Annexe de ce manuscrit (Article 2 - Supplementary data)

# Chapitre V : Evolution hydrothermale des parties profondes d'un paléo-réservoir géothermal dans l'arc de Guadeloupe : l'exemple de l'analogue exhumé de l'île de Terre-de-Haut (archipel des Saintes)

*Vu Ouest sur l'île de Terre-de-Haut, Les Saintes*

*Panorama de l'anse du Fond Curé à la Carrière de l'aérodrome*

*A gauche au loin un aperçu sur l'île de Basse-Terre*

# Chapitre V

## V.1. Préambule

La caractérisation de l'évolution tectono-métamorphique « standard » des roches volcaniques de l'arc volcanique de Guadeloupe, présenté au cours du chapitre IV, peut à présent nous servir de référence afin d'évaluer le caractère « anormal » de zones hydrothermalisées pouvant ainsi être considérées comme des « paléo-réservoirs » géothermaux exhumés.

En Guadeloupe, les nombreux travaux menés par le BRGM sur la province géothermale de Bouillante (Bouchot *et al.*, **2010**; Thinon *et al.*, **2010**; Calcagno *et al.*, **2012**; Gailler *et al.*, **2013**) permettent de bien connaître les caractéristiques structurales et minéralogiques du réservoir de Bouillante en surface et ce jusqu'à une profondeur de l'ordre de 1 km. Par contre à Bouillante, comme dans de nombreuses autres provinces géothermales, les parties profondes des réservoirs restent très peu connues.

Les coûts des forages profonds étant particulièrement élevés, nous avons cherché à étudier un « analogue exhumé » des parties profondes d'un réservoir géothermal en Guadeloupe.

Tout comme dans le chapitre précédent, nous avons étudié les terrains les plus anciens, en ciblant cette fois un secteur décrit comme une zone fortement hydrothermalisée, et cela au niveau de l'île de Terre-de-Haut dans l'archipel des Saintes (Jacques & Maury, **1988**). Cette zone avait été considérée, à titre d'hypothèse de travail, comme un paléo-réservoir géothermal (Verati *et al.*, **2016**).

Ce chapitre est présenté sous la forme d'un article soumis à la revue « *Journal of Volcanology and Geothermal Research* », dans lequel nous démontrons que la zone hydrothermalisée présente au centre de cette île est une partie, aujourd'hui exhumée, d'un paléo-réservoir géothermal. Elle va donc pouvoir nous servir d'analogue des parties profondes d'un réservoir géothermal de haute-température, présentant ainsi un nouvel outil dans l'exploration géothermal de haute-énergie.

Les principaux résultats présentés et discutés dans cet article sont :

- La caractérisation des structures et de la constitution de ce paléo-réservoir géothermal à partir d'investigations tectonique, géochimique, minéralogique et thermodynamique ;
- La caractérisation de l'évolution minéralogique de l'hydrothermalisme au cours du refroidissement de la structure par l'identification d'un stade de haute-température, d'un stade de basse-température et d'un stade d'altération supergène ;
- L'identification d'un important système de couloirs de schistosités, produits par un mécanisme de déformation ductile de type pression-dissolution, synchrone des transformations minéralogiques de haute-température des roches volcaniques ;

- La description d'un réseau de migration de fluides (verticaux et latéraux) et de chaleur dans les parties profondes d'un réservoir géothermal ;
- La démonstration, à partir d'une modélisation thermodynamique détaillée, que pour des roches différenciées (dacite, rhyodacite) d'un arc volcanique soumises à un hydrothermalisme de haute-température, ce n'est pas la fraction molaire d'$H_2O$ dans le fluide convectif qui contrôle le développement des paragénèses à chlorite et micas. En effet il suffit d'une fraction molaire d'$H_2O$ supérieure à 12% pour stabiliser cette association. Dans le cas particulier étudié, l'absence de waïrakite, qui est le zéolite le plus caractéristique des systèmes géothermaux de haute-enthalpie, s'explique par une pression supérieure à 0,9 kbar atteinte dans notre système ;
- La démonstration de l'existence d'un paléo-réservoir exhumé, de plus haute température que le système actif de Bouillante, et dont la paléo-profondeur est située entre -1,7 et -2,7 km ;
- La proposition d'un modèle conceptuel de fonctionnement des réservoirs géothermaux de haute-température dans le contexte de l'arc volcanique de Guadeloupe.

## V.2. Article 3 – Characterization of an exhumed high-energy geothermal paleo-reservoir: an example from Terre-de-Haut Island (Guadeloupe archipelago, Lesser Antilles arc)

Alexiane Favier[1-2], Jean-Marc Lardeaux[2-3], Michel Corsini[2], Chrystele Verati[2], Vivien Navelot[4], Yves Géraud[4], Marc Diraison[4], Sandra Ventalon[5] and Emile Voitus[6]

1: UMR 5243 Géosciences Montpellier, Université des Antilles-CNRS-Université de Montpellier

2: UMR 7329 Geoazur, Université de Nice Sophia Antipolis-CNRS

3: Czech Geological Survey, Centre for Lithospheric Research

4: UMR 7359 GeoRessources, Université de Lorraine-ENSG-CNRS

5 : UMR 8187 Laboratoire d'Océanologie et de Géosciences, Université de Lille

6 : ESPE, Université des Antilles

Cet article a été soumis à la revue Journal of Volcanology and Geothermal Research.

Keywords: exhumed paleo-reservoir, hydrothermal fluids pathways, high-enthalpy geothermal energy, Lesser Antilles arc

We present integrated structural, petrological, mineralogical and geochemical investigations, including thermodynamic modelling, realized on an exhumed geothermal paleo-reservoir identified in Terre-de-Haut Island (Guadeloupe archipelago). Based on an updated geological and structural

map, this work demonstrates, for the first time, the occurrence, at the paleo reservoir scale, of ductile schistose corridors generated by pressure-solution processes. We unravel first that the development of schistosity is coeval with high-temperature hydrothermalism and second this hydrothermal system was developed under Greenschist facies conditions at a depth of about 2 kilometers. We highlight, at shallow crustal depth, the occurrence of both vertical and lateral fluids and heat transfers in the volcanic arc and we propose a conceptual scheme for the thermo-mechanical evolution of this exhumed analogue of high-enthalpy geothermal reservoir.

### V.2.1. Introduction

Although the general tectonic settings favorable for geothermal activity are well known, and if, in many geothermal systems, a significant amount of geological and geophysical surface data are nowadays available to define and characterize the geothermal resources (see syntheses in Ledru & Guillou-Frottier, **2010**; Moeck, **2014**, with references therein), the nature, the structure and the mineralogical evolution of the deepest part of the reservoirs remain poorly documented. Deciphering the geological properties of the lowermost part of geothermal reservoirs is therefore still challenging, probably because of the high economic cost of exploratory drillings and the poor knowledge of mechanical properties of the hydrothermalized materials. As frequently implemented in the study of mineral and/or oil resources, an effective alternative to address this type of issue is the study of exhumed analogues (de Launay, **1934**; Bouma, **1962**; Middleton & Bouma, **1973**; Beck & Lehner, **1974**; Joseph & Lomas, **2004**).

On the west coast of Guadeloupe (Lesser Antilles magmatic arc), a high-energy geothermal system, favorable for electricity production, was identified in the 1970s in the Bouillante bay (Cormy *et al.*, **1970**; Demians d'Archimbaud & Munier-Jolain, **1976**; Demians d'Archimbaud & Surcin, **1976**). This geothermal field has been well characterized through geological, geochemical and geophysical investigations and several exploration and production wells (Iundt & Ouzounian, **1984**; Abou-Akar *et al.*, **1992**; Sanjuan & Brach, **1997**; Guillou-Frottier, **2003**; Lachassagne *et al.*, **2009**; Bouchot *et al.*, **2010**; Thinon *et al.*, **2010**; Calcagno *et al.*, **2012**; Gailler *et al.*, **2013**). However, in spite of these efforts, the nature, the architecture and the functioning of the deepest part of this reservoir are still under debate (Navelot *et al.*, **2018**). Because a possible exhumed analogue of such a geothermal reservoir has been recently identified in the Guadeloupe archipelago, precisely in Les Saintes Islands (Verati *et al.*, **2016**), this study aims first to clearly demonstrate that the considered Les Saintes hydrothermal area is really a paleo-geothermal reservoir (i.e. a convective system associated to a significant thermal anomaly with respect to the regional standard conductive geothermal gradient), and second to characterize its structural and mineralogical evolution in order to better understand the geological

properties of the high-enthalpy geothermal system in Guadeloupe archipelago and promote its sustainable development at the scale of the Lesser Antilles arc.

### V.2.2. Regional setting

#### *V.2.2.a. The Guadeloupe archipelago in the Lesser Antilles arc*

The 850 km-long curved Lesser Antilles arc is located at the convergent boundary between the Caribbean and the American plates (Hawkesworth & Powell, **1980**; Bouysse & Westercamp, **1988**; DeMets *et al.*, **2000**). It is the consequence of southwest-directed subduction of the American plates beneath the Caribbean one with a velocity about 2 cm/yr. (López *et al.*, **2006**). The crustal thickness of the upper plate crust, supporting the volcanic arc, was defined by geophysical investigations at around 28 km (Kopp *et al.*, **2011**; Gailler *et al.*, **2013**). The conductive geothermal gradient of the Lesser Antilles arc is now well established (Manga *et al.*, **2012**), and was measured around the Guadeloupe archipelago in a range between 69.3 ± 1.5 and 98.2 ± 8.8 °C/km (Figure V-1-**A**).

The northern part of the magmatic arc, including the Guadeloupe archipelago, is divided into two sub-parallel ridges (Westercamp, **1979**). The eastern one is an ancient arc formed by late Oligocene to Pleistocene carbonate platforms (Grande-Terre) while the western arc is composed of a recent chain of volcanic islands (Basse-Terre and Les Saintes) active since 5 Ma (Bouysse & Westercamp, **1990**). Basse-Terre Island consists of a cluster of volcanic complexes, frequently called « volcanic chains » (Figure V-1-**B**), and from north to south Samper et al., (**2007**) recognized: the oldest Basal Complex characterized by 4.28 to 2.67 Ma aged volcanism (Favier *et al.*, **2019**), the Septentrional Chain between 1.81 to 1.16 Ma, the Axial Chain active during 1.02 to 0.41 Ma, the Grande Découverte – Trois Rivières Complex (0.20 Ma-recent) including the present-day active La Soufrière volcano (Boudon *et al.*, **1987**, **2008**), and the Monts Caraïbes Chain built at around 0.55-0.47 Ma (Blanc, **1983**; Ricci *et al.*, **2017**). Southeast of Basse-Terre Island, Les Saintes archipelago are composed of two islands: Terre-de-Haut Island with 3.63 to 2.00 Ma aged volcanism and Terre-de-Bas Island younger than 1.00 Ma (Jacques *et al.*, **1984**; Jacques & Maury, **1988**; Zami *et al.*, **2014**).

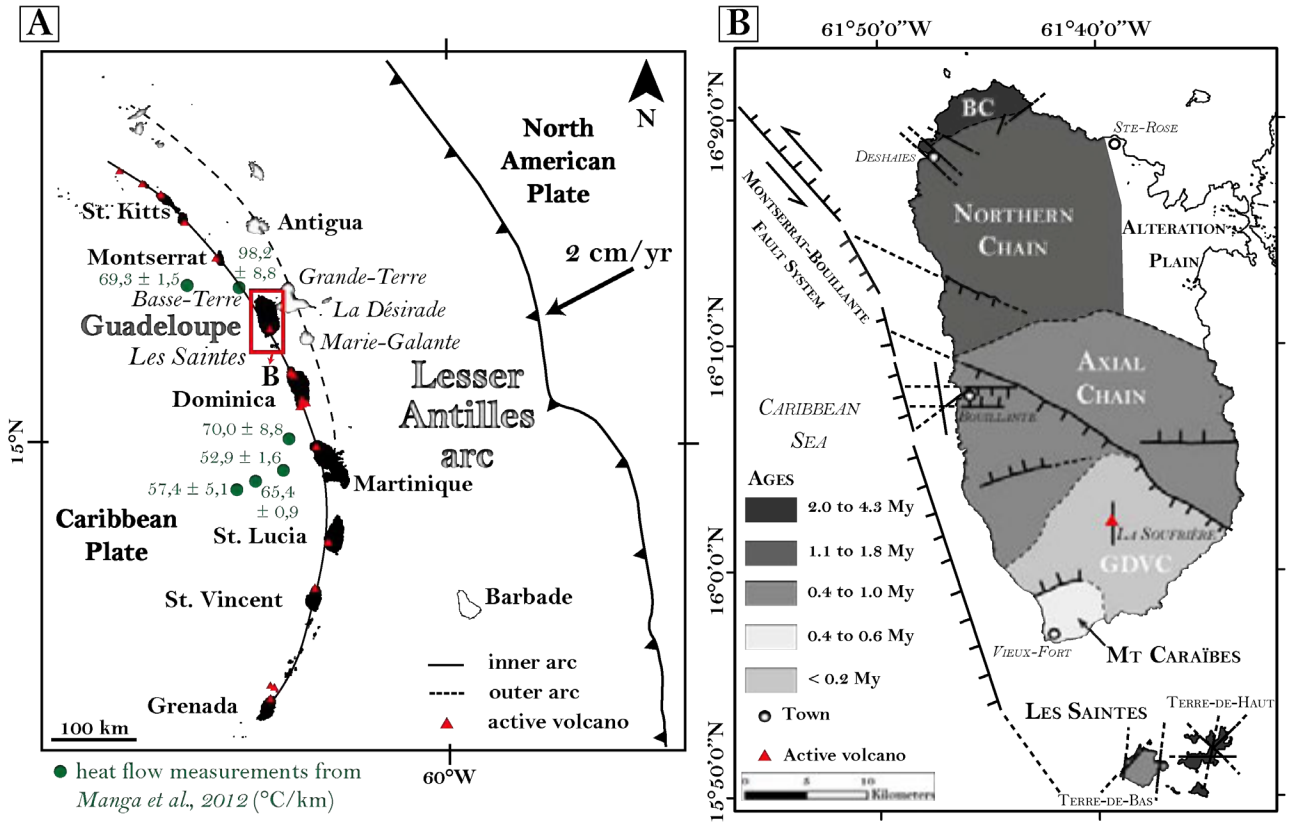


**Figure V-1: A) Geodynamic setting of the Lesser Antilles arc (after Feuillet *et al.*, 2001). B) Map of the active volcanic arc in Guadeloupe archipelago (i.e. Basse-Terre and Les Saintes) displaying the different volcanic complexes and the main tectonic structures (modified after Favier *et al.*, 2019; Boudon *et al.*, 1987; Calcagno *et al.*, 2015; Ricci *et al.*, 2017; Verati *et al.*, 2018), BC = Basal Complex; GDVC = Grande Decouverte Volcanic Complex.**

Regionally, four major directions of brittle faults have been identified: N50-N70, N90-N110, N120-N140 and N160-N10. Onshore and offshore investigations (Feuillet *et al.*, **2002**, **2010**, **2011**; Thinon *et al.*, **2010**; Corsini *et al.*, **2011**; Mathieu *et al.*, **2011**; Laigle *et al.*, **2013**; Lardeaux *et al.*, **2013**; Munch *et al.*, **2013**; Leclerc *et al.*, **2016**; Navelot *et al.*, **2018**; Legendre, **2018**) allow the reconstruction of the deformation history on the base of relative chronology criteria (i.e. superposed geometries). Statistically, the N160-N10 structures are regarded as the youngest fault system, while the N40-N50 structures are the oldest ones. According to many authors, the N120-N140 and the N90-N110 structures are synchronous and generated under a transtensive regime, and are presently active. Many studies (Bouysse, **1979**; Bouysse & Westercamp, **1990**; Favier *et al.*, **2019**; Feuillet *et al.*, **2002**, **2004**; Corsini *et al.*, **2011**; Lardeaux *et al.*, **2013**; De Min, **2014**; Navelot *et al.*, **2018**; Verati *et al.*, **2018**; Legendre, **2018**; Legendre *et al.*, **2018**) have emphasized the importance of the structural heritage, thus tectonic reactivation, on the present-day active finite deformation pattern. As a consequence, structures with different orientations can be solicited at the same time. Interestingly,

the active Bouillante geothermal field (Figure V-1-**B**) is located at an intersection between three of the main regional tectonic structures (Calcagno *et al.*, **2015**).

### *V.2.2.b. Terre-de-Haut in Les Saintes Islands*

Terre-de-Haut, the oldest volcanic complex from Les Saintes Islands, is rich in calk-alkaline lavas, debris and pyroclastic flows, but another significant geological feature is the abundance of lava domes and volcanic plugs (Jacques & Maury, **1988**; Verati *et al.*, **2016**). All the volcanic rocks are frequently fractured and deformed by superposed fault systems. Recent studies have clearly established the main characteristics of the finite brittle field on Terre-de-Haut Island (Verati *et al.*, **2016**; Navelot *et al.*, **2018**). These structural analyses revealed the existence of four main directions for the orientation of fault networks characterized by the following statistical structural directions: N000-N020, N050-N070, N090-N110 and N130-N140 trending fault systems (Verati *et al.*, **2016**). All these faults are generally strongly dipping, and when kinematic criteria are visible they are compatible with normal fault developments frequently associated to strike-slip movements. This brittle finite strain pattern is therefore consistent with the regional transtensive tectonic framework nowadays recognized at the scale of the whole Guadeloupe archipelago.

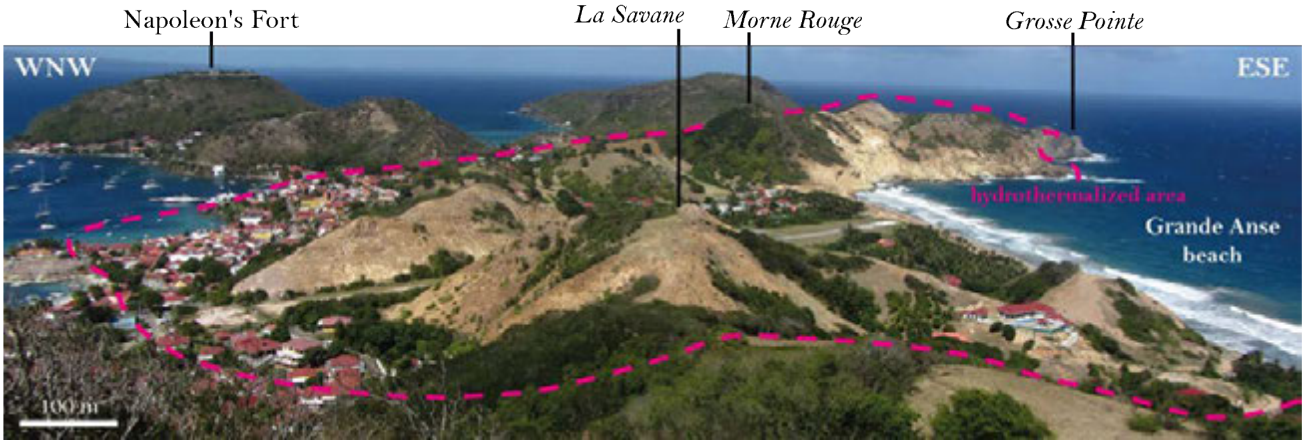


**Figure V-2 : Aerial view of a central portion of the Terre-de-Haut Island showing highly hydrothermalized area from Pré Cassin.**

However, the most striking geological feature of Terre-de-Haut Island is the occurrence, in the central part of this island, of huge hydrothermalized zone (Figure V-2), within which the initial magmatic structures and mineralogy have been completely erased, making impossible to distinguish between lava, debris or pyroclastic flows (Jacques & Maury, **1988**; Verati *et al.*, **2016**). The recognition of high-temperature hydrothermal mineral associations as well as the importance of fault networks led Verati et al. (**2016**) to interpret, as a working hypothesis, this hydrothermal zone as an exhumed paleo-geothermal reservoir. Such a hypothesis is consistent with the age of volcanic activity

(3-2 Ma) combined with the fact that Guadeloupe archipelago is subjected to intense weathering and erosion processes (Dessert *et al.*, **2015**). Indeed, because mechanical and chemical erosion rates of around 1-2 mm/yr are effective (Sak *et al.*, **2010**; Lloret *et al.*, **2011**; Rad *et al.*, **2013**; Ricci *et al.*, **2015a**, **b**), the central part of this island was overburden potentially by a minimum of two kilometers of volcanic materials. Moreover, the cumulative movements along the numerous normal faults are susceptible to favour the exhumation of the deep-seated hydrothermalized rocks. Furthermore, low-temperature mineral associations typical for surficial zones of geothermal fields have been recently described in this area (Beauchamps *et al.*, **2019**). Altogether, these data suggest that the Terre-de-Haut hydrothermal system is the best key target to find an exhumed analogue of a geothermal reservoir in the Guadeloupe archipelago.

### V.2.3. Material and methods

#### *V.2.3.a. Mapping lithology, structural analysis and sampling strategy*

We mapped accurately the various volcanic units by distinguishing the following formations: well developed soils, superficial quaternary sedimentary formations, debris flows, lava flows, lava domes and volcanic plugs.

More than a hundred measurements across the island of tectonic structures were acquired for this study, during seven fieldwork campaigns between 2010 and 2017 in order to characterize the superposed finite strain fields, the chronology of deformations and when possible kinematics of deformation.

Furthermore, to assess the state of transformation of volcanic rocks, we sampled fresh volcanic rocks, slightly hydrothermalized rocks and highly hydrothermalized rocks. The sampling was realized taking into account the rock deformation in the regional finite deformation gradient. As a result, the undeformed fresh volcanic rocks are considered as a standard reference (i.e. initial state) in order to quantify the effects of hydrothermalism and deformation.

#### *V.2.3.b. Whole rock geochemistry*

Whole rock major and trace element analyses were realized on 108 samples (localized in Figure V-3-**A** and Table V-1, and analytical results are provided in the supplementary data in Table X-1) in order to first improve the definition of the lithotypes defined on the geological map and second precise the magmatic characters of the sampled lava flows. We carefully selected the rock exposures to ensure that the main types of lava flows were sampled. Analyses were obtained by Inductively Plasma Atomic Emission Spectrometry (ICP-AES) and Inductively Coupled Mass Spectrometry (ICP-MS), for major and trace elements respectively, on rock powders at the Geochemical and Petrographical Research Center in Nancy (SARM laboratory, CNRS-CRPG, with the procedure proposed by Carignan *et al.*, **2001**).

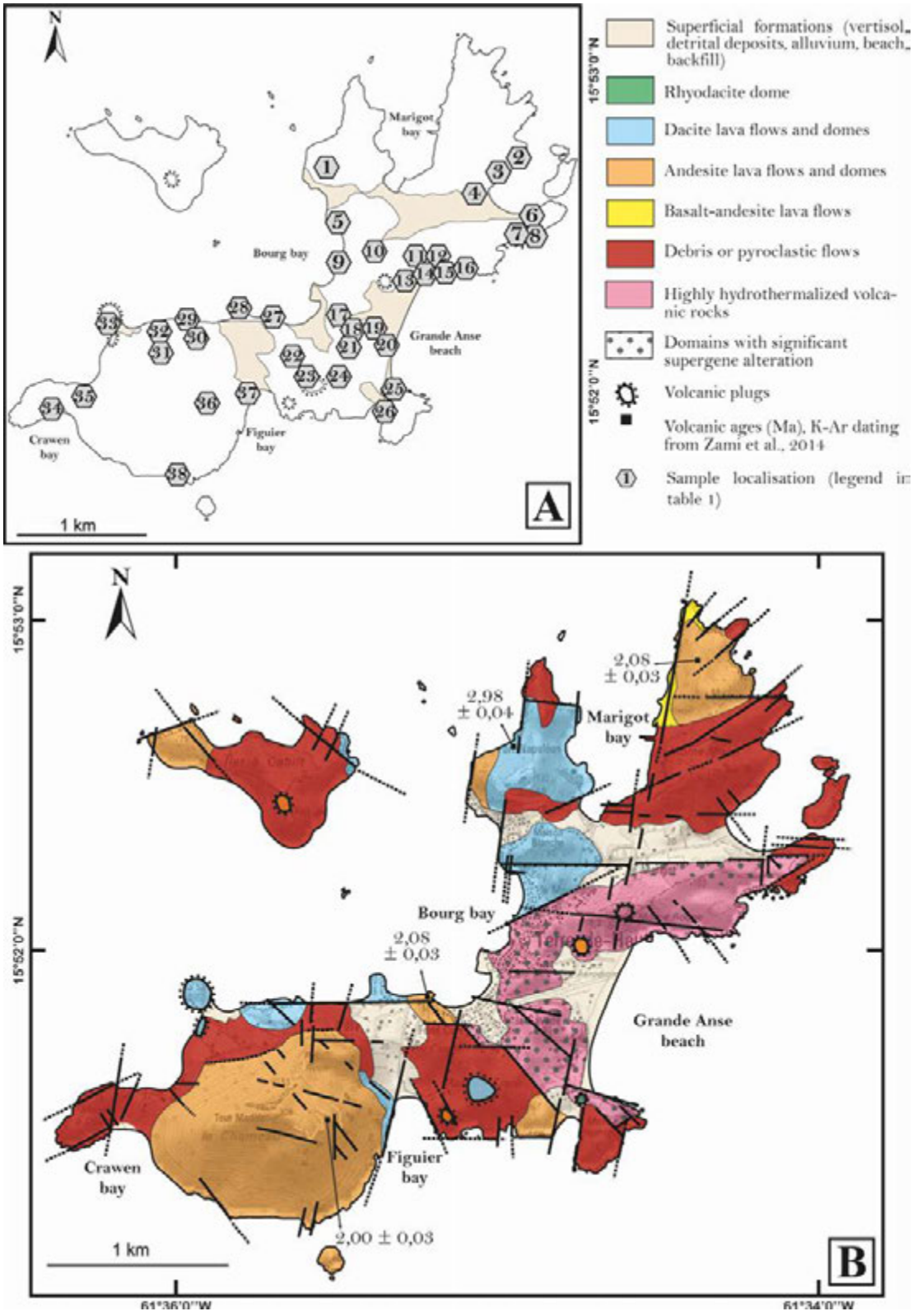


**Figure V-3: A) Sample localisations map, legend in Table V-1. B) Revisited geological map of Terre de Haut Island showing the main geological formations and the volcanic lithologies defined by their geochemistry and their mineralogy (modified after Jacques & Maury, 1988; Verati *et al.*, 2016). The heavy dark lines represent the main brittle faults identified in the field (modified after Verati *et al.*, 2016; Navelot *et al.*, 2018).**

**Table V-1: Sample location from Terre-de-Haut Island.**

| Localisation (fig.3-A) | Samples | Localisation (fig.3-A) | Samples | Localisation (fig.3-A) | Samples |
|---|---|---|---|---|---|
| 1 | 17TH26 | 14 | 16STH07; 16STH08; 16STH09a,b; 16STH10; GD-16-03; GD16-05 | 27 | 16STH23a,b |
| 2 | 17TH28 | 15 | 16STH11a,b; 16STH19; 16STH20; TH26a,b | 28 | 16STH24; 16STH25; 16STH26; 16STH27; 16STH28 |
| 3 | TH-23a,b,c,d,e | 16 | 16STH12; 16STH13; 16STH14; 16STH15a,b; 16STH16; 16STH17; 16STH18; 17TH16; 17TH17a,b; TH-27 | 29 | 16STH30; 16STH31; 16STH32 |
| 4 | 17TH29 | 17 | 16STH34; GD15-142 | 30 | 16STH29; 17TH24; TH-28 |
| 5 | TH-30a1,a2,b ; 16STH33 | 18 | 16STH35a,b; TH-24a,b,c; TH-25 | 31 | 17TH23 |
| 6 | TH-32a,b, TH-33 | 19 | 17TH01; 17TH02 | 32 | 17TH22 |
| 7 | GD-16-10 | 20 | 17TH03; 17TH04; 17TH15; 16STH21a,b | 33 | 17TH21 |
| 8 | 17TH30 | 21 | 17TH14; 16STH22 | 34 | 17TH18; 17TH19 |
| 9 | 17TH32a,b | 22 | 17TH12 | 35 | 17TH20 |
| 10 | 17TH31 | 23 | 17TH11 | 36 | 17TH25a,b; DC-10-09a,b; GD17-11 |
| 11 | SA-14 | 24 | 17TH09; 17TH10 | 37 | 17TH13; TH-29; GD-15-135 |
| 12 | 17TH33 | 25 | 17TH05; 17TH06; 17TH07; TH-25'; SA-12-08; GD-17-08 | 38 | GD-15-139; GD15-140; GD15-141 |
| 13 | 16STH01a,b; 16STH02; 16STH03; 16STH04a,b; 16STH05; 16STH06; GD16-06 | 26 | 17TH08; GD17-09 | | |

*V.2.3.c. Mineral chemistry*

In order to precise and quantify the petrological evolution of Terre-de-Haut, we investigated 126 thin sections. Mineral chemistry data were achieved by electron microprobe analyses, X-ray diffractometry and Raman spectrometry

Non-oriented powders of whole rocks (<70 μm) were analysed by an X-ray diffractor with XPert-Pro MPD system (Bragg Brentano geometry, Cu anticathode, KAlpha1 and KAlpha2 rays, PIXcel detector) at the CEMEF in Sophia-Antipolis Scientific Center.

Major elements analyses were performed at the "Service Commun de Microsonde" of Montpellier University on a Cameca-SX100 electron microprobe. The operating conditions were a 20 kV accelerating voltage and 10 nA beam current. The chemical analyses of metamorphic phases are presented in the supplementary data in Table X-2, Table X-3, Table X-4).

We used also Raman spectrometry to complete mineral determination. The spectra were recorded with a LabRam HR800UV Jobin-Yvon™ microspectrometer equipped with 1800 g/mm gratings and using 532 nm green laser excitation; acquisition time-span varied from 20 to 70 s during three accumulating cycles.

*V.2.3.d. Thermodynamic modeling*

Pressure and temperature conditions of hydrothermalism were quantified by standard thermometry on chlorites and thermodynamic modelling of representative samples using the THERIAK-DOMINO method (de Capitani & Petrakakis, **2010**) with the Holland and Powell database (**1996-2007**). These P-T calculations were carried out only on samples not or poorly affected by supergene alteration.

### V.2.4. Diversity of Terre-de-Haut lithologies

A first geological map of Terre-de-Haut was produced in the 1980's (Jacques & Maury, **1988**), and latter improved by geochronological and structural investigations (Zami *et al.*, **2014**; Verati *et al.*, **2016**). In order to continue the refinement of Terre-de-Haut geology, and to produce a revised geological map (Figure V-3**-B**), we first distinguished detrital deposits and alluviums within the so-called superficial sedimentary formations. In some places along the coast, sandy expanses form beaches and finally construction and extension works has been completed with backfill. Second, we refine the definition of volcanic domes and lava flows by systematic geochemical investigations taking into account the degree of post-volcanic transformation of these rocks (hydrothermalism).

We used standard geochemical diagrams, based on major elements distribution, only in the case of fresh volcanic rocks. In the Total Alkali versus Silica (TAS) diagram (Bas *et al.*, **1986**, Figure V-4**-A**), $SiO_2$ content ranges from 54 to 65 wt.% for lava flows and our sample compositions evolve from basalt-andesite to dacite. In the $K_2O$ versus $SiO_2$ diagram (Peccerillo & Taylor, **1976** for arc volcanic lavas, Figure V-4**-B**), the studied lavas fall within the fields of mostly Median-K to Low-K series for a restricted number of samples. In the $SiO_2$ versus Nb/Y diagram (Winchester & Floyd, **1977**, Figure V-4**-C**), the studied samples have a calk-alkaline affinity with an evolution from andesites to rhyodacites.

The Rare-Earth-Element (REE) diagram normalized to chondrite values (after Sun & McDonough, **1989**; Figure V-5**-A-B-C**) displays relatively constant slopes with Light-REE (LREE) enrichment for most samples, typical for insular arc related calk-alkaline lavas (Hawkesworth & Powell, **1980**; Labanieh, **2009**). Moreover, the multi-element diagram normalized to primitive mantle (Sun & McDonough, **1989**; Figure V-5**-D-E-F**) displays also typical patterns of calk-alkaline arc lavas, i.e. with Th, Pb, U and Large Ion Lithophile Element (LILE) enrichments, and also Nb and Ta depletions (Labanieh, **2009**).

The rhyodacitic samples show the most diversified geochemistry with especially strong Sr depletion, large K, Th, U enrichments, or K depletion. This geochemical variability can be either explained by different magmatic differentiation stages or by element mobility during alteration processes, especially for Sr and K.

However the positive Y and HREE anomaly of samples from "Morne à Craie" (17TH11) (Figure V-5**-E**) and the intrusion in southern part of Grande Anse beach (TH-25' and 17TH05) (Figure V-5**-F**) reflects supergene processes (Cotten *et al.*, **1995**), as also identified in REE spectra (Figure V-5**-B-C**).

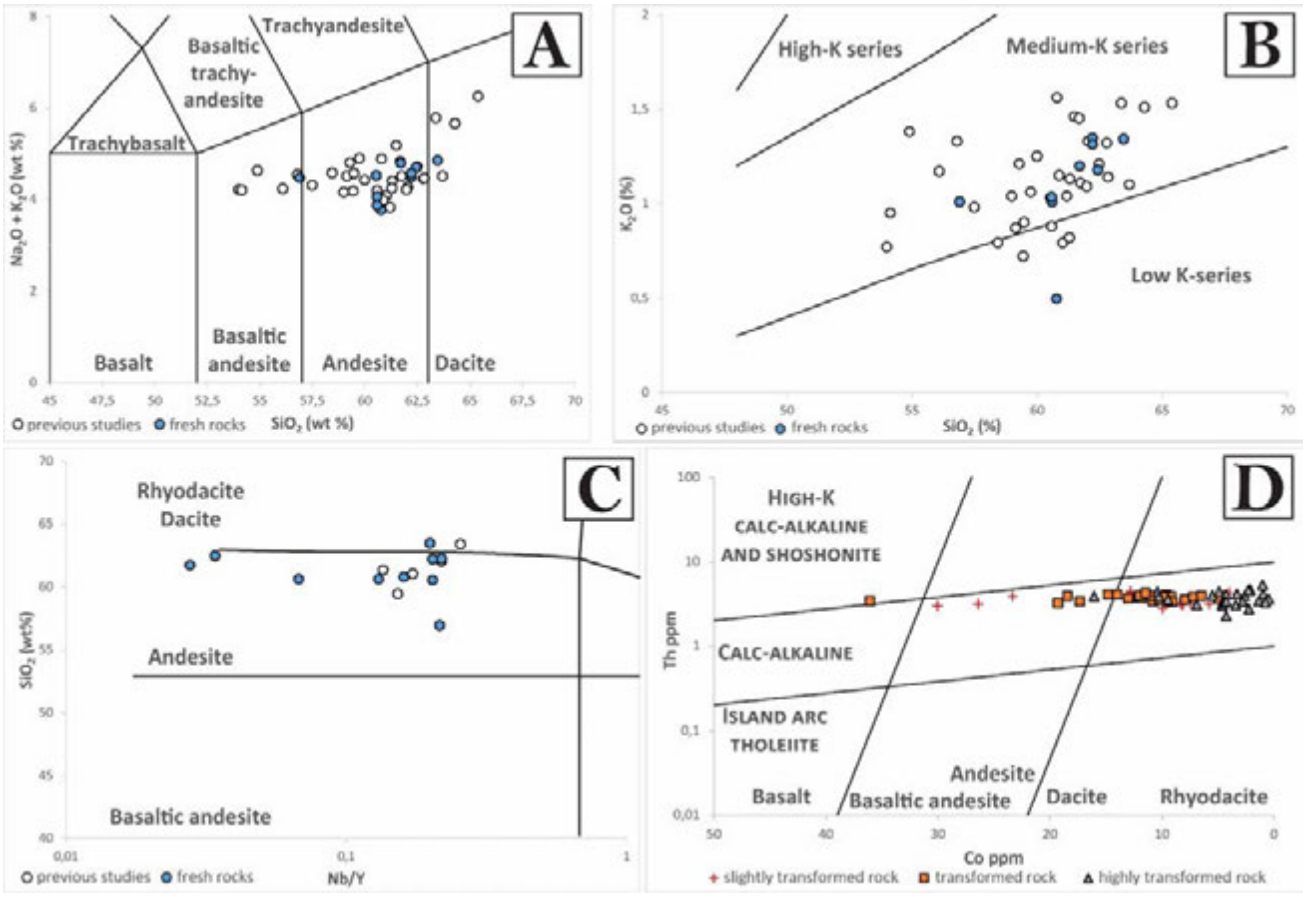


**Figure V-4: Geochemical characterization of lava flows. A) Total alkali vs. silica diagram after Bas et al. (1986), white circles represent previous data from: Jacques *et al.*, 1984; Jacques & Maury, 1988; Zami *et al.*, 2014; Navelot *et al.*, 2018. Blue circles correspond to our new analyses. B) SiO2 vs. K2O plot after Peccerillo and Taylor (1976), white circles represent previous data from: Jacques *et al.*, 1984; Jacques & Maury, 1988; Zami *et al.*, 2014; Navelot *et al.*, 2018. Blue circles correspond to our new analyses. C) SiO2 vs. Nb/Y diagram after Winchester & Floyd, 1977, white circles represent previous data from Jacques & Maury, 1988; Zami *et al.*, 2014; Navelot *et al.*, 2018. Blue circles correspond to our new analyses. D) Co vs. Th plot after Hastie *et al.*, 2007 showing the chemical characters of the studied rocks with respect to their degree of transformation.**

Major and some trace elements (mainly LILE and LREE) are severely mobile in altered lavas. Therefore to improve the geochemical characterization of our samples, particularly those affected by hydrothermal transformations, we selected diagrams based only on minor and trace elements considered as being the most immobile. Samples where LOI (loss on ignition) is below 1-2%, demonstrating that hydrothermalism and/or weathering are insignificant, are named slightly transformed rocks while when LOI is above 3% (as suggested by Samper *et al.*, **2007** to identify significantly altered volcanic rocks) they are named transformed or highly transformed rocks. Hydrothermal transformation and supergene alteration produce new mineral assemblages often associated with significant redistribution of chemical elements (Sturchio *et al.*, **1986**; Fulignati *et al.*, **1999**; Pandarinath *et al.*, **2008**; Salaün *et al.*, **2011**). Today, the Th-Co diagram proposed by Hastie et al. (**2007**) is considered as the best tool for the characterization of altered volcanic rocks. In this

diagram the studied rocks define a typical Medium K calk-alkaline volcanic serie (Figure V-4-**D**), characterized by a significant magmatic differentiation from basaltic-andesites to rhyodacites. Many lava domes and volcanic plugs correspond to andesites or rhyodacites. Lava flows are more diversified and we distinguished basalt-andesites, andesites, dacites and rhyodacites. Moreover, numerous volcanic formations are composed of debris flows and pyroclastic flows. We used therefore this diversified nomenclature in the proposed revised geological map (Figure V-3-**B**).

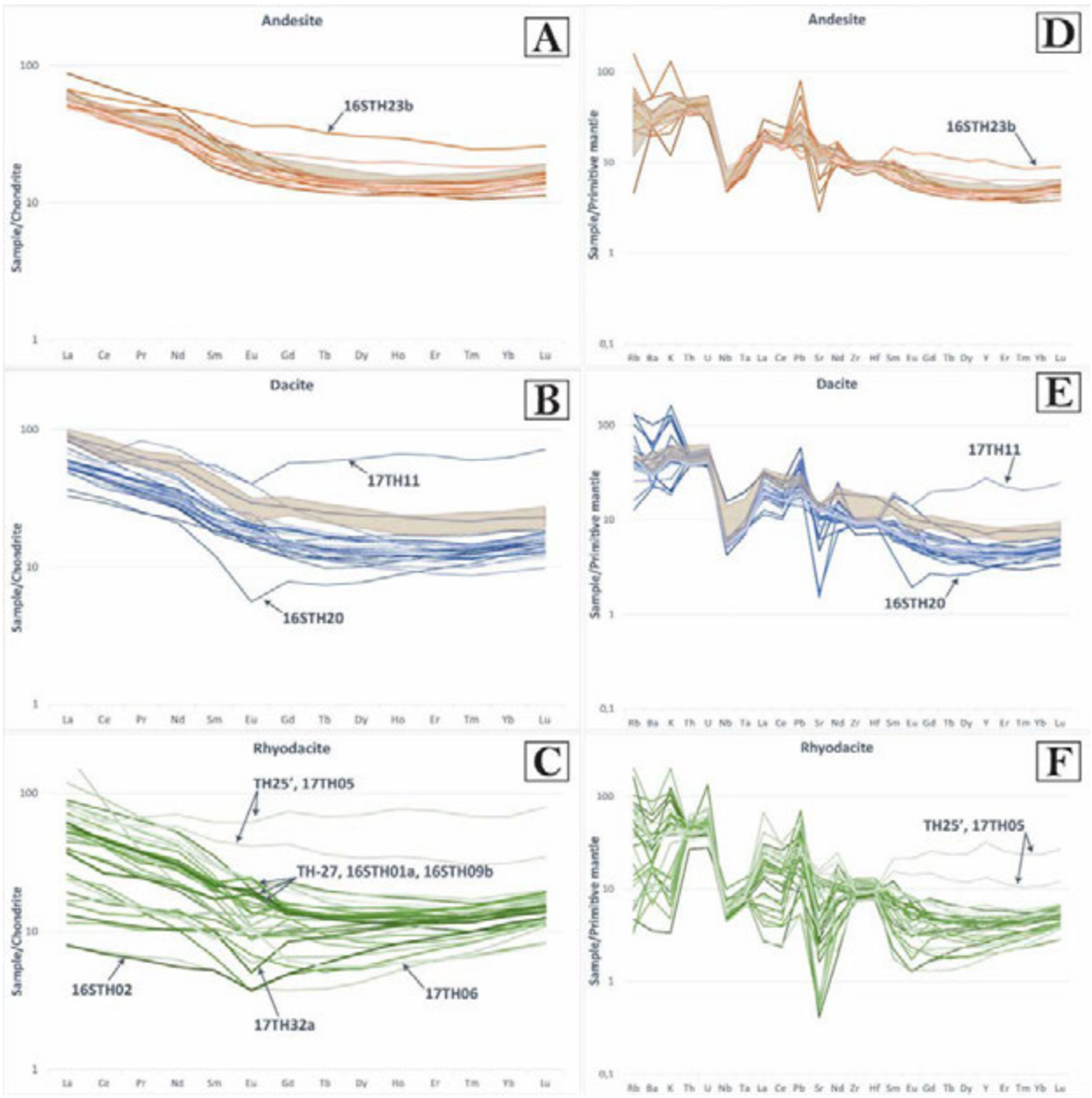


**Figure V-5: A) to C) Rare Earth Element (REE) patterns normalized to chondrite values (after Sun & McDonough, 1989) of the andesite, dacite and rhyodacite lava flows, respectively, used in this study. D) to F) Multi-element patterns normalized to primitive-mantle (after Sun & McDonough, 1989) for the same samples as in Fig. 5 A to C. The shaded bands corresponds to the range determined for Terre-de-Haut volcanic rocks from Zami *et al.*, 2014.**

In common trace element diagrams the lava flow samples are compared to other fresh volcanic rocks from Terre-de-Haut Island (Zami *et al.*, **2014**), in order to estimate the geochemical secondary evolution of the transformed rocks taking into account primary variations due to magmatic differentiation (andesitic, dacitic and rhyodacitic groups, Figure V-5). It is also a test of the proposed nomenclature in the geological map (Figure V-3**-B**).

Transformed andesite samples (Figure V-5**-A**) are similar to fresh volcanic andesites of Terre-de-Haut. A sample from south Bourg bay (16STH23b) displays enrichment in Middle-REE (MREE) and Heavy-REE (HREE) suggesting weathering and leaching process for this andesitic rock (Zhou *et al.*, **2013**).

Dacite samples (Figure V-5**-B**) display a consistent trend for most samples with enrichment in LREE. However, a sample from the top of "Morne à Craie" (17TH11) shows HREE enrichment and negative Ce anomaly, presumably indicating supergene alteration processes (Cotten *et al.*, **1995**; Zhou *et al.*, **2013**; Ricci *et al.*, **2017**). Another sample has a pattern that differs from the usual dacitic trend. It comes from the northern part of Grande Anse beach (16STH20) in a gypsum concentrated area and displays a large negative Eu anomaly suggesting plagioclase fractionation or interaction with mildly acidic low-temperature fluids (Bau, **1991**; Taylor & McLennan, **1995**).

Rhyodacite samples (Figure V-5**-C**), related to the most differentiated rocks, display the most various spectra with different degree of LREE enrichments. This feature can be either related to different magmatic differentiation stages or to secondary alteration events (hydrothermal and/or supergene alteration). Some samples show especially negative or positive Eu anomaly, suggesting either plagioclase fractionation or the interaction with secondary fluids (Bau, **1991**). For example, two severely hydrothermalized samples from the southern part of Bourg Bay area (17TH32a) and the northern part of Grande Anse beach (16STH02) reveal both LREE depletion and slightly negative Eu anomaly, related to typical high-temperature alteration under mildly acidic conditions (Bau, **1991**). Other hydrothermalized samples from the northern part (TH-27, 16STH01a, 16STH09b) and southern part (17TH06) of Grande Anse beach present a positive Eu anomaly due to acidic high-temperature hydrothermal fluids (Michard *et al.*, **1983**; Cotten *et al.*, **1995**). Samples from the southern part of Grande Anse beach (TH-25' and 17TH05), show high HREE enrichment and slight negative Ce anomaly, reflecting weathering processes under tropical conditions (Cotten *et al.*, **1995**; Zhou *et al.*, **2013**; Ricci *et al.*, **2017**), as already observed for the dacitic-sample (Figure V-5**-B**).

### V.2.5. Structural analysis

The main outcome of our structural study is the identification, for the first time in Terre-de-Haut Island, of schistose zones (Figure V-6), and thus ductile tectonic structures, in addition to the previously recognized brittle structures.

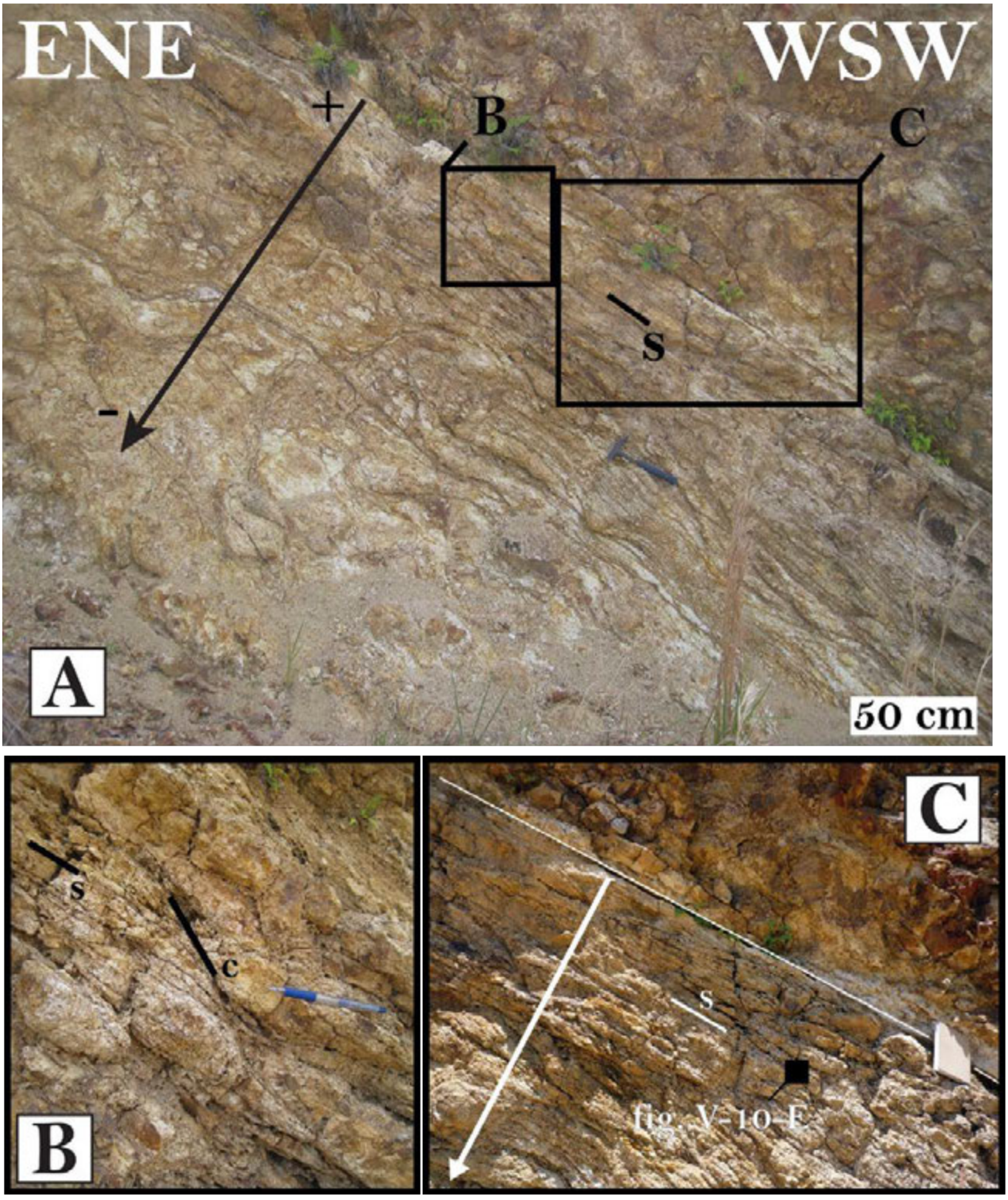


**Figure V-6: A) Schistose corridors showing a deformation gradient (from the aerodrome career). B) Local ductile strain pattern with S (schistosity) and C (shear planes) structure compatible with normal sense of shear. C) Zoom on schistose corridor with finite deformation gradient.**

These schistose zones are concentrated into decametre to hectometre corridors (Figure V-6**-A-C**), with ductile strain gradients. Stretching lineations are difficult to decipher, but in highly strained domains, strongly dipping lineations and local C/S structures indicate a normal sense of shear

(Figure V-6-**B**). At both local and map scale, the schistose zones are heterogeneously distributed and tend to anastomose forming lenticular pods (Figure V-7 and Figure V-8).

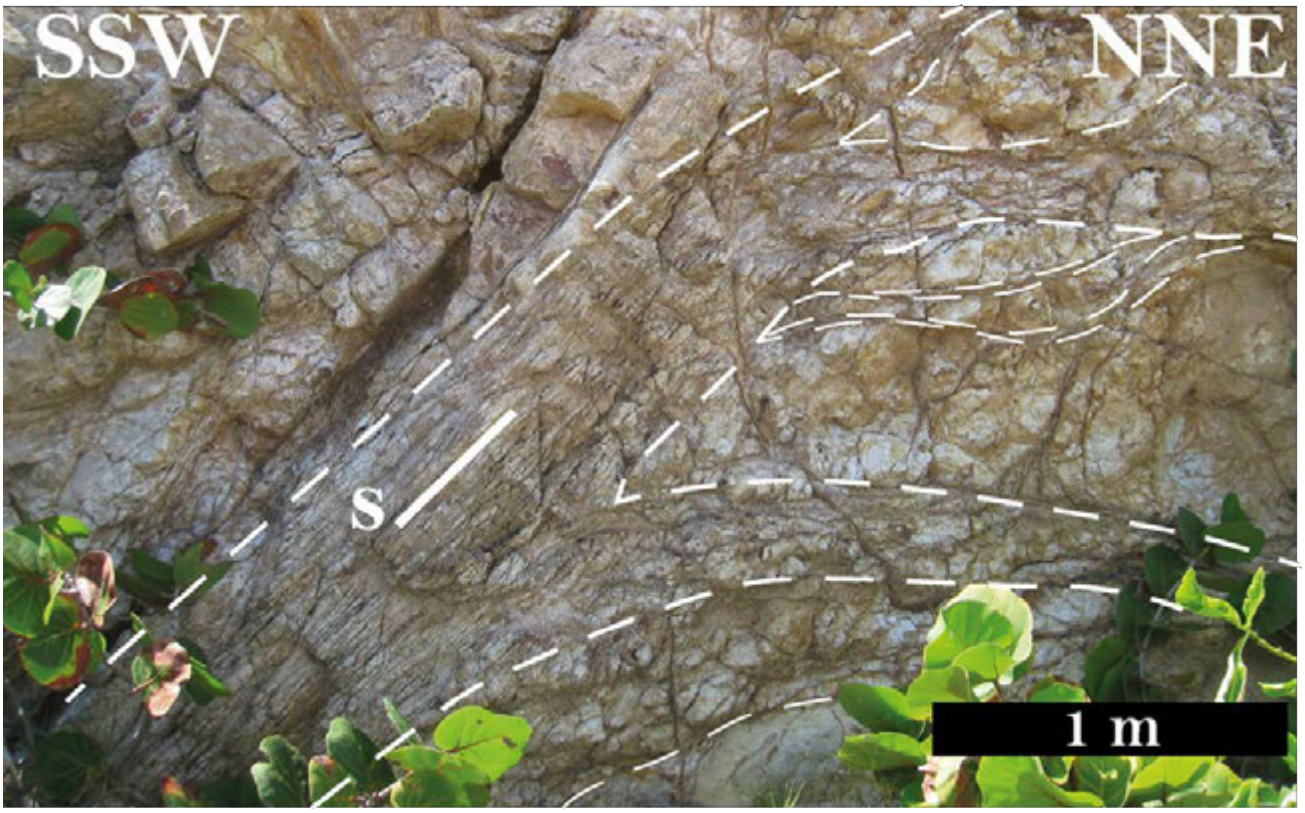


**Figure V-7: Schistose plans tend to anastomose forming lenticular pods. Outcrop from La Savane.**

Four directions of schistose corridors have been observed and measured in the field: (1) N030-N060, (2) N120-N150, (3) N080-N110, and (4) N160-N020, from the oldest to the youngest ones. The relative chronology is based on geometrical criteria (intersections, superimposed structures …) visible at the map scale (Figure V-8). The schistosity planes display variable dips (from 90 to 10°), but are more likely slightly dipping.

At the outcrop-scale, the geometry of the schistosity planes corresponds to spaced disjunctive cleavages (Powell, **1979**; Beach, **1982**; Passchier & Trouw, **2005**, Figure V-9-**A-B**).

In thin-section, the processes of schistosity formation correspond to pressure-solution mechanisms (Rutter, **1976**; Beach, **1979**; Figure V-10). Schistosity planes are underlined by local dissolution of minerals, frequently observed at the periphery of primary volcanic minerals (Figure V-10-**D-E**), but also by concentration of insoluble minerals. They are also highlighted by sulphur (pyrite mainly; Figure V-10-**B**), sulphates (gypsum, jarosite, barite; Figure V-10-**E**). Sometimes, opening of late veins filled with quartz, pyrite, calcite, gypsum and zeolites reworks schistosity planes (Figure V-10-**C**).

In the specific area of north of Grande Anse beach, we recognized hydrothermal tectonic breccias (in the sense of Sibson, **1977** and Jébrak, **1997**), with volcanic rock fragments cemented in fine-grained

matrix with cohesive texture. When these hydrothermal breccias are parallel, thus geometrically consistent to the schistose zones, they potentially reflect a local fluids overpressure under constant P-T conditions. On the other hand, when the breccias clearly intersect the ductile structures they could reflect a progressive transition of strain from ductile to brittle conditions during cooling of the studied system.

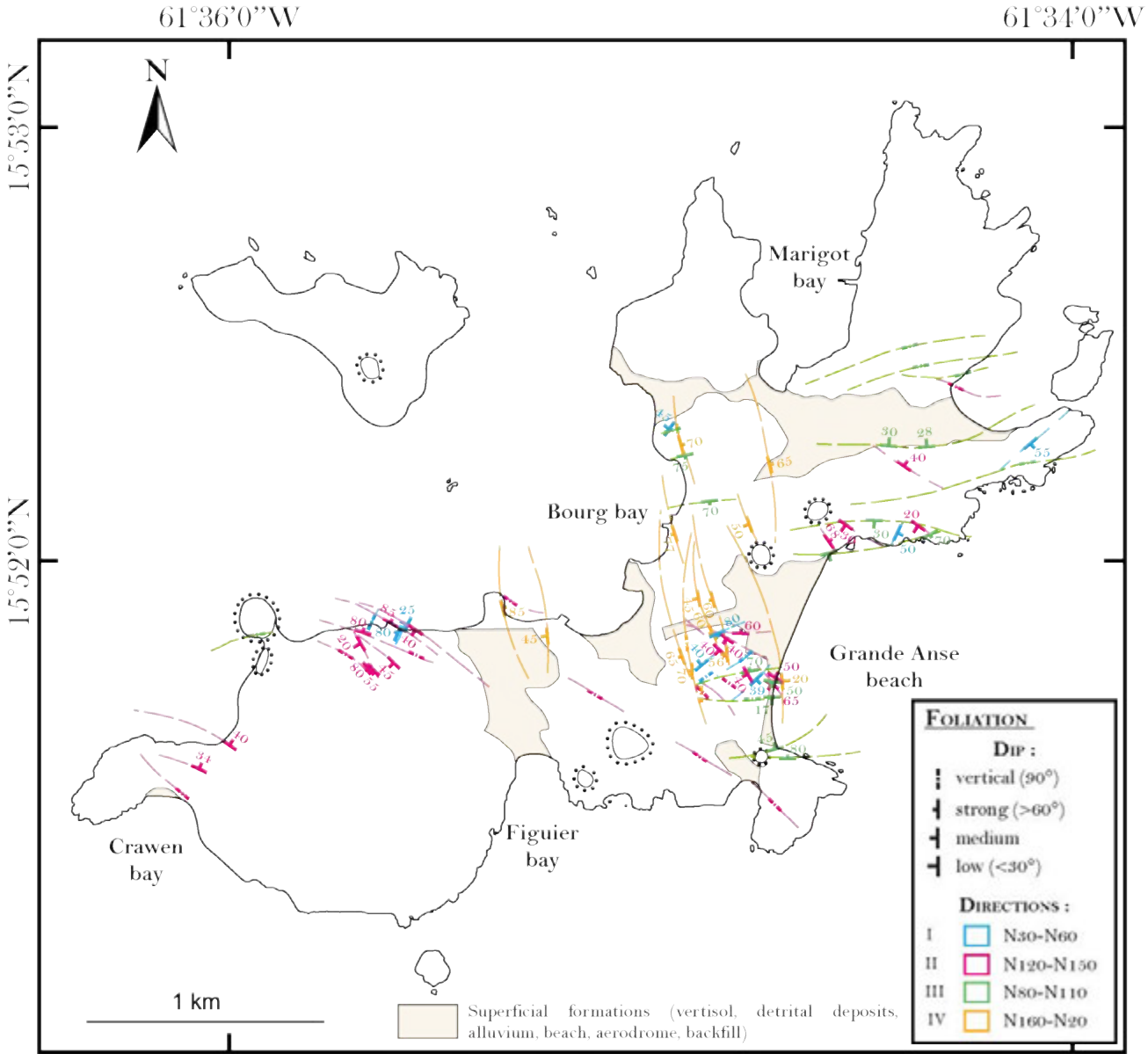


**Figure V-8: Tectonic sketch map of schistosity trajectories on the Terre-de-Haut Island according to field observations.**

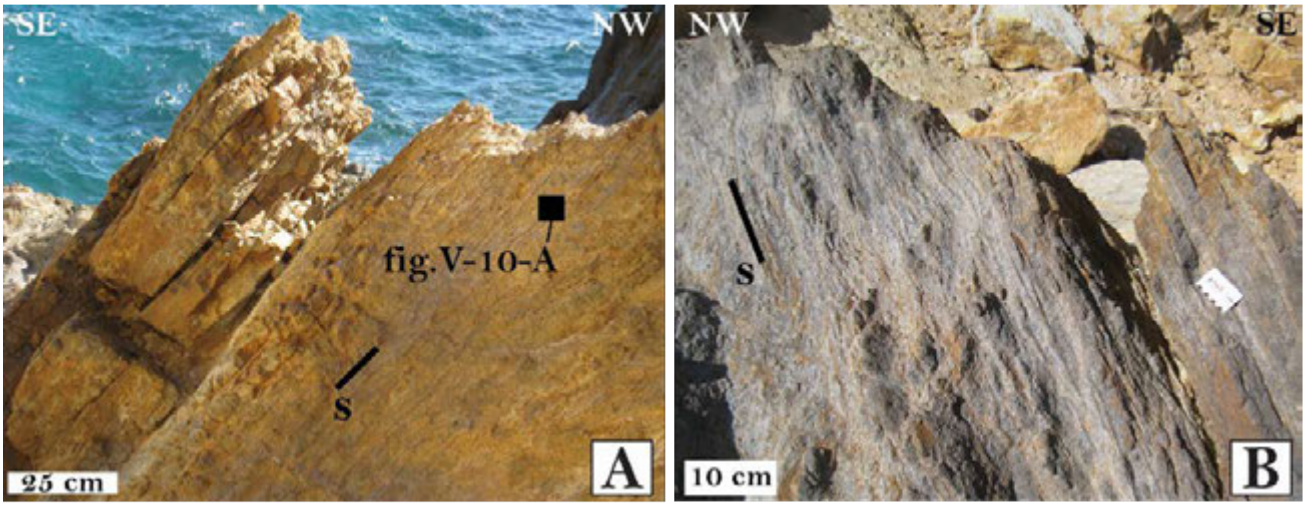


**Figure V-9: A) Highly hydrothermalized volcanic rock from North of Grande Anse beach with schistosity plane (s) expressed by spaced disjunctive cleavages. B) Moderatly hydrothermalized volcanic rock from North of Grande Anse beach with schistosity plane (s) corresponding to spaced disjunctive cleavages.**

### V.2.6. Petrography and mineralogy

Because of the heterogeneity of the hydrothermal transformations, of the finite deformation state and finally of the degree of supergene alteration depicted in Terre-de-Haut Island, we need to establish clear petrographic distinctions between fresh, slightly transformed, transformed, and highly transformed volcanic rocks. Mineral chemistry was performed on all rock types and selected microprobe analyses are presented in Table V-2 and in supplementary data Table X-2, Table X-3 and Table X-4.

(1) fresh rocks

The well-preserved lava flows and volcanic plugs are basaltic-andesite, andesite, dacite and rhyodacite. All these fresh rocks show porphyric textures with phenocrysts:

- Plagioclases (70-75%): the phenocrysts are mostly labradorite and less frequently bytownite. As previously underlined by Jacques and Maury (**1988**), some plagioclases are zoned, with bytwonite in the core and labradorite towards the rim.
- Ferromagnesian phases (20-25%): the orthopyroxenes are hypersthene, while the clinopyroxenes are augite. Brown amphibole compositions vary from hornblende to edenite or pargasite depending of the considered bulk-rock chemistry (see also Jacques & Maury, **1988**).
- And oxides (5%), ilmenite and/or titanomagnetite.

Several volcanic deposits, debris and pyroclastic flows, are also preserved from hydrothermal and supergene transformations. The fragments of volcanic rocks have well-developed porphyric textures with phenocrysts composed of plagioclases (65-74%), ortho- and clino- pyroxenes (25-29%), amphiboles (5-1%) and oxides (5%).

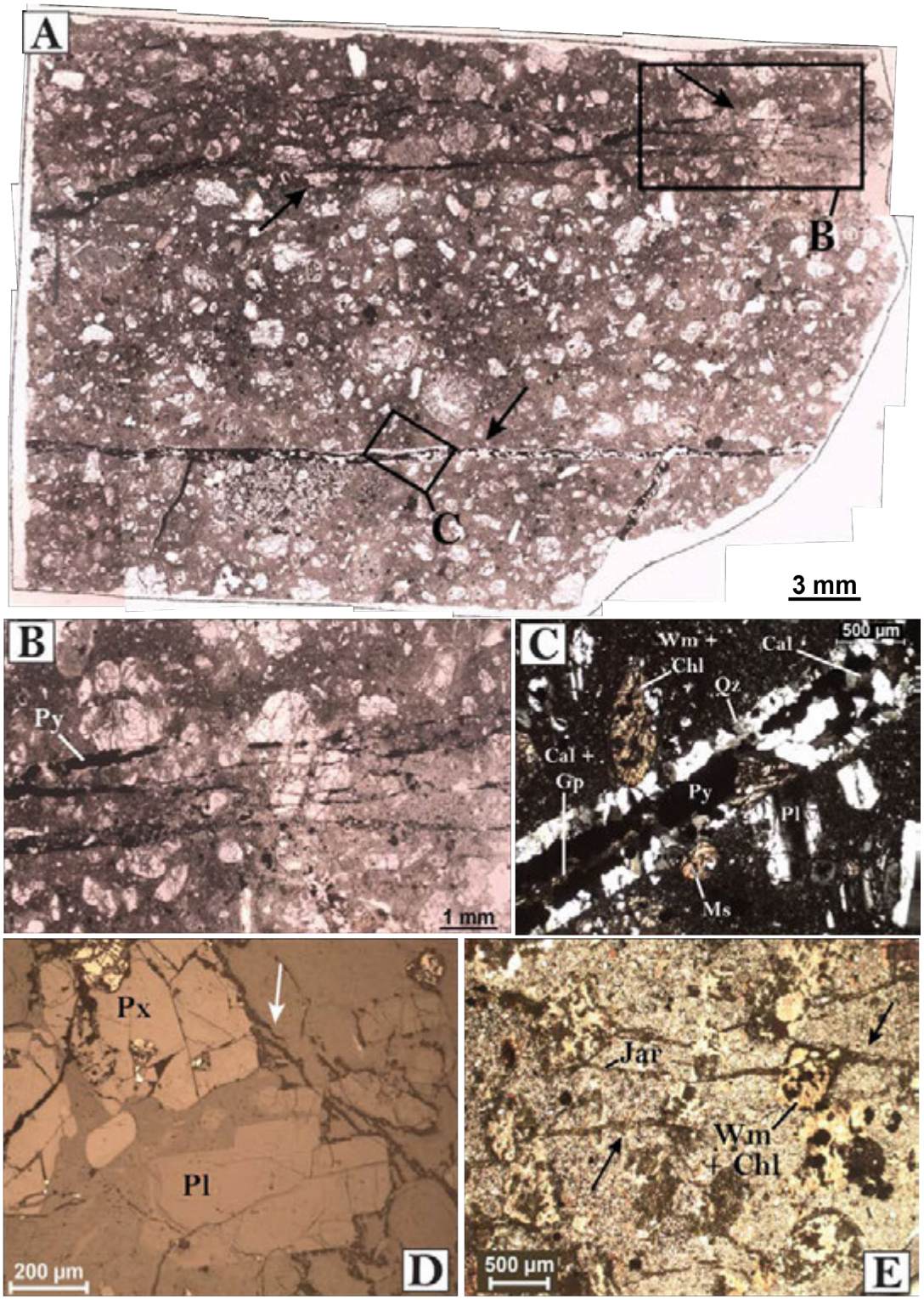


**Figure V-10: A) At the thin section scale, schistosity planes are underlined by insoluble residues. Sometimes the schistosity plane is reworked with opening of late veins. B) Zoom on the schistosity planes, underlined by pyrite, developed by pressure solution mechanisms. C) Zoom on a vein opened on the schistosity plane and filled with quartz, pyrite, calcite and gypsum. See, at the vein border, the local dissolution of volcanic minerals. D) Dissolution or pressure-solution mechanism at the periphery of volcanic minerals and concentration of insoluble. Sample from south of Grande Anse beach. E) Spaced disjunctive cleavages underlined by jarosite. Sample from the aerodrome career.**

(2) slightly transformed rocks

In these rocks, the primary volcanic textures are preserved, but we observed the limited development of reaction coronas around ferromagnesian volcanic phases (Figure V-11**-A-B**), mainly around ortho- and clino- pyroxenes. The neoformed minerals are actinolite, chlorite, muscovite and calcite. The lithologies most affected by these hydrothermal transformations are dacite and debris or pyroclastic flows, within which the neoformed phases represent 5 to 10% of the observed mineral composition.

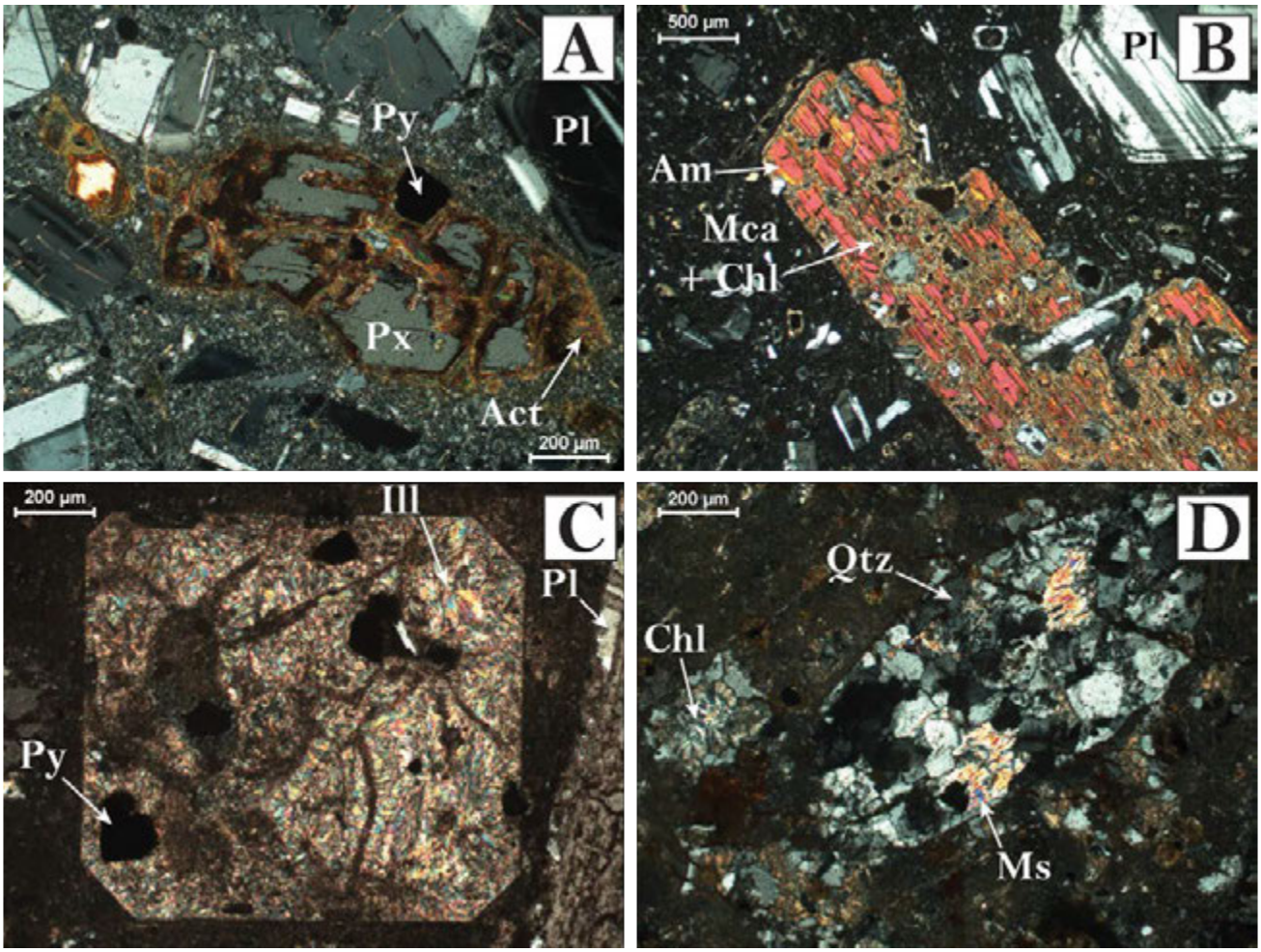


**Figure V-11: High-temperature pseudomorphic transformations of volcanic minerals. A) Reaction coronas around pyroxene, highlighted by actinolite, in a meta-andesite rock. Sample from south of Bourg bay (16STH23a). B) Replacement of volcanic amphibole by a mix of chlorite and mica, in meta-rhyodacite rock of pyroclastic flow. Sample from north of Crawen bay (17TH20b). C) Volcanic pyroxene replaced by white mica, in a meta-rhyodacite rock. Sample from north of Grande Anse beach (16STH19). D) Volcanic phase replaced by quartz, chlorite and/or muscovite, in a meta-rhyodacite rock. Sample from La Savane (16STH21a). Act = actinolite, Am = amphibole, Chl = chlorite, Qtz = quartz, Ill = illite, Mca = mica, Ms = muscovite, Pl = plagioclase, Px = pyroxene, Py = pyrite.**

(3) transformed rocks

In this category of rocks, we observe relicts of volcanic textures but more than 70% of the volcanic pyroxenes or amphiboles are transformed, as it is the case for more than 50% of the plagioclases. The hydrothermal phases can totally replace the initial volcanic phenocrysts (pseudomorphic

transformations, Figure V-11**-C-D**). The metamorphic minerals are typical of high-temperature hydrothermalism, such as quartz, epidote (clinozoisite in little sticks in Figure V-12**-B** and pistacite in colourless grains in Figure V-12**-E**), micas (illite in sheafs or spherules Figure V-11**-C**, muscovite Figure V-12**-A** and biotite), chlorite (Figure V-12**-C-D**), actinolite (Figure V-12**-F**), titanite (Figure V-12**-E**), talc (Figure V-12**-C**), and pyrophyllite, The most transformed lithologies are dacite and rhyodacite lava flows. Moreover, in veins, small-sized cracks or vacuoles, carbonates (micro-crystalline calcite grains with polysynthetic twins in Figure V-13**-A** and sub-automorphous calcite grains in Figure V-12**-F**), sulphates (Figure V-13**-B-C**), silice-polymorphs (quartz, chalcedony, cristobalite, Figure V-13**-D**), acicular or radial zeolites (Figure V-13**-D-E**) can also be observed. Finally, in a restricted number of samples a strong supergene alteration is marked by the complete transformation of volcanic phases by clay minerals.

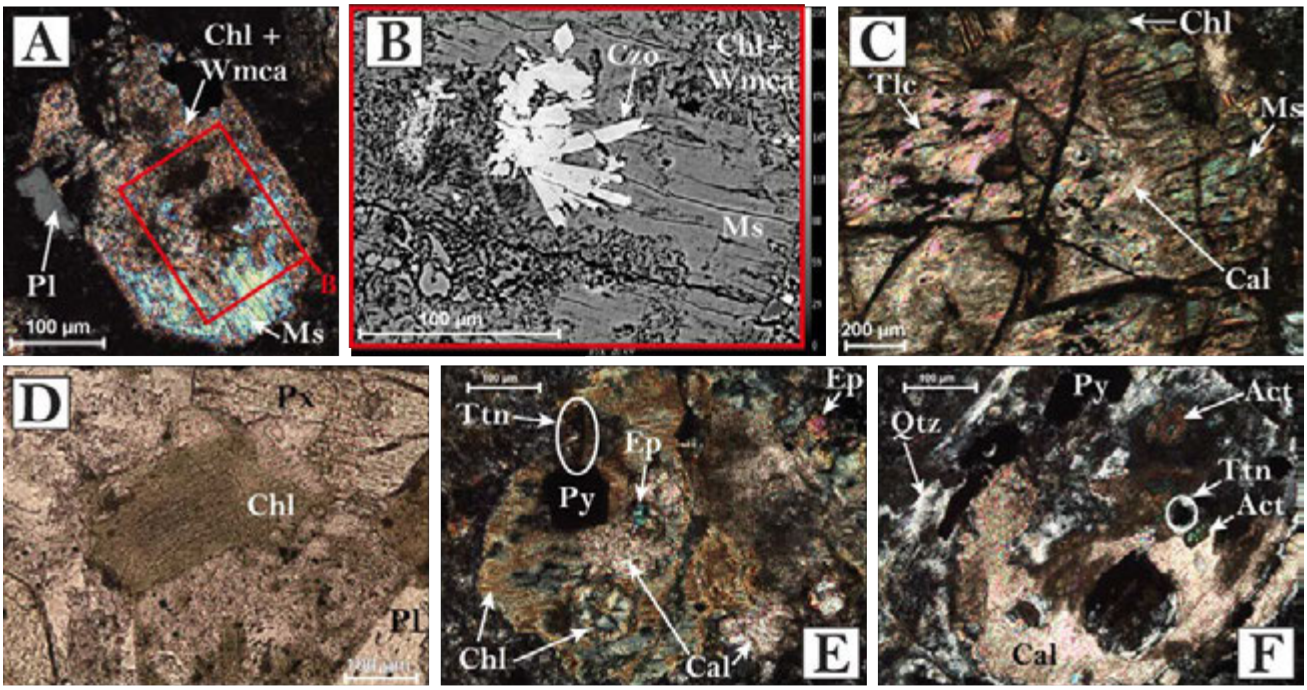


**Figure V-12: Diversity of secondary new phases developed at the expense of primary volcanic minerals. A) Pyroxene replaced by muscovite and a mix chlorite-white mica, in a meta-rhyodacite rock. Sample from north of Grande Anse beach (16STH16). B) BSE image. Zoom on clinozoisite and displaying contrast between fibrous muscovite and the mix chlorite-white mica. C) Volcanic phenocryst pseudomorphosed by multiple secondary new phases, in a meta-andesite rock. Sample from north of Grande Anse beach (SA-14). D) Fibrous green chlorite, in a meta-andesite rock. Sample from north of Grande Anse beach (SA-14). E) Pyroxene phenocryst replaced by numerous secondary new phases, in a meta-andesite rock. Sample from north of Grande Anse beach (SA-14). F) Crystallization of various secondary new phases at the expense of a volcanic phenocryst, in a meta-dacite rocks. Sample from north of Grande Anse beach (17TH16). Act = actinolite, Cal = calcite, Chl = chlorite, Czo = clinozoisite, Ep = epidote, Ms = muscovite, Qtz = quartz, Pl = plagioclase, Px = pyroxene, Py = pyrite, Tlc = talc, Ttn = titanite, Wmca = white mica.**

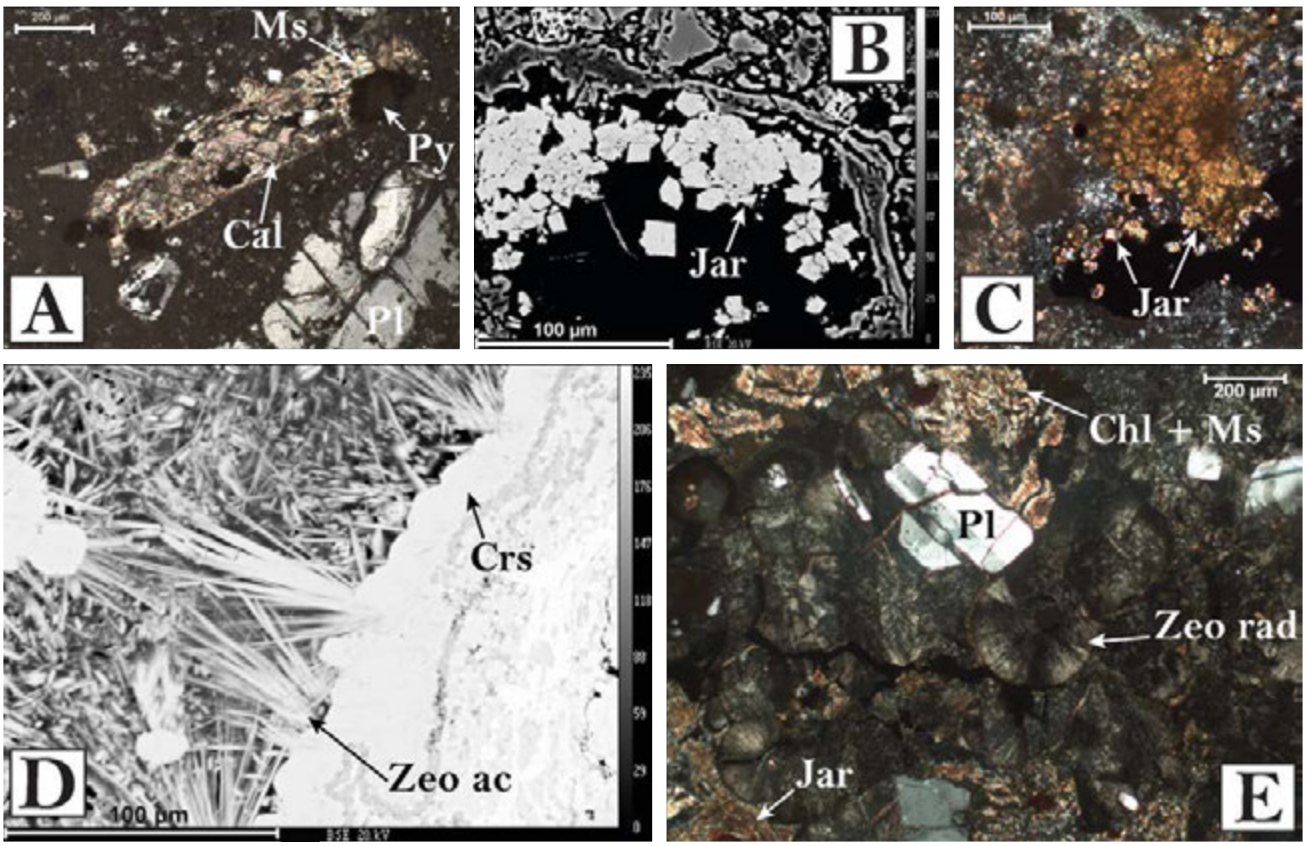


**Figure V-13: Examples of low-temperature secondary mineral crystallizations. A) Ferromagnesian phenocryst replaced by calcite, in a meta-dacite rock. Sample from north of Grande Anse beach (16STH11b). B) BSE image. Jarosite in border of cavity, in a meta-dacite rock of pyroclastic flow. Sample from north of le Chameau volcanic dome (17TH24). C) Jarosite in border of cavity, in a meta-dacite rock. Sample from north of Grande Anse beach (16STH20). D) BSE image. Cristobalite and acicular zeolite in border of cavity, in a meta-dacite rock of pyroclastic rock. Sample from north of le Chameau volcanic dome (16STH29). E) Jarosite and radial zeolite in matrix of a meta-dacite rock of pyroclatic flow. Sample from north of le Chameau volcanic dome (16STH29). Cal = calcite, Chl = chlorite, Crs = cristobalite, Jar = jarosite, Ms = muscovite, Pl = plagioclase, Py = pyrite, Zeo ac = acicular zeolite, Zeo rad = radial zeolite.**

(4) highly transformed rocks

These most hydrothermalized rocks are located in the central part of the island. Here, the primary volcanic textures have been completely erased, and in some cases phantoms of phenocryst shapes can be recognized. However, in most cases the whole rock is recrystallized (phenocrysts and matrix) into a fine-grained association of new phases including quartz-epidote-muscovite-chlorite-actinolite-titanite +/- talc and pyrophyllite.

In this central part of the island, a significant amount of low-temperature hydrothermal associations and supergene minerals including illite-smectite, smectite, kaolinite and halloysite have been recently described in detail (Beauchamps *et al.*, **2019**).

In order to highlight the importance and the spatial distribution of the previously described transformations, we propose a map of minerals occurrences at the scale of Terre-de-Haut Island

(Figure V-14), distinguishing high-temperature, low-temperature hydrothermal stages and supergene alterations.

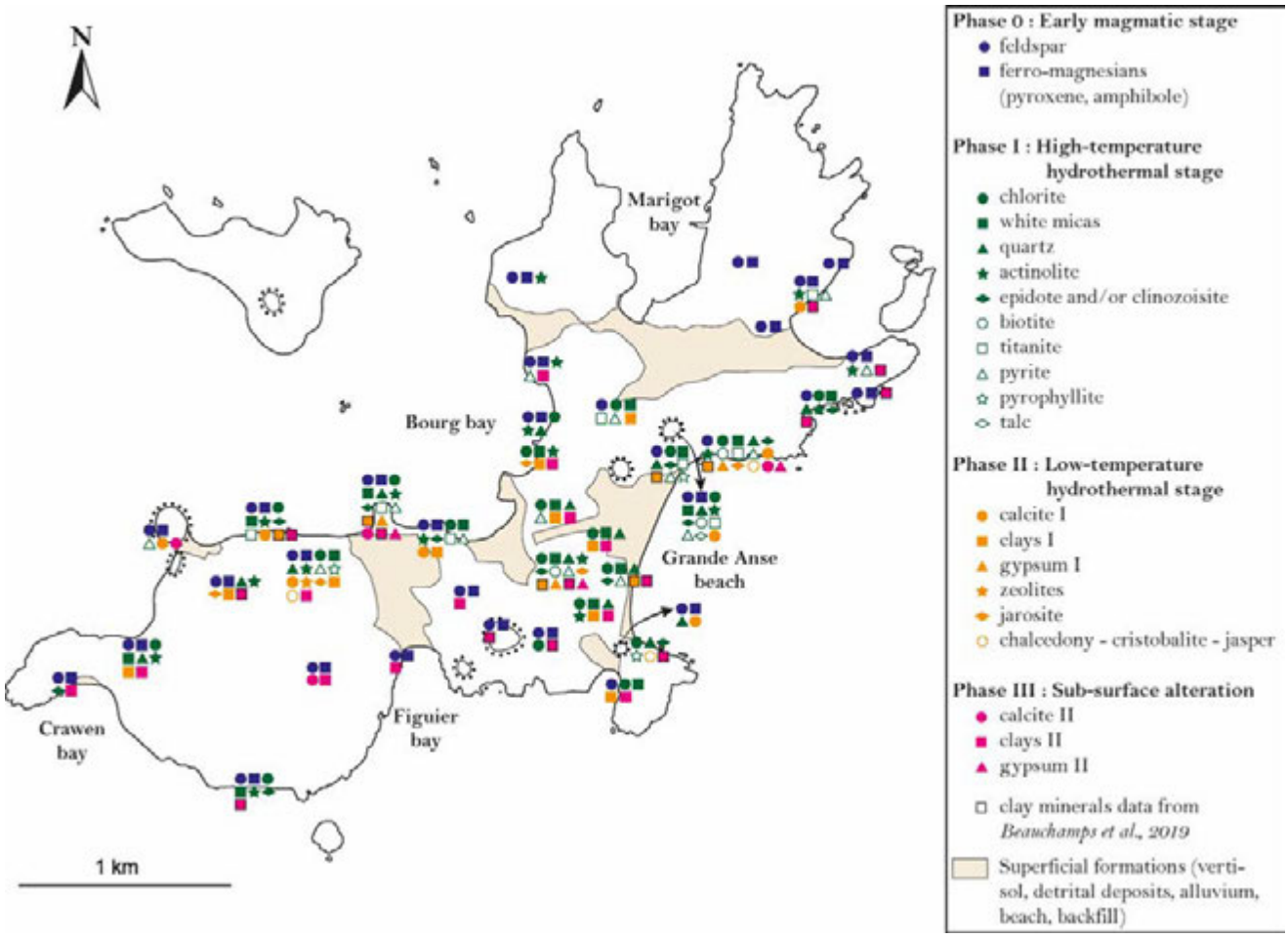


**Figure V-14: Distribution of mineral phases (volcanic, high and low temperature hydrothermal and sub-surface alteration) within the Terre-de-Haut Island.**

### V.2.7. Mineral equilibria modelling

First of all, and before any quantitative analysis of the P-T conditions of formation of Terre-de-Haut hydrothermal system, it must be specified that a mineral association involving the co-stability of chlorite+quartz+epidote+muscovite+albite+titanite+biotite+/-actinolite, and pyrite is stable, in volcanic rocks transformed in hydrothermal and geothermal systems, for a minimal temperature of about 300°C (Henley & Ellis, **1983**; Rancon, **1983**; White & Hedenquist, **1995**; Lagat, **2014**).

#### *V.2.7.a. Chlorite geothermometry*

Chlorite is a common phase in low-grade metamorphic rocks, and Cathelineau (**1988**) first proposed a geothermometer based on chemical composition of chlorite. Later on, more elaborated versions of this thermometer have been proposed, that are particularly well adapted for hydrothermalized rocks (Lanari *et al.*, **2014**; Bourdelle & Cathelineau, **2015**). Following these recent investigations, for Si-poor and Al-rich chlorites, the more appropriate calibration is the one proposed by Lanari et al.

(**2014**), while for Si-rich chlorites the calibration proposed by Bourdelle and Cathelineau (**2015**) is more adapted.

Because chlorite is stable over a wide temperature range in geothermal systems (< 100°C to > 350°C, Henley & Ellis, **1983**; Reyes, **1990**; White & Hedenquist, **1995**; Lagat, **2014**), it is critical to distinguish the possible variations of chlorite compositions with respect to their various microstructural crystallization sites. Indeed, we found the occurrence of chlorite in schistose corridors as well as in late (i.e.post-schistosity) veins or fractures. Out of the main schistose corridors, pale green chlorites are frequently observed, in association with low temperature minerals, within micro-cracks or vacuoles.

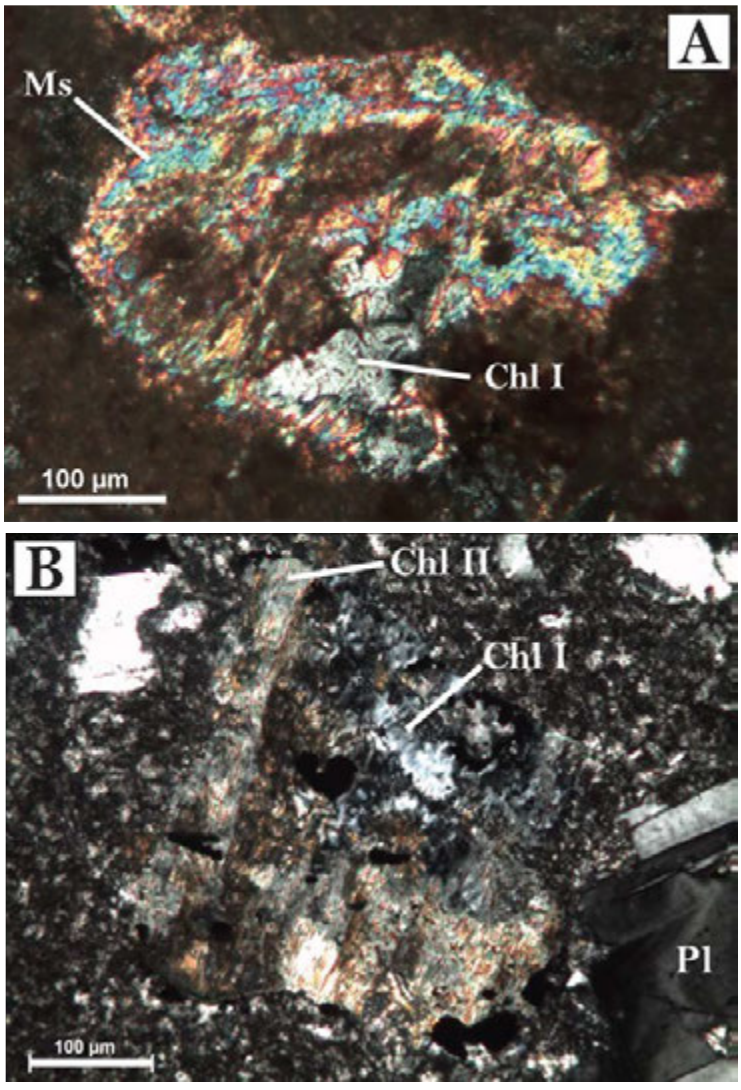


**Figure V-15: Chlorite morphologies. A) Ferromagnesian phenocryst pseudomorphosed by fibrous muscovite and grey automorphous crystals of chlorite (type I), in a meta-rhyodacite rock. Sample from north of Grande Anse beach (16STH19). B) Ferromagnesian phenocryst pseudomorphosed by grey automorphous crystals of chlorite (type I) and green-grey to yellow fibrous grains (type II), in a meta-dacite rock. Sample from north of Grande Anse beach (17TH16).**

**Table V-2: Microprobe analysis and chlorite thermometry on three samples from north of Grande Anse beach: 16STH19 (meta-rhyodacite), 17TH16 (meta-dacite) and SA-14 (meta-andesite).**

| Sample | 16STH19 | | | | | | | | | | 17TH16 | | | | | | | | | | SA-14 | | | | | |
|---|---|---|---|---|---|---|---|---|---|---|---|---|---|---|---|---|---|---|---|---|---|---|---|---|---|---|
| Chlorite analysis | grain 1 | | grain 2 | | grain 3 | grain 4 | grain 5 | grain 6 | | | grain 7 | | | grain 8 | grain 9 | grain 10 | grain 11 | | grain 12 | grain 13 | | | | | | |
| Chlorite type | I | I | I | I | I | I | I | I | II | II | I | I | II | I to II | II | II | I | II | I to II | II | | | | | | |
| Structural position | core | rims | core | rims | core | core | core | core | rims | rims | rims | rims | rims | rims | rims | rims | core | rims | rims | rims | | | | | | |
| **Mineral %wt** | | | | | | | | | | | | | | | | | | | | | | | | | | |
| $Al_2O_3$ | 20,57 | 20,30 | 20,08 | 20,22 | 20,18 | 20,11 | 20,27 | 17,15 | 17,12 | 16,27 | 16,98 | 16,77 | 16,05 | 15,40 | 17,04 | 16,95 | 15,83 | 15,01 | 14,99 | | | | | | | |
| $SiO_2$ | 27,32 | 27,01 | 25,66 | 25,51 | 25,45 | 25,69 | 25,53 | 31,02 | 30,94 | 31,60 | 29,71 | 29,69 | 31,37 | 32,50 | 31,94 | 30,16 | 32,15 | 31,33 | 32,98 | | | | | | | |
| $TiO_2$ | 0,01 | 0,06 | 0,00 | 0,00 | 0,01 | 0,01 | 0,02 | 0,01 | 0,04 | 0,04 | 0,16 | 0,02 | 0,01 | 0,02 | 0,02 | 0,06 | 0,05 | 0,01 | 0,03 | | | | | | | |
| $Na_2O$ | 0,00 | 0,00 | 0,19 | 0,00 | 0,05 | 0,04 | 0,02 | 0,03 | 0,02 | 0,04 | 0,02 | 0,00 | 0,02 | 0,05 | 0,05 | 0,11 | 0,11 | 0,08 | 0,14 | | | | | | | |
| MgO | 16,71 | 16,50 | 13,73 | 13,65 | 13,94 | 13,71 | 13,95 | 18,43 | 16,48 | 17,02 | 17,83 | 18,19 | 18,48 | 18,93 | 17,65 | 17,63 | 17,01 | 18,83 | 17,78 | | | | | | | |
| MnO | 0,29 | 0,33 | 0,37 | 0,23 | 0,30 | 0,34 | 0,26 | 1,82 | 1,57 | 1,44 | 1,75 | 2,15 | 1,37 | 1,56 | 1,83 | 0,69 | 0,75 | 0,73 | 0,66 | | | | | | | |
| FeO | 23,64 | 22,48 | 27,85 | 26,98 | 24,36 | 27,91 | 27,82 | 21,52 | 23,05 | 20,82 | 22,75 | 21,60 | 21,71 | 20,47 | 21,10 | 24,21 | 23,55 | 22,38 | 23,66 | | | | | | | |
| $K_2O$ | 0,00 | 0,00 | 0,00 | 0,00 | 0,00 | 0,00 | 0,00 | 0,01 | 0,02 | 0,08 | 0,02 | 0,01 | 0,02 | 0,02 | 0,02 | 0,04 | 0,04 | 0,01 | 0,05 | | | | | | | |
| CaO | 0,09 | 0,10 | 0,00 | 0,00 | 0,00 | 0,00 | 0,00 | 0,28 | 0,37 | 0,46 | 0,28 | 0,20 | 0,33 | 0,31 | 0,44 | 0,18 | 0,76 | 0,23 | 0,57 | | | | | | | |
| *Total* | *88,63* | *86,78* | *87,88* | *86,59* | *84,29* | *87,81* | *87,87* | *90,28* | *89,60* | *87,77* | *89,50* | *88,64* | *89,36* | *89,26* | *90,09* | *90,03* | *90,26* | *88,62* | *90,87* | | | | | | | |
| **Structural formulae** | | | | | | | | | | | | | | | | | | | | | | | | | | |
| Al | 2,50 | 2,50 | 2,53 | 2,57 | 2,60 | 2,54 | 2,55 | 2,02 | 2,05 | 1,97 | 2,04 | 2,03 | 1,91 | 1,82 | 2,01 | 2,03 | 1,88 | 1,81 | 1,76 | | | | | | | |
| $Al^{IV}$ | *1,19* | *1,17* | *1,26* | *1,25* | *1,22* | *1,26* | *1,28* | *0,76* | *0,68* | *0,54* | *0,88* | *0,89* | *0,70* | *0,55* | *0,61* | *0,87* | *0,57* | *0,69* | *0,55* | | | | | | | |
| $Al^{VI}$ | *1,31* | *1,33* | *1,27* | *1,32* | *1,38* | *1,28* | *1,27* | *1,26* | *1,37* | *1,43* | *1,16* | *1,14* | *1,21* | *1,27* | *1,40* | *1,16* | *1,31* | *1,12* | *1,21* | | | | | | | |
| Si | 2,81 | 2,83 | 2,74 | 2,75 | 2,78 | 2,74 | 2,72 | 3,11 | 3,14 | 3,24 | 3,03 | 3,05 | 3,17 | 3,27 | 3,19 | 3,06 | 3,24 | 3,20 | 3,29 | | | | | | | |
| Ti | 0,00 | 0,01 | 0,00 | 0,00 | 0,00 | 0,00 | 0,00 | 0,00 | 0,00 | 0,00 | 0,01 | 0,00 | 0,00 | 0,00 | 0,00 | 0,00 | 0,00 | 0,00 | 0,00 | | | | | | | |
| Na | 0,00 | 0,00 | 0,04 | 0,00 | 0,01 | 0,01 | 0,00 | 0,01 | 0,00 | 0,01 | 0,00 | 0,00 | 0,00 | 0,01 | 0,01 | 0,02 | 0,02 | 0,02 | 0,03 | | | | | | | |
| Mg | 2,56 | 2,57 | 2,19 | 2,19 | 2,27 | 2,18 | 2,22 | 2,75 | 2,50 | 2,60 | 2,71 | 2,79 | 2,79 | 2,84 | 2,63 | 2,67 | 2,55 | 2,87 | 2,65 | | | | | | | |
| Mn | 0,03 | 0,03 | 0,03 | 0,02 | 0,03 | 0,03 | 0,02 | 0,15 | 0,13 | 0,12 | 0,15 | 0,19 | 0,12 | 0,13 | 0,15 | 0,06 | 0,06 | 0,06 | 0,06 | | | | | | | |
| Fe | 2,04 | 1,97 | 2,49 | 2,43 | 2,23 | 2,49 | 2,48 | 1,80 | 1,96 | 1,78 | 1,94 | 1,86 | 1,84 | 1,72 | 1,76 | 2,06 | 1,98 | 1,91 | 1,98 | | | | | | | |
| K | 0,00 | 0,00 | 0,00 | 0,00 | 0,00 | 0,00 | 0,00 | 0,00 | 0,00 | 0,01 | 0,00 | 0,00 | 0,00 | 0,00 | 0,00 | 0,01 | 0,00 | 0,00 | 0,01 | | | | | | | |
| Ca | 0,01 | 0,01 | 0,00 | 0,00 | 0,00 | 0,00 | 0,00 | 0,03 | 0,04 | 0,05 | 0,03 | 0,02 | 0,04 | 0,03 | 0,05 | 0,02 | 0,08 | 0,02 | 0,06 | | | | | | | |
| Total (cations) | 9,94 | 9,92 | 10,02 | 9,97 | 9,92 | 9,99 | 10,00 | 9,88 | 9,83 | 9,79 | 9,93 | 9,93 | 9,87 | 9,82 | 9,81 | 9,93 | 9,83 | 9,91 | 9,83 | | | | | | | |
| *Ox. number* | *14* | *14* | *14* | *14* | *14* | *14* | *14* | *14* | *14* | *14* | *14* | *14* | *14* | *14* | *14* | *14* | *14* | *14* | *14* | | | | | | | |
| **Calculated temperature** | **328** | **289** | **375** | **360** | **318** | **376** | **379** | **150 - 185** | **135 - 163** | **100 - 145** | **180 - 250** | **180-240** | **145 - 200** | **115 - 150** | **115 - 160** | **210 - 250** | **120 - 150** | **160 - 200** | **123 - 155** | | | | | | | |

In order to quantify the maximal temperature suffered by the Terre-de-Haut hydrothermal system, we selected three samples from north of Grande Anse beach (16STH19, 17TH16, SA-14), thus in a significantly deformed domain, with well-developed schistose corridors. We also selected this area because it is a domain without evidence of supergene alteration (Figure V-3**-B** and Figure V-14). Moreover, in these selected samples chlorite developed in different microstructures as (1) grey automorphous crystals (Figure V-15**-A**), associated with muscovite, quartz and epidote, developed at the expense of magmatic pyroxenes, (2) green-grey to yellow fibrous grains (Figure V-15**-B**) associated with fibrous white micas, quartz, calcite, pyrite and/or talc, preferentially located at the rims of pseudomorphosed pyroxenes.

Interestingly, chlorite compositions evolve in relation with their microstructural position (see Table V-2), and even the type (1) grey automorphous grains display, in many cases, composition zoning from cores to rims. An increase of Si and a decrease of Al content is depicted from type (1) automorphous to type (2) fibrous chlorites.

Cores compositions of type (1) chlorites are Si-poor, thus we used the Lanari et al. (**2014**) calibration and this yield a temperature range of 255-380°C, with a calculated average temperature, taking into account the different samples, of 355°C (standard deviation=27). The rims of type (1) chlorites have higher Si-contents, thus in that case, and with the assumption that $Fe_{Total} = Fe^{2+}$, the Bourdelle and Cathelineau (**2015**) calibration is the most adapted. With this calibration the calculated temperatures range is 180-350 °C and the calculated average temperature, considering the different samples, of 252°C (standard deviation=57).

Type (2) fibrous chlorites have also high Si-contents, thus using the Bourdelle and Cathelineau (**2015**) calibration we obtained a temperature range of 115-250°C with a calculated average temperature, considering the different samples, of 175 °C (standard deviation=33).

All together, chlorite thermometers provide coherent estimation of the progressive cooling registered by the various generations of chlorites during their hydrothermal evolution through time.

*V.2.7.b. Pseudosection modelling*

The intensive parameters (pressure and temperature) corresponding to the high temperature hydrothermal stage, were calculated with the free energy minimization program Theriak-Domino (de Capitani & Petrakakis, **2010**, updated software v. 4 February 2017) and the internally consistent thermodynamic "tcdb55c2d" database (Holland & Powell, **2004**). Mixing models used for solid solutions are presented in appendix (Table X-5).

In order to be as close as possible to the equilibrium conditions at the scale of the whole rock, which are essential for the application of this type of method, we selected a highly transformed sample with a maximum of high temperature new phases expressed, but without mineralogical evidence of

supergene alteration. The best candidate for pseudosection modelling is, in such a case, a sample of rhyodacite (16STH19) selected from the most hydrothermalized area (north of Grande-Anse beach). P-T pseudosections were calculated in the system $SiO_2$-$Al_2O_3$-$TiO_2$-FeO-MnO-MgO-CaO-$Na_2O$-$K_2O$-$H_2O$, using the whole rock composition of the selected sample (Table V-3). The observed mineral assemblage involves albite + chlorite + muscovite + biotite + clinozoisite + epidote s.s. + quartz. Under tropical conditions, the iron oxidation state is always difficult to estimate. In order to test the effect of $Fe_2O_3$ in our models we calculated pseudosections with various amounts $Fe^{3+}$. When the later reaches 5%, we never find the mineral assemblage observed in the natural sample. Consequently, we consider that a model with total iron considered as FeO is the best approximation for pseudosections calculation.

**Table V-3: Whole-rock composition of 16STH19 sample and corresponding input in Theriak-Domino program.**

| Sample 16STH19 | | | |
|---|---|---|---|
| Composition (%) | | Input Theriak-Domino (mol) | |
| $SiO_2$ | 59.555 | Si | 50.489 |
| $Al_2O_3$ | 16.07 | Al | 16.058 |
| $Fe_2O_3$ | 1.772 | Fe | 1.129 |
| MnO | 0.103 | Mn | 0.074 |
| MgO | 3.055 | Mg | 3.862 |
| CaO | 5.531 | Ca | 5.024 |
| $Na_2O$ | 1.691 | Na | 2.78 |
| $K_2O$ | 1.299 | K | 1.405 |
| $TiO_2$ | 0.558 | Ti | 0.365 |
| $P_2O_5$ | 0.151 | P | 0.109 |
| LOI | 10.214 | H | 57.761 |
| *26.46 % $CO_{2\,total}$* | *2.703* | O | ? |
| *58.97 % $H_2O_{total}$* | *6.023* | | |
| *7.04 % FeO* | *0.719* | | |
| *7.53 % $S_{total}$* | *0.769* | | |

We considered the fluid phase in excess to be consistent with the conditions of a fluid-saturated hydrothermal system. However, in high-enthalpy geothermal systems, fluids have different origins (supergene waters, with or without sea-water component, volcanic –derived fluids and gases, with variable amounts of $CO_2$ or $SO_2$), it seems thus critical to test the effect of fluid composition on the modeled system. In a first approach, a pseudosection was calculated with 100% of $H_2O$ for the fluid composition. In this case, the observed mineral assemblage corresponds to the calculated field (360-375°C and 0.90-1.40 kbar) identified with bold-black characters in Figure V-16-**A** and is in agreement with the highest temperature values obtained by chlorite-geothermometry on type-1 chlorite cores obtained on this sample (16STH19, see Figure V-16-**B** and Table V-2). A temperature of about 365°C

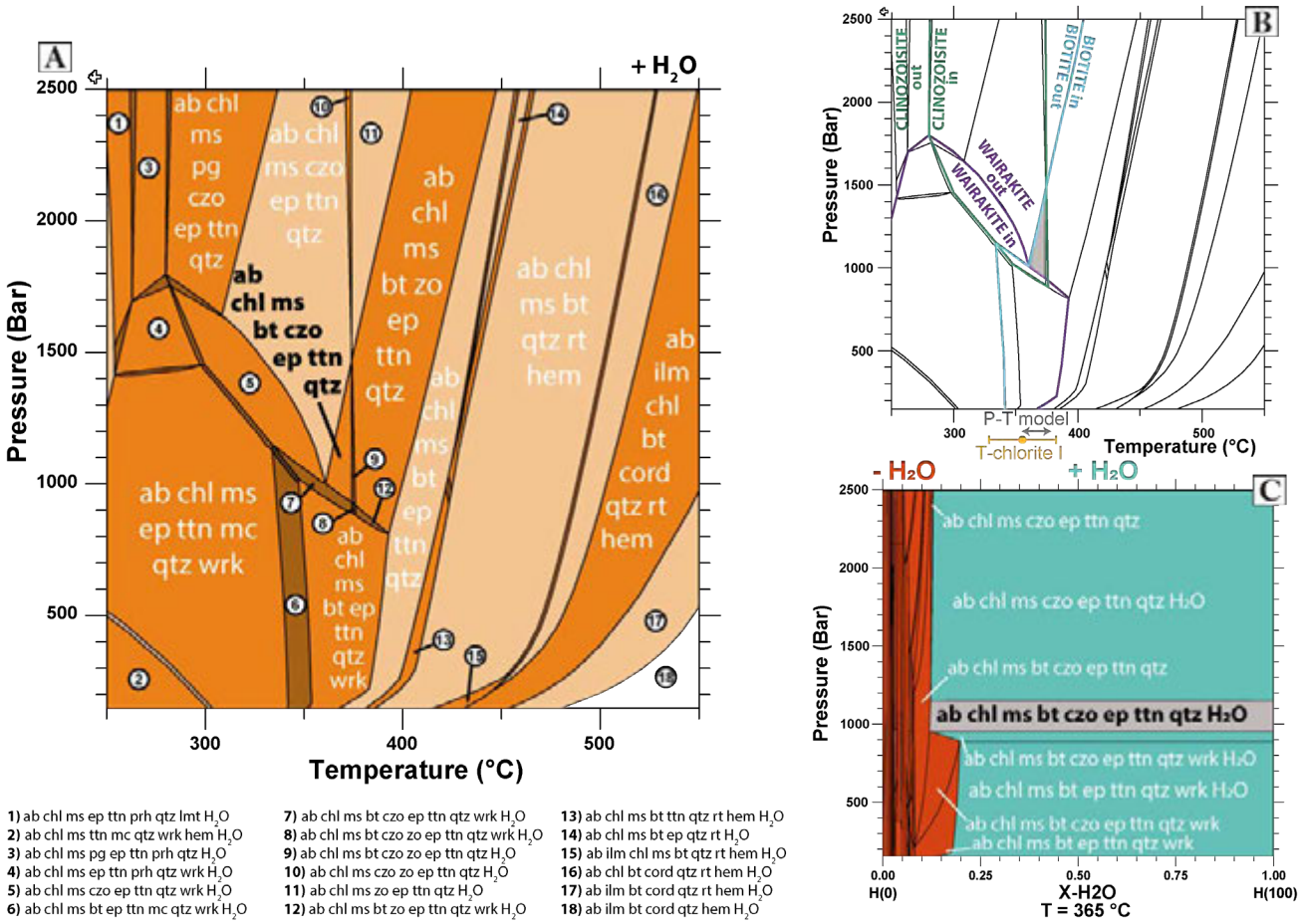


**1)** ab chl ms ep ttn prh qtz lmt $H_2O$
**2)** ab chl ms ttn mc qtz wrk hem $H_2O$
**3)** ab chl ms pg ep ttn prh qtz $H_2O$
**4)** ab chl ms ep ttn prh qtz wrk $H_2O$
**5)** ab chl ms czo ep ttn qtz wrk $H_2O$
**6)** ab chl ms bt ep ttn mc qtz wrk $H_2O$
**7)** ab chl ms bt czo ep ttn qtz wrk $H_2O$
**8)** ab chl ms bt czo zo ep ttn qtz wrk $H_2O$
**9)** ab chl ms bt czo zo ep ttn qtz $H_2O$
**10)** ab chl ms czo zo ep ttn qtz $H_2O$
**11)** ab chl ms zo ep ttn qtz $H_2O$
**12)** ab chl ms bt zo ep ttn qtz wrk $H_2O$
**13)** ab chl ms bt ttn qtz rt hem $H_2O$
**14)** ab chl ms bt ep qtz rt $H_2O$
**15)** ab ilm chl ms bt qtz rt hem $H_2O$
**16)** ab chl bt cord qtz rt hem $H_2O$
**17)** ab ilm bt cord qtz rt hem $H_2O$
**18)** ab ilm bt cord qtz hem $H_2O$

**Figure V-16: Mineral abbreviations are from Kretz, 1983. A) Calculated P-T pseudosection for meta-rhyodacite sample (16STH19) with H2O saturation and total iron as $Fe^{2+}$ with Theriak-Domino program (de Capitani & Petrakakis, 2010, updated software v. 4 February 2017) and "tcdb55c2d" database (Holland & Powell, 1998, 2004; updated Nov. 2003). The rock composition, given as mol.% oxide. Fields are colored with respect to their variances, darker colours indicate higher-variance assemblages. The stability field written in bold correspond to the observed assemblage. B) Simplified representation of P-T pseudosection with the stability field in grey and the main geothermal gradient consistent with regional thermal regime (Manga *et al.*, 2012; Verati *et al.*, 2018; Favier *et al.*, 2019). C) P-X(H2O) equilibrium phase diagram calculated at 365°C with the same composition in Figure 18-A, performed between 0 (H = 0) and 100 moles (H = 100). The field colored in grey corresponds to the observed assemblage.**

seems a coherent estimation to remain consistent with both methods. In a second time a specific P-$XH_2O$ pseudosection (with $XH_2O$ representing the variability of amount of water in the considered system) was calculated in order to decipher the effect of the amount of $H_2O$, in the fluid present in excess, on the pressure estimates (Figure V-16-**C**). The observed mineral assemblage is stable for a large range of $XH_2O$ values, i.e. between 12% and 100%. Moreover, in this specific sample, the chemical components of the LOI were analysed in the SARM Laboratory in Nancy (see Table V-3). This kind of analysis allows an estimation of the components in the fluid phase with respect to the bulk-rock chemistry of the analysed sample. In the 16STH19 sample, the amount of $H_2O$, in the fluid phase, is estimated at around 59%, with a $CO_2$ content of about 27%. The result of our thermodynamic modeling is totally consistent with this estimation, and indicates that regardless of the $XH_2O$ value,

if it is greater than 12%, the observed mineral assemblage remains stable. However for the $XH_2O$ values of interest, and for a temperature of about 365°C, the possible pressure range is restricted between 0.95 and 1.15 kbar. Indeed, in such a chemical system, for pressures lower than 0.9 kbar wairakite, commonly described in various geothermal fields, will be systematically present in the mineral association.

Altogether, the combination of chlorite thermometry and thermodynamic modeling yields to maximal ranges of P-T conditions of 360-375°C and 0.90-1.40 kbar (i.e. Greenschist facies conditions) for the development of the observed high temperature mineral assemblage in the meta-rhyodacite from the most hydrothermalized area of Terre-de-Haut Island.

## V.2.8. Discussion

### *V.2.8.a. Relationship between deformation and hydrothermalism: implications for fluid transfer pathways*

In the present day situation we observed in the field a system of brittle faults and in a general cross-section of Terre-de-Haut Island (Figure V-17), the main hydrothermal zone is localized within a WNW-ESE graben compatible with the regional transtensional context as proposed by Feuillet *et al.* (**2001, 2002**) and Leclerc *et al.* (**2014**, **2016**).

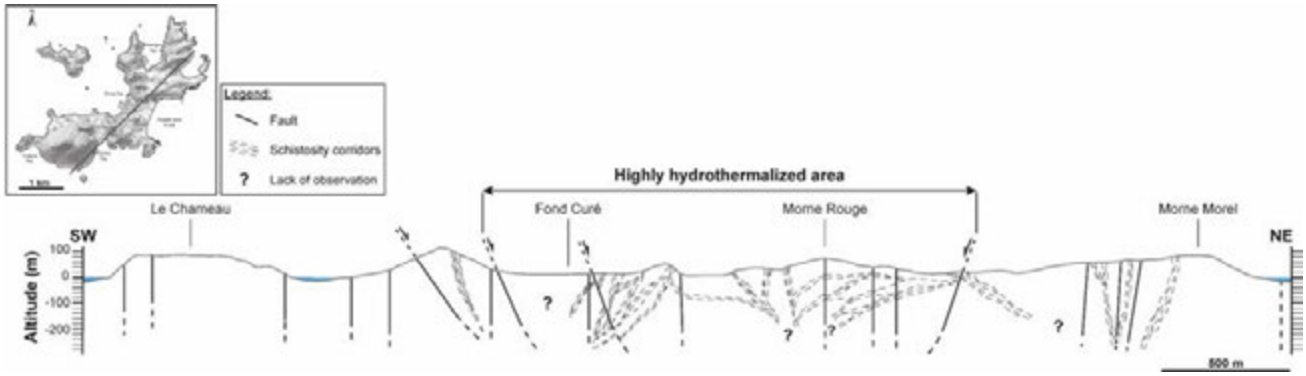


**Figure V-17: Cross-section NE-SW from Terre-de-Haut Island displaying brittle-ductile transition with faults network and schistosity planes, with the central part the highly hydrothermalized area in the WNW-ESE graben.**

However, the comparison between the structural and the mineralogical maps (Figure V-8 and Figure V-14) demonstrates that high-temperature hydrothermal phases are preferentially developed along the discontinuous and spaced cleavages concentrated in schistose corridors, indicating that their crystallization is contemporaneous with the development of such tectonic structures. As illustrated by the regional cross section (Figure V-17), brittle faults clearly crosscut the schistose corridors.

The observed schistosity planes being generated by pressure solution processes, the schistose corridors are markers of the circulation of high-temperature hydrothermal fluids. As shown in the detailed structural map (Figure V-8) and the regional cross-section (Figure V-17), these schistose domains show very specific geometries. In some cases, for example east of Fond Curé, schistose zones

tend to anastomose while in other domains, like west of Morne Rouge, sub-vertical schistose corridors clearly intersect other moderately dipping zones. However, and whatever the geometrical pattern is, in this hydrothermalized area, the primary volcanic structures are severely erased. In such a case we can propose, as a working hypothesis, that the poorly dipping schistosity planes developed at the expense of pre-existing, sub-horizontal, volcanic structures, particularly magmatic fluidality and lithological interfaces. Following this interpretation, the least dipping schistose corridors must be regarded as the result of tectonic reactivation of volcanic structures. On the other hand, the most dipping schistose corridors are neo-formed tectonic structures and they evolve, during progressive cooling of the studied area, from ductile to brittle structures. However, and whatever the mechanism of formation of schistose zones is, the observed finite structural pattern is particularly favourable to both vertical and lateral fluid transfers if the schistose zones are connected.

Through time, during the thermal evolution of the hydrothermal system, low-temperature hydrothermal phases continue to crystallize in schistose zones but also in fractures, veins and brittle faults. This means that during the cooling history of the hydrothermal system, tectonic structures continue to be preferential drains allowing the circulation of fluids. Moreover, in this specific area a recent study (Navelot *et al.*, **2018**) revealed also fluid transfers at the lithological interfaces between alternating lavas and debris flows. In these rocks, mineral transformations have a significant impact on their petrophysical properties, and the pyroclastic and debris flows are suitable horizons for storage and fluids flow.

*V.2.8.b. Terre-de-Haut hydrothermal domain: an exhumed paleo-geothermal system?*

A geothermal system represents a thermal anomaly, thus a significant deviation with respect to the regional standard conductive geothermal gradient. In the Guadeloupe archipelago, recent study (Manga *et al.*, **2012**) has revealed a steady-state conductive gradient between 69.3 ± 1.5 and 98.2 ± 8.8 °C/km. Furthermore, in the Basal Complex from Basse-Terre, thus in the most eroded piece of the active arc, arc-related metamorphism, dated between 4 and 2 Ma, has been recently evidenced, compatible with paleo-conductive geothermal gradient in the order of 70-100°C/km (Verati *et al.*, **2018**; Favier *et al.*, **2019**). Therefore, this type of conductive gradient remained stable during the last 4 Ma. In contrast to these regional standard values, in the Bouillante geothermal field, temperatures in the range of 230- 255°C are measured at depths between 475 m and 1.2 km (Sanjuan *et al.*, **2001**, **2004**; Guillou-Frottier, **2003**; Mas *et al.*, **2006**; Bouchot *et al.*, **2010**). In the highly hydrothermalized zone from Terre-de-Haut Island, we discovered the occurrence of high-temperature hydrothermal mineral parageneses that are stable under a temperature around 365 °C and very low-pressure conditions (Figure V-16**-A-C**). These conditions represent a significant thermal anomaly with respect to the regional standard geothermal gradient. Moreover, some of the observed mineral

associations as well as the microstructures of the reaction sites (i.e. progressive and/or complete replacement of pyroxenes by epidotes, chlorites, white micas, …) are similar to the ones described in hydrothermal rocks from the Bouillante well (Mas *et al.*, **2006**). But, the temperatures recorded by the Terre-de-Haut fossil hydrothermal system are higher than the temperatures proposed for the active Bouillante field. However, they are compatible with temperature ranges measured in drillings in different geothermal fields around the world (Browne, **1978**; Del Moro *et al.*, **1982**; Battaglia *et al.*, **1991**; White & Hedenquist, **1995**; Mas *et al.*, **2006**; Bogie *et al.*, **2008**; Bouchot & Genter, **2009**).

In addition to bearing the mineralogical traces of a strong thermal anomaly, the studied area is all the more comparable to a geothermal reservoir as it is a place of strong circulation of huge amount of hydrothermal fluids. These fluids are not exclusively composed with $H_2O$, but a minimal value of 12 moles of $H_2O$ in the fluids is necessary to produce the observed hydrothermal mineral assemblage (Figure V-16-**C**). High-temperature hydrothermal fluids circulation is effective enough to totally erase the primary volcanic structures, and as discussed in the previous section, tectonic structures constitute efficient drains for hydrothermal fluids circulation. All together, these data support the idea that the Terre-de-Haut hydrothermal domain constitutes an eroded, and thus exhumed, paleo-geothermal system. The latter can be used as an analogue of the deepest parts of active geothermal systems in the Lesser Antilles volcanic arc and can therefore serve to better constrain their operation modes.

*V.2.8.c. A conceptual scheme for deep parts of high-energy geothermal reservoirs in Guadeloupe archipelago*

The calculated P-T conditions for high-temperature hydrothermal mineral associations must be combined with the values of rhyodacites density in order to restore the depth of the Terre-de-Haut paleo-reservoir. For fresh rhyodacites, the dry bulk density is around 2.2 – 2.3 $kg/m^3.10^{-3}$ (Klein & Johnson, **1983**, for example), but in the Terre-de-Haut paleo-reservoir, the densities of hydrothermalized volcanic rocks were recently measured around 1.9 $kg/m^3.10^{-3}$ (Navelot *et al.*, **2018**), in agreement with the significant development of secondary micas and chlorite bearing assemblages in the meta-volcanites. Using this density value, the Terre-de Haut paleo-reservoir was located, 3 or 2 Ma ago (i.e. during the island volcanic activity, Zami *et al.*, **2014**), at a depth between 1.7 and 2.7 km. The timescale for exhumation of this paleo-reservoir is therefore consistent with erosion rates proposed for Guadeloupe archipelago (Sak *et al.*, **2010**; Lloret *et al.*, **2011**; Rad *et al.*, **2013s**; Ricci *et al.*, **2015a**, **b**).

With a standard conductive gradient in the order of 70-100°C/km which is stable since 4 Ma (Manga *et al.*, **2012**; Verati *et al.*, **2018**; Favier *et al.*, **2019**), the depth of the paleo brittle-ductile transition, in the Guadeloupe island arc crust, must be fixed at shallow crustal depths, around at 4-5 km. This value is consistent with the conditions recognized for example in the Tuscany magmatic arc in Italy

where the Larderello geothermal field is located (Bellani *et al.*, **2004**; Ranalli & Rybach, **2005**). In such a thermal context, brittle faults have to be progressively relayed by schistose corridors and rooted on the brittle-ductile transition horizon, as proposed by Ranalli and Rybach (**2005**). However, near Les Saintes archipelago, crustal seismicity is well documented with earthquakes hypocenters localized at minimal depths of 8 -12 km (Bazin *et al.*, **2010**, with references therein) indicating brittle behaviour of the arc crust. This apparent contradiction may result from a heterogeneous distribution of the heat flow at the arc scale or more likely from the difference in rheology that exists between the upper part of the arc crust, composed of a 5 to 8 km thick horizon of sediments and subduction related differentiated calc-alkaline volcanic rocks and the lowermost part of the Caribbean crust constituted by an old, Aptian-Albian, rigid oceanic plateau, rich in ultra-mafic rocks and thus subjected to brittle behaviour even at deeper crustal depths (Mauffret & Leroy, **1997**; Pindell & Barrett, **1997**; Kopp *et al.*, **2011**; Gailler *et al.*, **2013**).

In our conceptual scheme of geothermal reservoir (Figure V-18), with concentration of high-temperature hydrothermal fluid flows, the conductive high geothermal gradient, efficient only in the first few hundred meters, is relayed by a convective system up to a depth of at least 1 kilometre as demonstrated in the Bouillante geothermal field (Guillou-Frottier, **2003**). Close to the surface, on the upper part of the reservoir, the volcanic structures (lithological interfaces, fluidality, prismation) and the variations in petrophysical rock properties are important components of the fluid flow process (see discussion in Navelot *et al.*, **2018**). Faults also contribute to fluid-flow through the recharge of supergene fluids (meteoric water and seawater, Millot *et al.*, **2010**) in the geothermal system and leading the development of convective cells in the range of 500 m and 1 km. In addition, it is now necessary to consider that, in the lowermost domain of the reservoir, at depth near 2 kilometres, anastomosed schistose corridors become efficient drains for both vertical and lateral fluid circulations. In such a case, the nature and the spatial distribution of high-temperature hydrothermal mineral associations can be used to define the geometry and the critical volume of the deep parts of potential geothermal reservoirs in volcanic active arcs.

In the proposed conceptual scheme (Figure V-18), we restore the location of the Terre-de-Haut geothermal paleo-reservoir on the base of the calculated P-T conditions for hydrothermal peak. The primary volcanic structures are represented only in the uppermost part of the model because at 2 km depth they are erased and /or transposed by hydrothermally leaded tectonic and metamorphic transformations.

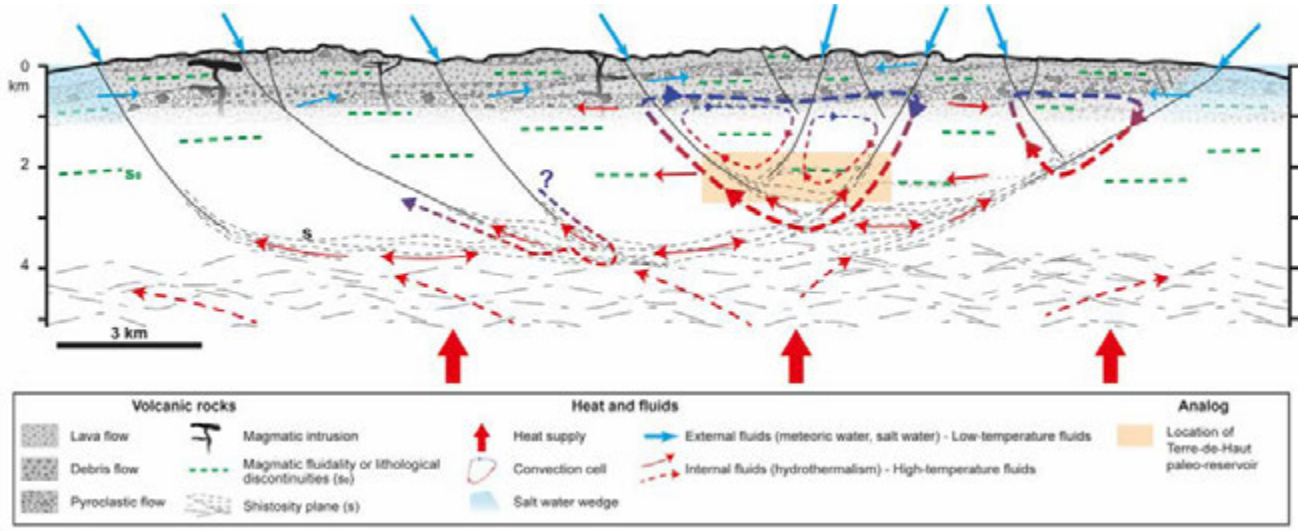


**Figure V-18: Conceptual model for volcanic arc related geothermal reservoir in the Guadeloupe island arc. This north-south cross section displays the plumbing system of a geothermal reservoir, from the surface to the deeper parts, with the different fluid flow contributions. The brittle/ductile transition is represented as a sub-horizontal horizon acting as a shear zone. The geometry of faults and schistose zones pattern is purely indicative. The geological formations are only illustrated schematically over the first kilometer of the cross-section.**

### V.2.9. Conclusions

1- We document and describe for the first time in Terre-de-Haut Island (Les Saintes volcanic archipelago) the occurrence of ductile deformation, i.e. schistose corridors generated by pressure solution processes, coeval with the development of high temperature hydrothermal mineral associations.

2- Using conventional thermometry and thermodynamic modelling we demonstrate that the hydrothermal system of Terre-de-Haut Island developed under Greenschist facies conditions at depths in the range of 1.7 – 2.7 kilometres.

3- The link between mineral transformations and ductile deformation suggest the occurrence of both vertical and lateral fluids and heat transfers in the crust of the studied volcanic arc.

4- Together with previous available structural, mineralogical and petrophysical data, this study clearly establishes that highly hydrothermalized area of Terre-de-Haut Island corresponds to an eroded and exhumed geothermal paleo-reservoir.

5- The temperatures of the geothermal system are higher in Terre-de-Haut than in the active Bouillante field. It is thus a key analogue for understanding the deepest parts of current active geothermal systems in the Lesser Antilles volcanic arc.

### V.2.10. Supplementary data

*Documents disponibles dans le chapitre Annexe de ce manuscrit* (Article 3 - Supplementary data).

### V.2.11. Acknowledgment

This paper is a contribution to the GEOTREF program, funded by French government with the program of "Investissements d'Avenir" and tutored by ADEME. We thank the researchers from the GEOTREF consortium for discussions during the fieldwork campaigns in Guadeloupe and during scientific meetings. The authors thank Gabriel Monge for his welcome to CEMEF laboratory for the use of the X-ray Diffraction device.

# Chapitre VI : Datation des systèmes hydrothermaux

*Fumerolles de la Soufrière*

# Chapitre VI

## VI.1. Préambule

Déterminer l'âge et la durée de vie des systèmes hydrothermaux, et donc potentiellement géothermaux, est un enjeu important à la fois scientifique et méthodologique. Il n'existe que peu d'études géochronologiques publiées sur ce type de systèmes, bien que dans les années 2000 des efforts importants aient été consacrés à cet enjeu (Grimes *et al.*, **1998**; Dalrymple *et al.*, **1999**; Arehart *et al.*, **2002**; Brockamp *et al.*, **2003**; Villa *et al.*, **2006**; Wilson *et al.*, **2008**; Oliveros *et al.*, **2008**; Hames *et al.*, **2009**; Márton *et al.*, **2010**; Verati *et al.*, **2014**; Oze *et al.*, **2017**).

En Guadeloupe, seule la brèche de Bouillante a fait l'objet d'une étude géochronologique récente par la méthode $^{40}Ar/^{39}Ar$ sur des adulaires (Verati *et al.*, **2014**). Un âge de 248,2 ± 50,2 ka a ainsi été obtenu pour cette brèche géothermale. Cet âge, qui converge avec celui du fonctionnement du système volcanique actif de la Grande-Découverte-Soufrière, et non pas avec l'âge connu pour la « chaine volcanique » de Bouillante appartenant à la Chaîne Axiale, pose alors la question de l'origine de la ressource géothermale à Bouillante.

Dans le cadre de ce travail de thèse, nous avons cherché à déterminer :

- L'âge et la durée du fonctionnement du paléo-réservoir géothermal exhumé identifié à Terre-de-Haut (Les Saintes). Pour cela il a fallu identifier des minéraux hydrothermaux susceptibles d'être datés. Ces résultats sont présentés sous la forme d'un article préparé en vue d'être soumis au journal *Chemical Geology* dans la première partie de ce chapitre. La présentation de cet article est suivie d'une courte discussion sur des perspectives qui pourraient permettre de mieux contraindre la durée de vie du système géothermal fossile de Terre-de-Haut ;
- L'âge des brèches hydrothermales identifiées au sein de la zone du PER du projet GEOTREF, et plus spécifiquement à Rocroy sur l'île de la Basse-Terre. Ces résultats sont présentés dans la seconde partie de ce chapitre.

## VI.2. Article 4 – $^{40}Ar/^{39}Ar$ dating of high enthalpy geothermal systems: first attempt from meta-pyroxenes of Les Saintes archipelago (Lesser Antilles arc, Guadeloupe)

Alexiane Favier[1-2], Chrystele Verati[2], Jean-Marc Lardeaux[2-3], Philippe Münch[4] and Christophe Renac[2]

1: UMR 5243 Géosciences Montpellier, Université des Antilles-CNRS-Université de Montpellier

2: UMR 7329 Geoazur, Université de Nice Sophia Antipolis-CNRS

3: Czech Geological Survey, Centre for Lithospheric Research

4: UMR 5243 Géosciences Montpellier, Université de Montpellier-CNRS-Université des Antilles

# Datation des systèmes hydrothermaux

Il s'agit d'un article méthodologique qui présente la possibilité de dater une phase hydrothermale potassique de haute-température, ici le mica blanc, observée au sein de pseudomorphoses de méta-pyroxènes par la méthode $^{40}Ar/^{39}Ar$.

Principaux résultats présentés dans cet article :

- L'établissement d'un protocole d'identification, de séparation et d'isolation d'une phase minérale potassique au sein d'une structure réactionnelle multi-phasée, et donc complexe, observée dans des méta-pyroxènes. Cette approche nécessite de combiner à la microscopie optique l'analyse des phases à la microsonde électronique et par diffraction des rayons X. Les séparations des mono-grains identifiés sont des processus longs qui impliquent des séparations magnétiques des phases dans différentes fractions de tailles de grains, des lavages succesifs dans des bains d'eau distillée et souvent sous ultrasons, et enfin la séparation manuelle finale de la phase choisie sous la loupe binoculaire. Nous présentons ainsi le premier essai de datation de méta-pyroxènes hydrothermaux par la méthode $^{40}Ar$-$^{39}Ar$ ;
- L'âge du fonctionnement à haute température du paléo-réservoir géothermal exhumé identifié à Terre-de-Haut (Les Saintes) est de 2,59 ± 0,12 Ma. Cet âge est cohérent avec les données géochronologiques disponibles sur le système volcanique de l'île de Terre-de-Haut, qui était actif entre -3 et -2 Ma.
- La confrontation entre l'âge de l'hydrothermalisme de haute-température et les âges des dômes volcaniques, non hydrothermalisés et intrusifs dans la zone hydrothermale, permet d'évaluer la durée maximale de fonctionnement du paléo-réservoir géothermal de Terre-de-Haut à 650 ka. Ce résultat est en accord avec les quelques données déjà publiées sur ce sujet et qui proposent des durées de vie comprises entre quelques centaines de milliers d'années et un million d'années pour les systèmes géothermaux.

Keywords: $^{40}Ar/^{39}Ar$ dating, geothermal system, Greenschist facies, sub-Greenschist facies, meta-pyroxene, white mica, muscovite, illite

### VI.2.1. Abstract

In this study, we investigate the potential of absolute dating of neoformed minerals developed, in geothermal system, under Greenschist facies conditions in volcanic arc context. The $^{40}Ar/^{39}Ar$ method is theoretically appropriate considering the common development of secondary K-bearing minerals in such P-T conditions. Our investigations concern white micas replacing pyroxene single grains within a meta-rhyodacite from a geothermal paleo-reservoir of Terre-de-Haut, Les Saintes archipelago (Lesser Antilles). After implementation of a specific separating protocol, and prior to Ar-

Ar dating, we analyzed the precise mineral assemblage within the transformed meta-pyroxene for two fractions sizes 315-500 µm and 160-315 µm, respectively. Thin section observations, electron microprobe and X-Ray diffraction analyses allows us to identify potassic-free phases (smectite, chlorite, feldspar) but also mixing of K-bearing phases like muscovite, illite, illite/smectites. The two fractions of meta-pyroxene display different Ar-Ar results. We demonstrate that crystallinity of K-bearing phases and the type of illite minerals play an important role in the Ar-Ar data interpretations. The 315-500 µm fraction, with higher muscovite crystallinity and without illite/smectite species, displays a well-defined Ar/Ar plateau age of 2.59 ± 0.12 Ma, interpreted as the best estimate of high temperature fluid circulation in the paleo-reservoir under Greenschist facies P-T conditions. Considering the available time constraints for volcanic activity in Terre-de-Haut Island, we propose a maximal lifetime of 650 ka for this paleo-reservoir. The 160-315 µm fraction, with least white mica crystallinity and detected illite/smectites, do not provide accurate Ar-Ar plateau age, likely due both to $^{39}$Ar recoil effect and high temperature system cooling to sub-greenschist facies conditions (< 200°C). Furthermore, using a theoretical model, we demonstrate that the substitution of muscovite by illite during the paleo-reservoir cooling can affect the K-Ar and thus the Ar-Ar ages only when the illite age is really younger than muscovite (very slow cooling) and/or the illitization is highly developed.

### VI.2.2. Introduction

Tectonic settings favorable for high enthalpy geothermal energy are mainly located in areas of emerged active volcanism, i.e. subduction, hotspot and rift zones (Arnórsson, **1995**; Bibby *et al.*, **1995**; Sasada *et al.*, **2000**; Ragnarsson, **2015**; Bertani, **2016**; Barcelona *et al.*, **2019**). Although many studies explore structural, mineralogical, geochemical and geophysical characteristics to better constrain the three-dimensional geometry of the plumbing system of active geothermal reservoirs, very few data are available on the duration of the geothermal activity in active (Grimes *et al.*, **1998**; Dalrymple *et al.*, **1999**; Arehart *et al.*, **2002**; Villa *et al.*, **2006**; Wilson *et al.*, **2008**; Verati *et al.*, **2014**; Oze *et al.*, **2017**), or in fossil geothermal systems (Brockamp *et al.*, **2003**; Oliveros *et al.*, **2008**; Hames *et al.*, **2009**; Márton *et al.*, **2010**). Indeed, very few minerals are available for geochronology at low-degree metamorphism and/or hydrothermalism, i.e. Zeolite, sub-Greenschist and Greenschist facies conditions. As far as the $^{40}$Ar/$^{39}$Ar technique is concerned, most analyses attempted so far have been carried out on sericite, adularia, alunite, celadonite and clay minerals (Dong *et al.*, **1995**; WoldeGabriel *et al.*, **1996**; Hall *et al.*, **1997**; Haines & van der Pluijm, **2008**; Oliveros *et al.*, **2008**; Clauer *et al.*, **2012**; Clauer, **2013**; Verati & Jourdan, **2014**; Verati *et al.*, **2014**; Oze *et al.*, **2017**). Unfortunately, K-bearing zeolites usually display very low retentivity of argon making this mineral difficult to date. K-rich clays could be used as dateable minerals, nevertheless $^{40}$Ar/$^{39}$Ar dating

requires encapsulation to prevent 39Ar recoil loss occurring during neutron irradiation, making the step-heating approach often inappropriate (Clauer, **2013**). Although adularia and sericite are considered suitable minerals for Ar-Ar method under low temperature metamorphism (Verati & Jourdan, **2014**; Verati *et al.*, **2014**; Oze *et al.*, **2017**), we need to find more dateable minerals for such geological conditions.

Our study consists to investigate the potentiality of the $^{40}Ar$-$^{39}Ar$ systematics on recently identified metamorphic K-bearing minerals from a fossil geothermal reservoir located in the Lesser Antilles arc. These K-rich phases were developed at the expense of volcanic pyroxenes during hydrothermal fluid circulations, under estimated P-T conditions of 360-380°C and 0.9-1.4 kbar, leading the development of the assemblage albite + chlorite + muscovite + biotite + clinozoisite + epidote + titanite + quartz at the rock sample scale (Favier et al., *submitted*). This study focuses on the identification the K-bearing phases present only in meta-pyroxenes, in order to consider how the Ar-Ar method can be appropriately applied. Dating the crystallization of these minerals can constrain the age and the duration of geothermal systems in subduction-related magmatic arc context.

### VI.2.3. Geological setting and previous mineralogical investigations

In the active Lesser Antilles arc, Les Saintes archipelago represents small volcanic islands (from the biggest to the smallest ones respectively: Terre-de-Bas, Terre-de-Haut, and their islets: Îlet à Cabris, Grand îlet and Îlet la Coche; Figure VI-1). These islands, in the framework of the Guadeloupe archipelago, are related to the recent active volcanic arc emplaced since 4.3 Ma (Bouysse, **1979**; Jacques *et al.*, **1984**; Bouysse & Westercamp, **1990**; Zami *et al.*, **2014**; Favier *et al.*, **2019**). Les Saintes Islands consist of typical calc-alkaline volcanic rocks, with ages ranging from 2.98 ± 0.04 Ma to 2.00 ± 0.03 for Terre-de-Haut Island, and less than 1 Ma for Terre- de- Bas Island (Zami *et al.*, **2014**). Volcanic formations correspond to rhyodacitic to andesitic domes, lava flows, and many debris flows (Figure VI-1).

In the island of Terre-de-Haut a highly hydrothermalized area (Figure VI-1) is well known since first petrographic and structural descriptions of Jacques and Maury (**1988**) and Verati et al. (**2016**) respectively. Last three years, several studies (Verati *et al.*, **2016**; Favier *et al.*, **2017**; Navelot *et al.*, **2018**; Beauchamps *et al.*, **2019**; Favier et al., *submitted*) have identified this hydrothermal system as an eroded and exhumed geothermal reservoir. The penetrating hydrothermal alteration prevents from easily identification of primary volcanic mineralogy (pyroxene, feldspar and glass), and thus from volcanic ages using common K-Ar and Ar-Ar methods. Nevertheless, related secondary K-bearing minerals were identified in transformed pyroxenes (i.e. meta-pyroxenes) from Terre-de-Haut Island (Favier et al., *submitted*), suggesting that geochronological K-Ar and/or Ar-Ar methods may be applied here to date low temperature events under sub-Greenschist to Greenschist facies

conditions (<380 °C) frequently recognized in high enthalpy geothermal systems (Henley & Ellis, **1983**; White & Hedenquist, **1990**; Groves *et al.*, **1998**; Goldfarb *et al.*, **2001**).

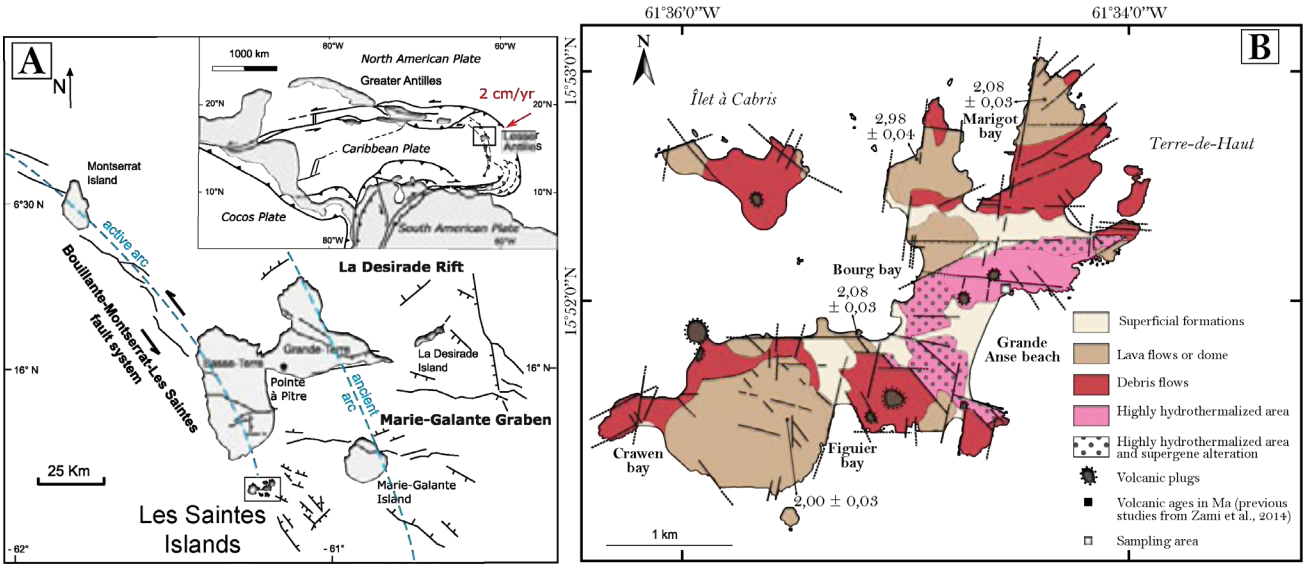


**Figure VI-1: A) Location of the Lesser Antilles arc system and Les Saintes archipelago (modified after Bouysse & Westercamp, 1990). Les Saintes Islands are located in the inner active arc since ca. 4.3 Ma (Bouysse, 1979; Jacques *et al.*, 1984; Bouysse & Westercamp, 1990; Zami *et al.*, 2014). B) Detailed map of volcanic formations in Les Saintes archipelago (i.e. Terre-de-Haut and Ilet à Cabris; Terre-de-Bas is not shown). Volcanic K-Ar ages from Zami *et al.*, 2014 are reported. Analyzed sample location is shown in the highly hydrothermalized area already identified by previous studies (Verati *et al.*, 2016; Navelot *et al.*, 2018; Favier et al., *submitted*).**

### VI.2.4.Materials and Methods

After recovering 35 samples in the field in the highly hydrothermalized area (Figure VI-2) of Terre-de-Haut Island, and subsequent preliminary observations in thin sections, we selected a meta-rhyodacite (16STH19) not affected by supergene alteration and containing meta-pyroxene crystals developed enough to perform mineralogical and geochronological investigations. After crushing the rock, we selected two different size fractions, i.e. 160-315 µm and 315-500 µm representing apparent meta-pyroxene size distribution in thin sections. A series of magnetic separation (Frantz separator) allow to remove sulphide and oxide crystals and to concentrate meta-pyroxenes in the less magnetic aliquot. The two different size fractions were repeatedly cleaned with an ultrasonic bath in distilled water. Further, air-dried grains with like-pyroxene shape and whitish colour were handpicked under a binocular microscope (Figure VI-3**-A-B**). To characterize precisely the mineralogy of these meta-pyroxenes we used appropriate X-Ray diffraction and electron microprobe methods.

**Figure VI-2: Outcrop of the sampled area showing intense rock transformations. Primary volcanic formations (i.e. lava and/or debris flows) cannot be recognized anymore.**

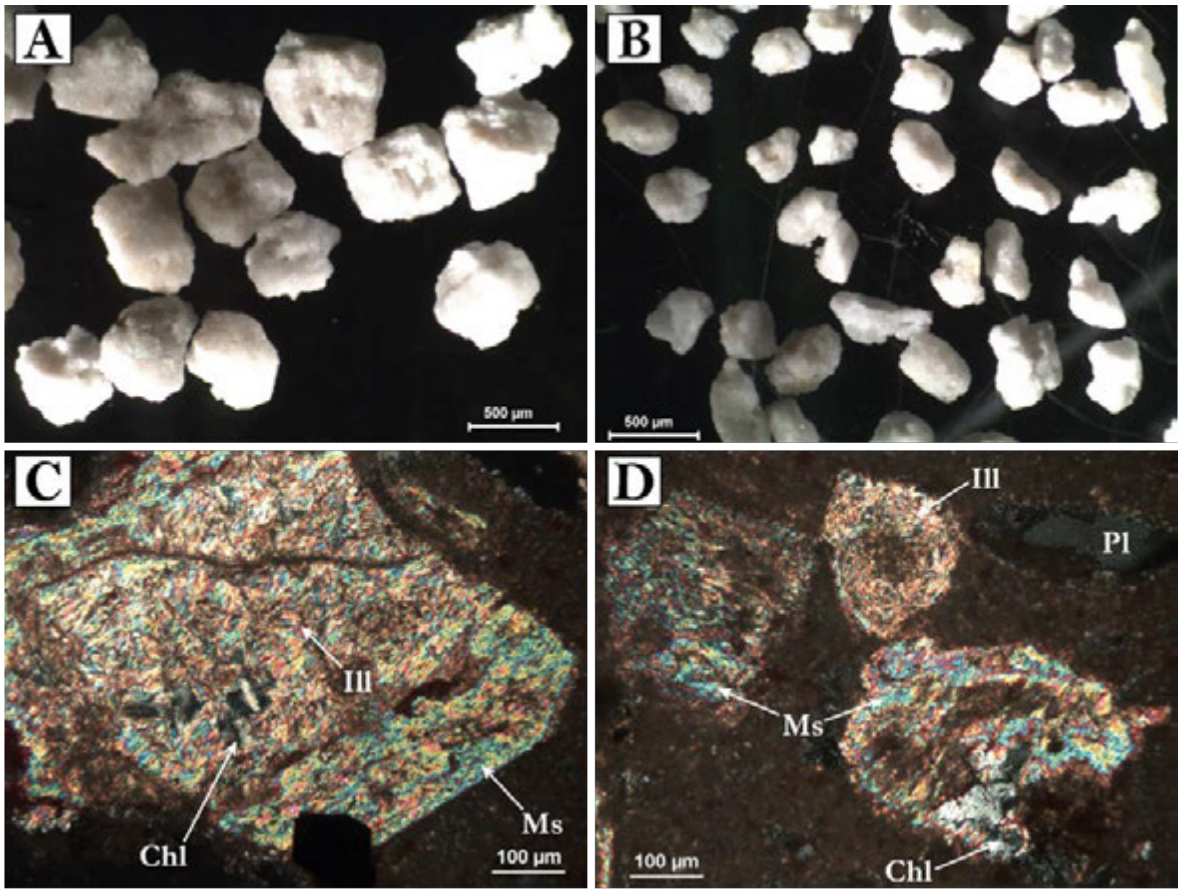


**Figure VI-3: Photographs of the grains used. A & B) Selected meta-pyroxene grains for 315-500 µm and 160-315 µm fraction respectively, after magnetic separation, HNO3 leaching and handpicking. C & D) : Cross-polarized photomicrographs of (C) a 315-500 µm grain and (D) several 160-315 µm grains. Ms = muscovite; Chl = chlorite; Ill = supposed illites in the indeterminate microcrystalline mixing; Pl = plagioclase.**

*VI.2.4.a. Electron microprobe analysis*

Electron Probe Micro-chemical Analysis (EPMA), using a CAMECA SX-100 electron microprobe at the "Service Commun de Microsonde" of Montpellier University, were performed on 16STH19 sample thin sections, to identify precisely the different minerals within the meta-pyroxenes. The operating conditions were a 20 kV accelerating voltage and 10 nA beam current.

*VI.2.4.b. X-ray diffraction method*

*Sample preparation*

An aliquot for the two different fractions of whitish grains (160-315 and 315-500 µm) was crushed to a fine powder (<70 µm) and was analysed by X-ray Diffraction (XRD) at CEMEF laboratory (Ecole des Mines in Sophia-Antipolis Scientific Center, France).

Secondly, in order to characterize fine phyllosilicates recognized in thin sections, we soak for 4 days whitish grains in a $CaCl_2$ solution (250 $g.l^{-1}$) to saturate interlayer spacing of clay minerals with Ca. Later, the mixture of grains and $CaCl_2$ was rinsed with demineralized water up to an electrical conductivity of 40 $\mu S.cm^{-1}$, and centrifuged to recover the dispersed particles in water. The fine-particles (<2 µm) were collected for phyllosilicate identification and deposited on a silica glass wafer. X-ray Diffraction (XRD) analyses were performed on these <2 µm samples at the same CEMEF laboratory. We used the X-ray diffractometer (Panalytical X'pert Pro) equipped with a PIXcel detector ($CuK_{\alpha 1+2}$, counting step 0.06°2θ, and 2.7 second per step). Diffraction patterns of powder (<70 µm) go from 3.5 to 75° 2θ, while the <2 µm size fractions were analysed from 2 to 35°.

The <2 µm phyllosilicate fractions were analysed under air-dried (AD) with 45% of relative humidity and with liquid ethylene glycol (EG) to identify smectites from other minerals (chlorite or illite).

*Decomposition of XRD patterns for <2µm samples*

A preliminary decomposition of AD and EG XRD patterns was performed using the Fityk 1.5 peak fitting software (Wojdyr, **2010**). The background was subtracted using the XRD pattern of the silica-glass wafer. The resulting pattern was fitted with Gaussian elementary curves optimized with the Levenburg-Marquardt algorithm. The different XRD patterns (AD and EG) were decomposed on bands of illite (001), mica (001), chlorite (002), EG-smectite (001) according to Lanson (**1997**). The Full Width at Half Maximum (FWHM) were used to described crystallinity or crystal ordering of phyllosilicates, with Kubler (micaceous phases, see below, Kübler, **1967**) and Arkai (chlorite, Árkai, **1991**) indexes. Further in the text, 10Å (001) peak with a FWHM lower than 0.17 will be described as muscovite, between 0.17 and 0.27 as illite-muscovite, between 0.27 and 0.53 as illite and higher than 0.53 as illite-smectite (Warr & Cox, **2016**). The relative proportions of phyllosilicates were estimated both on the surface and FWHM of decomposed peaks in EG patterns for (001).

*X-ray profile modelling method for <2µm samples*

XRD patterns (AD and EG) of <2 µm samples extracted from the two size- fractions (160-315 and 315-500 µm) were deconvoluted with the PyXRD Linux software developed by Dumon and van Ranst (**2016**). This program provides a graphic user interface to simultaneously compare oriented pattern (AD and EG) and calculated XRD profiles. The calculated XRD profiles represent the sum of mineral contributions with the number, nature (muscovite/illite, chlorite, smectite and interlayered illite/smectite), proportion and stacking sequences of the different layer types. The quality of the fit was estimated with the unweighted R parameter (Howard & Preston, **1989**). Finally, the distributions of coherent scattering domain sizes (CSDSs) were assumed to be lognormal and characterized by their mean value (Drits *et al.*, **1997**).

*VI.2.4.c. Ar-Ar dating*

Around 500 white grains of meta-pyroxene (Figure VI-3**-A-B**) were handpicked under a binocular microscope for each fraction (160-315 µm and 315-500 µm) and subsequently leached with hot $HNO_3$ (1N, 70°C) for a few hours to avoid residual oxide or sulphide inclusions. They were rinsed in distilled water and methanol and dried (<50°C). Selected grains were packed in aluminum foils for irradiation in the core of the Triga Mark II nuclear reactor of Pavia (Italia) with several aliquots of sanidine from the Taylor Creek Rhyolite standard (28.619 ± 0.034 Ma; Renne *et al.*, **2010**) as flux monitor. Argon isotopic interferences on K and Ca were determined by irradiation of KF and $CaF_2$ pure salts from which the following correction factors were obtained: $(^{40}Ar/^{39}Ar)_K = 9{,}69 \times 10^{-3} \pm 3.6 \times 10^{-5}$ at 1σ, $(^{38}Ar/^{39}Ar)_K = 1{,}297 \times 10^{-2} \pm 4.5 \times 10^{-4}$ at 1σ, $(^{39}Ar/^{37}Ar)_{Ca} = 7.27 \times 10^{-4} \pm 4.0 \times 10^{-5}$ at 1σ, and $(^{36}Ar/^{37}Ar)_{Ca} = 2.88 \times 10^{-4} \pm 1.6 \times 10^{-5}$ at 1σ. $^{40}Ar/^{39}Ar$ step heating analyses were performed at Geosciences Montpellier (France). We analysed four aliquots of bulk sample for the 315-500 µm fraction, and two aliquots for 160-315 µm. The gas extraction and purification line consists of: (a) an IR-CO2 laser of 100 kHz used at 3–20% power to heat samples during 180 s, (b) a lenses system for beam focusing, (c) a steel chamber, maintained at $10^{-8}$–$10^{-9}$ bar, with a copper holder in which 2 mm-diameter blind holes were milled, (d) two ZrAl getters for purification of gases. Argon isotopes were measured in static mode using an ARGUS VI mass spectrometer from Thermo-Fischer. Measurements were carried out in multi-collection mode using Faraday cups. Regularly analyzing air pipette volumes monitored the mass discrimination. The raw data of each step and blanks were processed, and ages were calculated using the ArArCALC software (Koppers, **2002**). Blanks were monitored after every three samples analyses. All parameters and relative abundance values for each experiment are provided in online supplementary data (file Ar/Ar experiments). They have been corrected for blanks, mass discrimination, and radioactive decay. Atmospheric $^{40}Ar$ was estimated using a value of the initial $^{40}Ar/^{36}Ar$ of 298.56 (Lee *et al.*, **2006**). Our criteria for the determination

of a plateau are as follows: a plateau must include at least 60% of released $^{39}Ar$, over a minimum of three consecutive steps agreeing at 95% confidence level. Plateau ages are given at the $2\sigma$ error level, and the plateau age uncertainties include analytical and J-value errors.

### VI.2.5. Results

*VI.2.5.a. Thin section observations*

In thin section (Figure VI-3**-C-D**), volcanic pyroxene is replaced by flaky material similar to white micas (muscovite), especially for the 315-500 µm grain size (Figure VI-3**-C**). Smaller patches of flaky particles suggest the occurrence of chlorite and illite with different size. In the two size fractions, a microcrystalline mixing of muscovite+illite+chlorite is present. Epidote and titanite were recognized in flaky particles or thin patches surrounding the pseudomorphosed pyroxenes. While muscovite patches are well developed in the 315-500 µm grain size, the smallest fraction displays less well-developed white micas (Figure VI-3**-C-D**).

*VI.2.5.b. Electron microprobe results*

The large flakes of white micas, chlorite and the smaller microcrystalline aggregates (see section VI.2.5.a) were analyzed for major element composition (online supplementary data, Table X-6), without considering the analyzed grain size. The structural formulae of minerals were calculated relative to a structure containing 11 oxygen atoms (muscovite, illite, illite/smectite) or 14 oxygen atoms (chlorite), assuming that the total iron content was composed of $Fe^{3+}$. In the $MR^3$-$2R^3$-$3R^2$ diagram (Figure VI-4), chlorite and white micas compositions are closed to pure chlorite (sudoite to donbassite types, (Wiewióra & Weiss, **1990**) and muscovite end-members respectively, while the microcrystalline mixing ranging between muscovite and chlorite compositions is compatible with the illite and illite/smectite domains (Figure VI-4).

*VI.2.5.c. XRD patterns decomposition and results*

X-ray diffraction analyses of bulk meta-pyroxene grains in the 160-315 and 315-500 grain sizes (<70 µm fraction and $3.5° < 2\theta < 75°$ range) consist of quartz, feldspar, illite-muscovite and chlorite, with no XRD peak of pyroxene. Minerals identification was established using Match! software (online supplementary data –Figure X-1). The FWHM of the quartz and feldspar vary from 0.12 to 0.18, suggesting that these phases are well crystallized. The mica (and chlorite) peaks are well expressed at low angle (2 to 20°), but are overlapped by feldspar and quartz, preventing the identification of mica polytype (1M, 2M, including 2M1 and 2M2, or 3T type).

X-ray patterns of the <2 µm fine-particle samples (oriented AD and EG) allow to identify less abundant and small particles roughly recognized in thin sections (315-500 µm in Figure VI-5**-A** and 160-315 µm in Figure VI-5**-D**), i.e. chlorite, smectite, mica, mica-illite and illite/smectite species. The

identified relative assemblages for the two meta-pyroxene fraction sizes are reported in Table VI-1. In decreasing order of significant abundances (Table VI-1 and in Table X-7), we record for the 315-500 µm fraction (Figure VI-5-**B**), (1) pure illite/muscovite with well- crystallized muscovite (small Kübler index of 0.12 for 001 mica and 0.53 for 001 illite), (2) pure smectite, (3) interstratified chlorite-smectite (Figure VI-5-**C**), (4) pure chlorite (0.34 with Arkai index), and (5) feldspar. For the 160-315 µm fraction (Figure VI-5-**E**), we distinguish (1) pure illite/muscovite (with Kübler index of 0.16 for 001 mica suggesting less well-crystallized muscovite than the bigger fraction; with 0.52 for 001 illite), (2) pure smectite, (3) interstratified illite-smectite (smectite-rich) species (Figure VI-5-**F**), (4) pure chlorite (Arkai index of 0.41), and (5) feldspar.

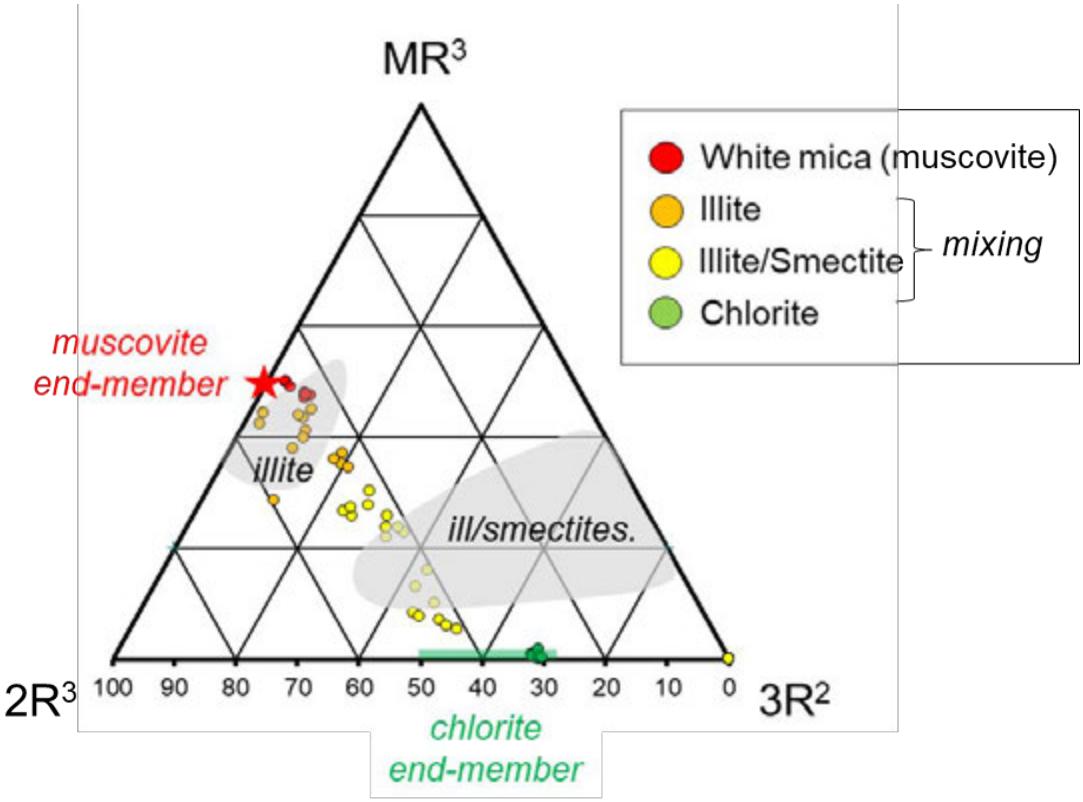


**Figure VI-4: $MR^3$-$2R^3$-$3R^2$ diagram (Velde, 1985) where are reported the electron microprobe results. In thin section, well-distinct muscovite and chlorite patches are near pure end-members. The numerous analyses on the undefined microcrystalline mixing indicate a more heterogeneous composition in the illite and illite/smectite domains. Data are reported in online supplementary data (EPMA data – Table X-6).**

**Table VI-1: Results of <2 µm mineral assemblages for the two meta-pyroxene fractions using AD state. Ãrkaï and Kübler index are also reported for detected chlorite, illite and white mica. Estimation of related Tmin values for illite and white mica are determined after Warr and Cox, 2016. Chl = chlorite, Fsp = feldspar, Ill = illite, I-S = illite-smectite interstratified, Musc = muscovite, Sm = smectite.**

| Sample | Ãrkai index | Kübler index | | Tmin values [001 illite] | Tmin values [001 mica] | <2µm assemblage |
|---|---|---|---|---|---|---|
| | 002 chlorite | 001 illite | 001 mica | (Warr and Cox, 2016) | (Warr and Cox, 2016) | |
| **16STH19-1_AD 315-500 µm** | 0.34 | 0.53 | 0.12 | >200°C | >350°C | Ill-Musc, Sm, Chl-Sm, Chl, Fsp |
| **16STH19-1_AD 160-315 µm** | 0.41 | 0.52 | 0.16 | >200°C | >300°C | Ill-Musc, Sm, I-S, Chl, Fsp |

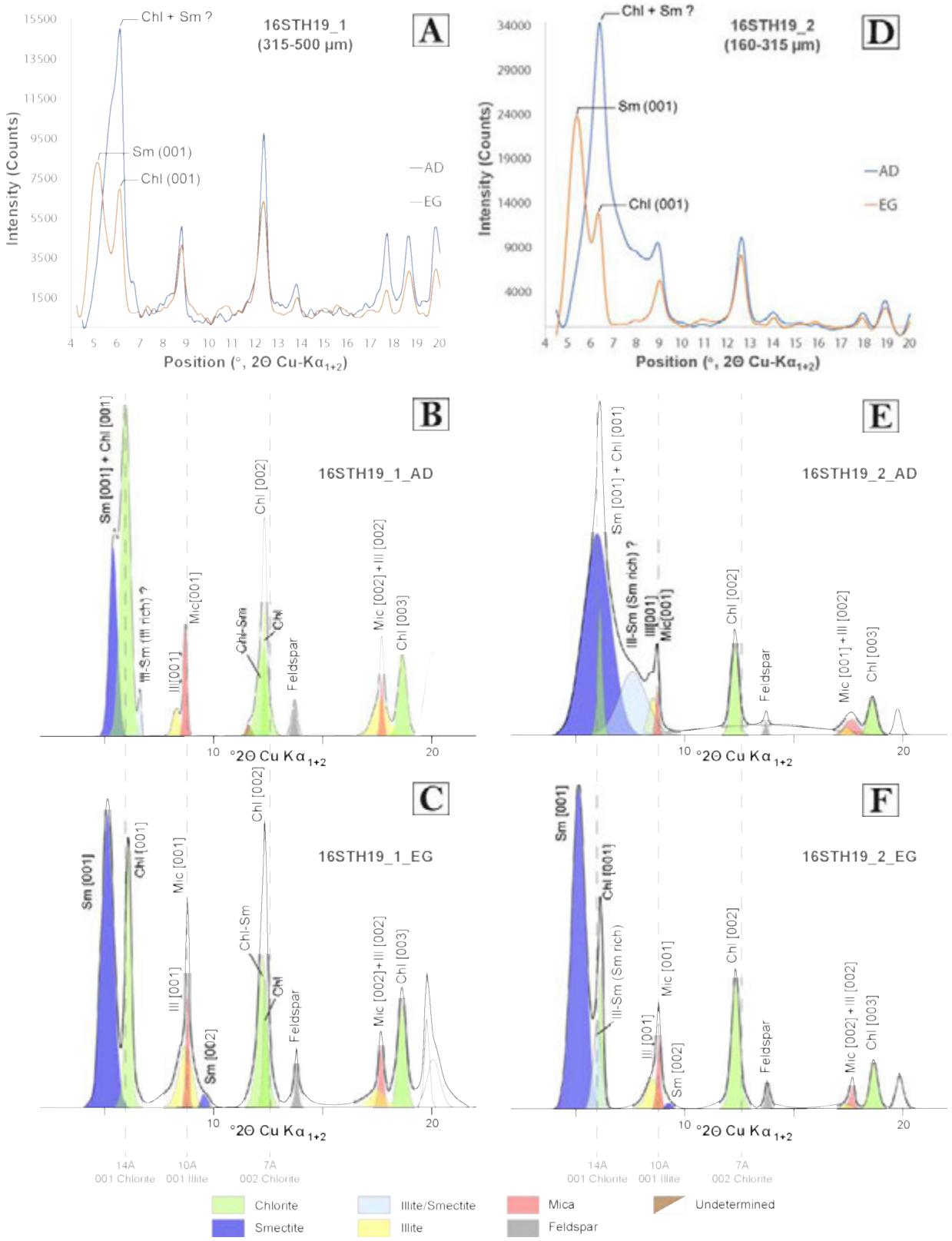


**Figure VI-5: X-Ray diffraction patterns for the 315-500 µm fraction (16STH19-1) and 160-315 µm fraction (16STH19-2) in AD (Air Dried) and EG (Ethylene Glycol) states. A & D: raw X-Ray patterns; B & E: decomposed and modelled X-Ray patterns in the AD state; C & F: decomposed and modelled X-Ray patterns in the EG state.**

*VI.2.5.d. Ar-Ar results*

All detailed data for each experiment is provided in online supplementary data (Ar/Ar experiments file) with a compilation of Ar-Ar results available in Table X-8.

*315-500 µm fraction*

The first experiment (16STH19B B7-B9) yielded a well-defined plateau age at 2.78 ± 0.23 Ma corresponding to 97.6% of $^{39}Ar$ released (Figure VI-6**-A**). The inverse isochron calculation yielded an identical age at 2.77 ± 0.33 Ma with an initial $^{40}Ar/^{36}Ar$ ratio at 299.9 ± 12.6 indicating that the trapped $^{40}Ar/^{36}Ar$ is indistinguishable from atmospheric $^{40}Ar/^{36}Ar$. The second and third experiments (16STH19 A9-A10 and 16STH19 B12) display concordant plateau ages at 2.45 ± 0.25 Ma and 2.62 ± 0.20 Ma, with 87.3% and 98.9% of $^{39}Ar$ released, respectively (Figure VI-6**-B-C**). Inverse isochron ages and related initial $^{40}Ar/^{36}Ar$ ratios for these two experiments are concordant with the first aliquot. The experiment 16STH19B B2 yielded less well-defined plateau age at 2.55 ± 0.44 Ma (Figure VI-6**-D**) with 61% of $^{39}Ar$ released, due to higher $^{40}Ar$ atmospheric contamination. Nevertheless, all plateau ages are concordant, thus we can statistically combine these four experiments. We retain the combined plateau age at 2.59 ± 0.12 Ma at 2σ (MSWD 0.39; initial $^{40}Ar/^{36}Ar$ ratio at 295.9 ± 5.5) for 315-500 µm meta-pyroxenes (Figure VI-6**-G**). K/Ca spectra (deduced from $^{39}Ar_K/^{37}Ar_{Ca}$ spectra) associated with the four plateau ages display relatively regular flat patterns, highlighting the chemical reproducibility of the step-heated phase(s).

*160-315 µm fraction*

The first experiment (16STH19A B1) displays disturbed spectra with a mini-plateau age at 1.87 ± 0.43 Ma (MSWD = 2.05, with 60.8% of 39Ar released; Figure VI-6**-E**). The first steps yield younger ages, suggesting radiogenic $^{40}Ar$ losses. The inverse isochron calculation yields a poorly defined age at 1.65 ± 0.66 Ma with an initial $^{40}Ar/^{36}Ar$ ratio at 305.9 ± 17 indicating that the initial argon in meta-pyroxene remains indistinguishable from atmospheric argon. The duplicated sample (16STH19A B1) shows the same characteristics, i.e. a concordant mini plateau age at 2.14 ± 0.38 Ma with apparent $^{40}Ar$ loss in the first steps. For the two experiments, K/Ca spectra displays relatively flat patterns similar to the 315-500 µm fraction experiments, suggesting degassing of isochemical phases during the step-heating of all experiments. These poorly defined plateau ages are younger than those of the 315-500 µm fraction, implying possible $^{40}Ar$ losses during late re-opening of hydrothermal phases. Nevertheless, it is difficult to consider that such isotopically disturbing events affect only the small meta-pyroxenes.

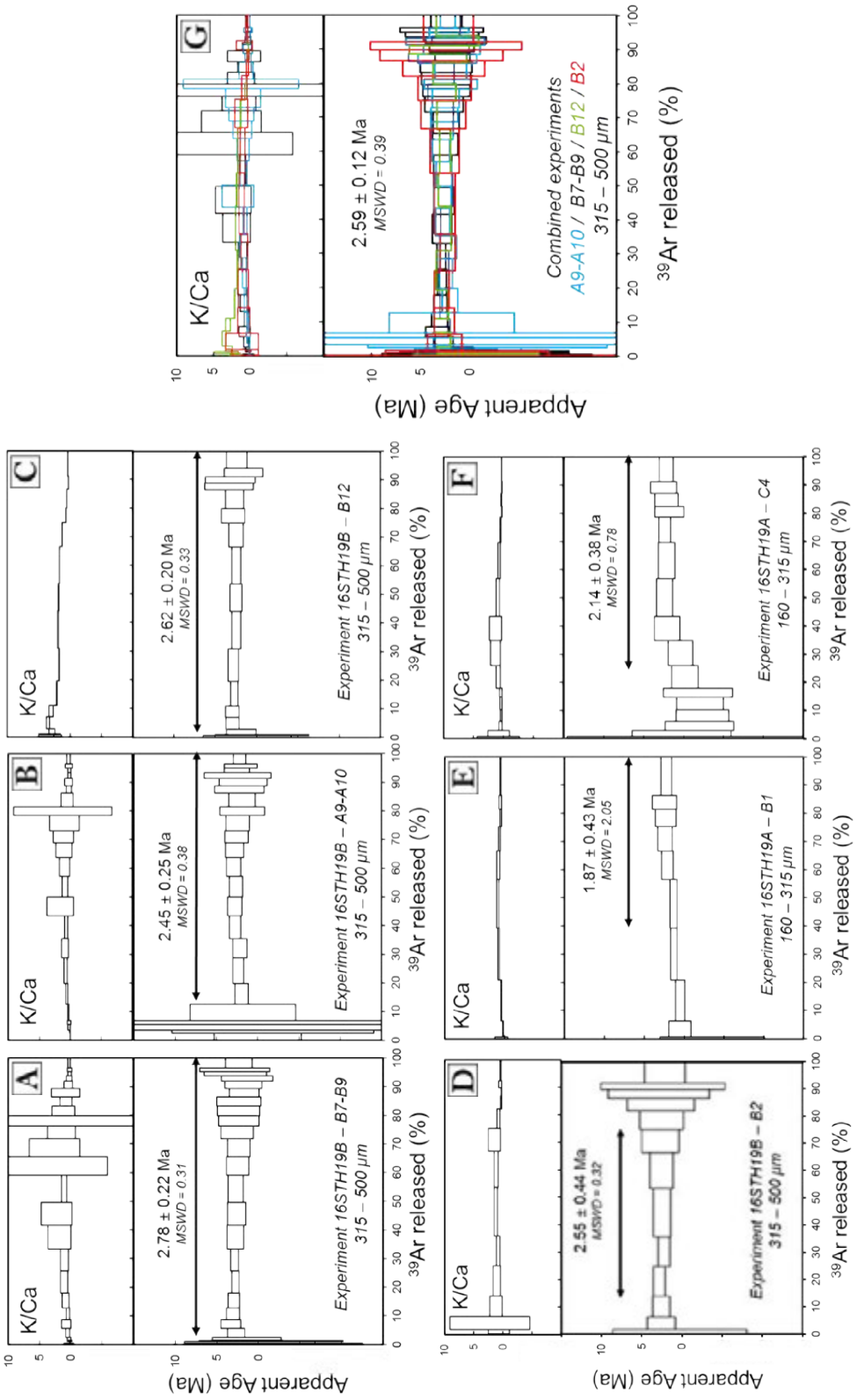


**Figure VI-6: $^{40}Ar/^{39}Ar$ age spectra and K/Ca spectra, as a function of $^{39}Ar$ released. The error boxes of each step are at the 2σ level. Arrows show the plateau age fraction. Error of the plateau age is given at the 2σ level. A, B, C & D: four individual experiments on the meta-pyroxene 315-500 µm fraction; E & F: two experiments on the 160-315 µm fraction; G: combined spectra of the four experiments A+B+C+D.**

### VI.2.6.Discussion

*VI.2.6.a. Interpretation of Ar-Ar data*

The K-rich phases, which can play a role on the obtained $^{40}Ar/^{39}Ar$ dataset, are well identified in our sample (section VI.2.5), they are: muscovite, illite and interstratified illite/smectite. Others phases without potassium (chlorite, smectite, quartz, feldspar, epidote, titanite or the missing pyroxene) can be neglected compared to K-bearing phases. Therefore we need to discuss our Ar-Ar results taking into account the mineralogical differences between the two meta-pyroxenes fractions.

*VI.2.6.b. Influence of K-rich phase crystallinity on Ar-Ar result interpretations*

We described some mineralogical differences between the 315-500 µm and the 160-315 µm fractions, especially illite and muscovite crystallinity. The 315-500 µm fraction, with muscovite and low Kübler index (0.12), displays well-defined plateau ages, while the 160-315 µm fraction, with higher index (0.16), provides a more disturbed Ar-Ar spectra. Moreover, the two fractions have quite the same illite Kübler index (0.53 – 0.52). Muscovite crystallinity is thus a key parameter for obtain a well-defined plateau age.

Additional mineralogical difference between the two fractions concerns the illite-type detected with X-Ray diffraction method. While the 315-500 µm fraction shows only one illite/muscovite type, the 160-315 µm fraction provides illite/smectite species also. If interstratified illite/smectite species are developed at the expense of muscovite as frequently observed in hydrothermal systems (Inoue *et al.*, **1992**; Inoue & Kitagawa, **1994**), it can perturb the previous K-bearing phase chronometer and thus explain the disturbed Ar-Ar spectra obtained on the 160-315 µm fraction. Nevertheless, while the well-defined Ar-Ar plateau ages for the 315-500 µm fraction are due to higher muscovite crystallinity, we suggest that the disturbed spectra of 160-315 µm fraction are related to the $^{39}Ar$ recoil effect as previously described for illite grains (Dong *et al.*, **1995**; Hall *et al.*, **1997**; Isik *et al.*, **2014**). The recoil effect, occurring during neutron irradiation, affects < 50 µm microcrystals (Jourdan *et al.*, **2007**) and here specifically illite/smectite species in the 160-315 µm fraction. We consider thus that the obtained mini-plateau ages on the small fraction are geological non-significant (see discussion in section VI.2.6.c). For the 315-500 µm fraction, the age of 2.59 ± 0.12 Ma is the best estimation for the high temperature (>350 °C) muscovite crystallization.

*VI.2.6.c. Influence of geothermal system cooling on Ar-Ar results*

The crystallinity of micaceous phases may be interpreted in term of temperature, according to Warr and Cox (**2016**) and Ji and Browne (**2000**), reaching a temperature domain above 300°C for mica-type and 200°C for illite (Tmin in the Table VI-1). These temperatures are in agreement with the temperature range (289-380°C) obtained by detailed mineralogical investigations (chlorite geo-

thermometry and thermodynamic modeling) performed on the studied sample (Favier et al., *submitted*).

Under low-grade metamorphism, the secondary micas developed at the expense of pyroxenes are often mixed illite and muscovite (Meyer & Hemley, **1967**; Merriman & Peacor, **1998**; Favier et al., *submitted*). Several studies demonstrated that white mica develops in epithermal to mesothermal systems (Guilbert & Park, **1986**; White & Hedenquist, **1990**; Groves *et al.*, **1998**; Hedenquist *et al.*, **2000**; Goldfarb *et al.*, **2001**) under sub-greenschist to greenschist facies conditions (<350°C). Illite crystallization (< 200°C) is generally the result of cooling of the geothermal system (ca. -150°C, Henley & Ellis, **1983**; Hedenquist *et al.*, **2000**; Ji & Browne, **2000**). In order to test the effect of the illite development on our muscovite age, we made a theoretical model showing how progressive illite formation modifies the K-Ar systematic of muscovite and ultimately can affect the accuracy of muscovite ages. We also discuss the significance of the younger ages obtained on the 160-315 µm fraction: are they related to illitization process or not?

We used the same calculations applied for sericitization of plagioclases in Verati & Jourdan (**2014**). We evaluated the K-Ar age reductions of the illitized muscovite with a two-components mixture between hydrothermal primary muscovite and secondary illite, considering that illitization occurs in a single stage.

Using the K-Ar age equation, for a given K content in muscovite ($^{40}K_{ms}$), radiogenic $^{40}Ar$ in illite-free muscovite with an age t is:

$$^{40}Ar = \frac{\lambda_e}{\lambda} {}^{40}K_{ms}(e^{\lambda t} - 1)$$

For a muscovite which is illitized at t' (t'<t), with X% of illite in the mixture, for a given K content in illite ($^{40}K_{ill}$), the total amount of K content in the mixture ($^{40}K_{tot}$), as well as the total amount of radiogenic $^{40}Ar$ ($^{40}Ar_{tot}$) in the mixture are:

$^{40}K_{tot} = (1 - X)^{40}K_{ms} + X^{40}K_{ill}$ with $^{40}Ar_{tot} = {}^{40}Ar_{ms} + {}^{40}Ar_{ill}$

We obtain:

$$^{40}Ar_{tot} = \frac{\lambda_e}{\lambda} {}^{40}K_{ms}(e^{\lambda t} - 1) + \frac{\lambda_e}{\lambda} {}^{40}K_{ill}(e^{\lambda t'} - 1)$$

We can define the apparent age t'' of the two-component mixture (illitized muscovite) as follow:

$$^{40}Ar_{tot} = \frac{\lambda_e}{\lambda} {}^{40}K_{tot}(e^{\lambda t''} - 1)$$

Previous equations may be combined to give:

$$\frac{\lambda_e}{\lambda} {}^{40}K_{tot}(e^{\lambda t''} - 1) = \frac{\lambda_e}{\lambda} {}^{40}K_{ms}(e^{\lambda t} - 1) + \frac{\lambda_e}{\lambda} {}^{40}K_{ill}(e^{\lambda t'} - 1)$$

We deduce the apparent K-Ar age t'' of the mixing:

$$t'' = \frac{1}{\lambda} ln\left[1 + \left(\frac{^{40}K_{ms}}{^{40}K_{tot}}\right)(e^{\lambda t} - 1) + \left(\frac{^{40}K_{ill}}{^{40}K_{tot}}\right)(e^{\lambda t'} - 1)\right] \quad (\textit{VI-1})$$

where $^{40}$Kms is the $^{40}$K content of muscovite, $^{40}K_{ill}$ is the $^{40}$K content of illite, $^{40}K^{tot}$ is the $^{40}$K content of the mixture, t is the K-Ar hydrothermal age of the muscovite, t' is the K-Ar age of the illitization event and λ is the total $^{40}$K decay constant (here 5.544 x$10^{-10}$ $yr^{-1}$ after Steiger & Jäger, **1977**).
The % of K-Ar age reduction AR is defined as:

$$AR = \frac{t - t''}{t} \quad (\textit{VI-2})$$

$^{40}K_{ms}/^{40}K_{tot}$ and $^{40}K_{ill}/^{40}K_{tot}$ ratio in equation (***VI-1***) are calculated with $M_{ms}$ = 398.71 $g.mol^{-1}$, $M_{ill}$ = 389.34 $g.mol^{-1}$, $\%K_2O_{ms}$ = 11.81%, $\%K_2O_{ill}$ = 7.26%. t value in equation (***VI-2***) is the K-Ar age of the muscovite, i.e. the total fusion age of combined Ar-Ar experiments for the 315-500 µm fraction (2.45 ± 0.27 Ma, see Table X-8 in online supplemenatry data).
According to the modelling of Verati & Jourdan (**2014**), the variable parameters in our study are the age of the illite (t') and the amount of illitization. In Figure VI-7-**A**, we plotted eight curves (different time span between muscovite crystallization and illitization) showing the %AR vs. % of illitization. The age difference between muscovite crystallyzation and illitization is the main parameter influencing the calculated K-Ar age reduction (Figure VI-7-**A**). When the time span between illitization and muscovite ranges between 0 to 10%, the decrease of the K-Ar age is not significant enough to provide a mixing K-Ar age discordant from the muscovite age, whatever the amount of illitization (2σ error of K-Ar age is bigger than the time span). This implyes that fast cooling rate (>150°C/200 ka) and illitization age cannot be determined under these conditions, and thus may not explained the younger ages obtained on the 160-315 µm fraction.
For a difference in age of 20% to 100% between muscovite crystallization and illitization, the related %AR remains low (<40%) for a high percent of alteration of 50%. High amounts of illitization (70% – 90%) do not reset totally the muscovite age totally whatever the time span between crystallization and illitization. An interpretation of our K-Ar dating on meta-pyroxene, as the age of muscovite/ illite mixing is thus inappropriate. However, high illitization of muscovite (>70%) may be responsible for apparent younger ages in the Ar-Ar spectra of the 160-315 µm fraction. In Figure VI-7-**B**, the K-Ar total fusion ages of the 160-315 µm fraction (two experiments at 1.6 ± 0.2 Ma and 1.2 ± 0.5 Ma, see the Table X-8 in the online supplementary data) are reported. These younger K-Ar ages due to illitization of muscovite can for instance be explained by 1) 50% to 60% of present day illitization, or 2) 60% to 75% of illitization at 500 ka, or 3) 85% à 100% of illitization at 1.35 Ma. Any event of illite formation older than 1.4 Ma, wathever the amount of illitization, explains the apparent younger K-

Ar age of the 160-315 µm meta-pyroxenes. Our thin section observations do not show such amount of illitization (>60%) for the small fraction, emphasizing that the $^{39}Ar$ recoil effect is responsible for the disturbed Ar-Ar spectra.

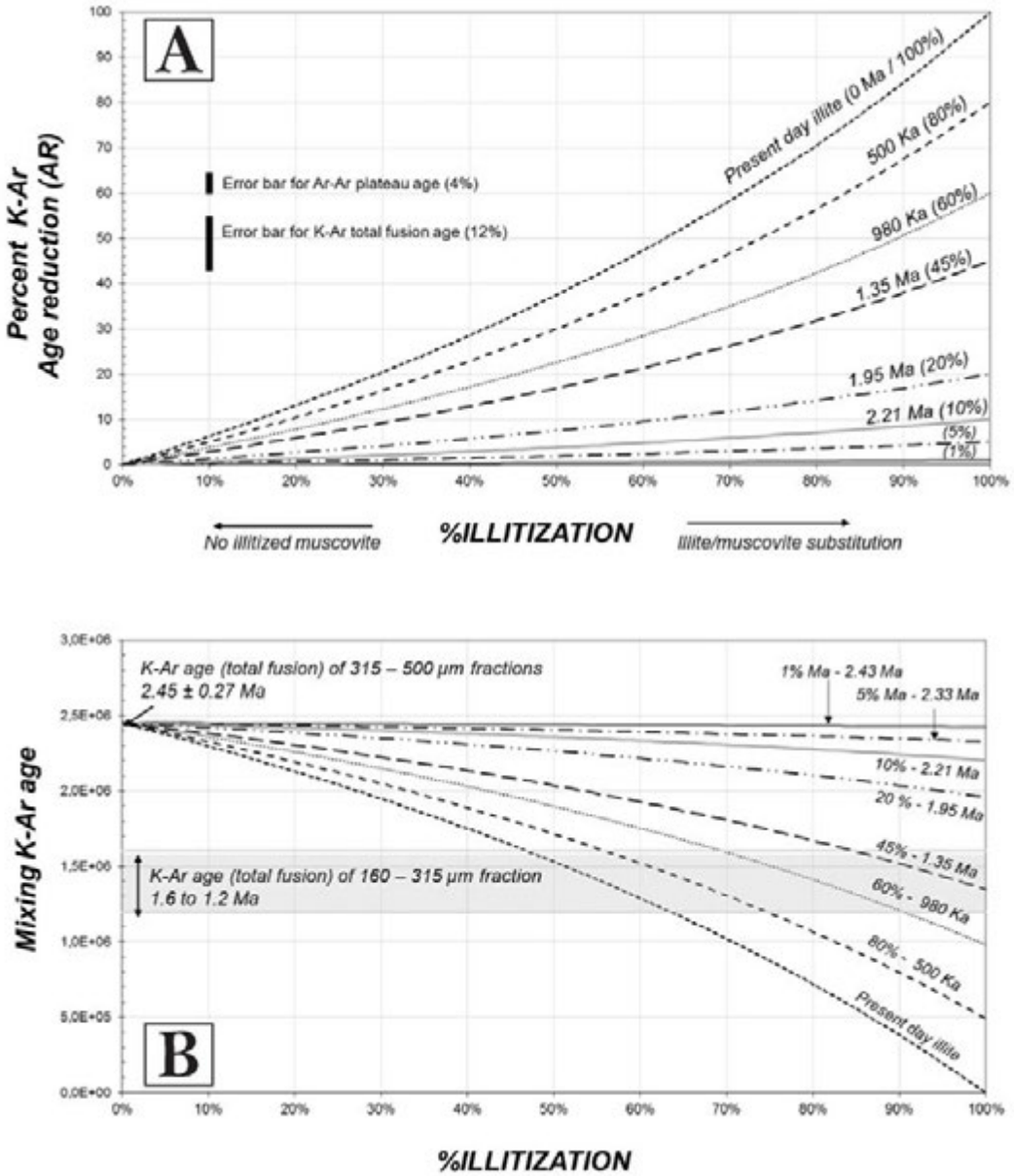


**Figure VI-7: A) Age Reduction parameter (%AR) vs % muscovite illitization. The curves are calculated for different t' (age of illitization). The age of the muscovite t = K-Ar total fusion age of 2.45 ± 0.27 Ma (see text for explanation). Age of the illitization (% time span / muscovite) is specified for each curve. Error bar for K-Ar total fusion and Ar-Ar plateau age is reported (after error at 2 σ in Table X-8, in online supplementary data). B) Theorical mixing K-Ar age vs % muscovite illitization. K-Ar age of 2.45 ± 0.27 Ma for the 315-500 µm fraction is reported. K-Ar ages (Ar-Ar total fusion of 1.6 Ma for B1 experiment, and 1.2 Ma for C4 experiment respectively) for the 160-315 µm meta-pyroxenes are also reported (grey area). Different theoretical curves are defined according to different age for the illitization (2.43 Ma to present day). For example, muscovite at 2.45 Ma can display an apparent K-Ar of 2.0 Ma with 50% of illitization occurring at 1.35 Ma.**

*VI.2.6.d. Implication for duration of an active geothermal system*

The combined plateau age at 2.59 ± 0.12 Ma at 2σ, obtained on the 315-500 µm fraction rich in muscovite, is the best age estimation of the high temperature hydrothermal system (>300°C) recognized in Terre-de-Haut Island. This age was obtained on a volcanic island within which other temporal constraints are available, thus a comparison of our results with ages of volcanic activity (emplacement of lava flows, volcanic domes or plugs, Figure VI-1**-B**) is highly significant. A first data set was obtained in the eighties (Jacques *et al.*, **1984**) by K/Ar technique on whole rock without considering the impact of hydrothermal and/or alteration processes on the obtained results. In this first data set, the only sample described as totally unaltered volcanic rock is located in a volcanic plug intrusive in the hydrothermalized zone, from North of Grande Anse area and dated at 1.94 ± 0.10 Ma (Jacques *et al.*, **1984**). Recent temporal data, with the use of the unspiked K-Ar technique (see discussion in Samper *et al.*, **2007**, **2009**), doing measurements on groundmass only with a selection of only fresh rocks, were obtained by Zami et al. (**2014**). All the ages obtained demonstrate a volcanic activity of Terre-de-Haut Island ranging from 2.98 ± 0.04 Ma to 2.00 ± 0.03 Ma. It must be underlined that an age around 2.00 ± 0.03 Ma was obtained on the unaltered and intrusive "Le Chameau" volcanic dome (Figure VI-1**-B**, Zami *et al.*, **2014**).

Our new results are clearly consistent with these previous investigations:

- First, the development of the studied geothermal system is coeval with the volcanic activity of this island.

- Second, altogether the whole temporal data set allows us to estimate a maximal duration of 650 ka of the geothermal system. This result is in agreement with the lifetimes proposed for other volcanic geothermal provinces or epithermal deposits where hydrothermal activity is ranging between a few hundred thousand years to a million years (Faure, **1986**; Deloule & Turcotte, **1989**; Nakai *et al.*, **1993**; Barnes, **1997**; Rowland & Sibson, **2004**).

## VI.2.7. Conclusion

1. We confirm that the $^{40}Ar/^{39}Ar$ method, coupled with a high-resolution mineralogical analysis, is a powerful technique for dating high enthalpy geothermal systems. Under Greenschist facies conditions, the degree of crystallinity of K-bearing phases is a key parameter for accurate Ar-Ar dating, especially for muscovite.

2. If crystallinity of K-rich phases is less defined, Ar-Ar spectra can display younger apparent ages which are not geologically relevant, due to $^{39}Ar$ recoil effect.

3. Ar-Ar spectra can also be disturbed by the replacement of high temperature K-bearing phases by younger K-rich ones during the geothermal reservoir cooling under sub-Greenschist facies (i.e. white mica illitization and/or interstratified illite/smectite substitution).

4. Muscovite in meta-pyroxenes, with high crystallinity index and less than 40% of illitization can provide accurate Ar-Ar plateau age of crystallization under Greenschist facies conditions. Nevertheless, illitization can have a fundamental impact on the Ar-Ar and K-Ar systematics only if the muscovite is highly illitized and/or if the illitization is much younger than the muscovite crystallization.

5. We propose the first example of dating hydrothermal muscovite crystallization developed at the expense of meta-pyroxenes within transformed arc-related calc-alkaline volcanic rocks. We obtain an age of 2.59 ± 0.12 Ma for the development of the Terre-de-Haut fossil geothermal reservoir, with a maximal duration estimated at 650 ka.

### VI.2.8. Supplementary data

*Documents disponibles dans le chapitre Annexe de ce manuscrit* (Article 4 – Supplementary data).

### VI.2.9. Ackowledgments

This paper is a contribution to the GEOTREF program, funded by the French government with the "Investissements d'Avenir" program and tutored by ADEME. We thank the researchers from the GEOTREF consortium for greatful discussions during the fieldwork campaigns in Guadeloupe and during scientific meetings. The authors thank Arthur Iemmolo for his technical support during $^{40}Ar/^{39}Ar$ analysis, Magaly Bonnefoy and Matthieu Zanti for sampling preparation, Gabriel Monge for his welcome to CEMEF for the use of the X-ray Diffraction device, Emile Voitus for his participation in the fieldwork campaigns and to the residents of the Terre-de-Haut Island.

## VI.3. Perspectives afin de mieux contraindre la durée de vie des systèmes géothermaux

Afin de contraindre d'avantage la durée du fonctionnement de la phase hydrothermale de haute-température nous avons également identifié des phases hydrothermales de plus basse-température dans le même secteur du Nord de Grande Anse ainsi qu'à l'échelle de l'île de Terre-de-Haut, en particulier des jarosites (voir partie V.2 du Chapitre V :).

La jarosite ($KFe^{3+}(SO_4)_2(OH)_6$) fait partie de la famille des sulfates et contient du potassium. Il s'agit donc d'une phase minérale potentiellement datable à partir des méthodes $^{40}Ar/^{39}Ar$ ou K-Ar. Des récentes études ont montré que les âges obtenus sur des jarosites peuvent être utilisés pour dater des processus de surface tels que l'altération météorique ou la circulation de fluides hydrothermaux acides et/ou oxydants de basse-température (80-240°C) en sub-surface (<200 m) en lien avec l'altération de minéraux sulfurés (Stoffregen *et al.*, **2000**; Lueth *et al.*, **2005**). L'âge obtenu correspond à l'âge de sa formation lors du refroidissement du système suite à l'arrêt du fonctionnement d'une source de chaleur (Lueth *et al.*, **2005**; Kula & Baldwin, **2011**). Ces phases minérales peuvent donc avoir une origine supergène ou hypogène et sont postérieures, au vu de leur relation structurale au sein des échantillons, à la mise en place de la phase potassique caractérisée et datée dans la partie précédente (VI.2). La mesure d'un tel âge permettrait également de contraindre le moment où de l'eau était encore présente dans ces roches, qui est une condition essentielle à la formation de jarosite, avant une phase de déshydratation régionale finale nécessaire à sa préservation (Elwood Madden *et al.*, **2009**).

La séparation de cette phase minérale ainsi que leurs faibles quantités prélevées dans les échantillons ne nous ont pas permis de réaliser leurs datations pendant la durée de la thèse, mais des tests avec la méthode de datation K-Ar vont avoir lieu par la suite. Pour éviter toute contamination de l'âge des silicates potassiques hydrothermaux issus de la phase de plus haute-température, présents dans les échantillons en question, des études préconisent un traitement à l'acide fluorhydrique (Samuels-Crow *et al.*, **2012**).

Si les résultats sont concluants, les âges obtenus pourront être un argument supplémentaire pour contraindre la limite supérieure de la durée du fonctionnement de la phase hydrothermale de haute-température à partir de la phase de plus basse-température postérieure.

## VI.4. Hydrothermalisme au niveau du système actif de la Basse-Terre – dans la zone du PER

Notre étude se concentre à présent sur l'île de la Basse-Terre de Guadeloupe, dans la zone du Permis Exclusif de Recherche (PER) attribué au projet GEOTREF (Figure VI-8**-A-B**).
Nous avons cherché à identifier des indices de manifestations de surface en lien avec l'activité géothermale ainsi que les structures tectoniques associées.

### VI.4.1. Etat des lieux des structures tectoniques et hydrothermales

En collaboration avec les partenaires impliqués dans le projet, nous nous sommes, dans un premier temps, attachés à relever les structures tectoniques dans la zone du PER, principalement le long du littoral afin d'avoir accès à des affleurements dégagés du couvert végétal en évitant les zones recouvertes par les formations relatives aux effondrements de flancs de volcans les plus récents qui masquent les structures.
Cela nous a permis de produire une nouvelle carte structurale du secteur (Figure VI-8**-B**), en complément des études précédentes, où nous retrouvons localement les quatre directions de failles bien connues à l'échelle régionale.

Nous avons également identifié une brèche hydrothermale au Sud de Vieux-Habitants, à la plage de Rocroy. Elle se localise au niveau des systèmes de failles N30-N50 et N80-N100 (Figure VI-8**-B**) et se situe au cœur d'une avalanche de débris grise à jaunâtre (Figure VI-9**-A-B**).

Nous nous sommes attachés à caractériser minéralogiquement cette brèche hydrothermale. Pour cela j'ai utilisé une approche multi-analytique sur l'échantillon 17PER03 prélevé dans cette brèche (Figure VI-9**-C**) :

- Les analyses chimiques de la poudre (<70 µm) de la roche totale des éléments majeurs et traces (Tableau VI-2) par la méthode ICP-AES (*Inductively Coupled Plasma Atomic Emission Spectrometry*) et ICP-MS (*Inductively Coupled Plasma Mass Spectrometry*) effectuées par le Service d'Analyse des Roches et Minéraux (SARM) à Vandœuvre-lès-Nancy (54). Elles nous ont permis d'identifier une perte au feu (ou *LOI* pour *Loss On Ignition*) de l'ordre de 13% indiquant une altération, éventuellement hydrothermale, importante de l'échantillon.

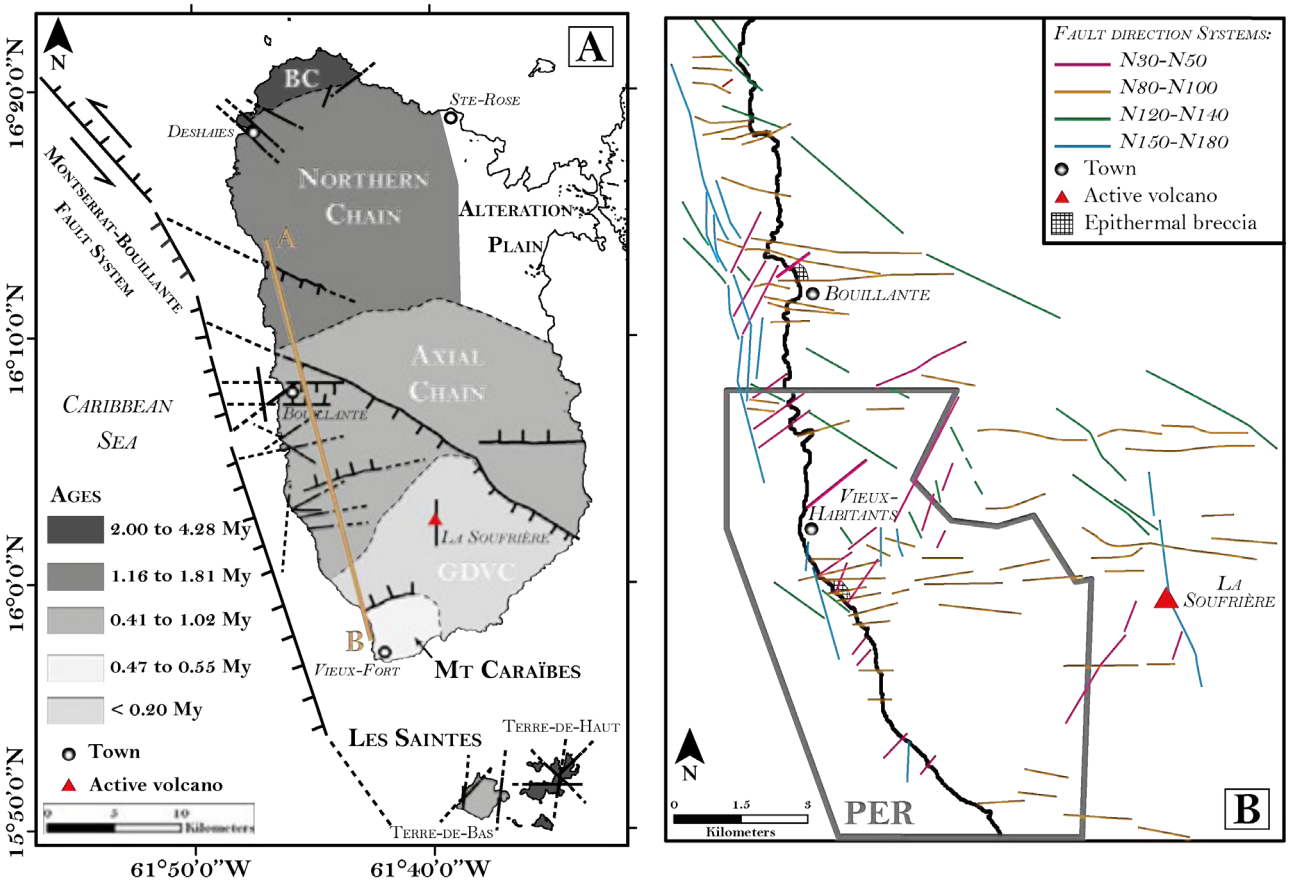


**Figure VI-8 : A) Carte de l'arc volcanique actif de l'archipel de Guadeloupe (l'île de Basse-Terre et l'archipel des Saintes) illustrant les différents complexes volcaniques et les principales structures tectoniques (modifiée d'après Verati *et al.*, 2018). Trait A-B localisant la coupe présentée en figure VI-15. B) Synthèse des données structurales de la zone Bouillante-PER à partir des observations de terrain complétées par les études précédentes (Feuillet *et al.*, 2002; Calcagno *et al.*, 2012; Lebrun *et al.*, 2017; Navelot, 2018).**

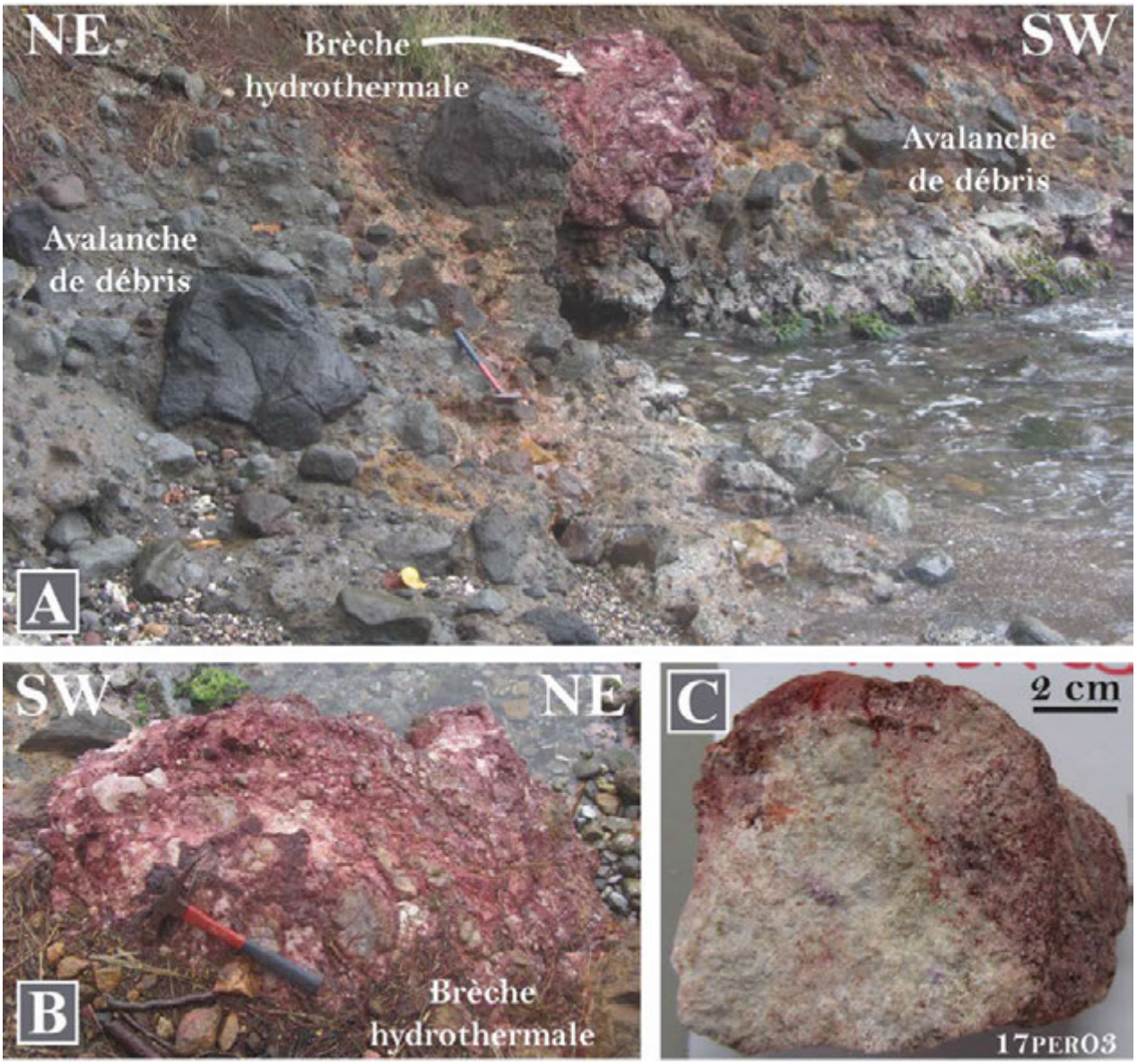


**Figure VI-9 : A) Affleurement de la plage de Rocroy illustrant les avalanches de débris grises et jaunâtres et la brèche hydrothermale rose et blanche. B) Zoom sur la brèche hydrothermale de Rocroy. C) Echantillon 17PER03 prélevé au cœur de la brèche hydrothermale de Rocroy.**

**Tableau VI-2: Composition chimique en éléments majeurs et traces sur roche totale de l'échantillon 17PER03**

| 17PER03 sample | | | | | | | |
|---|---|---|---|---|---|---|---|
| Major composition (%) | | Trace composition (ppm) | | | | | |
| $SiO_2$ | 62.79 | Be | 0.09 | Nb | 2.53 | Tb | 0.26 |
| $Al_2O_3$ | 21.78 | Sc | 20 | Mo | < L.D. | Dy | 1.62 |
| $Fe_2O_3$ | 0.22 | V | 116.46 | Cd | < L.D. | Ho | 0.36 |
| MnO | < L.D. | Cr | 5.24 | In | < L.D. | Er | 1.03 |
| MgO | 0.12 | Zn | < L.D. | Sn | 4.90 | Tm | 0.16 |
| CaO | 0.19 | Co | 0.24 | Sb | 0.17 | Yb | 1.17 |
| $Na_2O$ | 0.66 | Ni | < L.D. | Cs | 0.37 | Lu | 0.19 |
| $K_2O$ | 0.38 | Cu | 2.62 | Ba | 114.79 | Hf | 2.53 |
| $TiO_2$ | 0.85 | Ga | 13.56 | La | 6.83 | Ta | 0.18 |
| $P_2O_5$ | 0.16 | Ge | 2.67 | Ce | 17.36 | W | 4.95 |
| LOI | 13.06 | As | 4.40 | Pr | 2.24 | Pb | 1.14 |
| *3.27 % $CO_{2\ total}$* | *0.43* | Rb | 3.46 | Nd | 9.67 | Bi | 0.44 |
| *86.45 % $H_2O_{total}$* | *11.29* | Sr | 263.20 | Sm | 2.12 | Th | 1.48 |
| *0.93 % FeO* | *0.12* | Y | 8.87 | Eu | 0.42 | U | 0.29 |
| *9.35 % $S_{total}$* | *1.22* | Zr | 87.51 | Gd | 1.61 | | |

- La microscopie optique sur lame mince nous a permis d'identifier d'anciennes phases minérales volcaniques de type plagioclase, dont il ne reste que la forme, totalement remplacées par des phases argileuses, du quartz, parfois des alunites. La matrice est constituée de phases argileuses et d'oxydes de fer. Enfin des vacuoles sont totalement comblées par des alunites (Figure VI-10-**A**) parfois associées à du quartz.
- L'identification des alunites a été confirmée par des analyses :
    - A la microsonde électronique, effectuées au Service Commun de Microsonde de l'Université de Montpellier à Montpellier (34) sur un microsonde Cameca-SX100, selon les conditions suivantes : une tension d'accélération de 20kV, un courant de 10 nA et un temps d'analyse de 5 min par points ;
    - Au Microscope Electronique à Balayage (MEB), effectuées au Centre Commun de Microscopie Appliquée de l'Université de Nice-Sophia-Antipolis à Nice (06). Nous avons ainsi réussi à identifier de la pyrophyllite et de la kaolinite, associées aux alunites qui peuvent tendre vers des natroalunites avec des analyses avec un spectromètre à dispersion d'énergie (EDX, 20kV) couplé au MEB à canon à effet de champ JEOL 6700F (Tableau VI-3, Figure VI-11-**A**) ;
    - A la spectrométrie Raman, effectuées sur lame mince au Laboratoire d'Océanologie et de Géosciences de l'Université de Lille 1 à Villeneuve-d'Ascq (59), sur un LabRam HR800UV Jobin-Yvon™ équipé de réseaux de 1800 g/mm, utilisant une excitation

laser verte de 532 nm et dont la durée d'acquisition varie de 20 à 70 s pendant trois cycles. Le spectre obtenu est présenté en Figure VI-10-**B** et montre une bonne correspondance des pics avec ceux d'un standard d'alunites ;

- A la diffraction des Rayons-X sur la poudre (<70 µm) de la roche totale, effectuée au Centre de Mise en Forme des Matériaux MINES ParisTech à Sophia-Antipolis (06) à partir d'un système de diffractomètre XPert-Pro MPD (géométrie de Bragg Brentano, anticathode Cu, KAlpha1 et KAlpha2, détecteur PIXcel). Le spectre obtenu entre 3,6 et 75 °2θ nous a permis d'identifier un assemblage à kaolinite, quartz, alunite à natroalunite et un sulfate de fer de type greigite.

Pour cette brèche hydrothermale de Rocroy, à partir de l'échantillon étudié, nous obtenons donc l'assemblage minéralogique suivant :

- 20% de quartz [$SiO_2$]
- 10% d'alunites [$KAl_3(SO_4)_2(OH)_6$] (à natroalunite [$NaAl_3(SO_4)_2(OH)_6$])
- > 55% de kaolinite [$Al_2Si_2O_5(OH)_4$]
- < 5% de pyrophyllite [$Al_2Si_4O_{10}(OH)_2$]
- 10% d'oxyde de fer et de sulfate de fer [greigite $Fe_3S_4$]

L'alunite est la seule phase minérale potassique identifiée. C'est donc à partir de cette phase que nous nous sommes concentrés pour entreprendre la datation. Cela peut nous permettre d'obtenir l'âge de l'évènement hydrothermal post-dépôt volcanique qui a conduit à la mise en place de cette brèche. Ce sulfate peut également nous permettre d'étudier l'origine de cette brèche et des fluides qui ont circulés à partir d'analyses isotopiques, et donc de savoir si celle-ci est bien hydrothermale (ou hypogène) ou plutôt supergène. Nous avons donc cherché à isoler cette phase minérale.

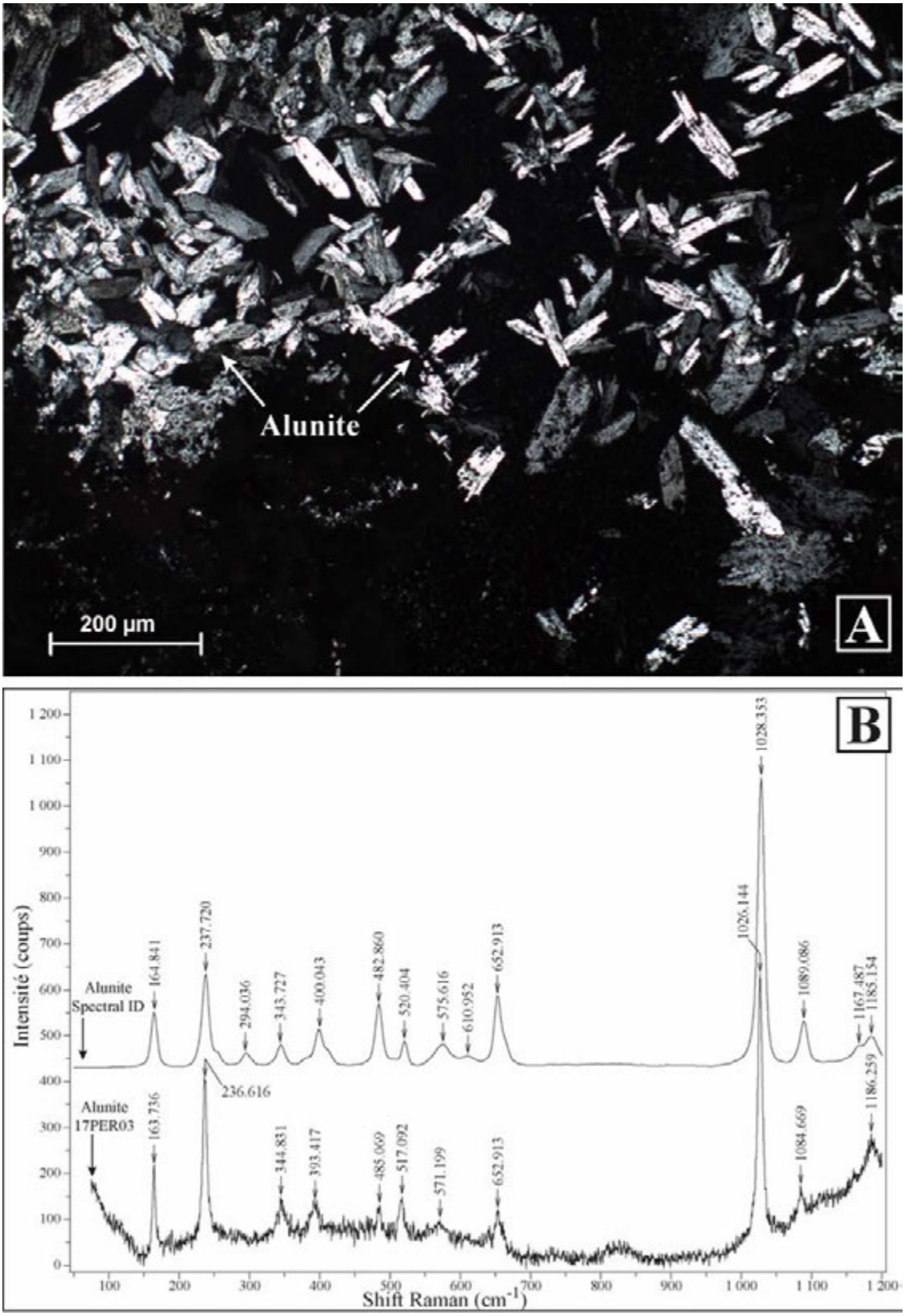


**Figure VI-10 : A) Alunites dans une vacuole, en Lumière Polarisée Analysée. B) Spectre Raman d'une alunite issue de l'échantillon 17PER03, obtenu à partir du logiciel d'acquisition Labspec et traité en comparant les spectres de la base de données du logiciel Spectral ID.**

**Tableau VI-3 : Analyses sur des grains triés d'alunites à natroalunites au MEB. HF = traitement à l'acide fluorhydrique sur les grains triés de l'échantillon 17PER03.**

| Composition des grains triés de l'échantillon 17PER03 (% massique) | | | | | | | | | |
|---|---|---|---|---|---|---|---|---|---|
| | pré-HF | | | | | | post-HF | | |
| | *n°29* | *n°33* | *n°41* | *n°53* | *n°76* | *n°81* | *n°1* | *n°2* | *n°3* |
| Si | 0,05 | 0,46 | 0,45 | 0,64 | | 0,26 | | | |
| Al | 19,5 | 19,8 | 19,5 | 19,3 | 20,4 | 18,1 | 19,7 | 21,7 | 19,1 |
| Na | 3,53 | 2,36 | 2,84 | 3,06 | 2,47 | 3,4 | 5,03 | 2,35 | 2,8 |
| K | 3,26 | 5,73 | 3,76 | 3,72 | 5,52 | 3,07 | 1,36 | 5,29 | 4,11 |
| S | 14 | 16,8 | 13,6 | 13,3 | 17 | 11,8 | 14,2 | 21,5 | 13,5 |
| Fe | | 0,11 | 0,29 | 0,07 | 0,45 | | | | |
| P | 0,15 | 0,16 | 0,48 | 0,14 | 0,18 | | 0,21 | 0,33 | 0,08 |
| Ca | | | 0,42 | | | | | 0,3 | |
| Ti | | | 0,12 | | | | | | |
| Cu | | | | | 0,26 | | | | |
| Cl | 0,26 | 0,22 | | | | | 0,33 | 0,32 | |
| Sr | | | | | | | 0,4 | 0,34 | |
| F | | | | | | | 0,43 | 0,62 | 1,21 |
| O | 59,2 | 54,2 | 58,6 | 59,8 | 53,7 | 63,3 | 58,3 | 47,3 | 59,2 |

### VI.4.2. Protocole de séparation de l'alunite

1) Détermination de la taille de la phase ciblée

Suite aux observations microscopiques sur lame mince, les alunites présentent une taille comprise entre 100 et 200 µm. Nous avons donc choisi de réduire en poudre l'échantillon et de le tamiser jusqu'à obtenir deux fractions granulométriques : une première entre 100 et 200 µm et une seconde supérieure à 200 µm. En dessous de 100 µm le tri des minéraux devient délicat sous loupe binoculaire. Après avoir rincé à l'eau les deux précédentes fractions obtenues, afin d'éliminer la fraction résiduelle la plus fine (éléments argileux), nous séchons à l'étuve la poudre à une température maximum de 45°C.

2) Séparation magnétique

Afin d'éliminer les éléments magnétiques (de type oxydes de fer), les fractions obtenues sont passées au séparateur magnétique (un Frantz) pour les purifier. Nous obtenons les fractions correctement séparées à une intensité de 2A. Nous isolons et conservons donc les fractions non magnétiques à 2A.

3) Vérification de la phase séparée

Les deux fractions obtenues sont observées sous une loupe binoculaire afin de ne conserver que les grains correspondant aux caractéristiques des alunites (de couleurs allant du blanc, au blanc jaunâtre et au blanc grisâtre ; d'aspect transparent à translucide ; un éclat vitreux ; des surfaces planes se fracturant de façon inégales). Nous sélectionnons quelques grains, puis nous réalisons au MEB des cartographies élémentaires afin de vérifier l'homogénéité des grains triés (Figure VI-11**-C-D-E**).
Dans ces fractions non-magnétiques, l'alunite est la seule phase de l'assemblage à contenir à la fois du potassium et du soufre, en comparaison des autres phases qui sont des silicates et donc contiennent du silicium. C'est ainsi que nous constatons qu'au sein d'un grain, supposé d'alunite, celui-ci est en réalité associé à d'autres phases telles que la pyrophyllite ou la kaolinite (Figure VI-11**-A-B**).

4) Attaque à l'acide des grains

En condition d'altération argileuse avancée, les relations de stabilité de l'alunite ($KAl_3(SO_4)_2(OH)_6$) avec les minéraux silicatés dans le système K-Al-Si-SO4 sont définies par les réactions suivantes (Hemley *et al.*, **1969**) pour former de la muscovite ($KAl_3Si_3O_{10}(OH)_2$, *équation* ***VI.1***), de la kaolinite ($KAl_3(SO_4)_2(OH)_6$, *équation* ***VI.2***, ou de la pyrophyllite), ou du feldspath potassique (l'adulaire $KAlSi_3O_8$, *équation* ***VI.3***) :

$KAl_3(SO_4)_2(OH)_{6\,(s)} + 3\ SiO_{2\,(s)} \Leftrightarrow KAl_3Si_3O_{10}(OH)_{2\,(s)} + 2\ SO_4^{2-}{}_{(aq)} + 4\ H^+{}_{(aq)}$ **(*VI.1*)**

$2\ KAl_3(SO_4)_2(OH)_{6\,(s)} + 6\ SiO_{2\,(s)} + 3\ H_2O \Leftrightarrow$

$3\ Al_2Si_2O5(OH)_{4\,(s)} + 4\ SO_4^{2-}{}_{(aq)} + 6\ H^+{}_{(aq)} + 2\ K^+{}_{(aq)}$ **(*VI.2*)**

$KAl_3(SO_4)_2(OH)_{6\,(s)} + 9\ SiO_{2\,(s)} + 2\ K^+{}_{(aq)} \Leftrightarrow 3\ KAlSi_3O_{8\,(s)} + 2\ SO_4^{2-}{}_{(aq)} + 6\ H^+{}_{(aq)}$ **(*VI.3*)**

Il est donc important d'éliminer les phases silicatées pouvant être présentes et en association avec l'alunite, pour avoir seulement le signal lié aux sulfates potassiques étudiés.

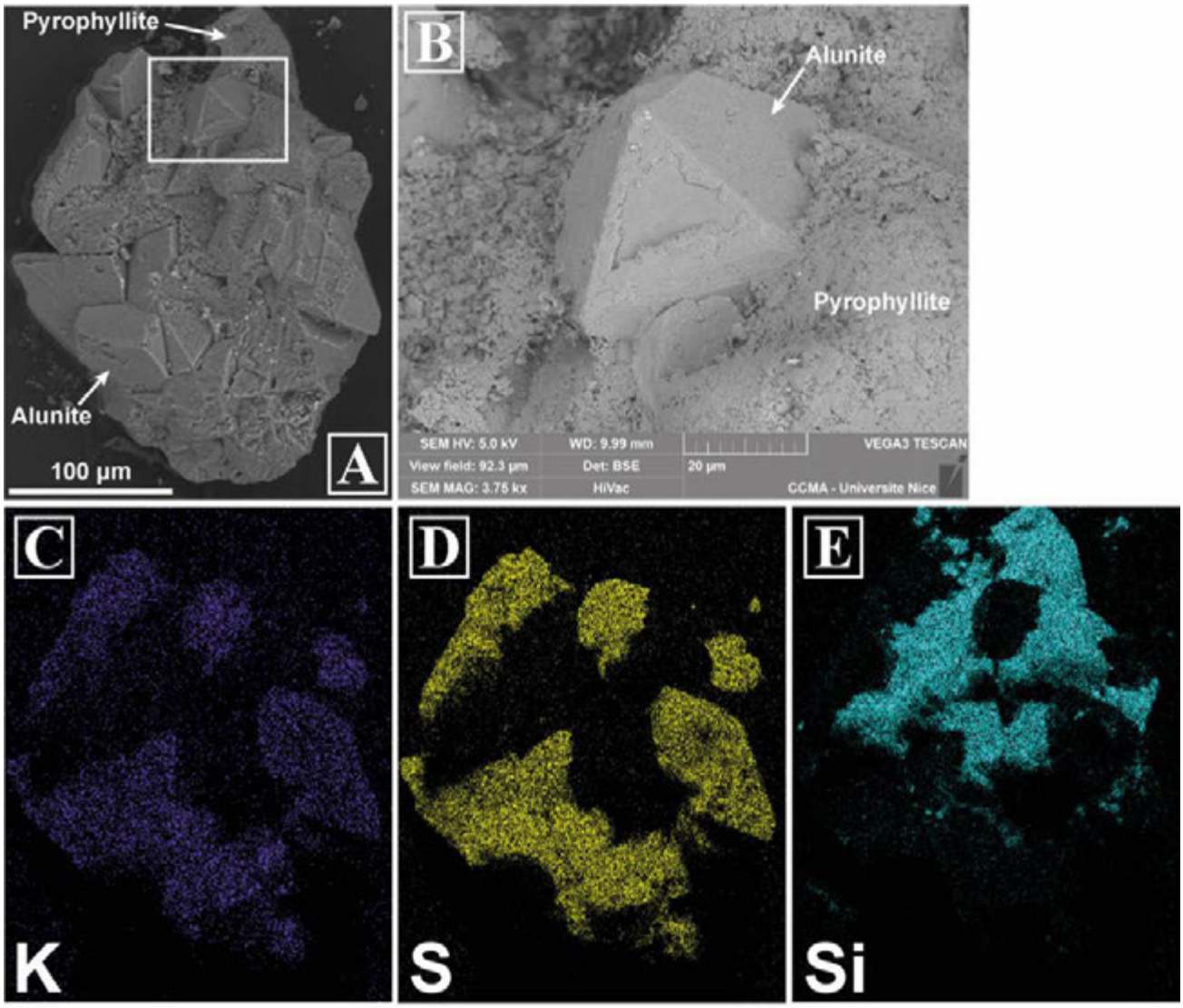


**Figure VI-11 : A) Image en électrons rétrodiffusés (BSE) d'un grain issu de l'échantillon 17PER03. B) Grossissement d'un fragment d'alunite au cœur de pyrophyllite (image BSE). C) Cartographie élémentaire en potassium. D) Cartographie élémentaire en soufre. E) Cartographie élémentaire en silicium.**

Afin de purifier les fractions en éliminant ces phases siliceuses contaminantes, nous décidons de procéder à un traitement à l'acide sur nos fractions à l'aide d'acide fluorhydrique (HF 10%) chauffé. L'aspect des grains a été modifié suite à cette attaque acide (Figure VI-12**,** Figure VI-13**-A)**, ils sont toujours blancs mais ont perdu de leur transparence et semblent plus grumeleux.

Afin de vérifier si la purification des grains a fonctionné nous procédons à nouveau à des cartographies élémentaires au MEB. Il est à présent possible de constater que les phases siliceuses ont été éliminées, seules les alunites ont été conservées, la cartographie du silicium ne donnant aucun résultat (Tableau VI-3**,** Figure VI-13**-B-C)**. Le risque de contamination par une autre phase minérale est donc éliminé.

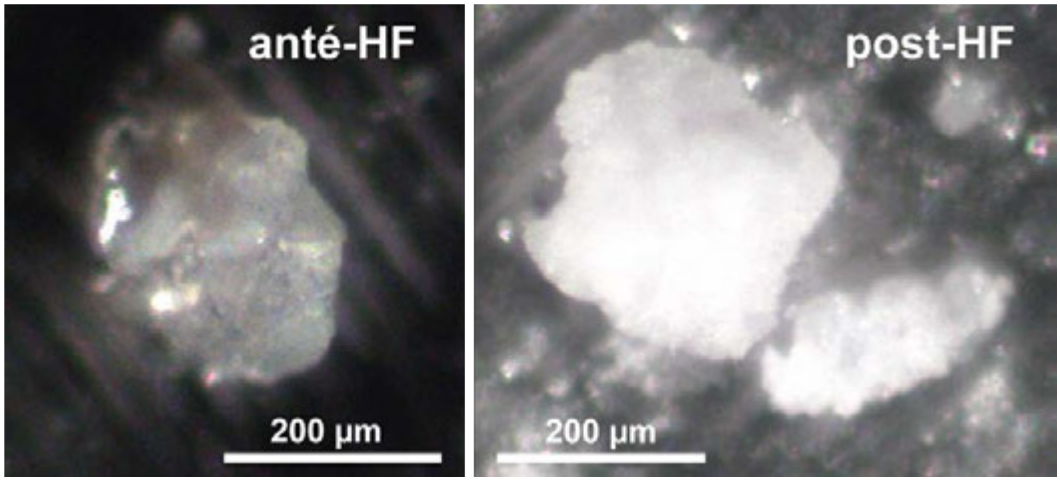


**Figure VI-12 : Grains issus de l'échantillon 17PER03 avant (à gauche) et après (à droite) traitement à l'acide fluorhydrique.**

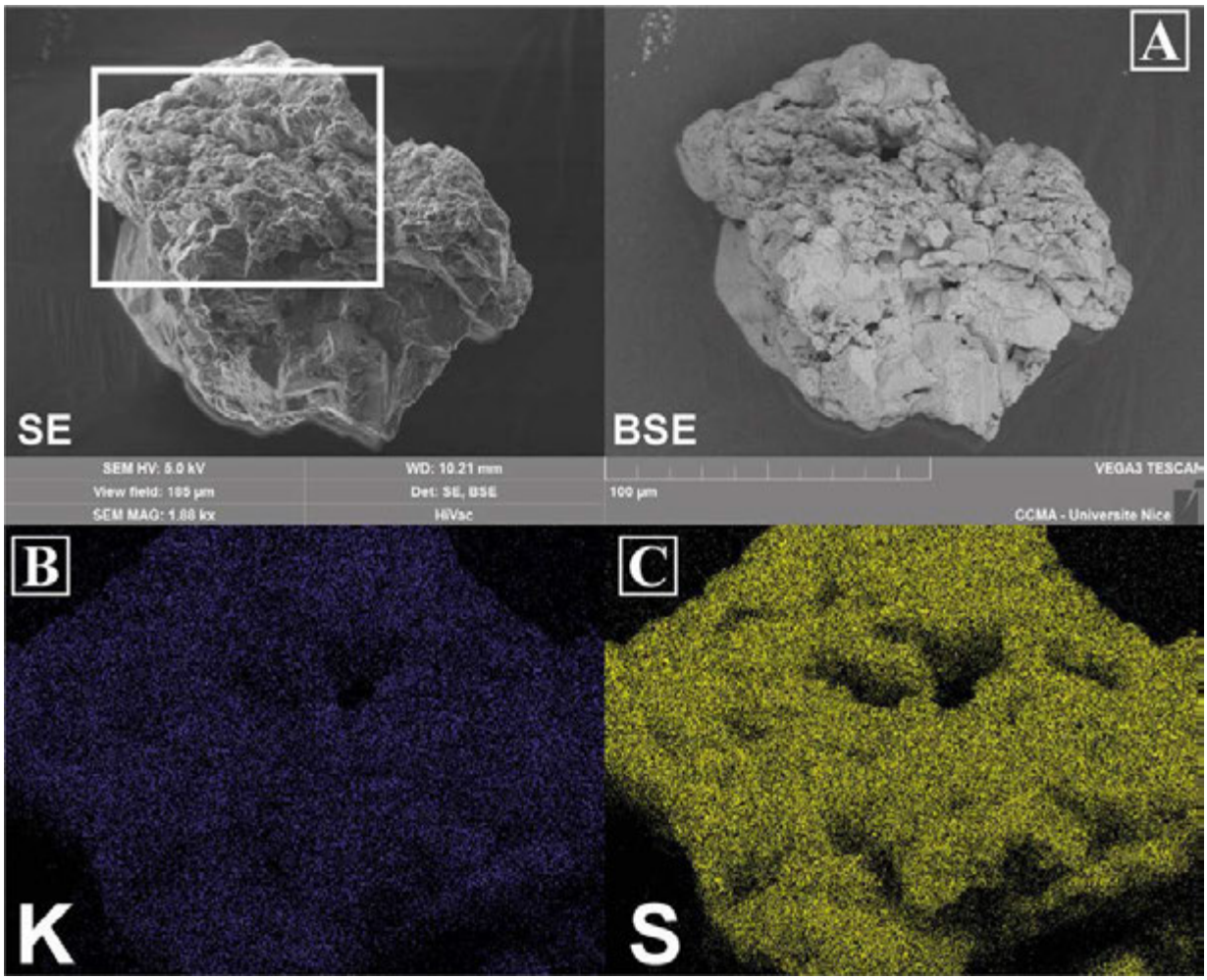


**Figure VI-13 : A) Image en électrons secondaires (SE, à gauche) et en électrons rétrodiffusés (BSE, à droite) d'un grain issu de l'échantillon 17PER03 après un traitement à l'acide fluorhydrique. B) Cartographie élémentaire en potassium. C) Cartographie élémentaire en soufre.**

5) Populations d'alunites

Nos deux fractions 100-200 µm et >200 µm nous ont permis d'obtenir des populations de grains d'alunites dont les poids respectifs sont de 658 mg et de 160 mg.

Nous choisissons de poursuivre nos investigations sur la fraction ayant le poids le plus important, c'est-à-dire au niveau de la fraction 100-200 µm, afin de pouvoir procéder à la fois à la datation de cette phase minérale et aux analyses isotopiques sur la même fraction granulométrique.

### VI.4.3.Datation K-Ar et analyses isotopiques

Afin de dater ces populations d'alunites nous avons choisi la méthode K-Ar plutôt que la méthode $^{40}Ar$-$^{39}Ar$ pour différentes raisons :

- Considérant l'âge estimé (< 1Ma) de cette phase potassique, nous avons besoin d'utiliser une méthode de datation absolue adaptée aux âges jeunes, pouvant mesurer de faible teneur en $^{40}Ar$. La rétention d'argon dans l'alunite supergénique à grains fins est similaire à celle de l'alunite hypogène à cristaux plus grossiers, ce qui permet de confirmer la fiabilité de l'utilisation de la méthode de datation K-Ar pour cette phase minérale (Itaya *et al.*, **1996**).
- L'hypothèse de l'âge jeune estimé nous contraint à analyser des quantités de populations d'alunites conséquentes (~300 mg) afin d'obtenir un signal d'argon radiogénique assez important. Dans le cadre de la méthode K-Ar les quantités analysées sont classiquement de l'ordre du gramme, alors que pour la méthode $^{40}Ar$-$^{39}Ar$ les quantités analysées ne dépassent pas quelques milligrammes pour les populations.
- Par ailleurs, au vu des âges attendus et de la quantité nécessaire, la présence de soufre en grande quantité est un frein à la mise en œuvre d'analyses $^{40}Ar$-$^{39}Ar$. En effet, la ligne d'extraction-purification des spectromètres Ar-Ar n'est généralement pas conçue pour analyser des sulfates en grande quantité. Il y a un risque de diminution de la vitesse de pompage au niveau des getters en cas de formation de $H_2SO_4$ dans la ligne (Itaya *et al.*, **1996**). Ceci peut entraîner une pollution non négligeable au niveau du spectromètre de masse lors du dégazage d'argon se produisant lors du chauffage de l'échantillon en compromettant souvent la qualité des analyses suivantes.
- Par ailleurs, la méthode de datation K-Ar ne nécessite pas d'irradiation des échantillons au préalable, cela permet de réduire la durée du protocole d'analyse (< 3 mois) et d'obtenir une mesure rapidement à un coût réduit par rapport à celui de la méthode $^{40}Ar$-$^{39}Ar$.

*VI.4.3.a. Résultat de la datation K-Ar sur la fraction K-Ar 100-200 µm d'alunites*

Après avoir effectué la séparation minérale au sein du laboratoire Geoazur, la population de grains d'alunites issues de la fraction 100-200 µm a été envoyés au sein du service de géochronologie d'Activation Laboratories (Actlabs) situé à Ancaster en Ontario au Canada pour que ces datations

soient réalisées selon la méthode K-Ar comme décrit ci-après. Nous avons décidé d'effectuer deux mesures (duplicate) sur cette même population de grains d'alunite pour une quantité d'environ 300 mg chacune, selon le protocole décrit ci-après.

Des portions de l'échantillon ont été introduit dans un récipient en aluminium, chargées dans le système d'échantillonnage de l'unité d'extraction, dégazées à ~100°C pendant 2 jours pour éliminer les gaz de surface (l'argon atmosphérique). L'argon est extrait de l'échantillon dans un four à double vide à 1700°C. La détermination de la teneur en argon radiogénique a été effectuée deux fois sur le spectromètre de masse MI-1201 IG par la méthode de dilution isotopique avec $^{38}Ar$ comme spike. Les gaz extraits ont été épurés dans un système de purification en deux étapes. L'argon pur est ensuite introduit dans un spectromètre de masse (de type Reinolds).

Il est à noter que le test a été effectué deux fois par échantillon pour assurer la cohérence du résultat. Pour le calcul de l'âge, les valeurs internationales des constantes ont été utilisées comme suit :

$\lambda_K$=0,581 x $10^{-10}y^{-1}$, $\lambda_{\beta-}$=4.962 x $10^{-10}y^{-1}$, $^{40}K$=0.01167 (at.%).

Deux standards mondialement reconnus (Bern 4M muscovite et la matrice de la rhyolite 1/65 « Asia ») ont permis l'étalonnage par le spike $^{38}Ar$ pour obtenir les résultats présentés en Tableau VI-4. L'âge obtenu est compris entre 151 ± 5 ka et 173 ± 5 ka, calculés avec une erreur de 2 σ.

**Tableau VI-4 : Synthèse des résultats obtenus suite aux datations K-Ar sur une population d'alunites de l'échantillon 17PER03**

| *Sample ID* | *Dated mineral* | *K, % ± σ* | *$^{40}$Ar rad. (ng/g)* | *%$^{40}$Ar air* | *Age, Ma* | *Error 2σ* |
|---|---|---|---|---|---|---|
| *17PER03-1* | alunite population | 3.87 ± 0.04 | 0.0466 | 97.9 | 0.173 | 0.05 |
| *17PER03-2* | alunite population | 3.90 ± 0.04 | 0.0407 | 97.6 | 0.151 | 0.05 |

*VI.4.3.b. Résultat des analyses isotopiques sur les alunites*

Afin de contraindre l'origine des fluides sulfatés à l'origine de la mise en place des alunites dans la brèche étudiée, des mesures isotopiques ont été effectuées au sein du service d'analyses isotopiques d'Activation Laboratories (Actlabs) situé à Ancaster en Ontario au Canada. Ces mesures sur sulfates sont effectuées sur des spectromètres de masse à rapport isotopique de l'oxygène ($^{18}O/^{16}O$, selon Stoffregen *et al.*, **1994**) et du soufre ($^{34}S/^{32}S$, selon Ueda & Krouse, **1986**).

Les mesures des isotopes ont été effectuées en double et une mesure moyenne a ainsi été obtenue, soit pour $\delta^{18}O_{sulfate}$ 16,0‰ (sur un total de 25,4 mg) et pour $\delta^{34}S_{sulfate}$ 11,4‰ (sur un total de 11,4 mg) (Tableau VI-5).

**Tableau VI-5 : Synthèse des résultats d'analyses isotopiques sur les alunites de l'échantillon 17PER03**

| Analyse | $\delta^{18}O_{sulfate}$ (‰) | | | $\delta^{34}S_{sulfate}$ (‰) | | |
|---|---|---|---|---|---|---|
| | original | duplicate | **moyenne** | original | duplicate | **moyenne** |
| *17PER03* | 15,9 | 16,2 | 16,0 | 11,4 | 11,3 | 11,4 |

*VI.4.3.c. Interprétation des résultats*

Au regard des analyses faites sur les alunites (à la microsonde, au MEB en Tableau VI-3, lors de la datation avec la méthode K-Ar en Tableau VI-4), nous remarquons que nous n'obtenons pas la formule structurale d'une alunite pure, mais une composition intermédiaire entre celle d'une alunite et d'une natroalunite (Tableau VI-6). Des minéraux de type natro-alunite avaient également été identifiés sur la Plage de Rocroy dans des études précédentes sans discuter leur origine (Bruzac, **2012**; Gadalia, **2013**).

**Tableau VI-6 : Compositions en pourcentage massique des pôles pures des phases minérales alunite et natroalunite.**

| Composition (% massique) | | |
|---|---|---|
| | **Alunite** | **Natroalunite** |
| **K** | **9,44** | |
| **Na** | | **5,77** |
| Al | 19,54 | 20,33 |
| H | 1,46 | 1,52 |
| S | 15,48 | 16,11 |
| O | 54,08 | 56,26 |

Compte tenu de l'attaque acide appliquée sur notre échantillon, les silicates associés à l'alunite ont été dissous, comme le confirmaient les analyses effectuées au MEB suite à l'attaque à l'HF en indiquant une composition intermédiaire des grains entre les pôles alunite et natroalunite. La valeur du potassium mesuré ($K_{total}$ , Tableau VI-4) sur quelques centaines de milligrammes dans l'échantillon de la fraction granulométrique 100-200 µm utilisé lors de la datation K-Ar, comprise entre 3,87 et 3,90 %, nous indique également une valeur inférieure à celle de l'alunite pure, mais cohérente avec la valeur moyenne de 3,59% obtenue avec les analyses effectuées au MEB post-HF (Tableau VI-3). Ainsi, nous pouvons estimer que la phase minérale présente dans notre échantillon et datée est une solution solide constituée à 41% d'alunite contre 59% de natroalunite.

La substitution du potassium par le sodium sur le site alcalin est significative au sein des alunites naturelles (Stoffregen *et al.*, **2000**). Cette substitution est fréquente à basse température en raison d'une carence en alcalins et d'une présence d'eau en excès (Ripmeester *et al.*, **1986**). Une seconde

substitution peut avoir lieu dans l'alunite, elle est alors couplée au phosphate et peut conduire à la substitution des cations monovalents (Na, K) par des cations divalents (Ca, Sr, Ba) (Allibone *et al.*, **1995**), ceci peut donc expliquer la présence de P, Ca, Sr en traces dans nos analyses (Tableau VI-3).

En principe, dans des conditions idéales (i.e. un système fermé), la datation des produits d'altération (ici une brèche hydrothermale) indique l'âge de l'activité hydrothermale ou de l'événement d'altération, qui est généralement associé à l'événement de minéralisation formant le système de dépôt (Vural, **2017**). La datation de l'âge des minéraux hydrothermaux donne donc l'âge de l'activité hydrothermale associée à la minéralisation (les alunites). Pour la population analysée par la méthode K-Ar, l'âge obtenu sur cette phase minérale sulfatée intermédiaire nous donne donc l'âge de cristallisation et donc l'âge des fluides qui ont circulé et conduit à la formation de cette brèche compris entre 146 et 178 ka.

L'alunite étudiée dans notre échantillon 17PER03 se présente sous la forme d'un minéral d'altération en association avec : kaolinite + quartz ± pyrophyllite, au sein d'une brèche. Cette association est classique des assemblages de l'altération argileuse avancée, et la présence de pyrophyllite témoigne d'une variante de haute-température (Meyer & Hemley, **1967**). Cette phase minérale peut être issue d'une altération supergène de basse-température (Bird *et al.*, **1989**; Stoffregen & Alpers, **1992**), d'une altération hydrothermale (Hemley *et al.*, **1969**; Cunningham *et al.*, **1984**; Bove *et al.*, **1990**), souvent associée à un système géothermal (Raymahashay, **1968**; Schoen *et al.*, **1974**; Aoki, **1983**). La présence d'alunite a également été signalée dans des roches métamorphique de bas degrés qui n'ont pas d'affinités hydrothermales (Wise, **1975**; Schoch *et al.*, **1989**; Ripp *et al.*, **1998**).

Afin de discuter son origine nous intégrons nos résultats dans un graphique $\delta^{18}O_{SO4}$ – $\delta^{34}S_{SO4}$ qui synthétise les différents environnements possibles (Figure VI-14).
Rye et al. (1992) définissent un champ du domaine magmatique-hydrothermal correspondant au dépôt d'alunite à partir d'eau purement magmatique et à une température comprise entre 200 et 400°C, typique des fluides magmatiques. Ce champ est contraint par des rapports $H_2S/SO_4$ compris entre 1 et 8 qui contrôlent l'état redox du système. Considérant les valeurs isotopiques du soufre et de l'oxygène, notre échantillon se situe en dehors de ce champ pour un rapport $H_2S/SO_4$ inférieur à 1. Ces alunites ne sont donc pas issues de fluides purement magmatiques, mais elles ont une affinité hydrothermale, donc hypogène, plutôt que supergène.

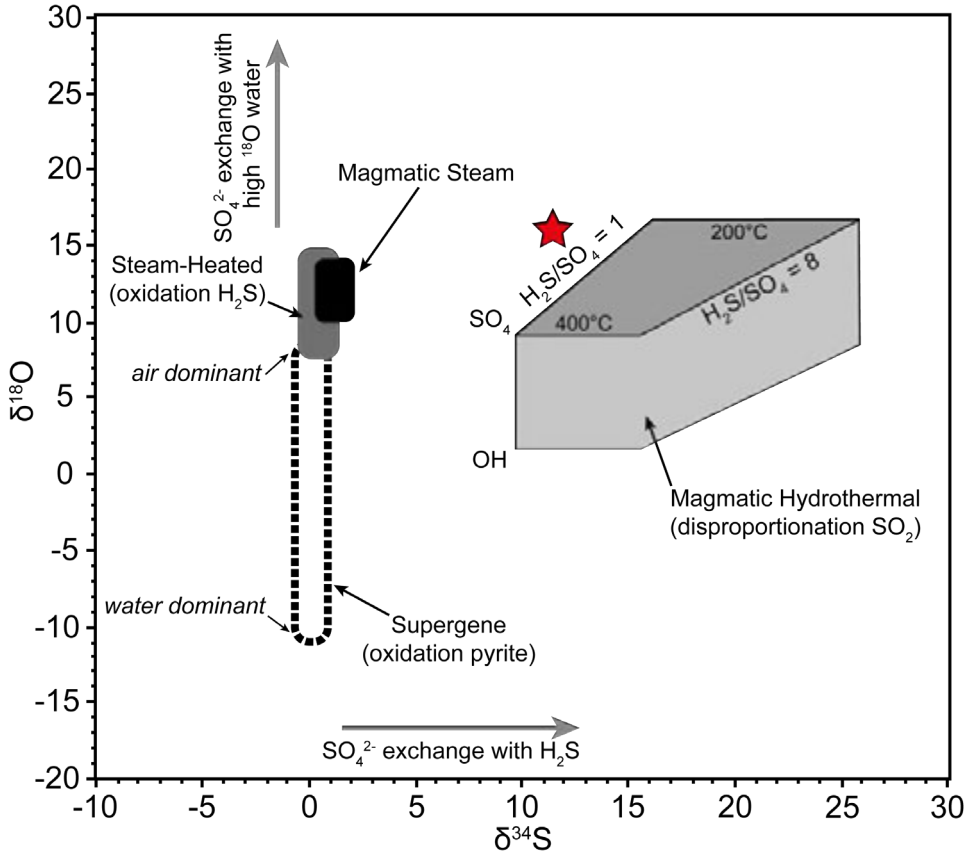


**Figure VI-14 : Valeurs de $\delta^{18}O^{SO4}$ – $\delta^{34}S_{SO4}$ relatifs aux champs soit magmatiques hydrothermaux, soit vapeur magmatique, soit steam-heated, soit supergène relatifs à l'origine des sulfates (d'après Rye *et al.*, 1992; Rye, 2005). L'étoile rouge indique le résultat pour les alunites de l'échantillon 17PER03.**

Nous avons alors voulu tester l'équilibre de l'alunite avec un fluide météorique-hydrothermal ayant un rapport $H_2S/SO_4$ inférieur à 1. Ce rapport indiquant un plus grand degré d'oxydation de ce fluide par rapport au fluide magmatique.

Ce travail a été réalisé en collaboration avec Christophe Renac du laboratoire Geoazur à Sophia-Antipolis. Nous avons cherché à estimer le domaine d'équilibre de l'alunite (hydrothermale) à l'aide du « package » R-CHNOSZ (Dick, **2019**) pour les associations minérales du champ de Rocroy. Dans un premier temps les températures et le pH ont été estimés. Par la suite le logiciel PHREEQC interactive version 3.5 (Charlton & Parkhurst, **2011**; Parkhurst & Appelo, **2013**) a été utilisé. Ce dernier permet d'estimer la composition d'un fluide en équilibre avec les associations de minéraux, dans différentes conditions de température et de pression (pression hydrostatique).

Suivant la première étape, l'alunite seule précipite à des conditions à l'équilibre à des pH très supérieurs à 9 et des températures comprises entre 100 et 300°C. Cependant la préservation du quartz à proximité des alunites est difficilement compatible avec la circulation d'un fluide basique (Knauss & Wolery, **1988**).

Nous avons donc fixé un assemblage correspondant à celui observé dans l'échantillon étudié : alunite+kaolinite+quartz+pyrophyllite. Cet assemblage est alors stable pour des températures similaires à celles obtenues précédemment (150-300°C) et pour des pH compris entre 6,6 et 4,9. Ces fluides à pH plutôt acides à neutres peuvent provenir d'infiltration d'eau de pluie mais ces fluides ne contiennent pas de soufre. Ces fluides infiltrés se chargent en sulfate en profondeur. Donc ce sont bien des fluides météoriques hydrothermaux récupérant une composante soufrée du système magmatique qui sont impliqués dans cette évolution. En effet, les conditions supergènes, en sub-surface, ne dépassent pas les 50°C.

Les domaines de températures calculés et les valeurs isotopiques semblent donc indiquer un domaine hypogène. Celui-ci n'est pas strictement à l'équilibre dans un environnement magmatique hydrothermal, il subit l'influence d'un dégazage (magmatic steam ou steam heated) avec une perte de $SO_2$ et $CO_2$ dissous sous forme de gaz.

Cette influence est confirmée par l'analyse des constituants de la perte au feu de notre échantillon (Carignan *et al.*, **2001**), présenté en Tableau VI-2, indiquant une estimation de la composition d'un fluide à 86,45 % d'$H_2O$, 9,35 % de S (soit $SO_2$), 3,27 % de $CO_2$ et 0,93 % de FeO.

### VI.4.4. Lien entre l'activité volcanique et géothermale du système actif de l'île de la Basse-Terre

La formation de cette brèche hydrothermale de Rocroy est issue d'environnement en présence de fluides hypogènes acides, oxydés et riches en sulfates de type « acid-sulfate » en lien avec une altération argileuse avancée formée à haute-température (150-300 °C). Cette brèche se compose d'un assemblage minéralogique à alunite + kaolinite + quartz ± pyrophyllite. Cette manifestation hydrothermale s'est mise en place au cœur d'un système de failles N30-N50 et N80-N100. L'âge de l'activité hydrothermale associée aux alunites est à présent daté entre 146 et 178 ka par la méthode K-Ar.

Il est important de confronter nos résultats à ceux obtenus sur le système de Bouillante. La brèche hydrothermale de Bouillante se situe à l'intersection entre trois systèmes de failles : N30-N50, N80-N100 et N150-N180 (Figure VI-8**-A,** Bouchot *et al.*, **2010**; Thinon *et al.*, **2010**; Calcagno *et al.*, **2012**). Elle se compose d'une altération potassique présentant un assemblage minéralogique à feldspath potassique de type adulaire + quartz + pyrite, issue de la circulation de fluides hypogènes neutres et réduits de haute-température (> 200 °C). Ce système est décrit comme pauvre en sulfate, bien qu'un second assemblage postérieur soit issu d'une altération argileuse avancée avec la présence de jarosite et de gypse. Enfin un troisième assemblage issu de l'altération argileuse est composé d'illite, smectite

et de calcite (Patrier *et al.*, **2013**). Cette activité hydrothermale a été datée à partir des adulaires à 248 ± 50 ka par la méthode $^{40}Ar/^{39}Ar$ (Verati *et al.*, **2014**).

Ces deux manifestations hydrothermales sont localisées dans le complexe volcanique de la Chaîne Axiale datée entre 1,02 Ma et 410 ka (Blanc, **1983**; Carlut *et al.*, **2000**; Samper *et al.*, **2007**; Ricci *et al.*, **2015a**, **b**, **2017**). Pourtant l'âge de leurs activités hydrothermales est concordant avec l'activité volcanique des complexes Grande-Découverte-Soufrière (GDVC) et pré-GDVC compris ente 310 ka et l'actuel (Blanc, **1983**; Carlut *et al.*, **2000**; Samper *et al.*, **2007**, **2009**; Ricci *et al.*, **2017**) comme l'hypothèse précédemment avancé par Verati et al. (**2014**).

Nous proposons une coupe transversale N-S d'une partie de l'île de la Basse-Terre illustrant les relations entre les complexes volcaniques, les structures fragiles et la localisation de ces brèches hydrothermales (Figure VI-15).

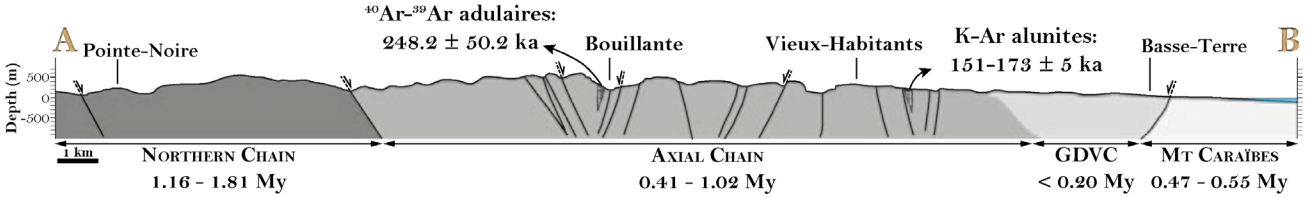


**Figure VI-15 : Coupe NNW-SSE de l'île de la Basse-Terre montrant la distribution spatio-temporelle des structures fragiles, des brèches hydrothermales et des complexes volcaniques (le résultat Ar-Ar d'après Verati *et al.*, 2014 et le résultat K-Ar provenant de cette étude). Trait de coupe localisé sur la figure VI-8-A.**

Par ailleurs, la composition de ces brèches est semblable à ce qui est décrit dans les systèmes épithermaux couramment associés aux centres magmatiques, combinant une infiltration de fluides magmatiques et une infiltration de fluides météoriques et oxygénés à faible profondeur et à une température comprise entre 50 et 200°C (Park & MacDiarmid, **1970**). Les sources chaudes et les paléo-systèmes géothermaux associés à ces dépôts sont classés en deux types principaux de degrés de sulfidation (Heald *et al.*, **1987**; Hedenquist, **1987**; Hedenquist *et al.*, **2000**) :

- Forte teneur en soufre ou *high-sulfidation* : ces dépôts se forment dans l'encaissant de roches siliceuses lixiviées par la circulation de fluides hypogènes acides, aussi appelés *acid-sulfate*, générés dans un environnement volcano-hydrothermal. Les roches se composent d'une association minéralogique à alunite-kaolinite-quartz. Ce type de système indique une forte oxydation du milieu, classique des fluides hypogènes acides. Ils sont issus d'un volcanisme de type rhyodacitique à rhyolitique. Les fluides près de la surface peuvent atteindre des températures de 200 à 300 °C, et sont enrichis en $SO_2$, HCl et NaCl. Il n'y a pas de réaction

entre les fluides et la roche encaissante, et ces dépôts témoignent d'une remontée rapide des fluides.

- Faible teneur en soufre ou *low-sulfidation* : ces dépôts indiquent des fluides hypogènes semblables à ceux piégés dans les sources chaudes des systèmes géothermaux. Les roches se composent d'une association minéralogique à adulaire-séricite-calcite. Ce type de système indique un milieu réducteur, les minéraux ainsi formés à partir de fluides à pH neutre, $H_2S$ en solution sert de ligand aux métaux (Au, Ag). Ils sont issus d'un volcanisme de type andésite (chlorite) ou rhyolite (séricite), en fonction d'un rapport séricite/chlorite.

Il semblerait donc qu'à Bouillante nous soyons en présence d'un système épithermal de type *low-sulfidation*, alors qu'à Rocroy il s'agit d'un système épithermal de type *high-sulfidation*.
Nous sommes donc en présence d'un système épithermal distal à l'échelle de l'île de la Basse-Terre. Dans ce type de système épithermal, les fluides initialement acides tendent à évoluer vers une neutralisation (Smith *et al.*, **2017**).

# Chapitre VII : Discussion des résultats obtenus

*Vue sur l'Anse du Bourg et le Chameau depuis le fort Napoléon*

*Île de Terre-de-Haut, Les Saintes*

L'objectif général du travail effectué dans le cadre de cette thèse était de caractériser l'évolution spatio-temporelle de l'hydrothermalisme au niveau de la plaque supérieure de l'arc des Petites-Antilles en Guadeloupe, et ses implications en terme de ressource géothermale et de fonctionnement des parties profondes des réservoirs de haute-énergie. Au terme de ces investigations, un certain nombre de résultats méritent d'être soulignés et discutés.

## VII.1. Hydrothermalisme et rhéologie de la croute supérieure de l'arc volcanique des Petites Antilles en Guadeloupe

En synergie avec une partie des doctorants impliqués dans le projet GEOTREF et à partir des données existantes, nous avons contribué tout d'abord à améliorer la cartographie structurale de l'île de la Basse-Terre. C'est ainsi qu'une carte de haute-résolution a été réalisée à l'échelle du PER, afin d'avoir un état des connaissances des données de structures tectoniques actuelles en surface au niveau de la zone d'intérêt. Ces données ont été présentées au sein des Chapitre IV : et Chapitre VI :. Elles permettent de présenter une carte volcano-tectonique de la région Ouest de l'archipel de Guadeloupe (Figure VII-1), avec la localisation des différents complexes volcaniques dont des âges et des limites ont été en partie ré-actualisés.

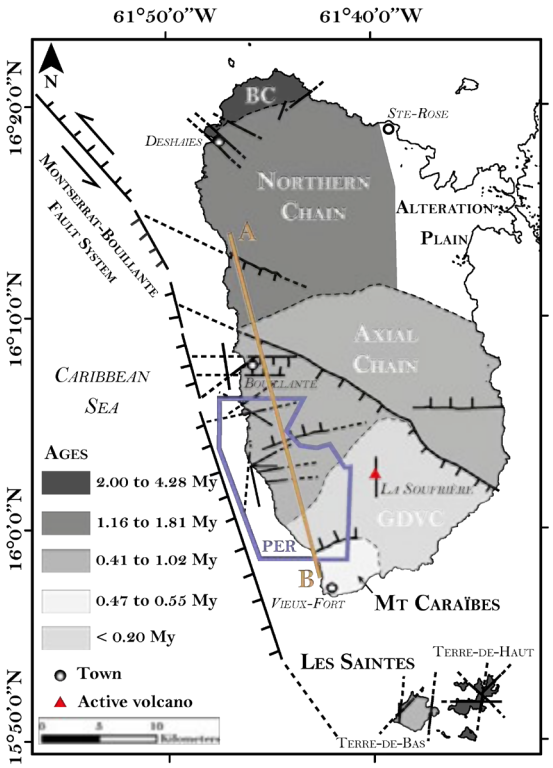


**Figure VII-1 : Carte de l'arc volcanique actif de l'archipel de Guadeloupe (l'île de la Basse-Terre et l'archipel des Saintes) illustrant les différents complexes volcaniques et les principales structures tectoniques identifiées (modifié d'après Verati *et al.*, 2018, BC = Basal Complex, PER = Permis Exclusif de Recherche).**

Afin d'étudier l'évolution thermomécanique des roches en contexte d'arc volcanique au cours du temps nous nous sommes concentrés sur la caractérisation de la minéralogie et des structures du complexe volcanique le plus ancien de l'île (le Complexe Basal). Ceci nous a ainsi permis de mettre en évidence :

- L'existence d'un métamorphisme hydrothermal de bas degré (faciès de type Schiste-Vert-Sub-Schiste-Vert à Zéolite, Figure VII-2) lié au fonctionnement même de l'arc volcanique en Guadeloupe,
- Un nouvel âge maximal de l'activité volcanique du Complexe Basal, avec la datation du Gros Morne de Deshaies à 4,28 ± 0,34 Ma, qui implique que ce métamorphisme hydrothermal soit actif depuis au moins quatre millions d'années,
- La mise en évidence d'une température comprise entre 250 et 300 °C à faible profondeur (3-4 km).

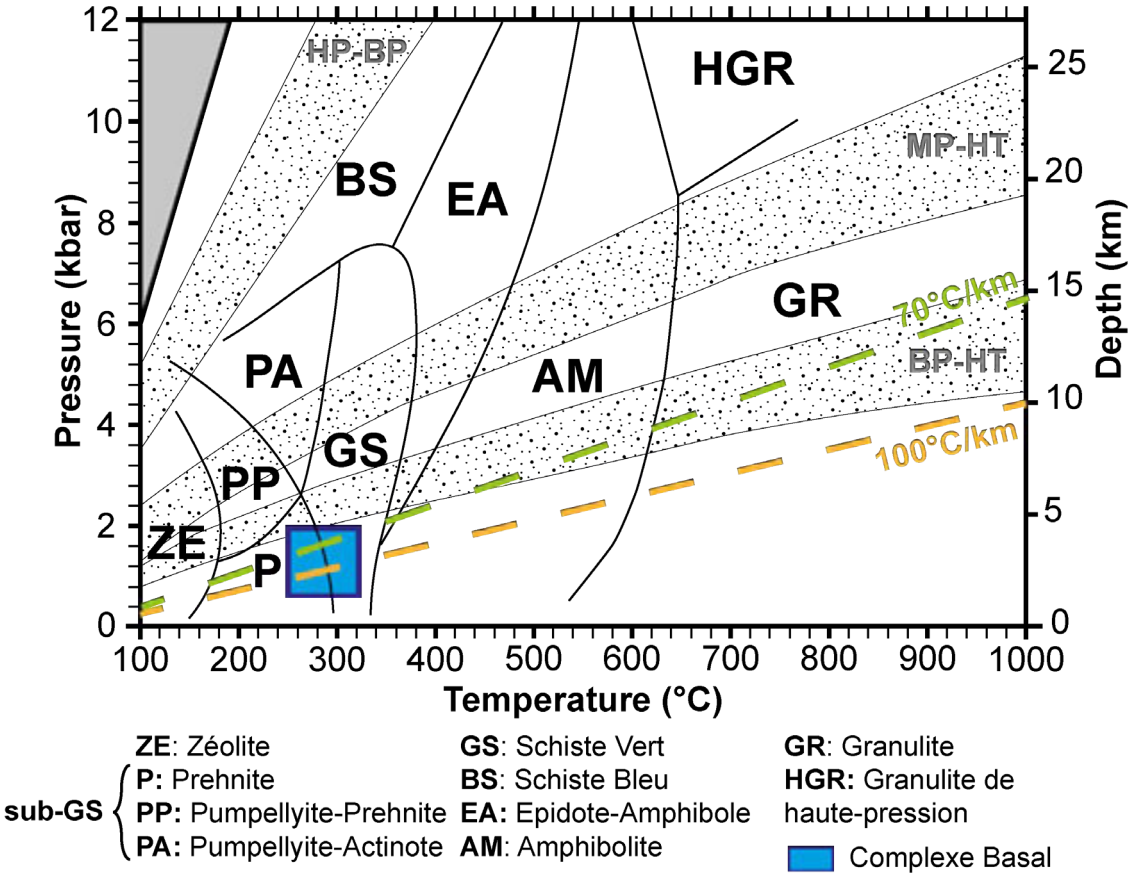


**Figure VII-2 : Faciès métamorphiques identifiés dans le Complexe Basal (limites des faciès modifié d'après Liou, 1987, gradients de température moyens entre 70 et 100°C/km d'après Manga *et al.*, 2012). Le rectangle bleu localise le pic métamorphique du Complexe Basal (La profondeur a été estimée à partir de la densité d'une rhyodacite fraîche comprise entre 2,2 et 2,3 g/cm³, d'après Klein & Johnson, 1983).**

Cette découverte a des conséquences importantes sur le comportement rhéologique des parties superficielles de la croûte de l'arc :

- Il existe à faible profondeur des structures tectoniques ductiles, de type schistosité de dissolution, contrôlées par les circulations de fluides sous contrainte (mécanisme de dissolution-recristallisation),
- La profondeur de la transition « fragile-ductile », qui dans une croûte continentale stable thermiquement est située de façon standard entre 12 et 15 kilomètres, doit être estimée entre 3 et 4 kilomètres dans une croûte d'arc actif. La position superficielle de transition rhéologique est alors le résultat de la combinaison d'un gradient thermique anormalement élevé et de l'action des fluides hydrothermaux sur les mécanismes de déformation des minéraux. (Figure VII-3).

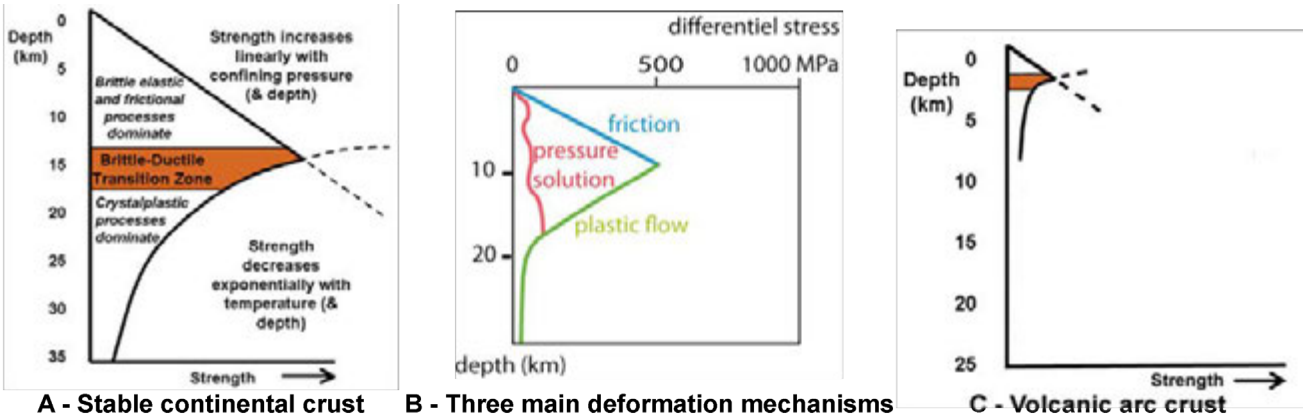


**Figure VII-3 : Diagrammes de l'évolution de la résistance mécanique de la croûte en fonction de la profondeur : A) En condition « standard », une croûte continentale standard montre une transition fragile-ductile aux alentours de 15 km (modifié d'après Sibson, 1984; Lachenbruch & Sass, 1992; Ranalli, 1995), B) Concurrence entre les trois mécanismes de déformation principaux de la croûte (Gratier *et al.*, 2013) : le régime de friction (en bleu), le régime sous pression fluide élevé avec un fluage contrôlé par la pression-dissolution qui diminue la résistance à la friction (en rose) et le régime de déformation plastique (en vert), C) En contexte d'arc volcanique, soumis à un gradient géothermique élevé contemporain de la circulation de fluides hydrothermaux, la transition fragile-ductile est située à faible profondeur (aux alentours de 3-4 km dans notre cas, d'après Ranalli & Rybach, 2005).**

En Guadeloupe, avec des températures de l'ordre de 300°C à 4 kilomètres de profondeur, la circulation de fluides hydrothermaux sous contraintes va favoriser le comportement plastique des minéraux, même à faible profondeur, en diminuant leur résistance au cisaillement (Gratier *et al.*, **2013**).

En conséquence, les structures fragiles sub-verticales identifiées en surface (Figure VII-4-**A**) sont nécessairement relayées par des couloirs schisteux qui s'enracinent sur l'horizon de la transition rhéologique (Figure VII-4-**B**). Cela nous permet d'envisager comment la géométrie des failles

normales, observées et mesurées en surface, évolue avec la profondeur. Deux coupes comparées illustrent cette évolution des structures tectoniques avec la profondeur au niveau de l'île de la Basse-Terre (Figure VII-4).

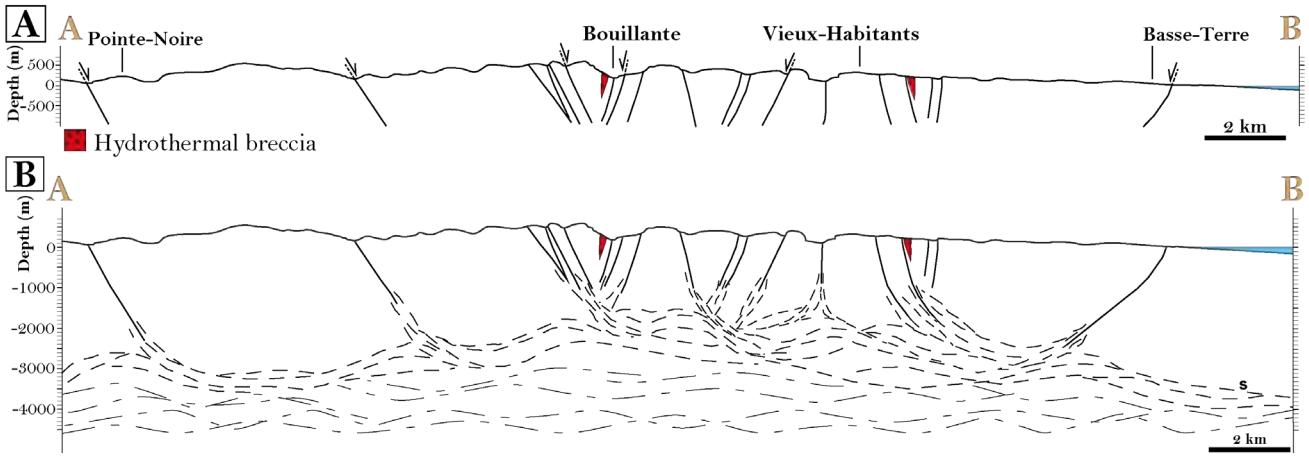


**Figure VII-4 : Coupe NNW-SSE localisée en figure VII-1. A) Représentation des structures tectoniques fragiles et des brèches identifiées en surface. B) Ajout des structures tectoniques ductiles avec la localisation de la transition fragile-ductile en profondeur à partir de 3-4 km.**

Grace à des mesures de flux de chaleur régional actuel effectuées à proximité de l'archipel de Guadeloupe, le gradient géothermique conductif est estimé entre 70,0 et 98.2 ± 8.8 °C/km (Manga *et al.*, **2012**). Les mesures effectuées sur nos échantillons nous ont permis de déterminer un paléo-gradient identique pour le Complexe Basal. Il semblerait donc que le flux de chaleur régional soit stable depuis les quatre derniers millions d'années. Le gradient géothermique conductif est donc stable avec une transition rhéologique située entre 3 et 4 km de profondeur à l'échelle de l'île de la Basse-Terre (Figure VII-5).

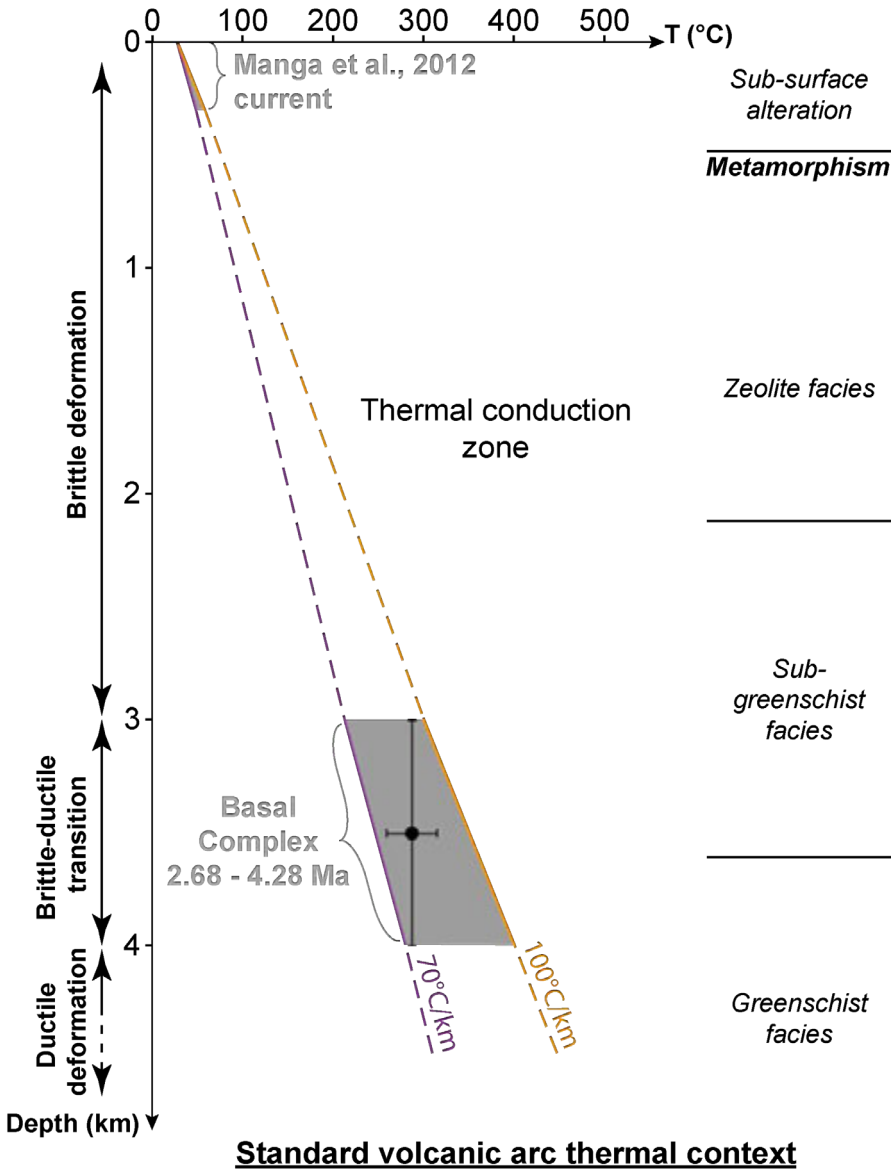


**Figure VII-5 : Evolution de la température avec la profondeur dans l'arc volcanique en Guadeloupe. Implications en termes de rhéologie, de régime de transfert de la chaleur et de distribution spatiale des faciès métamorphiques.**

## VII.2. Apport de l'étude d'analogue exhumé au fonctionnement des systèmes géothermaux de l'arc volcanique de Guadeloupe

L'étude de l'analogue exhumé (paléo-réservoir) sur l'île de Terre-de-Haut (Les Saintes), et dont les résultats sont décrits au sein des Chapitre V : et Chapitre VI :, nous a permis de mettre en évidence :

- La présence de structures tectoniques fragiles et ductiles superposées,
- La présence de transformations hydrothermales de haute-température, dont les assemblages minéralogiques correspondent au faciès des Schistes Verts, ainsi que des phases

hydrothermales de plus basse-température indiquant un refroidissement de la structure au cours du temps.

- Des transformations minéralogiques très variées, les plus abondantes en terme de nombre de phases néo-formées, sont issues de roches volcaniques initialement rhyodacitique à dacitique,
- Une température bien plus élevée qu'à Bouillante : 350-380°C entre 1,7 et 2,7 km (Figure VII-6).
- Un âge de la phase hydrothermale de haute température à 2,59 ± 0,12 Ma, nous permet d'estimer une durée de fonctionnement maximale du paléo-système géothermal à 650 ka.

La caractérisation de ce paléo-réservoir nous a permis de mieux comprendre la composition et le fonctionnement des parties profondes (entre 1,7 et 2,7 km) d'un réservoir géothermal de haute-énergie, dans le contexte de l'arc volcanique de Guadeloupe (Figure VII-6).

La température, mesurée au niveau du paléo-réservoir de Terre-de-Haut apparaît comme bien plus élevée que celle connue à Bouillante et implique la présence d'une forte anomalie du régime thermique il y a 2,6 Ma. Par ailleurs l'étude des minéralisations hydrothermales révèle des assemblages minéralogiques stables dans les conditions du faciès des Schistes Verts, en conditions saturées en fluides de haute température, drainés par des couloirs schisteux permettant la mise en place d'un système convectif conduisant à l'homogénéisation de la température dans le réservoir en profondeur (Figure VII-6).

Si nous comparons ces données au modèle de fonctionnement général proposé par Guillou-Frottier (**2003**) pour le réservoir de Bouillante, il faut alors considérer qu'il a existé en Guadeloupe des systèmes géothermaux de plus haute température que celui connu aujourd'hui et impliquant le développement d'une cellule convective jusqu'à des profondeurs plus importantes que celle proposée à Bouillante.

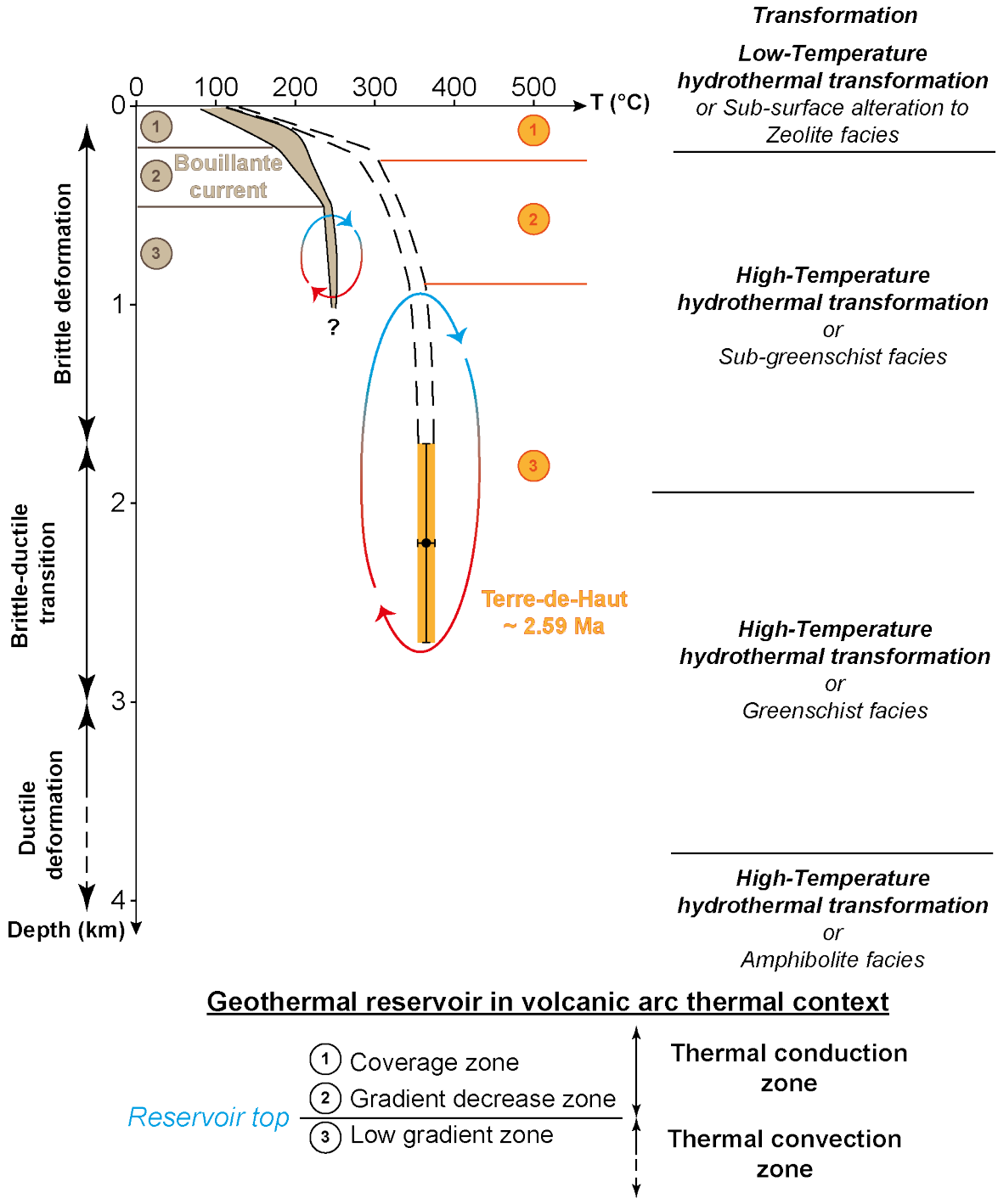


**Figure VII-6 : Evolution de la température avec la profondeur dans un contexte thermique perturbé par la convection dans un système géothermal, et leurs implications en terme de rhéologie, de régime de transfert de la chaleur et de faciès métamorphiques. Les données au niveau de Bouillante sont issues de mesures effectuées en puits par le BRGM (Guillou-Frottier, 2003).**

Par ailleurs, et c'est sans doute l'un des résultats les plus importants de cette étude, la structure des parties profondes des réservoirs géothermaux est caractérisée par la connexion de zones de transferts verticales et horizontales des fluides hydrothermaux. Cela nous conduit à proposer un modèle conceptuel de fonctionnement d'un réservoir géothermal en contexte d'arc volcanique (Figure VII-7).

En surface, les failles et les structures volcaniques permettent la recharge du système en fluides superficiels. En profondeur les fluides superficiels sont mélangés avec des fluides hydrothermaux d'origine volcanique conduisant à la mise en place d'un système convectif. Les transferts de fluides s'effectuent alors verticalement et latéralement grâce à des structures tectoniques ductiles (couloirs schisteux) et fragiles (failles). De plus, les circulations des fluides s'effectuent également le long des discontinuités géométriques d'origine volcanique (limites de coulées, fluidalité magmatique, limites de filons, …).

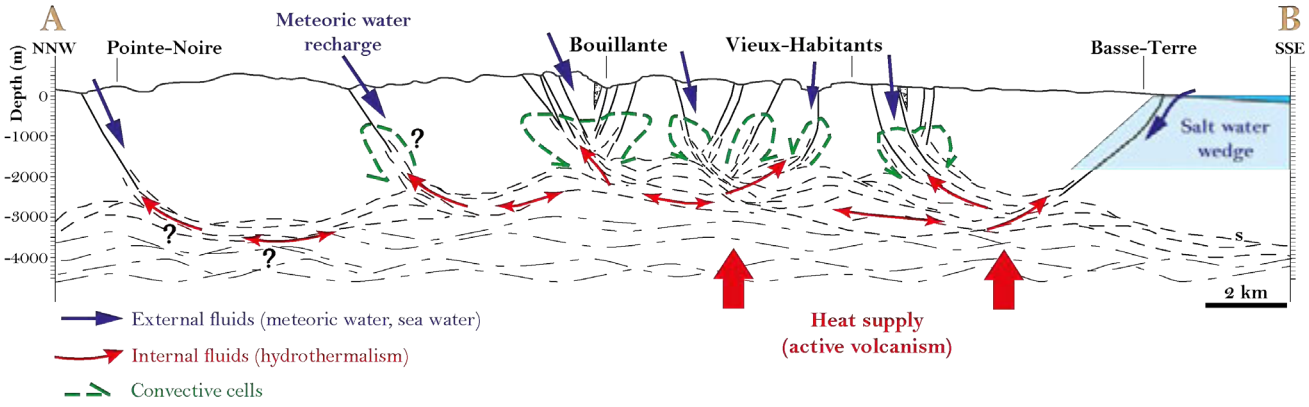


**Figure VII-7 : Modèle conceptuel des parties profondes du réservoir géothermal actif présent sous l'île de la Basse-Terre. Trait de coupe localisé en figure VII-1.**

Une des conséquences d'un tel modèle est que la ressource géothermale de haute-énergie dans l'arc volcanique de Guadeloupe pourrait être plus importante et de plus grande distribution spatiale que ce qui est envisagé jusqu'à présent.

## VII.3. Le système géothermal de Guadeloupe : évolution spatio-temporelle de l'hydrothermalisme et comparaison avec les systèmes métallogéniques

### VII.3.1. Distribution spatiale des contraintes temporelles dans l'arc récent de Guadeloupe

Afin de pouvoir interpréter l'évolution d'un système géothermal nous avons besoin de contraintes pétrologiques, structurales et temporelles. Pour cela il nous faut identifier des phases minérales néoformées (syn-tectoniques) et contemporaines de l'activité hydrothermale pour délimiter le réservoir et en déterminer l'âge et la durée de vie. Ces résultats ont été présentés au cours du Chapitre VI :.

Les contraintes temporelles sont délicates à acquérir pour différentes raisons. Les systèmes volcaniques actifs étant très jeunes (< 1Ma), la datation de l'activité géothermale associée nécessite d'une part d'identifier des phases minérales datables par des méthodes géochronologiques adaptées

et d'autre part d'en séparer des quantités importantes. Cela nécessite de mettre au point et de développer des méthodes spécifiques d'identification et de séparation de ces phases.

Dans l'arc volcanique de l'archipel de Guadeloupe nous disposons à présent de données chronologiques à la fois volcaniques et hydrothermales. Les contraintes temporelles présentées sur la carte en Figure VII-1 et la coupe en Figure VII-8 combinent les données de la littérature et les nouvelles données chronologiques acquise durant cette étude à savoir : l'âge du volcanisme au niveau du Complexe Basal et l'âge de la brèche hydrothermale de Rocroy située dans le périmètre du PER.

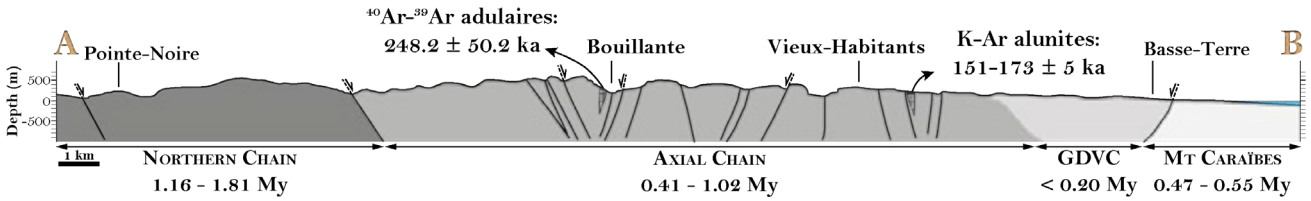


**Figure VII-8 : Coupe NNW-SSE, localisée en figure VII-1, montrant la distribution spatio-temporelle des structures fragiles et des brèches hydrothermales identifiées (le résultat Ar-Ar d'après Verati *et al.*, 2014 et le résultat K-Ar provenant de cette étude), ainsi que les complexes volcaniques de l'île de la Basse-Terre.**

Les âges des brèches hydrothermales de Rocroy et de Bouillante, situées au cœur de la Chaîne Axiale, sont vraisemblablement contemporaines de l'âge du système volcanique actif de Grande-Découverte-Soufrière (GDVC). La province géothermale de la Basse-Terre de Guadeloupe est alors un système de transfert de fluides et de chaleur distal du système volcanique actif aujourd'hui. C'est l'équivalent d'un système métallogénique de type « gîtes épithermaux Au-Ag » associés au volcanisme en contexte d'arc magmatique.

Ces nouvelles données nous montrent l'importance de l'acquisition de données temporelles sur l'hydrothermalisme dans les systèmes volcaniques pour comprendre l'origine de leurs mises en place et leurs évolutions au cours du temps.

### VII.3.2. Brèches hydrothermales et systèmes épithermaux

Les brèches hydrothermales de Bouillante et de Rocroy ont des significations différentes en termes de fluides, de compositions minéralogiques et chimiques, d'environnements et d'âges. La minéralogie de ces dépôts est contrôlée par un degré de sulfidation différent et représentent deux environnements géothermaux distincts (Heald *et al.*, **1987**; Hedenquist *et al.*, **2000**).

Au niveau de la brèche de Rocroy, il s'agit d'un gîte épithermal de type *high-sulfidation* (HS) ou *acid-sulfate*, marqué par des assemblages minéralogiques à quartz-alunites et dominé par des altérations de type argileuses avancées (Hedenquist *et al.*, **2000**; Jensen & Barton, **2000**) avec des fluides hypogènes acides riches en $Cl^-$ et $SO_4^{2-}$, dérivés d'une source magmatique, présentant une salinité

faible à modérée. Ce type de dépôts est généralement présent près de la surface à une profondeur inférieure à 1,5 km, pour une température comprise entre 150 et 300°C (Hedenquist & Lowenstern, **1994**). La présence de ces fluides acides complexifie l'exploitation de la ressource géothermale et demande une certaine adaptation des méthodes classiquement employées (Bogie & Lawless, **2000**).

A Bouillante, il s'agit d'un gîte épithermal de type *low-sulfidation* (LS) marqué par un assemblage minéralogique à adulaire-séricite et donc dominé par une altération potassique à argileuse avec des fluides alcalins chlorurés sodiques presque neutres et de très faible salinité, à une température de 250-260°C (Lachassagne *et al.*, **2009**; Patrier *et al.*, **2013**). Ce type de classification avait déjà été proposé pour ce site par des études précédentes (Bouchot & Genter, **2009**; Patrier *et al.*, **2013**). Ces dépôts sont généralement présents près de la surface jusqu'à une profondeur de 1 à 2 km, pour une température comprise entre 150 et 300°C et marquent une forte perméabilité typique des réservoirs géothermaux, ce qui en fait une cible idéale pour l'exploitation de la ressource (Hedenquist & Lowenstern, **1994**; Bogie & Lawless, **2000**).

L'identification de ces brèches hydrothermales témoigne d'une ébullition du fluide, dans le réservoir ou le système hydrothermal, entraînant une brèchification du matériel volcanique et une remontée des clastes en surface (Elder, **1981**).

Par ailleurs, des études ont permis de mettre en évidence une neutralisation latérale progressive des fluides initialement acides (gîtes HS), suite à leur éloignement de la source de chaleur magmatique, en réagissant avec les silicates présents dans les roches encaissantes en entraînant une diminution du rapport fluide-roche et une augmentation du rapport $HCO_3^-/SO_4^{2-}$ vers les gîtes LS (Arribas, **1995**; Hedenquist *et al.*, **2000**; Smith *et al.*, **2017**).

Les processus d'altérations hydrothermales sont liés à la circulation de fluides hydrothermaux qui transportent la chaleur et les constituants chimiques qui vont interagir avec l'encaissant rocheux. Le type d'altération est également influencé par la composition chimique de la roche et le gradient géothermique (Seedorff *et al.*, **2004**). La variation de la salinité du fluide hydrothermal avec la diminution de la température peut s'expliquer soit par l'atténuation de l'influence de la source de chaleur et la diminution du rapport fluide-roche, soit par l'ajout d'eau météorique dans le système (Zhu *et al.*, **2011**). Il s'avère qu'à Bouillante le fluide Na-Cl s'écoulant au travers de l'aquifère géothermique est composé approximativement de 60% d'eau de mer et de 40% d'eau météorique, pour un pH de l'ordre de 5,3 ± 0,3 et une salinité d'environ 20 g/L. Ce fluide est à comparer aux eaux de

surface captées dans les sources chaudes qui présentent une salinité à 1g/L et sont simplement des eaux de surface chauffées par conduction (Mas *et al.*, **2006**; Lachassagne *et al.*, **2009**).

### VII.3.3. Réservoirs géothermaux et gîtes métallogéniques hydrothermaux

Au cours de mes recherches je me suis retrouvée confrontée à un véritable problème de nomenclature pour définir les objets étudiés, dont l'étude se situe à la frontière de plusieurs disciplines. Entre géothermie, hydrothermalisme et pétrologie métamorphique les classifications changent mais les caractéristiques physico-chimiques des systèmes étudiés sont pourtant similaires.

Le paléo-réservoir de l'île de Terre-de-Haut se situe à la limite entre l'altération propylitique (ou le faciès Sub-Schiste-Vert) et le faciès métamorphique des Schistes-Verts. C'est dans les conditions P-T de ce dernier faciès que se situe la transition fragile ductile (Sibson, **1984**). Cette interface rhéologique entraîne une augmentation de la perméabilité (Richards, **2011**) et s'opère à des températures comprises entre 350 et 400 °C pour une profondeur entre 2 et 3 km. La transition fragile-ductile va permettre de localiser la circulation des fluides et la cristallisation de nouvelles minéralisations dans le système. Si nous comparons ces résultats aux nomenclatures employées pour décrire les gisements miniers en terme de température-profondeur, il devient délicat de continuer à parler, pour les parties inférieures des systèmes géothermaux, de processus épithermaux. C'est pourquoi il serait plus approprié de parler de gîtes mésothermaux (selon les classifications de Lindgren, **1933**; Evans, **1987**). Par ailleurs une sous-catégorie à un niveau intermédiaire entre les gîtes épi- et méso- thermaux a également été introduit sous le terme leptothermaux ($180 < T < 500$ °C entre 1,5 et 3 km, Graton, **1933**; Pélissonnier, **1962**) mais cette terminologie reste peu employée.

L'identification de zones d'altération dans un système géothermal actif permet alors de mieux identifier les cibles potentielles de forage, même si elles ne garantissent pas la présence d'une ressource ou d'un corps minéralisé (Zhu *et al.*, **2011**).

La comparaison entre les systèmes métallogéniques et géothermaux nous permet de proposer un modèle d'évolution spatio-temporelle d'un réservoir de haute-enthalpie et de ses parties profondes en contexte d'arc volcanique en Guadeloupe (Figure VII-9).
Ce schéma représente l'évolution distale volcanique hydrothermale et permet de mettre en évidence l'impact de l'éloignement à la source de chaleur (chambre magmatique) en terme de nature des fluides (composition évoluant d'acides à neutre, chemins de circulation), de gradient de température, de changement rhéologique et de la zonation de l'altération hydrothermale et des faciès métamorphiques.

Dans ce système de transferts de fluides hydrothermaux, nous pouvons ainsi replacer sur ce modèle les différents sites analysés et présentés dans ce manuscrit.

La brèche hydrothermale de Rocroy se situe dans la zone des dépôts épithermaux de type *high-sulfidation* (HS) à la limite entre le système volcanique et le système géothermal. La brèche hydrothermale de Bouillante se situe dans le domaine des dépôts épithermaux de type *low-sulfidation* (LS) du système géothermal. Le paléo-réservoir de Terre-de-Haut, il y a environ 2,6 Ma, se situait en profondeur à la transition fragile-ductile dans les dépôts mésothermaux du système géothermal, en dessous des dépôts épithermaux de type LS. Enfin, le Complexe Basal, il a y environ 4 Ma, se situait à la transition fragile-ductile en contexte d'arc volcanique « standard », c'est-à-dire en dehors d'un réservoir géothermal.

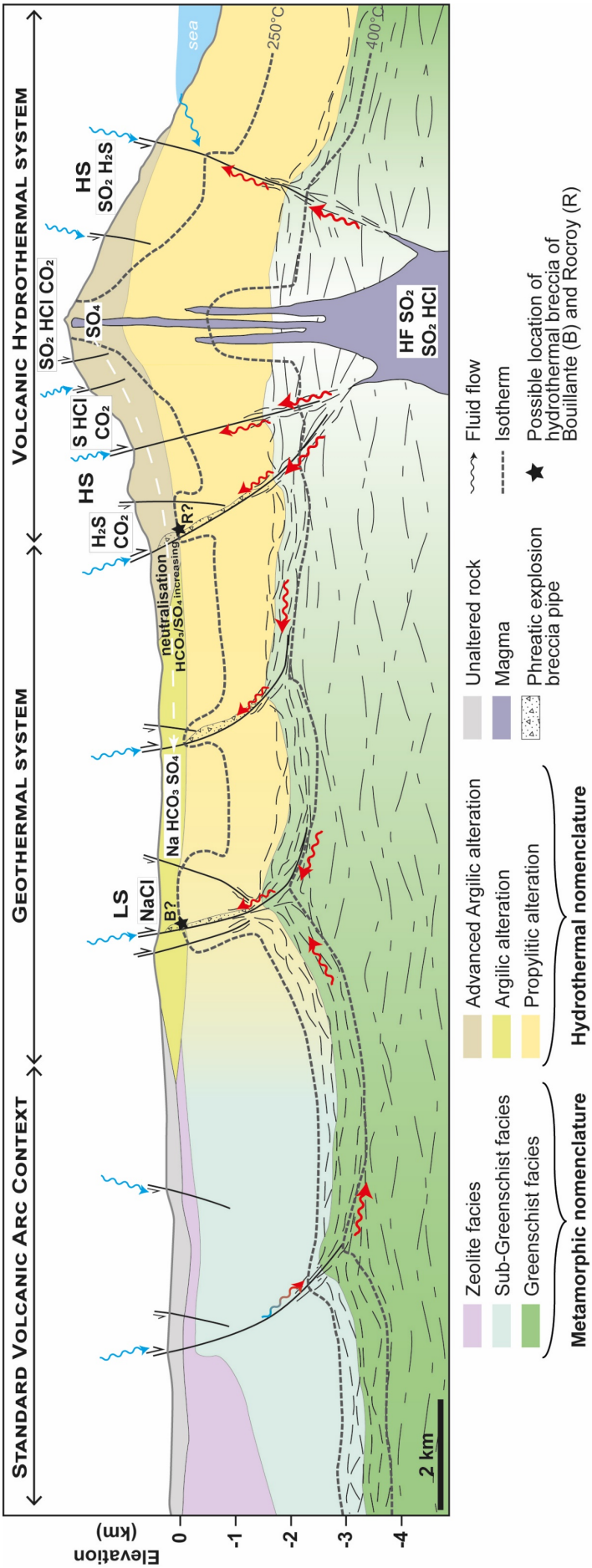
STANDARD VOLCANIC ARC CONTEXT
GEOTHERMAL SYSTEM
VOLCANIC HYDROTHERMAL SYSTEM
sea
250°C
400°C
HS
SO₂ H₂S
SO₂ HCl CO₂
SO₄
S HCl
CO₂
HS
H₂S
CO₂
R?
neutralisation
HCO₃/SO₄ increasing
LS
NaCl
B?
Na HCO₃ SO₄
HF SO₂
SO₂ HCl
2 km
Elevation (km)
0
-1
-2
-3
-4
Unaltered rock
Magma
Phreatic explosion breccia pipe
Fluid flow
Isotherm
Possible location of hydrothermal breccia of Bouillante (B) and Rocroy (R)
Advanced Argilic alteration
Argilic alteration
Propylitic alteration
Hydrothermal nomenclature
Zeolite facies
Sub-Greenschist facies
Greenschist facies
Metamorphic nomenclature

**Figure VII-9 : Coupe schématique illustrant un système distal de transferts hydrothermaux en contexte d'arc volcanique (modifié d'après Hedenquist *et al.*, 2000; Bogie *et al.*, 2005; Rye, 2005; Bouchot *et al.*, 2010; Richards, 2011; Moeck, 2014; Stimac *et al.*, 2015). LS = Low Sulfidation, HS = High Sulfidation**

# Chapitre VIII : Conclusions générales et perspectives

*Iguane et Bain Chaud, Anse Thomas*

*Bouillante, Basse-Terre*

# Chapitre VIII

Ce travail de thèse a permis d'apporter de nouvelles données structurales, pétrographiques, géochimiques et géochronologiques sur l'évolution de l'hydrothermalisme au niveau de l'arc volcanique actif des Petites Antilles en Guadeloupe. En complément des précédentes études réalisées, ces résultats permettent d'améliorer les connaissances sur le fonctionnement du système géothermal de l'île de la Basse-Terre. Plusieurs résultats importants peuvent ainsi être mis en évidence :

1) D'un point de vue cartographique avec :
    a. La mise à jour de la carte géologique du Nord de l'île de la Basse-Terre,
    b. La mise à jour de la carte géologique et structurale de l'île de Terre-de-Haut,
    c. La production d'une carte structurale à l'échelle du PER.

2) La définition d'une référence en terme d'évolution thermique et mécanique des roches en contexte d'arc volcanique avec :
    a. La découverte d'un métamorphisme de bas degré évoluant des faciès schiste-vert à zéolite et lié au fonctionnement de l'arc des Petites Antilles (métamorphisme d'arc),
    b. La démonstration de l'existence d'un gradient géothermique en conduction de l'ordre de 70 à 100 °C/km stable depuis 4 Ma (extension de la plus ancienne activité volcanique de l'île à partir d'une nouvelle datation d'un dôme volcanique du Complexe Basal à 4,28 ± 0,34 Ma),
    c. L'estimation de la localisation de la transition fragile-ductile aux environs 3-4 km de profondeur.

3) La caractérisation du fonctionnement des parties profondes d'un réservoir géothermal de haute-énergie avec :
    a. La démonstration de l'existence d'un paléo-réservoir géothermal exhumé sur l'île de Terre-de-Haut,
    b. La découverte d'une déformation de type ductile avec le développement de couloirs de schistosité de dissolution pouvant servir de drains pour les fluides caloporteurs. Ces zones à schistosité de dissolution constituent également un horizon de transfert de fluides à la transition fragile-ductile, à une profondeur comprise entre 1,7 et 2,7 km.
    c. Cet horizon qui peut également être interprété comme la base du réservoir permettant l'alimentation en fluides hydrothermaux du système, en connectant les failles normales de sub-verticales en surface aux plans de schistosité sub-horizontaux en profondeur,

d. La connaissance de l'extension et de l'évolution des transformations minéralogiques complexes des roches en profondeur permettant de proposer un modèle conceptuel incluant les conditions P-T-fluides nécessaires à la mise en place d'un réservoir de haute-enthalpie en contexte d'arc insulaire.

4) La mise au point de protocoles d'identification, d'analyse, de séparation et de datations des phases potassiques, par les méthodes Ar-Ar et K-Ar, dans les roches hydrothermalisées.

5) Les conséquences de ces nouveaux résultats sur l'exploration et l'exploitation de la ressource géothermale et plus particulièrement :
   a. L'estimation d'une durée maximale de fonctionnement pour ce type de réservoir géothermal à 650 ka, à partir de la datation d'une phase hydrothermale de haute-température à 2,59 ± 0,12 Ma,
   b. L'évolution de la composition des fluides en lien avec la distance à la source magmatique avec une neutralisation progressive distale, similaire à ce qui est proposé pour la genèse des gîtes épithermaux *high-sulfidation* à *low-sulfidation*,
   c. La découverte de nouveaux chemins de circulations de fluides permettant des transferts à la fois latéraux et verticaux, augmentant ainsi le potentiel énergétique de la Guadeloupe avec une ressource potentielle plus importante que celle estimée jusque-là,
   d. L'utilisation de l'hydrothermalisme pour la prospection et l'identification de zones favorables au développement de cellules convectives en profondeur et donc des cibles potentielles pour l'exploitation de la ressource géothermale.

A la suite de cette étude, différentes perspectives pourraient être envisagées :

1) Des études exploratoires similaires à celle-ci, avec une même démarche pluridisciplinaire, mériteraient d'être initiées à l'échelle de tout l'arc des Petites Antilles. Ainsi un métamorphisme régional d'arc avec un hydrothermalisme associé est sans doute présent sur d'autres îles de l'arc des Petites-Antilles. Il serait important de bien le mettre en évidence. De plus l'identification d'autres paléo-réservoirs exhumés permettrait d'affiner les caractéristiques des réservoirs à la fois régionalement et localement afin de poursuivre le développement de la géothermie de haute-énergie à l'échelle de l'arc. Le meilleur candidat se situe probablement au niveau de l'arc ancien Oligo-Miocène de l'île de la Martinique où affleure le Complexe Basal Oligocène aux presqu'îles de la Caravelle et de Sainte-Anne

(Germa *et al.*, **2011**). Une campagne de terrain en 2018 nous a déjà permis d'identifier des indices de déformation ductiles au niveau de ces presqu'îles et un potentiel paléo-réservoir exhumé au niveau de la Caravelle. Par ailleurs, des campagnes exploratoires sur l'île de St-Kitts ont également permis d'identifier des transformations hydrothermales typiques des réservoirs géothermaux dans la partie Sud-Est de l'île (comm. pers. Michel Corsini). Enfin la Dominique semble être une cible de choix au sein de l'arc récent. Elle présente l'activité volcanique la plus étendue spatialement avec ses trois complexes en dormance (Morne aux Diables, Morne Diablotin et Morne Trois Pitons), et son *Boiling Lake* rappelant les manifestations géothermales de Nouvelle-Zélande.

2) Les études géochimiques nécessiteraient également d'être approfondies afin de caractériser plus en détails les interactions « fluides-roches » :
    a. Il est possible d'effectuer des bilans de masse entre les roches fraîches et les roches affectées par une altération hydrothermale plus ou moins intense. Cela permettrait d'effectuer une estimation des mobilités élémentaires au sein des roches méta-volcaniques en fonction de leur composition et du type de fluide qui y circule. Cela permettrait également d'estimer les vitesses de transferts de ces fluides hydrothermaux.
    b. Il faudrait acquérir de nouvelles données isotopiques sur d'autres phases identifiées dans les provinces géothermales, en Guadeloupe comme dans d'autres îles d'arcs insulaires, telles que les jarosites, les pyrites, les gypses afin de caractériser l'origine de ces fluides impliqués dans leur formation (source hypogène ou supergène ou mixte).

3) D'un point de vue géochronologique il serait essentiel de dater systématiquement les phases hydrothermales et volcaniques à l'échelle de la zone d'intérêt explorée. Les âges et les durées de vie des systèmes géothermaux sont encore largement sous-déterminés. Notre étude démontre qu'il est possible de réaliser ce type d'investigation.

Ce travail de recherche s'inscrit au sein du projet GEOTREF, dans une démarche innovante impliquant différents partenaires afin d'acquérir de nouvelles données de surface et de sub-surface sur l'île de la Basse-Terre de Guadeloupe et plus particulièrement dans la zone d'intérêt du PER. Dans le cadre de ce projet différentes méthodes et disciplines ont été combinées (géologie, géophysique sismique et non sismique, pétrophysique, hydrogéologie, modélisation de réservoirs …). Il est important d'intégrer toutes ces nouvelles données obtenues au cours de la phase exploratoire du projet, afin de proposer des modèles ou des scénarios d'évolution des systèmes géothermaux et de

fonctionnement des réservoirs. Ces résultats et les hypothèses avancées vont pouvoir par la suite être testés et validés (ou non) lors de la phase des forages exploratoires qui devrait avoir lieu courant 2020-2021.

# Chapitre IX : Bibliographie

*Anse à la Barque, Marigot, île de la Basse-Terre*

**A**

ABOU-AKAR, A., MATRAY, J.-M., & BRACH, M. **1992**. *Etude Géochimique Du Fluide Géothermal Du Puits BO2 (Central EDF) et Des Sources Thermales de La Région de Bouillante (Guadeloupe), Report BRGM-R-36203 IRG SGN 92*. Orléans.

ADEME. **2012**. Le savoir-faire français dans le domaine de la géothermie : réseaux de chaleur et production d'électricité. 19.

ALLEMAND, P., DELACOURT, C., LAJEUNESSE, E., DEVAUCHELLE, O., & BEAUDUCEL, F. **2014**. Erosive effects of the storm Helena (1963) on Basse Terre Island (Guadeloupe — Lesser Antilles Arc). *Geomorphology*, 206, 79–86, doi: 10.1016/j.geomorph.2013.09.020.

ALLIBONE, A.H., CORDERY, G.R., MORRISON, G.W., JAIRETH, S., & LINDHORST, J.W. **1995**. Synchronous advanced argillic alteration and deformation in a shear zone-hosted magmatic hydrothermal Au-Ag deposit at the Temora (Gidginburg) Mine, New South Wales, Australia. *Economic Geology*, 90, 1570–1603, doi: 10.2113/gsecongeo.90.6.1570.

ANDREIEFF, P., BIZON, G., & BOUYSSE, P. **1981**. Revision de l'age des formations sedimentaires de l'ile de Saint- Martin: implications sur la chronologie du volcanisme de l'arc insulaire des Petites Antilles. *Comptes Rendus des Seances de l'Academie des Sciences, Serie 2: Mecanique, Physique, Chimie, Sciences de la Terre. Sciences de l'Univers*, 292, 79–82.

ANDREIEFF, P., BOUYSSE, P., & WESTERCAMP, D. **1987**. *Géologie de l'arc Insulaire Des Petites Antilles, et Évolution Géodynamique de l'Est-Caraïbes*. Université de Bordeaux I, Bordeaux.

AOKI, M. **1983**. *Modes of Occurrence and Mineralogical Properties of Alunite Solid Solution in Osorezean Geothermal Area*.

AREHART, G.., CHRISTENSON, B.., WOOD, C.., FOLAND, K.., & BROWNE, P.R.. **2002**. Timing of volcanic, plutonic and geothermal activity at Ngatamariki, New Zealand. *Journal of Volcanology and Geothermal Research*, 116, 201–214, doi: 10.1016/S0377-0273(01)00315-8.

ÁRKAI, P. **1991**. Chlorite crystallinity: an empirical approach and correlation with illite crystallinity, coal rank and mineral facies as exemplified by Palaeozoic and Mesozoic rocks of northeast Hungary. *Journal of Metamorphic Geology*, 9, 723–734, doi: 10.1111/j.1525-1314.1991.tb00561.x.

ARNÓRSSON, S. **1995**. Geothermal systems in Iceland: Structure and conceptual models—I. High-temperature areas. *Geothermics*, 24, 561–602, doi: 10.1016/0375-6505(95)00025-9.

ARRIBAS, A. **1995**. Characteristics of high sulfidation epithermal deposits, and their relation to magmatic fluid. *In*: Thompson, J. F. H. (ed.) *Magmas, Fluids, Ore Deposits*. 419–454.

AVÉ LALLEMANT, H.G. & SISSON, V.B. **2005**. Exhumation of eclogites and blueschists in northern Venezuela: constraints from kinematic analysis of deformation structures. *Geological Society of America, Special Paper 394*, 193–206.

**B**

BALDI, P., BELLANI, S., CECCARELLI, A., FIORDELISI, A., SQUARCI, P., & TAFFI, L. **1995**. Geothermal anomalies and structural features of southern Tuscany. *In*: *World Geothermal Congress Proceedings, Florence*. Florence, 1287–2391.

BARBARIN, B. **1990**. Granitoids: Main petrogenetic classifications in relation to origin and tectonic setting. *Geological Journal*, 25, 227–238, doi: 10.1002/gj.3350250306.

BARCELONA, H., YAGUPSKY, D., VIGIDE, N., & SENGER, M. **2019**. Structural model and slip-dilation tendency analysis at the Copahue geothermal system: Inferences on the reservoir geometry. *Journal of Volcanology and Geothermal Research*, 375, 18–31, doi: 10.1016/j.jvolgeores.2019.03.007.

BARELLI, A., CAPPETTI, G., & STEFANI, G. **1995**. Results of deep drilling in the Larderello-Travale/Radicondoli geothermal area. *In*: *World Geothermal Congress 1995*. Florence, Italy, 1275–1278.

BARELLI, A., BERTINI, G., BUONASORTE, G., CAPPETTI, G., & FIORDELISI, A. **2000**. Recent Deep Exploration Results at the Margins of the Larderello Travale Geothermal System. *In*: *Proccedings World Geothermal Congress 2000*. Kyushu-Tohoku, Japan, 6.

BARNES, H.L. **1997**. *Geochemistry of Hydrothermal Ore Deposits*. John Wiley & Sons.

# Bibliographie


BARTOLE, R. **1995**. The North Tyrrhenian?Northern Apennines post-collisional system: constraints for a geodynamic model. *Terra Nova*, 7, 7–30, doi: 10.1111/j.1365-3121.1995.tb00664.x.

BAS, M.J.L., MAITRE, R.W.L., STRECKEISEN, A., & ZANETTIN, B. **1986**. A Chemical Classification of Volcanic Rocks Based on the Total Alkali-Silica Diagram. *Journal of Petrology*, 27, 745–750, doi: 10.1093/petrology/27.3.745.

BATINI, F., BROGI, A., LAZZAROTTO, A., LIOTTA, D., & PANDELI, E. **2003**. Geological features of Larderello-Travale and Mt. Amiata geothermal areas (southern Tuscany, Italy). *Episodes*, 26, 239–244.

BATTAGLIA, S., GIANELLI, G., ROSSI, R., & CAVARRETTA, G. **1991**. The sulphur springs geothermal field, St. Lucia, lesser Antilles: Hydrothermal mineralogy of wells SL-1 and SL-2. *Journal of South American Earth Sciences*, 4, 1–12, doi: 10.1016/0895-9811(91)90014-C.

BAU, M. **1991**. Rare-earth element mobility during hydrothermal and metamorphic fluid-rock interaction and signifiance of the oxidation state of europium. *Chemical Geology*, 93, 219–230, doi: 10.1016/0009-2541(91)90115-8.

BAUMGARTNER, P.O., BANDINI, A., & DENYER, P. **2004**. Jurassic-Lower Cretaceous radiolarites in Central America and the Caribbean – remnants of Pacific ocean floor. *In*: *Second Swiss Geosciences Meeting Abstract*. Lausanne, 1–2.

BAZIN, S., FEUILLET, N., DUCLOS, C., CRAWFORD, W., NERCESSIAN, A., BENGOUBOU-VALÉRIUS, M., BEAUDUCEL, F., & SINGH, S.C. **2010**. The 2004–2005 Les Saintes (French West Indies) seismic aftershock sequence observed with ocean bottom seismometers. *Tectonophysics*, 489, 91–103, doi: 10.1016/j.tecto.2010.04.005.

BEACH, A. **1979**. Pressure solution as a metamorphic process in deformed terrigenous sedimentary rocks. *Lithos*, 12, 51–58, doi: 10.1016/0024-4937(79)90062-8.

BEACH, A. **1982**. Chemical processes in deformation at low metamorphic grades: Pressure solution and hydraulic fracturing. *Episodes*, N° 4, 22–25.

BEAUCHAMPS, G., LEDESERT, B., HEBERT, R., NAVELOT, V., & FAVIER, A. **2019**. The characterisation of an exhumed high - temperature paleo - geothermal system on Terre - de - Haut Island ( the Les Saintes archipelago , Guadeloupe ) in terms of clay minerals and petrophysics. *Geothermal Energy*, 1–18, doi: 10.1186/s40517-019-0122-y.

BECK, R.H. & LEHNER, P. **1974**. Oceans, New Frontier in Exploration. *The American Association of Petroleum Geologists Bulletin*, 58, 376–395.

BELLANI, S., BROGI, A., LAZZAROTTO, D., LIOTTA, D., & RANALLI, G. **2004**. Heat flow, deep temperatures and extensional structures in the Larderello Geothermal Field (Italy) : constraints on geothermal fluid flow. *Journal of Volcanology and Geothermal Research*, 132, 15–29, doi: 10.1016/S0377-0273(03)00418-9.

BERTANI, R. **2016**. Geothermal power generation in the world 2010–2014 update report. *Geothermics*, 60, 31–43, doi: 10.1016/j.geothermics.2015.11.003.

BERTANI, R. & CAPPETTI, G. **1995**. Numerical simulation of the Monteverdi zone western border of Larderello geothermal field. *In*: *World Geothermal Congress 1995*. Florence, Italy, 1735–1740.

BERTANI, R. & ROMAGNOLI, P. **2017**. *2016 Italy Country Report*. Pisa, Italy.

BERTINI, G., CAPPETTI, G., DINI, I., & LOVARI, F. **1995**. Deep drilling results and updating of geothermal knowledge of the Monte Amiata area. *In*: *World Geothermal Congress 1995*. Florence, Italy, 1283–1286.

BERTINI, G., CASINI, M., GIANELLI, G., & PANDELI, E. **2006**. Geological structure of a long-living geothermal system, Larderello, Italy. *Terra Nova*, 18, 163–169, doi: 10.1111/j.1365-3121.2006.00676.x.

BIBBY, H.M., CALDWELL, T.G., DAVEY, F.J., & WEBB, T.H. **1995**. Geophysical evidence on the structure of the Taupo Volcanic Zone and its hydrothermal circulation. *Journal of Volcanology and Geothermal Research*, 68, 29–58, doi: 10.1016/0377-0273(95)00007-H.

BIRD, M.I., ANDREW, A.S., CHIVAS, A.R., & LOCK, D.E. **1989**. An isotopic study of surficial alunite in Australia: 1. Hydrogen and sulphur isotopes. *Geochimica et Cosmochimica Acta*, 53, 3223–3237,

doi: 10.1016/0016-7037(89)90103-8.

BLANC, F. **1983**. *Corrélations Chronologiques et Géochimiques Des Formations Volcaniques Du Sud de La Basse-Terre de Guadeloupe (Petites Antilles) : Début Du Cycle Récent.* Université Scientifique et Médicale de Grenoble, Grenoble.

BOGIE, I. & LAWLESS, J. **2000**. Application of mineral deposit concepts to geothermal exploration. *In*: *Proccedings World Geothermal Congress 2000.* Kyushu-Tohoku, Japan, 1003–1008.

BOGIE, I., LAWLESS, J. V., RYCHAGOV, S., & BELOUSOV, V. **2005**. Magmatic-related hydrothermal systems: classification of the types of geothermal systems and their ore mineralization. *In*: *Proceedings of Geoconference in Russia, Kuril.*

BOGIE, I., KUSUMAH, Y.I., & WISNANDARY, M.C. **2008**. Overview of the Wayang Windu geothermal field, West Java, Indonesia. *Geothermics*, 37, 347–365, doi: 10.1016/j.geothermics.2008.03.004.

BONNET, A.L., CORRIVEAU, L., & GOODFELLOW, W.D. **2007**. Alteration vectors to metamorphosed hydrothermal systems in gneissic terranes. *Geological Association of Canada, Mineral Deposits Division, Special Publication*, 5, 1035–1049.

BOUCHOT, V. & GENTER, A. **2009**. Exploration guides for active high-temperature geothermal systems as modern analogs for epithermal paleosystems. *In*: *Geothermal Resources Council 2009 Annual Meeting October 4-7 2009, Reno, Nevada, USA.* Reno, Nevada, USA.

BOUCHOT, V., TRAINEAU, H., GUILLOU-FROTTIER, L., THINON, I., BALTASSAT, J.-M., FABRIOL, H., BOURGEOIS, B., & LASNE, E. **2010**. Assessment of the Bouillante Geothermal Field (Guadeloupe, French West Indies): Toward a Conceptual Model of the High Temperature Geothermal System. *In*: *World Geothermal Congress 2010, April 2010.* Bali, Indonesia, International Geothermal Association.

BOUDON, G., SEMET, M.P., & VINCENT, P.M. **1987**. Magma and hydrothermally driven sector collapses: The 3100 and 11,500 y. B.P. eruptions of la Grande Decouverte (la Soufrière) volcano, Guadeloupe, French West Indies. *Journal of Volcanology and Geothermal Research*, 33, 317–323, doi: 10.1016/0377-0273(87)90021-7.

BOUDON, G., DAGAIN, J., SEMET, M.P., WESTERCAMP, D., BARAT, A., BOUYSSE, P., & FEUILLARD, M. **1988**. *Notice Explicative de La Carte Géologique à 1/20.000 Du Massif Volcanique de La Soufrière (Département de La Guadeloupe, Petites Antilles).* Paris.

BOUDON, G., SEMET, M.P., & VINCENT, P.M. **1989**. The Evolution of La Grande Découverte (La Soufrière) Volcano, Guadeloupe (F.W.I.). *In*: *J. Latter (Ed.), Volcanic Hazards : Assessment Monitoring. IAVCEI Proceedings in Volcanology, Berlin.* Springer, Berlin, Heidelberg, 86–109., doi: 10.1007/978-3-642-73759-6_5.

BOUDON, G., SEMET, M.P., & VINCENT, P.M. **1992**. Les Eruptions a ecroulement de flanc sur le volcan de la Grande-Decouverte (La Soufriere) de Guadeloupe; implications sur le risque volcanique. *Bulletin de la Société Géologique de France*, 163, 159–167.

BOUDON, G., SEMET, M.P., KOMOROWSKI, J.-C., VILLEMANT, B., & MICHEL, A. **2003**. Was the last magmatic eruption of la Soufrière, Guadeloupe, in 1440 AD, triggered by partial collapse of the volcano? *In*: *EGS - AGU - EUG Joint Assembly, Abstracts from the Meeting Held in Nice.*

BOUDON, G., LE FRIANT, A., KOMOROWSKI, J.-C., DEPLUS, C., & SEMET, M.P. **2007**. Volcano flank instability in the Lesser Antilles Arc: Diversity of scale, processes, and temporal recurrence. *Journal of Geophysical Research: Solid Earth*, 112, doi: 10.1029/2006BJ004674.

BOUDON, G., KOMOROWSKI, J.C., VILLEMANT, B., & SEMET, M.P. **2008**. A new scenario for the last magmatic eruption of La Soufrière of Guadeloupe (Lesser Antilles) in 1530 A.D. Evidence from stratigraphy radiocarbon dating and magmatic evolution of erupted products. *Journal of Volcanology and Geothermal Research*, 178, 474–490, doi: 10.1016/j.jvolgeores.2008.03.006.

BOUMA, A.H. **1962**. *Sedimentology of Some Flysch Deposits: A Graphic Approach to Facies Interpretation.* Amsterdam, Elsevier.

BOUMA, A.H. & RAVENNE, C. **2004**. The Bouma Sequence (1962) and the resurgence of geological interest in the French Maritime Alps (1980s): the influence of the Gres d'Annot in the developing ideas of turbidite systems. *In*: Joseph, P. & Lomas, S. A. (eds) *Deep-Water*

*Sedimentation in the Alpine Basin of SE France: New Perspectives on the Gres d'Annot and Related Systems*. Geological Society of London, Special Publication, 27–38.

BOURDELLE, F. & CATHELINEAU, M. **2015**. Low-temperature chlorite geothermometry: a graphical representation based on a T-R2+-Si diagram. *European Journal of Mineralogy*, 27, 617–626, doi: 10.1127/ejm/2015/0027-2467.

BOUYSSE, P. **1979**. Caractères morphostructuraux et évolution géodynamique de l'arc insulaire des Petites Antilles (campagne ARCANTE 1). *Bulletin du Bureau de Recherches Géologiques et Minières*, 2, 185–210.

BOUYSSE, P. **1980**. Sur l'existence d'un volcan sous-marin dans l'archipel de Guadeloupe. Commentaires sur le problème du volcanisme sous-marin historique dans l'arc insulaire des Petites Antilles. *Bulletin du Bureau de Recherches Géologiques et Minières*, IV, 3–14.

BOUYSSE, P. **1983**. The Lesser Antilles arc: structure and geodynamic evolution. *Initial Reports of the Deep Sea Drilling Project*, 78, 83–103.

BOUYSSE, P. & GARRABÉ, F. **1984**. Evolution tectonique néogène des îles calcaires de l'archipel de Guadeloupe. *Comptes Rendus de l'Académie des Sciences de Paris*, II, 763–766.

BOUYSSE, P. & GUENNOC, P. **1983**. Données sur la structure de l'arc insulaire des Petites Antilles, entre Ste-Lucie et Anguilla. *Marine Geology*, 53, 131–166.

BOUYSSE, P. & WESTERCAMP, D. **1988**. Effets de la subduction de rides océaniques sur l'évolution d'un arc insulaire: l'exemple des Petites Antilles. *Géologie de la France*, 2/3, 2–38.

BOUYSSE, P. & WESTERCAMP, D. **1990**. Subduction of Atlantic aseismic ridges and Late Cenozoic evolution of the Lesser Antilles island arc. *Tectonophysics*, 175, 349–380, doi: 10.1016/0040-1951(90)90180-G.

BOUYSSE, P., SCHMIDT-EFFING, R., & WESTERCAMP, D. **1983**. La Désirade island (Lesser Antilles) revisited: Lower Cretaceous radiolarian cherts and arguments against an ophiolitic origin for the basal complex. *Geology*, 11, 244–247.

BOUYSSE, P., BAUBRON, J.C., RICHARD, M., MAURY, R.C., & ANDREIEFF, P. **1985a**. Evolution de la terminaison nord de l'arc interne des Petites Antilles. *Bulletin de la Societe Geologique de France*, 1, 181–188, doi: 10.2113/gssgfbull.I.2.181.

BOUYSSE, P., ANDREIEFF, P., RICHARD, M., BAUBRON, J.C., MASCLE, A., MAURY, R.C., & WESTERCAMP, D. **1985b**. *Géologie de La Ride d'Aves et Des Pentes Sous-Marines Du Nord Des Petites Antilles: Esquisse Bathymétrique à 1/1000000 de l'est-Caraïbe*.

BOUYSSE, P., WESTERCAMP, D., ANDREIEFF, P., BAUBRON, J.C., & SCOLARI, G. **1985c**. Le volcanisme sous-marin néogène récent au large des côtes Caraïbes des Antilles françaises: relations avec le volcanisme à terre et évolution du front volcanique. *Géologie de la France*, 1, 101–114.

BOUYSSE, P., MASCLE, A., MAUFFRET, A., MERCIER DE LEPINAY, B., JANY, I., LECLERC-VANHOEVE, A., & MONJARET, M.C. **1988**. Reconnaissance de structures tectoniques et volcaniques sous-marines de l'arc interne des Petites Antilles (Kick'em Jenny, Qualibou, Montagne Pelée, NW de la Guadeloupe). *Marine Geology*, 81, 261–287.

BOUYSSE, P., WESTERCAMP, D., & ANDREIEFF, P. **1990**. The Lesser Antilles island arc. *In*: Moore, J. C. & Mascle, A. (eds) *Proceedings of the Ocean Drilling Program Scientific Results*. 29–44.

BOVE, D.J., RYE, R.O., & HON, K. **1990**. *Evolution of the Red Mountain Alunite Deposits, Lake City, Colo.*

BRIDEN, J.C., REX, D.C., FALLER, A.M., & TOMBLIN, J.F. **1979**. K-Ar Geochronology and Palaeomagnetism of Volcanic Rocks in the Lesser Antilles Island Arc. *Philosophical Transactions of the Royal Society A: Mathematical, Physical and Engineering Sciences*, 291, 485–528, doi: 10.1098/rsta.1979.0040.

BROCKAMP, O., CLAUER, N., & ZUTHER, M. **2003**. Authigenic sericite record of a fossil geothermal system: the Offenburg trough, central Black Forest, Germany. *International Journal of Earth Sciences*, 92, 843–851, doi: 10.1007/s00531-003-0368-1.

BROGI, A., LAZZAROTTO, A., LIOTTA, D., & RANALLI, G. **2003**. Extensional shear zones as imaged by reflection seismic lines: the Larderello geothermal field (central Italy). *Tectonophysics*, 363, 127–139, doi: 10.1016/S0040-1951(02)00668-6.

BROWN, E.H. **1977**. Phase equilibria among pumpellyite, lawsonite, epidote and associated minerals in low grade metamorphic rocks. *Contributions to Mineralogy and Petrology*, 64, 123–136, doi: 10.1007/BF00371507.

BROWN, G.M., HOLLAND, J.G., SIGURDSSON, H., TOMBLIN, J.F., & ARCULUS, R.J. **1977**. Geochemistry of the Lesser Antilles volcanic island arc. *Geochimica et Cosmochimica Acta*, 41, 785–801, doi: 10.1016/0016-7037(77)90049-7.

BROWN, M. **2010**. Paired metamorphic belts revisited. *Gondwana Research*, 18, 46–59, doi: 10.1016/j.gr.2009.11.004.

BROWNE, P.R.L. **1978**. Hydrothermal alteration in active geothermal fields. *Annu. Rev. Earth and Planetary Science Letters*, 6, 229–250.

BROWNE, P.R.L. & ELLIS, A.J. **1970**. The Ohaki-Broadlands hydrothermal area, New Zealand; mineralogy and related geochemistry. *American Journal of Science*, 269, 97–131, doi: 10.2475/ajs.269.2.97.

BRUZAC, S. **2012**. *Evolution Spatio-Temporelle Des Phénomènes d'altération Hydrothermale de Haute Température En Guadeloupe et Relation Hydrothermale/Propriété Réservoir, Rapport Intermédiaire*. Orléans, France.

BURKE, K. **1988**. Tectonic Evolution of the Caribbean. *Annual Review of Earth and Planetary Sciences*, 16, 201–230, doi: 10.1146/annurev.ea.16.050188.001221.

**C**

CALAIS, E., HAN, J.Y., DEMETS, C., & NOCQUET, J.M. **2006**. Deformation of the North American plate interior from a decade of continuous GPS measurements. *Journal of Geophysical Research: Solid Earth*, 111, 1–23, doi: 10.1029/2005JB004253.

CALAIS, É., SYMITHE, S., MERCIER DE LÉPINAY, B., & PRÉPETIT, C. **2016**. Plate boundary segmentation in the northeastern Caribbean from geodetic measurements and Neogene geological observations. *Comptes Rendus Geoscience*, 348, 42–51, doi: 10.1016/j.crte.2015.10.007.

CALCAGNO, P., BOUCHOT, V., THINON, I., & BOURGINE, B. **2012**. A new 3D fault model of the Bouillante geothermal province combining onshore and offshore structural knowledge (French West Indies). *Tectonophysics*, 526–529, 185–195, doi: 10.1016/j.tecto.2011.08.012.

CALCAGNO, P., BOUCHOT, V., THINON, I., BOURGINE, B., & GUILLEMIN, C. **2015**. 3D Fault Model of the Bouillante Geothermal Province Interpreted from Onshore and Offshore Structural Knowledge (French West Indies). *In*: *Proceedings World Geothermal Congress 2015*. 1–6.

CAMELI, G.M., DINI, I., & LIOTTA, D. **1993**. Upper crustal structure of the Larderello geothermal field as a feature of post-collisional extensional tectonics (Southern Tuscany, Italy). *Tectonophysics*, 224, 413–423.

CAMELI, G.M., CECCARELLI, A., DINI, I., & MAZZOTTI, A. **2000**. Contribution of the seismic reflection method to the location of deep fractured levels in the geothermal fields of Southern Tuscany (central Italy). *In*: *Proceedings World Geothermal Congress 2000 Kyushu - Tohoku, Japan*. 1025–1029.

CAPPETTI, G., PASSALEVA, G., & SABATELLI, F. **2000**. Italy country update report 1995- 1999. *In*: *World Geothermal Congress Proceedings 2000*. Kyushu-Tohoku, Japan, 109–116.

CAREY, B., DUNSTALL, M., MCCLINTOCK, S., WHITE, B., BIGNALLI, G., LUKETINA, K., ROBSON, B., ZARROUK, S., & SEWARD, A. **2015**. 2015 New Zealand Country Update. *In*: *World Geothermal Congress Proceedings 2015*. Melbourne, Australia, 18.

CARIGNAN, J., HILD, P., MEVELLE, G., MOREL, J., & YEGHICHEYAN, D. **2001**. Routine Analyses of Trace Elements in Geological Samples using Flow Injection and Low Pressure On-Line Liquid Chromatography Coupled to ICP-MS: A Study of Geochemical Reference Materials BR, DR-N, UB-N, AN-G and GH. *Geostandards and Geoanalytical Research*, 25, 187–198, doi: 10.1111/j.1751-908X.2001.tb00595.x.

CARLUT, J., QUIDELLEUR, X., COURTILLOT, V., & BOUDON, G. **2000**. Paleomagnetic directions and K/Ar dating of 0 to 1 Ma lava flows from La Guadeloupe Island (French West Indies): Implications for time-averaged field models. *Journal of Geophysical Research: Solid Earth*, 105,

835–849, doi: 10.1029/1999JB900238.

CARMIGNANI, L., DECANDIA, F.A., FANTOZZI, P.L., LAZZAROTTO, A., LIOTTA, D., & MECCHERI, M. **1994**. Tertiary extensional tectonics in Tuscany (Northern Apennines, Italy). *Tectonophysics*, 238, 295–315, doi: 10.1016/0040-1951(94)90061-2.

CARSLAW, H.S. & JAEGER, J.C. **1959**. *Conduction of Heat in Solids*. London, Oxford Univ. Press.

CASE, J.E., MAC DONALD, W.D., & FOX, P.J. **1990**. Caribbean crustal provinces: seismic and gravity evidence. *In*: Dengo, G. & Case, J. E. (eds) *The Geology of North America*. Geological Society of America, 15–36.

CATHELINEAU, M. **1988**. Cation site occupancy in chlorites and illites as a function of Temperature. *Clay Minerals*, 23, 471–485.

CHAMBEFORT, I., LEWIS, B., WILSON, C.J.N., RAE, A.J., COUTTS, C., BIGNALL, G., & IRELAND, T.R. **2014**. Stratigraphy and structure of the Ngatamariki geothermal system from new zircon U–Pb geochronology: Implications for Taupo Volcanic Zone evolution. *Journal of Volcanology and Geothermal Research*, 274, 51–70, doi: 10.1016/j.jvolgeores.2014.01.015.

CHARLTON, S.R. & PARKHURST, D.. **2011**. Modules based on the geochemical model PHREEQC for use in scripting and programming languages. *Computers & Geosciences*, 37, 1653–1663.

CHENEVOY, M. & PIBOULE, M. **2007**. *Hydrothermalisme: Spéciation Métallique Hydrique et Systèmes Hydrothermaux*. Grenoble, France.

CLAUER, N. **2013**. The K-Ar and 40Ar/39Ar methods revisited for dating fine-grained K-bearing clay minerals. *Chemical Geology*, 354, 163–185, doi: 10.1016/j.chemgeo.2013.05.030.

CLAUER, N., ZWINGMANN, H., LIEWIG, N., & WENDLING, R. **2012**. Comparative 40Ar/39Ar and K–Ar dating of illite-type clay minerals: A tentative explanation for age identities and differences. *Earth-Science Reviews*, 115, 76–96, doi: 10.1016/j.earscirev.2012.07.003.

COMBS, J. & MUFFLER, L.J.P. **1973**. Exploration for geothermal resources. Riverside, University of California, 95–128.

CORDEY, F. & CORNEE, J.-J. **2009**. New radiolarian assemblages from La Desirade Island basement complex (Guadeloupe, Lesser Antilles arc) and Caribbean tectonic implications. *Bulletin de la Societe Geologique de France*, 180, 399–409, doi: 10.2113/gssgfbull.180.5.399.

CORMY, G., DEMIANS D'ARCHIMBAUD, J., & SURCIN, J. **1970**. Prospection geothermique aux antilles françaises, guadeloupe et Martinique. *Geothermics*, 2, 57–72, doi: 10.1016/0375-6505(70)90006-4.

CORNEE, J.-J., LETICEE, J.-L., MÜNCH, P., QUILLEVERE, F., LEBRUN, J.-F., MOISSETTE, P., BRAGA, J.-C., MELINTE-DOBRINESCU, M., DE MIN, L., OUDET, J., & RANDRIANASOLO, A. **2012**. Sedimentology, palaeoenvironments and biostratigraphy of the Pliocene-Pleistocene carbonate platform of Grande-Terre (Guadeloupe, Lesser Antilles forearc). *Sedimentology*, 59, 1426–1451, doi: 10.1111/j.1365-3091.2011.01311.x.

CORSINI, M. **2011**. La centrale géothermique de Bouillante (Guadeloupe). *UVED*. World Wide Web Address: http://unt.unice.fr/uved/bouillante/.

CORSINI, M., LARDEAUX, J.M., VERATI, C., VOITUS, E., & BALAGNE, M. **2011**. Discovery of lower cretaceous synmetamorphic thrust tectonics in French lesser antilles (La Désirade Island, Guadeloupe): Implications for Caribbean geodynamics. *Tectonics*, 30, 1–15, doi: 10.1029/2011TC002875.

COTTEN, J., LE DEZ, A., BAU, M., CAROFF, M., MAURY, R.C., DULSKI, P., FOURCADE, S., BOHN, M., & BROUSSE, R. **1995**. Origin of anomalous rare-earth element and yttrium enrichments in subaerially exposed basalts: Evidence from French Polynesia. *Chemical Geology*, 119, 115–138, doi: 10.1016/0009-2541(94)00102-E.

CREASEY, S.C. **1966**. Hydrothermal alteration. Tucson, University of Arizona, 51–74.

CUNNINGHAM, C.G., RYE, R.O., STEVEN, T.A., & MEHNERT, H.H. **1984**. Origins and exploration significance of replacement and vein-type alunite deposits in the Marysvale volcanic field, west central Utah. *Economic Geology*, 79, 50–71, doi: 10.2113/gsecongeo.79.1.50.

**D**

DAGAIN, J. **1981**. *La Mise En Place Du Massif Volcanique Madeleine-Soufrière, Basse-Terre de Guadeloupe, Antilles*. Université Paris Sud, Orsay.

DALLMEYER, D.R. & LIOTTA, D. **1998**. Extension, uplift of rocks and cooling ages in thinned crustal provinces: the Larderello geothermal area (inner Northern Apennines, Italy). *Geological Magazine*, 135, 193–202, doi: 10.1017/S0016756898008309.

DALRYMPLE, G.B., GROVE, M., LOVERA, O.M., HARRISON, T.M., HULEN, J.B., & LANPHERE, M.A. **1999**. Age and thermal history of the Geysers plutonic complex (felsite unit), Geysers geothermal field, California: a 40Ar/39Ar and U–Pb study. *Earth and Planetary Science Letters*, 173, 285–298, doi: 10.1016/S0012-821X(99)00223-X.

DE CAPITANI, C. & PETRAKAKIS, K. **2010**. The computation of equilibrium assemblage diagrams with Theriak-Domino software. *American Mineralogist*, 95, 1006–1016.

DE CARITAT, P., HUTCHEON, I., & WALSHE, J. **1993**. Chlorite geothermometry: a review. *Clays and Clay Minerals*, 41, 219–239.

DE LAUNAY, L. **1934**. Les grands types de gisements. In: Introduction aux Etudes minières coloniales. *Soc. edit. géograph., maritimes et coloniales, Paris*, 1–17.

DE MIN, L. **2014**. *Sismo-Stratigraphie Multi-Échelles d'un Bassin d'avant-Arc : Le Bassin de Marie-Galante, Petites Antilles*. University of Antilles and Guyane, Pointe-à-Pitre, Guadeloupe.

DE MIN, L., LEBRUN, J.-F., CORNEE, J.-J., MÜNCH, P., LETICEE, J.L., QUILLEVERE, F., MELINTE-DOBRINESCU, M., RANDRIANASOLO, A., MARCAILLOU, B., & ZAMI, F. **2015**. Tectonic and sedimentary architecture of the Karukéra spur: A record of the Lesser Antilles fore-arc deformations since the Neogene. *Marine Geology*, 363, 15–37, doi: 10.1016/j.margeo.2015.02.007.

DE REYNAL DE SAINT-MICHEL, A. **1966**. *Carte Géologique à l'échelle 1:50 000 Du Département de La Guadeloupe - Feuilles de Basse-Terre et Des Saintes*. Paris.

DEL MORO, A., PUXEDDU, M., RADICATI DI BROZOLO, F., & VILLA, I.M. **1982**. Rb-Sr and K-Ar ages on minerals at temperatures of 300°-400°C from deep wells in the Larderello geothermal field (Italy). *Contributions to Mineralogy and Petrology*, 81, 340–349, doi: 10.1007/BF00371688.

DELOULE, E. & TURCOTTE, D.L. **1989**. The flow of hot brines in cracks and the formation of ore deposits. *Economic Geology*, 84, 2217–2225, doi: 10.1016/0009-2541(88)90581-5.

DEMETS, C., JANSMA, P.E., MATTIOLI, G.S., DIXON, T.H., FARINA, F., BILHAM, R., CALAIS, E., & MANN, P. **2000**. GPS geodetic constraints on Caribbean-North America Plate Motion. *Geophysical Research Letters*, 27, 437–440, doi: 10.1029/1999GL005436.

DEMIANS D'ARCHIMBAUD, J. & MUNIER-JOLAIN, J.P. **1976**. *Les Progrès de l'exploration Géothermique à Bouillante En Guadeloupe*.

DEMIANS D'ARCHIMBAUD, J. & SURCIN, J. **1976**. Recherches d'énergies géothermique en Guadeloupe. *Bulletin du Bureau de Recherches Géologiques et Minières*, 4, 365–373.

DEPLUS, C., LE FRIANT, A., BOUDON, G., KOMOROWSKI, J.-C., VILLEMANT, B., HARFORD, C., SEGOUFIN, J., & CHEMINEE, J.-L. **2001**. Submarine evidence for large-scale debris avalanches in the Lesser Antilles Arc. *Earth and Planetary Science Letters*, 192, 145–157, doi: 10.1016/S0012-821X(01)00444-7.

DESSERT, C., LAJEUNESSE, E., LLORET, E., CLERGUE, C., CRISPI, O., GORGE, C., & QUIDELLEUR, X. **2015**. Controls on chemical weathering on a mountainous volcanic tropical island: Guadeloupe (French West Indies). *Geochimica et Cosmochimica Acta*, 171, 216–237, doi: 10.1016/j.gca.2015.09.009.

DICK, J.M. **2019**. CHNOSZ: Thermodynamic Calculations and Diagrams for Geochemistry. *Frontiers in Earth Science*, 7, doi: 10.3389/feart.2019.00180.

DICKINSON, W.R. & SEELY, D.R. **1979**. Structure and Stratigraphy of Forearc Regions. *AAPG Bulletin*, 63, 2–31.

DICKSON, M.H. & FANELLI, M. **2013**. *Geothermal Energy: Utilization and Technology*. Taylor and Francis Group.

DIXON, T.H., FARINA, F., DEMETS, C., JANSMA, P., MANN, P., & CALAIS, E. **1998**. Relative motion between the Caribbean and North American plates and related boundary zone deformation from a decade of GPS observations. *Journal of Geophysical Research: Solid Earth*, 103, 15157–15182, doi: 10.1029/97JB03575.

DONG, H., HALL, C.M., PEACOR, D.R., & HALLIDAY, A.N. **1995**. Mechanisms of Argon Retention in Clays Revealed by Laser 40Ar-39Ar Dating. *Science*, 267, 355–359, doi: 10.1126/science.267.5196.355.

DRITS, V., SRODON, J., & EBERL, D.D. **1997**. XRD Measurement of Mean Crystallite Thickness of Illite and Illite/Smectite: Reappraisal of the Kubler Index and the Scherrer Equation. *Clays and Clay Minerals*, 45, 461–475, doi: 10.1346/CCMN.1997.0450315.

**E-F**

EDGAR, T.N., EWING, J.I., & HENNION, J. **1971**. Seismic Refraction and Reflection in Caribbean Sea. *AAPG Bulletin*, 55, 833–870.

ELDER, J.W. **1981**. *Geothermal Systems*. London, Academic Press.

ELWOOD MADDEN, M.E., MADDEN, A.S., & RIMSTIDT, J.D. **2009**. How long was Meridiani Planum wet? Applying a jarosite stopwatch to determine the duration of aqueous diagenesis. *Geology*, 37, 635–638, doi: 10.1130/G25639A.1.

EPPELBAUM, L., KUTASOV, I., & PILCHIN, A. **2014**. Thermal Properties of Rocks and Density of Fluids. *In*: *Applied Geothermics*. 99–149., doi: 10.1007/978-3-642-34023-9_2.

ERNST, W.G. **1976**. Mineral chemistry of eclogites and related rocks from the Voltri Group, western Liguria, Italy. *Schweizerische Mineralogische und Petrographische Mitteiungen*, 56, 293–343.

EVANS, A.M. **1987**. *An Introduction to Ore Geology*, 2e édition. Oxford, Blackwell Scientific Publication.

FAURE, G. **1986**. *Principles of Isotope Geology*. New-York, John Wiley & Sons.

FAVIER, A., NAVELOT, V., VERATI, C., LARDEAUX, J.M., CORSINI, M., DIRAISON, M., GERAUD, Y., MERCIER DE LEPINAY, J., & MUNSCHY, M. **2017**. Characterization of geothermal paleosystem in the Lesser Antilles volcanic arc: structural, petrographic, thermodynamic and petrophysics analysis of Terre-de-Haut (Les Saintes archipelago, Lesser Antilles). *In*: *19th EGU General Assembly, Vienne 2017*. 18920.

FAVIER, A., LARDEAUX, J.-M., LEGENDRE, L., VERATI, C., PHILIPPON, M., CORSINI, M., MÜNCH, P., & VENTALON, S. **2019**. Tectono-metamorphic evolution of shallow crustal levels within active volcanic arcs. Insights from the exhumed Basal Complex of Basse-Terre (Guadeloupe, French West Indies). *BSGF - Earth Sciences Bulletin*, 190, 22, doi: 10.1051/bsgf/2019011.

FAVIER, A., VERATI, C., LARDEAUX, J.-M., MÜNCH, P., RENAC, C., & CORSINI, M. ***submitted***. Characterization of an exhumed high-energy geothermal paleo-reservoir: An example from Terre-de-Haut Island (Guadeloupe archipelago, Lesser Antilles arc). *Journal of Volcanology and Geothermal Research*.

FEUILLET, N. **2000**. *Sismotectonique Des Petites Antilles. Liaison Entre Activité Sismique et Volcanique*. Université Paris 7 Denis Diderot, Paris.

FEUILLET, N., MANIGHETTI, I., & TAPPONNIER, P. **2001**. Extension active perpendiculaire à la subduction dans l'arc des Petites Antilles (Guadeloupe, Antilles françaises). *Comptes Rendus de l'Academie de Sciences - Serie IIa: Sciences de la Terre et des Planetes*, 333, 583–590, doi: 10.1016/S1251-8050(01)01543-9.

FEUILLET, N., MANIGHETTI, I., TAPPONNIER, P., & JACQUES, E. **2002**. Arc parallel extension and localization of volcanic complexes in Guadeloupe, Lesser Antilles. *Journal of Geophysical Research*, 107 (B12), ETG 3 1-29, doi: 10.1029/2001JB000308.

FEUILLET, N., TAPPONNIER, P., MANIGHETTI, I., VILLEMANT, B., & KING, G.C.P. **2004**. Differential uplift and tilt of Pleistocene reef platforms and Quaternary slip rate on the Morne-Piton normal fault (Guadeloupe, French West Indies). *Journal of Geophysical Research: Solid Earth*, 109, 1–18, doi: 10.1029/2003JB002496.

FEUILLET, N., LECLERC, F., TAPPONNIER, P., BEAUDUCEL, F., BOUDON, G., LE FRIANT, A., DEPLUS, C., LEBRUN, J.-F., NERCESSIAN, A., SAUREL, J.-M., & CLÉMENT, V. **2010**. Active faulting induced

by slip partitioning in Montserrat and link with volcanic activity: New insights from the 2009 GWADASEIS marine cruise data. *Geophysical Research Letters*, 37, n/a-n/a, doi: 10.1029/2010GL042556.

FEUILLET, N., BEAUDUCEL, F., & TAPPONNIER, P. **2011**. Tectonic context of moderate to large historical earthquakes in the Lesser Antilles and mechanical coupling with volcanoes. *Journal of Geophysical Research: Solid Earth*, 116, 1–26, doi: 10.1029/2011JB008443.

FITCH, T.J. **1972**. Plate convergence, transcurrent faults, and internal deformation adjacent to Southeast Asia and the western Pacific. *Journal of Geophysical Research*, 77, 4432–4460, doi: 10.1029/JB077i023p04432.

FULIGNATI, P., GIONCADA, A., & SBRANA, A. **1999**. Rare-earth element (REE) behaviour in the alteration facies of the active magmatic–hydrothermal system of Vulcano (Aeolian Islands, Italy). *Journal of Volcanology and Geothermal Research*, 88, 325–342, doi: 10.1016/S0377-0273(98)00117-6.

**G**

GADALIA, A. **2013**. *Exploration Géothermique de La Zone de Vieux-Habitants (Guadeloupe) - Etat Des Connaissances Géologiques - BRGM/RP-62569-FR*. Orléans, France.

GADALIA, A., GSTALTER, N., & WESTERCAMP, D. **1988**. La chaîne volcanique de Bouillante, Basse-Terre de Guadeloupe (Petites Antilles) : Identité pétrographique, volcanologique et géodynamique. *Géologie de la France*, 101–130.

GAILLER, L.S., MARTELET, G., THINON, I., BOUCHOT, V., LEBRUN, J.F., & MÜNCH, P. **2013**. Crustal structure of Guadeloupe islands and the Lesser Antilles arc from a new gravity and magnetic synthesis. *Bulletin de la Societe Geologique de France*, 184, 77–97, doi: 10.2113/gssgfbull.184.1-2.77.

GARIBALDI, C. **2010**. *Determination Des Temperatures Profondes Du Bassin Du Sud-Est De La France Et Relations Entre Anomalies Thermiques, Geologie Et Circulations Hydrothermales Par Modelisation 3D*.

GAUCHAT, K. **2004**. *Geochemistry of Desirade Island Rocks (Guadeloupe, Fench Antilles)*. University of Lausanne, Lausanne, Switzerland.

GEOTREF. **2017**. *Rapport de Synthèse Des Études Géologiques : Contribution à l'étude Du Potentiel Géothermique Du PER de Vieux-Habitants (Basse-Terre de La Guadeloupe) - Document Interne Confidentiel*.

GERMA, A., QUIDELLEUR, X., LABANIEH, S., CHAUVEL, C., & LAHITTE, P. **2011**. The volcanic evolution of Martinique Island: Insights from K-Ar dating into the Lesser Antilles arc migration since the Oligocene. *Journal of Volcanology and Geothermal Research*, 208, 122–135, doi: 10.1016/j.jvolgeores.2011.09.007.

GIUNTA, G. & OLIVERI, E. **2009**. Some remarks on the Caribbean Plate kinematics: facts and remaining problems. *Geological Society, London, Special Publications*, 328, 57–75, doi: 10.1144/SP328.2.

GIUNTA, G. & ORIOLI, S. **2011**. The Caribbean Plate Evolution: Trying to Resolve a Very Complicated Tectonic Puzzle. *In*: Sharkov, E. V. (ed.) *New Frontiers in Tectonic Research: General Problems, Sedimentary Basins and Island Arcs*. Werde Science, 221–248.

GOLDFARB, R.., GROVES, D.., & GARDOLL, S. **2001**. Orogenic gold and geologic time: a global synthesis. *Ore Geology Reviews*, 18, 1–75, doi: 10.1016/S0169-1368(01)00016-6.

GOMEZ, S., BIRD, D., & MANN, P. **2018**. Deep crustal structure and tectonic origin of the Tobago-Barbados ridge. *Interpretation*, 6, T471–T484, doi: 10.1190/INT-2016-0176.1.

GRANT, M.A. & BIXLEY, P.F. **2011**. Geothermal Reservoirs. *In*: *Geothermal Reservoir Engineering*. Elsevier, 1–8., doi: 10.1016/B978-0-12-383880-3.10001-0.

GRATIER, J.-P., DYSTHE, D.K., & RENARD, F. **2013**. The Role of Pressure Solution Creep in the Ductility of the Earth's Upper Crust. *In*: *Advances in Geophysics*. 47–179., doi: 10.1016/B978-0-12-380940-7.00002-0.

GRATON, L.C. **1933**. The depth zones in ore deposition. *Economic Geology*, 28, 513–555.

GRIMES, S., RICKARD, D., HAWKESWORTH, C., VAN CALSTEREN, P., & BROWNE, P. **1998**. A U–Th

calcite isochron age from an active geothermal field in New Zealand. *Journal of Volcanology and Geothermal Research*, 81, 327–333, doi: 10.1016/S0377-0273(98)00005-5.

GROVES, D.., GOLDFARB, R.., GEBRE-MARIAM, M., HAGEMANN, S.., & ROBERT, F. **1998**. Orogenic gold deposits: A proposed classification in the context of their crustal distribution and relationship to other gold deposit types. *Ore Geology Reviews*, 13, 7–27, doi: 10.1016/s0169-1368(97)00012-7.

GUILBERT, J.M. & PARK, C.F.J. **1986**. *The Geology of Ore Deposits*. New York, W. H. Freeman and Compagny.

GUILLOU-FROTTIER, L. **2003**. *Compilation et Analyse Des Données Thermiques Sur Le Champ Géothermique de Bouillante. Premières Interprétations Pour Le Fonctionnement Du Champ Géothermique. Rapport Final. BRGM/RP-52452-FR.*

**H**

HAINES, S.H. & VAN DER PLUIJM, B.A. **2008**. Clay quantification and Ar–Ar dating of synthetic and natural gouge: Application to the Miocene Sierra Mazatán detachment fault, Sonora, Mexico. *Journal of Structural Geology*, 30, 525–538, doi: 10.1016/j.jsg.2007.11.012.

HALL, C.M., HIGUERAS, P.L., KESLER, S.E., LUNAR, R., DONG, H., & HALLIDAY, A.N. **1997**. Dating of alteration episodes related to mercury mineralization in the Almadén district, Spain. *Earth and Planetary Science Letters*, 148, 287–298, doi: 10.1016/S0012-821X(97)00041-1.

HAMES, W., UNGER, D., SAUNDERS, J., & KAMENOV, G. **2009**. Early Yellowstone hotspot magmatism and gold metallogeny. *Journal of Volcanology and Geothermal Research*, 188, 214–224, doi: 10.1016/j.jvolgeores.2009.07.020.

HASTIE, A.R., KERR, A.C., PEARCE, J.A., & MITCHELL, S.F. **2007**. Classification of altered volcanic island arc rocks using immobile trace elements: Development of the Th-Co discrimination diagram. *Journal of Petrology*, 48, 2341–2357, doi: 10.1093/petrology/egm062.

HAWKESWORTH, C.J. & POWELL, M. **1980**. Magma genesis in the Lesser Antilles island arc. *Earth and*, 51, 297–308.

HEALD, P., FOLEY, N.K., & HAYBA, D.O. **1987**. Comparative anatomy of volcanic-hosted epithermal deposits: acid–sulfate and adularia–sericite types. *Economic Geology*, 1–26.

HEDENQUIST, J.W. **1987**. Mineralization associated with volcanic-related hydrothermal systems in the Circum-Pacific basin. *In*: *Circum Pacific Energy and Mineral Ressources Conference, American Association of Petroleum Geologists, 4th, Singapore, Transactions*. 513–524.

HEDENQUIST, J.W. & LOWENSTERN, J.B. **1994**. The role of magmas in the formation of hydrothermal ore deposits. *Nature*, 370, 519–527, doi: 10.1038/370519a0.

HEDENQUIST, J.W., ARRIBAS, A.J., & GONZALEZ-URIEN, E. **2000**. Exploration for epithermal gold deposits. *In*: *SEG Review*. 245–277.

HEISE, W., CALDWELL, T.G., BIBBY, H.M., & BANNISTER, S.C. **2008**. Three-dimensional modelling of magnetotelluric data from the Rotokawa geothermal field, Taupo Volcanic Zone, New Zealand. *Geophysical Journal International*, 173, 740–750, doi: 10.1111/j.1365-246X.2008.03737.x.

HEMLEY, J.J., HOSTETLER, P.B., GUDE, A.J., & MOUNTJOY, W.T. **1969**. Some stability relations of alunite. *Economic Geology*, 64, 599–612, doi: 10.2113/gsecongeo.64.6.599.

HENLEY, R.W. & ELLIS, A.J. **1983**. Geothermal systems ancient and modern: a geochemical review. *Earth-Science Reviews*, 19, 1–50, doi: 10.1016/0012-8252(83)90075-2.

HOLLAND, T.J.B. & POWELL, R. **1998**. An internally consistent thermodynamic data set for phases of petrological interest. *Journal of Metamorphic Geology*, 16, 309–343.

HOLLAND, T.J.B. & POWELL, R. **2004**. An internally consistent thermodynamic data set for phases of petrological interest. *Journal of Metamorphic Geology*, 16, 309–343, doi: 10.1111/j.1525-1314.1998.00140.x.

HOWARD, S.A. & PRESTON, K.D. **1989**. Profile fitting of powder diffraction patterns. *In*: *Modern Powder Diffraction*. 217–275.

**I-J**

INOUE, A. & KITAGAWA, R. **1994**. Morphological characteristics of illite clay minerals from a hydrothermal system. *American Mineralogist*, 79, 700–711.

INOUE, A., UTADA, M., & WAKITA, K. **1992**. Smectite-to-illite conversion in natural hydrothermal systems. *Applied Clay Science*, 7, 131–145, doi: 10.1016/0169-1317(92)90035-L.

INOUE, A., MEUNIER, A., PATRIER-MAS, P., RIGAULT, C., BEAUFORT, D., & VIEILLARD, P. **2009**. Application of Chemical Geothermometry to Low-Temperature Trioctahedral Chlorites. *Clays and Clay Minerals*, 57, 371–382, doi: 10.1346/CCMN.2009.0570309.

ISIK, V., UYSAL, I.T., CAGLAYAN, A., & SEYITOGLU, G. **2014**. The evolution of intraplate fault systems in central Turkey: Structural evidence and Ar-Ar and Rb-Sr age constraints for the Savcili Fault Zone. *Tectonics*, 33, 1875–1899, doi: 10.1002/2014TC003565.

ITAYA, T., ARRIBAS, A., & OKADA, T. **1996**. Argon release systematics of hypogene and supergene alunite based on progressive heating experiments from 100 to 1000°C. *Geochimica et Cosmochimica Acta*, 60, 4525–4535, doi: 10.1016/S0016-7037(97)82784-6.

IUNDT, F. & OUZOUNIAN, G. **1984**. *Prospection Géothermique de La Région de Bouillante - Vieux Habitants Guadeloupe, Rapport Du B.R.G.M 84 SGN 063 GTH*. Orléans, France.

JACQUES, D. & MAURY, R.C. **1988**. Carte géologique au 1/20 000e, département de la Guadeloupe, Les Saintes. *BRGM, Service Géologique National, Orléans*.

JACQUES, D., MAURY, R.C., & BELLON, H. **1984**. *Geology and K-Ar geochronology of Les Saintes island, guadeloupe, Frend West-Indies Géologie et géochronologie 40K-40Ar des îles des Saintes (Guadeloupe)*. Gauthier-Villars.

JAMES, K.H. **2003**. A simple synthesis of Caribbean Geology. *In*: *AAPG International Conference Extended Abstracts*. Barcelona.

JAMES, K.H. **2006**. Arguments for and against the Pacific origin of the Caribbean Plate: discussion, finding for an inter-American origin. *Geologica Acta*, 4, 279–302.

JAMES, K.H. **2009**. In situ origin of the Caribbean: discussion of data. *Geological Society, London, Special Publications*, 328, 77–125, doi: 10.1144/SP328.3.

JARRARD, R.D. **1986**. Terrane motion by strike-slip faulting of forearc slivers. *Geology*, 14, 780, doi: 10.1130/0091-7613(1986)14<780:TMBSFO>2.0.CO;2.

JÉBRAK, M. **1997**. Hydrothermal breccias in vein-type ore deposits: A review of mechanisms, morphology and size distribution. *Ore Geology Reviews*, 12, 111–134, doi: 10.1016/S0169-1368(97)00009-7.

JENSEN, E.P. & BARTON, M.D. **2000**. *Gold Deposits Related to Alkaline Magmatism*, Gold in 20. Hagemann, S. . & Brown, P. E. (eds). Littleton, Colorado, Society of Economic Geologists.

JI, J. & BROWNE, P.R.L. **2000**. Relationship between illite crystallinity and temperature in active geothermal systems of New Zealand. *Clays and Clay Minerals*, 48, 139–144.

JOHNSTON, J.M., PELLERIN, L.., & HOHMANN, G.W. **1992**. Evaluation of electromagnetic methods for geothermal reservoir detection. *Transactions - Geothermal Resources Council*.

JOSEPH, PHILIPPE & LOMAS, SIMON A. **2004**. Deep-water sedimentation in the Alpine Foreland Basin of SE France: New perspectives on the Grès d'Annot and related systems—an introduction Joseph, P & Lomas, S A (eds). *Geological Society, London, Special Publications*, 221, 1–16, doi: 10.1144/GSL.SP.2004.221.01.01.

JOURDAN, F., MATZEL, J.P., & RENNE, P.R. **2007**. 39Ar and 37Ar recoil loss during neutron irradiation of sanidine and plagioclase. *Geochimica et Cosmochimica Acta*, 71, 2791–2808, doi: 10.1016/j.gca.2007.03.017.

**K**

KERR, A.C., TARNEY, J., MARRINER, G.F., NIVIA, A., KLAVER, G.T., & SAUNDERS, A.D. **1996**. The geochemistry and tectonic setting of late Cretaceous Caribbean and Colombian volcanism. *Journal of South American Earth Sciences*, 9, 111–120, doi: 10.1016/0895-9811(96)00031-4.

KERR, A.C., MARRINER, G.F., TARNEY, J., NIVIA, A., SAUNDERS, A.D., THIRLWALL, M.F., & SINTON, C.W. **1997**. Cretaceous Basaltic Terranes in Western Colombia: Elemental, Chronologicaland Sr-Nd Isotopic Constraints on Petrogenesis. *Journal of Petrology*, 38, 677–702, doi:

10.1093/petrology/38.6.677.

KERR, A.C., TARNEY, J., NIVIA, A., MARRINER, G.F., & SAUNDERS, A.D. **1998**. The internal structure of oceanic plateaus: inferences from obducted Cretaceous terranes in western Colombia and the Caribbean. *Tectonophysics*, 292, 173–188, doi: 10.1016/S0040-1951(98)00067-5.

KERR, A.C., WHITE, R. V., THOMPSON, P.M.E., TARNEY, J., & SAUNDERS, A.D. **2003**. No Oceanic Plateau - No Caribbean Plate? The Seminal Role of an Oceanic Plateau in Caribbean Plate Evolution. *In*: *The Circum-Gulf of Mexico and the Caribbean: Hydrocarbon Habitats, Basin Formation, and Plate Tectonics: AAPG Memoir 79*. 126–168.

KLEIN, D.P. & JOHNSON, G.R. **1983**. *Density, Porosity and Magnetic Properties of Rock Specimens from Southwestern Arizona*.

KNAUSS, K.G. & WOLERY, T.J. **1988**. The dissolution kinetics of quartz as a function of pH and time at 70°C. *Geochimica et Cosmochimica Acta*, 52, 43–53, doi: 10.1016/0016-7037(88)90055-5.

KOMOROWSKI, J.C., BOUDON, G., SEMET, M.P., VILLEMANT, B., & HAMMOUYA, G. **2002**. Recurrent flank-collapses at Soufriére of Guadeloupe Volcano: implications of acid hydrothermal fluids on edifice stability Mount Pelée 1902–2002; explosive volcanism in subduction zones. *In*: *IPGP-INSU-IAVCEI International Congress, Ile de La Martinique*. Martinique.

KOMOROWSKI, J.C., BOUDON, G., SEMET, M.P., BEAUDUCEL, F., ANTENOR-HARBAZAC, C., BAZIN, S., & HAMMOUYA, G. **2005**. Guadeloupe. *In*: *Volcanic Atlas of the Lesser Antilles*. 65–102.

KOPP, H. **2013**. Invited review paper: The control of subduction zone structural complexity and geometry on margin segmentation and seismicity. *Tectonophysics*, 589, 1–16, doi: 10.1016/j.tecto.2012.12.037.

KOPP, H., WEINZIERL, W., BECEL, A., CHARVIS, P., EVAIN, M., FLUEH, E.R., GAILLER, A., GALVE, A., HIRN, A., KANDILAROV, A., KLAESCHEN, D., LAIGLE, M., PAPENBERG, C., PLANERT, L., & ROUX, E. **2011**. Deep structure of the central Lesser Antilles Island Arc: Relevance for the formation of continental crust. *Earth and Planetary Science Letters*, 304, 121–134, doi: 10.1016/j.epsl.2011.01.024.

KOPPERS, A.A.P. **2002**. ArArCALC—software for 40Ar/39Ar age calculations. *Computers & Geosciences*, 28, 605–619, doi: 10.1016/S0098-3004(01)00095-4.

KRETZ, R. **1983**. Symbols for rock-forming minerals. *American Mineralogist*, 68, 277–279.

KRUPP, R.E. & SEWARD, T.M. **1987**. The Rotokawa geothermal systems, New Zealand: an active epithermal gold-depositing environment. *Economic Geology*, 82, 1109–1129.

KÜBLER, B. **1967**. La cristallinité de l`illite et les zones tout à fait supérieures du métamorphisme. *In*: *Étages Tectoniques, Colloque de Neuchâtel 1966*. La Baconniere, Neuchâte, 105–121.

KULA, J. & BALDWIN, S.L. **2011**. Jarosite, argon diffusion, and dating aqueous mineralization on Earth and Mars. *Earth and Planetary Science Letters*, 310, 314–318, doi: 10.1016/j.epsl.2011.08.006.

**L**

LABANIEH, S. **2009**. *Géochimie de l'île de La Martinique Aux Petites Antilles*. Université Joseph-Fourier - Grenoble I, Grenoble.

LACHASSAGNE, P., MARECHAL, J., & SANJUAN, B. **2009**. Hydrogeological model of a high energy geothermal field (Bouillante area, Guadeloupe, French West Indies). *Hydrogeology Journal, Springer Verlag*, 17, 1589–1606.

LACHENBRUCH, A.H. & SASS, J.H. **1992**. Heat flow from Cajon Pass, fault strength, and tectonic implications. *Journal of Geophysical Research*, 97, 4995–5015, doi: 10.1029/91JB01506.

LAGAT, J. **2014**. Hydrothermal Alteration Mineralogy in Geothermal Fields With Case Examples From Olkaria Domes Geothermal Field , Kenya. *In*: *Short Course IX on Exploration for Geothermal Resources*. Lake Bogoria and Lake Naivasha, Kenya, 1–24.

LAIGLE, M., BECEL, A., DE VOOGD, B., SACHPAZI, M., BAYRAKCI, G., LEBRUN, J.-F., & EVAIN, M. **2013**. Along-arc segmentation and interaction of subducting ridges with the Lesser Antilles Subduction forearc crust revealed by MCS imaging. *Tectonophysics*, 603, 32–54, doi: 10.1016/j.tecto.2013.05.028.

Lanari, P., Wagner, T., & Vidal, O. **2014**. A thermodynamic model for di-trioctahedral chlorite from experimental and natural data in the system MgO-FeO-Al2O3-SiO2-H2O: Applications to P-T sections and geothermometry. *Contributions to Mineralogy and Petrology*, 167, 1–19, doi: 10.1007/s00410-014-0968-8.

Laplaige, P., Durimel, H., & Mompelat, J. **2013**. Développement de la géothermie dans la Caraïbe. *Géosciences*, 26–35.

Lardeaux, J.M., Münch, P., Corsini, M., Cornee, J.-J., Verati, C., Lebrun, J.-F., Quillevere, F., Melinte-Dobrinescu, M., Leticee, J.L., Fietzke, J., Mazabraud, Y., Cordey, F., & Randrianasolo, A. **2013**. La Désirade island (Guadeloupe, French West Indies): A key target for deciphering the role of reactivated tectonic structures in Lesser Antilles arc building. *Bulletin de la Societe Geologique de France*, 184, 21–34, doi: 10.2113/gssgfbull.184.1-2.21.

Laurencin, M. **2017**. *Etude de La Géométrie, de La Nature et Des Déformations de Subduction Des Petites Antilles Du Nord*. Université de Bretagne occidentale, Brest.

Lebrun, J.-F., Fabre, M., & equipe de la campagne oceanographique GEOTREF 2015 (N/O Antea). **2017**. *Livrable 10.4.2 - Résumé Quant Aux Structures Du Plateau Insulaire de La Basse-Terre. Livrable GEOTREF, ADEME-Teranov, Document Interne*.

Leclerc, F. & Feuillet, N. **2019**. Quaternary coral reef complexes as powerful markers of long-term subsidence related to deep processes at subduction zones: Insights from Les Saintes (Guadeloupe, French West Indies). *Geosphere*, 15, 983–1007, doi: 10.1130/GES02069.1.

Leclerc, F., Feuillet, N., Cabioch, G., Deplus, C., Lebrun, J.F., Bazin, S., Beauducel, F., Boudon, G., LeFriant, A., De Min, L., & Melezan, D. **2014**. The Holocene drowned reef of Les Saintes plateau as witness of a long-term tectonic subsidence along the Lesser Antilles volcanic arc in Guadeloupe. *Marine Geology*, 355, 115–135, doi: 10.1016/j.margeo.2014.05.017.

Leclerc, F., Feuillet, N., & Deplus, C. **2016**. Interactions between active faulting, volcanism, and sedimentary processes at an island arc: Insights from Les Saintes channel, Lesser Antilles arc. *Geochemistry, Geophysics, Geosystems*, 17, 2781–2802, doi: 10.1002/2016GC006337.

Ledru, P. & Guillou-Frottier, L. **2010**. Reservoir Definition. *In*: Huenges, E. (ed.) *Geothermal Energy Systems: Exploration, Development, and Utilization*. Potsdam, Germany, 1–36.

Lee, J.-Y., Marti, K., Severinghaus, J.P., Kawamura, K., H-S., Y., Lee, J.B., & Kim, J.S. **2006**. A redetermination of the isotopic abundances of atmospheric Ar. *Geochimica et Cosmochimica Acta*, 4507–4512.

Legendre, L. **2018**. *Evolution Tectonique Du Nord de l'arc Des Petites Antilles*. Université des Antilles, Pointe-à-Pitre, Guadeloupe.

Legendre, L., Philippon, M., Münch, P., Leticee, J.L., Noury, M., Maincent, G., Cornee, J.J., Caravati, A., Lebrun, J.F., & Mazabraud, Y. **2018**. Trench Bending Initiation: Upper Plate Strain Pattern and Volcanism. Insights From the Lesser Antilles Arc, St. Barthelemy Island, French West Indies. *Tectonics*, 37, 2777–2797, doi: 10.1029/2017TC004921.

Lemale, J. **2015**. *La Géothermie - 2e Édition*, Le Moniteu. Dunod (ed.). Paris.

Leticee, J.-L., Cornee, J.-J., Münch, P., Fietzke, J., Philippon, M., Lebrun, J.-F., De Min, L., & Randrianasolo, A. **2019**. Decreasing uplift rates and Pleistocene marine terraces settlement in the central lesser Antilles fore-arc (La Désirade Island, 16°N). *Quaternary International*, 508, 43–59, doi: 10.1016/j.quaint.2018.10.030.

Lindgren, W. **1913**. *Mineral Deposits, 1e Ed.*, Mc Graw-Hi.

Lindgren, W. **1933**. *Mineral Deposits, 4e Ed.*, Mc Graw-Hi.

Liotta, D. & Ranalli, G. **1999**. Correlation between seismic reflectivity and rheology in extended lithosphere: southern Tuscany, inner Northern Apennines, Italy. *Tectonophysics*, 315, 109–122, doi: 10.1016/S0040-1951(99)00292-9.

Liou, J.G. **1987**. Very low-grade metamorphism of volcanic and volcaniclastic rocks-mineral assemblages and mineral facies. *Low Temperature Metamorphism*, 59–112.

Lloret, E., Dessert, C., Gaillardet, J., Albéric, P., Crispi, O., Chaduteau, C., & Benedetti, M.F. **2011**. Comparison of dissolved inorganic and organic carbon yields and fluxes in the

watersheds of tropical volcanic islands, examples from Guadeloupe (French West Indies). *Chemical Geology*, 280, 65–78, doi: 10.1016/j.chemgeo.2010.10.016.

LÓPEZ, A.M., STEIN, S., DIXON, T., SELLA, G., CALAIS, E., JANSMA, P., WEBER, J., & LAFEMINA, P. **2006**. Is there a northern Lesser Antilles forearc block? *Geophysical Research Letters*, 33, 2–5, doi: 10.1029/2005GL025293.

LOWRIE, W. **1997**. *'Fundamentals of Geophysics', 2nd Ed.*, Paperback. Cambridge University Press (ed.). Cambridge, UK.

LUETH, V.W., RYE, R.O., & PETERS, L. **2005**. "Sour gas" hydrothermal jarosite: ancient to modern acid-sulfate mineralization in the southern Rio Grande Rift. *Chemical Geology*, 215, 339–360, doi: 10.1016/j.chemgeo.2004.06.042.

LUND, J.W. **2004**. 100 years of geothermal power production. *GHC Bulletin*, 9.

LUZIEUX, L.D.A., HELLER, F., SPIKINGS, R., VALLEJO, C.F., & WINKLER, W. **2006**. Origin and Cretaceous tectonic history of the coastal Ecuadorian forearc between 1°N and 3°S: Paleomagnetic, radiometric and fossil evidence. *Earth and Planetary Science Letters*, 249, 400–414, doi: 10.1016/j.epsl.2006.07.008.

**M-N**

MACDONALD, R., HAWKESWORTH, C.J., & HEATH, E. **2000**. The Lesser Antilles volcanic chain: a study in arc magmatism. *Earth Science Reviews*, 49, 1–76, doi: 10.1016/S0012-8252(99)00069-0.

MANGA, M., HORNBACH, M.J., LE FRIANT, A., ISHIZUKA, O., STRONCIK, N., ADACHI, T., ALJAHDALI, M., BOUDON, G., BREITKREUZ, C., FRAASS, A., FUJINAWA, A., HATFIELD, R., JUTZELER, M., KATAOKA, K., LAFUERZA, S., MAENO, F., MARTINEZ-COLON, M., MCCANTA, M., MORGAN, S., PALMER, M.R., SAITO, T., SLAGLE, A., STINTON, A.J., SUBRAMANYAM, K.S. V, TAMURA, Y., TALLING, P.J., VILLEMANT, B., WALL-PALMER, D., & WANG, F. **2012**. Heat flow in the Lesser Antilles island arc and adjacent back arc Grenada basin. *Geochemistry, Geophysics, Geosystems*, 13, 1–19, doi: 10.1029/2012GC004260.

MANN, P., TAYLOR, F.W., EDWARDS, R.L., & KU, T.-L. **1995**. Actively evolving microplate formation by oblique collision and sideways motion along strike-slip faults: An example from the northeastern Caribbean plate margin. *Tectonophysics*, 246, 1–69, doi: 10.1016/0040-1951(94)00268-E.

MANN, P., CALAIS, E., RUEGG, J.-C., DEMETS, C., JANSMA, P.E., & MATTIOLI, G.S. **2002**. Oblique collision in the northeastern Caribbean from GPS measurements and geological observations. *Tectonics*, 21, 7-1-7–26, doi: 10.1029/2001TC001304.

MANZELLA, A., RUGGIERI, G., GIANELLI, G., & PUXEDDU, M. **1998**. Plutonic-geothermal systems of southern Tuscany: a review of the crustal models. *Mem. Soc. Geol. It*, 52, 283–294.

MÁRTON, I., MORITZ, R., & SPIKINGS, R. **2010**. Application of low-temperature thermochronology to hydrothermal ore deposits: Formation, preservation and exhumation of epithermal gold systems from the Eastern Rhodopes, Bulgaria. *Tectonophysics*, 483, 240–254, doi: 10.1016/j.tecto.2009.10.020.

MAS, A., GUISSEAU, D., PATRIER MAS, P., BEAUFORT, D., GENTER, A., SANJUAN, B., & GIRARD, J.P. **2006**. Clay minerals related to the hydrothermal activity of the Bouillante geothermal field (Guadeloupe). *Journal of Volcanology and Geothermal Research*, 158, 380–400, doi: 10.1016/j.jvolgeores.2006.07.010.

MATHIEU, L. **2010**. *The Structure of Guadeloupe , Maderas and Mt Cameroon Volcanoes and the Impact of Strike-Slip Movements*. Université Blaise Pascal - Clermont-Ferrand II, Clermont-Ferrand; Trinity College Dublin.

MATHIEU, L., VAN WYK DE VRIES, B., PILATO, M., & TROLL, V.R. **2011**. The interaction between volcanoes and strike-slip, transtensional and transpressional fault zones: Analogue models and natural examples. *Journal of Structural Geology*, 33, 898–906, doi: 10.1016/j.jsg.2011.03.003.

MATHIEU, L., VAN WYK DE VRIES, B., MANNESSIEZ, C., MAZZONI, N., SAVRY, C., & TROLL, V.R. **2013**. The structure and morphology of the Basse Terre Island, Lesser Antilles volcanic arc. *Bulletin of Volcanology*, 75, 1–15, doi: 10.1007/s00445-013-0700-y.

MATTINSON, J.M., PESSAGNO, E.A., MONTGOMERY, H., & HOPSON, C.A. **2008**. Late Jurassic age of oceanic basement at La Désirade Island, Lesser Antilles arc. *In*: *Special Paper 438: Ophiolites, Arcs, and Batholiths: A Tribute to Cliff Hopson*. Geological Society of America, 175–190., doi: 10.1130/2008.2438(06).

MAUFFRET, A. & LEROY, S. **1997**. Seismic stratigraphy and structure of the Caribbean igneous province. *Tectonophysics*, 283, 61–104, doi: 10.1016/S0040-1951(97)00103-0.

MAURY, R.C., WESTBROOK, G.K., BAKER, P.E., BOUYSSE, P., & WESTERCAMP, D. **1990**. Chapter 5: Geology of the Lesser Antilles. *In*: Dengo, G. & Case, J. E. (eds) *The Geology of North America, Vol. H*. Boulder, Colorado, 141–166.

MCCANN, W.R. & SYKES, L.R. **1986**. REPLY [to "Comment on 'Subduction of aseismic ridges beneath the Caribbean Plate: Implications for the tectonics and seismic potential of the northeastern Caribbean' by W. R. McCann and L. R. Sykes"]. *Journal of Geophysical Research*, 91, 787–791, doi: 10.1029/JB091iB01p00787.

MEIDAV, T. **1998**. Progress in geothermal exploration technology. *Bulletin Geothermal Resources Council*, 27, 81–178.

MERRIMAN, R.J. & PEACOR, D.R. **1998**. Very Low-Grade Metapelites: Mineralogy, Microfabrics and Measuring Reaction Progress. *In*: *Low-Grade Metamorphism*. Oxford, UK, Blackwell Publishing Ltd., 10–60., doi: 10.1002/9781444313345.ch2.

MEYER, C. & HEMLEY, J.J. **1967**. Wall rock alteration. *In*: *Geochemistry of Hydrothermal Ore Deposits*. New-York, 166–235.

MICHARD, A., ALBARÈDE, F., MICHARD, G., MINSTER, J.F., & CHARLOU, J.L. **1983**. Rare-earth elements and uranium in high-temperature solutions from East Pacific Rise hydrothermal vent field (13 °N). *Nature*, 303, 795–797, doi: 10.1038/303795a0.

MIDDLETON, G. V. & BOUMA, A.H. **1973**. Turbidites and Deep Water Sedimentation: Frontmatter. *In*: Geology, S. for S. (ed.) *SEPM Pacific Section Short Course*. Anaheim.

MILICICH, S.D., WILSON, C.J.N., BIGNALL, G., PEZARO, B., & BARDSLEY, C. **2013**. Reconstructing the geological and structural history of an active geothermal field: A case study from New Zealand. *Journal of Volcanology and Geothermal Research*, 262, 7–24, doi: 10.1016/j.jvolgeores.2013.06.004.

MILLOT, R., SCAILLET, B., & SANJUAN, B. **2010**. Lithium isotopes in island arc geothermal systems: Guadeloupe, Martinique (French West Indies) and experimental approach. *Geochimica et Cosmochimica Acta*, 74, 1852–1871, doi: 10.1016/j.gca.2009.12.007.

MILLOT, R., HEGAN, A., & NÉGREL, P. **2012**. Geothermal waters from the Taupo Volcanic Zone, New Zealand: Li, B and Sr isotopes characterization. *Applied Geochemistry*, 27, 677–688, doi: 10.1016/j.apgeochem.2011.12.015.

MINISSALE, A. **1991**. The Larderello geothermal field: a review. *Earth-Science Reviews*, 31, 133–151, doi: 10.1016/0012-8252(91)90018-B.

MIYASHIRO, A. **1961**. Evolution of Metamorphic Belts. *Journal of Petrology*, 2, 277–311, doi: 10.1093/petrology/2.3.277.

MOECK, I.S. **2014**. Catalog of geothermal play types based on geologic controls. *Renewable and Sustainable Energy Reviews*, 37, 867–882, doi: 10.1016/j.rser.2014.05.032.

MONTGOMERY, H., PESSAGNO, E.A., LEWIS, J.F., & SCHELLEKENS, J. **1994**. Paleogeography of Jurassic fragments in the Caribbean. *Tectonics*, 13, 725–732, doi: 10.1029/94TC00455.

MULDER, T. & ALEXANDER, J. **2001**. The physical character of subaqueous sedimentary density flows and their deposits. *Sedimentology*, 48, 269–299, doi: 10.1046/j.1365-3091.2001.00360.x.

MUNCH, P., LEBRUN, J.F., CORNÉE, J.-J., THINON, I., GUENNOC, P., MARCAILLOU, B.J., BEGOT, J., BERTRAND, G., DE BERC, S.B., BISCARRAT, K., CLAUD, C., DE MIN, L., FOURNIER, F., GAILLER, L., GRAINDORGE, D., LÉTICÉE, J.L., MARIE, L., MAZABRAUD, Y., MELINTE-DOBRINESCU, M., MOISSETTE, P., QUILLÉVÉRÉ, F., VERATI, C., & RANDRIANASOLO, A. **2013**. Pliocene to Pleistocene carbonate systems of the Guadeloupe archipelago, french lesser antilles: A land and sea study (the KaShallow project). *Bulletin de la Societe Geologique de France*, 184, 99–110, doi:

10.2113/gssgfbull.184.1-2.99.

MÜNCH, P., CORNEE, J.-J., LEBRUN, J.-F., QUILLEVERE, F., VERATI, C., MELINTE-DOBRINESCU, M., DEMORY, F., SMITH, B., JOURDAN, F., LARDEAUX, J.-M., DE MIN, L., LETICEE, J.-L., & RANDRIANASOLO, A. **2014**. Pliocene to Pleistocene vertical movements in the forearc of the Lesser Antilles subduction: insights from chronostratigraphy of shallow-water carbonate platforms (Guadeloupe archipelago). *Journal of the Geological Society*, 171, 329–341, doi: 10.1144/jgs2013-005.

NAKAI, S., HALLIDAY, A.N., KESLER, S.E., JONES, H.D., KYLE, J.R., & LANE, T.E. **1993**. Rb-Sr dating of sphalerites from Mississippi Valley-type (MVT) ore deposits. *Geochimica et Cosmochimica Acta*, 57, 417–427, doi: 10.1016/0016-7037(93)90440-8.

NAVELOT, V. **2018**. *Caractérisations Structurale et Pétrophysique d'un Système Géothermique En Contexte Volcanique d'arc de Subduction. Exemple de l'archipel de Guadeloupe*. Université de Lorraine.

NAVELOT, V., GERAUD, Y., FAVIER, A., DIRAISON, M., CORSINI, M., LARDEAUX, J.-M., VERATI, C., MERCIER DE LEPINAY, J., LEGENDRE, L., & BEAUCHAMPS, G. **2018**. Petrophysical properties of volcanic rocks and impacts of hydrothermal alteration in the Guadeloupe Archipelago (West Indies). *Journal of Volcanology and Geothermal Research*, 360, 1–21, doi: 10.1016/j.jvolgeores.2018.07.004.

NEILL, I., GIBBS, J.A., HASTIE, A.R., & KERR, A.C. **2010**. Origin of the volcanic complexes of La Désirade, Lesser Antilles: Implications for tectonic reconstruction of the Late Jurassic to Cretaceous Pacific-proto Caribbean margin. *Lithos*, 120, 407–420, doi: 10.1016/j.lithos.2010.08.026.

**O-P**

OLIVEROS, VER., AGUIRRE, L., MORATA, D., SIMONETTI, A., VERGARA, M., BELMAR, M., & CALDERÓN, S. **2008**. Geochronology of very low-grade Mesozoic Andean metabasites; an approach through the K–Ar, 40 Ar/ 39 Ar and U–Pb LA-MC-ICP-MS methods. *Journal of the Geological Society*, 165, 579–584, doi: 10.1144/0016-76492007-113.

OREC-GUADELOUPE. **2018**. *Les Chiffres Clés de l'énergie En Guadeloupe - Bilan 2017*.

OZE, C., CATTELL, H., & GROVE, M. **2017**. 40 Ar/ 39 Ar dating and thermal modeling of adularia to constrain the timing of hydrothermal activity in magmatic settings. *Geology*, 45, 43–46, doi: 10.1130/G38405.1.

PANDARINATH, K., DULSKI, P., TORRES-ALVARADO, I.S., & VERMA, S.P. **2008**. Element mobility during the hydrothermal alteration of rhyolitic rocks of the Los Azufres geothermal field, Mexico. *Geothermics*, 37, 53–72, doi: 10.1016/j.geothermics.2007.10.002.

PARK, C.F.J. & MACDIARMID, R.A. **1970**. *Ore Deposits*. San Francisco, Freeman and Company.

PARKHURST, D.L. & APPELO, C.A.J. **2013**. *Description of Input and Examples for PHREEQC Version 3--A Computer Program for Speciation, Batch- Reaction, One-Dimensional Transport, and Inverse Geochemical Calculations*.

PASSCHIER, C.W. & TROUW, R.A.J. **2005**. *Microtectonics*, 2nd Ed. Springer, Berlin, Heidelberg.

PATRIER, P., BRUZAC, S., PAYS, R., BEAUFORT, D., BOUCHOT, V., VERATI, C., & GADALIA, A. **2013**. Occurrence of K-feldspar-bearing hydrothermal breccias in the Bouillante geothermal field (Basse Terre - Guadeloupe). *Bulletin de la Societe Geologique de France*, 184, 119–128, doi: 10.2113/gssgfbull.184.1-2.119.

PECCERILLO, A. & TAYLOR, S.R. **1976**. Geochemistry of eocene calc-alkaline volcanic rocks from the Kastamonu area, Northern Turkey. *Contributions to Mineralogy and Petrology*, 58, 63–81, doi: 10.1007/BF00384745.

PELISSONNIER, H. **1962**. Classifications métallogéniques : problèmes et essais de synthèse. *Chronique Mines d'Outremer et Recherche Minière*, 43-57;83-95.

PINDELL, J.L. & BARRETT, S.F. **1997**. Geological evolution of the Caribbean region: A plate tectonic perspective. *In*: Dengo, G. & Case, J. E. (eds) *The Geology of North America, Vol. H*. Boulder, Colorado, Geological Society of America, 405–432.

PINDELL, J.L. & KENNAN, L. **2009**. Tectonic evolution of the Gulf of Mexico, Caribbean and northern

South America in the mantle reference frame: an update. *Geological Society, London, Special Publications*, 328, 1.1-55, doi: 10.1144/SP328.1.

PIRAJNO, F. **2009**. *Hydrothermal Processes and Mineral Systems - Volume I*. Dordrecht, Springer Netherlands, doi: 10.1007/978-1-4020-8613-7.

PITCHER, W.S. **1983**. Granite type and tectonic environment. *In*: Hsu, K. (ed.) *Mountain Building Process*. London, Academic Press, 19–40.

PITCHER, W.S. **1993**. *The Nature and Origin of Granites*, 1st editio. London, Chapman & Hall.

POLLACK, H.N., HURTER, S.J., & JOHNSON, J.R. **1993**. Heat flow from the Earth's interior: Analysis of the global data set. *Reviews of Geophysics*, 31, 267, doi: 10.1029/93RG01249.

POWELL, C.M. **1979**. A morphological classification of rock cleavage. *Tectonophysics*, 58, 21–34, doi: 10.1016/0040-1951(79)90320-2.

**R**

RAD, S., LOUVAT, P., GORGE, C., GAILLARDET, J., & ALLÈGRE, C.J. **2006**. River dissolved and solid loads in the Lesser Antilles: New insight into basalt weathering processes. *Journal of Geochemical Exploration*, 88, 308–312, doi: 10.1016/j.gexplo.2005.08.063.

RAD, S., ALLEGRE, C.J., & LOUVAT, P. **2007**. Hidden erosion on volcanic islands. *Earth and Planetary Science Letters*, 262, 109–124, doi: 10.1016/j.epsl.2007.07.019.

RAD, S., CERDAN, O., RIVÉ, K., & GRANDJEAN, G. **2011**. Age of river basins in Guadeloupe impacting chemical weathering rates and land use. *Applied Geochemistry*, 26, S123–S126, doi: 10.1016/j.apgeochem.2011.03.046.

RAD, S., RIVÉ, K., VITTECOQ, B., CERDAN, O., & ALLÈGRE, C.J. **2013a**. Chemical weathering and erosion rates in the Lesser Antilles: An overview in Guadeloupe, Martinique and Dominica. *Journal of South American Earth Sciences*, 45, 331–344, doi: 10.1016/j.jsames.2013.03.004.

RAD, S., RIVÉ, K., VITTECOQ, B., CERDAN, O., & ALLÈGRE, C.J. **2013b**. Chemical weathering and erosion rates in the Lesser Antilles: An overview in Guadeloupe, Martinique and Dominica. *Journal of South American Earth Sciences*, 45, 331–344, doi: 10.1016/j.jsames.2013.03.004.

RAGNARSSON, A. **2015**. Geothermal development in Iceland 2010–2014. *In*: *Proceedings World Geothermal Congress 2015*. Melbourne, Australia, 15.

RANALLI, G. **1995**. *Rheology of the Earth - 2nd Edition*, Chapman &. London, UK.

RANALLI, G. & RYBACH, L. **2005**. Heat flow, heat transfer and lithosphere rheology in geothermal areas: Features and examples. *Journal of Volcanology and Geothermal Research*, 148, 3–19, doi: 10.1016/j.jvolgeores.2005.04.010.

RANCON, J.P. **1983**. *Applications Thermométriques de l'étude Des Minéraux Hydrothermaux En Géothermie Haute-Énergie*. Orléans, France.

RAYMAHASHAY, B.C. **1968**. A geochemical study of rock alteration by hot springs in the Paint Pot Hill area, Yellowstone Park. *Geochimica et Cosmochimica Acta*, 32, 499–522, doi: 10.1016/0016-7037(68)90042-2.

RAZZANO, F. & CEI, M. **2015**. Geothermal Power Generation in Italy 2010-2014 Update Report. *In*: *Proccedings World Geothermal Congress 2015*. Melbourne, Australia, 10.

RENNE, P.R., MUNDIL, R., BALCO, G., MIN, K., & LUDWIG, K.R. **2010**. Joint determination of 40K decay constants and 40Ar*/40K for the Fish Canyon sanidine standard, and improved accuracy for 40Ar/39Ar geochronology. *Geochimica et Cosmochimica Acta*, 74, 5349–5367, doi: 10.1016/j.gca.2010.06.017.

REYES, A.G. **1990**. Petrology of Philippine geothermal systems and the application of alteration mineralogy to their assessment. *Journal of Volcanology and Geothermal Research*, 43, 279–309, doi: 10.1016/0377-0273(90)90057-M.

RICCI, J. **2014**. *Evolution Spatio-Temporelle Du Volcanisme de Basse-Terre (Guadeloupe, Petites Antilles) Revisitée à Partir de Nouvelles Données Géochronologiques, Géochimiques et Géomorphologiques*. Université Paris-Sud, Paris.

RICCI, J., LAHITTE, P., & QUIDELLEUR, X. **2015a**. Construction and destruction rates of volcanoes within tropical environment: Examples from the Basse-Terre Island (Guadeloupe, Lesser

Antilles). *Geomorphology*, 228, 597–607, doi: 10.1016/j.geomorph.2014.10.002.

RICCI, J., QUIDELLEUR, X., & LAHITTE, P. **2015b**. Volcanic evolution of central Basse-Terre Island revisited on the basis of new geochronology and geomorphology data. *Bulletin of Volcanology*, 77, 84, doi: 10.1007/s00445-015-0970-7.

RICCI, J., QUIDELLEUR, X., PALLARES, C., & LAHITTE, P. **2017**. High-resolution K-Ar dating of a complex magmatic system: The example of Basse-Terre Island (French West Indies). *Journal of Volcanology and Geothermal Research*, 345, 142–160, doi: 10.1016/j.jvolgeores.2017.07.013.

RICCI, J., CARLUT, J., & VALET, J.-P. **2018**. Paleosecular variation recorded by Quaternary lava flows from Guadeloupe Island. *Scientific Reports*, 8, 10147, doi: 10.1038/s41598-018-28384-z.

RICHARDS, J.P. **2011**. Magmatic to hydrothermal metal fluxes in convergent and collided margins. *Ore Geology Reviews*, 40, 1–26, doi: 10.1016/j.oregeorev.2011.05.006.

RIPMEESTER, J.A., RATCLIFFE, C.I., DUTRIZAC, J.E., & JAMBOR, J.L. **1986**. Hydronium ion in the alunite-jarosite group. *The Canadian Mineralogist*, 24, 435–447.

RIPP, G.S., KANAKIN, S. V., & SHCHERBAKOVA, M.N. **1998**. Phosphate mineralization in metamorphosed high-alumina rocks of the Ichetuyskoye ore occurrence. *Zapiski Vseross Mineral Obshch*, 127, 98–108.

ROSENBERG, M.D., BIGNALL, G., & RAE, A.J. **2009**. The geological framework of the Wairakei–Tauhara Geothermal System, New Zealand. *Geothermics*, 38, 72–84, doi: 10.1016/j.geothermics.2009.01.001.

ROSSETTI, F., FACCENNA, C., JOLIVET, L., FUNICIELLO, R., TECCE, F., & BRUNET, C. **1999**. Syn- versus post-orogenic extension: the case study of Giglio Island (Northern Tyrrhenian Sea, Italy). *Tectonophysics*, 304, 71–93, doi: 10.1016/S0040-1951(98)00304-7.

ROWLAND, J. V. & SIBSON, R.H. **2004**. Structural controls on hydrothermal flow in a segmented rift system, Taupo Volcanic Zone, New Zealand. *Geofluids*, 4, 259–283, doi: 10.1111/j.1468-8123.2004.00091.x.

RUTTER, E.H. **1976**. The kinetics of rock deformation by pressure solution. *Philosophical Transactions of the Royal Society London*, 283, 203–219, doi: 10.1098/rsta.1976.0079.

RYBACH, L. **2007**. Geothermal sustainability. *In*: *Proceedings European Geothermal Congress*. Unterhaching, Germany, 5.

RYE, R.O. **2005**. A review of the stable-isotope geochemistry of sulfate minerals in selected igneous environments and related hydrothermal systems. *Chemical Geology*, 215, 5–36, doi: 10.1016/j.chemgeo.2004.06.034.

RYE, R.O., BETHIKE, P.M., & WASSERMAN, M.D. **1992**. The stable isotope geochemistry of acid sulfate alteration. *Economic Geology*, 87, 225–262.

**S**

SAK, P.B., NAVARRE-SITCHLER, A.K., MILLER, C.E., DANIEL, C.C., GAILLARDET, J., BUSS, H.L., LEBEDEVA, M.I., & BRANTLEY, S.L. **2010**. Controls on rind thickness on basaltic andesite clasts weathering in Guadeloupe. *Chemical Geology*, 276, 129–143, doi: 10.1016/j.chemgeo.2010.05.002.

SALAÜN, A., VILLEMANT, B., GÉRARD, M., KOMOROWSKI, J.-C., & MICHEL, A. **2011**. Hydrothermal alteration in andesitic volcanoes: Trace element redistribution in active and ancient hydrothermal systems of Guadeloupe (Lesser Antilles). *Journal of Geochemical Exploration*, 111, 59–83, doi: 10.1016/j.gexplo.2011.06.004.

SAMPER, A. **2007**. *Etude Géochronologique, Aspects Géomorphologiques et Géochimiques Du Volcanisme de l'île de Basse Terre (Guadeloupe), et Datation Des Structures d'effondrement de Flanc Majeures de l'Arc Des Petites Antilles*. Université Paris Sud - Paris XI.

SAMPER, A., QUIDELLEUR, X., LAHITTE, P., & MOLLEX, D. **2007**. Timing of effusive volcanism and collapse events within an oceanic arc island: Basse-Terre, Guadeloupe archipelago (Lesser Antilles Arc). *Earth and Planetary Science Letters*, 258, 175–191, doi: 10.1016/j.epsl.2007.03.030.

SAMPER, A., QUIDELLEUR, X., KOMOROWSKI, J.-C., LAHITTE, P., & BOUDON, G. **2009**. Effusive history of the Grande Découverte Volcanic Complex, southern Basse-Terre (Guadeloupe,

French West Indies) from new K–Ar Cassignol–Gillot ages. *Journal of Volcanology and Geothermal Research*, 187, 117–130, doi: 10.1016/j.jvolgeores.2009.08.016.

SAMUELS-CROW, K.E., LUETH, V.W., PETERS, L., & MCINTOSH, W.C. **2012**. 40Ar/39Ar geochronology of jarosite: The effectiveness of HF in removing silicate contaminants. *Chemical Geology*, 314–317, 23–32, doi: 10.1016/j.chemgeo.2012.04.032.

SANJUAN, B. & BRACH, M. **1997**. *Etude Hydrogéochimique Du Champ Géothermique de Bouillante (Guadeloupe)*. Orléans, France.

SANJUAN, B. & TRAINEAU, H. **2008**. Development of the Bouillante geothermal field (Guadeloupe, French West Indies). *IGA News, Quaterly n°73*, 5–9.

SANJUAN, B., BRACH, M., & LASNE, E. **2001**. Bouillante geothermal fluid: mixing and water/rock interaction processes at 250°C. *In*: Cidu, R. (ed.) *Proceedings of the 10th International Symposium on Water/Rock Interactions (WRI10), Vol. 2, 10-15 July 2001*. Villasimius, Italy, A.A. Balkema publishers, 911–914.

SANJUAN, B., LE NINDRE, Y.M., MENJOZ, A., SBAI, A., BRACH, M., & LASNE, E. **2004**. *Travaux de Recherche Liés Au Développement Du Champ Géothermique de Bouillante (Guadeloupe), Report BRGM/RP-53136-FR*. Orléans, France.

SASADA, M., TAGUCHI, S., & HEDENQUIST, J.W. **2000**. Japanese geothermal systems developments in the 1990s-Preface. *Geothermics*, 29, 123–126.

SCHOCH, A.E., BEUKES, G.J., VAN DER WESTHUIZEN, W.A., & DE BRUIYN, H. **1989**. Natroalunite from Koenabib, Pofadder district, South Africa. *South African Journal of Geology*, 92, 20–28.

SCHOEN, R., WHITE, D.E., & HEMLEY, J.J. **1974**. Argillization by Descending Acid at Steamboat Springs, Nevada. *Clays and Clay Minerals*, 22, 1–22, doi: 10.1346/CCMN.1974.0220104.

SEEDORFF, E., DILLES, J.H., PROFFETT, J.M., EINAUDI, M.T., ZURCHER, L., STAVAST, W.J., BARTON, M.D., & JOHNSON, D.A. **2004**. Porphyry-related deposits: characteristics and origin of hypogene features. *Economic Geology 100th Anniversary Volume*, 251–298.

SEMET, M.P., ANSAULT, A., MICHEL, A., VILLEMANT, B., BOUDON, G., & KOMOROWSKI, J.C. **2002**. The 1440 eruption of la Soufrière, Guadeloupe: a textbook example of magma mixing? Explosive volcanism in subduction zones. *In*: *IPGP-INSU-IAVCEI International Congress, Ile de La Martinique*. 62.

SERRI, G., INNOCENTI, F., & MANNETI, P. **1993**. Geochemical and petrological evidence of the subduction of delaminated Adriatic continental lithosphere in the genesis of the Neogene-Quaternary magmatism of central Italy. *Tectonophysics*, 223, 117–147.

SHANKS, P.W.C. **2012**. Hydrothermal Alteration. *In*: *Volcanogenic Massive Sulfide Occurence Model*. U.S. Geological Survey Scientific Investigations Report 2010-5070, 12.

SIBSON, R.H. **1977**. Fault rocks and fault mechanisms. *Journal of the Geological Society*, 133, 191–213, doi: 10.1144/gsjgs.133.3.0191.

SIBSON, R.H. **1984**. Roughness at the base of the seismogenic zone: Contributing factors. *Journal of Geophysical Research: Solid Earth*, 89, 5791–5799, doi: 10.1029/JB089iB07p05791.

SINCLAIR, H.D. **1997**. Flysch to molasse transition in peripheral foreland basins: the role of the passive margin versus slab breakoff. *Geology*, 25, 1123–1126.

SMITH, D.J., NADEN, J., JENKIN, G.R.T., & KEITH, M. **2017**. Hydrothermal alteration and fluid pH in alkaline-hosted epithermal systems. *Ore Geology Reviews*, 89, 772–779, doi: 10.1016/j.oregeorev.2017.06.028.

SPEED, R.C. **1985**. Cenozoic collision of the Lesser Antilles Arc and continental South America and the origin of the El Pilar Fault. *Tectonics*, 4, 41–69, doi: 10.1029/TC004i001p00041.

SPIKINGS, R.A., WINKLER, W., HUGHES, R.A., & HANDLER, R. **2005**. Thermochronology of allochthonous terranes in Ecuador: Unravelling the accretionary and post-accretionary history of the Northern Andes. *Tectonophysics*, 399, 195–220, doi: 10.1016/j.tecto.2004.12.023.

STACEY, F.D. **1992**. *'Physics of the Earth', 3rd Edition*, Brookfield. Brisbane.

STEIGER, R.H. & JÄGER, E. **1977**. Subcommission on geochronology: Convention on the use of decay constants in geo- and cosmochronology. *Earth and Planetary Science Letters*, 36, 359–362, doi:

10.1016/0012-821X(77)90060-7.

STEINER, A. **1977**. The Wairakei geothermal area, North Island, New Zealand. *Geological Survey Bulletin*, 90.

STIMAC, J., GOFF, F., & GOFF, C.J. **2015**. Intrusion-Related Geothermal Systems. *In*: *The Encyclopedia of Volcanoes*. Elsevier, 799–822., doi: 10.1016/B978-0-12-385938-9.00046-8.

STOFFREGEN, R.E. & ALPERS, C.N. **1992**. Observations on the unit-cell dimensions, H2O contents, and δD values of natural and synthetic alunite. *American Mineralogist*, 77, 1092–1098.

STOFFREGEN, R.E., RYE, R.O., & WASSERMAN, M.D. **1994**. Experimental studies of alunite: I. 18O-16O and D-H fractionation factors between alunite and water at 250–450°C. *Geochimica et Cosmochimica Acta*, 58, 903–916, doi: 10.1016/0016-7037(94)90514-2.

STOFFREGEN, R.E., ALPERS, C.N., & JAMBOR, J.L. **2000**. Alunite-Jarosite Crystallography, Thermodynamics, and Geochronology. *Reviews in Mineralogy and Geochemistry*, 40, 453–479, doi: 10.2138/rmg.2000.40.9.

STURCHIO, N.C., MUEHLENBACHS, K., & SEITZ, M.G. **1986**. Element redistribution during hydrothermal alteration of rhyolite in an active geothermal system: Yellowstone drill cores Y-7 and Y-8. *Geochimica et Cosmochimica Acta*, 50, 1619–1631, doi: 10.1016/0016-7037(86)90125-0.

SUN, S. -S. & MCDONOUGH, W.F. **1989**. Chemical and isotopic systematics of oceanic basalts: implications for mantle composition and processes. *Geological Society, London, Special Publications*, 42, 313–345, doi: 10.1144/GSL.SP.1989.042.01.19.

**T-U**

TAYLOR, S.R. & MCLENNAN, S.M. **1995**. The geochemical evolution of the continental crust. *Reviews of Geophysics*, 33, 241, doi: 10.1029/95RG00262.

THAIN, I., REYES, A.G., & HUNT, T. **2006**. *A Practical Guide to Exploiting Low Temperature Geothermal Resources*.

THINON, I., GUENNOC, P., BITRI, A., & TRUFFERT, C. **2010**. Study of the Bouillante Bay (West Basse-Terre Island shelf): contribution of geophysical surveys to the understanding of the structural context of Guadeloupe (French West Indies - Lesser Antilles). *Bulletin de la Societe Geologique de France*, 181, 51–65, doi: 10.2113/gssgfbull.181.1.51.

TURCOTTE, D.L. & SCHUBERT, G. **2002**. *Geodynamics*. Cambridge University Press, Cambridge.

TURNER, S., HAWKESWORTH, C., VAN CALSTEREN, P., HEATH, E., MACDONALD, R., & BLACK, S. **1996**. U-series isotopes and destructive plate margin magma genesis in the Lesser Antilles. *Earth and Planetary Science Letters*, 142, 191–207, doi: 10.1016/0012-821X(96)00078-7.

UEDA, A. & KROUSE, H.R. **1986**. Direct conversion of sulphide and sulphate minerals to SO2 for isotope analyses. *GEOCHEMICAL JOURNAL*, 20, 209–212, doi: 10.2343/geochemj.20.209.

**V**

VALLEJO, C., SPIKINGS, R.A., LUZIEUX, L., WINKLER, W., CHEW, D., & PAGE, L. **2006**. The early interaction between the Caribbean Plateau and the NW South American Plate. *Terra Nova*, 18, 264–269, doi: 10.1111/j.1365-3121.2006.00688.x.

VAN BENTHEM, S., GOVERS, R., SPAKMAN, W., & WORTEL, R. **2013**. Tectonic evolution and mantle structure of the Caribbean. *Journal of Geophysical Research: Solid Earth*, 118, 3019–3036, doi: 10.1002/jgrb.50235.

VARET, J. **2011**. La géothermie. *L'encyclopédie du développement durable*, 12.

VELDE, B. **1985**. *A Physico-Chemical Explanation of Their Occurrence. Developments in Sedimentology*. Amsterdam, Elsevier.

VERATI, C. & JOURDAN, F. **2014**. Modelling effect of sericitization of plagioclase on the 40 K/ 40 Ar and 40 Ar/ 39 Ar chronometers: implication for dating basaltic rocks and mineral deposits. *Geological Society, London, Special Publications*, 378, 155–174, doi: 10.1144/SP378.14.

VERATI, C., PATRIER-MAS, P., LARDEAUX, J.-M., & BOUCHOT, V. **2014**. Timing of geothermal activity in an active island-arc volcanic setting: First 40Ar/39Ar dating from Bouillante geothermal field (Guadeloupe, French West Indies). *Geological Society, London, Special*

*Publications*, 378, 285–295, doi: 10.1144/SP378.19.

VERATI, C., MAZABRAUD, Y., LARDEAUX, J.-M., CORSINI, M., SCHNEIDER, D., VOITUS, E., & ZAMI, F. **2016**. Tectonic evolution of Les Saintes archipelago (Guadeloupe, French West Indies): relation with the Lesser Antilles arc system. *Bulletin de la Société Géologique de France*, 187, 3–10, doi: 10.2113/gssgfbull.187.1.3.

VERATI, C., LARDEAUX, J.-M., FAVIER, A., CORSINI, M., PHILIPPON, M., & LEGENDRE, L. **2018**. Arc-related metamorphism in the Guadeloupe archipelago (Lesser Antilles active island arc): First report and consequences. *Lithos*, 320–321, 592–598, doi: 10.1016/j.lithos.2018.08.005.

VILLA, I.M., RUGGIERI, G., PUXEDDU, M., & BERTINI, G. **2006**. Geochronology and isotope transport systematics in a subsurface granite from the Larderello–Travale geothermal system (Italy). *Journal of Volcanology and Geothermal Research*, 152, 20–50, doi: 10.1016/j.jvolgeores.2005.09.011.

VURAL, A. **2017**. K-Ar Dating for Determining the Age of Mineralization as Alteration Product: A Case Study of Antimony Mineralization Vein Type in Granitic Rocks of Gümüşhane Area, Turkey. *Acta Physica Polonica A*, 132, 792–795, doi: 10.12693/APhysPolA.132.792.

**W**

WADGE, G. **1984**. Comparison of volcanic production rates and subduction rates in Lesser Antilles and Central America. *Geology*, 12, 555–558.

WARR, L.N. & COX, S.C. **2016**. Correlating illite (Kübler) and chlorite (Árkai) "crystallinity" indices with metamorphic mineral zones of the South Island, New Zealand. *Applied Clay Science*, 134, 164–174, doi: 10.1016/j.clay.2016.06.024.

WESTERCAMP, D. **1979**. Diversity, structural control and origin of recent volcanism in the Lesser Antilles island arc. *Bulletin du Bureau de Recherches Géologiques et Minières*, Sect. IV, 211–226.

WESTERCAMP, D. & TAZIEFF, H. **1980**. *Guide Géologiques Régionaux, Martinique, Guadeloupe, Saint-Martin, La Désirade*, Elsevier M. Paris.

WHITE, A.F. & BLUM, A.E. **1995**. Effects of climate on chemical_ weathering in watersheds. *Geochimica et Cosmochimica Acta*, 59, 1729–1747, doi: 10.1016/0016-7037(95)00078-E.

WHITE, D.E. **1955**. Thermal springs and epithermal ore deposits. *Economic Geology 50th Anniversary volume*, 99–154.

WHITE, D.E. **1965**. *Geothermal Energy*. Washington.

WHITE, D.E. **1973**. Characteristics of geothermal ressources and problems of utilization. *In*: Paul and Otte, C. (ed.) *Geothermal Energy-Ressources, Production, Stimulation*. Stanford Universal Press, 69–94.

WHITE, D.E., MUFFLER, L.J.P., & TRUESDELL, A.H. **1971**. Vapor-Dominated Hydrothermal Systems Compared with Hot-Water Systems. *Economic Geology*, 66, 75–97.

WHITE, N.C. & HEDENQUIST, J.W. **1990**. Epithermal environments and styles of mineralization: Variations and their causes, and guidelines for exploration. *Journal of Geochemical Exploration*, 36, 445–474, doi: 10.1016/0375-6742(90)90063-G.

WHITE, N.C. & HEDENQUIST, J.W. **1995**. Epithermal gold deposits: styles, characteristics and exploration. *SEG Newsletter*, 23, 1–9.

WHITE, W.M. & DUPRÉ, B. **1986**. Sediment subduction and magma genesis in the Lesser Antilles: Isotopic and trace element constraints. *Journal of Geophysical Research*, 91, 5927, doi: 10.1029/JB091iB06p05927.

WIEWIÓRA, A. & WEISS, Z. **1990**. Crystallochemical classifications of phyllosilicates based on the unified system of projection of chemical composition: II. The chlorite group. *Clay Minerals*, 25, 83–92, doi: 10.1180/claymin.1990.025.1.09.

WILSON, C.J.N., HOUGHTON, B.F., MCWILLIAMS, M.O., LANPHERE, M.A., WEAVER, S.D., & BRIGGS, R.M. **1995**. Volcanic and structural evolution of Taupo Volcanic Zone, New Zealand: a review. *Journal of Volcanology and Geothermal Research*, 68, 1–28, doi: 10.1016/0377-0273(95)00006-G.

WILSON, C.J.N., CHARLIER, B.L.A., FAGAN, C.J., SPINKS, K.D., GRAVLEY, D.M., SIMMONS, S.F., & BROWNE, P.R.L. **2008**. U–Pb dating of zircon in hydrothermally altered rocks as a correlation

tool: Application to the Mangakino geothermal field, New Zealand. *Journal of Volcanology and Geothermal Research*, 176, 191–198, doi: 10.1016/j.jvolgeores.2008.04.010.

WINCHESTER, J.A. & FLOYD, P.A. **1977**. Geochimical discrimination of different magma series and their differentiation products using immobile elements. *Chemical Geology*, 20, 325–343, doi: 10.1016/0009-2541(77)90057-2.

WISE, W. **1975**. Solid solution between the alunite, woodhouseite, and crandallite mineral serie. *Neues Jahrbuch für Mineralogie Monatshefte*, 540–545.

WOHLETZ, K. & HEIKEN, G. **1992**. *Volcanology and Geothermal Energy*. United States.

WOJDYR, M. **2010**. Fityk : a general-purpose peak fitting program. *Journal of Applied Crystallography*, 43, 1126–1128, doi: 10.1107/S0021889810030499.

WOLDEGABRIEL, G., BROXTON, D.E., & BYERS, F.M. **1996**. Mineralogy and temporal relations of coexisting authigenic minerals in altered silicic tuffs and their utility as potential low-temperature dateable minerals. *Journal of Volcanology and Geothermal Research*, 71, 155–165, doi: 10.1016/0377-0273(95)00064-X.

www.geothermie-perspectives.fr. **2019**. *Géothermie360*. World Wide Web Address: http://www.geothermie-perspectives.fr.

**Z**

ZAMI, F., QUIDELLEUR, X., RICCI, J., LEBRUN, J.-F., & SAMPER, A. **2014**. Initial sub-aerial volcanic activity along the central Lesser Antilles inner arc: New K–Ar ages from Les Saintes volcanoes. *Journal of Volcanology and Geothermal Research*, 287, 12–21, doi: 10.1016/j.jvolgeores.2014.09.011.

ZHOU, L., ZHANG, Z., LI, Y., YOU, F., WU, C., & ZHENG, C. **2013**. Geological and geochemical characteristics in the paleo-weathering crust sedimentary type REE deposits, western Guizhou, China. *Journal of Asian Earth Sciences*, 73, 184–198, doi: 10.1016/j.jseaes.2013.04.011.

ZHU, Y., AN, F., & TAN, J. **2011**. Geochemistry of hydrothermal gold deposits: A review. *Geoscience Frontiers*, 2, 367–374, doi: 10.1016/j.gsf.2011.05.006.

# Chapitre X : Annexes

Dépôts pyroclastiques au Sud de la Basse-Terre, Monts-Caraïbes

# Chapitre X

## X.1. Fiches de tâches du projet GEOTREF

| **Tâche N° 2.1 - Etude des affleurements, des analogues de terrain et des données régionales** | | | |
|---|---|---|---|
| **N°lot: 2** | **Début:** T0 | **Fin:** T0 + 12 | **Durée:** 12 |
| **Tâche(s) antécédente(s) :** | **Tâche (s) suivante (s):** 5.1 – 6.1 – 6.2 – 6.6 – 6.7 – 6.8 – 6.10 –7.1 – 7.2 – 7.8– 8.1 – 8.3 – 8.4 – 8.5 – 10.1 – 10.4 – 10.5 – 11.8 – 12.1 – 12.2 | | |
| **Description synthétique de la tâche :** Etude structurale et de la pétrologie : failles (localisation, orientation du plan de faille), fractures et autres objets géologiques pour réaliser des schémas géologiques et structuraux. Etudes des caractéristiques (propriétés), pétrophysiques de la matrice et des matériaux composant les zones de failles et fractures. Trois cadres géodynamiques seront investigués : des roches magmatiques et métamorphiques dans un contexte extensif, des roches volcaniques en contexte extensif, des roches volcaniques en contexte de subduction. La géométrie des réservoirs est assez bien caractérisée pour les systèmes extensifs, peu de données sont disponibles dans ces systèmes de subduction ou ceux structurés lors des phases de compressions. Les différents types de porosités à chacune des unités seront définis, porosité de fractures, porosité primaire de matrice, porosité secondaire liée aux circulations de fluides secondaires. Ce schéma, construit à partir de l'étude d'analogue permettra de proposer un premier modèle de réservoir mal contraint à ce jour et qui peut avoir des implications sur la compréhension de signaux précurseurs aux éruptions volcaniques par exemple ou à la définition des gites à oxydes et sulfures. Associés aux résultats de la tache 2.2, les résultats obtenus ici permettront de préciser les lois d'échelle contrôlant la géométrie du réservoir, en termes de longueur et d'espacement des structures notamment. | | | |
| **Etat de l'art :** La dynamique des réservoirs est contrôlée par les éléments qui composent le réseau poreux de ces réservoirs [1] [2] [3]. Ces éléments peuvent être de type structural avec des failles et des fractures et peuvent être également comprendre des éléments matriciels, les proportions entre ces différents éléments dans un réservoir dépendent de la nature pétrographique de la formation hôte et du contexte géodynamique [4] [5] [6]. Dans les formations sédimentaires, les structures matricielles sont principalement primaires et peuvent avoir un rôle important au côté des structures tectoniques [7]. Alors que dans les formations de socles, la porosité matricielle est souvent développée lors de processus secondaires entrainant l'altération des phases primaires [8]. Des caractérisations de réservoirs géothermiques en systèmes volcaniques existent principalement pour les systèmes extensifs, principalement en Islande, les réservoirs des systèmes volcaniques en systèmes compressifs sont peu décrits malgré de nombreux sites géothermiques exploités (Philippines, Italie). La définition pluriscalaire des réservoirs géothermiques est déterminante dans la modélisation aussi bien des propriétés de transferts que des interactions eaux- roches avec l'identification des structures kilométriques à micrométriques. Grâce à une sélection d'échantillons représentatifs des différents faciès pétrographiques et structuraux, une description pétrophysique des différents faciès. | | | |
| **Connaissances indispensables à la réalisation de la tâche :**<br>• Connaissance des réservoirs fracturés (CNRS/GeoRessources, GeoAzur, UAG, GEC) et des altérations associées.<br>• Expérience des partenaires sur les études géologiques de terrain | | | |
| **Description des travaux :**<br>Les travaux de cette tâche seront réalisés en collaboration entre les partenaires, et devront conduire à :<br>• L'élaboration de méthodes permettant de faire la liaison entre les données de surface et les propriétés pétrophysiques et d'écoulement de fond.<br>• Fournir une description relativement précise des éléments devant figurer dans les schémas conceptuels. | | | |

**Moyens utilisés:**

- Etat de l'art.
- Expérimentations préliminaires.
- Cartographie.
- Mesures de la porosité par saturation à l'hélium, à l'eau et par injection de mercure, de la perméabilité, de la conductivité thermique, de la vitesse de propagation des ondes.
- Caractérisation pétrographique par observations en microscopie électronique et optique, par diffraction de Rx sur poudre.
- Mesures géophysiques de sub-surfaces, magnétiques, électrique et sismique.
- Réalisation de travaux de r&d dans le cadre de la thèse 1(codirection UAG et GeoAzur) et de la thèse 2 (direction GeoRessources)

**Objectifs – résultats attendus (et indicateurs associés)**

Modèle de réservoir pétrographique et pétrophysique.

**Sous-traitants envisagés :**

GEC : prestation de sous-traitance pour DRX répartie entre les tâches 2.1, 5.1 et 10.1 (14000€)

**Livrables de la tâche:**

- **L2.1.1:** *Date prévue:* T30
  *Description du contenu* : Méthodes de liaison des propriétés pétrophysique de surface et de fond et description des schémas conceptuels de réservoirs
  *Partenaires impliqués* : **GeoAzur**, GEC, GeoRessources, UA.

| Tâche N° 4.3 - Datation des systèmes hydrothermaux | | | |
|---|---|---|---|
| **N°lot: 4** | **Début:** T0 | **Fin:** T0 + 24 | **Durée:** 24 |
| **Tâche(s) antécédente(s):** | **Tâche (s) suivante (s):** 6.9 – 7.2 – 7.3 – 7.8 – 8.1 – 8.3 – 8.4 – 8.5 – 10.3 – 10.5 – 11.3 – 12.1 – 12.4 | | |

**Description synthétique de la tâche :** caractérisation pétro-géochimique des phases minérales liées aux circulations fluides. Datation par la méthode $^{39}Ar/^{40}Ar$ de ces minéralisations

**Etat de l'art :** Les vitesses de transfert des fluides dans la croûte et les cinétiques des altérations hydrothermales dans les zones de subduction sont aujourd'hui peu ou pas connues. L'étude des altérations hydrothermales et de minéralisations associées nécessite un développement méthodologique significatif vu les spécificités chimiques et le caractère récent des formations volcaniques considérées.

**Connaissances indispensables à la réalisation de la tâche :**

- Identification sur le terrain des minéralisations associées aux circulations hydrothermales

**Description des travaux :**

- cartographie structurale
- échantillonnage
- Séparation des phases minérales en laboratoire
- Irradiation des échantillons dans un réacteur nucléaire
- datations $^{40}Ar/^{39}Ar$

**Moyens utilisés:**

- Datation par la méthode $^{40}Ar/^{39}Ar$ :
  - chauffage des échantillons au laser
  - Analyse par spectrométrie en phase gazeuse
- caractérisation pétrographique et géochimique:
  - microsonde ionique

**Objectifs – résultats attendus (et indicateurs associés)**
Datation des minéralisations hydrothermales et estimation des vitesses de transfert

**Sous-traitants envisagés:**

**Livrables de la tâche:**

- **L4.3.1:** *Date prévue:* T24
  *Description du contenu* : Rapport sur les résultats des analyses des altérations hydrothermales.
  *Partenaires impliqués:* CNRS / **GeoAzur**

| Tâche N° 10.3 - Etudes manifestations géochimiques de surface | | | |
|---|---|---|---|
| **N°lot: 10** | **Début:** TO | **Fin:** ~~TO + 12 mois~~ | **Durée:** 2 mois |
| **Tâche(s) antécédente(s):** 1.2 – Lot 4 | | **Tâche (s) suivante (s):** 10.5 – 10.6 – 11.2 – 12.1 – 12.4 | |
| **Description synthétique de la tâche :** Mise en pratique des travaux méthodologiques et r&d du lot 4.<br>Prélèvements, analyses et interprétation des manifestations de surface et des altérations hydrothermales | | | |
| **Etat de l'art :**<br>cf. Lot 4 | | | |
| **Connaissances indispensables à la réalisation de la tâche :**<br>• Localisation des manifestations de surface et des altérations hydrothermales | | | |
| **Description des travaux:**<br>• Prélèvements et analyses des manifestations géochimiques de surface (eau, gaz)<br>• Géochronologie des altérations hydrothermales | | | |
| **Moyens utilisés:**<br>• Sous-traitance et prélèvements sur site | | | |
| **Objectifs – résultats attendus (et indicateurs associés)**<br>• Géothermométrie des manifestations de surface<br>• Typologie des fluides des manifestations de surface/caractérisation géochimique<br>• Datation des minéralisations hydrothermales<br>• Estimation des vitesses de transfert et cinétiques des altérations hydrothermales | | | |
| **Sous-traitants envisagés :**<br>Société externe pour la mesure des températures en forage. | | | |
| **Livrables de la tâche:**<br>• **L10.3.1:** *Date prévue*: ~~T12~~T24<br>*Description du contenu:* Rapport d'étude<br>*Partenaires impliqués* : UAG et GeoAzur | | | |

| Tâche N° 10.5 - Evaluation qualité de la ressource géothermique | | | |
|---|---|---|---|
| **N°lot: 10** | **Début:** TO | **Fin:** TO + 21 mois | **Durée:** 21 mois |
| **Tâche(s) antécédente(s):** 1.2 – Lot 2 – Lot 3 – Lot 4 – 7.1 – 7.2 – 7.8 – 10.1 – 10.2 – 10.3 – 10.4 | **Tâche (s) suivante (s):** 10.6 – 11.7 | | |

**Description synthétique de la tâche :** Evaluation de la qualité de la ressource géothermique : choix de modèle(s) géologiques conceptuel(s), estimation de la température, de l'extension et de la capacité du réservoir. Exploitation si possible des données géophysiques pour construire un premier modèle structural et géologique. Conception préliminaire de l'exploitation du réservoir (zone centrale de production, zone de réinjection, localisation de la centrale). Qualification de la ressource : critères favorables, critères défavorables, risques d'échec. Décision quant à la réalisation de l'étude de faisabilité.

**Etat de l'art :**

Actuellement, la méthode volumétrique de Muffler P. et Cataldi R. (1977) est celle qui actuellement la plus employée. Elle est fondée sur la détermination analytique de l'énergie calorifique stockée dans un volume déterminé de roche situé entre la surface du sol et une profondeur de 3 km ; c'est ce que l'on appelle la ressource géothermique de base accessible (RGBA). La petite partie de la RGBA qu'il est possible d'extraire jusqu'à la surface est appelée Ressource géothermique.

La méthode volumétrique de Muffler est considérée dans la profession comme la méthode la plus fiable parmi toutes les solutions à disposition lors des étapes intermédiaires d'exploration, lorsque l'on ne connaît que quelques paramètres fondamentaux du système géothermique. Dans la bibliographie, parmi les exemples d'application réussie de cette méthode figure le cas de l'évaluation du potentiel géothermique aux États-Unis d'Amérique (Muffler, 1979). À noter néanmoins que pour parvenir à une valeur précise dans l'évaluation du potentiel énergétique d'un champ géothermique, il est indispensable de passer par l'étape de faisabilité et de découverte de la ressource, qui implique de réaliser une campagne de puits profonds d'exploration et de réaliser des tests de production en vue de déterminer, entre autres paramètres fondamentaux : la pression, le débit massique, l'enthalpie et la composition chimique des fluides (salinité, gaz...).

Application de méthodes et approches issues de la r&d (lots 2 à 4)

**Connaissances indispensables à la réalisation de la tâche :**

- Imagerie géophysique de la zone concernée

**Description des travaux:**

- Analyse de l'ensemble des données de préfaisabilité disponibles (surface, géophysique, marine, …)
- Application de critères d'évaluation de la ressource issus de la r&d (lots 2 à 4)

**Moyens utilisés:**

- Méthodes et approches issues de la r&d (lots 2 à 4)

**Objectifs – résultats attendus (et indicateurs associés)**

- Interprétation des données de préfaisabilité
- Modèle conceptuel 3D géoréferencé
- Evaluation de la ressource géothermique à partir de critères établis

**Sous-traitants envisagés:**

-

**Livrables de la tâche:**

- **L10.5.1:** *Date prévue*: T21
  *Description du contenu:* Rapport d'étude
  *Partenaires impliqués* : **KIDOVA,** Georessoucres, GeoAzur, IPGS, LHyGeS

| Tâche N° 12.2 - Etudes géol. de surface et télédétection | | | |
|---|---|---|---|
| **N°lot : 12** | **Début :** TO + 36 mois | **Fin :** TO + 48 mois | **Durée :** 12 mois |
| **Tâche(s) antécédente(s) :** Lot 2 – 10.1 | | **Tâche (s) suivante (s) :** aucune | |
| **Description synthétique de la tâche :** Rédaction dans un manuel méthodologique collectif et pluridisciplinaire sur la géothermie haute énergie en milieux fracturés, de l'approche méthodologique sur le thème l'exploitation de données en liaison avec les études géologiques de surface. | | | |
| **Etat de l'art :** | | | |
| **Connaissances indispensables à la réalisation de la tâche :**<br>• | | | |
| **Description des travaux :**<br>• Rédaction<br>• Relecture<br>• Encadrement d'un Master | | | |
| **Moyens utilisés :**<br>• | | | |
| **Objectifs – résultats attendus (et indicateurs associés)**<br>• | | | |
| **Sous-traitants envisagés :**<br>• | | | |
| **Livrables de la tâche :**<br>• **L12.2.1 :** *Date prévue*: T48<br>*Description du contenu* : Rédaction dans un manuel méthodologique collectif et pluridisciplinaire sur la géothermie haute énergie en milieux fracturés, de l'approche méthodologique sur le thème l'exploitation de données en liaison avec les études géologiques de surface<br>*Partenaires impliqués* : KIDOVA, CNRS/Georessources et Geoazur, GEC | | | |

## X.2. Article 1 - Supplementary data

**Table A-1: Results of paleotensors obtained by field data inversion in the Basal Complex of the Basse-Terre de Guadeloupe.**

| n/nt | $\sigma_1$ | $\sigma_2$ | $\sigma_3$ | R' | $\alpha_w$ | $QR_w$ | $QR_t$ |
|---|---|---|---|---|---|---|---|
| 83/96 | 52/320 | 38/131 | 05/224 | 0,68 | 10,2 | C | C |

**Table A-2: 40Ar/39Ar analyses results, ArArCalc files.**

Fichiers Excel en ligne sur le site du BSGF

BT22_A.xls

BT22_B.xls

BT22_A-B.xls

Table A-3: New major element data set of whole-rock samples analysed for this study.

| Latitude | Longitude | Localisation | Sample | Volcanic formation | Transformation state | $SiO_2$ | $Al_2O_3$ | $Fe_2O_3$ | MnO | MgO | CaO | $Na_2O$ | $K_2O$ | $TiO_2$ | $P_2O_5$ | LOI | Total |
|---|---|---|---|---|---|---|---|---|---|---|---|---|---|---|---|---|---|
| | | | | | | (wt %) | | | | | | | | | | | |
| 16°21'10.77" N | 61°43'29.60" W | BT1 | BT1_01 | debris flow | fresh | 56,76 | 17,23 | 8,46 | 0,17 | 3,69 | 7,32 | 3,12 | 1,07 | 0,68 | < L.D. | 0,59 | 99,08 |
| 16°21'10.77" N | 61°43'29.60" W | | BT1_02 | debris flow | fresh | 63,02 | 16,85 | 6,16 | 0,04 | 0,52 | 2,86 | 3,43 | 1,61 | 0,57 | < L.D. | 5,00 | 100,06 |
| 16°21'10.77" N | 61°43'29.60" W | | BT1_03 | debris flow | sub-metamorphized | 62,75 | 16,65 | 7,21 | 0,10 | 1,15 | 2,30 | 2,91 | 1,65 | 0,61 | < L.D. | 4,13 | 99,44 |
| 16°21'14.78" N | 61°43'29.80" W | | BT1_04 | debris flow | metamorphized | 64,05 | 16,44 | 6,42 | 0,05 | 0,54 | 3,04 | 3,51 | 1,64 | 0,57 | < L.D. | 4,21 | 100,46 |
| 16°21'14.78" N | 61°43'29.80" W | | BT1_05 | debris flow | metamorphized | 58,47 | 16,47 | 8,37 | 0,13 | 2,67 | 5,92 | 3,21 | 1,29 | 0,87 | < L.D. | 2,85 | 100,24 |
| 16°21'26.14" N | 61°43'45.71" W | BT2 | BT2_01 | debris flow | sub-metamorphized | 63,90 | 16,96 | 6,25 | 0,05 | 0,57 | 3,13 | 3,46 | 1,63 | 0,59 | < L.D. | 3,81 | 100,34 |
| 16°21'32.40" N | 61°44'46.07" W | BT3 | BT3_01 | debris flow | metamorphized and weathered | 60,61 | 15,69 | 7,60 | 0,04 | 0,47 | 1,67 | 3,96 | 1,32 | 0,71 | < L.D. | 7,84 | 99,90 |
| 16°21'16.79" N | 61°45'26.61" W | BT4 | BT4_01 | lava flow | sub-metamorphized | 60,88 | 15,39 | 8,62 | 0,16 | 1,67 | 5,23 | 4,07 | 1,52 | 1,04 | 0,23 | 1,30 | 100,09 |
| 16°21'16.79" N | 61°45'26.61" W | | BT4_02 | lava flow | sub-metamorphized | 60,78 | 15,61 | 8,73 | 0,09 | 1,19 | 4,56 | 4,11 | 1,55 | 1,05 | 0,23 | 2,35 | 100,25 |
| 16°21'18.89" N | 61°45'29.84" W | BT5 | BT5_01 | lava flow | fresh | 61,12 | 15,35 | 8,69 | 0,17 | 1,77 | 5,25 | 3,98 | 1,51 | 1,04 | 0,23 | 1,56 | 100,67 |
| 16°21'18.33" N | 61°45'29.91" W | | BT5_02 | lava flow | metamorphized | 60,72 | 15,50 | 8,67 | 0,09 | 1,37 | 4,55 | 4,01 | 1,56 | 1,05 | 0,23 | 3,08 | 100,82 |
| 16°21'18.16" N | 61°45'30.80" W | BT6 | BT6_01 | lava flow | fresh | 61,42 | 15,93 | 7,22 | 0,09 | 1,39 | 4,86 | 4,19 | 1,61 | 1,09 | 0,22 | 2,32 | 100,35 |
| 16°21'20.24" N | 61°45'35.13" W | BT7 | BT7_01 | lava flow | fresh | 59,93 | 15,36 | 8,51 | 0,10 | 1,50 | 5,10 | 4,01 | 1,54 | 1,03 | 0,22 | 1,98 | 99,27 |
| 16°21'06.61" N | 61°45'52.43" W | BT8 | BT8_01 | lava flow | fresh | 58,13 | 16,00 | 9,13 | 0,12 | 1,86 | 5,44 | 3,94 | 1,25 | 1,06 | < L.D. | 2,73 | 99,68 |
| 16°21'07.10" N | 61°46'00.11" W | BT9 | BT9_01 | lava flow | metamorphized | 60,34 | 16,50 | 8,19 | 0,04 | 0,57 | 1,73 | 4,02 | 1,60 | 1,01 | < L.D. | 6,24 | 100,24 |
| 16°21'06.22" N | 61°46'00.55" W | | BT9_02 | lava flow | metamorphized | 61,41 | 16,30 | 7,92 | 0,05 | 0,34 | 2,40 | 3,95 | 1,56 | 0,97 | < L.D. | 4,90 | 99,78 |
| | 61°46'02.35" W | BT10 | BT10_01 | lava flow | sub-metamorphized | 62,02 | 15,77 | 7,72 | 0,08 | 0,70 | 3,95 | 4,66 | 1,48 | 0,94 | 0,23 | 2,44 | 100,01 |
| 16°21'03.08" N | 61°46'08.53" W | BT11 | BT11_01 | lava flow | metamorphized | 64,28 | 15,10 | 6,69 | 0,12 | 0,79 | 3,62 | 4,64 | 1,57 | 0,78 | 0,24 | 2,70 | 100,52 |
| 16°21'03.63" N | 61°46'08.43" W | BT12 | BT12_01 | lava flow | metamorphized | 59,77 | 18,03 | 6,83 | 0,15 | 1,82 | 6,30 | 4,17 | 1,07 | 0,77 | 0,20 | 1,91 | 101,01 |
| 16°21'04.04" N | 61°46'08.47" W | | BT12_02 | lava flow | fresh | 59,87 | 18,09 | 6,82 | 0,10 | 1,74 | 6,35 | 4,07 | 1,01 | 0,76 | 0,20 | 1,84 | 100,85 |
| 16°20'37.41" N | 61°46'41.42" W | BT13 | BT13_01 | lava flow | metamorphized and weathered | 49,25 | 20,59 | 9,98 | 0,31 | 0,93 | 0,07 | 1,60 | 0,19 | 1,15 | < L.D. | 16,76 | 100,83 |
| 16°20'37.12" N | 61°46'41.22" W | BT14 | BT14_01 | lava flow | metamorphized and weathered | 49,30 | 18,88 | 9,06 | 0,09 | 1,12 | 2,85 | 2,88 | 0,28 | 1,08 | < L.D. | 13,18 | 98,71 |
| 16°20'37.12" N | 61°46'41.22" W | | BT14_02 | lava flow | sub-metamorphized | 58,38 | 17,64 | 8,15 | 0,17 | 1,22 | 4,88 | 3,88 | 0,71 | 0,92 | 0,14 | 3,65 | 99,71 |
| 16°20'37.02" N | 61°46'41.19" W | | BT14_03 | lava flow | metamorphized | 59,59 | 17,11 | 7,62 | 0,17 | 1,38 | 4,82 | 3,86 | 0,99 | 0,84 | 0,14 | 4,32 | 100,81 |
| 16°20'36.79" N | 61°46'41.03" W | | BT14_04 | lava flow | metamorphized and weathered | 54,04 | 19,72 | 9,41 | 0,14 | 0,48 | 1,98 | 3,09 | 0,28 | 1,06 | < L.D. | 11,13 | 101,33 |
| 16°20'36.48" N | 61°46'40.85" W | | BT14_05 | lava flow | metamorphized and weathered | 56,42 | 17,93 | 8,83 | 0,10 | 0,47 | 2,58 | 3,06 | 0,62 | 0,99 | < L.D. | 9,71 | 100,71 |
| 16°20'36.48" N | 61°46'40.85" W | | BT14_06 | lava flow | sub-metamorphized | 60,49 | 16,68 | 7,86 | 0,13 | 2,07 | 5,83 | 3,69 | 1,12 | 0,84 | < L.D. | 1,65 | 100,36 |
| 16°20'35.30" N | 61°46'40.41" W | BT15 | BT15_01 | lava flow | fresh | 60,23 | 16,24 | 7,48 | 0,20 | 1,64 | 5,29 | 3,84 | 1,24 | 0,85 | < L.D. | 2,42 | 99,44 |
| 16°20'16.34" N | 61°47'05.71" W | BT16 | BT16_01 | lava flow | metamorphized | 64,89 | 15,74 | 6,05 | 0,07 | 0,32 | 3,12 | 4,44 | 1,57 | 0,74 | < L.D. | 2,91 | 99,85 |
| 16°20'16.63" N | 61°47'06.00" W | | BT16_02 | lava flow | sub-metamorphized | 64,88 | 15,61 | 5,52 | 0,04 | 0,31 | 3,38 | 4,66 | 1,53 | 0,74 | 0,16 | 3,21 | 100,02 |
| 16°19'57.30" N | 61°47'02.59" W | BT17 | BT17_01 | lava flow | metamorphized | 56,14 | 18,55 | 7,18 | 0,05 | 1,26 | 5,85 | 3,06 | 0,71 | 0,77 | 0,13 | 6,21 | 99,89 |
| 16°19'48.99" N | 61°47'15.91" W | BT18 | BT18_01 | lava flow | metamorphized | 57,87 | 16,25 | 8,16 | 0,13 | 2,70 | 7,28 | 3,09 | 1,09 | 0,76 | 0,11 | 2,35 | 99,80 |
| 16°19'29.55" N | 61°47'13.41" W | BT19 | BT19_01 | lava flow | metamorphized | 57,11 | 16,57 | 6,73 | 0,11 | 2,39 | 8,57 | 3,03 | 1,08 | 0,78 | 0,11 | 3,38 | 99,85 |
| 16°19'51.85" N | 61°45'46.18" W | BT20 | BT20_01 | lava flow | sub-metamorphized | 61,42 | 16,31 | 6,87 | 0,17 | 1,61 | 5,18 | 4,54 | 1,05 | 0,88 | < L.D. | 1,03 | 99,06 |
| 16°19'02.54" N | 61°47'50.25" W | BT21 | BT21_02 | debris flow | metamorphized | 54,82 | 17,28 | 8,38 | 0,09 | 2,17 | 5,41 | 2,90 | 0,55 | 0,72 | 0,11 | 7,75 | 100,18 |
| 16°18'49.59" N | 61°47'47.73" W | BT22 | BT22_01 | lava flow | fresh | 62,43 | 16,35 | 6,91 | 0,12 | 2,10 | 5,98 | 3,50 | 1,10 | 0,57 | < L.D. | 1,19 | 100,25 |
| 16°18'44.29" N | 61°47'45.84" W | BT23 | BT23_01 | lava flow | altered | 60,61 | 16,05 | 7,18 | 0,10 | 2,01 | 5,23 | 3,29 | 1,10 | 0,64 | < L.D. | 3,12 | 99,32 |

**Table A-4: New trace element data set of whole-rock samples analysed for this study.**

| Latitude | Longitude | Localisation | Sample | Volcanic formation | Transformation state | Sc 45 | Co 59 | Ga 70 | Rb 85 | Sr 88 | Y 89 | Zr 90 | Nb 93 | Ba 137 | La 139 | Ce 140 |
|---|---|---|---|---|---|---|---|---|---|---|---|---|---|---|---|---|
| | | | | | | (ppm) | | | | | | | | | | |
| 16°21'10.77" N | 61°43'29.60" W | BT1 | BT1_01 | debris flow | fresh | 28,75 | 20,96 | 16,79 | 23,91 | 254,78 | 23,58 | 93,11 | 2,42 | 163,27 | 7,3601 | 17,6463 |
| 16°21'10.77" N | 61°43'29.60" W | | BT1_02 | debris flow | fresh | 19,51 | 6,48 | 17,62 | 39,84 | 139,84 | 104,77 | 80,80 | 2,74 | 376,51 | 33,8406 | 63,1569 |
| 16°21'10.77" N | 61°43'29.60" W | | BT1_03 | debris flow | sub-metamorphized | 19,33 | 10,69 | 17,00 | 42,21 | 115,65 | 16,45 | 91,22 | 2,94 | 248,06 | 9,0785 | 11,2771 |
| 16°21'14.78" N | 61°43'29.80" W | | BT1_04 | debris flow | metamorphized | 19,68 | 8,61 | 17,45 | 42,43 | 149,16 | 113,84 | 99,78 | 2,83 | 240,84 | 49,7133 | 64,9337 |
| 16°21'14.78" N | 61°43'29.80" W | | BT1_05 | debris flow | metamorphized | 33,20 | 16,33 | 17,19 | 31,64 | 190,50 | 131,50 | 111,84 | 3,49 | 177,60 | 9,3509 | 23,9535 |
| 16°21'26.14" N | 61°43'45.71" W | BT2 | BT2_01 | debris flow | sub-metamorphized | 19,25 | 7,51 | 17,21 | 36,84 | 149,74 | 41,66 | 83,08 | 2,73 | 265,30 | 6,017 | 13,5204 |
| 16°21'32.40" N | 61°44'46.07" W | BT3 | BT3_01 | debris flow | metamorphized and weathered | 19,53 | 15,06 | 17,65 | 22,16 | 88,06 | 4,67 | 80,38 | 2,93 | 206,60 | 2,5309 | 6,2273 |
| 16°21'16.79" N | 61°45'26.61" W | BT4 | BT4_01 | lava flow | sub-metamorphized | 30,29 | 13,38 | 18,04 | 31,22 | 189,02 | 38,26 | 159,66 | 4,78 | 247,33 | 11,2155 | 26,4171 |
| 16°21'16.79" N | 61°45'26.61" W | | BT4_02 | lava flow | sub-metamorphized | 30,62 | 9,29 | 18,11 | 31,56 | 174,64 | 35,23 | 159,78 | 4,81 | 215,75 | 9,4738 | 22,7386 |
| 16°21'18.89" N | 61°45'29.84" W | BT5 | BT5_01 | lava flow | fresh | 29,88 | 13,27 | 16,69 | 29,90 | 164,68 | 70,91 | 144,52 | 4,45 | 257,29 | 10,5819 | 25,4757 |
| 16°21'18.33" N | 61°45'29.91" W | | BT5_02 | lava flow | metamorphized | 30,74 | 9,21 | 17,07 | 30,62 | 155,45 | 54,91 | 148,19 | 4,59 | 198,28 | 10,2132 | 20,2025 |
| 16°21'18.16" N | 61°45'30.80" W | BT6 | BT6_01 | lava flow | fresh | 29,37 | 10,87 | 18,35 | 35,24 | 178,68 | 55,92 | 161,58 | 5,09 | 206,99 | 12,8296 | 24,7762 |
| 16°21'20.24" N | 61°45'35.13" W | BT7 | BT7_01 | lava flow | fresh | 28,86 | 9,98 | 17,54 | 31,91 | 184,20 | 35,70 | 157,20 | 4,92 | 200,00 | 9,983 | 22,34 |
| 16°21'06.61" N | 61°45'52.43" W | BT8 | BT8_01 | lava flow | fresh | 33,26 | 13,10 | 18,47 | 24,97 | 194,40 | 29,00 | 130,70 | 3,91 | 182,00 | 8,306 | 19,69 |
| 16°21'07.10" N | 61°46'00.11" W | BT9 | BT9_01 | lava flow | metamorphized | 26,57 | 4,42 | 19,28 | 30,14 | 104,34 | 18,97 | 168,04 | 5,31 | 196,57 | 3,4764 | 6,3916 |
| 16°21'06.22" N | 61°46'00.55" W | | BT9_02 | lava flow | metamorphized | 27,70 | 5,04 | 19,58 | 30,34 | 142,65 | 22,17 | 175,23 | 5,14 | 227,96 | 4,2281 | 7,0922 |
| | 61°46'02.35" W | BT10 | BT10_01 | lava flow | sub-metamorphized | 26,80 | 14,03 | 19,08 | 29,73 | 183,49 | 31,00 | 157,71 | 5,09 | 239,40 | 10,3903 | 22,51 |
| 16°21'03.08" N | 61°46'08.53" W | BT11 | BT11_01 | lava flow | metamorphized | 20,55 | 5,85 | 17,37 | 31,05 | 180,21 | 34,59 | 175,39 | 5,38 | *307,38* | 11,6552 | 26,5177 |
| 16°21'03.63" N | 61°46'08.43" W | BT12 | BT12_01 | lava flow | metamorphized | 21,27 | 11,71 | 16,22 | 18,11 | 218,63 | 56,05 | 109,71 | 3,60 | 175,56 | 9,1621 | 21,6649 |
| 16°21'04.04" N | 61°46'08.47" W | | BT12_02 | lava flow | fresh | 20,81 | 9,12 | 16,39 | 18,01 | 219,04 | 28,62 | 111,38 | 3,61 | 149,62 | 8,3889 | 20,2489 |
| 16°20'37.41" N | 61°46'41.42" W | BT13 | BT13_01 | lava flow | metamorphized and weathered | 32,98 | 25,89 | 19,93 | 1,87 | 25,52 | 19,45 | 148,51 | 4,86 | 176,82 | 16,7594 | 29,2037 |
| 16°20'37.12" N | 61°46'41.22" W | BT14 | BT14_01 | lava flow | metamorphized and weathered | 30,35 | 8,97 | 18,66 | 3,00 | 124,81 | 14,66 | 144,55 | 4,56 | 77,35 | 6,6639 | 14,6648 |
| 16°20'37.12" N | 61°46'41.22" W | | BT14_02 | lava flow | sub-metamorphized | 27,10 | 13,62 | 17,71 | 5,44 | 196,77 | 28,41 | 133,99 | 4,56 | 225,95 | 9,6497 | 22,5213 |
| 16°20'37.02" N | 61°46'41.19" W | | BT14_03 | lava flow | metamorphized | 26,54 | 12,01 | 16,35 | 9,42 | 176,94 | 27,45 | 117,83 | 3,85 | 205,33 | 7,8848 | 18,222 |
| 16°20'36.79" N | 61°46'41.03" W | | BT14_04 | lava flow | metamorphized and weathered | 31,02 | 12,28 | 19,11 | 1,80 | 114,28 | 39,00 | 144,36 | 4,63 | 150,29 | 16,8469 | 23,2931 |
| 16°20'36.48" N | 61°46'40.85" W | | BT14_05 | lava flow | metamorphized and weathered | 28,39 | 8,62 | 17,03 | 5,23 | 112,97 | 19,64 | 130,33 | 4,23 | 188,78 | 3,9912 | 10,8308 |
| 16°20'36.48" N | 61°46'40.85" W | | BT14_06 | lava flow | sub-metamorphized | 28,14 | 12,86 | 16,40 | 22,02 | 198,31 | 35,28 | 118,55 | 3,74 | 205,72 | 10,9366 | 20,2767 |
| 16°20'35.30" N | 61°46'40.41" W | BT15 | BT15_01 | lava flow | fresh | 26,92 | 15,40 | 15,73 | 23,99 | 186,10 | 40,75 | 121,90 | 3,96 | 235,70 | 9,147 | 20,71 |
| 16°20'16.34" N | 61°47'05.71" W | BT16 | BT16_01 | lava flow | metamorphized | 20,71 | 4,20 | 16,09 | 28,18 | 166,61 | 32,84 | 174,50 | 4,61 | 244,77 | 9,6574 | 23,1594 |
| 16°20'16.63" N | 61°47'06.00" W | | BT16_02 | lava flow | sub-metamorphized | 19,79 | 3,21 | 15,62 | 27,37 | 172,39 | 32,96 | 163,38 | 4,71 | 225,58 | 8,7101 | 19,2782 |
| 16°19'57.30" N | 61°47'02.59" W | BT17 | BT17_01 | lava flow | metamorphized | 21,36 | 11,96 | 17,11 | 7,58 | 205,97 | 26,37 | 91,16 | 2,92 | 130,85 | 6,4009 | 14,6599 |
| 16°19'48.99" N | 61°47'15.91" W | BT18 | BT18_01 | lava flow | metamorphized | 28,32 | 18,12 | 15,93 | 23,81 | 180,47 | 22,61 | 108,16 | 3,41 | 159,80 | 6,9835 | 17,3955 |
| 16°19'29.55" N | 61°47'13.41" W | BT19 | BT19_01 | lava flow | metamorphized | 29,73 | 19,60 | 16,77 | 24,05 | 187,34 | 25,38 | 109,08 | 3,40 | 162,06 | 7,5891 | 18,7679 |
| 16°19'51.85" N | 61°45'46.18" W | BT20 | BT20_01 | lava flow | sub-metamorphized | 21,23 | 7,56 | 14,52 | 21,88 | 228,68 | 37,04 | 103,55 | 3,42 | 175,82 | 8,4178 | 18,6977 |
| 16°19'02.54" N | 61°47'50.25" W | BT21 | BT21_02 | debris flow | metamorphized | 22,49 | 18,00 | 15,97 | 4,67 | 184,68 | 17,32 | 88,14 | 2,63 | 129,96 | 6,2428 | 13,9336 |
| 16°18'49.59" N | 61°47'47.73" W | BT22 | BT22_01 | lava flow | fresh | 17,45 | 11,16 | 15,44 | 21,43 | 247,32 | 27,02 | 107,60 | 2,85 | 224,14 | 8,9947 | 20,4057 |
| 16°18'44.29" N | 61°47'45.84" W | BT23 | BT23_01 | lava flow | altered | 18,02 | 10,10 | 15,15 | 23,72 | 215,60 | 25,12 | 101,70 | 3,04 | 199,60 | 7,736 | 16,83 |
| 16°18'55.23" N | 61°46'44.45" W | BT24 | BT24_01 | lava flow | fresh | 23,79 | 16,49 | 16,67 | 31,81 | 266,25 | 29,48 | 115,03 | 3,54 | 213,98 | 10,1871 | 23,3239 |
| 16°18'59.59" N | 61°46'06.65" W | BT25 | BT25_01 | lava flow | altered | 25,95 | 16,02 | 16,19 | 31,78 | 244,85 | 24,60 | 117,47 | 2,91 | 202,07 | 8,3884 | 19,7934 |
| 16°18'59.59" N | 61°46'06.65" W | | BT25_02 | lava flow | altered | 25,09 | 13,00 | 15,77 | 33,65 | 201,12 | 25,86 | 121,12 | 3,06 | 215,91 | 9,3762 | 20,6105 |
| 16°18'12.21" N | 61°45'47.53" W | BT26 | BT26_01 | lava flow | altered | 23,25 | 16,09 | 16,65 | 31,21 | 257,83 | 41,32 | 116,65 | 3,65 | 210,33 | 12,1001 | 25,1816 |

| Sample | Pr 141 | Nd 146 | Sm 147 | Eu 151 | Gd 157 | Tb 159 | Dy 163 | Ho 165 | Er 167 | Tm 169 | Yb 173 | Lu 175 | Hf 177 | Ta 181 | Pb 208 | Th 232 | U 238 |
|---|---|---|---|---|---|---|---|---|---|---|---|---|---|---|---|---|---|
| | (ppm) | | | | | | | | | | | | | | | | |
| BT1_01 | 2,4045 | 10,9155 | 3,0419 | 0,887 | 3,2391 | 0,5724 | 3,7965 | 0,8569 | 2,4282 | 0,3532 | 2,5242 | 0,4026 | 2,7047 | 0,218 | 2,881 | 2,192 | 0,7161 |
| BT1_02 | 13,9853 | 61,8204 | 15,6983 | 4,9707 | 15,1075 | 2,5751 | 16,5305 | 3,5768 | 9,8649 | 1,4308 | 9,8189 | 1,5918 | 2,4975 | 0,2997 | 4,0375 | 3,9395 | 1,4782 |
| BT1_03 | 3,1994 | 13,6232 | 3,4393 | 1,0555 | 2,9156 | 0,5005 | 3,1364 | 0,6434 | 1,7812 | 0,2738 | 2,0055 | 0,3198 | 2,7257 | 0,3095 | 3,2802 | 4,0776 | 1,0661 |
| BT1_04 | 23,8016 | 109,0689 | 29,3749 | 9,6657 | 27,573 | 4,6125 | 26,785 | 4,931 | 12,2019 | 1,737 | 11,709 | 1,5936 | 3,0455 | 0,3196 | 3,7121 | 4,0883 | 1,3662 |
| BT1_05 | 4,6475 | 28,6983 | 12,3781 | 3,6629 | 15,235 | 2,7518 | 18,6693 | 4,3237 | 12,0324 | 1,7493 | 11,6752 | 1,838 | 3,3583 | 0,2976 | 7,2017 | 2,9389 | 1,203 |
| BT2_01 | 2,0592 | 11,9137 | 4,8343 | 1,8623 | 6,0016 | 1,1356 | 7,6315 | 1,6638 | 4,5705 | 0,6678 | 4,5467 | 0,6998 | 2,58 | 0,309 | 3,9508 | 3,9866 | 1,2012 |
| BT3_01 | 0,5498 | 2,3963 | 0,7583 | 0,5938 | 0,7658 | 0,1418 | 0,9756 | 0,2044 | 0,61 | 0,0975 | 0,7429 | 0,1246 | 2,5564 | 0,315 | 5,047 | 4,204 | 0,3824 |
| BT4_01 | 3,8961 | 18,2765 | 5,2601 | 1,3918 | 5,6413 | 0,9854 | 6,5783 | 1,4367 | 4,008 | 0,5891 | 3,9873 | 0,6158 | 4,6377 | 0,39 | 4,3492 | 2,7358 | 0,9556 |
| BT4_02 | 3,307 | 15,5319 | 4,5092 | 1,3308 | 4,9098 | 0,8731 | 5,9569 | 1,3244 | 3,715 | 0,5429 | 3,6888 | 0,5788 | 4,5459 | 0,393 | 3,5722 | 2,7756 | 1,0234 |
| BT5_01 | 3,9185 | 19,078 | 6,1791 | 1,8959 | 8,0718 | 1,5568 | 11,1646 | 2,6483 | 7,6585 | 1,1272 | 7,8911 | 1,2274 | 4,0879 | 0,3673 | 5,395 | 2,4884 | 0,8887 |
| BT5_02 | 3,7726 | 18,2422 | 5,5149 | 1,5781 | 6,7666 | 1,1814 | 7,9838 | 1,8363 | 5,1004 | 0,7298 | 4,8638 | 0,7684 | 4,3234 | 0,3599 | 3,875 | 2,5179 | 0,8933 |
| BT6_01 | 4,3401 | 20,3754 | 5,6965 | 1,5043 | 6,6422 | 1,1569 | 7,7565 | 1,8234 | 5,0907 | 0,7302 | 4,9644 | 0,7802 | 4,7815 | 0,4003 | 3,6357 | 4,293 | 1,2823 |
| BT7_01 | 3,658 | 17,37 | 5,033 | 1,409 | 5,32 | 0,909 | 6,003 | 1,35 | 3,652 | 0,524 | 3,547 | 0,552 | 4,464 | 0,393 | 3,9826 | 2,5 | 0,985 |
| BT8_01 | 2,977 | 13,89 | 4,202 | 1,29 | 4,414 | 0,76 | 4,919 | 1,107 | 2,955 | 0,436 | 2,898 | 0,434 | 3,682 | 0,332 | 4,3566 | 1,87 | 0,733 |
| BT9_01 | 1,0574 | 5,1487 | 1,6593 | 0,9533 | 1,9491 | 0,4061 | 3,0203 | 0,7272 | 2,176 | 0,3427 | 2,4885 | 0,3839 | 4,8739 | 0,4146 | 3,5521 | 2,6343 | 1,0158 |
| BT9_02 | 1,3205 | 6,8126 | 2,1399 | 1,236 | 2,4336 | 0,472 | 3,4105 | 0,8054 | 2,4336 | 0,3726 | 2,6446 | 0,4175 | 5,0095 | 0,409 | 3,2868 | 2,6159 | 0,9138 |
| BT10_01 | 3,5871 | 16,9423 | 4,7757 | 1,4583 | 4,9734 | 0,8339 | 5,3824 | 1,1641 | 3,1625 | 0,4472 | 2,9662 | 0,4445 | 4,5175 | 0,4622 | 3,6818 | 2,4024 | 0,8969 |
| BT11_01 | 3,9763 | 18,907 | 5,3049 | 1,5033 | 5,5522 | 0,9497 | 6,1073 | 1,3025 | 3,6101 | 0,5185 | 3,4462 | 0,5178 | 5,0522 | 0,441 | 6,0645 | 2,6398 | 0,9408 |
| BT12_01 | 3,3923 | 16,7088 | 5,2407 | 1,5456 | 6,5139 | 1,1946 | 8,3858 | 1,9571 | 5,4955 | 0,8181 | 5,4696 | 0,8682 | 3,2035 | 0,2719 | 2,161 | 1,4968 | 0,5315 |
| BT12_02 | 3,212 | 15,2167 | 4,4048 | 1,3005 | 4,6074 | 0,7862 | 5,1172 | 1,1104 | 3,0662 | 0,4374 | 3,0287 | 0,4582 | 3,1624 | 0,2735 | 2,2062 | 1,5096 | 0,5544 |
| BT13_01 | 4,1055 | 18,1004 | 4,5195 | 1,1083 | 4,3468 | 0,7543 | 4,2625 | 0,947 | 2,3748 | 0,396 | 2,4199 | 0,4029 | 4,3312 | 0,3755 | 7,842 | 2,5917 | 0,4591 |
| BT14_01 | 2,5926 | 12,1869 | 3,5119 | 1,1225 | 3,2468 | 0,5507 | 3,0642 | 0,6275 | 1,5525 | 0,2331 | 1,4606 | 0,2256 | 4,1137 | 0,394 | 3,9148 | 2,5474 | 0,5706 |
| BT14_02 | 3,1917 | 14,8436 | 4,1532 | 1,2622 | 4,3746 | 0,7404 | 4,8701 | 1,0764 | 3,0157 | 0,4463 | 3,1707 | 0,4932 | 3,8296 | 0,3712 | 4,2742 | 2,3865 | 0,5233 |
| BT14_03 | 2,5859 | 12,0428 | 3,444 | 1,1447 | 3,7591 | 0,6758 | 4,5625 | 1,0437 | 2,917 | 0,4395 | 3,0463 | 0,4662 | 3,3872 | 0,3033 | 3,9537 | 2,0078 | 0,587 |
| BT14_04 | 3,9997 | 17,7911 | 4,756 | 1,2417 | 5,1804 | 0,9784 | 6,2175 | 1,4817 | 3,9661 | 0,649 | 4,1841 | 0,6832 | 4,117 | 0,3777 | 4,5129 | 2,5138 | 0,5842 |
| BT14_05 | 1,22 | 5,365 | 1,6347 | 0,8419 | 1,9062 | 0,3998 | 3,0822 | 0,7405 | 2,2184 | 0,3566 | 2,5978 | 0,4089 | 3,7677 | 0,3435 | 4,4312 | 2,2491 | 0,5072 |
| BT14_06 | 3,6367 | 16,8047 | 4,7074 | 1,2897 | 5,2474 | 0,903 | 6,0098 | 1,315 | 3,6668 | 0,5282 | 3,6497 | 0,5762 | 3,3481 | 0,3066 | 3,3478 | 1,9704 | 0,6692 |
| BT15_01 | 2,989 | 14,06 | 3,997 | 1,138 | 4,785 | 0,823 | 5,832 | 1,361 | 3,854 | 0,585 | 3,958 | 0,624 | 3,592 | 0,359 | 3,883 | 2,014 | 0,773 |
| BT16_01 | 3,7829 | 18,5367 | 5,5577 | 1,5117 | 5,5542 | 0,9531 | 6,07 | 1,2914 | 3,519 | 0,4959 | 3,3997 | 0,499 | 5,0108 | 0,3831 | 3,4448 | 2,6719 | 0,8988 |
| BT16_02 | 3,1878 | 15,1696 | 4,5827 | 1,4391 | 4,7522 | 0,8593 | 5,7222 | 1,2913 | 3,6387 | 0,5439 | 3,7569 | 0,5734 | 4,8015 | 0,3435 | 3,7922 | 2,6364 | 0,8741 |
| BT17_01 | 2,3205 | 11,1317 | 3,2827 | 1,0803 | 3,5701 | 0,635 | 4,2213 | 0,9511 | 2,6286 | 0,3874 | 2,6448 | 0,4006 | 2,6769 | 0,2279 | 2,1272 | 1,359 | 0,3785 |
| BT18_01 | 2,3754 | 10,8735 | 3,121 | 0,8826 | 3,3505 | 0,5858 | 3,9121 | 0,8784 | 2,4134 | 0,356 | 2,5086 | 0,3892 | 3,1693 | 0,2927 | 1,8583 | 2,034 | 0,6794 |
| BT19_01 | 2,488 | 11,4059 | 3,2331 | 0,9073 | 3,5868 | 0,6398 | 4,2947 | 0,9567 | 2,7064 | 0,4015 | 2,8342 | 0,4523 | 3,1228 | 0,2889 | 2,3724 | 2,0645 | 0,9936 |
| BT20_01 | 3,182 | 15,5363 | 4,9058 | 1,5435 | 5,5502 | 0,9599 | 6,4951 | 1,4183 | 3,9098 | 0,5529 | 3,8256 | 0,5901 | 2,9991 | 0,2628 | 4,6554 | 1,6085 | 0,5838 |
| BT21_02 | 2,1432 | 9,8584 | 2,7911 | 0,8742 | 2,8949 | 0,506 | 3,2415 | 0,7061 | 1,8893 | 0,2748 | 1,9234 | 0,2875 | 2,6155 | 0,2047 | 2,5815 | 1,5541 | 0,4257 |
| BT22_01 | 3,0282 | 14,1964 | 4,017 | 1,0119 | 4,1828 | 0,719 | 4,6523 | 1,0199 | 2,8564 | 0,4126 | 2,87 | 0,4422 | 3,1004 | 0,2407 | 3,7229 | 1,9741 | 0,716 |
| BT23_01 | 2,647 | 12,57 | 3,655 | 0,942 | 3,898 | 0,668 | 4,455 | 0,966 | 2,772 | 0,404 | 2,82 | 0,445 | 2,931 | 0,231 | 4,8932 | 1,793 | 0,694 |
| BT24_01 | 3,0623 | 13,7001 | 3,7398 | 0,9907 | 3,8465 | 0,6757 | 4,6057 | 1,0354 | 2,9719 | 0,4431 | 3,1202 | 0,4885 | 3,31 | 0,2834 | 3,5779 | 2,9907 | 1,0743 |
| BT25_01 | 2,6677 | 12,1343 | 3,3863 | 0,893 | 3,5621 | 0,6159 | 4,1341 | 0,9142 | 2,5913 | 0,3809 | 2,7098 | 0,4169 | 3,3722 | 0,2456 | 4,767 | 2,9447 | 0,9926 |
| BT25_02 | 3,0412 | 13,8594 | 3,8998 | 0,9565 | 4,0149 | 0,6871 | 4,5221 | 0,9864 | 2,7987 | 0,4051 | 2,7838 | 0,4276 | 3,5143 | 0,2625 | 3,805 | 3,0992 | 1,0112 |
| BT26_01 | 3,6174 | 16,575 | 4,5742 | 1,2233 | 5,0467 | 0,8892 | 6,1754 | 1,3884 | 4,11 | 0,612 | 4,328 | 0,6897 | 3,3397 | 0,2926 | 3,5482 | 3,044 | 1,0207 |

## Table A-5: Microprobe analysis of metamorphic phases. Ox = oxygen number

| Dacite | | | | | | Rhyodacite | | | | | | | |
|---|---|---|---|---|---|---|---|---|---|---|---|---|---|
| Sample | BT6_01 | BT6_01 | Sample | BT6_01 | BT6_01 | Sample | BT9_02 | BT9_01 | BT9_01 | BT9_01 | Sample | BT9_02 | BT9_02 | BT9_02 |
| Mineral wt% | *Albite* | *Andesine* | Mineral wt% | *Epidote (clinozoisite)* | *Epidote (clinozoisite)* | Mineral %wt | *Titanite* | *Pyrophyllite* | *Anorthoclase* | *Andesine* | Mineral %wt | *Chlorite* | *Chlorite* | *Muscovite* |
| | | | | | | | | | | | | | | |
| SiO2 | 68,05 | 58,45 | SiO2 | 38,65 | 38,95 | SiO2 | 31,56 | 48,59 | 65,09 | 57,98 | SiO2 | 27,88 | 26,97 | 48,13 |
| TiO2 | 0 | 0,06 | TiO2 | 0 | 0 | TiO2 | 33,22 | 0,13 | 0,07 | 0,06 | TiO2 | 0,00 | 0,00 | 0,04 |
| Al2O3 | 19,49 | 25,35 | Al2O3 | 26,08 | 27,35 | Al2O3 | 3,23 | 32,55 | 19,15 | 25,15 | Al2O3 | 20,17 | 19,31 | 28,67 |
| FeO | 0,23 | 1,03 | FeO | 9,28 | 6,98 | FeO | 2,78 | 4,65 | 0,72 | 1,02 | FeO | 23,83 | 26,81 | 6,71 |
| MnO | 0 | 0,02 | MnO | 0,12 | 0,09 | MnO | 0,02 | 0,16 | 0,00 | 0,02 | MnO | 0,31 | 0,28 | 0,05 |
| MgO | 0 | 0,02 | MgO | 0,05 | 0,01 | MgO | 0,15 | 1,12 | 0,04 | 0,02 | MgO | 16,14 | 14,56 | 0,07 |
| CaO | 1,13 | 8,06 | CaO | 23,96 | 23,76 | CaO | 27,25 | 0,03 | 0,86 | 8,00 | CaO | 0,03 | 0,03 | 0,02 |
| Na2O | 10,89 | 6,38 | Na2O | 0,01 | 0 | Na2O | 0,02 | 0,05 | 6,19 | 6,33 | Na2O | 0,00 | 0,02 | 0,03 |
| K2O | 0,12 | 0,52 | K2O | 0 | 0 | K2O | 0,01 | 0,47 | 7,20 | 0,50 | K2O | 0,00 | 0,00 | 9,75 |
| Total | 99,91 | 99,89 | Total | 98,15 | 97,14 | Total | 98,24 | 87,75 | 99,40 | 99,11 | Total | 88,36 | 87,98 | 93,47 |
| | | | | | | | | | | | | | | |
| | | | | | | Si | 1,05 | 1,51 | 2,95 | 2,63 | Si | 2,88 | 2,85 | 3,33 |
| Si | 2,98 | 2,63 | Si | 3,02 | 3,05 | Ti | 0,83 | 0,00 | 0,00 | 0,00 | AlIV | 1,12 | 1,15 | 0,67 |
| Ti | 0,00 | 0,00 | Ti | 0,00 | 0,00 | Al | 0,13 | 1,19 | 1,02 | 1,34 | AlVI | 1,33 | 1,26 | 1,67 |
| Al | 1,01 | 1,34 | Al | 2,41 | 2,52 | Fe | 0,08 | 0,12 | 0,03 | 0,04 | Fe | 2,06 | 2,37 | 0,39 |
| Fe | 0,01 | 0,04 | Fe3+ | 0,55 | 0,41 | Mn | 0,00 | 0,00 | 0,00 | 0,00 | Mn | 0,03 | 0,03 | 0,00 |
| Mn | 0,00 | 0,00 | Mn | 0,01 | 0,01 | Mg | 0,01 | 0,05 | 0,00 | 0,00 | Mg | 2,48 | 2,29 | 0,01 |
| Mg | 0,00 | 0,00 | Mg | 0,01 | 0,00 | Ca | 0,97 | 0,00 | 0,04 | 0,39 | Ca | 0,00 | 0,00 | 0,00 |
| Ca | 0,05 | 0,39 | Ca | 2,01 | 1,99 | Na | 0,00 | 0,00 | 0,54 | 0,56 | Na | 0,00 | 0,00 | 0,00 |
| Na | 0,93 | 0,56 | Na | 0,00 | 0,00 | K | 0,00 | 0,02 | 0,42 | 0,03 | K | 0,00 | 0,00 | 0,86 |
| K | 0,01 | 0,03 | K | 0,00 | 0,00 | | | | | | Ti | 0,00 | 0,00 | 0,02 |
| | | | | | | | | | | | | | | |
| Total | 4,981 | 4,99 | Total | 7,998 | 7,984 | Total (cations) | 3,06 | 2,902 | 5,011274 | 4,9889951 | Total (cations) | 9,897 | 9,95 | 6,932 |
| | *8 Ox* | *8 Ox* | | *12,5 Ox* | *12,5 Ox* | | *5 Ox* | *5 Ox* | *8 Ox* | *8 Ox* | | *14 Ox* | *14 Ox* | *11 Ox* |

| Basalt-andesite | | | | | | | | | | | Debris flow | | | | |
|---|---|---|---|---|---|---|---|---|---|---|---|---|---|---|---|
| Sample | BT13_01 | BT13_01 | BT13_01 | BT13_01 | Sample | BT13_01 | Sample | BT13_01 | Sample | BT13_01 | BT13_01 | Sample | BT1_04 | BT1_04 | BT1_04 | BT1_04 |
| Mineral %wt | *Chlorite* | *Chlorite* | *Muscovite* | *Muscovite* | Mineral %wt | *Epidote (clinozoisite)* | Mineral %wt | *Actinolite* | Mineral %wt | *Prehnite* | *Prehnite* | Mineral %wt | *Pyrophyllite* | *Anthophyllite* | *Andesine* | *Labradorite* |
| | | | | | | | | | | | | | | | | |
| SiO2 | 27,66 | 27,47 | 47,96 | 48,07 | SiO2 | 38,83 | SiO2 | 51,96 | SiO2 | 42,77 | 43,28 | SiO2 | 35,56 | 52,84 | 55,87 | 55,27 |
| TiO2 | 0,02 | 0 | 0,03 | 0,03 | TiO2 | 0 | TiO2 | 0,083 | TiO2 | 0,00 | 0,00 | TiO2 | 0,06 | 0,14 | 0,01 | 0,02 |
| Al2O3 | 19,99 | 19,35 | 27,13 | 28,13 | Al2O3 | 27,64 | Al2O3 | 2,87 | Al2O3 | 23,94 | 24,41 | Al2O3 | 26,73 | 0,78 | 27,14 | 27,97 |
| FeO | 27,06 | 27,53 | 6,27 | 6,48 | FeO | 7,36 | FeO | 17,12 | Fe Tot. * | 1,61 | 1,23 | FeO | 7,43 | 25,00 | 0,32 | 0,38 |
| MnO | 0,61 | 0,32 | 0,04 | 0,06 | MnO | 0,12 | MnO | 0,38 | MnO | 0,04 | 0,02 | MnO | 0,04 | 0,85 | 0,00 | 0,01 |
| MgO | 12,87 | 13,48 | 0,09 | 0,17 | MgO | 0,03 | MgO | 12,83 | MgO | 0,06 | 0,01 | MgO | 0,35 | 20,29 | 0,00 | 0,01 |
| CaO | 0,03 | 0,02 | 0,02 | 0,02 | CaO | 24,38 | CaO | 12,47 | CaO | 26,94 | 26,87 | CaO | 0,15 | 1,00 | 9,56 | 10,36 |
| Na2O | 0,04 | 0,01 | 0,28 | 0,49 | Na2O | 0 | Na2O | 0,3 | Na2O | 0,00 | 0,00 | Na2O | 0,05 | 0,00 | 5,66 | 5,38 |
| K2O | 0,01 | 0 | 9,66 | 9,89 | K2O | 0 | K2O | 0,11 | K2O | 0,00 | 0,00 | K2O | 0,03 | 0,00 | 0,41 | 0,45 |
| Total | 88,29 | 88,18 | 91,48 | 93,34 | Total | 98,36 | Total | 98,12 | Total | 95,36 | 95,82 | Total | 70,40 | 100,96 | 98,98 | 99,83 |
| | | | | | | | | | | | | | | | | |
| Si | 2,91 | 2,90 | 3,39 | 3,34 | Si | 2,99 | Si | 7,59 | Si | 2,97 | 2,98 | Si | 1,42 | 7,58 | 2,54 | 2,50 |
| AlIV | 1,09 | 1,10 | 0,61 | 0,66 | Ti | 0,00 | AlIV | 0,41 | Ti | 0,00 | 0,00 | Ti | 0,00 | 0,02 | 0,00 | 0,00 |
| AlVI | 1,39 | 1,31 | 1,64 | 1,64 | Al | 2,51 | AlVI | 0,08 | Al | 1,96 | 1,98 | Al | 1,26 | 0,13 | 1,45 | 1,49 |
| Fe | 2,38 | 2,43 | 0,37 | 0,38 | Fe3+ | 0,47 | Fe2+ | 1,84 | Fe3+ | 0,08 | 0,06 | Fe | 0,25 | 3,00 | 0,01 | 0,01 |
| Mn | 0,05 | 0,03 | 0,00 | 0,00 | Mn | 0,01 | Fe3+ * | 0,25 | Mn | 0,00 | 0,00 | Mn | 0,00 | 0,10 | 0,00 | 0,00 |
| Mg | 2,02 | 2,12 | 0,01 | 0,02 | Mg | 0,00 | Mn | 0,05 | Mg | 0,01 | 0,00 | Mg | 0,02 | 4,34 | 0,00 | 0,00 |
| Ca | 0,00 | 0,00 | 0,00 | 0,00 | Ca | 2,01 | Mg | 2,79 | Ca | 2,00 | 1,98 | Ca | 0,01 | 0,15 | 0,47 | 0,50 |
| Na | 0,01 | 0,00 | 0,04 | 0,07 | Na | 0,00 | Ca | 1,95 | Na | 0,00 | 0,00 | Na | 0,00 | 0,00 | 0,50 | 0,47 |
| K | 0,00 | 0,00 | 0,87 | 0,88 | K | 0,00 | Na | 0,09 | K | 0,00 | 0,00 | K | 0,00 | 0,00 | 0,02 | 0,03 |
| Ti | 0,00 | 0,00 | 0,00 | 0,00 | | | K | 0,02 | | | | | | | | |
| | | | | | | | Ti | 0,01 | | | | | | | | |
| Total (cations) | 9,855 | 9,896 | 6,938 | 6,981 | Total (cations) | 8 | Total (cations) | 15,081 | Total (cations) | 7,015 | 7,002 | Total (cations) | 2,96 | 15,33 | 4,99 | 5,00 |
| | *14 Ox* | *14 Ox* | *11 Ox* | *11 Ox* | | *12,5 Ox* | | *23 Ox* | | *11 Ox* | *11 Ox* | | *5 Ox* | *23 Ox* | *8 Ox* | *8 Ox* |
| | | | | | | | * Fe3+ after Schumacher (1977) | | * Fe Tot= Fe2O3 | | | | | | | |

**Table A-6: All stable mineralogical assemblages listed in Figure 13. Mineral abbreviations are from Kretz, 1983.**

| Figure | Number | Mineralogical assemblages |
|---|---|---|
| 13-A | 1 | ab chl ms pg czo ttn rieb qtz H2O |
| 13-A | 2 | ab chl ms pg czo ep ttn rieb qtz H2O |
| 13-A | 3 | ab chl ms pg ep ttn rieb prh qtz H2O |
| 13-A | 4 | ab ilm chl ms pg ep rieb qtz wrk H2O |
| 13-A | 5 | ab ilm chl ms pg ep ttn qtz wrk H2O |
| 13-A | 6 | ab ilm chl ms pg ep ttn rieb qtz H2O |
| 13-A | 7 | ab ilm chl ms pg czo ep ttn qtz H2O |
| 13-A | 8 | ab ilm chl ms pg czo ep qtz H2O |
| 13-A | 9 | ab chl ms pg ttn rieb mc qtz lmt H2O |
| 13-A | 10 | ab ilm chl ms pg ttn rieb qtz wrk H2O |
| 13-A | 11 | ab chl ms pg ep ttn rieb qtz wrk H2O |
| 13-A | 12 | ab ilm chl ms pg ep qtz wrk H2O |
| 13-A | 13 | ab ilm chl ms ep rieb qtz wrk H2O |
| 13-A | 14 | ab ilm chl ms ep qtz  wrk H2O |
| 13-A | 15 | ab ilm chl ms ep qtz H2O |
| 13-A | 16 | ab ilm chl ms pg ep rieb qtz H2O |
| 13-A | 17 | ab ilm chl ms ep  rieb qtz mag H2O |
| 13-A | 18 | ab ilm chl ms ep qtz wrk mag H2O |
| 13-A | 19 | ab ilm chl ms ep rieb qtz wrk mag H2O |
| 13-A | 20 | ab ilm chl ms rieb qtz wrk mag H2O |
| 13-A | 21 | ab ilm chl ms bt rieb qtz wrk mag H2O |
| 13-A | 22 | ab ilm chl ms bt qtz wrk mag H2O |
| 13-A | 23 | ab ilm chl ms bt ep qtz wrk mag H2O |
| 13-B | 24 | ab chl ms pg cam ttn qtz lmt H2O |
| 13-B | 25 | ab chl pg cam ttn mc qtz lmt H2O |
| 13-B | 26 | ab chl ms pg ttn mic qtz lmt H2O |
| 13-B | 27 | ab chl ms pg ttn prh qtz lmt H2O |
| 13-B | 28 | ab ilm chl ms czo ttn qtz wrk H2O |
| 13-B | 29 | ab ilm chl ms bt czo ttn qtz wrk H2O |
| 13-B | 30 | ab ilm chl ms bt ttn qtz wrk H2O |
| 13-B | 31 | ab ilm chl ms ttn mc qtz wrk H2O |
| 13-B | 32 | ab ilm chl ms bt mic qtz wrk H2O |
| 13-C | 33 | ab ilm chl ms pg bt czo rieb qtz |
| 13-C | 34 | ab ilm chl ms pg czo ttn rieb qtz |
| 13-C | 35 | ab ilm ms bt czo ep rieb qtz |
| 13-C | 36 | ab ilm ms bt ep rieb qtz |
| 13-C | 37 | ab ilm ms pg bt ep rieb qtz |
| 13-C | 38 | ab ilm chl ms pg ep rieb qtz |
| 13-C | 39 | ab ilm chl ms ep qtz |
| 13-C | 40 | ab ilm chl ms ep qtz wrk |
| 13-C | 41 | ab ilm chl ms pg ep qtz wrk |
| 13-C | 42 | ab ilm chl ms ep rieb qtz wrk |
| 13-C | 43 | ab ilm chl ms pg rieb qtz wrk |
| 13-C | 44 | ab ilm chl ms pg ttn rieb qtz wrk |
| 13-C | 45 | ab ilm chl ms pg ep ttn qtz wrk |
| 13-C | 46 | ab ilm chl ms pg ep ttn rieb qtz |
| 13-C | 47 | ab chl ms pg ep ttn rieb qtz wrk |
| 13-D | 48 | ab chl ms czo ttn qtz wrk |
| 13-D | 49 | ab chl ms ttn qtz wrk |
| 13-D | 50 | ab ilm chl ms pg ttn qtz wrk |
| 13-D | 51 | ab ilm chl ms czo ttn qtz wrk |
| 13-D | 52 | ab ilm chl ms czo mc qtz |
| 13-D | 53 | ab ilm chl ms czo ttn mc qtz |
| 13-D | 54 | ab ilm chl ms bt qtz wrk |
| 13-D | 55 | ab ilm chl ms bt czo mc qtz |

**Appendix-A: Raman spectrometry spectra used to complete mineral determination.**

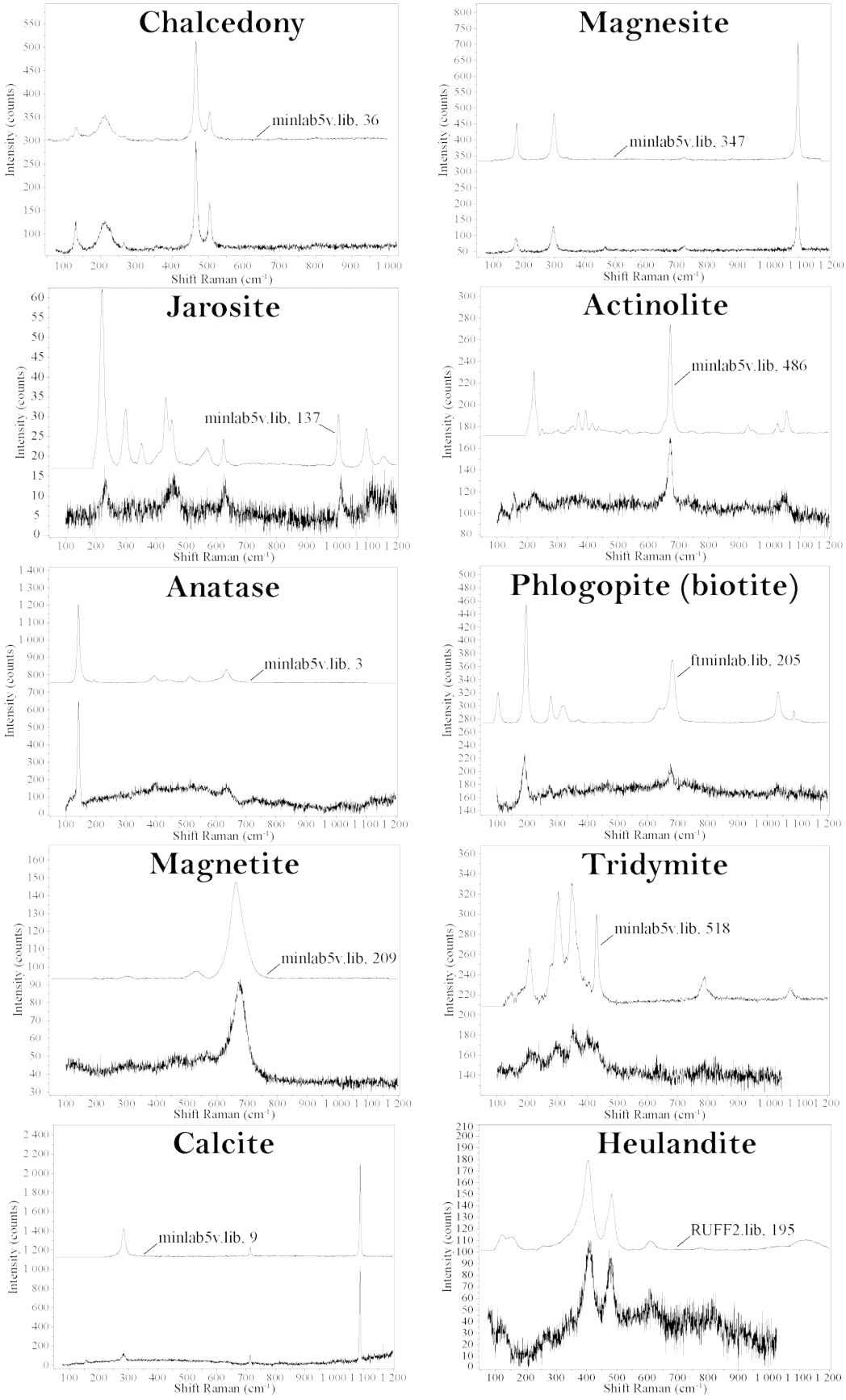

## X.3. Article 2 - Supplementary data

**Table A-1: Co-Th contents of the studied samples.**

| Sample sites | Location | Co (ppm) | Th (ppm) | protolite |
|---|---|---|---|---|
| BT1 sample #1 | Amandiers Beach | 20.9634 | 2.192 | andesite |
| BT1 sample #2 | Amandiers Beach | 6.4822 | 3.9395 | dacite |
| BT1 sample #3 | Amandiers Beach | 10.6922 | 4.0776 | dacite |
| BT1 sample #4 | Amandiers Beach | 8.6122 | 4.0883 | dacite |
| BT2 | Nogent Point | 7.5127 | 3.9866 | dacite |
| BT4 | Rifflet Point | 4.2044 | 2.6719 | rhyodacite |
| BT5 sample #1 | Perle Creek | 12.8586 | 1.9704 | dacite |
| BT5 sample #2 | Perle Creek | 8.6235 | 2.2491 | dacite |
| BT5 sample #3 | Perle Creek | 12.283 | 2.5138 | dacite |
| BT5 sample #4 | Perle Creek | 13.7989 | 2.3783 | dacite |
| BT5 sample #5 | Perle Creek | 12.0096 | 2.0078 | dacite |
| BT5 sample #6 | Perle Creek | 15.2418 | 2.1898 | andesite |
| BT6 | Tillet Creek | 5.8508 | 2.6398 | rhyodacite |
| BT7 | Tillet Creek | 5.0387 | 2.6159 | rhyodacite |
| BT8 sample #1 | Clugny Beach | 13.3794 | 2.7358 | dacite |
| BT8 sample #2 | Clugny Beach | 9.2941 | 2.7756 | dacite |
| BT9 sample #1 | Grande Anse Beach | 18.0032 | 1.5541 | andesite |
| BT9 sample #2 | Grande Anse Beach | 16.328 | 2.9389 | andesite |
| BT10 | Breton Point | 18.121 | 2.034 | andesite |
| BT11 | Rifflet Point | 11.963 | 1.359 | dacite |
| BT12 sample #1 | Clugny Beach | 10.872 | 4.293 | dacite |
| BT12 sample #2 | Clugny Beach | 12.4475 | 2.6983 | dacite |
| BT14 | Tillet Creek | 4.4227 | 2.6343 | rhyodacite |

**Table A-2: Electron microprobe analyses and structural formula of metamorphic minerals.**

| Sample | BT7 | BT7 | BT7 | Sample | BT7 | BT14 | Sample | BT6 | BT6 | BT6 | BT6 |
|---|---|---|---|---|---|---|---|---|---|---|---|
| Mineral % wt | **Chlorite** | **Chlorite** | **Muscovite** | Mineral % wt | **Titanite** | **Pyrophyllite** | Mineral wt% | **Albite** | **Andesine** | **Epidote** | **Epidote** |
| SiO2 | 27.88 | 26.97 | 48.13 | SiO2 | 31.56 | 48.59 | SiO2 | 68,05 | 58,45 | 38,65 | 38,95 |
| TiO2 | 0.00 | 0.00 | 0.04 | TiO2 | 33.22 | 0.13 | TiO2 | 0 | 0,06 | 0 | 0 |
| Al2O3 | 20.17 | 19.31 | 28.67 | Al2O3 | 3.23 | 32.55 | Al2O3 | 19,49 | 25,35 | 26,08 | 27,35 |
| FeO | 23.83 | 26.81 | 6.71 | FeO | 2.78 | 4.65 | FeO | 0,23 | 1,03 | 9,28 | 6,98 |
| MnO | 0.31 | 0.28 | 0.05 | MnO | 0.02 | 0.16 | MnO | 0 | 0,02 | 0,12 | 0,09 |
| MgO | 16.14 | 14.56 | 0.07 | MgO | 0.15 | 1.12 | MgO | 0 | 0,02 | 0,05 | 0,01 |
| CaO | 0.03 | 0.03 | 0.02 | CaO | 27.25 | 0.03 | CaO | 1,13 | 8,06 | 23,96 | 23,76 |
| Na2O | 0.00 | 0.02 | 0.03 | Na2O | 0.02 | 0.05 | Na2O | 10,89 | 6,38 | 0,01 | 0 |
| K2O | 0.00 | 0.00 | 9.75 | K2O | 0.01 | 0.47 | K2O | 0,12 | 0,52 | 0 | 0 |
| Total | *88.36* | *87.98* | *93.47* | Total | *98.24* | *87.75* | *Total* | *99,91* | *99,89* | *98,15* | *97,14* |
| | | | | | | | | | | | |
| Si | 2.876 | 2.850 | 3.329 | Si | 1.048 | 1.509 | Si | 2,981 | 2,629 | 3,024 | 3,049 |
| $Al^{IV}$ | 1.124 | 1.150 | 0.671 | Ti | 0.830 | 0.003 | Ti | 0 | 0,002 | 0 | 0 |
| $Al^{VI}$ | 1.328 | 1.255 | 1.666 | Al | 0.126 | 1.191 | Al | 1,007 | 1,344 | 2,405 | 2,523 |
| Fe | 2.056 | 2.369 | 0.388 | Fe | 0.077 | 0.121 | Fe | 0,008 | 0,039 | 0,546 | 0,411 |
| Mn | 0.027 | 0.025 | 0.003 | Mn | 0.001 | 0.004 | Mn | 0 | 0,001 | 0,008 | 0,006 |
| Mg | 2.482 | 2.294 | 0.007 | Mg | 0.007 | 0.052 | Mg | 0 | 0,001 | 0,006 | 0,001 |
| Ca | 0.003 | 0.003 | 0.001 | Ca | 0.969 | 0.001 | Ca | 0,053 | 0,388 | 2,009 | 1,993 |
| Na | 0.000 | 0.004 | 0.004 | Na | 0.001 | 0.003 | Na | 0,925 | 0,556 | 0,001 | 0 |
| K | 0.000 | 0.000 | 0.860 | K | 0.000 | 0.019 | K | 0,006 | 0,03 | 0 | 0 |
| Ti | 0.000 | 0.000 | 0.020 | | | | | | | | |
| | | | | | | | | | | | |
| Total (cations) | *9.897* | *9.950* | *6.932* | Total (cations) | *3.060* | *2.902* | *Total (cations)* | *4,981* | *4,99* | *7,998* | *7,984* |
| | *14 Ox* | *14 Ox* | *12 Ox* | | *5 Ox* | *5 Ox* | *6 Ox* | *8 Ox* | *8 Ox* | *12,5 Ox* | *12,5 Ox* |

**Table A-3: Solution models used for computation of equilibrium assemblage diagrams and a-x modelling.**

| **Mineral and Solution models** | **Reference** | |
|---|---|---|
| Biotite | White et al., 2007 | White, R.W., Powell, R. & Holland, T.J.B., 2007. Progress relating to calculation of partial melting equilibria for metapelites and felsic gneisses. Journal of Metamorphic Geology, 25, 511–527. |
| Chlorite | Holland et al., 1998 | Holland, T.J.B., Baker, J. & Powell, R., 1998. Mixing properties and activity–composition relationships of chlorites in thesystem MgO–Al2O3–SiO2–H2O. European Journal of Mineralogy, 10, 395–406. |
| Clino-Amphibole (sensu-lato naming) | Diener and Powell, 2012 | Diener, J.F.A., Powell, R., 2012. Revised activity–composition models for clinopyroxene and amphibole. Journal of Metamorphic Geology,30,131-142. |
| Plagioclase | Holland and Powell, 2003 | Holland, TJB & Powell, R (2003) Activity-composition relations for phases in petrological calculations: an asymmetric multicomponent formulation. Contributions to Mineralogy and Petrology, 145, 492-501. |
| Hematite<br>Ilmenite | White et al., 2007 | White, R.W., Powell, R. & Holland, T.J.B., 2007. Progress relating to calculation of partial melting equilibria for metapelites and felsic gneisses. Journal of Metamorphic Geology, 25, 511–527. |
| White Mica | Coggon and Holland, 2002 | Coggon, R. & Holland, T.J.B., 2002. Mixing properties of phengitic micas and revised garnet–phengite thermobarometers. Journal of Metamorphic Geology, 20, 683–696. |
| Epidote | Holland and Powell, 1998 | Holland, T.J.B. & Powell, R., 1998. An internally-consistent thermodynamic dataset for phases of petrological interest. Journal of Metamorphic Geology, 16, 309–344. |
| Laumontite<br>Magnetite<br>Microcline<br>Prehnite<br>Quartz<br>Titanite<br>Wairakite | Minerals considered as pure end members. | |

**Table A-4: Major element contents (weight % oxides) of andesine pseudomorph.**

| | wt% |
|---|---|
| $SiO_2$ | 63.73 |
| $Al_2O_3$ | 18.44 |
| FeO | 7.61 |
| MnO | 0.01 |
| MgO | 0.53 |
| CaO | 3.08 |
| $Na_2O$ | 4.32 |
| $K_2O$ | 1.36 |
| $TiO_2$ | 0.89 |
| Total | 99.97 |

| | Mole numbers for domino input | |
|---|---|---|
| | 100% $Fe^{2+}$ | 90% $Fe^{2+}$ - 10% $Fe^{3+}$ |
| Si | 70.18 | 69.64 |
| Al | 23.94 | 23.85 |
| Fe [$Fe^{2+}$] | 7.01 | 6.98 |
| O ($Fe^{3+}$) | | 0.7 |
| Mg | 0.87 | 0.87 |
| Ca | 3.63 | 3.62 |
| Na | 9.22 | 9.19 |
| K | 1.91 | 1.9 |
| Ti | 0.76 | 0.75 |
| O | (?)* | (?)* |

*? for the oxygen amount instructs the program to assign exactly the stoichiometric oxygen atoms to the other elements.

**Appendix A-1: The Co-Th discrimination diagram (from Hastie et al., 2007).**

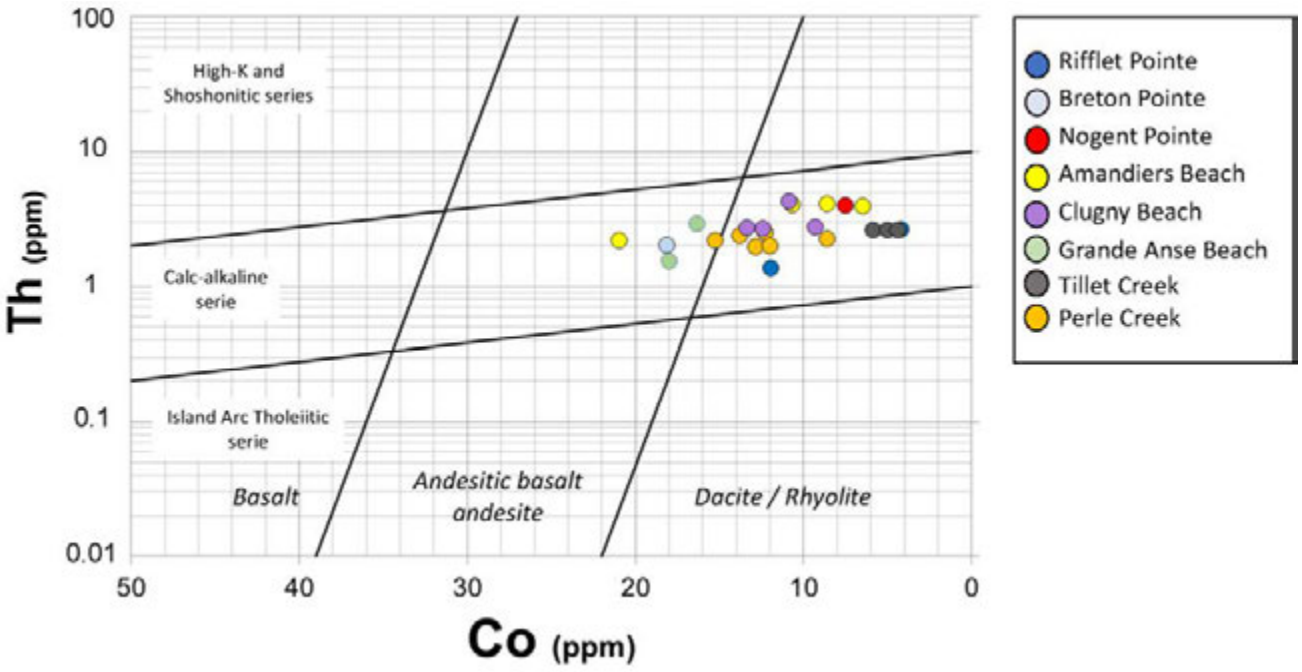

**Appendix A-2: XRD spectra of BT17 sample (spectra interpreted using Match! Software).**

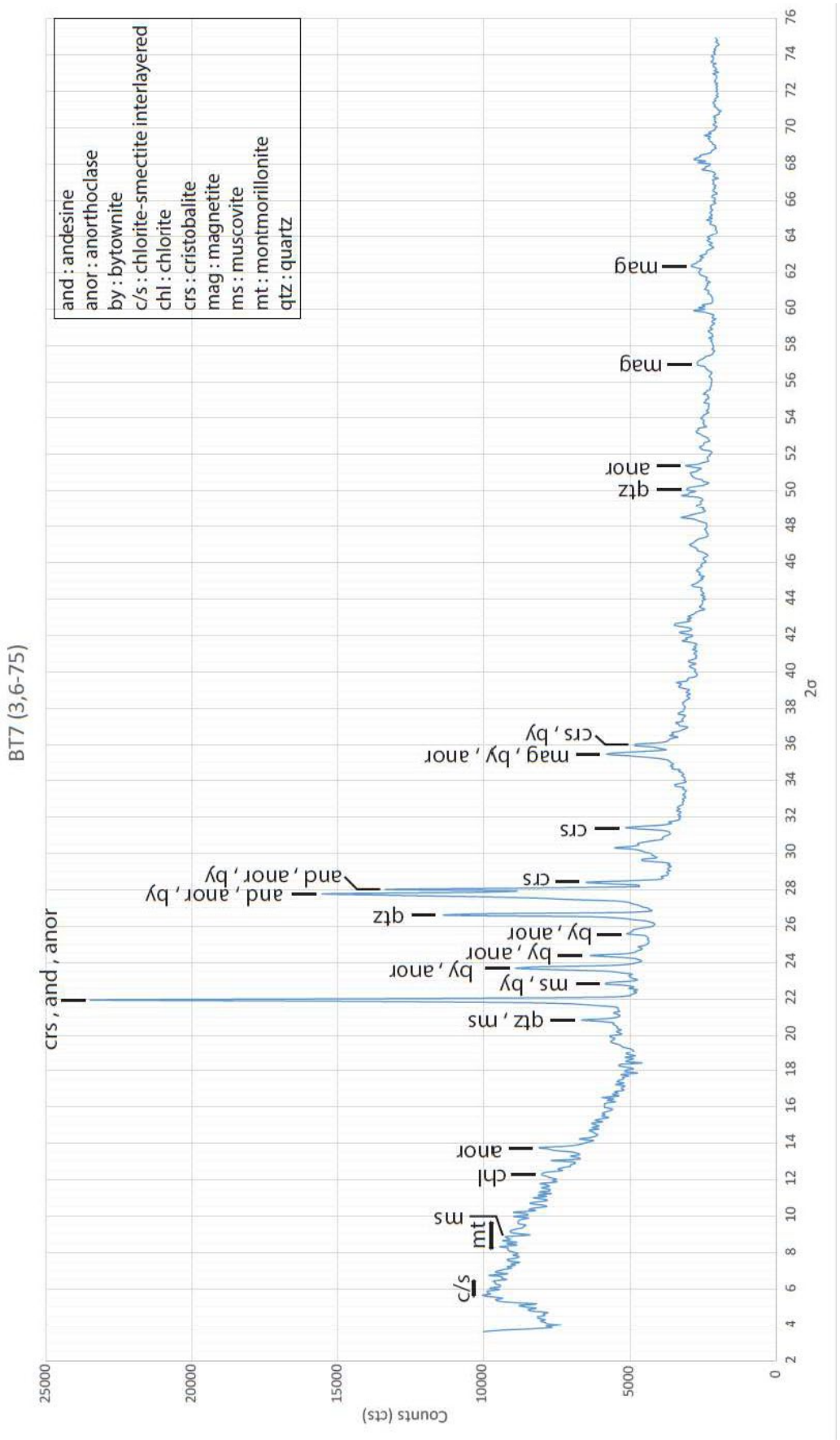

## X.4. Article 3 - Supplementary data

**Table X-1: Table of whole rock major and trace element analyses.**

| Echantillon | Localisation (Fig.3-A) | Formation | Transformation state | $SiO_2$ | $Al_2O_3$ | $Fe_2O_3$ | MnO | MgO | CaO | $Na_2O$ | $K_2O$ | $TiO_2$ | $P_2O_5$ | LOI | Total |
|---|---|---|---|---|---|---|---|---|---|---|---|---|---|---|---|
| | | | | % | % | % | % | % | % | % | % | % | % | % | % |
| TH-30b | 5 | lava flow | fresh untransformed | 60,47 | 17,07 | 6,405 | 0,1353 | 1,228 | 6,11 | 3,446 | 1,079 | 0,531 | 0,23 | 2,17 | 98,88 |
| 16STH33 | 5 | lava flow | fresh untransformed | 61,23 | 17,773 | 5,602 | 0,0562 | 0,917 | 5,997 | 3,528 | 1,041 | 0,477 | 0,2 | 4,31 | 101,12 |
| SA-12.08 | 25 | volcanic plug | fresh untransformed | 61,36 | 16,803 | 5,575 | 0,1816 | 1,996 | 6,301 | 3,082 | 1,021 | 0,511 | 0,2 | 4,22 | 101,25 |
| 17TH05 | 25 | volcanic plug | fresh untransformed | 60,43 | 16,79 | 5,33 | 0,17 | 1,82 | 6,08 | 2,83 | 1,03 | 0,46 | 0,19 | 4,59 | 99,72 |
| 17TH11 | 23 | volcanic plug | fresh untransformed | 61,73 | 16,86 | 6,07 | 0,15 | 1,66 | 5,83 | 3,48 | 1,16 | 0,52 | 0,21 | 1,2 | 98,85 |
| DC10-09b | 36 | volcanic dome | fresh untransformed | 57,27 | 17,873 | 8,525 | 0,1906 | 2,911 | 7,652 | 3,484 | 1,016 | 0,87 | 0,2 | 0,63 | 100,62 |
| TH-25' | 25 | volcanic plug | fresh untransformed | 60,53 | 16,893 | 5,603 | 0,1841 | 2,161 | 6,321 | 2,837 | 0,912 | 0,5 | 0,21 | 4,39 | 100,54 |
| GD15.135 | 37 | lava flow | fresh untransformed | 63,06 | 17,028 | 4,941 | 0,0988 | 1,362 | 5,703 | 3,484 | 1,332 | 0,533 | 0,15 | 1,66 | 99,35 |
| DC10-09a | 36 | volcanic dome | fresh untransformed | 62,98 | 15,598 | 6,874 | 0,1414 | 2,212 | 5,174 | 3,186 | 1,361 | 0,521 | 0,15 | 3 | 101,19 |
| GD17.11 | 36 | volcanic dome | fresh untransformed | 62,4 | 16,278 | 6,376 | 0,1333 | 2,005 | 5,614 | 3,268 | 1,316 | 0,502 | 0,15 | 2,25 | 100,28 |
| 17TH26a | 1 | lava flow | slighty transformed | 65,64 | 16,618 | 3,722 | 0,0548 | 0,584 | 4,418 | 4,543 | 1,439 | 0,54 | 0,19 | 1,52 | 99,28 |
| 17TH32b | 9 | lava flow | slighty transformed | 62,44 | 17,105 | 4,701 | 0,1146 | 1,629 | 6,207 | 3,334 | 1,179 | 0,521 | 0,17 | 1,46 | 98,86 |
| TH-29 | 37 | lava flow | slighty transformed | 62,71 | 15,945 | 6,015 | 0,1897 | 1,837 | 4,868 | 3,416 | 1,47 | 0,458 | < L.D. | 2,29 | 99,19869 |
| 16STH25 | 28 | lava flow | slighty transformed | 64,25 | 17,818 | 3,803 | < L.D. | 0,55 | 5,541 | 3,834 | 1,228 | 0,496 | 0,15 | 2,89 | 100,56 |
| 16STH26 | 28 | lava flow | slighty transformed | 59,91 | 16,298 | 8,554 | 0,599 | 0,952 | 5,565 | 3,314 | 1,13 | 0,432 | 0,22 | 3,18 | 100,15 |
| 16STH32 | 29 | lava flow | slighty transformed | 62,97 | 17,61 | 4,696 | 0,0998 | 0,935 | 6,366 | 3,644 | 1,133 | 0,51 | 0,15 | 1,26 | 99,37 |
| 17TH22 | 32 | lava flow | slighty transformed | 61,88 | 17,283 | 5,525 | 0,0829 | 1,454 | 5,55 | 3,291 | 1,063 | 0,541 | 0,16 | 2,53 | 99,36 |
| 16STH24 | 28 | lava flow | slighty transformed | 62,48 | 17,123 | 5,711 | 0,1707 | 1,569 | 5,983 | 3,504 | 1,113 | 0,474 | 0,21 | 2,69 | 101,02 |
| 16STH31 | 29 | lava flow | slighty transformed | 61,6 | 17,305 | 5,532 | 0,0613 | 1,126 | 5,824 | 3,239 | 1,171 | 0,606 | 0,16 | 3,74 | 100,35 |
| 17TH24 | 30 | lava flow | slighty transformed | 59,93 | 16,06 | 4,924 | 0,1001 | 2,111 | 3,281 | 1,886 | 0,508 | 0,588 | 0,15 | 9,71 | 99,24 |
| 17TH21 | 33 | volcanic plug | slighty transformed | 59,79 | 16,36 | 6,185 | 0,1 | 1,659 | 6,364 | 3,379 | 1,101 | 0,491 | 0,16 | 3,27 | 98,84 |
| GD15.141 | 38 | lava flow | slighty transformed | 61,62 | 16,3 | 6,717 | 0,1427 | 2,19 | 5,825 | 3,2 | 1,344 | 0,525 | 0,15 | 2,54 | 100,55 |
| 16STH23b | 27 | lava flow | slighty transformed | 62,38 | 17,798 | 5,66 | 0,0898 | 1,361 | 6,48 | 3,085 | 0,679 | 0,5 | 0,2 | 2,36 | 100,59 |
| 16STH27 | 28 | lava flow | slighty transformed | 62,4 | 17,203 | 5,592 | 0,1048 | 1,332 | 6,271 | 3,609 | 0,981 | 0,535 | 0,22 | 3,1 | 101,34 |
| GD15.140 | 38 | lava flow | slighty transformed | 59,75 | 16,318 | 6,798 | 0,196 | 2,387 | 4,96 | 2,494 | 0,734 | 0,555 | 0,16 | 5,79 | 100,14 |
| 16STH03 | 13 | pyroclastic flow | slighty transformed | 64,71 | 15,5 | 5,201 | 0,1052 | 1,028 | 4,596 | 2,889 | 1,255 | 0,523 | 0,16 | 4,17 | 100,14 |
| SA-14 | 11 | volcanic plug | slighty transformed | 60,97 | 16,26 | 6,757 | 0,1927 | 2,93 | 6,772 | 2,911 | 1,295 | 0,549 | 0,14 | 2,11 | 100,88 |
| TH-27 | 16 | debris flow | slighty transformed | 60,43 | 19,16 | 2,558 | 0,0659 | 2,578 | 4,822 | 3,254 | 0,493 | 0,963 | < L.D. | 5,09 | 99,41389 |
| 17TH31 | 10 | debris flow | slighty transformed | 62,85 | 18,405 | 2,752 | 0,043 | 0,693 | 4,583 | 3,079 | 1,295 | 0,573 | 0,17 | 5,64 | 100,09 |
| 16STH23a | 27 | lava flow | slighty transformed | 60,92 | 17,043 | 7,456 | 0,2076 | 2,163 | 6,717 | 3,118 | 0,9 | 0,49 | 0,23 | 1,12 | 100,36 |
| GD15.139 | 38 | lava flow | slighty transformed | 60 | 16,318 | 6,781 | 0,1548 | 2,457 | 4,939 | 3,447 | 1,095 | 0,533 | 0,16 | 4,16 | 100,04 |
| GD16.10 | 7 | debris flow | transformed | 57,44 | 19,133 | 6,395 | 0,0617 | 1,477 | 6,227 | 3,425 | 0,299 | 0,645 | < L.D. | 5,05 | 100,1527 |
| 16STH04b | 13 | undetermined | transformed | 64,48 | 13,658 | 6,975 | 0,0332 | 1,318 | 1,795 | 1,125 | 1,399 | 0,488 | 0,12 | 8,54 | 99,93 |
| 16STH05 | 13 | undetermined | transformed | 64,59 | 16,313 | 5,082 | 0,017 | 0,569 | 1,981 | 1,76 | 2,873 | 0,568 | 0,14 | 6,79 | 100,68 |
| 16STH08 | 14 | undetermined | transformed | 57,57 | 15,31 | 6,683 | 0,0472 | 1,779 | 3,812 | 0,529 | 1,491 | 0,468 | 0,13 | 12,88 | 100,7 |
| 16STH11a | 15 | undetermined | transformed | 61,91 | 16,705 | 3,249 | 0,1611 | 2,497 | 5,552 | 3,045 | 1,086 | 0,549 | 0,16 | 5,02 | 99,93 |
| 16STH11b | 15 | undetermined | transformed | 60,3 | 16,313 | 5,25 | 0,0998 | 2,207 | 4,994 | 2,98 | 1,347 | 0,503 | 0,14 | 5,74 | 99,88 |
| 16STH12 | 16 | undetermined | transformed | 59,93 | 16,595 | 5,174 | 0,0481 | 2,23 | 5,015 | 3,067 | 1,022 | 0,508 | 0,14 | 5,85 | 99,57 |
| 16STH14 | 16 | undetermined | transformed | 60,83 | 17,255 | 4,425 | 0,1492 | 2,448 | 4,886 | 3,107 | 1,148 | 0,526 | 0,14 | 4,79 | 99,71 |
| 16STH15b | 16 | undetermined | transformed | 60,83 | 17,105 | 4,779 | 0,1837 | 2,032 | 4,695 | 3,027 | 1,514 | 0,581 | 0,14 | 5,34 | 100,21 |

| Echantillon | As | Ba | Be | Bi | Cd | Ce | Co | Cr | Cs | Cu | Dy |
|---|---|---|---|---|---|---|---|---|---|---|---|
| | ppm | ppm | ppm | ppm | ppm | ppm | ppm | ppm | ppm | ppm | ppm |
| TH-30b | 0,4565 | 208,7682 | 0,8141 | < L.D. | 0,1116 | 30,1641 | 8,5522 | 2,0126 | 0,4087 | 11,8522 | 4,023 |
| 16STH33 | < L.D. | 204,5272 | 0,7755 | 0,2915 | 0,0609 | 27,2875 | 6,163 | 3,5551 | 0,3276 | 14,5508 | 3,2295 |
| SA-12.08 | 0,6663 | 208,8095 | 0,7979 | 0,0628 | 0,1223 | 33,1177 | 7,9915 | 2,2168 | 2,726 | 8,7885 | 4,6472 |
| 17TH05 | 0,9539 | 229,0287 | 0,9124 | 0,0666 | 0,1276 | 37,3679 | 7,7182 | 0,5865 | 3,2143 | 8,3613 | 8,6431 |
| 17TH11 | 0,7158 | 212,2816 | 0,8758 | < L.D. | 0,0549 | 34,5421 | 9,6566 | 1,5565 | 0,5717 | 9,1062 | 15,7442 |
| DC10-09b | < L.D. | 201,3942 | 0,7351 | 0,2052 | 0,0997 | 31,6212 | 14,0793 | 11,447 | 0,4526 | 20,8021 | 4,9709 |
| TH-25' | 0,8229 | 206,5825 | 0,945 | < L.D. | 0,1309 | 38,7464 | 9,639 | 2,7318 | 4,4536 | 11,937 | 17,667 |
| GD15.135 | 4,0853 | 252,2657 | 0,7933 | 1,5265 | 0,1118 | 28,5382 | 31,3625 | 1,5909 | 0,7069 | 20,2959 | 3,2766 |
| DC10-09a | < L.D. | 232,2765 | 0,7399 | < L.D. | 0,0524 | 24,4147 | 10,206 | 3,1446 | 0,6033 | 15,2752 | 2,8577 |
| GD17.11 | < L.D. | 246,1602 | 0,7494 | < L.D. | 0,1328 | 27,5899 | 32,5841 | 2,4594 | 0,613 | 16,1789 | 3,3861 |
| 17TH26a | 0,5332 | 311,4438 | 1,249 | 0,0497 | 0,0851 | 46,364 | 3,9536 | 0,7762 | 0,3303 | 16,4043 | 6,0126 |
| 17TH32b | 0,5079 | 218,7118 | 0,7759 | 0,145 | 0,7634 | 31,5147 | 12,9995 | 1,5491 | 0,4415 | 17,082 | 3,8943 |
| TH-29 | 0,2509 | 282,2108 | 0,7822 | < L.D. | 0,101 | 39,0674 | 12,8061 | 2,8156 | 0,4599 | 18,7627 | 3,9371 |
| 16STH25 | 1,9798 | 232,3759 | 0,8961 | 0,0917 | 0,038 | 22,7772 | 0,557 | 3,7093 | 0,3445 | 10,7431 | 2,7297 |
| 16STH26 | < L.D. | 206,2064 | 0,8329 | < L.D. | 0,2926 | 27,7487 | 8,091 | 3,3284 | 0,5689 | 10,1541 | 3,5775 |
| 16STH32 | 0,5479 | 231,2377 | 0,8209 | 0,0936 | 0,0741 | 27,5807 | 11,4443 | 2,6923 | 0,4929 | 15,3231 | 3,1949 |
| 17TH22 | < L.D. | 208,1382 | 0,7152 | 0,0908 | < L.D. | 28,062 | 9,3208 | 1,3032 | 0,52 | 16,1727 | 3,2989 |
| 16STH24 | < L.D. | 228,8008 | 0,8439 | < L.D. | 0,1918 | 27,8838 | 8,1775 | 3,5973 | 0,2454 | 12,351 | 3,1156 |
| 16STH31 | < L.D. | 222,1313 | 0,7933 | 0,0811 | 0,0693 | 27,5529 | 9,3922 | 2,4488 | 0,5207 | 21,5945 | 2,966 |
| 17TH24 | 0,7205 | 108,4606 | 0,4953 | 0,258 | 0,1002 | 26,5847 | 6,7951 | 2,3392 | 0,9227 | 11,3711 | 2,5961 |
| 17TH21 | < L.D. | 202,6322 | 0,7687 | 0,35 | 0,0529 | 28,1483 | 8,4115 | 4,1202 | 0,4521 | 12,5563 | 3,4644 |
| GD15.141 | 1,6363 | 228,9785 | 0,7855 | 0,2738 | 0,2229 | 26,9004 | 23,3047 | 1,9931 | 3,2829 | 18,287 | 3,119 |
| 16STH23b | 1,2532 | 137,9983 | 0,8728 | < L.D. | 0,0385 | 35,5809 | 9,6574 | 2,6353 | 0,4753 | 11,8829 | 7,7241 |
| 16STH27 | < L.D. | 199,9975 | 0,8641 | 0,0568 | 0,0502 | 29,4762 | 7,4544 | 2,3534 | 0,3069 | 12,578 | 3,8525 |
| GD15.140 | 2,1526 | 164,046 | 0,6856 | 0,1685 | 0,2242 | 25,5884 | 30,0282 | 1,9114 | 6,756 | 17,8687 | 3,2452 |
| 16STH03 | < L.D. | 220,5754 | 0,7369 | 0,0471 | 0,0706 | 27,4773 | 9,9649 | 33,3216 | 0,5229 | 28,0993 | 2,568 |
| SA-14 | 0,762 | 241,8016 | 0,7253 | < L.D. | 0,0676 | 25,3352 | 13,2914 | 16,3491 | 0,6053 | 30,8559 | 3,1162 |
| TH-27 | 5,021 | 143,3665 | 0,8555 | 0,2292 | 0,0539 | 28,8752 | 5,7896 | 2,0201 | 0,1584 | < L.D. | 3,3169 |
| 17TH31 | < L.D. | 234,0827 | 0,8367 | < L.D. | 0,048 | 27,9742 | 4,4974 | 2,0623 | 0,6759 | 18,2131 | 2,9746 |
| 16STH23a | 1,368 | 173,6702 | 0,8114 | 0,0531 | 0,1036 | 29,2443 | 9,9252 | 2,5732 | 0,4339 | 7,2629 | 3,687 |
| GD15.139 | < L.D. | 202,3721 | 0,684 | < L.D. | 0,0896 | 27,0653 | 26,4119 | 1,4011 | 3,4913 | 17,1923 | 3,528 |
| GD16.10 | 1,4236 | 171,7455 | 0,8283 | < L.D. | 0,3405 | 27,9965 | 14,7731 | 1,1768 | 0,2304 | 24,6167 | 3,3923 |
| 16STH04b | 1,3246 | 133,0661 | 0,7872 | 0,0491 | 0,1436 | 20,9264 | 19,2801 | 16,8467 | 0,774 | 274,8483 | 3,9218 |
| 16STH05 | 0,5734 | 449,6002 | 0,6502 | 0,0644 | 0,0622 | 40,7253 | 10,7879 | 14,8765 | 0,5301 | 71,5254 | 4,5594 |
| 16STH08 | 2,3601 | 362,3001 | 0,758 | 0,1525 | 0,3808 | 43,5252 | 10,1769 | 4,6592 | 0,4327 | 44,0875 | 3,0894 |
| 16STH11a | 6,145 | 237,1358 | 0,7729 | < L.D. | 0,1543 | 24,4011 | 9,6007 | 2,4419 | 0,2472 | 17,1255 | 3,3615 |
| 16STH11b | 33,923 | 237,9161 | 0,7527 | 0,2481 | 0,2016 | 26,5004 | 12,116 | 2,912 | 0,1833 | 21,3565 | 3,0871 |
| 16STH12 | 14,6709 | 374,0999 | 0,8126 | 0,0857 | 0,0416 | 29,6904 | 13,9776 | 2,7103 | 0,2193 | 44,5716 | 4,1345 |
| 16STH14 | 16,1294 | 271,1534 | 0,7222 | 0,1397 | 0,0373 | 32,871 | 11,7735 | 2,5278 | 0,2559 | 10,6306 | 3,1011 |
| 16STH15b | 16,9935 | 301,1608 | 0,6763 | < L.D. | 0,0873 | 27,0685 | 11,9925 | 2,9078 | 0,3032 | 30,4568 | 3,007 |

| Echantillon | Er | Eu | Ga | Gd | Ge | Hf | Ho | In | La | Lu | Mo |
|---|---|---|---|---|---|---|---|---|---|---|---|
| | ppm | ppm | ppm | ppm | ppm | ppm | ppm | ppm | ppm | ppm | ppm |
| TH-30b | 2,5374 | 1,1864 | 18,3728 | 3,7935 | 1,4704 | 2,8397 | 0,8924 | 0,0559 | 14,047 | 0,452 | 0,5241 |
| 16STH33 | 1,9726 | 1,1207 | 18,029 | 3,1349 | 1,3043 | 2,7111 | 0,6951 | 0,0459 | 12,7934 | 0,3263 | < L.D. |
| SA-12.08 | 2,9522 | 1,2549 | 17,0322 | 4,4862 | 1,4752 | 2,814 | 1,0386 | 0,0503 | 15,1649 | 0,5048 | 0,7904 |
| 17TH05 | 5,4742 | 2,3886 | 17,7269 | 8,8601 | 1,6439 | 2,9563 | 1,988 | 0,0453 | 18,6572 | 0,8787 | 0,8206 |
| 17TH11 | 10,7606 | 2,3325 | 17,7637 | 11,7096 | 1,6309 | 3,0122 | 3,7655 | 0,0468 | 17,2869 | 1,8163 | 0,5931 |
| DC10-09b | 3,1154 | 1,3706 | 15,3821 | 4,5961 | 1,436 | 3,1245 | 1,1235 | 0,057 | 14,0923 | 0,4805 | 1,2854 |
| TH-25' | 12,3417 | 3,5837 | 18,2016 | 15,1714 | 1,5479 | 2,9586 | 4,3729 | 0,0571 | 20,3705 | 2,0204 | 0,8559 |
| GD15.135 | 2,0952 | 1,0115 | 17,4029 | 2,9952 | 1,4099 | 2,9544 | 0,738 | 0,0562 | 13,572 | 0,3806 | 0,7526 |
| DC10-09a | 1,8274 | 0,8926 | 15,5761 | 2,6928 | 1,4659 | 2,8392 | 0,639 | 0,0322 | 12,3232 | 0,323 | 0,5693 |
| GD17.11 | 2,1334 | 1,0035 | 16,6655 | 3,1324 | 1,4521 | 2,9543 | 0,7406 | 0,0422 | 13,5672 | 0,3747 | 0,7195 |
| 17TH26a | 3,6586 | 1,6963 | 17,2608 | 5,5643 | 1,4895 | 5,4158 | 1,3158 | 0,0451 | 21,3113 | 0,5844 | 0,6526 |
| 17TH32b | 2,4097 | 1,1162 | 18,0109 | 3,5921 | 1,4423 | 3,0309 | 0,8512 | 0,0432 | 14,1136 | 0,4017 | 0,6864 |
| TH-29 | 2,3834 | 1,1374 | 16,6655 | 3,9172 | 1,605 | 2,9941 | 0,845 | 0,0423 | 19,9035 | 0,4334 | 0,6319 |
| 16STH25 | 1,8365 | 1,092 | 17,5024 | 2,4524 | 1,1714 | 2,9616 | 0,6317 | < L.D. | 11,7285 | 0,3613 | 0,5406 |
| 16STH26 | 2,3864 | 1,0568 | 16,0351 | 3,2109 | 1,3335 | 2,5557 | 0,8079 | 0,0402 | 13,2502 | 0,4349 | 0,6919 |
| 16STH32 | 2,0093 | 1,0558 | 16,9488 | 2,9606 | 1,2804 | 3,0456 | 0,7075 | 0,0459 | 13,6548 | 0,344 | < L.D. |
| 17TH22 | 1,9809 | 1,0866 | 17,21 | 3,2257 | 1,4762 | 2,9682 | 0,7144 | 0,0439 | 12,8637 | 0,3331 | < L.D. |
| 16STH24 | 1,9198 | 1,0561 | 16,5534 | 2,9971 | 1,2236 | 2,7527 | 0,6781 | 0,0426 | 13,0588 | 0,3365 | 0,7015 |
| 16STH31 | 1,8048 | 1,0267 | 16,6859 | 2,9556 | 1,2881 | 2,8134 | 0,6484 | 0,0586 | 13,0232 | 0,2957 | < L.D. |
| 17TH24 | 1,5011 | 1,103 | 17,0341 | 2,8916 | 0,9044 | 2,3185 | 0,5455 | 0,0495 | 11,4054 | 0,271 | 0,5053 |
| 17TH21 | 2,2489 | 0,9956 | 16,3221 | 3,0981 | 1,4351 | 2,8969 | 0,7766 | 0,0351 | 12,9446 | 0,4186 | < L.D. |
| GD15.141 | 2 | 0,9458 | 16,3896 | 2,8781 | 1,3139 | 2,7147 | 0,6922 | 0,0505 | 13,0502 | 0,3685 | < L.D. |
| 16STH23b | 4,4869 | 2,0993 | 18,7649 | 7,4874 | 1,4837 | 2,876 | 1,6712 | 0,0775 | 15,8434 | 0,6594 | 0,502 |
| 16STH27 | 2,3609 | 1,1673 | 17,4785 | 3,5859 | 1,3424 | 2,7391 | 0,8495 | 0,0607 | 13,6917 | 0,399 | 0,5193 |
| GD15.140 | 2,0477 | 1,0445 | 15,9485 | 3,0925 | 1,4014 | 2,6537 | 0,7123 | 0,0624 | 11,4865 | 0,339 | < L.D. |
| 16STH03 | 1,4798 | 0,9376 | 14,9848 | 2,7159 | 1,2473 | 2,2208 | 0,5416 | 0,0381 | 14,399 | 0,2507 | 0,5814 |
| SA-14 | 2,0201 | 0,9253 | 15,8611 | 2,8497 | 1,4132 | 2,6514 | 0,7209 | 0,0533 | 12,0042 | 0,3659 | 0,8451 |
| TH-27 | 2,347 | 1,4145 | 19,1042 | 2,9768 | 1,1463 | 4,0345 | 0,7631 | 0,0544 | 12,4286 | 0,4875 | 0,7523 |
| 17TH31 | 1,7313 | 1,1022 | 19,4081 | 3,0329 | 1,2306 | 3,1205 | 0,6302 | 0,04 | 13,3024 | 0,2872 | 0,7918 |
| 16STH23a | 2,3952 | 1,1528 | 17,8473 | 3,507 | 1,4408 | 2,627 | 0,8331 | 0,0865 | 13,3092 | 0,42 | 0,7197 |
| GD15.139 | 2,1891 | 1,0437 | 16,5263 | 3,2316 | 1,378 | 2,8577 | 0,7695 | 0,0535 | 12,7662 | 0,3739 | < L.D. |
| GD16.10 | 1,8431 | 1,3834 | 19,5672 | 3,6863 | 1,3368 | 3,1864 | 0,6921 | 0,0485 | 15,659 | 0,2846 | < L.D. |
| 16STH04b | 2,329 | 1,07 | 15,8113 | 3,8161 | 1,4978 | 2,3704 | 0,8574 | 0,059 | 12,9262 | 0,3772 | 0,6875 |
| 16STH05 | 2,239 | 2,3492 | 15,906 | 5,599 | 1,4371 | 2,6341 | 0,8426 | 0,0728 | 22,4023 | 0,3738 | 0,6454 |
| 16STH08 | 1,9247 | 1,1353 | 15,2164 | 3,4764 | 0,9701 | 2,6624 | 0,6725 | 0,5432 | 20,7707 | 0,3617 | 1,1816 |
| 16STH11a | 2,2265 | 0,8877 | 16,3415 | 2,9765 | 1,1267 | 2,8449 | 0,7689 | 0,0509 | 11,3761 | 0,4078 | 1,0989 |
| 16STH11b | 2,0048 | 0,9125 | 15,6124 | 2,7718 | 1,1855 | 2,6752 | 0,6985 | 0,0613 | 12,182 | 0,3714 | 2,0286 |
| 16STH12 | 2,3791 | 1,3824 | 16,2183 | 4,1389 | 1,0511 | 2,7697 | 0,8695 | < L.D. | 13,2944 | 0,3957 | 0,9716 |
| 16STH14 | 2,0516 | 1,0053 | 16,5161 | 2,8937 | 1,2181 | 2,8471 | 0,695 | 0,0393 | 16,0149 | 0,3744 | 0,9069 |
| 16STH15b | 2,0077 | 0,9067 | 16,4319 | 2,6163 | 1,1362 | 2,9476 | 0,6858 | 0,0564 | 13,1116 | 0,3823 | 0,7787 |

| Echantillon | Nb | Nd | Ni | Pb | Pr | Rb | Sc | Sb | Sm | Sn | Sr |
|---|---|---|---|---|---|---|---|---|---|---|---|
| | ppm | ppm | ppm | ppm | ppm | ppm | ppm | ppm | ppm | ppm | ppm |
| TH-30b | 3,8923 | 17,1432 | < L.D. | 3,8023 | 4,0534 | 26,1371 | 11,35 | 0,0911 | 3,9404 | < L.D. | 312,5498 |
| 16STH33 | 3,7307 | 14,9288 | 3,4586 | 4,2656 | 3,546 | 24,6551 | 9,21 | < L.D. | 3,3966 | 0,9756 | 300,0037 |
| SA-12.08 | 4,0084 | 19,1612 | < L.D. | 4,3511 | 4,4639 | 41,6081 | 9,25 | 0,0924 | 4,559 | 1,0105 | 310,9473 |
| 17TH05 | 4,1142 | 26,687 | < L.D. | 4,4228 | 5,5473 | 53,374 | 9 | 0,1002 | 6,9423 | 1,1551 | 312,5111 |
| 17TH11 | 4,285 | 27,0579 | < L.D. | 3,5188 | 5,871 | 29,2397 | 10,58 | < L.D. | 8,4711 | 1,0746 | 288,7074 |
| DC10-09b | 6,1573 | 18,9761 | 6,5915 | 6,6938 | 4,3256 | 19,4873 | 16,14 | 0,0915 | 4,7241 | 1,1238 | 337,1109 |
| TH-25' | 4,0506 | 32,7688 | < L.D. | 4,7846 | 6,4244 | 50,6492 | 9,85 | 0,0841 | 9,4559 | < L.D. | 337,2208 |
| GD15.135 | 4,0082 | 14,459 | 2,0009 | 6,9212 | 3,5585 | 36,5882 | 12,45 | 0,1206 | 3,2463 | 2,7683 | 268,737 |
| DC10-09a | 3,755 | 12,7872 | 2,5795 | 3,9159 | 3,193 | 33,9525 | 11,93 | < L.D. | 2,8979 | 0,8514 | 220,121 |
| GD17.11 | 3,9583 | 14,6484 | 6,4838 | 5,4142 | 3,5654 | 36,9297 | 11,64 | 0,1017 | 3,2708 | 1,5198 | 247,0394 |
| 17TH26a | 11,0686 | 25,5371 | < L.D. | 4,7856 | 6,01 | 25,7897 | 10,11 | 0,0785 | 5,9355 | 1,6651 | 294,1204 |
| 17TH32b | 4,0131 | 16,2786 | < L.D. | 3,5907 | 3,8995 | 30,0581 | 10,88 | < L.D. | 3,7755 | 1,0868 | 277,6659 |
| TH-29 | 3,8709 | 20,1784 | 8,7552 | 4,1701 | 5,1235 | 37,9516 | 10,44 | 0,0538 | 4,1515 | < L.D. | 248,1141 |
| 16STH25 | 4,0253 | 12,613 | 2,0507 | 5,4525 | 3,097 | 26,5303 | 8,74 | 0,2671 | 2,7716 | 0,8278 | 297,9983 |
| 16STH26 | 3,479 | 14,5359 | 2,6108 | 5,5486 | 3,471 | 23,8213 | 8,11 | 0,1684 | 3,2784 | 1,6595 | 289,041 |
| 16STH32 | 3,9951 | 14,1442 | 2,1522 | 3,2552 | 3,4478 | 27,7645 | 10,53 | 0,1074 | 3,2008 | 1,012 | 290,0364 |
| 17TH22 | 3,8886 | 15,2525 | < L.D. | 3,4537 | 3,6509 | 24,3836 | 12,37 | 0,072 | 3,459 | 1,0105 | 266,5853 |
| 16STH24 | 3,561 | 14,5047 | 2,1082 | 2,8619 | 3,514 | 22,2674 | 9,04 | < L.D. | 3,1926 | 0,7898 | 284,7426 |
| 16STH31 | 3,9551 | 14,4636 | 2,1561 | 3,8708 | 3,4941 | 29,5292 | 13,88 | 0,1039 | 3,1734 | 1,1085 | 260,2103 |
| 17TH24 | 3,5806 | 16,1959 | < L.D. | 3,5397 | 3,5823 | 8,3848 | 13,45 | 0,0704 | 3,6962 | 1,0669 | 293,4747 |
| 17TH21 | 3,8015 | 14,2609 | < L.D. | 2,8693 | 3,4829 | 27,5743 | 10,39 | < L.D. | 3,1868 | 0,6622 | 271,8292 |
| GD15.141 | 3,8595 | 13,6106 | 2,0365 | 4,2854 | 3,3719 | 39,6628 | 12,22 | 0,1089 | 3,0352 | 1,4855 | 239,5612 |
| 16STH23b | 3,9215 | 22,9527 | < L.D. | 2,0238 | 4,9696 | 23,3678 | 8,62 | 0,0701 | 6,5737 | 1,2786 | 282,9667 |
| 16STH27 | 3,8837 | 16,1059 | < L.D. | 2,5338 | 3,8293 | 21,6476 | 11,14 | 0,0847 | 3,733 | 0,9435 | 296,4421 |
| GD15.140 | 3,5719 | 14,1431 | 3,9085 | 3,5026 | 3,3306 | 20,6645 | 12,15 | 0,4244 | 3,2609 | 1,2288 | 236,3323 |
| 16STH03 | 3,026 | 14,857 | 7,7704 | 3,1768 | 3,6834 | 30,0764 | 15,81 | < L.D. | 3,0686 | 0,9031 | 304,4162 |
| SA-14 | 3,522 | 12,7022 | 5,4916 | 2,8711 | 3,1791 | 31,5717 | 16,63 | 0,1872 | 2,9674 | 0,9532 | 256,1978 |
| TH-27 | 7,172 | 15,242 | < L.D. | 3,6897 | 3,6358 | 8,9017 | 18,62 | 0,2861 | 3,4334 | < L.D. | 280,0529 |
| 17TH31 | 4,0529 | 15,0337 | < L.D. | 3,695 | 3,6088 | 33,5895 | 12,38 | < L.D. | 3,4299 | 0,9671 | 253,1946 |
| 16STH23a | 3,6839 | 16,0194 | < L.D. | 2,4785 | 3,7902 | 24,6508 | 8,89 | 0,1102 | 3,7092 | 1,0553 | 286,0814 |
| GD15.139 | 3,7571 | 14,8202 | < L.D. | 3,7432 | 3,5353 | 30,5466 | 12,19 | 0,0998 | 3,3528 | 1,1493 | 237,7966 |
| GD16.10 | 4,2082 | 18,9004 | < L.D. | 4,0087 | 4,5006 | 2,9214 | 14,13 | 0,1522 | 4,2653 | 1,5715 | 306,0099 |
| 16STH04b | 3,3946 | 14,5971 | 5,8395 | 6,2015 | 3,384 | 30,6598 | 14,63 | 0,1453 | 3,4977 | 0,9815 | 95,6306 |
| 16STH05 | 3,5578 | 33,6758 | 6,506 | 6,3796 | 7,9173 | 64,2017 | 13,84 | 0,0946 | 7,7523 | 2,0791 | 135,2441 |
| 16STH08 | 3,3781 | 22,2477 | 3,6015 | 4,197 | 5,5629 | 26,7887 | 12,49 | 0,2016 | 4,4811 | 1,4262 | 60,97 |
| 16STH11a | 3,7624 | 12,7677 | 2,9109 | 7,5772 | 3,0478 | 24,151 | 13,15 | 0,5023 | 3,0413 | 0,8297 | 223,5863 |
| 16STH11b | 3,5942 | 13,2871 | 3,0934 | 7,2114 | 3,2132 | 28,2268 | 12,6 | 0,5109 | 2,9858 | 1,5155 | 225,5414 |
| 16STH12 | 3,6974 | 16,9477 | 3,1449 | 4,5699 | 3,9003 | 21,7773 | 12,5 | 0,3391 | 4,3066 | 1,4004 | 258,5763 |
| 16STH14 | 3,7163 | 15,1484 | 2,2965 | 7,2237 | 3,8489 | 22,9925 | 12,25 | 0,6403 | 3,1706 | 1,1304 | 231,9152 |
| 16STH15b | 3,7597 | 12,8266 | 2,8182 | 6,9585 | 3,2366 | 34,008 | 13,53 | 0,7095 | 2,7817 | 1,3726 | 228,0427 |

| Echantillon | Ta | Tb | Th | Tm | U | V | W | Y | Yb | Zn | Zr |
|---|---|---|---|---|---|---|---|---|---|---|---|
| | ppm | ppm | ppm | ppm | ppm | ppm | ppm | ppm | ppm | ppm | ppm |
| TH-30b | 0,3183 | 0,6233 | 3,1308 | 0,3727 | 0,7968 | 61,4164 | < L.D. | 24,1824 | 2,6963 | 86,362 | 101,0801 |
| 16STH33 | 0,2939 | 0,5059 | 3,1344 | 0,2942 | 0,8161 | 53,3755 | < L.D. | 18,3223 | 2,0609 | 82,1907 | 97,8486 |
| SA-12.08 | 0,3251 | 0,7177 | 3,2678 | 0,4336 | 0,8679 | 51,6405 | < L.D. | 30,6034 | 3,1292 | 98,6845 | 102,4166 |
| 17TH05 | 0,3384 | 1,3539 | 3,4803 | 0,7712 | 0,9354 | 50,8235 | < L.D. | 60,6667 | 5,3076 | 132,9595 | 104,7214 |
| 17TH11 | 0,3403 | 2,1966 | 3,4982 | 1,5246 | 0,9684 | 58,8475 | < L.D. | 125,3368 | 10,7089 | 101,5116 | 108,1801 |
| DC10-09b | 0,4598 | 0,7839 | 2,7578 | 0,4624 | 0,719 | 122,5045 | < L.D. | 28,4703 | 3,1251 | 56,3504 | 114,7523 |
| TH-25' | 0,3429 | 2,5429 | 3,3869 | 1,7354 | 0,9018 | 56,4477 | < L.D. | 145,8115 | 11,5486 | 176,4262 | 105,2768 |
| GD15.135 | 0,5137 | 0,5135 | 4,2001 | 0,3239 | 1,1551 | 90,9493 | 163,0236 | 20,1006 | 2,3251 | 74,9394 | 104,5124 |
| DC10-09a | 0,343 | 0,4548 | 3,9263 | 0,2784 | 0,971 | 80,308 | < L.D. | 17,1433 | 2,0114 | 67,2059 | 98,0539 |
| GD17.11 | 0,5873 | 0,517 | 4,2388 | 0,325 | 1,1124 | 81,5231 | 158,4907 | 19,4145 | 2,3505 | 82,9237 | 102,8632 |
| 17TH26a | 0,8103 | 0,9381 | 4,2616 | 0,5485 | 1,1513 | 25,5857 | < L.D. | 31,9583 | 3,8551 | 66,0084 | 201,2034 |
| 17TH32b | 0,3373 | 0,5949 | 3,8069 | 0,3655 | 1,0156 | 83,0067 | < L.D. | 23,2535 | 2,593 | 92,3955 | 104,6093 |
| TH-29 | 0,3644 | 0,6223 | 4,4137 | 0,3563 | 1,1304 | 75,2117 | < L.D. | 23,9213 | 2,5875 | 65,6544 | 107,2856 |
| 16STH25 | 0,3273 | 0,422 | 3,4052 | 0,2956 | 0,9391 | 48,8978 | < L.D. | 16,0786 | 2,1679 | 12,1786 | 102,2522 |
| 16STH26 | 0,2986 | 0,5411 | 3,1181 | 0,3634 | 0,854 | 50,7893 | < L.D. | 22,1767 | 2,6077 | 110,447 | 89,0744 |
| 16STH32 | 0,3217 | 0,4939 | 3,6241 | 0,3028 | 0,9593 | 75,0463 | < L.D. | 18,9026 | 2,1544 | 64,7544 | 108,4293 |
| 17TH22 | 0,3232 | 0,5203 | 3,4291 | 0,3025 | 0,8422 | 89,3531 | < L.D. | 19,0104 | 2,136 | 63,2979 | 103,3029 |
| 16STH24 | 0,3052 | 0,4894 | 3,1159 | 0,2878 | 0,822 | 53,4085 | < L.D. | 18,5412 | 2,0967 | 95,0466 | 97,5598 |
| 16STH31 | 0,3099 | 0,4792 | 3,3205 | 0,2646 | 0,8645 | 99,2938 | < L.D. | 17,3889 | 1,8431 | 75,2053 | 102,0698 |
| 17TH24 | 0,2731 | 0,4314 | 2,7318 | 0,2276 | 0,7058 | 101,5608 | < L.D. | 13,2105 | 1,6736 | 92,0137 | 83,1434 |
| 17TH21 | 0,3157 | 0,5286 | 3,2119 | 0,3526 | 0,8276 | 81,4714 | < L.D. | 22,2598 | 2,5192 | 78,9583 | 104,083 |
| GD15.141 | 0,4461 | 0,4743 | 3,8802 | 0,3113 | 1,0511 | 88,0263 | 91,2631 | 19,1576 | 2,2531 | 78,0298 | 98,0095 |
| 16STH23b | 0,3 | 1,2158 | 3,1327 | 0,6295 | 0,8201 | 51,1381 | < L.D. | 48,9112 | 4,2319 | 92,7103 | 101,9629 |
| 16STH27 | 0,3219 | 0,5926 | 3,1666 | 0,361 | 0,8476 | 64,1251 | < L.D. | 22,8259 | 2,5364 | 103,7619 | 95,8342 |
| GD15.140 | 0,465 | 0,5053 | 2,9952 | 0,306 | 0,8353 | 66,3573 | 122,7896 | 18,4322 | 2,1766 | 68,5155 | 95,3533 |
| 16STH03 | 0,2879 | 0,4181 | 3,4643 | 0,2196 | 0,9014 | 106,495 | < L.D. | 14,6902 | 1,5731 | 97,008 | 77,4498 |
| SA-14 | 0,3208 | 0,4962 | 3,6348 | 0,3167 | 0,9596 | 113,219 | < L.D. | 18,7514 | 2,2238 | 69,7399 | 93,455 |
| TH-27 | 0,535 | 0,495 | 3,1987 | 0,3854 | 0,9377 | 115,4723 | < L.D. | 20,0278 | 2,8982 | 32,1305 | 145,3062 |
| 17TH31 | 0,3454 | 0,4754 | 4,0433 | 0,2543 | 1,041 | 86,938 | < L.D. | 17,0376 | 1,8015 | 78,5953 | 113,9298 |
| 16STH23a | 0,2873 | 0,5751 | 2,8329 | 0,3588 | 0,7572 | 51,0988 | < L.D. | 22,5555 | 2,6172 | 69,9314 | 96,6662 |
| GD15.139 | 0,4728 | 0,547 | 3,1588 | 0,3318 | 0,8566 | 79,1303 | 110,2892 | 19,7856 | 2,4121 | 72,2291 | 101,7947 |
| GD16.10 | 0,4631 | 0,5704 | 4,0559 | 0,268 | 0,5801 | 92,4443 | 75,0901 | 17,1405 | 1,8636 | 66,1525 | 110,3506 |
| 16STH04b | 0,2767 | 0,6225 | 3,235 | 0,333 | 0,8422 | 115,9895 | < L.D. | 26,9908 | 2,3598 | 105,1497 | 81,0563 |
| 16STH05 | 0,3053 | 0,8194 | 3,3904 | 0,3297 | 0,8136 | 92,5213 | < L.D. | 19,167 | 2,4038 | 51,6423 | 88,6373 |
| 16STH08 | 0,2992 | 0,5078 | 3,5382 | 0,3027 | 0,7997 | 67,9472 | < L.D. | 18,404 | 2,2054 | 222,3722 | 92,9823 |
| 16STH11a | 0,3478 | 0,492 | 3,9826 | 0,3451 | 1,0545 | 95,0321 | < L.D. | 20,8312 | 2,5103 | 91,6873 | 100,084 |
| 16STH11b | 0,3102 | 0,4712 | 3,7638 | 0,3106 | 0,9829 | 81,3015 | 0,979 | 18,4467 | 2,2637 | 83,2068 | 92,427 |
| 16STH12 | 0,329 | 0,6679 | 4,042 | 0,3542 | 1,0989 | 91,0534 | < L.D. | 23,7932 | 2,5199 | 29,0334 | 98,8057 |
| 16STH14 | 0,3394 | 0,4713 | 3,7084 | 0,3123 | 0,9976 | 106,024 | < L.D. | 18,1691 | 2,3056 | 33,8058 | 98,2738 |
| 16STH15b | 0,3536 | 0,4397 | 3,9557 | 0,3187 | 1,0648 | 105,702 | < L.D. | 18,1012 | 2,3441 | 82,9061 | 101,1634 |

| Echantillon | Localisation (Fig.3-A) | Formation | Transformation state | $SiO_2$ | $Al_2O_3$ | $Fe_2O_3$ | MnO | MgO | CaO | $Na_2O$ | $K_2O$ | $TiO_2$ | $P_2O_5$ | LOI | Total |
|---|---|---|---|---|---|---|---|---|---|---|---|---|---|---|---|
| | | | | % | % | % | % | % | % | % | % | % | % | % | % |
| 16STH17 | 16 | undetermined | transformed | 61,07 | 17,43 | 4,934 | 0,1775 | 1,129 | 4,289 | 2,71 | 1,269 | 0,52 | 0,19 | 7,58 | 101,3 |
| 17TH33 | 12 | undetermined | transformed | 60,29 | 15,905 | 7,236 | 0,1803 | 2,633 | 5,409 | 2,467 | 1,094 | 0,533 | 0,13 | 3,37 | 99,25 |
| 17TH16 | 16 | undetermined | transformed | 60,25 | 16,373 | 6,373 | 0,3074 | 2,465 | 5,65 | 2,754 | 1,064 | 0,539 | 0,15 | 4,2 | 100,12 |
| 16STH28 | 28 | undetermined | transformed | 64,87 | 18,423 | 2,321 | 0,0477 | 1,161 | 5,704 | 3,342 | 1,087 | 0,554 | 0,22 | 3,6 | 101,32 |
| 16STH09b | 14 | undetermined | transformed | 58,06 | 15,3 | 5,924 | 0,035 | 1,604 | 4,331 | 0,651 | 0,965 | 0,487 | 0,13 | 12,99 | 100,48 |
| 16STH16 | 16 | undetermined | transformed | 62,47 | 16,99 | 2,999 | 0,1264 | 2,579 | 3,596 | 2,96 | 0,52 | 0,487 | 0,1 | 7,13 | 99,96 |
| 16STH18 | 16 | undetermined | transformed | 60,39 | 15,233 | 7,621 | 0,0689 | 1,732 | 2,652 | 1,692 | 1,945 | 0,397 | 0,16 | 7,85 | 99,73 |
| TH-26a | 15 | undetermined | transformed | 59,85 | 15,815 | 5,416 | 0,085 | 2,884 | 3,914 | 1,161 | 1,551 | 0,562 | < L.D. | 8,05 | 99,28801 |
| GD16.03 | 14 | undetermined | transformed | 58,94 | 15,02 | 6,226 | 0,0792 | 2,915 | 4,507 | 2,187 | 0,855 | 0,503 | < L.D. | 8,55 | 99,7822 |
| 17TH17a | 16 | undetermined | transformed | 62,28 | 16,743 | 4,777 | 0,0507 | 1,856 | 4,026 | 2,906 | 0,452 | 0,522 | 0,15 | 5,32 | 99,08 |
| 17TH17b | 16 | undetermined | transformed | 63,17 | 16,635 | 4,989 | 0,0424 | 1,598 | 3,273 | 2,658 | 0,669 | 0,556 | 0,15 | 6,31 | 100,05 |
| 17TH07 | 25 | undetermined | transformed | 63,29 | 20,243 | 1,637 | < L.D. | 0,261 | 1,499 | 1,989 | 1,168 | 0,494 | 0,13 | 9,49 | 100,201 |
| GD17.08 | 25 | undetermined | transformed | 59,97 | 16,448 | 7,26 | 0,2013 | 2,113 | 6,027 | 2,918 | 0,893 | 0,489 | 0,21 | 3,75 | 100,27 |
| GD17.09 | 26 | pyroclastic flow | transformed | 64,88 | 17,883 | 3,113 | 0,0184 | 0,47 | 4,321 | 3,147 | 1,217 | 0,529 | 0,12 | 4,63 | 100,34 |
| 16STH29 | 30 | pyroclastic flow | transformed | 60,61 | 15,945 | 5,276 | 0,0381 | 1,031 | 5,062 | 2,847 | 1,505 | 0,498 | 0,15 | 7 | 99,96 |
| 16STH07 | 14 | undetermined | highly transformed | 61,72 | 18,593 | 4,377 | 0,0218 | 0,666 | 1,171 | 0,973 | 0,23 | 0,612 | 0,1 | 12,16 | 100,62 |
| 16STH09a | 14 | undetermined | highly transformed | 59,5 | 16,818 | 4,771 | 0,0171 | 1,936 | 1,443 | 0,54 | 2,628 | 0,608 | 0,21 | 12,71 | 101,17 |
| GD16.05 | 14 | undetermined | highly transformed | 66,25 | 18,338 | 2,873 | < L.D. | 0,448 | 0,531 | 0,445 | 3,991 | 0,615 | < L.D. | 5,82 | 99,31099 |
| 17TH32a | 9 | undetermined | highly transformed | 69,88 | 13,12 | 1,917 | 0,024 | 1,264 | 0,426 | 0,744 | 0,161 | 0,717 | < L.D. | 11,3 | 99,55302 |
| 16STH10 | 14 | undetermined | highly transformed | 58,47 | 16,268 | 5,402 | 0,0577 | 2,858 | 1,457 | 0,429 | 2,336 | 0,593 | 0,14 | 13,24 | 101,25 |
| 16STH19 | 15 | undetermined | highly transformed | 59,01 | 15,923 | 1,756 | 0,1023 | 3,027 | 5,48 | 1,676 | 1,287 | 0,553 | 0,15 | 10,12 | 99,08 |
| GD16.06 | 13 | undetermined | highly transformed | 59,72 | 15,928 | 7,753 | 0,0959 | 3,098 | 1,876 | 1,285 | 0,529 | 0,522 | 0,13 | 8,78 | 99,72 |
| GD15.142 | 17 | lava flow | highly transformed | 60,34 | 19,938 | 7,558 | 0,0302 | 0,759 | 0,101 | 0,132 | 3,242 | 0,501 | < L.D. | 6,46 | 99,0612 |
| 16STH35a | 18 | undetermined | highly transformed | 68,53 | 14,633 | 2,545 | 0,0399 | 0,698 | 0,098 | 0,161 | 1,66 | 0,565 | < L.D. | 12,19 | 101,1199 |
| 16STH35b | 18 | undetermined | highly transformed | 67 | 14,995 | 3,193 | 0,0574 | 0,934 | 0,082 | 0,103 | 0,4 | 0,561 | < L.D. | 12,71 | 100,0354 |
| TH-24a | 18 | undetermined | highly transformed | 66,03 | 15,595 | 6,464 | 0,033 | 0,588 | < L.D. | 0,06 | 0,12 | 0,643 | < L.D. | 11,09 | 100,623 |
| TH-24c | 18 | undetermined | highly transformed | 65,14 | 16,243 | 6,093 | 0,0187 | 0,199 | 0,208 | 0,443 | 0,191 | 0,576 | < L.D. | 10,83 | 99,9417 |
| 16STH01a | 13 | undetermined | highly transformed | 67,55 | 18,45 | 2,531 | < L.D. | 0,324 | 0,247 | 0,649 | 2,73 | 0,561 | 0,15 | 6,26 | 99,452 |
| 16STH01b | 13 | undetermined | highly transformed | 69,02 | 16,84 | 3,835 | < L.D. | 0,245 | 0,17 | 0,695 | 3,156 | 0,655 | 0,17 | 4,58 | 99,36599 |
| 16STH02 | 13 | undetermined | highly transformed | 92,13 | 1,036 | 4,73 | 0,0186 | 0,074 | 0,071 | 0,062 | 0,085 | 0,774 | < L.D. | 1,32 | 100,3006 |
| 16STH34 | 17 | undetermined | highly transformed | 59,31 | 22,253 | 0,591 | 0,0191 | 0,312 | 0,095 | 0,255 | 0,329 | 0,466 | < L.D. | 15,65 | 99,28011 |
| 16STH21a | 20 | undetermined | highly transformed | 62,91 | 15,708 | 4,537 | 0,0321 | 0,984 | 0,53 | 1,132 | 1,821 | 0,549 | 0,17 | 13,06 | 101,43 |
| 16STH21b | 20 | undetermined | highly transformed | 63,78 | 15,243 | 5,886 | 0,0299 | 0,847 | 0,318 | 0,815 | 1,368 | 0,755 | < L.D. | 11,98 | 101,0219 |
| 16STH20 | 15 | undetermined | highly transformed | 67,12 | 15,685 | 3,292 | 0,0215 | 0,729 | 0,906 | 0,547 | 3,271 | 0,584 | < L.D. | 7,72 | 99,8755 |
| TH-25 | 18 | undetermined | highly transformed | 64,65 | 16,795 | 3,088 | 0,0431 | 1,116 | 1,653 | 0,166 | 5,024 | 0,54 | < L.D. | 7,38 | 100,4551 |
| 17TH01 | 19 | undetermined | highly transformed | 67,73 | 18,795 | 0,241 | < L.D. | 0,418 | 0,081 | 0,681 | 0,232 | 0,62 | < L.D. | 10,73 | 99,52801 |
| 17TH02 | 19 | undetermined | highly transformed | 67,95 | 18,418 | 0,774 | < L.D. | 0,29 | 0,106 | 0,326 | 0,316 | 0,653 | < L.D. | 10,42 | 99,253 |
| 16STH22 | 21 | undetermined | highly transformed | 58,01 | 16,888 | 11,54 | 0,022 | 0,291 | 0,067 | 0,078 | 0,772 | 0,476 | 0,26 | 11,88 | 100,29 |
| 17TH03 | 20 | undetermined | highly transformed | 60,9 | 9,81 | 14,705 | < L.D. | 0,34 | 0,198 | 2,009 | 0,264 | 0,557 | 0,24 | 10,82 | 99,84299 |
| 17TH06 | 25 | undetermined | highly transformed | 63,8 | 20,183 | 2,043 | 0,0174 | 0,548 | 0,656 | 1,352 | 1,136 | 0,543 | < L.D. | 10,32 | 100,5984 |
| 16STH13 | 16 | undetermined | highly transformed | 63,44 | 11,708 | 11,407 | 0,0267 | 1,408 | 0,517 | 0,514 | 3,149 | 0,478 | < L.D. | 7,6 | 100,2477 |

| Echantillon | As | Ba | Be | Bi | Cd | Ce | Co | Cr | Cs | Cu | Dy |
|---|---|---|---|---|---|---|---|---|---|---|---|
| | ppm | ppm | ppm | ppm | ppm | ppm | ppm | ppm | ppm | ppm | ppm |
| 16STH17 | 6,1931 | 188,8038 | 0,8313 | 0,2847 | 0,0384 | 27,8418 | 7,8809 | 2,2987 | 0,7966 | 5,2776 | 3,4376 |
| 17TH33 | 1,4176 | 275,235 | 0,7585 | 0,0568 | 0,0424 | 25,9829 | 7,1671 | 11,3081 | 0,1281 | 41,2588 | 3,1441 |
| 17TH16 | 3,8755 | 241,7578 | 0,6631 | < L.D. | 0,0669 | 27,5846 | 9,1546 | 1,1604 | 0,232 | 21,3476 | 3,444 |
| 16STH28 | 10,6974 | 202,2048 | 0,9108 | < L.D. | 0,2198 | 34,7258 | 9,4633 | 3,3368 | 0,3812 | 212,1904 | 4,0607 |
| 16STH09b | 1,3037 | 236,651 | 0,6829 | 0,0971 | 0,3974 | 16,091 | 9,0574 | 4,5812 | 0,3223 | 44,4507 | 3,2036 |
| 16STH16 | 30,9393 | 153,6595 | 0,8025 | 0,6178 | 0,0279 | 25,9059 | 9,9245 | 5,1436 | 0,2375 | 21,405 | 2,8708 |
| 16STH18 | 7,1532 | 155,1786 | 1,0579 | 0,3491 | 0,1006 | 17,9074 | 12,9807 | 2,47 | 0,3356 | 7,8809 | 4,2402 |
| TH-26a | 3,1207 | 126,8781 | 0,7971 | 0,3368 | 0,0918 | 25,4572 | 6,4786 | 4,4461 | 0,6723 | 8,3261 | 3,7025 |
| GD16.03 | 6,5638 | 182,6993 | 0,655 | 1,3582 | 0,0827 | 26,4325 | 17,3096 | 2,0817 | 0,3039 | 27,9385 | 2,8927 |
| 17TH17a | 37,0775 | 165,1166 | 0,7282 | 0,3142 | 0,4464 | 30,9202 | 10,8943 | 1,3359 | 0,5029 | 28,1384 | 3,3059 |
| 17TH17b | 59,4304 | 182,4485 | 0,6479 | 0,8173 | 0,1068 | 26,9167 | 11,4329 | 1,7989 | 0,7641 | 38,5732 | 3,2848 |
| 17TH07 | < L.D. | 177,3078 | 1,0385 | 0,1382 | < L.D. | 40,3056 | 4,9515 | 0,7966 | 0,4615 | 7,1652 | 4,1364 |
| GD17.08 | 1,0209 | 207,4139 | 0,8306 | < L.D. | 0,1126 | 29,7707 | 36,0226 | 0,8007 | 3,5981 | 8,3903 | 3,6546 |
| GD17.09 | 0,6677 | 221,3489 | 0,8738 | < L.D. | 0,0331 | 48,9018 | 18,4029 | 0,6012 | 0,9108 | 8,9161 | 6,0582 |
| 16STH29 | 0,6621 | 164,9672 | 0,7106 | 0,0472 | 0,0576 | 26,5057 | 7,8765 | 2,2029 | 0,6995 | 21,1438 | 2,7345 |
| 16STH07 | 2,4224 | 104,8012 | 0,4358 | 0,3974 | 0,0395 | 19,5274 | 0,9548 | 5,0682 | 0,1099 | 34,0729 | 2,6679 |
| 16STH09a | 1,0159 | 437,9999 | 0,6908 | 0,109 | 0,0722 | 46,4285 | 4,6096 | 3,4216 | 0,659 | 10,0011 | 4,6437 |
| GD16.05 | 18,5827 | 420,4506 | 0,565 | 1,143 | 0,0449 | 37,6125 | 10,3743 | 3,4974 | 1,2742 | 86,3482 | 2,5421 |
| 17TH32a | 2,1267 | 123,1559 | 0,1601 | < L.D. | 0,0272 | 7,1789 | 0,4672 | 0,7654 | 0,1849 | 4,4958 | 2,5453 |
| 16STH10 | 1,1657 | 370,1801 | 0,7368 | 0,1148 | 0,1703 | 9,8468 | 6,8775 | 3,5359 | 0,5895 | 13,4522 | 2,8511 |
| 16STH19 | 2,5358 | 171,3805 | 0,6841 | 0,0544 | < L.D. | 28,9439 | 1,3458 | 3,666 | 0,2644 | 3,9483 | 3,1763 |
| GD16.06 | 2,1609 | 136,3278 | 0,684 | < L.D. | 0,2179 | 27,407 | 16,0462 | 2,3247 | 0,2337 | 9,648 | 3,4753 |
| GD15.142 | 8,3036 | 370,6367 | 0,6793 | 1,3122 | 0,1889 | 28,9641 | 4,3719 | 0,7951 | 2,487 | 27,5921 | 3,132 |
| 16STH35a | 0,6823 | 262,4867 | 0,6199 | 0,4374 | 0,1108 | 34,2974 | 2,6327 | 2,4915 | 0,717 | 16,0939 | 2,1227 |
| 16STH35b | 1,4396 | 47,9233 | 0,4673 | 0,1015 | 0,0724 | 6,9608 | 5,4807 | 3,3669 | 0,2785 | 22,4191 | 2,2696 |
| TH-24a | 10,2056 | 55,0091 | 0,3257 | < L.D. | < L.D. | 20,2372 | 4,8936 | 1,5061 | 0,2425 | 23,377 | 3,2918 |
| TH-24c | 2,3881 | 104,2038 | 213,933 | 1,6642 | < L.D. | 25,0578 | 3,273 | 3,7987 | 0,3581 | 23,0085 | 1,9338 |
| 16STH01a | 1,1022 | 621,8782 | 0,9886 | 0,1539 | 0,0279 | 27,8298 | 4,6232 | 3,7969 | 0,9005 | 40,4332 | 2,9532 |
| 16STH01b | 1,2158 | 703,8156 | 0,6349 | 0,082 | 0,0371 | 42,3617 | 9,452 | 3,1664 | 0,9448 | 17,3478 | 2,7156 |
| 16STH02 | 3,1862 | 24,6698 | 0,3018 | 0,214 | 0,0483 | 4,2013 | 4,2828 | 2,9591 | 0,1738 | 73,4101 | 1,7783 |
| 16STH34 | 0,9509 | 122,0737 | 0,7875 | 0,3926 | 0,0286 | 8,1965 | 2,7734 | 2,0887 | 0,6418 | 15,2931 | 1,4051 |
| 16STH21a | 21,7661 | 481,7101 | 0,6959 | < L.D. | 0,12 | 52,3475 | 4,2592 | 2,1454 | 0,2349 | 30,1992 | 2,273 |
| 16STH21b | 27,9519 | 360,6594 | 0,5795 | 0,1199 | 0,0527 | 4,3723 | 4,4684 | 3,5117 | 0,2061 | 32,7423 | 1,0848 |
| 16STH20 | 13,5177 | 385,3916 | 1,5941 | 0,4386 | 0,1104 | 19,3351 | 10,2663 | 4,6299 | 1,1013 | 7,8071 | 1,9565 |
| TH-25 | 3,7207 | 479,5984 | 0,6953 | 0,9091 | < L.D. | 13,1647 | 0,7624 | 2,6125 | 1,0225 | 10,1529 | 3,8191 |
| 17TH01 | 4,4905 | 66,0448 | 0,3398 | 0,051 | 0,1514 | 41,5976 | 2,1184 | 2,8769 | 0,1199 | 6,4285 | 3,0558 |
| 17TH02 | 11,5527 | 116,1575 | 0,4301 | 0,1397 | 0,0901 | 27,3433 | 2,2615 | 2,8798 | 0,1476 | 3,5807 | 2,5418 |
| 16STH22 | 46,674 | 68,6967 | 0,862 | 0,0844 | 0,0655 | 10,4802 | 3,4351 | 7,6869 | 0,3383 | 35,5492 | 1,7211 |
| 17TH03 | 66,5354 | 78,9745 | 0,4264 | 2,9019 | 0,0312 | 55,5665 | 1,0127 | 1,3354 | 0,1853 | 33,4523 | 3,7126 |
| 17TH06 | < L.D. | 170,4709 | 0,4778 | 0,2477 | < L.D. | 11,1083 | 2,2154 | 0,7182 | 1,3428 | 3,8025 | 1,4137 |
| 16STH13 | 35,962 | 180,8244 | 0,4201 | 4,3852 | 0,0451 | 11,9591 | 4,264 | 2,6172 | 0,7996 | 11,0788 | 1,3652 |

| Echantillon | Er | Eu | Ga | Gd | Ge | Hf | Ho | In | La | Lu | Mo |
|---|---|---|---|---|---|---|---|---|---|---|---|
| | ppm | ppm | ppm | ppm | ppm | ppm | ppm | ppm | ppm | ppm | ppm |
| 16STH17 | 2,183 | 1,0383 | 16,4516 | 3,2958 | 0,8537 | 3,0206 | 0,7721 | < L.D. | 12,5761 | 0,3989 | < L.D. |
| 17TH33 | 2,0518 | 0,9354 | 16,0805 | 2,8857 | 1,4448 | 2,7778 | 0,6985 | 0,0605 | 12,4949 | 0,3737 | 0,7029 |
| 17TH16 | 2,1823 | 1,0314 | 16,7594 | 3,0876 | 1,6152 | 2,8611 | 0,7823 | 0,0562 | 12,7918 | 0,4012 | 0,8334 |
| 16STH28 | 2,4281 | 1,2758 | 18,8516 | 4,0078 | 1,3184 | 2,9157 | 0,8674 | 0,0537 | 15,8447 | 0,4059 | 0,7331 |
| 16STH09b | 2,136 | 1,0782 | 14,2932 | 2,7077 | 0,9487 | 2,6091 | 0,7337 | 0,2749 | 8,781 | 0,3815 | 0,6379 |
| 16STH16 | 1,9738 | 0,8474 | 16,5578 | 2,4573 | 0,8565 | 2,998 | 0,6683 | 0,03 | 12,4395 | 0,3842 | < L.D. |
| 16STH18 | 2,7729 | 0,9513 | 16,9159 | 3,1572 | 1,1776 | 2,9433 | 0,9605 | 0,0401 | 7,8241 | 0,4691 | 0,7179 |
| TH-26a | 2,4033 | 0,7795 | 16,8343 | 3,2477 | 0,9859 | 2,9501 | 0,8307 | 0,0417 | 10,5793 | 0,4132 | 1,1183 |
| GD16.03 | 1,9019 | 0,841 | 15,1456 | 2,6373 | 0,9263 | 2,489 | 0,6651 | 0,0609 | 12,7705 | 0,3505 | < L.D. |
| 17TH17a | 2,1319 | 1,158 | 16,6519 | 3,0951 | 1,3824 | 2,9543 | 0,734 | 0,0886 | 13,9967 | 0,4047 | 0,7581 |
| 17TH17b | 2,1355 | 0,8777 | 15,5177 | 2,8937 | 1,4764 | 3,1397 | 0,7365 | 0,1007 | 12,3748 | 0,416 | 0,7847 |
| 17TH07 | 2,5423 | 1,4016 | 18,6857 | 3,9562 | 1,3084 | 3,0247 | 0,8904 | 0,0367 | 16,0226 | 0,4112 | < L.D. |
| GD17.08 | 2,3256 | 1,1257 | 17,4793 | 3,399 | 1,509 | 2,9705 | 0,8259 | 0,0551 | 13,2492 | 0,4224 | 0,8518 |
| GD17.09 | 3,2666 | 1,9957 | 19,1916 | 6,783 | 1,3058 | 3,2581 | 1,2298 | 0,0411 | 23,3784 | 0,5396 | < L.D. |
| 16STH29 | 1,5953 | 0,984 | 15,5403 | 2,8086 | 1,0967 | 2,3952 | 0,5739 | 0,0444 | 12,0497 | 0,2697 | 0,565 |
| 16STH07 | 2,0042 | 0,525 | 16,574 | 2,0281 | 0,9456 | 3,1192 | 0,6392 | 0,1333 | 9,415 | 0,3926 | 0,8113 |
| 16STH09a | 2,7862 | 1,1813 | 17,6183 | 4,692 | 1,1493 | 2,8533 | 0,9981 | 0,1734 | 21,1213 | 0,4303 | 0,6249 |
| GD16.05 | 1,9777 | 0,8173 | 17,9275 | 2,3904 | 0,8883 | 3,3339 | 0,6227 | < L.D. | 19,5343 | 0,4183 | < L.D. |
| 17TH32a | 1,9638 | 0,2917 | 17,7791 | 1,7312 | 0,8999 | 3,6748 | 0,6226 | 0,0562 | 3,1236 | 0,3945 | 0,6626 |
| 16STH10 | 2,023 | 0,5333 | 18,228 | 2,1139 | 0,5341 | 2,6784 | 0,6764 | 0,0793 | 4,5072 | 0,3782 | 0,9264 |
| 16STH19 | 2,001 | 0,8756 | 16,4097 | 2,8729 | 0,9648 | 2,5441 | 0,7086 | 0,0552 | 13,5987 | 0,3478 | 0,7934 |
| GD16.06 | 2,2653 | 1,1633 | 16,406 | 3,1468 | 1,1441 | 2,9854 | 0,789 | 0,1297 | 12,0961 | 0,4086 | 0,7924 |
| GD15.142 | 2,0498 | 1,0736 | 17,4476 | 3,0177 | 0,9522 | 2,7652 | 0,6889 | 0,081 | 11,391 | 0,3887 | 1,1426 |
| 16STH35a | 1,4071 | 0,8001 | 15,6214 | 2,5467 | 1,254 | 3,278 | 0,4607 | 0,076 | 17,0195 | 0,3147 | < L.D. |
| 16STH35b | 1,5648 | 0,5263 | 16,9312 | 1,904 | 1,389 | 3,2836 | 0,5306 | 0,0446 | 2,7238 | 0,3221 | < L.D. |
| TH-24a | 2,4083 | 0,5014 | 19,8358 | 2,5037 | 1,4033 | 3,5117 | 0,7898 | 0,0707 | 9,2553 | 0,4524 | < L.D. |
| TH-24c | 1,4012 | 0,5241 | 17,8464 | 1,9748 | 1,8361 | 3,2297 | 0,4588 | 0,0334 | 11,3947 | 0,3006 | 0,7977 |
| 16STH01a | 1,9022 | 1,1579 | 15,9329 | 2,8433 | 1,5428 | 2,7595 | 0,6492 | 0,0446 | 14,5063 | 0,3559 | 0,5947 |
| 16STH01b | 1,6529 | 1,4266 | 15,4831 | 2,9924 | 1,4739 | 3,0975 | 0,5682 | 0,05 | 20,7719 | 0,3119 | 0,7197 |
| 16STH02 | 1,4891 | 0,2177 | 0,9778 | 1,0098 | 1,2272 | 3,2467 | 0,4621 | 0,0454 | 1,8867 | 0,3185 | 1,0754 |
| 16STH34 | 1,2163 | 0,3918 | 16,7175 | 1,1428 | 1,0794 | 2,7841 | 0,3622 | 0,2277 | 3,7714 | 0,2896 | 0,7744 |
| 16STH21a | 1,8451 | 0,5824 | 17,0316 | 2,0024 | 1,3127 | 2,9639 | 0,5737 | < L.D. | 46,1801 | 0,4241 | 0,7353 |
| 16STH21b | 1,0279 | 0,2239 | 15,1573 | 0,7733 | 1,2671 | 2,9624 | 0,2948 | < L.D. | 1,8263 | 0,2779 | 1,045 |
| 16STH20 | 1,6061 | 0,3229 | 17,5547 | 1,6132 | 1,0559 | 2,9224 | 0,495 | 0,1198 | 8,6532 | 0,3597 | 0,7392 |
| TH-25 | 2,344 | 0,7465 | 20,3638 | 3,203 | 1,1173 | 2,8791 | 0,8543 | 0,574 | 5,7185 | 0,3721 | 3,9676 |
| 17TH01 | 2,1789 | 0,6351 | 18,1079 | 3,0725 | 1,6591 | 3,5561 | 0,7128 | 0,077 | 19,6293 | 0,4316 | < L.D. |
| 17TH02 | 1,8972 | 0,6064 | 18,5097 | 2,2639 | 1,1591 | 3,4226 | 0,6088 | 0,0675 | 13,3266 | 0,4034 | 1,2824 |
| 16STH22 | 1,3065 | 0,3441 | 14,9532 | 1,3431 | 1,1629 | 2,4101 | 0,4147 | 0,0621 | 3,9575 | 0,2896 | 1,4021 |
| 17TH03 | 2,3628 | 1,3318 | 11,2973 | 4,3506 | 0,8671 | 3,671 | 0,8134 | 0,3403 | 28,0476 | 0,4663 | 0,9757 |
| 17TH06 | 1,0267 | 0,6081 | 18,5073 | 1,2723 | 1,2493 | 2,8042 | 0,3346 | 0,0315 | 5,5968 | 0,2072 | < L.D. |
| 16STH13 | 1,012 | 0,2144 | 13,6404 | 1,0011 | 1,4299 | 2,38 | 0,3324 | 0,107 | 6,1551 | 0,2107 | 14,8478 |

| Echantillon | Nb | Nd | Ni | Pb | Pr | Rb | Sc | Sb | Sm | Sn | Sr |
|---|---|---|---|---|---|---|---|---|---|---|---|
| | ppm | ppm | ppm | ppm | ppm | ppm | ppm | ppm | ppm | ppm | ppm |
| 16STH17 | 3,8683 | 15,1014 | < L.D. | 2,5672 | 3,5849 | 28,145 | 10,2 | 0,1776 | 3,536 | 1,806 | 216,828 |
| 17TH33 | 3,5805 | 12,889 | 4,959 | 1,9048 | 3,1193 | 23,1158 | 15,75 | 0,4872 | 3,0106 | 1,1244 | 241,7166 |
| 17TH16 | 3,8634 | 13,9701 | < L.D. | 5,8314 | 3,4092 | 22,799 | 12,7 | 0,4382 | 3,1395 | 1,1318 | 230,1807 |
| 16STH28 | 4,0231 | 18,8663 | 2,2731 | 3,9106 | 4,4885 | 22,7916 | 11,16 | 0,5533 | 4,4036 | 0,9593 | 288,0977 |
| 16STH09b | 3,2664 | 9,9396 | 3,5094 | 6,3145 | 2,3383 | 18,7154 | 11,92 | 0,2163 | 2,6234 | 1,6703 | 72,0722 |
| 16STH16 | 4,0187 | 12,4344 | 3,5391 | 2,5797 | 3,0892 | 8,1312 | 9,36 | 0,1655 | 2,6706 | 1,501 | 220,3348 |
| 16STH18 | 3,6699 | 10,284 | 2,1582 | 5,2526 | 2,3611 | 48,9454 | 7,84 | 0,333 | 2,8151 | 2,1156 | 129,8916 |
| TH-26a | 3,8618 | 13,3875 | < L.D. | 7,1574 | 2,9632 | 35,0753 | 14,93 | 0,1662 | 3,2312 | < L.D. | 121,6225 |
| GD16.03 | 3,3361 | 12,607 | < L.D. | 10,179 | 3,1667 | 14,3585 | 12,76 | 0,1677 | 2,7247 | 1,8832 | 140,9714 |
| 17TH17a | 3,8744 | 15,6083 | < L.D. | 8,2155 | 3,8214 | 10,2593 | 12,21 | 1,2882 | 3,3855 | 1,5729 | 205,753 |
| 17TH17b | 4,0673 | 13,5415 | < L.D. | 7,2733 | 3,3367 | 16,5147 | 12,5 | 1,7447 | 3,075 | 2,0414 | 176,4767 |
| 17TH07 | 4,1988 | 21,0386 | < L.D. | 5,4065 | 5,1712 | 30,7379 | 7,95 | < L.D. | 4,7057 | 0,9285 | 100,2716 |
| GD17.08 | 4,1508 | 15,6347 | < L.D. | 6,4952 | 3,7129 | 42,3404 | 9,66 | 0,1607 | 3,6112 | 1,2447 | 311,1159 |
| GD17.09 | 4,522 | 31,4764 | < L.D. | 6,1236 | 7,1641 | 33,9829 | 9,84 | 0,0675 | 7,2488 | 1,001 | 262,9174 |
| 16STH29 | 3,2775 | 14,2621 | < L.D. | 3,5948 | 3,3921 | 26,4725 | 11,19 | 0,0773 | 3,2798 | 0,8996 | 248,238 |
| 16STH07 | 4,0869 | 9,2591 | 2,0643 | 1,7004 | 2,3337 | 3,8142 | 15,17 | 0,4121 | 2,0837 | 1,4199 | 60,6327 |
| 16STH09a | 4,1825 | 24,5429 | 4,2024 | 6,9668 | 6,0414 | 54,6068 | 14,35 | 0,1298 | 5,3837 | 1,6472 | 54,2314 |
| GD16.05 | 4,3291 | 16,7899 | < L.D. | 4,2819 | 4,3655 | 80,5285 | 13,74 | 0,5718 | 3,1906 | 4,1713 | 32,1747 |
| 17TH32a | 5,2269 | 4,7611 | < L.D. | 1,6029 | 1,0231 | 2,1573 | 16,58 | 2,7306 | 1,5442 | 1,5393 | 43,2627 |
| 16STH10 | 3,4523 | 6,3699 | 6,5412 | 4,5372 | 1,4066 | 51,3766 | 16,39 | 0,0898 | 1,8524 | 2,7513 | 53,4256 |
| 16STH19 | 3,4319 | 13,9532 | 2,1816 | 3,1134 | 3,4636 | 26,5331 | 12,93 | 0,1737 | 3,0957 | 1,1554 | 134,0375 |
| GD16.06 | 3,858 | 13,2891 | 3,1628 | 4,9313 | 3,2085 | 13,9979 | 13,08 | 0,1322 | 3,2017 | 3,003 | 94,4784 |
| GD15.142 | 3,6694 | 20,1136 | < L.D. | 14,8417 | 4,387 | 99,579 | 12,77 | 0,3118 | 4,0851 | 2,8242 | 134,1101 |
| 16STH35a | 3,9631 | 17,7824 | 2,1083 | 3,8597 | 4,1584 | 45,0901 | 13,96 | 0,1259 | 3,6104 | 1,1244 | 92,7631 |
| 16STH35b | 4,0647 | 4,9116 | 5,4464 | 0,9942 | 0,9732 | 11,7053 | 14,34 | 0,1109 | 1,5982 | 0,7841 | 10,4482 |
| TH-24a | 4,3017 | 10,5253 | < L.D. | 3,0318 | 2,4578 | 2,4107 | 13,6 | 0,2342 | 2,6235 | < L.D. | 13,2876 |
| TH-24c | 4,1074 | 10,6322 | < L.D. | 8,9364 | 2,6653 | 3,7201 | 9,31 | 0,162 | 2,1635 | 2,6362 | 81,7695 |
| 16STH01a | 4,4176 | 14,3095 | 4,1319 | 12,9369 | 3,5567 | 64,7326 | 12,09 | 0,1385 | 3,2782 | 2,1494 | 92,8092 |
| 16STH01b | 4,5402 | 21,1517 | 4,3119 | 10,6293 | 5,3564 | 82,296 | 10,25 | 0,3596 | 4,1238 | 2,6163 | 98,697 |
| 16STH02 | 5,5604 | 2,5704 | 2,585 | 2,2499 | 0,5955 | 2,9534 | 4,04 | 0,4058 | 0,7968 | 1,4189 | 8,7296 |
| 16STH34 | 3,2069 | 6,6524 | 3,2902 | 6,5248 | 1,2367 | 7,751 | 6,21 | 0,1406 | 1,5528 | 2,8121 | 41,5307 |
| 16STH21a | 3,9184 | 10,3114 | < L.D. | 6,0754 | 3,6187 | 33,8191 | 13,6 | 0,7625 | 2,1028 | 0,6308 | 230,9896 |
| 16STH21b | 4,61 | 2,9288 | 2,7971 | 0,987 | 0,6251 | 26,3043 | 8,39 | 0,9225 | 0,7868 | 0,9499 | 43,6689 |
| 16STH20 | 3,9691 | 9,7809 | 3,0827 | 4,0059 | 2,4026 | 83,8231 | 14,04 | 0,8456 | 1,8644 | 9,525 | 35,7818 |
| TH-25 | 3,6251 | 5,975 | < L.D. | 8,8611 | 1,4456 | 129,3422 | 15,32 | 0,269 | 2,1092 | 7,1069 | 195,5159 |
| 17TH01 | 4,5174 | 19,7267 | 2,914 | 2,4024 | 5,0181 | 4,6872 | 15,81 | 0,4316 | 3,8852 | 1,1765 | 11,2005 |
| 17TH02 | 4,5443 | 13,5824 | < L.D. | 5,4675 | 3,2817 | 6,8386 | 16,36 | 0,4666 | 2,8943 | 1,1435 | 77,9753 |
| 16STH22 | 3,1491 | 5,9232 | 3,8684 | 2,1997 | 1,4186 | 18,1829 | 19,89 | 1,3678 | 1,4256 | 1,3696 | 14,7589 |
| 17TH03 | 4,69 | 23,9209 | < L.D. | 10,2588 | 6,3634 | 4,1645 | 10,73 | 0,5775 | 4,7399 | 2,2948 | 167,5759 |
| 17TH06 | 4,0057 | 5,8327 | < L.D. | 2,1831 | 1,3396 | 30,6447 | 10,26 | < L.D. | 1,3473 | 0,9459 | 73,7749 |
| 16STH13 | 3,2813 | 4,8396 | < L.D. | 7,74 | 1,3244 | 102,6224 | 10,1 | 1,355 | 1,0002 | 3,9335 | 34,3698 |

| Echantillon | Ta | Tb | Th | Tm | U | V | W | Y | Yb | Zn | Zr |
|---|---|---|---|---|---|---|---|---|---|---|---|
| | ppm | ppm | ppm | ppm | ppm | ppm | ppm | ppm | ppm | ppm | ppm |
| 16STH17 | 0,3111 | 0,5484 | 3,5726 | 0,3421 | 0,947 | 64,5407 | < L.D. | 20,4427 | 2,4736 | 50,7799 | 107,1079 |
| 17TH33 | 0,3211 | 0,4741 | 3,8045 | 0,3102 | 1,0021 | 114,9678 | < L.D. | 19,5465 | 2,2693 | 65,0372 | 97,1724 |
| 17TH16 | 0,336 | 0,5118 | 3,8664 | 0,3491 | 1,0398 | 89,3327 | < L.D. | 20,3964 | 2,4407 | 79,2388 | 99,7133 |
| 16STH28 | 0,3351 | 0,6391 | 3,4268 | 0,3699 | 0,911 | 66,6378 | < L.D. | 23,041 | 2,6036 | 78,8998 | 100,2147 |
| 16STH09b | 0,2968 | 0,4789 | 3,3352 | 0,3233 | 0,7813 | 67,9594 | < L.D. | 19,8159 | 2,3435 | 86,3354 | 90,6659 |
| 16STH16 | 0,3297 | 0,4346 | 3,8523 | 0,3168 | 1,0407 | 59,7869 | < L.D. | 17,4489 | 2,3272 | 32,3761 | 110,1349 |
| 16STH18 | 0,326 | 0,6027 | 3,6531 | 0,4326 | 0,9516 | 49,0632 | < L.D. | 24,3084 | 3,0914 | 58,6248 | 101,0091 |
| TH-26a | 0,334 | 0,5572 | 3,9252 | 0,3686 | 1,0202 | 102,6296 | < L.D. | 22,4234 | 2,5836 | 68,3945 | 104,3071 |
| GD16.03 | 0,3503 | 0,4426 | 3,3904 | 0,295 | 0,9262 | 88,9019 | 56,9708 | 17,337 | 2,1439 | 50,8582 | 81,7135 |
| 17TH17a | 0,3579 | 0,5008 | 3,9786 | 0,3306 | 1,0959 | 89,4762 | < L.D. | 19,5894 | 2,3869 | 218,0115 | 101,0814 |
| 17TH17b | 0,3651 | 0,4841 | 4,2218 | 0,338 | 1,1472 | 95,2726 | < L.D. | 19,4712 | 2,4738 | 60,7984 | 106,7594 |
| 17TH07 | 0,3351 | 0,6505 | 3,6217 | 0,3757 | 0,9072 | 52,5401 | < L.D. | 24,4152 | 2,5598 | 113,2304 | 106,4014 |
| GD17.08 | 0,5727 | 0,56 | 3,4212 | 0,3633 | 0,9002 | 56,0466 | 170,1318 | 22,0574 | 2,6078 | 97,0636 | 106,8677 |
| GD17.09 | 0,5195 | 1,0152 | 3,9212 | 0,4842 | 1,0312 | 50,7053 | 80,0098 | 32,0451 | 3,3926 | 97,1009 | 113,2517 |
| 16STH29 | 0,2561 | 0,4419 | 2,6435 | 0,2361 | 0,6639 | 85,2428 | < L.D. | 14,9357 | 1,7152 | 57,6713 | 83,9934 |
| 16STH07 | 0,3399 | 0,3753 | 4,1642 | 0,3207 | 1,0653 | 93,7741 | < L.D. | 17,3999 | 2,4008 | 55,9596 | 110,4638 |
| 16STH09a | 0,3454 | 0,7404 | 3,0383 | 0,4055 | 0,797 | 90,9892 | < L.D. | 26,3353 | 2,811 | 60,8926 | 102,2289 |
| GD16.05 | 0,408 | 0,3686 | 4,3846 | 0,3281 | 1,1737 | 106,6943 | 32,7625 | 17,1457 | 2,4851 | < L.D. | 114,3872 |
| 17TH32a | 0,4393 | 0,3411 | 3,6226 | 0,321 | 1,2195 | 101,8005 | < L.D. | 16,74 | 2,4074 | 25,1896 | 138,0204 |
| 16STH10 | 0,2971 | 0,3965 | 3,0955 | 0,3244 | 0,8437 | 136,3834 | < L.D. | 18,9458 | 2,3592 | 57,0789 | 93,6405 |
| 16STH19 | 0,3049 | 0,4806 | 3,436 | 0,3053 | 0,9131 | 97,3724 | < L.D. | 19,2147 | 2,1823 | 22,465 | 87,707 |
| GD16.06 | 0,3932 | 0,5331 | 3,8886 | 0,3512 | 0,9201 | 80,7337 | 26,5166 | 21,494 | 2,4924 | 37,559 | 103,3847 |
| GD15.142 | 0,3304 | 0,4801 | 3,4574 | 0,3203 | 0,9625 | 104,2217 | 23,6054 | 17,9632 | 2,3533 | 40,7106 | 95,9391 |
| 16STH35a | 0,3407 | 0,3541 | 3,9482 | 0,2326 | 1,0808 | 59,9248 | < L.D. | 12,2802 | 1,798 | 48,393 | 110,5219 |
| 16STH35b | 0,3449 | 0,3343 | 3,9854 | 0,2563 | 1,105 | 62,9885 | < L.D. | 13,9353 | 1,8929 | 76,1793 | 111,8878 |
| TH-24a | 0,389 | 0,4515 | 4,4433 | 0,388 | 1,1309 | 109,6795 | < L.D. | 19,6434 | 2,7956 | 50,541 | 119,8478 |
| TH-24c | 0,355 | 0,3038 | 4,1637 | 0,2332 | 1,0675 | 45,9663 | < L.D. | 13,3465 | 1,737 | 51,612 | 113,05 |
| 16STH01a | 0,3222 | 0,4624 | 3,2762 | 0,297 | 0,7723 | 73,3002 | < L.D. | 16,8521 | 2,2113 | 47,3142 | 97,5249 |
| 16STH01b | 0,3614 | 0,4383 | 3,5478 | 0,2547 | 0,7564 | 78,3665 | < L.D. | 14,3609 | 1,9027 | 16,5889 | 110,8288 |
| 16STH02 | 0,3582 | 0,2206 | 2,2853 | 0,2548 | 0,5924 | 21,4611 | < L.D. | 11,9167 | 1,9359 | 17,079 | 115,3211 |
| 16STH34 | 0,308 | 0,1905 | 3,4065 | 0,2112 | 1,0183 | 37,1538 | < L.D. | 9,598 | 1,6559 | 30,1882 | 96,6645 |
| 16STH21a | 0,3328 | 0,3277 | 4,1267 | 0,3035 | 0,9981 | 116,6269 | < L.D. | 16,0142 | 2,3706 | 54,2045 | 102,9594 |
| 16STH21b | 0,3474 | 0,1431 | 3,296 | 0,1788 | 0,9022 | 42,9399 | < L.D. | 8,2338 | 1,47 | 52,871 | 102,2314 |
| 16STH20 | 0,3347 | 0,2742 | 3,8554 | 0,2689 | 0,9819 | 90,659 | < L.D. | 13,9772 | 2,1011 | 9,138 | 102,7507 |
| TH-25 | 0,31 | 0,5606 | 3,3224 | 0,3339 | 0,9367 | 123,6865 | < L.D. | 18,7664 | 2,3138 | 13,8444 | 99,4103 |
| 17TH01 | 0,4142 | 0,4796 | 4,6838 | 0,3474 | 1,5855 | 80,6246 | < L.D. | 18,3664 | 2,6392 | 11,5245 | 126,3574 |
| 17TH02 | 0,3844 | 0,3695 | 4,5884 | 0,3109 | 1,263 | 99,739 | < L.D. | 16,8182 | 2,3914 | 39,3701 | 120,2305 |
| 16STH22 | 0,2648 | 0,2459 | 3,0556 | 0,2151 | 0,8908 | 143,713 | < L.D. | 10,8696 | 1,6591 | 110,8209 | 84,2718 |
| 17TH03 | 0,423 | 0,6113 | 5,3227 | 0,3804 | 1,436 | 60,215 | < L.D. | 21,7711 | 2,8433 | 12,8003 | 132,9818 |
| 17TH06 | 0,3118 | 0,2094 | 2,7628 | 0,1662 | 0,7629 | 68,2543 | < L.D. | 9,0877 | 1,2198 | 71,378 | 97,7921 |
| 16STH13 | 0,2831 | 0,1989 | 3,4095 | 0,169 | 2,7898 | 47,3475 | 0,8862 | 9,0349 | 1,2599 | 22,1408 | 84,0559 |

**Table X-2: Electron microprobe analyses and structural formula of volcanic phases.**

| Sample | DC-10-09a | | 17TH05 | | SA-14 | 16STH32b | | | | 17TH24a | | | | 17TH16 | 16STH16 | | 16STH19 |
|---|---|---|---|---|---|---|---|---|---|---|---|---|---|---|---|---|---|
| Transformation state | Fresh | | Fresh | | Slighty transformed | Slighty transformed | | | | Slighty transformed | | | | Transformed | Transformed | | Highly transformed |
| | Untransformed | | Untransformed | | | | | | | | | | | | | | |
| Mineral % wt | Hypersthene | Hypersthene | Labradorite | Labradorite | Bytownite | Hypersthene | Augite | Hypersthene | Hypersthene | Hypersthene | Labradorite | Labradorite | Labradorite | Labradorite | Labradorite | Labradorite | Labradorite |
| $Al_2O_3$ | 0.68 | 0.79 | 27.86 | 30.57 | 31.59 | 0.88 | 1.28 | 0.88 | 0.88 | 1.26 | 27.92 | 28.67 | 28.23 | 29.03 | 29.40 | 28.24 | |
| $SiO_2$ | 53.19 | 54.62 | 55.48 | 51.15 | 48.62 | 51.90 | 52.27 | 51.70 | 56.51 | 52.45 | 55.25 | 53.79 | 55.11 | 52.52 | 52.58 | 54.09 | |
| $TiO_2$ | 0.11 | 0.10 | 0.00 | 0.03 | 0.03 | 0.14 | 0.30 | 0.13 | 0.13 | 0.19 | 0.02 | 0.04 | 0.00 | 0.01 | 0.04 | 0.00 | |
| $Na_2O$ | 0.02 | 0.00 | 5.26 | 3.58 | 2.76 | 0.00 | 0.24 | 0.03 | 0.03 | 0.05 | 4.97 | 4.83 | 5.01 | 4.97 | 4.82 | 5.37 | |
| MgO | 18.96 | 24.14 | 0.00 | 0.02 | 0.01 | 18.42 | 13.23 | 17.98 | 18.25 | 19.33 | 0.02 | 0.02 | 0.01 | 0.01 | 0.02 | 0.02 | |
| MnO | 1.24 | 0.67 | 0.01 | 0.00 | 0.01 | 1.18 | 0.60 | 1.36 | 1.29 | 1.16 | 0.01 | 0.02 | 0.00 | 0.01 | 0.02 | 0.00 | |
| FeO | 26.85 | 20.53 | 0.35 | 0.37 | 0.42 | 27.78 | 11.87 | 28.34 | 28.29 | 26.50 | 0.54 | 0.37 | 0.39 | 0.34 | 0.33 | 0.30 | |
| $K_2O$ | 0.01 | 0.00 | 0.16 | 0.08 | 0.07 | 0.01 | 0.00 | 0.00 | 0.01 | 0.00 | 0.14 | 0.13 | 0.16 | 0.14 | 0.12 | 0.20 | |
| CaO | 1.15 | 1.49 | 11.14 | 14.18 | 15.22 | 1.10 | 20.26 | 1.21 | 1.19 | 1.31 | 11.10 | 11.94 | 11.00 | 11.81 | 11.99 | 10.75 | |
| Total | 102.20 | 102.34 | 100.26 | 99.98 | 98.71 | 101.42 | 100.05 | 101.63 | 106.59 | 102.23 | 99.98 | 99.82 | 99.91 | 98.84 | 99.32 | 98.97 | |
| | | | | | | | | | | | | | | | | | |
| **Al** | **0.03** | **0.03** | **1.48** | **1.64** | **1.73** | **0.04** | **0.06** | **0.04** | **0.04** | **0.06** | **1.49** | **1.53** | **1.50** | **1.57** | **1.58** | **1.52** | |
| **Si** | **1.98** | **1.97** | **2.50** | **2.33** | **2.25** | **1.97** | **1.97** | **1.96** | **2.02** | **1.96** | **2.49** | **2.44** | **2.49** | **2.41** | **2.40** | **2.47** | |
| **Ti** | **0.00** | **0.00** | **0.00** | **0.00** | **0.00** | **0.00** | **0.01** | **0.00** | **0.00** | **0.01** | **0.00** | **0.00** | **0.00** | **0.00** | **0.00** | **0.00** | |
| **Na** | **0.00** | **0.00** | **0.46** | **0.32** | **0.25** | **0.00** | **0.02** | **0.00** | **0.00** | **0.00** | **0.44** | **0.43** | **0.44** | **0.44** | **0.43** | **0.47** | |
| **Mg** | **1.06** | **1.30** | **0.00** | **0.00** | **0.00** | **1.04** | **0.74** | **1.02** | **0.97** | **1.08** | **0.00** | **0.00** | **0.00** | **0.00** | **0.00** | **0.00** | |
| **Mn** | **0.04** | **0.02** | **0.00** | **0.00** | **0.00** | **0.04** | **0.02** | **0.04** | **0.04** | **0.04** | **0.00** | **0.00** | **0.00** | **0.00** | **0.00** | **0.00** | |
| **Fe** | **0.84** | **0.62** | **0.01** | **0.01** | **0.02** | **0.88** | **0.37** | **0.90** | **0.84** | **0.83** | **0.02** | **0.01** | **0.01** | **0.01** | **0.01** | **0.01** | |
| **K** | **0.00** | **0.00** | **0.01** | **0.00** | **0.00** | **0.00** | **0.00** | **0.00** | **0.00** | **0.00** | **0.01** | **0.01** | **0.01** | **0.01** | **0.01** | **0.01** | |
| **Ca** | **0.05** | **0.06** | **0.54** | **0.69** | **0.76** | **0.04** | **0.82** | **0.05** | **0.05** | **0.05** | **0.54** | **0.58** | **0.53** | **0.58** | **0.59** | **0.53** | |
| **Total (cations)** | **4.00** | **4.01** | **5.00** | **5.01** | **5.01** | **4.01** | **4.00** | **4.02** | **3.96** | **4.01** | **4.98** | **5.01** | **4.98** | **5.03** | **5.02** | **5.01** | |
| | **6 Ox** | **6 Ox** | **8 Ox** | **8 Ox** | **8 Ox** | **6 Ox** | **6 Ox** | **6 Ox** | **6 Ox** | **6 Ox** | **8 Ox** | **8 Ox** | **8 Ox** | **8 Ox** | **8 Ox** | **8 Ox** | |

**Table X-3: Electron microprobe analyses of low-temperature hydrothermal phases.**

| **Sample** | DC-10-09a | 17TH05 | 16STH32b | 17TH16 | 17TH16 | 17TH16 | 17TH16 | SA-14 | SA-14 | SA-14 | SA-14 | 17TH24a | 17TH24a | 16STH35a[2] |
|---|---|---|---|---|---|---|---|---|---|---|---|---|---|---|
| **Transformation state** | Fresh Untransformed | Fresh Untransformed | Slighty transformed | Transformed | Transformed | Transformed | Transformed | Transformed | Transformed | Transformed | Transformed | Transformed | Transformed | Highly transformed |
| **Mineral %wt** | Calcite | Calcite | Calcite | Calcite | Calcite | Calcite | Calcite | Calcite | Calcite | Calcite | Calcite | Jarosite to Natrojarosite | Jarosite | Jarosite to Natrojarosite |
| $Al_2O_3$ | 0.01 | 0.12 | 0.00 | 0.19 | 0.12 | 0.04 | 0.00 | 0.10 | 0.01 | 0.02 | 0.00 | 4.23 | 3.07 | 10.16 |
| $SiO_2$ | 0.16 | 0.92 | 0.21 | 0.56 | 0.33 | 0.37 | 0.21 | 0.38 | 0.14 | 0.24 | 0.25 | 0.11 | 0.26 | 0.09 |
| $TiO_2$ | 0.00 | 0.01 | 0.01 | 0.03 | 0.00 | 0.03 | 0.00 | 0.00 | 0.01 | 0.00 | 0.03 | 0.02 | 0.04 | 0.04 |
| $Na_2O$ | 0.12 | 0.00 | 0.03 | 0.01 | 0.00 | 0.00 | 0.02 | 0.04 | 0.03 | 0.00 | 0.06 | 3.92 | 2.78 | 3.89 |
| MgO | 0.10 | 0.07 | 0.07 | 0.23 | 0.12 | 0.02 | 0.17 | 0.00 | 0.00 | 0.00 | 0.15 | 0.02 | 0.00 | 0.00 |
| MnO | 0.17 | 0.18 | 0.17 | 0.65 | 0.36 | 0.25 | 0.22 | 0.46 | 0.55 | 0.08 | 0.17 | 0.00 | 0.02 | 0.01 |
| FeO | 0.91 | 0.50 | 0.74 | 0.56 | 0.50 | 0.26 | 0.70 | 0.06 | 0.32 | 0.27 | 0.84 | 41.24 | 42.93 | 36.58 |
| $K_2O$ | 0.00 | 0.05 | 0.01 | 0.01 | 0.00 | 0.01 | 0.00 | 0.13 | 0.00 | 0.00 | 0.01 | 1.32 | 2.95 | 0.99 |
| CaO | 53.12 | 51.92 | 51.65 | 55.56 | 55.95 | 56.72 | 51.57 | 42.71 | 54.95 | 56.88 | 52.30 | 1.33 | 0.15 | 0.09 |
| $SO_2$ | 0.00 | 0.04 | 0.00 | 0.00 | 0.00 | 0.00 | 0.00 | 0.00 | 0.00 | 0.03 | 0.00 | 24.30 | 21.84 | 25.30 |
| Total | 54.59 | 53.81 | 52.89 | 57.81 | 57.38 | 57.71 | 52.88 | 43.98 | 56.01 | 57.55 | 53.82 | 76.54 | 74.16 | 77.18 |

**Table X-4: Electron microprobe analyses and structural formula of high-temperature hydrothermal phases.**

| Sample | 16STH16 | | SA-14 | | | | |
|---|---|---|---|---|---|---|---|
| Transformation state | Transformed | | Transformed | | | | |
| Mineral % wt | clinozoisite | clinozoisite | actinote | actinote | titanite | epidote | talc |
| $Al_2O_3$ | 28.50 | 27.83 | 4.48 | 3.02 | 4.06 | 24.15 | 0.17 |
| $SiO_2$ | 37.22 | 35.64 | 50.80 | 51.47 | 33.80 | 38.46 | 64.35 |
| $TiO_2$ | 0.15 | 0.00 | 0.25 | 0.24 | 28.73 | 0.11 | 0.02 |
| $Na_2O$ | 0.01 | 0.01 | 0.33 | 0.31 | 0.09 | 0.00 | 0.10 |
| MgO | 0.36 | 0.35 | 11.38 | 12.74 | 1.66 | 0.12 | 29.92 |
| MnO | 1.35 | 1.03 | 0.98 | 1.05 | 0.18 | 0.73 | 0.02 |
| FeO | 3.23 | 2.14 | 19.90 | 18.28 | 3.82 | 12.38 | 1.06 |
| $K_2O$ | 0.07 | 0.03 | 0.20 | 0.22 | 0.05 | 0.00 | 0.01 |
| CaO | 22.19 | 22.15 | 10.40 | 11.81 | 26.00 | 22.83 | 0.04 |
| Total | 93.08 | 89.18 | 98.72 | 99.14 | 98.39 | 98.78 | 95.69 |
| | | | | | | | |
| **Al** | **2.63** | **2.67** | **0.78** | **0.52** | **0.16** | **2.20** | **0.01** |
| **Si** | **2.91** | **2.90** | **7.49** | **7.54** | **1.11** | **2.97** | **4.05** |
| **Ti** | **0.01** | **0.00** | **0.03** | **0.03** | **0.71** | **0.01** | **0.00** |
| **Na** | **0.00** | **0.00** | **0.09** | **0.09** | **0.01** | **0.00** | **0.01** |
| **Mg** | **0.04** | **0.04** | **2.50** | **2.78** | **0.08** | **0.01** | **2.81** |
| **Mn** | **0.09** | **0.07** | **0.12** | **0.13** | **0.01** | **0.05** | **0.00** |
| **Fe** | **0.21** | **0.15** | **2.45** | **2.24** | **0.11** | **0.80** | **0.06** |
| **K** | **0.01** | **0.00** | **0.04** | **0.04** | **0.00** | **0.00** | **0.00** |
| **Ca** | **1.86** | **1.93** | **1.64** | **1.85** | **0.92** | **1.89** | **0.00** |
| **Total (cations)** | **7.76** | **7.76** | **15.14** | **15.22** | **3.11** | **7.93** | **6.94** |
| | **12 Ox** | **12 Ox** | **23 Ox** | **23 Ox** | **5 Ox** | **12 Ox** | **11 Ox** |

| Sample | 17TH24a | 16STH16 | | | | 16STH19 | | |
|---|---|---|---|---|---|---|---|---|
| Transformation state | Transformed | Transformed | | | | Highly transformed | | |
| Mineral % wt | illite | illite | illite | muscovite | muscovite | illite | muscovite | muscovite |
| $Al_2O_3$ | 27.91 | 31.46 | 30.78 | 32.44 | 33.19 | 23.76 | 29.31 | 28.94 |
| $SiO_2$ | 53.38 | 48.16 | 48.63 | 49.45 | 49.41 | 51.97 | 47.13 | 47.96 |
| $TiO_2$ | 0.07 | 0.10 | 0.08 | 0.04 | 0.07 | 0.00 | 0.09 | 0.01 |
| $Na_2O$ | 0.30 | 0.08 | 0.08 | 0.11 | 0.15 | 0.00 | 0.03 | 0.08 |
| MgO | 2.86 | 4.97 | 4.32 | 1.63 | 1.55 | 0.84 | 0.61 | 0.43 |
| MnO | 0.08 | 0.26 | 0.21 | 0.07 | 0.06 | 0.00 | 0.10 | 0.02 |
| FeO | 2.04 | 0.63 | 0.87 | 0.16 | 0.13 | 7.93 | 5.79 | 7.41 |
| $K_2O$ | 7.90 | 9.07 | 8.42 | 10.00 | 9.92 | 4.89 | 9.87 | 9.94 |
| CaO | 0.22 | 0.13 | 0.17 | 0.10 | 0.13 | 0.00 | 0.01 | 0.03 |
| Total | 94.76 | 94.86 | 93.56 | 94 | 64.61 | 89.39 | 92.94 | 94.82 |
| | | | | | | | | |
| **$Al^{IV}$** | **0.50** | **0.81** | **0.75** | **0.71** | **0.74** | **0.36** | **0.73** | **0.71** |
| **$Al^{VI}$** | **1.66** | **1.64** | **1.67** | **1.83** | **1.84** | **1.61** | **1.67** | **1.63** |
| **Si** | **3.50** | **3.19** | **3.25** | **3.29** | **3.26** | **3.64** | **3.27** | **3.29** |
| **Ti** | **0.00** | **0.01** | **0.00** | **0.00** | **0.00** | **0.00** | **0.01** | **0.00** |
| **Na** | **0.04** | **0.01** | **0.01** | **0.01** | **0.02** | **0.00** | **0.00** | **0.01** |
| **Mg** | **0.28** | **0.49** | **0.43** | **0.16** | **0.15** | **0.09** | **0.06** | **0.04** |
| **Mn** | **0.00** | **0.01** | **0.01** | **0.00** | **0.00** | **0.00** | **0.01** | **0.00** |
| **Fe** | **0.11** | **0.03** | **0.05** | **0.01** | **0.01** | **0.47** | **0.34** | **0.43** |
| **K** | **0.66** | **0.77** | **0.72** | **0.85** | **0.83** | **0.44** | **0.87** | **0.87** |
| **Ca** | **0.02** | **0.01** | **0.01** | **0.01** | **0.01** | **0.00** | **0.00** | **0.00** |
| **Total (cations)** | **6.77** | **6.97** | **6.90** | **6.87** | **6.86** | **6.60** | **6.96** | **6.98** |
| | **11 Ox** | **11 Ox** | **11 Ox** | **11 Ox** | **11 Ox** | **11 Ox** | **11 Ox** | **11 Ox** |

**Table X-5: Table of mixing models solid solution used in tcdb55c2d database of Theriak-Domino software.**

| Solution models Mineral | Abbreviation Kretz, 1983 | Reference | End-members |
|---|---|---|---|
| Biotite | bt | White et al., 2007 | phlogopite, annite2, obiotite, eastonite, tbiotite |
| Chlorite | chl | Holland et al., 1998 | Al-free-chlorite, clinochlore, daphnite, amesite, Mn-chlorite |
| Feldspar | ab | Baldwin et al., 2005 | sanidine, high-albite, anorthite |
| Ilmenite | ilm | White et al., 2007 | Oilmenite, Dilmenite, hematite |
| White Mica | ms pg<br>ms<br>pg | Cogon and Holland, 2002 | muscovite, celadonite, Fe-celadonite, paragonite |

## X.5. Article 4 – Supplementary data

**Table X-6: Electron microprobe analyses and structural formula of high-temperature hydrothermal phases.**

| Mineral | Illite-Smectite | | | | | | | | | | | | | | | |
|---|---|---|---|---|---|---|---|---|---|---|---|---|---|---|---|---|
| analysis number | 1 / 1 | 3 / 1 | 4 / 1 | 5 / 1 | 9 / 1 | 10 / 1 | 14 / 1 | 27 / 1 | 15 / 1 | 31 / 1 | 32 / 1 | 35 / 1 | 37 / 1 | 45 / 1 | 46 / 1 | 41 / 1 |
| **Element (%wt oxide)** | | | | | | | | | | | | | | | | |
| Al2O3 | 29.94 | 27.44 | 24.62 | 26.14 | 28.18 | 26.20 | 26.10 | 29.84 | 27.03 | 27.48 | 28.15 | 29.55 | 24.73 | 24.48 | 23.31 | 29.26 |
| SiO2 | 45.55 | 41.51 | 36.88 | 41.59 | 43.51 | 43.05 | 40.07 | 43.79 | 41.66 | 39.69 | 41.78 | 42.79 | 40.01 | 39.45 | 39.11 | 42.76 |
| TiO2 | 0.09 | 0.08 | 0.07 | 0.09 | 0.06 | 0.06 | 0.09 | 0.04 | 0.09 | 0.03 | 0.03 | 0.02 | 0.02 | 0.14 | 0.16 | 0.03 |
| Na2O | 0.08 | 0.05 | 0.03 | 0.03 | 0.07 | 0.03 | 0.03 | 0.10 | 0.04 | 0.06 | 0.11 | 0.09 | 0.03 | 0.02 | 0.03 | 0.09 |
| MgO | 9.42 | 11.88 | 19.28 | 14.57 | 9.57 | 8.53 | 14.04 | 10.24 | 12.18 | 16.50 | 10.59 | 7.92 | 19.18 | 15.24 | 13.65 | 10.57 |
| MnO | 0.82 | 0.76 | 1.28 | 0.98 | 0.65 | 0.55 | 1.08 | 0.65 | 0.97 | 0.90 | 0.64 | 0.48 | 0.90 | 1.12 | 1.23 | 0.52 |
| FeO | 0.94 | 1.70 | 2.81 | 1.96 | 1.34 | 1.33 | 1.77 | 1.21 | 1.53 | 1.69 | 1.34 | 0.98 | 1.96 | 2.04 | 1.79 | 1.21 |
| K2O | 6.51 | 5.19 | 2.20 | 3.33 | 6.00 | 6.64 | 3.68 | 3.93 | 4.58 | 3.70 | 3.46 | 6.04 | 1.17 | 3.85 | 3.99 | 3.79 |
| CaO | 0.21 | 0.26 | 0.37 | 0.38 | 0.30 | 0.25 | 0.31 | 0.34 | 0.28 | 0.31 | 0.45 | 0.26 | 0.66 | 0.30 | 0.38 | 0.53 |
| Total | 93.56 | 88.88 | 87.53 | 89.07 | 89.68 | 86.64 | 87.18 | 90.14 | 88.35 | 90.36 | 86.54 | 88.12 | 88.64 | 86.65 | 83.65 | 88.76 |
| **Structural formula** | | | | | | | | | | | | | | | | |
| **Al** | 2.36 | 2.29 | 2.11 | 2.17 | 2.33 | 2.24 | 2.22 | 2.41 | 2.26 | 2.26 | 2.37 | 2.47 | 2.05 | 2.11 | 2.08 | 2.41 |
| **Si** | 3.05 | 2.94 | 2.68 | 2.93 | 3.05 | 3.13 | 2.89 | 3.01 | 2.96 | 2.77 | 2.99 | 3.03 | 2.82 | 2.88 | 2.96 | 2.98 |
| **Ti** | 0.00 | 0.00 | 0.00 | 0.01 | 0.00 | 0.00 | 0.01 | 0.00 | 0.00 | 0.00 | 0.00 | 0.00 | 0.00 | 0.01 | 0.01 | 0.00 |
| **Na** | 0.01 | 0.01 | 0.00 | 0.00 | 0.01 | 0.00 | 0.00 | 0.01 | 0.01 | 0.01 | 0.01 | 0.01 | 0.00 | 0.00 | 0.00 | 0.01 |
| **Mg** | 0.94 | 1.26 | 2.09 | 1.53 | 1.00 | 0.92 | 1.51 | 1.05 | 1.29 | 1.72 | 1.13 | 0.84 | 2.01 | 1.66 | 1.54 | 1.10 |
| **Mn** | 0.05 | 0.05 | 0.08 | 0.06 | 0.04 | 0.03 | 0.07 | 0.04 | 0.06 | 0.05 | 0.04 | 0.03 | 0.05 | 0.07 | 0.08 | 0.03 |
| **Fe** | 0.05 | 0.10 | 0.17 | 0.12 | 0.08 | 0.08 | 0.11 | 0.07 | 0.09 | 0.10 | 0.08 | 0.06 | 0.12 | 0.12 | 0.11 | 0.07 |
| **K** | 0.56 | 0.47 | 0.20 | 0.30 | 0.54 | 0.62 | 0.34 | 0.34 | 0.41 | 0.33 | 0.32 | 0.55 | 0.11 | 0.36 | 0.38 | 0.34 |
| **Ca** | 0.02 | 0.02 | 0.03 | 0.03 | 0.02 | 0.02 | 0.02 | 0.02 | 0.02 | 0.02 | 0.03 | 0.02 | 0.05 | 0.02 | 0.03 | 0.04 |
| **Total (cation)** | 7.04 | 7.14 | 7.37 | 7.13 | 7.06 | 7.06 | 7.16 | 6.96 | 7.11 | 7.26 | 6.98 | 7.01 | 7.21 | 7.24 | 7.19 | 6.98 |
| **O (fixed)** | 11 | 11 | 11 | 11 | 11 | 11 | 11 | 11 | 11 | 11 | 11 | 11 | 11 | 11 | 11 | 11 |

| Mineral | Illites | | | | | | | | |
|---|---|---|---|---|---|---|---|---|---|
| analysis number | 25 / 1 . | 26 / 1 . | 13 / 1 . | 2 / 1 . | 16 / 1 . | 22 / 1 . | 23 / 1 . | 15 | 34 / 1 . |
| | | | | | | | | | |
| **Element (%wt oxide)** | | | | | | | | | |
| Al2O3 | 32.65 | 31.72 | 29.34 | 31.46 | 30.78 | 35.00 | 34.94 | 23.76 | 31.41 |
| SiO2 | 48.10 | 47.53 | 46.90 | 48.16 | 48.63 | 50.51 | 49.31 | 51.97 | 45.63 |
| TiO2 | 0.03 | 0.04 | 0.09 | 0.10 | 0.08 | 0.01 | 0.03 | 0.00 | 0.07 |
| Na2O | 0.16 | 0.14 | 0.09 | 0.08 | 0.08 | 0.19 | 0.22 | 0.00 | 0.06 |
| MgO | 4.44 | 4.97 | 4.95 | 4.97 | 4.32 | 0.97 | 1.06 | 0.84 | 3.74 |
| MnO | 0.29 | 0.34 | 0.27 | 0.26 | 0.21 | 0.03 | 0.02 | 0.00 | 0.19 |
| FeO | 0.61 | 0.73 | 0.70 | 0.63 | 0.87 | 0.22 | 0.27 | 7.93 | 0.45 |
| K2O | 6.17 | 6.93 | 7.42 | 9.07 | 8.42 | 7.59 | 6.64 | 4.89 | 7.85 |
| CaO | 0.29 | 0.24 | 0.21 | 0.13 | 0.17 | 0.19 | 0.32 | 0.00 | 0.19 |
| Total | 92.74 | 92.64 | 89.99 | 94.87 | 93.56 | 94.72 | 92.79 | 89.39 | 89.58 |
| | | | | | | | | | |
| **Structural formula** | | | | | | | | | |
| **Al** | **2.55** | **2.50** | **2.39** | **2.45** | **2.42** | **2.67** | **2.71** | **1.96** | **2.57** |
| **Si** | **3.19** | **3.18** | **3.24** | **3.19** | **3.25** | **3.27** | **3.25** | **3.64** | **3.17** |
| **Ti** | **0.00** | **0.00** | **0.00** | **0.01** | **0.00** | **0.00** | **0.00** | **0.00** | **0.00** |
| **Na** | **0.02** | **0.02** | **0.01** | **0.01** | **0.01** | **0.02** | **0.03** | **0.00** | **0.01** |
| **Mg** | **0.44** | **0.50** | **0.51** | **0.49** | **0.43** | **0.09** | **0.10** | **0.09** | **0.39** |
| **Mn** | **0.02** | **0.02** | **0.02** | **0.01** | **0.01** | **0.00** | **0.00** | **0.00** | **0.01** |
| **Fe** | **0.03** | **0.04** | **0.04** | **0.03** | **0.05** | **0.01** | **0.01** | **0.46** | **0.03** |
| **K** | **0.52** | **0.59** | **0.65** | **0.77** | **0.72** | **0.63** | **0.56** | **0.44** | **0.70** |
| **Ca** | **0.02** | **0.02** | **0.02** | **0.01** | **0.01** | **0.01** | **0.02** | **0.00** | **0.01** |
| **Total (cation)** | **6.80** | **6.87** | **6.89** | **6.97** | **6.90** | **6.72** | **6.69** | **6.59** | **6.89** |
| **O (fixed)** | **11** | **11** | **11** | **11** | **11** | **11** | **11** | **11** | **11** |

| Mineral | Chlorite | | | | | | | | | | | | |
|---|---|---|---|---|---|---|---|---|---|---|---|---|---|
| analysis number | 28 / 1 . | 24 / 1 . | 36 / 1 . | 17 / 1 . | 19 / 1 . | 21 / 1 . | 1 | 7 | 8 | 9 | 11 | 13 | 2 |
| | | | | | | | | | | | | | |
| **Element (%wt oxide)** | | | | | | | | | | | | | |
| Al203 | 23.10 | 23.77 | 23.49 | 25.72 | 25.70 | 24.60 | 20.30 | 20.18 | 20.08 | 20.22 | 20.11 | 20.27 | 20.57 |
| SiO2 | 34.37 | 35.21 | 37.94 | 38.83 | 37.86 | 37.62 | 27.01 | 25.45 | 25.66 | 25.51 | 25.69 | 25.53 | 27.32 |
| TiO2 | 0.05 | 0.03 | 0.03 | 0.00 | 0.06 | 0.03 | 0.06 | 0.01 | 0.00 | 0.00 | 0.01 | 0.02 | 0.01 |
| Na2O | 0.03 | 0.01 | 0.04 | 0.02 | 0.03 | 0.02 | 0.00 | 0.05 | 0.19 | 0.00 | 0.04 | 0.02 | 0.00 |
| MgO | 19.42 | 22.40 | 20.90 | 18.26 | 18.53 | 22.26 | 16.50 | 13.94 | 13.73 | 13.65 | 13.71 | 13.95 | 16.71 |
| MnO | 1.15 | 1.27 | 1.05 | 0.97 | 1.09 | 1.24 | 0.33 | 0.30 | 0.37 | 0.23 | 0.34 | 0.26 | 0.29 |
| FeO | 2.29 | 2.41 | 2.30 | 1.94 | 2.03 | 2.29 | 22.48 | 24.36 | 27.85 | 26.98 | 27.91 | 27.82 | 23.64 |
| K2O | 0.18 | 0.24 | 0.76 | 0.29 | 0.28 | 0.31 | 0.00 | 0.00 | 0.00 | 0.00 | 0.00 | 0.00 | 0.00 |
| CaO | 0.51 | 0.38 | 0.55 | 0.62 | 0.55 | 0.41 | 0.10 | 0.00 | 0.00 | 0.00 | 0.00 | 0.00 | 0.09 |
| Total | 81.10 | 85.71 | 87.06 | 86.65 | 86.12 | 88.78 | 86.78 | 84.29 | 87.88 | 86.59 | 87.81 | 87.87 | 88.63 |
| | | | | | | | | | | | | | |
| **Structural formula** | | | | | | | | | | | | | |
| **Al** | **2.68** | **2.62** | **2.54** | **2.76** | **2.78** | **2.05** | **2.50** | **2.60** | **2.53** | **2.57** | **2.53** | **2.55** | **2.49** |
| **Si** | **3.38** | **3.30** | **3.48** | **3.54** | **3.48** | **2.66** | **2.83** | **2.78** | **2.74** | **2.75** | **2.74** | **2.72** | **2.81** |
| **Ti** | **0.00** | **0.00** | **0.00** | **0.00** | **0.00** | **0.00** | **0.00** | **0.00** | **0.00** | **0.00** | **0.00** | **0.00** | **0.00** |
| **Na** | **0.01** | **0.00** | **0.01** | **0.00** | **0.00** | **0.00** | **0.00** | **0.01** | **0.04** | **0.00** | **0.01** | **0.00** | **0.00** |
| **Mg** | **2.85** | **3.13** | **2.86** | **2.48** | **2.54** | **2.35** | **2.57** | **2.27** | **2.19** | **2.19** | **2.18** | **2.22** | **2.56** |
| **Mn** | **0.10** | **0.10** | **0.08** | **0.07** | **0.08** | **0.07** | **0.03** | **0.03** | **0.03** | **0.02** | **0.03** | **0.02** | **0.03** |
| **Fe** | **0.19** | **0.19** | **0.18** | **0.15** | **0.16** | **0.14** | **1.97** | **2.23** | **2.49** | **2.43** | **2.49** | **2.48** | **2.03** |
| **K** | **0.02** | **0.03** | **0.09** | **0.03** | **0.03** | **0.03** | **0.00** | **0.00** | **0.00** | **0.00** | **0.00** | **0.00** | **0.00** |
| **Ca** | **0.05** | **0.04** | **0.05** | **0.06** | **0.05** | **0.03** | **0.01** | **0.00** | **0.00** | **0.00** | **0.00** | **0.00** | **0.01** |
| **Total (cation)** | **9.29** | **9.40** | **9.29** | **9.10** | **9.14** | **7.33** | **9.92** | **9.92** | **10.02** | **9.97** | **9.99** | **10.00** | **9.94** |
| **O (fixed)** | **14** | **14** | **14** | **14** | **14** | **14** | **14** | **14** | **14** | **14** | **14** | **14** | **14** |

| Mineral | Muscovite | | | | | | | | | |
|---|---|---|---|---|---|---|---|---|---|---|
| analysis number | 3 | 4 | 5 | 18 / 1 . | 30 / 1 . | 33 / 1 . | 6 | 10 | 12 | 14 |
| | | | | | | | | | | |
| **Element (%wt oxide)** | | | | | | | | | | |
| Al203 | 28.59 | 28.94 | 29.31 | 32.44 | 33.19 | 32.43 | 28.69 | 28.75 | 28.52 | 29.35 |
| SiO2 | 48.05 | 47.96 | 47.13 | 49.45 | 49.41 | 48.85 | 48.11 | 47.89 | 48.19 | 47.07 |
| TiO2 | 0.06 | 0.01 | 0.09 | 0.04 | 0.07 | 0.10 | 0.05 | 0.07 | 0.07 | 0.12 |
| Na2O | 0.04 | 0.08 | 0.03 | 0.11 | 0.15 | 0.08 | 0.03 | 0.01 | 0.03 | 0.05 |
| MgO | 0.28 | 0.43 | 0.61 | 1.63 | 1.55 | 2.21 | 0.47 | 0.29 | 0.57 | 0.69 |
| MnO | 0.07 | 0.02 | 0.10 | 0.07 | 0.06 | 0.10 | 0.06 | 0.12 | 0.04 | 0.07 |
| FeO | 6.62 | 7.41 | 5.79 | 0.16 | 0.13 | 0.27 | 6.41 | 6.63 | 6.37 | 5.81 |
| K2O | 9.81 | 9.94 | 9.87 | 10.00 | 9.92 | 9.84 | 9.75 | 9.88 | 9.79 | 9.79 |
| CaO | 0.03 | 0.03 | 0.01 | 0.10 | 0.13 | 0.07 | 0.02 | 0.01 | 0.02 | 0.00 |
| Total | 93.55 | 94.82 | 92.94 | 93.99 | 94.60 | 93.96 | 93.59 | 93.65 | 93.60 | 92.95 |
| | | | | | | | | | | |
| **Structural formula** | | | | | | | | | | |
| **Al** | **2.33** | **2.34** | **2.40** | **2.54** | **2.58** | **2.54** | **2.33** | **2.34** | **2.32** | **2.40** |
| **Si** | **3.32** | **3.29** | **3.27** | **3.29** | **3.26** | **3.25** | **3.32** | **3.31** | **3.33** | **3.27** |
| **Ti** | **0.00** | **0.00** | **0.00** | **0.00** | **0.00** | **0.00** | **0.00** | **0.00** | **0.00** | **0.01** |
| **Na** | **0.01** | **0.01** | **0.00** | **0.01** | **0.02** | **0.01** | **0.00** | **0.00** | **0.00** | **0.01** |
| **Mg** | **0.03** | **0.04** | **0.06** | **0.16** | **0.15** | **0.22** | **0.05** | **0.03** | **0.06** | **0.07** |
| **Mn** | **0.00** | **0.00** | **0.01** | **0.00** | **0.00** | **0.01** | **0.00** | **0.01** | **0.00** | **0.00** |
| **Fe** | **0.38** | **0.42** | **0.34** | **0.01** | **0.01** | **0.01** | **0.37** | **0.38** | **0.37** | **0.34** |
| **K** | **0.87** | **0.87** | **0.87** | **0.85** | **0.83** | **0.84** | **0.86** | **0.87** | **0.86** | **0.87** |
| **Ca** | **0.00** | **0.00** | **0.00** | **0.01** | **0.01** | **0.01** | **0.00** | **0.00** | **0.00** | **0.00** |
| **Total (cation)** | **6.94** | **6.98** | **6.96** | **6.87** | **6.87** | **6.89** | **6.94** | **6.95** | **6.94** | **6.96** |
| **O (fixed)** | **11** | **11** | **11** | **11** | **11** | **11** | **11** | **11** | **11** | **11** |

**Table X-7: XRD pattern decompositions.**

| Sample | Position | Intensity | Area | FWHM | Interpretation |
|---|---|---|---|---|---|
| 16STH19-1_AD 315-500 µm | 5.81 | 10900.6 | 13177.4 | 1.14 | Chlorite-Smectite (001) |
| | 6.12 | 6828.17 | 1946.31 | 0.27 | |
| | 6.69 | 1939.5 | 195.95 | 0.15 | Illite-Smectite [Illite-rich] ? |
| | 8.67 | 2200.51 | 1229.94 | 0.53 | Illite (001) |
| | 8.80 | 3695.56 | 466.4 | 0.12 | Mica (001) |
| | 12.34 | 8267.05 | 2970.77 | 0.34 | Chlorite (002) |
| | 13.76 | 1294.95 | 353.38 | 0.26 | Feldspar |
| | 17.68 | 3442.68 | 1164.31 | 0.32 | Illite-Mica (002) |
| | 18.64 | 3529.18 | 1370.53 | 0.36 | Chlorite (003) |
| 16STH19-1_EG 315-500 µm | 5.14 | 6569.07 | 4575.52 | 0.65 | Smectite (001) |
| | 6.09 | 5696.10 | 2019.63 | 0.33 | Chlorite (001) |
| | 8.72 | 1406.39 | 1054.28 | 0.7 | Illite (001) |
| | 8.8 | 3104.77 | 476.93 | 0.14 | Mica (001) |
| | 9.52 | 627.18 | 125.44 | 0.38 | Smectite (002) |
| | 12.25 | 3449.96 | 1846.5 | 0.5 | Chlorite (002) [Chlorite-Smectite] |
| | 12.37 | 3058.74 | 665.46 | 0.2 | Chlorite (002) [Chlorite] |
| | 13.81 | 986.34 | 186.23 | 0.18 | Feldspar |
| | 17.68 | 1393.94 | 388.12 | 0.26 | Illite-Mica (002) |
| | 18.65 | 2294.22 | 1024.21 | 0.42 | Chlorite (003) |
| 16STH19-2_AD 160-315 µm | 6.03 | 24011.50 | 37594.5 | 1.47 | Smectite (001) |
| | 6.16 | 15974.50 | 4718.98 | 0.28 | Chlorite (001) |
| | 7.66 | 7573.89 | 12103 | 1.5 | Illite-Smectite [Smectite rich] ? |
| | 8.59 | 4501.99 | 2484.71 | 0.52 | Illite (001) |
| | 8.79 | 6198.99 | 1044.39 | 0.16 | Mica (001) |
| | 12.36 | 10918.90 | 4723.47 | 0.41 | Chlortite (002) |
| | 13.77 | 1633.76 | 304.01 | 0.17 | Feldspar |
| | 17.69 | 2276.70 | 1779.93 | 0.73 | Mica-Illite (002) |
| | 18.68 | 4448.59 | 2135.17 | 0.45 | Chlorite (003) |
| 16STH19-2_EG 160-315 µm | 5.13 | 20976.90 | 16870.4 | 0.76 | Smectite (001) |
| | 5.99 | 5787.09 | 2748.14 | 0.45 | Illite-Smectite [Smectite rich] |
| | 6.15 | 9599.99 | 2267.96 | 0.22 | Chlorite (001) |
| | 8.63 | 2445.41 | 2243.11 | 0.86 | Illite (001) |
| | 8.80 | 4848.96 | 960.84 | 0.19 | Mica (001) |
| | 9.68 | 572.07 | 85.81 | 0.31 | Smectite (002) |
| | 12.34 | 8428.02 | 3833.68 | 0.43 | Chlortite (002) |
| | 13.79 | 1304.07 | 231.96 | 0.17 | Feldspar |
| | 17.68 | 1748.83 | 455.48 | 0.24 | Illite-Mica (002) |
| | 18.68 | 2925.63 | 1371.33 | 0.44 | Chlorite (003) |

**Table X-8: Compiled Ar-Ar results.**

| | K-Ar total fusion (Ma) | 2σ | Plateau age (Ma) | 2σ | MSWD | % $^{39}$Ar released | Isochron age (Ma) | 2σ | $^{40}$Ar/$^{36}$Ar i | 2σ |
|---|---|---|---|---|---|---|---|---|---|---|
| 315 - 500 µm fraction | | | | | | | | | | |
| Experiments: | | | | | | | | | | |
| #B7-B8 | 2.53 | 0.32 | 2.78 | 0.22 | 0.31 | 98% | 2.77 | 0.33 | 299.9 | 12.6 |
| #A9 A10 | 2.27 | 0.75 | 2.45 | 0.25 | 0.38 | 87% | 2.59 | 0.31 | 292.6 | 9 |
| #B12 | 2.57 | 0.25 | 2.62 | 0.2 | 0.33 | 99% | 2.57 | 0.31 | 297.4 | 8.5 |
| #B2 | 2.52 | 0.62 | 2.55 | 0.44 | 0.32 | 61% | 2.88 | 1.54 | 277.2 | 109 |
| Combined experiments | 2.45 | 0.27 | 2.59 | 0.12 | 0.39 | 90% | 2.67 | 0.17 | 295.9 | 5.5 |
| | | | | | | | | | | |
| 160 - 315 µm fraction | | | | | | | | | | |
| Experiments: | | | | | | | | | | |
| #B1 | 1.58 | 0.25 | 1.87 | 0.43 | 2.05 | 61% | 1.65 | 0.66 | 305.9 | 17.8 |
| #C4 | 1.16 | 0.53 | 2.14 | 0.38 | 0.78 | 74% | 2.21 | 0.49 | 296.7 | 12.9 |
| | | | | | | | | | | |

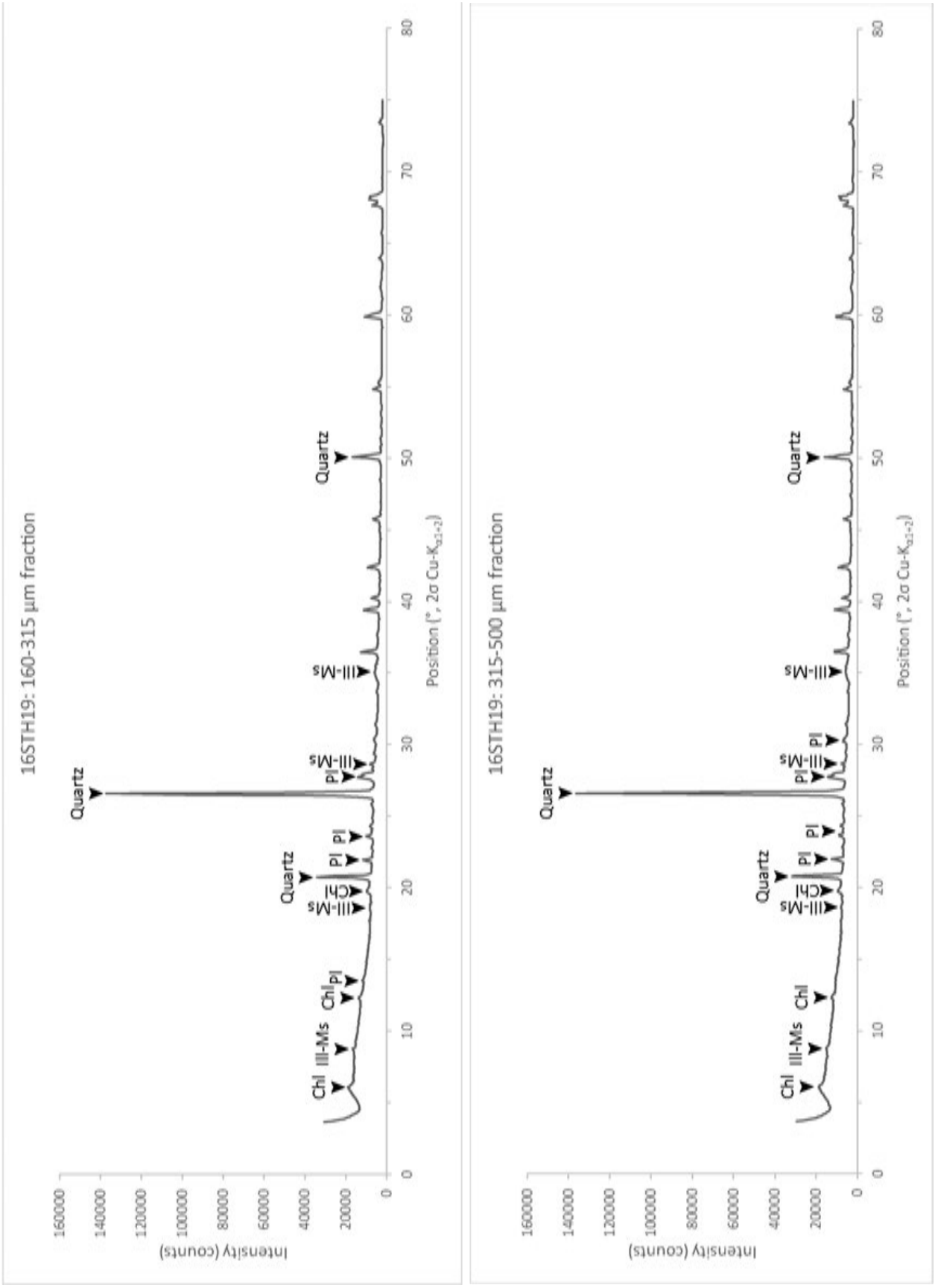


**Figure X-1: XRD bulk meta-pyroxenes sample**

## X.6. Article 5 – Petrophysical properties of volcanic rocks and impacts of hydrothermal alteration in the Guadeloupe Archipelago (West Indies)

Journal of Volcanology and Geothermal Research 360 (2018) 1–21

Contents lists available at ScienceDirect

Journal of Volcanology and Geothermal Research

journal homepage: www.elsevier.com/locate/jvolgeores

# Petrophysical properties of volcanic rocks and impacts of hydrothermal alteration in the Guadeloupe Archipelago (West Indies)

Vivien Navelot [a,*], Yves Géraud [a], Alexiane Favier [b,c], Marc Diraison [a], Michel Corsini [b], Jean-Marc Lardeaux [b], Chrystèle Verati [b], Jeanne Mercier de Lépinay [d], Lucie Legendre [c], Gildas Beauchamps [e]

[a] Université de Lorraine, UMR 7359 GeoRessources, Ecole Nationale Supérieure de Géologie, 2 Rue du Doyen Marcel Roubault, Vandoeuvre-lès-Nancy 54500, France
[b] Université Côte d'Azur, CNRS - Observatoire de la Côte d'azur - IRD - UMR 7329 Géoazur, 250 Rue Albert Einstein, Valbonne 06560, France
[c] Université des Antilles, UMR 5243 Geosciences Montpellier, Campus de Fouillole, Pointe à Pitre 97159, Guadeloupe, France
[d] Université de Strasbourg, Institut de Physique du Globe de Strasbourg, UMR 7516 CNRS, 5 Rue René Descartes, Strasbourg 67084, France
[e] Université de Cergy Pontoise, Laboratoire Géosciences et Environnement Cergy, 1 Rue Descartes, Neuville-sur-Oise 95000, France

ARTICLE INFO

*Article history:*
Received 16 January 2018
Received in revised form 12 June 2018
Accepted 17 July 2018
Available online 21 July 2018

*Keywords:*
Andesites
Debris flows
Pyroclastics
Petrophysical properties
Hydrothermal alteration

ABSTRACT

The results of the GEOTREF project presented here aim to develop high enthalpy geothermal energy in fractured reservoirs. They focus on active volcanic islands, especially the Basse-Terre Island (Guadeloupe Archipelago). As part of this project we measured several petrophysical properties to better understand how fluids flow in the hydrothermal system, provide a set of parameters to modelers and build datasets for future interpretation of well logs. The thermo-physical rock properties of bulk and grain density, porosity, permeability, compressional wave velocity, thermal conductivity and diffusivity, specific heat capacity of outcropping volcanic rocks from the Guadeloupe Archipelago (Lesser Antilles) were measured and a dataset was built. According to field observations, samples were grouped into three lithological classes and then separated by their degree of alteration according to macroscopic aspects and optical microscopy results. Geochemical data were obtained, and magnetic minerals identified by combining anisotropy of magnetic susceptibility and variation of magnetic susceptibility with temperature.

The lithotypes investigated were lava flows, debris flows and pyroclastics (gathering ash, pumice and scoria deposits). For lavas and debris flows, three degrees of alteration were defined; fresh, slightly to moderately altered and highly hydrothermalized. Only fresh pyroclastics were studied because the altered state was not outcropping.

Typically, samples are composed of andesite and belong to tholeiitic and calc-alkaline series. Lava porosity consists of high-density cooling joints and vesicles of different shapes, whereas pores in debris flows and pyroclastics are located both between and within particles. Median porosities and permeabilities are clearly distinct for lavas (4% and $6 \cdot 10^{-18}$ m$^2$), debris flows (33% and $4 \cdot 10^{-14}$ m$^2$) and pyroclastics (34% and $8 \cdot 10^{-13}$ m$^2$). The porosity difference implies a thermal conductivity twice to three times higher for lavas (1.68 W·m$^{-1}$·K$^{-1}$). Specific heat capacity of all lithothypes is similar (0.75–0.97 kJ·kg$^{-1}$·K$^{-1}$).

Advancing hydrothermal alteration removes magnetic minerals and transforms initial rocks. The original plagioclases and pyroxenes in neoformed chlorite, white micas, quartz, epidote and clay minerals are replaced. This modifies the shape of the pore network. Furthermore, hydrothermal alteration results in a reduction of pore throat diameter. It tends to decrease petrophysical differences between lavas and debris flows, increasing the porosity and permeability of effusive rocks, while the opposite effects are observed for debris flows.

© 2018 Elsevier B.V. All rights reserved.

### 1. Introduction

Geothermal exploitation is well-developed in magmatic-volcanic fields where convection dominates heat transfer (Moeck, 2014). Such fields lie above subduction areas like in the Western Pacific (Heise et al., 2016; McNamara et al., 2016; Mielke et al., 2016; Ratouis and Zarrouk, 2016; Wilmarth and Stimac, 2015). This geological context is favorable because it is associated with a strong heat flux. Active subduction occurs in the Atlantic Ocean, along the Caribbean archipelago (Fig. 1a). The geothermal potential of the Caribbean is proved, and several sites are in the prospecting phase (Bertani, 2016). Currently, only the Bouillante field (Guadeloupe Island) is operating. Seven exploratory and production wells were drilled for the development of the Bouillante

* Corresponding author at: UMR 7359 GeoRessources, Ecole Nationale Supérieure de Géologie, 2 Rue du Doyen Marcel Roubault, BP 10162, 54505 Vandoeuvre-lès-Nancy cedex, France.
*E-mail address:* vivien.navelot@univ-lorraine.fr (V. Navelot).

https://doi.org/10.1016/j.jvolgeores.2018.07.004
0377-0273/© 2018 Elsevier B.V. All rights reserved.

field (Bézèlgues-Courtade and Bes-de-Berc, 2007). Even after forty years of exploration and production, the understanding of the Bouillante geothermal system is still limited. This is due to the high complexity of its geological context. The structural framework and location of fluid flow pathways are well-defined (Calcagno et al., 2012). The composition of hydrothermal fluid is well-documented (Bouchot et al.,

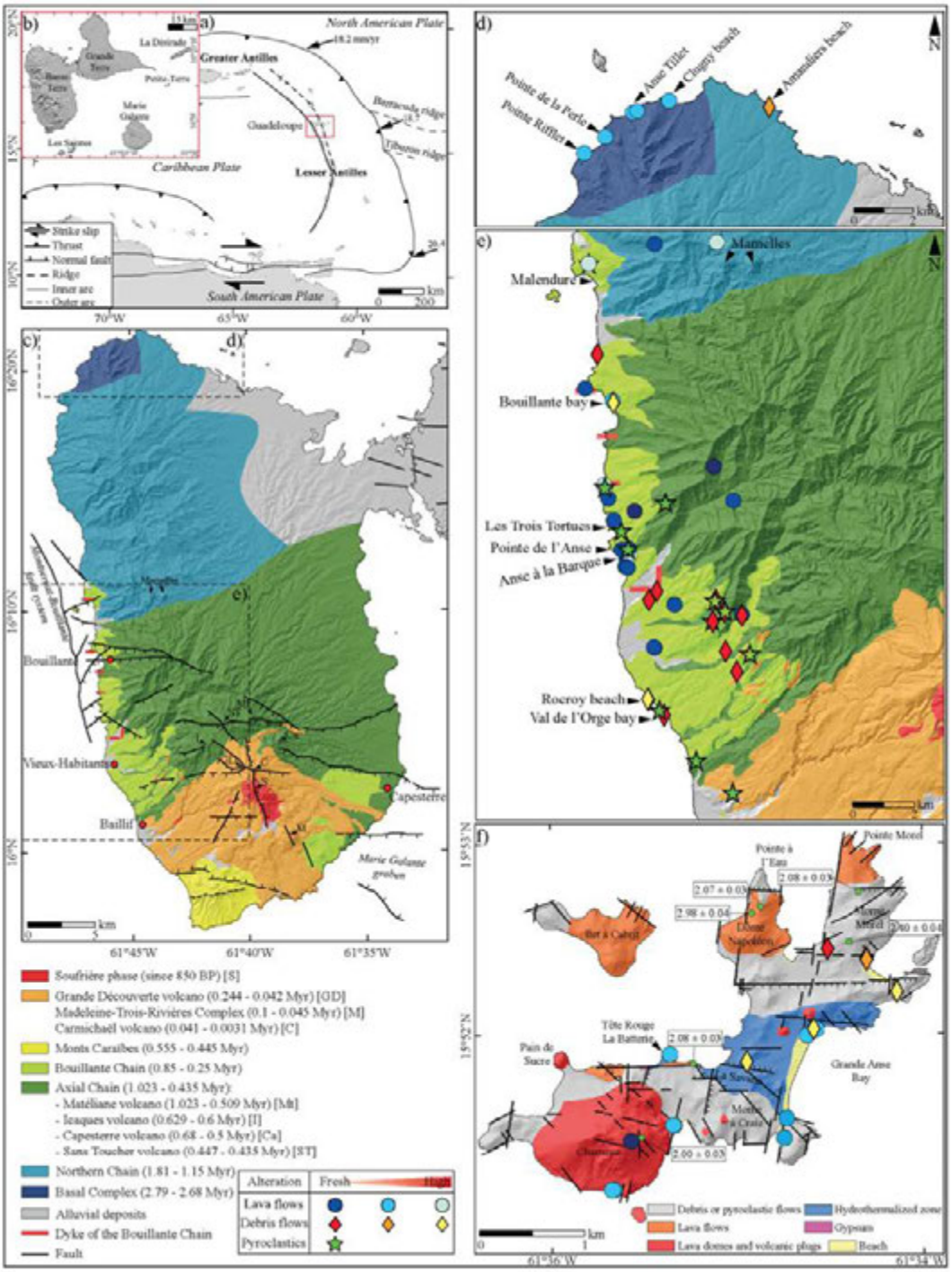

2008; Iundt and Ouzounian, 1985; Sanjuan et al., 2010, 2004, 2001, 2000; Sanjuan and Brach, 1998; Traineau et al., 2014). However, the origins of fluid and heat are still subject to debate. Only limited data have been published, and conceptual models for both fluid flow (Lachassagne et al., 2009; Lopez et al., 2011), and the reservoir geometry (Bouchot et al., 2010, 2008) remain weak.

There is a clear lack of petrological, thermal and physical data concerning volcanic rocks of Guadeloupe. Therefore, it is difficult to identify the targeted volcanic formations and the impact of hydrothermal alteration on rocks. As part of the exploration and development of high enthalpy geothermal energy to develop geothermal reservoir models, the characterization of petrophysical properties of rocks in the Vieux-Habitants area at different degrees of hydrothermal alteration (Fig. 1c) was performed. To this end, a comprehensive set of fresh or hydrothermally altered outcropping rocks was collected and outcrop analogue studies were carried out. These provide important information about geo-body size and geometry (Howell et al., 2014). They are also an inexpensive way of investigating petrophysical properties on a large set of samples. Outcrop studies are commonly used for geothermal exploration (Aretz et al., 2015; Lenhardt and Götz, 2015, 2011). Previous reservoir characterizations were carried out on similar rocks in several areas like New Zealand (Cant et al., 2018; Mielke et al., 2016, 2015; Siratovich et al., 2014), the Philippines (Stimac et al., 2004), the Faroe Islands (Ólavsdóttir et al., 2015) and Mexico (Lenhardt and Götz, 2011). These studies were performed on samples from both outcrops and cores. They supplied large datasets of petrophysical properties, providing information that could constrain numerical models to real measured properties. Overall, they highlighted: 1 - decreasing porosity and permeability with increasing depth; 2 - a decrease of porosity associated with hydrothermal alterations that result in an increase of thermal conductivity; 3 - the observation of better matrix porosity and permeability for breccia and pyroclastics than for lava.

The samples studied came from Basse-Terre Island (Basal Complex, Northern Chain and Vieux-Habitants-Bouillante areas) and Terre-de-Haut Island (Fig. 1b–f). The study described in this paper aims to characterize petrophysical matrix properties for lava flows, debris flows and pyroclastics. The long-term aim is to build a database, improve the interpretation of forthcoming borehole logging, understand how fluids flow in the different lithological classes and provide parameters for static and dynamic 3D reservoir models. These properties have been measured both on fresh rocks from the Vieux-Habitants-Bouillante area and on older rocks exhumed from the Basal Complex and Terre-de-Haut. Older rocks could have been buried under the same thermal and pressure conditions as rocks of the currently exploited Bouillante geothermal field. Indeed, the central part of Terre-de-Haut was defined as an exhumed geothermal system by Verati et al. (2016). The volcanic activity of the Basal Complex occurred coevally with Terre-de-Haut (Zami et al., 2014). We can presume that the Basal Complex was buried before its exhumation and placed at a relatively high temperature, according to an abnormally high geothermal gradient calculated in this area (Manga et al., 2012). The objectives of the data set are: 1 – to determine petrophysical properties of the pyroclastic and debris flow matrices: importantly, these are not only concentrated onto lava blocks (Bernard, 1999; Bernard et al., 2007); 2 – to define the role of hydrothermal alterations and weathering on petrography, microstructures, and their resulting petrophysical properties; 3 – to identify the contribution of different lithotypes to the reservoir geometry. Based on a first exploratory mission we decided to focus on two islands; Terre-de-Haut and Basse-Terre. These are in approximately the same geodynamic context and have a similar volcanic activity.

## 2. Geological context

The Guadeloupe Archipelago is located at the convergent boundary between the North American and Caribbean tectonic plates (Fig. 1a). This convergence is accommodated by the subduction of the North and South American lithospheres under the Caribbean plate, at the relatively low velocity of approximately 2 $cm \cdot yr^{-1}$ (DeMets et al., 2000; Symithe et al., 2015). This subduction produced two successive volcanic arcs (Bouysse, 1983). The outer, older, volcanic arc was active from the Eocene to Early Miocene era. It includes several islands e.g. Grande-Terre of Guadeloupe, Marie-Galante and Petite-Terre (Fig. 1b). These are topped by the Pliocene to Holocene carbonate platforms (Munch et al., 2014) and eastern Martinique (Bouysse and Westercamp, 1990). The inner volcanic arc began its activity during the Pliocene epoch and is still active. It encompasses several islands such as Saint Kitts and Nevis, Dominica and Montserrat. Some of these islands are renowned for their seismic activity and have a well-known history of eruptions (Feuillet et al., 2010, 2002). Three islands of the Guadeloupe Archipelago belong to the more recent volcanic arc (Bouysse and Westercamp, 1990): Terre-de-Bas and Terre-de-Haut in Les Saintes Archipelago and Basse-Terre with its active volcano "La Soufrière" (Fig. 1b and c). The activity of the Grande Découverte-Soufrière Complex is a major human safety issue, especially since its last major eruption in 1976, even though this was limited to a seismic crisis and a phreatic eruption (Komorowski et al., 2005). Many studies since this date have revealed a large amount of geological, geochemical and geophysical data concerning this well-monitored volcano (e.g. Coutant et al., 2012; Gaudin et al., 2016, 2015, 2013; Lesparre et al., 2016; Pozzi et al., 1979; Rosas-Carbajal et al., 2016; Samper et al., 2009). Moreover, the recent offshore seismic activity between Les Saintes and Dominica gave a new impetus to studies of the Archipelago's structural framework (Bazin et al., 2010; Escartín et al., 2016; Feuillet et al., 2011; Leclerc et al., 2016, 2014).

### 2.1. Geology of Basse-Terre Island

Basse-Terre is a late Tertiary to Quaternary volcanic island, with a volcano that is still active, and which belongs to the inner arc of the Lesser Antilles. The island is made of composite volcanoes built-up by spaced pulses of activity (Davidson and De Silva, 2000). It consists of six major eruptive complexes that are successively placed from North to South according to a NNW-SSE to NW-SE direction (Fig. 1c). However, several volcanic edifices and seamounts are located distant to this general alignment and others do not enter into the progressive southward migration (Mathieu, 2010). The oldest volcanic complex is the Basal Complex outcrop in the northern part of the island. This was active between 2.79 ± 0.04 Myr ago and 2.68 ± 0.04 Myr ago (K-Ar ages, Samper et al. (2007)) and forms the Basse-Terre substratum. It is made of sub-aerial lava flows and eroded volcanic edifices (Mathieu, 2010). The calc-alkaline Northern Chain, dating from 1.81 ± 0.03 Myr to 1.15 ± 0.02 Myr ago (K-Ar ages, Samper et al. (2007)), consists of voluminous lava flows and andesite and dacite domes (Komorowski et al., 2005). The Axial and Bouillante Chains composed of Pitons de Bouillante, Matéliane, Icaques, Capesterre and Sans Toucher volcanoes were formed between 1.023 ± 0.025 Myr and 0.435 ± 0.008 Myr ago (K-Ar ages, Samper et al. (2007)). These chains are characterized by

**Fig. 1.** a) Geodynamic setting of the Lesser Antilles arc (modified from Bouysse and Westercamp, 1990; Feuillet et al., 2002; Symithe et al., 2015). b) The Guadeloupe Archipelago. 5 m resolution DEM from IGN (Institut national de l'information géographique et forestière). c) Simplified geological map of Basse-Terre Island with major volcanic complexes and structures shown (Boudon, 1988; Mathieu, 2010). Groundmass K/Ar ages are from Blanc, 1983; Carlut et al., 2000; Ricci et al., 2015b, 2015a, 2017; Samper et al., 2007, 2009. Major faults are from Calcagno et al., 2012; Feuillet et al., 2002; Leclerc et al., 2016. d and e) Location map of samples studied with the different rock types and their degree of alteration: d) Basal Complex in the Northern part of Basse-Terre Island; e) Vieux-Habitants-Bouillante area. f) Location of samples studied and simplified geological map of Terre-de-Haut with the dominant lithotypes in each area indicated. Tectonic sketch map of the main faults. Modified from Jacques and Maury (1988a) and Verati et al. (2016) according to field observations. K-Ar ages (Myr) are from Zami et al., 2014. (For interpretation of the references to color in this figure legend, the reader is referred to the web version of this article.)

voluminous hyaloclastites covered by lava flows. On the West Coast, the volcanic activity is essentially phreatomagmatic and there is a wide range of magma compositions: olivine basalts, andesites, dacites and quartz-bearing rhyolites (Komorowski et al., 2005). The Monts Caraïbes were active from 0.555 Myr to 0.445 Myr ago (K-Ar ages, Samper et al. (2007)). Both the inactive Trois-Rivières-Madeleine Complex and the still active Grande Découverte-Soufrière Complex are younger than 0.25 Myr (K-Ar ages, Samper et al. (2007)). They are characterized by an effusive activity, which produces voluminous domes, lava flows and a more limited volume of pyroclastics (block-and-ash flows and ash and scoria flows).

The geology of the Guadeloupe Archipelago has been extensively studied since the 1970s, in particular for its geothermal resource (Bouchot et al., 2011, 2010; Calcagno et al., 2012; Patrier et al., 2003; Sanjuan and Brach, 2015, 1998). Indeed, a high-temperature (250–260 °C) geothermal field was identified in Bouillante (Fig. 1c) in the 1970s (Bouchot et al., 2010). This geothermal field has been exploited since 1985 for electricity generation. Since 2005, this geothermal plant has had a capacity of 15 MWe (Sanjuan and Traineau, 2008). This Bouillante geothermal field developed in a regional key geodynamic area is located at the intersection of the Lesser Antilles major tectonic structures (Calcagno et al., 2012; Thinon et al., 2010), accommodating the oblique convergence between the Caribbean and North American plates. Two regional fault systems come together in this area. The NW-SE Montserrat-Bouillante fault system is composed of several 'en echelon' oblique normal strike-slip faults that accommodate a sinistral motion. The ESE-WNW to E-W Bouillante-Capesterre normal fault system could be the western termination of the E-W Marie-Galante graben system.

### 2.2. Geology of Terre-de-Haut Island

Les Saintes Archipelago, which includes the Terre-de-Haut Island, represents the emerging part of a plateau largely covered by plio-quaternary reef carbonates (Andreieff et al., 1979). The Terre-de-Haut Island is entirely composed of medium-K calc-alkaline andesite rocks (Jacques et al., 1984; Zami et al., 2014). This composition is typical of the central part of the recent active arc in the Lesser Antilles. The volcanic activity on the Terre-de-Haut Island began approximately at the same time as on Basse-Terre (Samper, 2007). Three volcanic phases between 2.98 ± 0.04 Myr and 2.00 ± 0.03 Myr, built the Terre-de-Haut Island (Jacques et al., 1984; Jacques and Maury, 1988b, 1988a; Zami et al., 2014). Phase I, at 2.98 ± 0.04 Myr (K-Ar age), consists of dacite lava flows and explosive breccia from the Napoléon dome (Fig. 1f). Phase II, at 2.40 ± 0.04 Myr, built up the Morne Morel, starting with explosive phreato-magmatic activity and continuing with the placing of pyroclastic flows. Phase III, from 2.08 ± 0.03 Myr to 2.00 ± 0.03 Myr, completed the build-up of the island with the development of the Pointe Morel basic andesite flows associated with the phreato-magmatic deposit and the dark andesite lava flow with two pyroxenes in the central part of Terre-de-Haut. This phase ended with the positioning of the Chameau dome and several other intrusions. The central part of the Terre-de-Haut is affected by high hydrothermal alterations that limit dating of this area, since rocks are totally transformed (Fig. 1f). Verati et al. (2016) characterized this area as an exhumed geothermal system and described paragenesis associated with hydrothermal alterations.

### 2.3. Hydrothermal alteration

Hydrothermal alterations in the central part of Terre-de-Haut consist in the development of smectite, kaolinite, and veins of quartz, pyrite and gypsum (Jacques and Maury, 1988a). Verati et al. (2016) specified the high-temperature association. They observed three such events. The first is composed of chlorite and epidote aggregates developed as pseudomorphs of primary magmatic clinopyroxenes and plagioclases. The second consists in chlorite, serpentine and oxide aggregates developed at the expense of orthopyroxenes. Veins filled either by chalcedony, pyrite and quartz, or chlorite, smectite and goethite aggregates re-cut these new minerals. The third comes from an advanced argilitic alteration consisting in the development of kaolinite, illite and smectite (montmorillonite). High gypsum and pyrite contents are observed in the most altered areas. All of these elements match a high-temperature hydrothermal paragenesis developed in an epithermal context (Patrier et al., 2013).

Verati et al. (2016) also demonstrated that the development of this highly hydrothermalized area is controlled by the intersection of two major normal fault systems N090-N110 and N130-140 (Fig. 1f), which have approximately the same directions as those observed in the Bouillante geothermal field (Fig. 1c).

## 3. Material and methods

### 3.1. Samples

According to field observations, we distinguished three major classes of rock type: lava flows, coarse breccia and pyroclastics. Breccia gathers coarse and poorly sorted heterogeneous deposits like debris avalanches, debris flows and lahars. Coarse breccia is further called debris flows because this is the dominant brecciated rock type. Debris flows are composed of fine-grained matrices (from clay to fine pebbles) that support a significant content of cobbles and boulders. Pyroclastics group fine-grained indurated and homogeneous deposits containing ashes, pumices and scoria. The largest elements are decimeter-sized pumices. Lava and debris flows can also be separated into three groups according their degree of alteration. The aim is not to distinguish weathering and hydrothermal alterations, but to understand the general impacts of alteration on petrophysical properties. Weathering and hydrothermal alterations of samples are not separated, but a difference is made between fresh, slightly to moderately altered, and highly altered samples (Fig. 2). Fresh samples are the more numerous, because altered samples are restricted to very limited areas (see Table 2 for distribution of samples by lithotypes). Only fresh pyroclastics were sampled, because the altered states did not outcrop in the areas studied. Alteration was defined firstly according macroscopic observations and secondly using a selection of representative thin sections. To be comprehensive, each outcropping lithological class was sampled.

Fresh samples were collected in the Vieux-Habitants-Bouillante area and on Terre-de-Haut Island. Samples with slight to moderate weathering and/or hydrothermal alteration were collected in the Basal Complex, the Northern Chain, the Bouillante Chain and Terre-de-Haut Island. Finally, the highly hydrothermalized samples were collected in Mamelles massif and in the exhumed geothermal system of Terre-de-Haut (Fig. 1d, e and f).

Samples were taken directly from outcrops as oriented blocks and parallelepipeds were cut to measure magnetic susceptibility, P-wave velocity, thermal conductivity and diffusivity. For lava, the size of parallelepipeds is consistent with the spacing of cooling joints. For pyroclastics and debris flows, the sample limits are not constrained by fractures or cooling joints and cutting the cubes is easier. The size of blocks is comprised between 4 and 10 cm in thickness and approximately 10 cm both for length and width. 25 mm diameter plugs were drilled to measure porosity, permeability and density (see Section 4.2.2 for representativeness). For coarse debris flows, physical measurements on plugs were limited to matrix notably because the size of cobbles and boulders exceeds the capacity of the measuring instruments.

The surfaces of friable blocks were flattened, and porosity measurements were carried out on pieces of rock of similar plug sizes. Before performing measurements, each sample was dried in an oven until a constant weight was reached. The drying temperature was set at 60 °C to avoid any change in mineralogy.

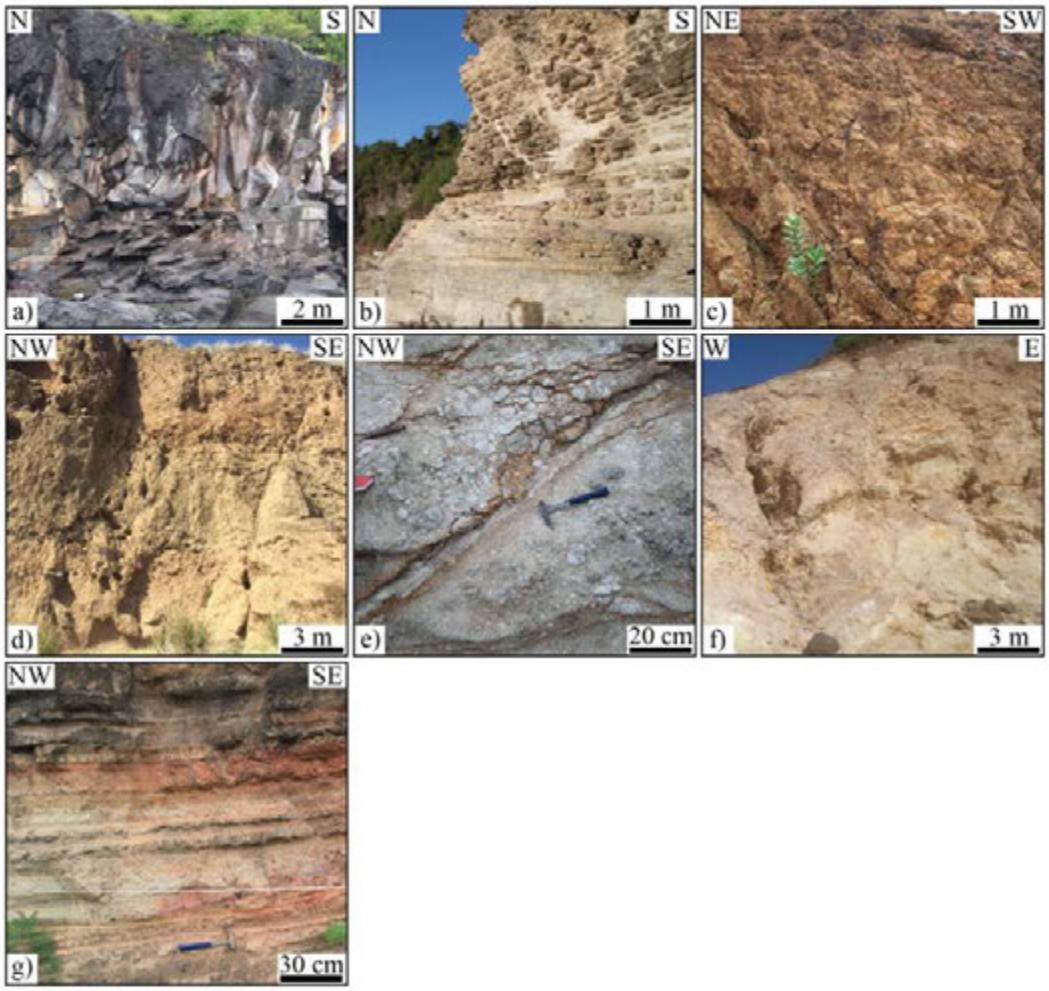


**Fig. 2.** The seven lithotypes analyzed. Lava flows are on the first line: a) fresh lava flow from Les Trois Tortues (location Fig. 1e); b) moderately hydrothermalized lava flow from Anse Tillet (Fig. 1d); c) highly hydrothermalized lava flow in La Savane (Fig. 1f). Coarse volcano sedimentary deposits are represented on the second line: d) coarse debris flow from the Val de l'Orge bay (Fig. 1e); e) moderately hydrothermalized debris flow from the Amandiers beach (Fig. 1d); f) highly hydrothermalized debris flow from Grande Anse Bay (Fig. 1f). g) Pyroclastics from Les Trois Tortues.

### 3.2. Petrography study

Thin sections were produced for a selection of representative samples to study petrography of the different lithological classes. Several studies were performed on all thin sections to specify the separation of each sample in a distinct alteration intensity class. This classification relies on macroscopic features (change of structure, color) and microscopic features (intensity of mineral replacement, type of neo-formed minerals). It revealed that macroscopic observations were sufficient to classify each sample in an altered class. Primary minerals from fresh samples were determined under an optical microscope. According to Bernard (1999), Clauser and Huenges (1995), Mielke et al. (2017), mineral composition has a significant impact on petrophysical properties. Unfortunately, no phase counting done on minerals was linked to petrophysical properties, because only phenocrysts can be counted. Microliths from the groundmass are too small to be determined accurately. Minerals and phases formed during alteration processes are small (cf. Fig. 5c and f) and are characterized by standard X-ray techniques, on a powder with a particle size of 70–80 μm. X-ray diffraction was carried out using a Bruker D2 phaser, with Cu K-alpha radiation. The major mineral element compositions were determined in thin sections using a CAMECA SX-100 instrument equipped with five wavelength-dispersive X-ray spectrometers (WDS). The analyses were done with 20 kV accelerating voltage, a focused beam of 10 nA and counting times of 20–30 s. Finally, magnetic minerals were investigated through reflected light and magnetic susceptibility variation with temperature (detailed in Section 3.2.2). The objective of the magnetic mineral determination is to understand whether the negative anomaly of magnetic susceptibility observed by Gailler et al. (2014) in the Bouillante geothermal province could be linked to variation in mineral content of the hydrothermally altered samples.

#### 3.2.1. Chemical analyses

Geochemical analyses were only carried out on lava flows, to compare our results to previous studies and to identify the chemical

diversity of lava flows (Ricci et al., 2015a, 2015b, 2017; Samper et al., 2007; Zami et al., 2014). Whole-rock major and trace element analyses were performed at the Service d'Analyze des Roches et des Minéraux (SARM, CNRS, Nancy, France). Major element contents were determined by ICP-AES (Thermo Fischer ICap 6500) and trace element concentrations by ICP-MS (Thermo Elemental X7). Only major elements, and especially total alkali and silica, are exploited in this article.

#### 3.2.2. Magnetic susceptibility

Three parameters were measured: the magnetic susceptibility; the magnetic fabric; the determination of magnetic minerals. The first consists of measuring the total magnetic susceptibility directly on outcrops (Morgan et al., 2017) or on parallelepiped samples in the laboratory with a GF SM-20 Instruments model handheld magnetic susceptibility meter. The SM-20 has a $10^{-6}$ SI (International system of units) sensitivity in the range of 0–999 · $10^{-3}$ SI. This is well below the values observed in the areas studied. The second parameter consists in measuring the anisotropy of magnetic susceptibility (AMS) on oriented cores (2.1 cm height and 2.5 cm diameter) with an MFK1-A Kappabridge (AGICO) in a constant field of 200 $A \cdot m^{-1}$ at the operating frequency of 976 Hz, using the 3-D rotator (Hrouda et al., 2015). AMS is also a reliable method to assess the magnetic fabric computing anisotropy degree of rocks (Jelinek, 1981). The last criterion is measured using the evolution of magnetic susceptibility with temperature. This is an efficient method to identify magnetic minerals carrying the AMS (Panaiotu et al., 2011). The apparatus used is approximately the same as AMS with an MFK1-A Kappabridge, constant magnetizing field and operating frequency. However, the device is coupled to a CS-L Cryostat and CS-4 Furnace, which allows the study of bulk magnetic susceptibility for temperatures of between −194 °C and 700 °C. Variation of this parameter with temperature was measured on samples reduced to a thin powder. Measurements are performed under argon at three temperature intervals: between −194 °C and 20 °C using liquid nitrogen, between 20 °C and 700 °C (heating curve), and finally between 700 °C and 20 °C (cooling curve). The determination of magnetic transitions during heating/cooling cycles like the Curie temperature, the Vervey transition for magnetite and the Morin transition for hematite are indicators to identify magnetic minerals (Butler, 1998; Chadima, 2011). In this study, susceptibility vs. temperature curves are measured on lava flows with a different alteration degree to identify the impact of hydrothermal alteration on magnetic minerals.

### 3.3. Thermal and physical measurements

#### 3.3.1. Porosity and density

Quantifying porosity is fundamental to estimate the volume available for fluid flow and storage. Only connected porosity was quantified. Three complementary methods using different saturation fluids have been selected to handle every sample.

The triple weighing method is defined by the RILEM norm (try n°I.1, 1978). This is a reliable low-cost method, which allows 50 samples to be handled with volumes of between 10 and 50 $cm^3$ each time. It is non-destructive for cohesive samples without increasing argilaceous alteration. After a 48 h immersion, the saturated and hydrostatic masses were measured to calculate effective porosity, sample volume and bulk density. As some volcanic materials are insufficiently cohesive or contain clays, saturation with water causes their destruction. Thus, fragile samples were not processed by this method.

Grain density depends on mineralogy and unconnected porosity since samples were not reduced into a thin powder, which could remove every isolated pore. This was measured using a Micromeritics® model AccuPyc II 1340 gas pycnometer which allows sample volumes of between 10 and 50 $cm^3$ to be handled (Aretz et al., 2015). It also allows the calculation of effective porosity using bulk density from triple weighing.

Measurements of connected porosity using water or helium are easy to perform and are non-destructive methods. However, they do not provide any information about pore throat diameter. Mercury porosimetry was used to assess this parameter avoiding any of the former problems encountered with argilaceous rocks (Sizun, 1995; Washburn, 1921). Measurements have been performed with a Micromeritics® model AutoPore IV 9500 v1.09. This model investigates pore throat diameters from 360 μm to 5.7 nm. Moreover, it provides a great deal of information such as the pore size distribution, the total pore volume, the grain and bulk density (Belghoul, 2007; Giesche, 2006). Bulk densities of low cohesive samples were determined using this method.

#### 3.3.2. Matrix permeability

Intrinsic permeability $K$ measurements were performed with a nitrogen permeameter under low confining pressure (20 bars). This covers a wide range of permeability ($10^{-11}$ $m^2$ to $10^{-19}$ $m^2$). The Klinkenberg effect was not taken into account to remove the slip-flow phenomenon between gas molecules and solid walls (Klinkenberg, 1941). Indeed, permeability measurements did not exhibit such an effect. Permeability measurements were performed on 25 mm diameter plugs for sufficiently cohesive lithotypes. For other samples, parallelepipeds were cut and included in fast-setting epoxy resin to form 40 mm diameter plugs. Some pyroclastics like ashes and highly hydrothermalized rocks were not cohesive enough to be measured.

The number of measurements per sample is variable because some lavas were measured both parallel and perpendicular to the lava flow. In most cases, only one plug was measured for each sample because the measurement took approximately 2 h. The size of plugs and the number of measurements per sample is limited by the permeameter design that allows accurate measurements but cannot be repeated for several plugs per sample taking into account our large sample set. Therefore, plugs were chosen that were the best representative of the sample.

#### 3.3.3. Thermal conductivity

Thermal conductivity λ and diffusivity $D$ were measured using a Thermal Conductivity Scanner from Lippmann & Rauen GbR. The technique is based on the change in surface temperature after a known and set heat input and could be applied to a wide range of geological materials (Boulanouar et al., 2013; Rosener, 2007; Stanek, 2013; Surma and Geraud, 2003). The measuring instrument includes a mobile plate composed of three thermal sensors and a heat source. The device has an accuracy of 3% in the measuring range from 0.2 to 25 $W \cdot m^{-1} \cdot K^{-1}$. The procedure is described in detail by Popov et al. (2016, 1999). Temperature measurement is every 1 mm step.

For thermal diffusivity, the two standards have different thermal conductivity and diffusivity values. Therefore, temperature is additionally measured after heating, with a third temperature sensor. Temperature measurement occurs every 2 mm step. The combination of bulk density, thermal conductivity and diffusivity allows the calculation of specific heat capacity $c_p$.

λ and $D$ were measured in the three directions of blocks and then averaged to take into account possible anisotropy of rocks linked to specific mineral orientation, porosity and structure of the pore space.

#### 3.3.4. P-wave velocity

The measurement of compressional wave velocity (P-wave) was performed on dry samples using the ultrasonic velocity method with the Proceeq® brand PunditLab model (Bertrand, 2017; Bossennec et al., 2018; Haffen, 2012). This is a non-destructive test based on the transmission of an acoustic pulse. The instrument is composed of two 54 kHz piezoelectric P transducers (a transmitter and a receiver) and a pulse generator. The acoustic emission that reaches the receiver is converted into an electrical signal acquired with a computer-controlled oscilloscope. The operating frequency was constant at 54 kHz and a shear gel was applied to ensure a better connection. Compressional wave

velocity was measured in the three directions of blocks and then averaged. Shear waves were not studied, because of the difficulty to pick the first S-wave that arrives in low cohesive samples.

## 4. Results

### 4.1. Petrology and geochemistry

A large amount of geochemical data is available both for Terre-de-Haut and Basse-Terre (e.g. Gadalia, 2013; Jacques et al., 1984; Jacques and Maury, 1988b; Samper et al., 2007, 2009). Samples of this study are complementary in location to those of previous works, since Samper et al. (2009, 2007) concentrated mostly on volcanic edifices and not on the coast.

Major elements were measured for 33 samples, including 22 fresh lava flows and 11 slightly altered lava flows. Although the $SiO_2$ content varies between 55 and 65%, most samples are andesites and basaltic andesites from the Axial Chain. Only a few dacite samples from Terre-de-Haut and the Basal Complex are observed (Fig. 3a). According to Peccerillo and Taylor (1976), most samples belong to the calk-alcaline series, with 8 samples located between Beaugendre and Grande Rivière de Vieux-Habitants valleys belonging to low differentiated lavas (in the tholeitic domain). Basse-Terre and Terre-de-Haut lavas belong to the medium and low K types ($K_2O$: 0.55–1.56 wt%, Fig. 3b). Our geochemical data are consistent with previous studies that confirm the representative nature of the set of samples studied.

#### 4.1.1. Macroscopic and thin section observations

All fresh lavas have porphyric textures and color from light to dark grey (Fig. 4). No specific mineral orientation was observed. Using thin section counting with JMicroVision software (Roduit, 2007), phenocrysts represent 31% (20.7% to 43.2% on 7600 points of 30 thin sections) of fresh lavas and are mostly composed of plagioclase (≈80%) and to a lesser extent clinopyroxene and orthopyroxene (≈15%) and iron oxides (magnetite and hematite, ≈5%). This distribution is in agreement with parageneses found in previous studies (Boudon et al., 2008; Samper et al., 2007). The matrix is always composed of microlites of the same minerals and no glass is observed (Fig. 5a). The porosity is mostly composed of different shaped vesicles and micro-cracks crossing the matrix and phenocrysts. The structure and texture of fresh lavas is preserved in slightly to moderately altered lavas. These are of various colors: greenish, white, medium grey and red (Fig. 4). They are composed on average of 20% of phenocrysts (4.4% to 36% on 4000 points on 16 thin sections). The alteration began to dissolve the borders and the central part of pyroxene minerals but does not affect plagioclases. Chlorite, actinolite and pyrite appeared during this alteration phase (Fig. 5b). Neoformed minerals represent 30% of the minerals present in phenocrysts. The porosity is composed of pores formed during dissolution in pyroxenes, initial cooling joints, small pores in the matrix, micro-cracks crossing both phenocrysts and matrix and very rare vesicles. Hydrothermally altered lavas exhibit homogeneous light grey to white colors (Fig. 4). Hydrothermal alteration changed significantly the macroscopic aspect of lava. It produced a total replacement of microlites, pyroxenes and plagioclases phenocrysts by quartz, white micas, pyrite and calcite (Fig. 5c), reducing phenocryst content to only 6% (2000 points on 8 thin sections).

Fresh debris flows and pyroclastics consist of the same minerals as fresh lavas, but their rock colors are much more heterogeneous because debris flows are composed of conglomerates of clasts (lavas, pyroclasts) and fine-grained matrices. Ash deposits have well-marked bedding caused by the homogeneous size of deposits. Pyroclastics are often poorly cohesive because there is no matrix to link elements together (Fig. 4). Their cohesion depends on the degree of welding. The porosity of debris flow is extremely different to that of lavas. Indeed, the genesis of coarse deposits does not produce cooling structures or vesicles. However, the arrangement of particles creates pores of sizes depending on the particle size (Fig. 5d). This porosity is added to the initial porosity of cobbles and boulders encompassing debris flows. Slightly to moderately altered debris flows that are mostly sampled in the Basal Complex are greenish to purplish (Fig. 4). These debris flows are composed of the same minerals observed in slightly to moderately altered lavas. There is a clear decrease of inter-particular porosity compensated by partial dissolution of phenocrysts (Fig. 5e). Highly hydrothermalized debris flows are mainly sampled on Terre-de-Haut. Overall, such debris flows are white to yellow in color and contain large amounts of illite, chlorite, smectite in the matrix and gypsum, pyrite and calcite in fractures and

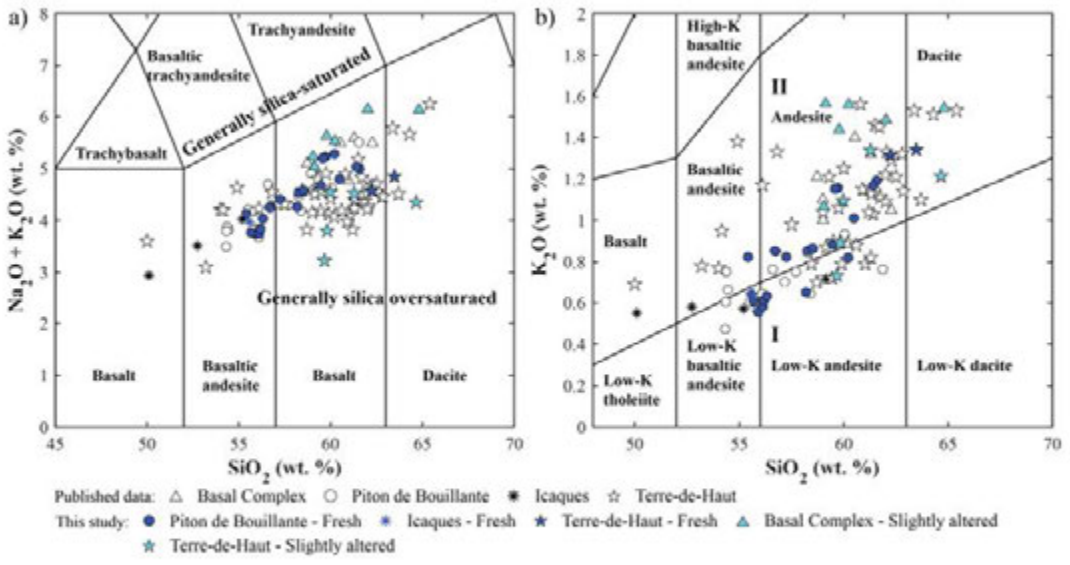


**Fig. 3.** Geochemical characterization of lava flows. a) Total alkali vs. silica diagram after Bas et al. (1986); b) $SiO_2$ vs. $K_2O$ plot after Peccerillo and Taylor (1976). I – calc-alkaline series; II – high-K calc-alkaline-series. Published geochemical data: Basal Complex, Pitons de Bouillante and Icaques (Ricci et al., 2017); Terre-de-Haut (Jacques et al., 1984; Zami et al., 2014).

| Classification | Location | Minerals / *Porosity* | Samples |
|---|---|---|---|
| Fresh lavas | Axial Chain<br>Bouillante Chain<br>Terre-de-Haut | **Plagioclases ++++**<br>**Pyroxenes ++**<br>**Iron oxides +**<br>*Initial vesicles*<br>*Cooling joints*<br>*Micro-cracks*<br>*Fractures* | |
| Slightly to moderatelely altered lavas | Basal Complex<br>Bouillante Chain<br>Terre-de-Haut | **Plagioclases ++++**<br>**Pyroxenes +**<br>**Iron oxides +**<br>**Chlorite, Micas +**<br>*Dissolution*<br>*Cooling joints*<br>*Cracks*<br>*Fractures* | |
| Highly hydrothermalized lavas | Northern Chain<br>Terre-de-Haut | **Plagioclases ++**<br>**Calcite, Pyrite ++**<br>**Clay Minerals ++**<br>**Micas, Chlorite +**<br>*Dissolution*<br>*Cooling joints*<br>*Cracks*<br>*Fractures* | |
| Fresh debris flows | Axial Chain<br>Bouillante Chain<br>Terre-de-Haut | **Plagioclases ++++**<br>**Pyroxenes ++**<br>**Iron oxides +**<br>**Plant residues +**<br>*Interparticular*<br>*Intraparticular*<br>*Micro-cracks*<br>*Fractures* | |
| Slightly to moderately altered debris flows | Basal Complex<br>Terre-de-Haut | **Plagioclases +++**<br>**Pyroxenes +**<br>**Iron oxides +**<br>**Chlorite, Quartz +**<br>**Pyrophyllite**<br>*Dissolution*<br>*Cracks*<br>*Fractures* | |
| Highly hydrothermalized debris flows | Axial Chain<br>Bouillante Chain<br>Terre-de-Haut | **Plagioclases ++**<br>**Pyroxenes +**<br>**Qz, Gp, Calcite ++**<br>**Chlorite, Epidote +**<br>**White micas +**<br>*Dissolution*<br>*Cracks*<br>*Fractures* | 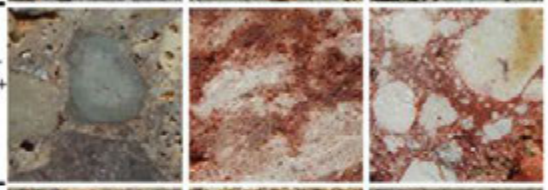 |
| Fresh pyroclastics | Bouillante Chain<br>Grande-Decouverte volcano | **Plagioclases ++++**<br>**Pyroxenes ++**<br>**Iron oxides +**<br>*Interparticular*<br>*Intraparticular*<br>*Cracks*<br>*Vesicles* | |

**Fig. 4.** Short description of the seven lithological classes with macroscopic pictures of the different rocks in each class. Each picture is 3.5 cm in size. Qz – quartz; Gp – Gypsum.

bedding planes (Fig. 5f). Patchy alterations are common due to the higher porosity of pyroclast cobbles relative to debris flow matrix. These rocks are composed of 5% of plagioclases (80–90% transformed) and 95% of neoformed minerals. The well-known hydrothermal breccia from the Bouillante bay that permitted the first Ar-Ar dating of the Bouillante field (Patrier et al., 2013; Verati et al., 2013) was classified in this lithotype. It is an entirely re-crystallized and silicified multicolored rock (Fig. 4, first row, line 6). Pores are essentially composed of cracks and dissolution voids, which result in the disappearance of initial phenocrysts and particles.

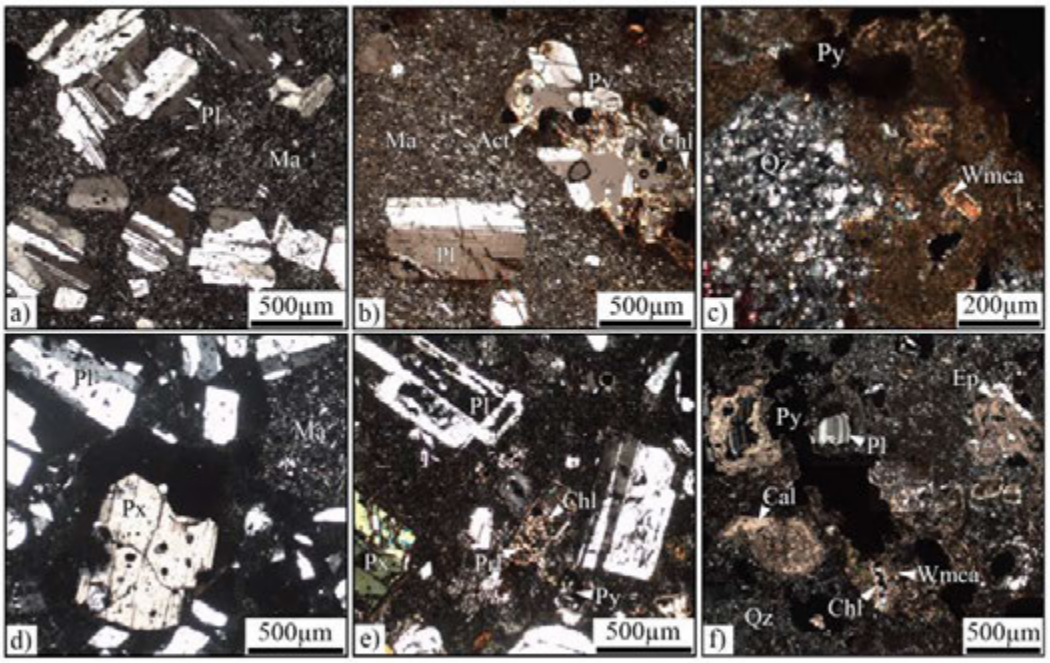


**Fig. 5.** Thin section photomicrographs of lava and debris flows (cross polarized light). Lava flows are on the top line: a) fresh lava flow from Les Trois Tortues; b) moderately hydrothermalized lava flow from Anse Tillet; c) highly hydrothermalized lava flow in La Savane. Coarse volcano sedimentary deposits are represented on the line below with: d) coarse debris flow from the Val de l'Orge bay; e) moderately hydrothermalized debris flow from the Amandiers beach and f) highly hydrothermalized debris flow from Grande Anse Bay. Abbreviations: Act - actinolite, Cal - calcite, Chl - chlorite, Ep - epidote, Ma - microlithic matrix, Pl - plagioclase, Pyl - pyrophyllite, Px - pyroxene, Py - pyrite, Qz - quartz, Wmca - white mica.

*4.1.2. Magnetic susceptibility data*

Measurement of magnetic susceptibility was performed using three methods. The quickest and easiest consisted in measuring susceptibility directly on outcrops or on rock blocks with sufficiently flat surfaces. It permitted susceptibility values to be obtained for every sample in contrast to the AMS method, which needs samples strong enough to be plugged. Median values of total magnetic susceptibility are $11.6 \cdot 10^{-3}$ and $7.5 \cdot 10^{-3}$ SI respectively for fresh lavas and debris flows which is slightly higher than pyroclastics $6.6 \cdot 10^{-3}$ SI (Table 1). This intensity of magnetic signal cannot only be explained by the presence of paramagnetic pyroxenes and it indicates relatively high amounts of magnetic minerals (Hrouda et al., 2015). Total magnetic susceptibility of slightly to moderately altered lavas and debris flows has higher median values than fresh samples ($12 \cdot 10^{-3}$ and $17.2 \cdot 10^{-3}$ SI respectively). The first phase of alteration that transforms initial minerals (pyroxenes and plagioclases) and concentrates iron oxides leads to a slight increase of magnetic susceptibility. Finally, samples affected by advancing hydrothermal alteration have the same median value of $0.1 \cdot 10^{-3}$ SI. The total transformation of initial minerals by hydrothermal alteration also removes magnetic minerals. These results are in agreement with those obtained by Gailler et al. (2014). The trends are similar for lavas and debris flows. Results obtained with AMS are approximately the same for lavas but display a lower signal for debris flows. This may be due to a reduced number of samples. However, the general behavior with advancing alterations remains the same. The slight increase of magnetic susceptibility with moderate alteration and the reduction of magnetization with advancing hydrothermal alterations are also obvious. High temperature hydrothermal alteration removes magnetic minerals. AMS highlights the fact that magnetic fabrics of lavas are weakly anisotropic (a corrected degree of anisotropy lies between 1.002 and 1.054). This anisotropy is logically oriented in the direction of lava flow determined in the field using closely spaced cooling joints, which

**Table 1**
Summary of magnetic susceptibility measurements on outcrops and blocks with handheld susceptibility meter and using AMS.

| | Total susceptibility [$\times 10^{-3}$ SI] | Lava flow | | | Debris flow | | | Pyroclastics |
|---|---|---|---|---|---|---|---|---|
| | | Fresh | Slightly to moderately altered | Highly altered | Fresh | Slightly to moderately altered | Highly altered | Fresh |
| Field susceptibility meter | Average | 13.92 | 13.34 | 5.99 | 9.36 | 13.19 | 0.94 | 8.84 |
| | **Median** | **11.60** | **11.97** | **0.09** | **7.54** | **17.17** | **0.14** | **6.60** |
| | Min–max | 2.06–26.8 | 3.58–27.62 | −0.04–21.47 | 3.89–24.9 | 3.96–18.37 | −0.17–5.04 | 4.88–19.33 |
| | n | 41 | 23 | 7 | 20 | 7 | 7 | 14 |
| AMS | Average | 15.68 | 12.86 | 0.02 | 5.84 | 5.38 | 1.57 | 15.55 |
| | **Median** | **12.05** | **13.36** | **0.02** | **4.65** | **5.38** | **0.29** | **15.59** |
| | Min–max | 3.54–32.7 | 0.57–20.91 | 0.02–0.02 | 4.19–9.34 | 5.37–5.4 | 0.24–4.17 | 11.15–21.13 |
| | n | 157 | 28 | 1 | 5 | 2 | 3 | 9 |

are parallel to each other and to the lava flow margins (Mathieu, 2010). This preferential mineral orientation in lavas was not observed during thin section observations.

Thermomagnetic curves obtained on a selected set of lavas with different degrees of alteration (Fig. 6) provide information about the nature of minerals that supply a magnetic signal. The most striking feature is the difference between heating and cooling curves. For fresh and slightly to moderately altered samples, the heating curve runs much higher than the cooling curve. The opposite relationship exists for highly hydrothermalized samples from the central part of Terre-de-Haut Island. This major difference between heating and cooling curves indicates that the assembly of magnetic minerals is unstable. Furthermore, it could be caused by post-magmatic alterations occurring during magma cooling (Hrouda et al., 2015). Fresh lava samples show

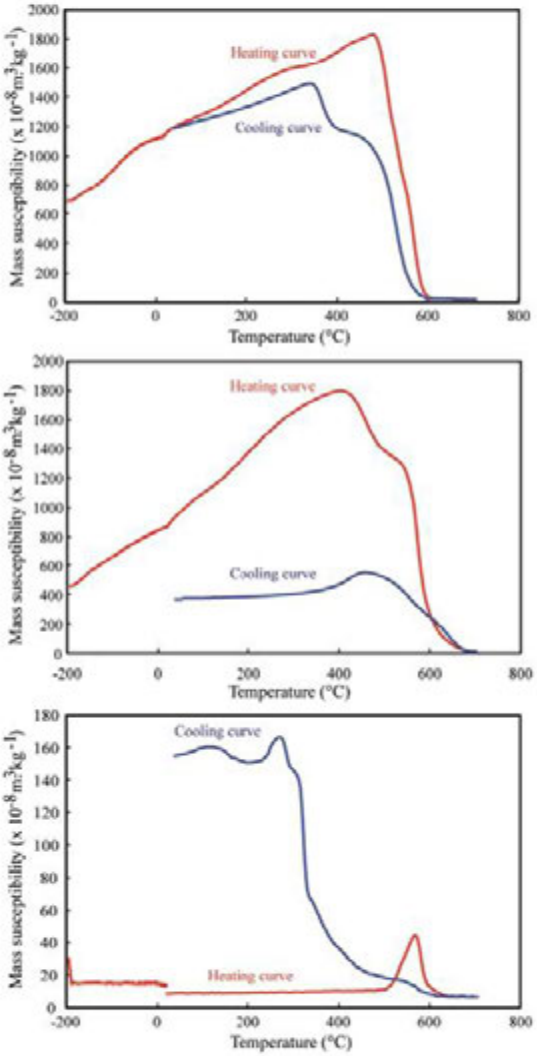


**Fig. 6.** Evolution of magnetic susceptibility to temperature for lavas undergoing 3 alteration stages. From top to bottom, fresh andesite lava flow from Duché (Vieux-Habitants area), moderately hydrothermalized andesite lava flow from Pointe Rifflet (Basal Complex) and highly hydrothermalized lava flow from Grande Anse Bay (Terre-de-Haut).

a constant substantial decrease of mass susceptibility between 480 and 600 °C, which may indicate the presence of titanomagnetite and magnetite. The heating curve of the moderately altered sample exhibits two susceptibility decreases. The first one is a medium decrease between 400 and 540 °C and the second one is a major drop between 540 and 600 °C, certainly due to the presence of maghemite and titanomagnetite. A coupled analysis using reflected light microscopy and XRD confirmed these results. It also highlights a progressive transformation of magnetite into maghemite along micro-cracks in moderately altered lavas. Highly hydrothermalized lavas have a mass susceptibility two orders of magnitude lower than fresh lavas. The susceptibility between −194 and 700 °C is almost unchanged, except for one peak at 560 °C. Thin section analysis shows the absence of magnetite and maghemite in these rocks, which explains the large decrease in the magnetic signal. Iron oxides are totally replaced by pyrite and hematite during hydrothermal alteration.

### 4.2. Thermal and physical properties

Table 2 summarizes median values and ranges for all properties measured.

#### 4.2.1. Porosity and pore throat diameter

The measurement of porosity using mercury as the saturation fluid was carried out on 99 samples. Fig. 7 displays the results for a selection of representative samples from the seven lithological classes. We represented common mercury injection curves with bar charts to simplify the interpretation. An empirical lower limit of 40% of the maximal mercury intrusion was established to remove every pore throat diameter below this limit. The diameter corresponding to the maximal intrusion was defined as the percolation threshold (Fig. 7, diamonds). The narrower the bars are, the more homogeneous the pore network is. Fresh lava flows can be divided into two groups. The first one corresponds to low porosity samples without vesicles ($\Phi < 5\%$), pore throat diameters below 0.5 μm and percolation thresholds generally of <0.05 μm. Porosity is essentially derived from micropores in the microlithic matrix and microcracks crossing the matrix and phenocrysts. The second group is comprised of lavas with vesicles of different shapes and porosities higher than 5%. Their pore network is more homogeneous than those of the first group and is often limited to a small injection interval with percolation thresholds higher than 1 μm. Some samples with millimeter size vesicles have a minor part of porosity that cannot be detected because pore throat diameters are above the detection bounds. Porosity is essentially composed of well-opened vuggy pores, or tight, elongated vesicles, oriented in the direction of magma flow. Slightly to moderately altered lavas have a wide porosity range (1.4–27.6%) with pore throat diameters below 0.01 μm. The pore network of planar bedding samples from the Basal Complex (GD15.01 and GD15.42) has a very limited pore throat diameter range. Highly hydrothermalized lavas from Terre-de-Haut have porosities higher than 15% and there is no pore throat diameter larger than 5 μm. Weathering and hydrothermal alterations increase the homogeneity of the pore network and reduce the variability of throat diameters in lavas.

Fresh debris flows and pyroclastics have high porosity values. These range between 15% for coarse volcanic breccia to more than 60% for some pumice deposits. The injection of mercury concerns a wider range of pore throat diameters than in the case of fresh lavas, even if the major part of porosity has thresholds below 50 μm. Two individual pore networks may explain this heterogeneity: intra-clast pores with thresholds below 0.05 μm, and intergranular porosity with pore throats of between 0.05 and 50 μm. For the majority of samples, percolation thresholds are close to 5 μm. Slightly to moderately altered and hydrothermalized debris flows have similar porosity values, but the injection of mercury is more continuous below 5 μm. Moreover, percolation thresholds tend to decrease progressively with advancing

**Table 2**
Statistical overview of measured thermo-physical properties. $\rho_b$: bulk density, $\rho_s$: grain density, $\Phi_{Hg}$: mercury porosity, $\Phi_w$: water porosity, $\Phi_{He}$: helium porosity, K: permeability (measurement limits $10^{-19}$–$10^{-11}$ $m^2$), $V_P$: P-wave velocity, λ: thermal conductivity, D: thermal diffusivity, $c_p$: specific heat capacity. n: number of measurements.

| Lithological class | Alteration | | $\rho_b$ [g·cm$^{-3}$] | $\rho_s$ [g·cm$^{-3}$] | $\Phi_{Hg}$ [%] | $\Phi_W$ [%] | $\Phi_{He}$ [%] | K [m$^2$] | $V_P$ [m·s$^{-1}$] | λ [W·m$^{-1}$·K$^{-1}$] | D [×10$^{-6}$ m$^2$·s$^{-1}$] | $C_P$ [kJ·kg$^{-1}$·K$^{-1}$] |
|---|---|---|---|---|---|---|---|---|---|---|---|---|
| Andesite lava | Fresh | **Median** | **2.64** | **2.75** | **4.00** | **3.59** | **3.85** | **6E−18** | **4589** | **1.68** | **0.88** | **0.75** |
| | *28 blocks* | Average | 2.61 | 2.75 | 6.61 | 4.98 | 5.32 | 2E−14 | 4627 | 1.62 | 0.84 | 0.76 |
| | | Min–max | 2.17–2.77 | 2.61–2.85 | 1.1–22.8 | 0.03–19.7 | 1.4–23.9 | 1E−19–8E−13 | 2876–6233 | 0.76–1.98 | 0.5–0.97 | 0.7–0.82 |
| | | n | 210 | 80 | 31 | 209 | 55 | 46 | 34 | 50 | 25 | 28 |
| | Slightly to moderately altered | **Median** | **2.49** | **2.62** | **5.91** | **4.07** | **4.63** | **4E−15** | **4490** | **1.65** | **0.75** | **0.89** |
| | *16 blocks* | Average | 2.42 | 2.61 | 11.03 | 7.89 | 10.72 | 8E−15 | 3947 | 1.52 | 0.72 | 0.89 |
| | | Min–max | 1.6–2.64 | 2.5–2.74 | 1.4–27.6 | 0.04–32.2 | 1.2–35.9 | 1E−19–1E−13 | 1412–5362 | 0.78–1.88 | 0.46–0.92 | 0.78–1.06 |
| | | n | 33 | 26 | 15 | 32 | 19 | 17 | 16 | 25 | 14 | 16 |
| | Highly altered | **Median** | **2.00** | **2.73** | **20.44** | **22.88** | **25.84** | **2E−14** | **1837** | **1.66** | **0.92** | **0.97** |
| | *6 blocks* | Average | 2.05 | 2.71 | 19.16 | 22.63 | 25.99 | 1E−13 | 1668 | 1.71 | 0.97 | 0.92 |
| | | Min–max | 1.97–2.25 | 2.61–2.8 | 14.2–21.5 | 18.6–26.1 | 24.7–27.6 | 1E−17–5E−13 | 500–2660 | 1.38–2.08 | 0.66–1.4 | 0.69–1.06 |
| | | n | 6 | 7 | 4 | 5 | 4 | 4 | 5 | 9 | 6 | 6 |
| Debris flow | Fresh | **Median** | **1.63** | **2.60** | **32.56** | **34.18** | **37.52** | **4E−14** | **2059** | **0.67** | **0.47** | **0.88** |
| | *22 blocks* | Average | 1.74 | 2.58 | 32.67 | 32.34 | 35.67 | 5E−13 | 2020 | 0.73 | 0.48 | 0.89 |
| | | Min–max | 1.33–2.29 | 2.3–2.8 | 15.4–46.5 | 15.9–44.8 | 15.9–45.6 | 1E−16–7E−12 | 635–3330 | 0.43–1.36 | 0.28–0.86 | 0.6–1.19 |
| | | n | 25 | 44 | 21 | 25 | 22 | 16 | 23 | 33 | 20 | 22 |
| | Slightly to moderately altered | **Median** | **1.97** | **2.62** | **23.55** | **25.37** | **28.25** | **1E−15** | **2379** | **1.02** | **0.59** | **0.90** |
| | *6 blocks* | Average | 1.99 | 2.61 | 23.90 | 24.18 | 26.38 | 6E−15 | 2200 | 1.07 | 0.62 | 0.87 |
| | | Min–max | 1.84–2.14 | 2.52–2.67 | 17.9–28.7 | 19.1–29.1 | 19.6–29.4 | 2E−16–3E−14 | 1370–2695 | 0.92–1.3 | 0.56–0.79 | 0.72–0.93 |
| | | n | 7 | 10 | 6 | 6 | 5 | 5 | 9 | 12 | 6 | 6 |
| | Highly altered | **Median** | **1.50** | **2.62** | **30.44** | **41.47** | **36.26** | **5E−16** | **1636** | **0.85** | **0.44** | **0.97** |
| | *8 blocks* | Average | 1.65 | 2.59 | 33.71 | 35.82 | 33.22 | 2E−13 | 1683 | 0.97 | 0.59 | 1.00 |
| | | Min–max | 1.21–2.3 | 2.36–2.7 | 15.4–52.4 | 11.9–50.6 | 12–48.4 | 7E−18–5E−13 | 790–3623 | 0.5–1.81 | 0.42–1.1 | 0.72–1.62 |
| | | n | 7 | 9 | 7 | 5 | 4 | 3 | 8 | 11 | 8 | 8 |
| Pyroclastics | Fresh | **Median** | **1.52** | **2.65** | **34.24** | **41.96** | **42.33** | **8E−13** | **1642** | **0.54** | **0.40** | **0.88** |
| | *15 blocks* | Average | 1.53 | 2.61 | 37.81 | 43.53 | 44.82 | 2E−12 | 1767 | 0.56 | 0.41 | 0.86 |
| | | Min–max | 0.62–2.42 | 2.21–2.79 | 20.2–63 | 21.6–74 | 21.6–76.1 | 2E−14–1E−11 | 500–3584 | 0.26–1.11 | 0.29–0.57 | 0.63–1.12 |
| | | n | 20 | 30 | 16 | 17 | 16 | 10 | 17 | 25 | 14 | 15 |

hydrothermal alteration. Values close to 0.05 μm are observed for the most transformed samples.

*4.2.2. Density vs. porosity*

Bulk and grain densities were measured on all lithotypes investigated (Fig. 8a). There is no clear trend between these two properties. Maximal median values of grain density are observed for fresh and highly hydrothermalized lava flows (2.75 and 2.73 g·cm$^{-3}$ respectively). Slightly to moderately altered lavas, debris flows and pyroclastics have similar grain densities comprised between 2.6 and 2.65 g·cm$^{-3}$. Grain densities exhibit a significant dispersion between 2.21 and 2.85 g·cm$^{-3}$ with only three samples below 2.4 g·cm$^{-3}$. It can be explained as a larger amount of porosity inaccessible to helium but accessible to water because their bulk densities are not abnormally low compared to other debris flows and pyroclastic samples. Grain densities of fresh lavas range between 2.61 and 2.85 g·cm$^{-3}$. Such a difference may be caused mostly by the $SiO_2$ content, which varies inversely to the grain density and secondarily to unconnected porosity. The partial transformation of minerals in slightly to moderately altered lavas decreases the grain density in comparison to fresh lavas. CaAl-pyroxenes ($\rho_s$ = 3.36 - Schön, 2015) are replaced by chlorite ($\rho_s$ = 2.8 - Schön, 2015) and pyrophyllite ($\rho_s$ = 2.65–2.9, *www.mindat.org*). The surprisingly high grain density of hydrothermalized lavas is due to the high pyrite content ($\rho_s$ = 5.011 - Schön, 2015), which compensates for the lower density of porous clay minerals. The major part of debris flows and pyroclastics have similar grain densities to lavas between 2.55 and 2.8 g·cm$^{-3}$. This result seems logical for fresh debris flows, since they are formed from the dismantling of unstable volcanic edifice slopes composed of pyroclastics and lavas. In contrast to lavas, the hydrothermally altered debris flows do not contain pyrite. They incorporate a large amount of low density gypsum $\rho_s$ = 2.305 (Schön, 2015), compensated by calcite, 2.71 (Schön, 2015), and quartz, 2.648 (Schön, 2015) which give grain densities similar to those of fresh debris flows.

Remarkably, bulk densities range from 0.62 to 2.77 g·cm$^{-3}$ for pumice deposits and fresh lava respectively. They mirror mercury porosity values (Fig. 8b). Overall, the majority of lavas follow the general trend on the contrary to the slight dispersion of debris flows and pyroclastics.

High porosity debris flows and pyroclastics generally have a lower grain density than lavas. Three presumptions could explain this general trend:

- Fresh debris flows and pyroclastics have a dense magnetic mineral content, which is slightly lower than that of fresh lavas. Indeed, porosities of debris flows and pyroclastics are significantly higher than those of fresh lavas. Thus, their mineral proportion including magnetic minerals like magnetite, $\rho_s$ = 5.2 (Schön, 2015), is lower. This is an assumption that is unlikely to be true because lava and debris flows have approximately the same magnetic susceptibility (Table 1);
- In contrast to entirely crystallized lavas, debris flows are composite rocks with crystallized clasts similar to lava flows embedded in a poorly organized matrix. According to Vallance and Iverson (2015), this clay-rich matrix may result from leaching in hydrothermal systems on volcanic edifice flanks. This removes mobile elements and decomposes framework silicates, in particular to form clay minerals. These latter could trap porosity between clay layers such that it is not accessible to helium and may be included in the grain density value;
- The last hypothesis remains the existence of a representative elementary volume for debris flows and pyroclastics. This problem is

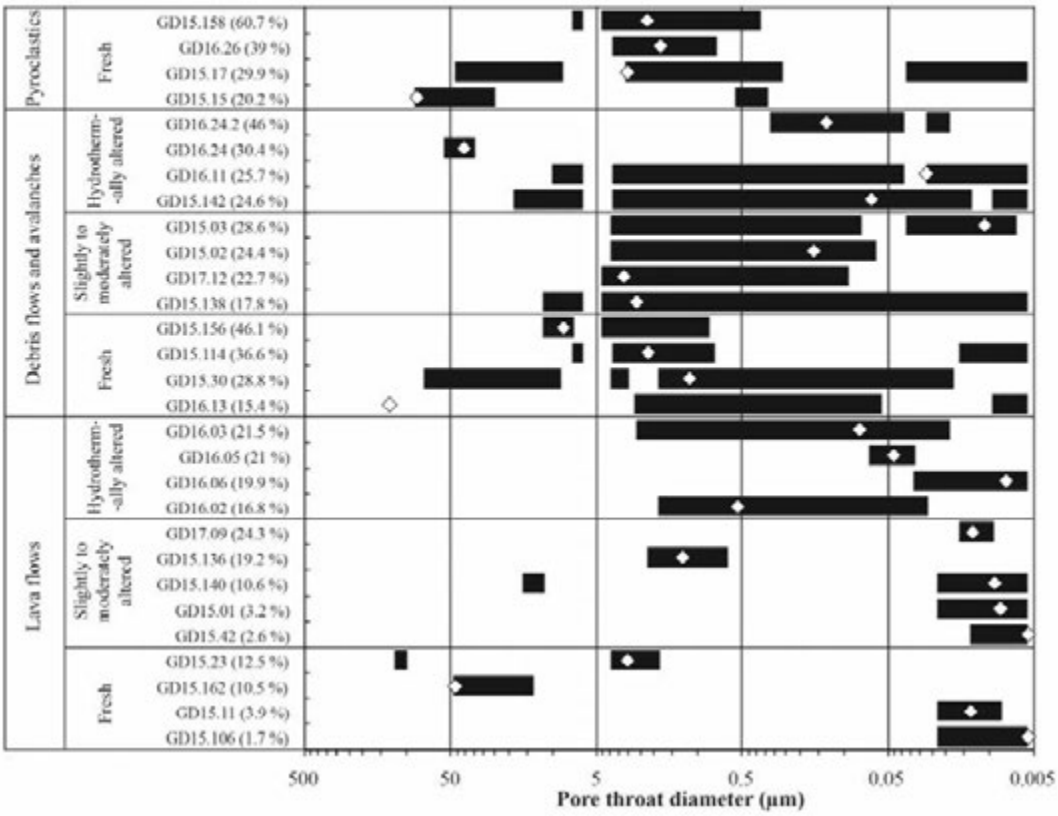


**Fig. 7.** Pore throat diameter of selected samples from the seven lithotypes investigated. Samples from all lithotypes are sorted by ascending porosity. Bars represent pore throat diameters corresponding to at least 40% of the maximal mercury injection. Diamond symbols represent the percolation threshold where the peak injection of mercury occurs.

rather inexistent in lavas since the whole rock has a general homogeneity even if fracture and vesicle content differ according to the lava flow profile. In contrast, a debris flow evolves a lot between its proximal part on the volcano flank and its distal end. It acquires a progressive inverse grading with thin elements at the base and coarse blocks at the top and loads progressively with exotic particles. Downstream sampling at the base of a debris flow shows a clay content that is not typical of the whole flow. Moreover, our sampling could not take into account clasts that are coarser than thin pebbles. Cobbles and boulders in debris avalanches and flows were not studied. These are often composed of andesites, with lower porosities and higher densities than the matrix of the debris flow. Therefore, the size of the debris flow samples used for physical laboratory measurements limits the representativeness of the study to the preponderant matrix part. From these results, if clasts were taken into account, we could infer that the total porosity of a debris flow might be slightly lower and the grain density slightly higher than our measurements. Taking into consideration this effect needs a medium-scale analysis which is not within the scope of this paper.

*4.2.3. Permeability vs. porosity*

Permeability measurements (Fig. 8c) exhibit 8 orders of magnitude difference between the lowest and the highest permeable samples. This difference is probably underestimated since a few samples are outside of the detection limits of the measurement apparatus ($10^{-19}$–$10^{-11}$ m$^2$). In agreement with porosity results, pyroclastics and debris flows are more permeable than lavas. Pyroclastics have a permeability higher than $10^{-14}$ m$^2$. The relationship between porosity and permeability is not clear and cannot be described by a simple equation. However, there is a logical increase of permeability with increasing porosity. Two conducts can be distinguished depending on the porosity value:

1 - Samples with porosities lower than 10% are only represented by lavas and show a steep increase in permeability (dashed line). Samples with the same porosity values may vary over 2 or 3 orders of magnitude of permeability. The pore network is controlled by cracks and a planar organization of elongated vesicles. Cracks efficiently improve the connectivity of initially poorly connected vesicles. The relationship between porosity and permeability has a fissure-type conduct. Fractal equations presented by Pape et al. (1999) were tested but none provided a good correlation coefficient;

2 - Samples with porosity higher than 10%, mostly represented by debris flows and pyroclastics have a gentle slope (dotted line). In contrast to lavas, matrix porosity is higher than crack and fracture porosity. The increase of permeability along with porosity is more restricted than in the first group. It is caused by the higher tortuosity of pore network connecting inter-and intra-particular porosities in pyoclastics and debris flow. This contrasts with the much straighter cracks and elongated vesicle networks seen in lavas.

*4.2.4. Thermal conductivity and P-wave velocity vs. porosity*

Fig. 8d shows an obvious decrease of thermal conductivity with increasing porosity. This relationship can be decomposed into one of

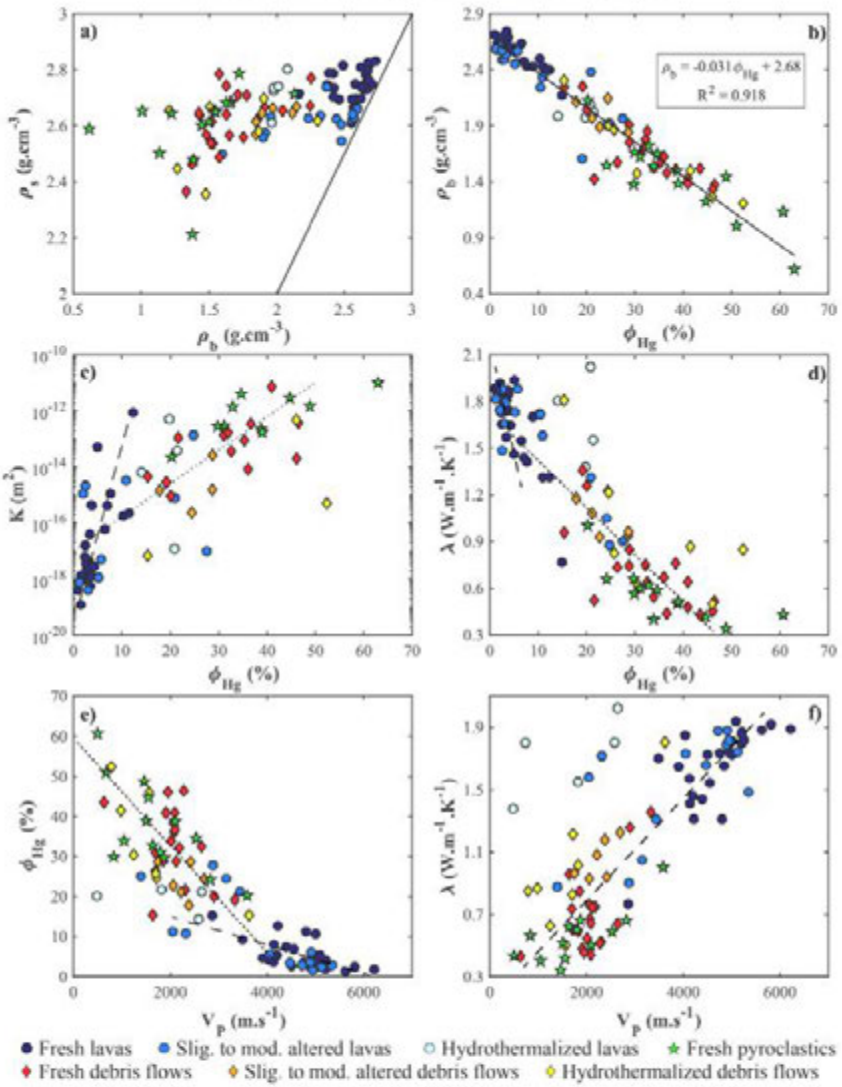


**Fig. 8.** Thermo-physical rock properties of all lithotypes investigated: a) grain density (gas pycnometer) versus bulk density (triple weighing); b) bulk density versus mercury porosity; c) nitrogen permeability versus mercury porosity; d) thermal conductivity in dry conditions versus mercury porosity; e) Mercury porosity versus compressional wave velocity in dry conditions; f) thermal conductivity versus compressional wave velocity in dry conditions. Average values ($\rho_s$, $V_P$, λ) for each sample. Slig. to mod.: slightly to moderately.

two different linear graphs. The first of these is for lavas (dashed line) and has a steep slope caused by a wide range of thermal conductivities (1.4 to 1.9 W·m$^{-1}$·K$^{-1}$) in a narrow range of porosity (1–7%). This phenomenon highlights the importance of vesicles acting as isolators on thermal conductivity. The latter seems to decrease with increasing vesicle content and elongation. The second graph for debris flows and pyroclastics (dotted line) has a gentle slope and a large dispersion on either side of the linear trend.

A clear decrease of P-wave velocity is observed with increasing porosity (Fig. 8e). The higher and more heterogeneous is the porosity, the lower is the P-wave velocity. For a small range of porosity (2–5%), there is a 2500 m·s$^{-1}$ velocity range. This phenomenon is the same as that which we observed in Fig. 8d for thermal conductivity.

Good relationships of both thermal conductivity and P-wave velocity with porosity indicate that this is the major factor that controls these former properties. However, the difference of a few samples within the general trend may result in petrographic heterogeneities or strengths of contacts between minerals in rocks.

*4.2.5. Thermal conductivity vs. P-wave velocity*

Thermal conductivity and P-wave velocity measurements on all dry samples highlight a linear trend. Fig. 8f displays two well-separated groups: lavas with conductivities and velocities generally higher than 1.3 W·m$^{-1}$·K$^{-1}$ and 3500 m·s$^{-1}$ and debris flows and pyroclastics generally with values below these limits.

Thermal conductivity and P-wave velocities are directly linked, since they depend principally on mineralogy, porosity and fracture filling,

whether these be open or sealed fractures (Mielke et al., 2017). Fresh lavas and the majority of slightly to moderately altered ones are entirely crystallized and have low porosities. This implies velocities greater than 4000 $m \cdot s^{-1}$. However, the development of fracture networks creating porosities higher than 15% sharply decreases the velocities to values close to those of volcano-sedimentary deposits. Highly hydrothermalized lavas are completely outside of the linear trend. Their P-wave velocities are lower than 3000 $m \cdot s^{-1}$ and one sample estimated at 500 $m \cdot s^{-1}$ has a velocity below the detection limit. This is attributed to three elements: a high dissolution porosity, a large number of micro-cracks, and the almost complete recrystallization of rocks in microlithes of white micas, chlorite, quartz and clay minerals with weak contacts between them. Nevertheless, hydrothermalized lavas have thermal conductivities that are similar to, and sometimes higher than, fresh lavas. This could be explained by the large amount of pyrite that have a high thermal conductivity (Clauser and Huenges, 1995). Pyroclastics and debris flows have low P-wave velocities and thermal conductivities due to their high inter-particular porosity acting as insulation. Particles of debris flows and pyroclastics are poorly cemented. In contrast, lavas have an entirely crystallized matrix without glass conferring a good continuity between microlithic groundmass and phenocrysts.

## 5. Discussion

### 5.1. Comparison to other published petrophysical data

Very few studies concerning both petrographic analyses and thermo-physical measurements for these kinds of volcanic rocks are available. To date, to our knowledge, no study comparing field measurements and cores has been published. However, numerous analyses provide very valuable measurements to characterize: 1 - wells in active geothermal fields (Cant et al., 2018; Mielke et al., 2016; Rejeki et al., 2005; Stimac et al., 2004; Wyering et al., 2014); 2 - transport properties of pyroclastic rocks (Bernard, 1999; Bernard et al., 2007); 3 - geothermal reservoir potential from outcrop analogues (Lenhardt and Götz, 2015, 2011; Pola et al., 2014, 2012); 4 - pore network and mechanical properties of andesites (Farquharson et al., 2015; Heap et al., 2015; Heap and Kennedy, 2016).

Unfortunately, the comparison of published data on debris flow and pyroclastics with Guadeloupe data is difficult. Even the terminology of volcanic deposits is somewhat arbitrary and authors usually name deposits according to the process that led to their formation (e.g. indurated block-and-ash flows, Peléean "nuées ardentes", tuff). Normally, researchers did not characterize physical properties of the ash and pumice matrices, but mostly considered the lava blocks which bring no significant information to these deposits since they also characterize lava flows (e.g. Bernard, 1999; Bernard et al., 2007; Heap et al., 2015). Therefore, the comparison of measured properties from Guadeloupe concerning debris flows and pyroclastic matrices leaves a lot to be desired.

Table 3 summarizes major thermo-physical properties published to study geothermal systems. Bulk density, porosity, permeability, thermal conductivity, specific heat capacity and compressional wave velocity were all analyzed.

The authors extensively studied lava flows and lava blocks from block-and-ash flows. The results may be explained by simpler measurements on lavas than on lower cohesion pyroclastics and debris flows (e.g. Bernard et al., 2007; Lenhardt and Götz, 2011; Mielke et al., 2016). Fresh lavas from Guadeloupe are mostly dense. Therefore, they generally have lower porosity and matrix permeability compared to vesiculated blocks from Martinique. A local comparison with dense lavas from Montagne Pelée (Martinique) displays porosity similarities (Bernard et al., 2007). Farquharson et al. (2015), Heap et al. (2015). Heap and Kennedy (2016) worked on andesite stratovolcanoes either on Volcán de Colima (Mexico) or Mt. Ruapehu (New Zealand), studying porosity-permeability relationships and the mechanical behavior of andesite rocks. They observed higher porosities (10.6–17%) for lavas that showed 3 to 4 orders of magnitude higher permeability. On the contrary, andesite affected by high temperature alterations has surprisingly low porosity and permeability levels, respectively 4.4% and $5.10^{-17}$ $m^2$. For the same porosities, Guadeloupe and New-Zealand lavas have approximately the same thermal conductivities and compressional wave velocities (4–2.3–4.2%, 1.68–1.70–1.68 $W \cdot m^{-1} \cdot K^{-1}$, 4589–4300–4500 $m \cdot s^{-1}$; Mielke et al., 2016). Lavas with higher porosities display significant drops in thermal conductivity and P-wave velocities (Mielke et al., 2016). This confirms that thermal conductivity and compressional wave velocity are mainly controlled by porosity and the structure of the pore network. However, in the Tauhara geothermal field Mielke et al. (2015) observed a decrease of porosity and permeability with increasing depth, consecutive with advancing hydrothermal alterations. In contrast, upon advancing hydrothermal alteration, Guadeloupe lavas display an increase in both porosity and permeability. In Guadeloupe, the increase of micro-crack density in altered lavas and the replacement of plagioclases and pyroxenes by more porous minerals are the dominant features of porosity evolution whereas primary porosity clogging is less important. A similar feature was observed in Solfatara (Italy - Pola et al., 2012) where hydrothermal alteration progressively increases porosity. Pola et al. (2012) highlighted a slight decrease of porosity in totally altered lava related to large pores filled by new minerals.

Both fresh Debris flows from Guadeloupe and Ischia tuff (Italy - Pola et al., 2012) have porosities above 25%. Hydrothermal alteration tends to maintain this value at approximately 30% and slightly decreases permeabilities to around $10^{-15}$–$10^{-16}$ $m^2$ (Mielke et al., 2015; Pola et al., 2012). New minerals formed in large primary pores reduce pore throat diameters and this may explain the one order of magnitude decrease in permeability.

Overall, fresh pyroclastics from Guadeloupe exhibit lower porosities (34%) and permeability ($8.10^{-13}$ $m^2$) than scoria and pumice deposits from Volcán de Colima and Montagne Pelée. A major drop in these properties was observed by Lenhardt and Götz (2011) in slightly altered densely welded ash-flow deposits. Only a few data are available for highly altered pyroclastics, but core data display porosities higher than 10%, permeability of around $10^{-14}$ $m^2$ with thermal conductivity half as high as that of lavas (Mielke et al., 2015; Wyering et al., 2014). Highly altered outcropping pyroclastic sequences from Solfatara (Pola et al., 2012) have a porosity above 40%. Such porosities and permeabilities measured on ouctrop and cores show that pore collapse in pyroclastics does not totally close pores.

To conclude, the comparison of outcrop and core data exhibits many similarities. Advanced hydrothermal alteration improves porosity and permeability of lavas and these properties are unchanged or reduced in pyroclastics and debris flows. Altered samples have mostly porosities higher than 20% and permeabilities comprised between $10^{-14}$ and $10^{-16}$ $m^2$. However, these properties were only measured on matrices at a small scale. Thus, at a larger scale, the major role of fractures and faults on hydrothermal fluid flow and storage (Cox et al., 2015; Cox, 2010; Faulkner et al., 2010; Micklethwaite et al., 2015; Pinti et al., 2017; Rowland and Sibson, 2004; Rowland and Simmons, 2012; Scibek et al., 2016; Sibson, 1996, 1994; Sibson and Rowland, 2003; Simpson and Bignall, 2016; Tardani et al., 2016; Wilson and Rowland, 2016) was not taken into account.

### 5.2. Storage and fluid flow properties in a lava flow

Section 4.2.3 highlighted a wide variability of porosity and permeability especially for lava flows (Fig. 8c). To illustrate this heterogeneity and discuss the evolution of storage and fluid flow properties within a lava flow, petrophysical properties of four samples coming from the Pointe de l'Anse lava flow were isolated (Fig. 9). Four layers are visible on a 1.5 × 1.5 m outcrop section. From the bottom to the top: a 20 cm

**Table 3**
Comparison with other published petrophysical data. Outcrop data are either median values (regular character) or mean values (italics). Core measurements are median values (bold characters). The number of samples is in brackets. Detail abbreviations: D – dome; BAF - block-and-ash flows; NA – nuées ardentes. Alteration degree: F - fresh; SA - slightly altered; MA - moderately altered; HA - highly altered. References: 1 - Bernard, 1999; 2 - Bernard et al., 2007; 3 - Lenhardt and Götz, 2011; 4 - Lenhardt and Götz, 2015; 5 - Pola et al., 2012; 6 - Pola et al., 2014; 7 - Wyering et al., 2014; 8 - Mielke et al., 2015; 9 - Farquharson et al., 2015; 10 - Heap et al., 2015; 11 - Mielke et al., 2016; 12 - Heap and Kennedy, 2016.

| Lithological class | Detail | | Country | Alteration degree | $\rho_b$ [g·cm$^{-3}$] | Φ [%] | K [m$^2$] | λ [W·m$^{-1}$·K$^{-1}$] | $C_P$ [kJ·kg$^{-1}$·K$^{-1}$] | VP [m·s$^{-1}$] | Ref |
|---|---|---|---|---|---|---|---|---|---|---|---|
| Lava | | Andesite | FR | F | 2.64 (210) | 4 (31) | 6E−18 (46) | 1.68 (50) | 0.75 (28) | 4589 (34) | This study |
| | D | Lava block | FR | F | | 12.1 (1) | 4E−15 (1) | 1.07 (1) | | 2078 (1) | 1–2 |
| | D | Lava block | FR | F | | 9.8 (1) | 2E−15 (1) | 1.2 (1) | | 2501 (1) | 1–2 |
| | D | Dense lava flows | FR | F | | 3.5 (3) | 1E−16 (3) | 1.565 (2) | | 4645 (3) | 1–2 |
| | | *Adesite - Dacite* | *MX* | *F* | | *30 (5)* | *1E−15 (24)* | *1.5 (24)* | | | *3–4* |
| | | | *IT* | *F* | *2.38 (11)* | *11.0 (3)* | | | | *4390 (11)* | *5–6* |
| | | Andesite | MX | | 2.40 (9) | 10.6 (9) | 6E−14 (9) | | | | 9 |
| | | Andesite | MX | F | | 11.2 (8) | | | | | 10 |
| | | Andesite | NZ | F | 2.55 (32) | 2.3 (32) | 2E−15 (12) | 1.70 (36) | 0.72 (30) | 4300 (30) | 11 |
| | | Andesite | NZ | F | 2.32 (3) | 10.1 (3) | 5E−16 (3) | 1.61 (3) | 0.58 (3) | 3700 (3) | 11 |
| | | Andesite | NZ | F | 2.38 (8) | 13.0 (8) | 1E−13 (7) | 1.19 (8) | 0.52 (8) | 3200 (7) | 11 |
| | | Andesite | NZ | F | 2.59 (8) | 4.2 (8) | 5E−16 (7) | 1.68 (8) | 0.63 (8) | 4500 (8) | 11 |
| | | Andesite | NZ | F | | 16.9 (19) | 4E−14 (19) | | | | 12 |
| | BAF | Dense lava blocks | FR | F | | 7 (2) | 6E−16 (2) | 1.5 (2) | | 4995 (2) | 1–2 |
| | BAF | Vesicular lava blocks | FR | F | | 26.45 (4) | 1E−12 (4) | 0.9 (3) | | 2845 (4) | 1–2 |
| | BAF | Vesicular lava blocks | FR | F | | 28 (6) | 5E−12 (6) | 1.165 (2) | | 2310 (4) | 1–2 |
| | BAF | Vesicular lava blocks | MX | F | | 16.95 (16) | | | | | 10 |
| | NA | Vesicular lava blocks | FR | F | | 17.15 (10) | 5E−14 (10) | | | 3647 (6) | 1–2 |
| | NA | Vesicular lava blocks | FR | F | | 25.1 (5) | 1E−12 (5) | 0.91 (2) | | 2537 (5) | 1–2 |
| | | Andesite | FR | SA–MA | 2.49 (33) | 5.91 (15) | 4E−15 (17) | 1.65 (25) | 0.89 (16) | 4490 (16) | This study |
| | | | IT | SA | 2.50 (5) | 15.0 (3) | | | | 4140 (5) | 5–6 |
| | | | IT | MA | 1.94 (7) | 18.6 (3) | | | | 3160 (7) | 5–6 |
| | | **Andesite** | **NZ** | **SA** | **2.37 (24)** | **9.52 (24)** | **4E−17 (24)** | **1.32 (24)** | **0.74 (24)** | | **8** |
| | | Andesite | FR | HA | 2.00 (6) | 20.44 (4) | 2E−14 (4) | 1.66 (9) | 0.97 (6) | 1837 (5) | This study |
| | | | *IT* | *HA* | *1.65 (8)* | *32.0 (3)* | | | | *3110 (8)* | *5–6* |
| | | | *IT* | *HA* | *1.50 (7)* | *26.8 (3)* | | | | *2790 (7)* | *5–6* |
| | | **Andesite** | **NZ** | **SA–HA** | **2.53 (15)** | **6.84 (15)** | | | | **4154 (15)** | **7** |
| | | Andesite | MX | HA | | 7.6 (7) | | | | | 10 |
| | | Andesite | NZ | HA | | 4.4 (8) | 5E−17 (8) | | | | 12 |
| Debris flow | | Lahar, Avalanches | FR | F | 1.63 (25) | 32.56 (21) | 4E−14 (16) | 0.67 (33) | 0.88 (22) | 2059 (23) | This study |
| | | *Tuff* | *IT* | *F* | *1.54 (4)* | *25.5 (3)* | | | | *1140 (4)* | *5–6* |
| | | Lahar | MX | F | | 24 (7) | | | | | 10 |
| | | Lahar, Avalanches | FR | SA - MA | 1.97 (7) | 23.55 (6) | 1E−15 (5) | 1.02 (12) | 0.90 (6) | 2379 (9) | This study |
| | | Lahar, Avalanches | FR | HA | 1.5 (7) | 30.44 (7) | 5E−16 (3) | 0.85 (11) | 0.97 (8) | 1636 (8) | This study |
| | | *Tuff breccia* | *MX* | *HA* | | *15.2 (5)* | *2E−14 (5)* | *0.8 (6)* | | | *3–4* |
| | | *Mass flow deposits* | | | | | | | | | |
| | | *Tuff* | *IT* | *HA* | *1.81 (3)* | *29.7 (3)* | | | | *2250 (3)* | *5–6* |
| | | **Andesite breccia** | **NZ** | **HA** | **2.66 (12)** | **1.68 (12)** | | | | **4163 (12)** | **7** |
| | | **Andesite breccia** | **NZ** | **HA** | **1.71 (12)** | **38.67 (12)** | **1E−15 (12)** | **0.72 (12)** | **0.66 (12)** | | **8** |
| Pyroclastics | | Scoria, Pumice and Ashes | FR | F | *1.52 (20)* | *34.24 (16)* | *8E−13 (10)* | *0.54 (25)* | *0.88 (15)* | *1642 (17)* | This study |
| | | Block-and-ash flow Indurated ashes | FR | F | | 13.9 (6) | 6E−15 (6) | 1.33 (2) | | 3970 (5) | 1–2 |
| | | Scoriaceous blocks | FR | F | | 35.2 (3) | 2E−12 (3) | 0.57 (3) | | 3421 (3) | 1–2 |
| | | Pumices | FR | F | | 57.4 (7) | 8E−13 (6) | | | 1986 (5) | 1–2 |
| | | Scoria | MX | | 1.43 (4) | 46.7 (4) | 4E−13 (4) | | | | 9 |
| | | Pumice | MX | | 1.07 (4) | 58.25 (4) | 2E−12 (4) | | | | 9 |
| | | Scoria | NZ | | | 60.9 (2) | 3E−11 (2) | | | | 12 |
| | AF | *Incipiently welded* | *MX* | *SA* | | *37.7 (7)* | *5E−15 (7)* | *0.5 (5)* | | | *3–4* |
| | AF | *Partially welded* | *MX* | *SA* | | *33.0 (25)* | *6E−14 (25)* | *0.6 (17)* | | | *3–4* |
| | AF | *Moderately welded* | *MX* | *SA* | | *21.3 (29)* | *2E−14 (29)* | *0.9 (33)* | | | *3–4* |
| | AF | *Densely welded* | *MX* | *SA* | | *1.6 (6)* | *4E−16 (6)* | *1.7 (13)* | | | *3–4* |
| | | *Ignimbrite* | *IT* | *SA* | *0.98 (13)* | *65.0 (3)* | | | | *1140 (13)* | *5–6* |
| | | **Ash tuffs** | **NZ** | **SA - HA** | **1.57 (125)** | **40.56 (125)** | **3E−14 (125)** | **0.79 (125)** | **0.63 (125)** | | **8** |
| | | **Ignimbrite** | **NZ** | **HA** | **2.35 (37)** | **10.90 (37)** | | | | **3489 (36)** | **7** |
| | | *Pyroclastic* | *IT* | *HA* | *1.48 (8)* | *41.5 (3)* | | | | *2180 (8)* | *5–6* |
| | | *Pyroclastic* | *IT* | *HA* | *1.54 (9)* | *44.8 (3)* | | | | *2060 (9)* | *5–6* |
| | | *Pyroclastic* | *IT* | *HA* | *1.43 (7)* | | | | | *1650 (7)* | *5–6* |
| | | **Tuffs** | **NZ** | **HA** | **2.12 (10)** | **17.64 (10)** | | | | **2798 (10)** | **7** |

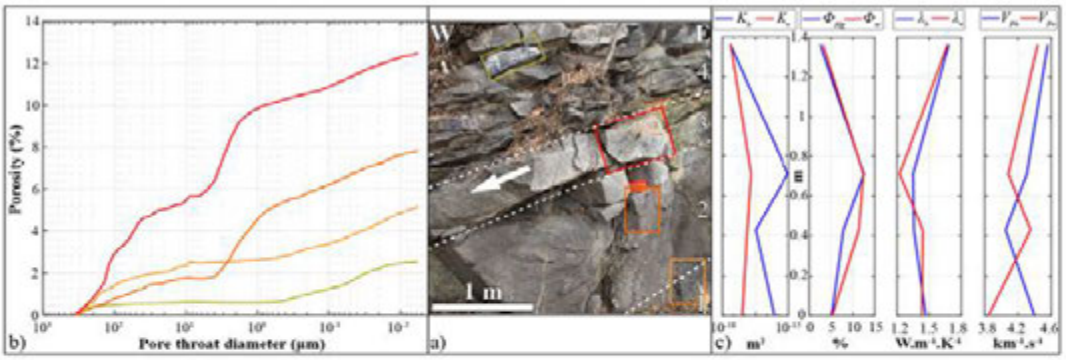


**Fig. 9.** Profile of measured physical properties on 4 samples from the same lava flow in Pointe de l'Anse (location shown in Fig. 1e). a) Picture of the outcropping lava flow with the locations of samples (insets). Dashed lines limit the 4 different zones in the lava flow: 1 - elongated vesicle rich layer; 2 - vertically fractured layer with thin spherical vesicles; 3 - vuggy vesicle-rich layer; 4 - densely fractured zone without vesicles. The white arrow indicates the direction of magma flow. b) mercury injection curves. c) 4 plots summarize principal physical properties. Permeability, thermal conductivity and P-wave velocity are measured parallel and perpendicular to magmatic foliation. The second plot displays porosity measurements using mercury injection and a triple weighing method.

thick vesicular layer of centimeter size had wide-open elongated vesicles; a 50 cm layer with thin bubble vesicles and half meter fractures; a 20 cm thick connected spherical vesicle-rich layer and a 60 cm thick layer with regularly spaced planar cooling joints. This structure in sub-parallel planar layers having different contents of vesicles and densities of fractures creates a strong vertical anisotropy (Yi et al., 2015).

The results show a wide dispersion of matrix porosity (2.5–12.5%) and a 5 orders of magnitude difference of permeability ($10^{-17}$–$10^{-12}$ m²). The comparison of permeability measurements performed parallel and perpendicular to magmatic foliation (Fig. 9) highlights that vesicles predominantly control the anisotropy of matrix permeability. This was confirmed by the lowest porous and permeable sample, which is the only isotropic sample analyzed for permeability. Thermal conductivity and P-wave velocity exhibit the same anisotropy since areas with vesicles result in a large decrease of the two properties. Only one sample has a better thermal conductivity and P-wave velocity perpendicular to magmatic foliation, rather than parallel to it. For this sample, the vertical fracture corridor creates a larger decrease of both properties than the vesicle plane does. At the matrix scale, these results show that lavas have poor reservoir properties. However, at a larger scale, several geothermal, groundwater and hydrocarbon reservoirs are hosted in lava flows (Feng, 2008; Hadi et al., 2005; Wang and Chen, 2015). The Rotokawa geothermal reservoir in New Zealand is composed of low porosity andesites whose fluid flow is structurally controlled (Siratovich et al., 2014). Murphy et al. (2004) have shown that highly permeable natural fractures play a predominant role in fluid flow, compared to the surrounding rock matrix. The existence of columnar cooling joints in lavas provides high permeability pathways (Rowland and Sibson, 2004), which could decrease the anisotropy attributed to vesicles aligned along magmatic foliation.

The Pointe de l'Anse lava flow contains mostly planar and vertical columnar joints. A striking feature is the difference in the number of planar fractures in the different layers. The density of fractures varies inversely with the vesicle content. Cooling joints are mostly concentrated in vesicle-poor layers. Vesicles tend to inhibit brittle behavior. They are transformed by ductile behavior during cooling, which explains their elongated shapes and allows a better connection of pore network, thus increasing permeability. Preferential hydrothermal fluid flow in lava flows should occur in both vesicle layers and cooling joints during burial.

### 5.3. General impact of alteration on thermo-physical properties

Cross-plots of physical properties of studied rocks (Fig. 8) highlighted the large variability of thermo-physical parameters. Two trends are clearly distinguishable on every plot between fresh lava flows on the one hand and fresh debris flows and pyroclastics on the other hand. Altered samples form an intermediary group. Advancing alteration tends to decrease initial thermo-physical differences between fresh rock types. Fresh pyroclastics and debris flows show high intergranular porosity with large pore throat diameters resulting in good permeability. Fluids can easily flow into the matrix, transforming initial minerals into secondary ones due to hydrothermal alterations. These could result in a patchy alteration depending on the clast nature (Mielke et al., 2015). Lava clasts tend to be less altered than the fine-grained matrix (Fig. 10a) in contrast to porous pumice clasts. On a small scale, matrices of fresh lava flows have poor fluid flow properties compared to debris flows and pyroclastics, even if they are affected by micro-cracks. These limit the development of pervasive alterations. Fortunately, lava flows are affected by dense networks of cooling joints, which are approximately parallel or perpendicular to magmatic foliation (Aydin and Degraff, 1988; Degraff and Aydin, 1993; Massiot et al., 2017; Mathieu, 2010). Joints divide lava flow bodies into a large number of geometric blocks whose shapes depend on the orientation of the joints. Therefore, the lava flow should not be considered as a unique massive body but as multiple blocks a few decimeters in size, limited by fractures. Intersections of joints create a large number of preferential pathways for fluid to enter the lava (Fig. 10b–c). Lava flows form a quasi-porous medium at the medium to large scale and can act as an aquifer, whereas matrices of small blocks are very impermeable. Very rare lava flows are affected by spheroidal weathering. Fluids flowing in joints progressively propagate to impermeable and impervious matrices, creating "onion skin" fractures (Jamtveit et al., 2009, 2008). In this way a fresh core is separated from an altered multi-layer rind (Sak et al., 2010). Fractures that appear by spalling divide lava blocks into thin layers with improved porosity and permeability. Therefore, the lava may be easily transformed by hydrothermal alteration during burial.

Long-term circulation of hydrothermal fluids tends to completely transform the matrices of every lithotype. Hydrothermal alteration transforms initial minerals into secondary phases like clay minerals with lower thermal conductivity (Clauser and Huenges, 1995) and compressional wave velocity (Schön, 2015). These neoformed minerals fill the initial vesicles of lavas and inter-particular porosity of debris flow and pyroclastics, reducing pore throat diameters (Fig. 7). A secondary porosity appears due to the replacement of low porosity plagioclase and pyroxene by high porosity clay minerals and the development of micro-cracks upon temperature increase ("thermal cracking", Mielke et al., 2016). The new porosity has lower pore throat diameters and

**Fig. 10.** Alteration of debris and lava flows. a) Differential alteration in a coarse debris flow from the Rocroy beach (location shown in Fig. 1e). Slightly hydrothermalized andesitic blocks are included in a whitish to reddish highly hydrothermalized matrix where the initial minerals are totally transformed. b and c) Spheroidal weathering in Tête Rouge La Batterie lava flow (Fig. 1f). The lava flow is cut by a set of sub-horizontal and vertical joints, which divide the lava flow in cubic blocks of andesites typically around few decimeters in size. Every block is affected by "onion-skin" fractures separating a "fresh" core from an altered rind. The rusty colored striation is a combination of Liesegang bands and "onion-skin" fractures (Jamtveit et al., 2011). The preferential fluid circulation from joints toward andesite block interior creates a gradual alteration degree improved by the intersection of closely spaced joints.

forms a more homogenous pore network. Highly altered pyroclastics do not outcrop in Guadeloupe. Thus, it is difficult to predict if their large open pores collapse with overburden pressure and hydrothermal alteration. Rejeki et al. (2005) measured porosities in lapilli of 10–15% at a 7000 ft depth in the Darajat geothermal field. Mielke et al. (2015) observed a permeability increase in ash tuff by a few percent with advancing hydrothermal alteration in the Tauhara geothermal field. Moreover, published cross-sections of active Bouillante (Lachassagne et al., 2009; Mas et al., 2006) and Lahendong (Indonesia - Brehme et al., 2014) geothermal fields localized production zones in tuff, lahars and volcanic breccia and secondary permeable zones in massive lavas. Therefore, hydrothermal alteration and overburden pressures are not sufficient to close the pore network of pyroclastics and debris flows which could actively act as aquifers.

### 5.4. Thoughts concerning a model of the Guadeloupe geothermal system

Measurements of physical parameters and an understanding of the impact of advancing hydrothermal alterations allow the proposal of a first explanation of the development of a geothermal system in active volcanic islands like Basse-Terre (Fig. 11). We propose a brief scenario of several steps to explain the transformation of fresh volcanic rocks into highly altered rocks:

1 - The relatively rich silica content produced mainly andesite lava (Fig. 3). Field observations show that lavas are mainly located close to the emission center. The proportion of lavas progressively decreases toward the coast of the island. A cross-section of the island between the emission center and the coast is composed of an alternation of lavas, debris flows, pyroclastics and debris avalanches (Fig. 4). This alternation of lithotypes creates a major planar anisotropy perpendicular to the volcano flank, notably decreasing the vertical permeability. However, this is compensated for by dykes and faults cross cutting the lithotype layers (Rowland and Sibson, 2004; Scibek et al., 2016). The viscous magma is favorable for the development of unstable steep flanks responsible for debris avalanches made up of meter size blocks. In this context explosive volcanism results in large amounts of pyroclastic material (Boudon et al., 2008) deposited on the volcano slopes (Fig. 11, stage 0).

2 - The tropical climate with several meters of rainfall per year on the volcano summit generates a high hydraulic gradient between the summit and the coast. Deposits linked to explosive volcanism (ash and pumice, blocks, bombs etc.) are saturated with water and may be reworked later into debris flows on the volcano slopes. Due to their suitable physical properties, pyroclastics and debris flows are loaded with meteoric water on the volcano flanks (Fig. 11, stage 1). Since lavas are surrounded by formations saturated with fluid, water progressively infiltrates lavas along cooling joints, autobrecciated and vesicular areas.

3 - When all lithotypes are buried under new volcanic materials (Fig. 11, stage 2), they are subject to high temperatures (higher than 200 °C) at shallow depth, due to an unusual temperature gradient (Manga et al., 2012) and low overburden pressures. This is demonstrated by the presence of high temperature neo-formed minerals in altered rocks of the exhumed geothermal system on Terre-de-Haut (muscovite, epidote, Fig. 5c and f). Using lithium isotopic measurements, Millot et al. (2010) demonstrated a mixing zone of meteoric water and seawater below the transition zone that lies between andesite volcanic flows and basaltic dykes. This zone would be situated at a depth ranging from 3 to 5 km. The resulting fluid is transported vertically by faults that create convection cells (Bouchot et al., 2008). The tectonic context is ideal because major structures have different orientations (e.g. Calcagno et al., 2012) creating many fault intersections that are suitable for fluid ascent. Moreover, these faults may be well-connected to fractured lavas, improving the large scale porosity and permeability of the system. Thus, the resulting hot fluid flows from faults to highly-fractured lavas and high matrix porosity lithotypes begin the transformation of the initial minerals (Fig. 5).

4 - Burial of volcanic lithotypes continues (Fig. 11, stage 3). Overburden pressure is presumed to decrease the size of large pores in debris flows and pyroclastics, but it could be partly compensated by the fluid pressure (Traineau et al., 2014). The porosity of all lithotypes is filled with hot hydrothermal fluids. According to temperature profiles acquired in production wells, the temperature of fluid reaches 240–260 °C and remains unchanged at depths ranging between 500 and 1800 m (Bouchot et al., 2010, 2008; Mas et al., 2006; Sanjuan et al., 2004, 2000). Transformation of initial minerals in pyroclastics and debris flows slightly decreases their porosities and permeabilities, but it increases their thermal conductivity. Replacement processes induce fractures and cracks in lavas (Jamtveit et al., 2009) significantly increasing reacting surfaces, porosity and permeability, even if vesicles are progressively sealed by clay minerals. Published well logs of the Bouillante field (Sanjuan et al.,

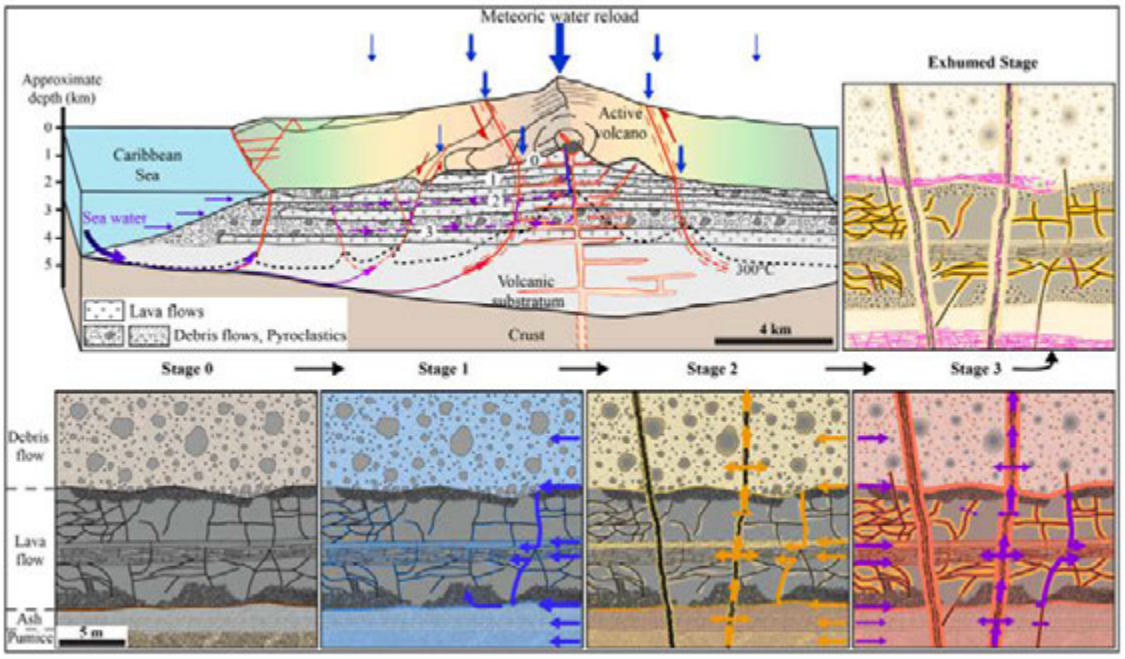


**Fig. 11.** Conceptual geological model of a geothermal system in Basse-Terre Island. The width of volcanic deposits was increased in the model to improve visibility, but the deposit size is respected in every zoom area for a 20 m thick volcano lithostratigraphical single unit. Stage 0 - General organization of fresh deposits after a pulse of volcanic activity of the stratovolcano. Stage 1 - Saturation of primary porosity with meteoric water on the volcano flank. Arrow size is proportional to fluid flow. Stage 2 - Tectonic constraints induce fractures and faults crossing deposits. A mix of seawater and meteoric water replaces meteoric water due to major faults. The resulting fluid impregnates all deposits and replacement of initial minerals begins. Stage 3 - Volcanic lithotypes are buried between 500 and 2000 m. The temperature of fluid (≈250 °C) increases the velocity of mineral transformation. Contacts between volcano-sedimentary units and lava flow are preferential pathways for fluids. Initial cooling joints are extended as far as neighbor joints, to form continuous structures. Stage 4 - Hydrothermally transformed lithotypes are exhumed upon volcano-erosion. Exhumation of the geothermal system partly fills fractures with gypsum, pyrite and gypsum. (For interpretation of the references to color in this figure legend, the reader is referred to the web version of this article.)

2004) allow the production area to be ranked: 1 – a major production in highly fractured areas, but the corresponding lithotypes are not described because of total loss; 2 – a medium production in tuffs; 3 – a minor production in lava flows. The circulation of hydrothermal fluid contributes to the total replacement of initial minerals. However, information obtained in the field, in the exhumed geothermal system, shows that lavas are less transformed than debris flows. This is most probably because of a less permeable matrix. Indeed, the highly hydrothermalized Grande Anse cliffs (Terre-de-Haut Island) exhibit a vertical succession of lavas and debris flows where the limits between lithotypes are well-defined. Debris flows are totally transformed, while lavas have preserved their initial structures. Therefore, the original anisotropy linked with initial volcanic deposits persists during the activity of the geothermal system;

5 - Several explanations may account for the end of the geothermal system, like the migration of volcanic activity or the development of new major faults that transport hydrothermal fluid elsewhere. Erosion of the volcanic chain contributes to the exhumation of the geothermal system (Fig. 11, exhumed stage). Field evidence obtained in the central part of Terre-de-Haut highlight that the final cooling stage of the geothermal system before exhumation consists in partial filling of fractures and bedding by a large amount of gypsum, pyrite and calcite (Figs. 2f and 11, exhumed stage, pink veins). Gypsum veins are predominantly located in highly altered debris flows indicating the preservation of high porosity and permeability of debris flows in the reservoir. Finally, weathering may occur on exhumed rocks. XRD analyses display a low kaolinite content showing that weathering of altered rocks is very limited.

## 6. Conclusion

The study presented here provides a dataset of thermo-physical properties for rocks of andesitic composition formed by explosive and effusive volcanism. Lithotypes studied are: 1 - lava flows with different vesicle contents; 2 – coarse breccia mostly composed of debris flows; 3 – pyroclastics including ash, pumice and scoria deposits. All lithological classes were divided according to alteration advancement. This work covers both fresh and hydrothermalized data, and is a cheap and effective way to counter the lack of in-depth information brought about by exploration wells, which are not available in the area of interest. The dataset comprises the following measurements on matrices: bulk and grain densities, mercury, water and helium porosities, permeability, P-wave velocity, thermal conductivity and diffusivity, calculation of specific heat capacity. These parameters are all essential to build realistic reservoir models that allow evaluation of the resource potential in the Vieux-Habitants area.

The study exhibits major heterogeneities between the different lithotypes and identifies clear boundaries separating lavas, pyroclastics and debris flows. On a small scale, fresh lavas have low porosity and permeability but high thermal conductivity, whereas the opposite features are observed in debris flows and pyroclastics. Field observations revealed a distinct mechanical behavior with high density fractures in lavas. This was partially caused by cooling and localized fracture corridors in pyroclastics and debris flows. High density cooling joints in lavas resulted in a significant improvement of porosity and permeability on a larger scale.

The impacts of hydrothermal alteration are: 1 - a disappearance of highly magnetic minerals resulting in rocks without magnetic signals,

which could improve the prospection of geothermal fields by geophysics and 2 - a general replacement of primary minerals by secondary phases that modify the initial pore network, notably reducing pore throat diameters. The impact of alterations on thermo-physical properties is contrasted for lava and debris flows since it produces an increase of porosity and permeability of lavas and a decrease in debris flows. Thermal conductivity remains constant in lavas, whereas it increases significantly in debris flows due to partial clogging of inter particular porosity.

Finally, comparisons with other published data, especially the work of Mielke et al. (2016, 2015), Pola et al. (2012), Siratovich et al. (2014), demonstrated remarkable correlations between thermo-physical properties acquired from outcropped samples and cores from geothermal fields. Therefore, outcrop measurements of altered samples should be considered at least as a first approximation to representatives of deep rocks.

## Acknowledgements

This paper is a contribution to the program GEOTREF funded by the French government in the frame of the program "Investissements d'Avenir" and tutored by ADEME. Partners of the GEOTREF project are Teranov, Kidova, Mines ParisTech, ENS Paris, GeoAzur, Georessources, IMFT, IPGS, LHyGes, UA, UCP-GEC.

## References

Andreieff, P., Bouysse, P., Westercamp, D., 1979. Reconnaissance géologique de l'arc insulaire des Petites Antilles. Résultats d'une campagne à la mer de prélèvements de roches entre Sainte-Lucie et Anguilla (No. 80SGN086MAR). Bureau de Recherches Géologiques et Minières.

Aretz, A., Baer, K., Götz, A., Sass, I., 2015. Outcrop analogue study of Permocarboniferous geothermal sandstone reservoir formations (northern Upper Rhine Graben, Germany): impact of mineral content, depositional environment and diagenesis on petrophysical properties. Int. J. Earth Sci. https://doi.org/10.1007/s00531-015-1263-2.

Aydin, A., Degraff, J.M., 1988. Evolution of polygonal fracture patterns in lava flows. Science 239, 471–476. https://doi.org/10.1126/science.239.4839.471.

Bas, M.J.L., Maitre, R.W.L., Streckeisen, A., Zanettin, B., 1986. A chemical classification of volcanic rocks based on the total alkali-silica diagram. J. Petrol. 27, 745–750. https://doi.org/10.1093/petrology/27.3.745.

Bazin, S., Feuillet, N., Duclos, C., Crawford, W., Nercessian, A., Bengoubou-Valerius, M., Beauducel, F., Singh, S.C., 2010. The 2004–2005 Les Saintes (French West Indies) seismic aftershock sequence observed with ocean bottom seismometers. Tectonophysics 489, 91–103. https://doi.org/10.1016/j.tecto.2010.04.005.

Belghoul, A., 2007. Caractérisation pétrophysique et hydrodynamique du socle cristallin (French). Université de Montpellier 2 Sciences et Techniques du Languedoc, Montpellier.

Bernard, M.-L., 1999. Etude expérimentale des propriétés physiques des roches pyroclastiques de la Montagne Pelée (French). Université de Paris 07, France.

Bernard, M.-L., Zamora, M., Géraud, Y., Boudon, G., 2007. Transport properties of pyroclastic rocks from Montagne Pelée volcano (Martinique, Lesser Antilles). J. Geophys. Res. 112, B05205. https://doi.org/10.1029/2006JB004385.

Bertani, R., 2016. Geothermal power generation in the world 2010–2014 update report. Geothermics 60, 31–43. https://doi.org/10.1016/j.geothermics.2015.11.003.

Bertrand, L., 2017. Etude des réservoirs géothermiques développés dans le socle et à l'interface avec les formations sédimentaires. Université de Lorraine.

Bézèlgues-Courtade, S., Bes-de-Berc, S., 2007. Inventaire et caractérisation des sources thermales de Guadeloupe (No. BRGM/RP-55060-FR).

Blanc, F., 1983. Corrélations chronologiques et géochimiques des formations volcaniques du sud de la basse terre de Guadeloupe (petites Antilles): début du cycle récent. (phd thesis). Université Scientifique et Médicale de Grenoble.

Bossennec, C., Géraud, Y., Moretti, I., Mattioni, L., Stemmelen, D., 2018. Pore network properties of sandstones in a fault damage zone. J. Struct. Geol. 110, 24–44. https://doi.org/10.1016/j.jsg.2018.02.003.

Bouchot, V., Traineau, H., Sanjuan, B., Gadalia, A., Guillou-Frottier, L., Thinon, I., Fabriol, H., Bourgeois, B., Baltassat, J.-M., Pajot, G., Jousset, P., Lasne, E., Genter, A., 2008. Modèle conceptuel du champ géothermique haute température de Bouillante, Guadeloupe, Antilles françaises. Rapport final. (Rapport BRGM No. RP-57252-FR). BRGM.

Bouchot, V., Traineau, H., Guillou-Frottier, L., Thinon, I., Baltassat, J.-M., Fabriol, H., Bourgeois, B., Lasne, E., 2010. Assessment of the Bouillante Geothermal Field (Guadeloupe, French West Indies): Toward a Conceptual Model of the High Temperature Geothermal System. Presented at the World Geothermal Congress 2010 (8 pp.).

Bouchot, V., Sanjuan, B., Calcagno, P., Gloaguen, E., Thinon, I., Gailler, L., Baltassat, J.-M., Bourgeois, B., Lerouge, C., Gadalia, A., Bourdon, E., Traineau, H., Patrier-Mas, P., Beaufort, D., Verati, C., 2011. The high-temperature geothermal system of Bouillante (Guadeloupe, French West Indies). 19ème Conférence Géologique de La Caraibe 2011. Le Gosier, Guadeloupe, France.

Boudon, G., 1988. Carte géologique du massif volcanique de la Soufrière. Département de la Guadeloupe, Petites Antilles [WWW Document].

Boudon, G., Komorowski, J.-C., Villemant, B., Semet, M.P., 2008. A new scenario for the last magmatic eruption of La Soufrière of Guadeloupe (Lesser Antilles) in 1530 A.D. Evidence from stratigraphy radiocarbon dating and magmatic evolution of erupted products. J. Volcanol. Geotherm. Res. 178, 474–490. https://doi.org/10.1016/j.jvolgeores.2008.03.006 (Evaluating Explosive Eruption Risk at European Volcanoes Contribution from the EXPLORIS Project 178).

Boulanouar, A., Rahmouni, A., Boukalouch, M., Samaouali, A., Géraud, Y., Harnafi, M., Sebbani, J., 2013. Determination of thermal conductivity and porosity of building stone from ultrasonic velocity measurements. Geomaterials 03, 138–144. https://doi.org/10.4236/gm.2013.34018.

Bouysse, P., 1983. The Lesser Antilles Island Arc: Structure and Geodynamic Evolution (Service Géologique National). Bureau de Recherches Géologiques et Minières.

Bouysse, P., Westercamp, D., 1990. Subduction of Atlantic aseismic ridges and Late Cenozoic evolution of the Lesser Antilles island arc. Tectonophysics 175, 349–380.

Brehme, M., Moeck, I., Kamah, Y., Zimmermann, G., Sauter, M., 2014. A hydrotectonic model of a geothermal reservoir – a study in Lahendong, Indonesia. Geothermics 51, 228–239. https://doi.org/10.1016/j.geothermics.2014.01.010.

Butler, R.F., 1998. Paleomagnetism: Magnetic Domains to Geologic Terranes. 23 (Electronic edition).

Calcagno, P., Bouchot, V., Thinon, I., Bourgine, B., 2012. A new 3D fault model of the Bouillante geothermal province combining onshore and offshore structural knowledge (French West Indies). Tectonophysics 526–529, 185–195. https://doi.org/10.1016/j.tecto.2011.08.012 (Modelling in Geosciences).

Cant, J.L., Siratovich, P.A., Cole, J.W., Villeneuve, M.C., Kennedy, B.M., 2018. Matrix permeability of reservoir rocks, Ngatamariki geothermal field, Taupo Volcanic Zone, New Zealand. Geotherm. Energy 6 (2). https://doi.org/10.1186/s40517-017-0088-6.

Carlut, J., Quidelleur, X., Courtillot, V., Boudon, G., 2000. Paleomagnetic directions and K/Ar dating of 0 to 1 Ma lava flows from La Guadeloupe Island (French West Indies): implications for time-averaged field models. J. Geophys. Res. Solid Earth 105, 835–849. https://doi.org/10.1111/j.1365-246X.1971.tb03616.x.

Chadima, M., 2011. Application of Magnetic Susceptibility Susceptibility as a Function of Temperature, Field and Frequency.

Clauser, C., Huenges, E., 1995. Thermal conductivity of rocks and minerals. In: Ahrens, T.J. (Ed.), Rock Physics & Phase Relations. American Geophysical Union, pp. 105–126 https://doi.org/10.1029/RF003p0105.

Coutant, O., Bernard, M.L., Beauducel, F., Nicollin, F., Bouin, M.P., Roussel, S., 2012. Joint inversion of P-wave velocity and density, application to La Soufrière of Guadeloupe hydrothermal system. Geophys. J. Int. 191, 723–742. https://doi.org/10.1111/j.1365-246X.2012.05644.x.

Cox, S.F., 2010. The application of failure mode diagrams for exploring the roles of fluid pressure and stress states in controlling styles of fracture-controlled permeability enhancement in faults and shear zones. Geofluids 10, 217–233. https://doi.org/10.1111/j.1468-8123.2010.00281.x.

Cox, S.C., Menzies, C.D., Sutherland, R., Denys, P.H., Chamberlain, C., Teagle, D.a.H., 2015. Changes in hot spring temperature and hydrogeology of the Alpine Fault hanging wall, New Zealand, induced by distal South Island earthquakes. Geofluids 15, 216–239. https://doi.org/10.1111/gfl.12093.

Davidson, J., De Silva, S., 2000. Composite volcanoes. Encyclopedia of Volcanoes. Haraldur Sigurdsson, p. 1442.

Degraff, J.M., Aydin, A., 1993. Effect of thermal regime on growth increment and spacing of contraction joints in basaltic lava. J. Geophys. Res. 98, 6411–6430. https://doi.org/10.1029/92JB01709.

DeMets, C., Jansma, P.E., Mattioli, G.S., Dixon, T.H., Farina, F., Bilham, R., Calais, E., Mann, P., 2000. GPS geodetic constraints on Caribbean-North America Plate Motion. Geophys. Res. Lett. 27, 437–440. https://doi.org/10.1029/1999GL005436.

Escartín, J., Leclerc, F., Olive, J.-A., Mevel, C., Cannat, M., Petersen, S., Augustin, N., Feuillet, N., Deplus, C., Bezos, A., Bonnemains, D., Chavagnac, V., Choi, Y., Godard, M., Haaga, K.A., Hamelin, C., Ildefonse, B., Jamieson, J.W., John, B.E., Leleu, T., MacLeod, C.J., Massot-Campos, M., Nomikou, P., Paquet, M., Rommevaux-Jestin, C., Rothenbeck, M., Steinführer, A., Tominaga, M., Triebe, L., Campos, R., Gracias, N., Garcia, R., Andreani, M., Vilaseca, G., 2016. First direct observation of coseismic slip and seafloor rupture along a submarine normal fault and implications for fault slip history. Earth Planet. Sci. Lett. 450, 96–107. https://doi.org/10.1016/j.epsl.2016.06.024.

Farquharson, J., Heap, M.J., Varley, N.R., Baud, P., Reuschle, T., 2015. Permeability and porosity relationships of edifice-forming andesites; a combined field and laboratory study. J. Volcanol. Geotherm. Res. 297, 52–68. https://doi.org/10.1016/j.jvolgeores.2015.03.016.

Faulkner, D.R., Jackson, C.A.L., Lunn, R.J., Schlische, R.W., Shipton, Z.K., Wibberley, C.A.J., Withjack, M.O., 2010. A review of recent developments concerning the structure, mechanics and fluid flow properties of fault zones. J. Struct. Geol. 32, 1557–1575. https://doi.org/10.1016/j.jsg.2010.06.009 (Fault Zones).

Feng, Z., 2008. Volcanic rocks as prolific gas reservoir: a case study from the Qingshen gas field in the Songliao Basin, NE China. Mar. Pet. Geol. 25, 416–432. https://doi.org/10.1016/j.marpetgeo.2008.01.008 (Geology of Giant gas Fields in China).

Feuillet, N., Manighetti, I., Tapponnier, P., Jacques, E., 2002. Arc parallel extension and localization of volcanic complexes in Guadeloupe, Lesser Antilles. J. Geophys. Res. 107. https://doi.org/10.1029/2001JB000308.

Feuillet, N., Leclerc, F., Tapponnier, P., Beauducel, F., Boudon, G., Le Friant, A., Deplus, C., Lebrun, J.-F., Nercessian, A., Saurel, J.-M., Clément, V., 2010. Active faulting induced by slip partitioning in Montserrat and link with volcanic activity: new insights from the 2009 GWADASEIS marine cruise data. Geophys. Res. Lett. 37, L00E15. https://doi.org/10.1029/2010GL042556.

Feuillet, N., Beauducel, F., Jacques, E., Tapponnier, P., Delouis, B., Bazin, S., Vallée, M., King, G.C.P., 2011. The Mw = 6.3, November 21, 2004, Les Saintes earthquake

(Guadeloupe): tectonic setting, slip model and static stress changes. J. Geophys. Res. 116, B10301. https://doi.org/10.1029/2011JB008310.
Gadalia, A., 2013. Exploration géothermique de la zone de Vieux Habitants. Etat des connaissances géologiques. (Rapport d'avancement No. BRGM/RP-62569-FR).
Gailler, L.-S., Bouchot, V., Martelet, G., Thinon, I., Coppo, N., Baltassat, J.-M., Bourgeois, B., 2014. Contribution of multi-method geophysics to the understanding of a high-temperature geothermal province: the Bouillante area (Guadeloupe, Lesser Antilles). J. Volcanol. Geotherm. Res. 275, 34–50. https://doi.org/10.1016/j.jvolgeores.2014.02.002.
Gaudin, D., Beauducel, F., Allemand, P., Delacourt, C., Finizola, A., 2013. Heat flux measurement from thermal infrared imagery in low-flux fumarolic zones: example of the Ty fault (La Soufrière de Guadeloupe). J. Volcanol. Geotherm. Res. 267, 47–56. https://doi.org/10.1016/j.jvolgeores.2013.09.009.
Gaudin, D., Finizola, A., Delcher, E., Beauducel, F., Allemand, P., Delacourt, C., Brothelande, E., Peltier, A., Di Gangi, F., 2015. Influence of rainfalls on heat and steam fluxes of fumarolic zones: six months records along the Ty fault (Soufrière of Guadeloupe, Lesser Antilles). J. Volcanol. Geotherm. Res. 302, 273–285. https://doi.org/10.1016/j.jvolgeores.2015.06.015.
Gaudin, D., Beauducel, F., Coutant, O., Delacourt, C., Richon, P., de Chabalier, J.-B., Hammouya, G., 2016. Mass and heat flux balance of La Soufrière volcano (Guadeloupe) from aerial infrared thermal imaging. J. Volcanol. Geotherm. Res. 320, 107–116. https://doi.org/10.1016/j.jvolgeores.2016.04.007.
Giesche, H., 2006. Mercury porosimetry: a general (practical) overview. Part. Part. Syst. Charact. 23, 9–19. https://doi.org/10.1002/ppsc.200601009.
Hadi, J., Harrison, C., Keller, J., Rejeki, S., 2005. Overview of Darajat Reservoir Characterization: A Volcanic Hosted Reservoir. Presented at the World Geothermal Congress, Antalya, Turkey, p. 11.
Haffen, S., 2012. Caractéristiques géothermiques du réservoir gréseux du Bundsandstein d'Alsace. Université de Strasbourg, Strasbourg.
Heap, M.J., Kennedy, B.M., 2016. Exploring the scale-dependent permeability of fractured andesite. Earth Planet. Sci. Lett. 447, 139–150. https://doi.org/10.1016/j.epsl.2016.05.004.
Heap, M.J., Farquharson, J.I., Baud, P., Lavallée, Y., Reuschle, T., 2015. Fracture and compaction of andesite in a volcanic edifice. Bull. Volcanol. 77. https://doi.org/10.1007/s00445-015-0938-7.
Heise, W., Caldwell, T.G., Bertrand, E.A., Hill, G.J., Bennie, S.L., Palmer, N.G., 2016. Imaging the deep source of the Rotorua and Waimangu geothermal fields, Taupo Volcanic Zone, New Zealand. J. Volcanol. Geotherm. Res. 314, 39–48. https://doi.org/10.1016/j.jvolgeores.2015.10.017 (The Lake Rotomahana Geothermal System and Effects of the 1886 Mt. Tarawera Eruption).
Howell, J.A., Martinius, A.W., Good, T.R., 2014. The application of outcrop analogues in geological modelling: a review, present status and future outlook. Geol. Soc. Lond., Spec. Publ. 387, SP387.12. https://doi.org/10.1144/SP387.12.
Hrouda, F., Buriánek, D., Krejčí, O., Chadima, M., 2015. Magnetic fabric and petrology of Miocene sub-volcanic sills and dykes emplaced into the SW Flysch Belt of the West Carpathians (S Moravia, Czech Republic) and their volcanological and tectonic implications. J. Volcanol. Geotherm. Res. 290, 23–38. https://doi.org/10.1016/j.jvolgeores.2014.12.001.
Iundt, F., Ouzounian, G., 1985. Comparaison entre les eaux thermales et les fluides de forages géothermiques dans la région de Bouillante (Guadeloupe). (Rapport BRGM No. 85 SGN 351 GTH). BRGM.
Jacques, D., Maury, R., 1988a. Carte géologique à 1/20000, département de la Guadeloupe. BRGM, Service Géologique Nationale, Orléans.
Jacques, D., Maury, R., 1988b. L'archipel des Saintes (Guadeloupe, Petites Antilles): géologie et pétrologie. Géol. Fr. 11.
Jacques, D., Maury, R.C., Bellon, H., 1984. Géologie et géochronologie $^{40}K$-$^{40}Ar$ des îles des Saintes (Guadeloupe). Comptes-rendus des séances de l'Académie des sciences. Série 2, Mécanique-physique, chimie, sciences de l'univers, sciences de la terre 299, pp. 721–726.
Jamtveit, B., Malthe-Sorenssen, A., Kostenko, O., 2008. Reaction enhanced permeability during retrogressive metamorphism. Earth Planet. Sci. Lett. 267, 620–627. https://doi.org/10.1016/j.epsl.2007.12.016.
Jamtveit, B., Putnis, C.V., Malthe-Sorenssen, A., 2009. Reaction induced fracturing during replacement processes. Contrib. Mineral. Petrol. 157, 127–133. https://doi.org/10.1007/s00410-008-0324-y.
Jamtveit, B., Kobchenko, M., Austrheim, H., Malthe-Sorenssen, A., Royne, A., Svensen, H., 2011. Porosity evolution and crystallization-driven fragmentation during weathering of andesite. J. Geophys. Res. 116. https://doi.org/10.1029/2011JB008649 (@CitationB12204-@CitationB12204).
Jelinek, V., 1981. Characterization of the magnetic fabric of rocks. Tectonophysics 79, T63–T67. https://doi.org/10.1016/0040-1951(81)90110-4.
Klinkenberg, L.J., 1941. The Permeability of Porous Media to Liquids and Gases. Presented at the Drilling and Production Practice. American Petroleum Institute.
Komorowski, J.-C., Boudon, G., Michel, S., Beauducel, F., Anténor-Habazac, C., Bazin, S., Hammouya, G., 2005. Guadeloupe. Volcanic Hazard Atlas of the Lesser Antilles. Seismic Research Unit, University of the West Indies. p. 279.
Lachassagne, P., Marechal, J.C., Sanjuan, B., 2009. Hydrogeological model of a high-energy geothermal field (Bouillante area, Guadeloupe, French West Indies). Hydrogeol. J. 17, 1589. https://doi.org/10.1007/s10040-009-0486-3.
Leclerc, F., Feuillet, N., Cabioch, G., Deplus, C., Lebrun, J.F., Bazin, S., Beauducel, F., Boudon, G., Lefriant, A., de Min, L., Melezan, D., 2014. The Holocene drowned reef of Les Saintes Plateau as witness of a long-term tectonic subsidence along the Lesser Antilles volcanic arc in Guadeloupe. Mar. Geol. 355, 115–135. https://doi.org/10.1016/j.margeo.2014.05.017.
Leclerc, F., Feuillet, N., Deplus, C., 2016. Interactions between active faulting, volcanism, and sedimentary processes at an island arc: insights from Les Saintes channel, Lesser Antilles arc. Geochem. Geophys. Geosyst. 17, 2781–2802. https://doi.org/10.1002/2016GC006337.
Lenhardt, N., Götz, A.E., 2011. Volcanic settings and their reservoir potential: an outcrop analog study on the Miocene Tepoztlán Formation, Central Mexico. J. Volcanol. Geotherm. Res. 204, 66–75. https://doi.org/10.1016/j.jvolgeores.2011.03.007.
Lenhardt, N., Götz, A.E., 2015. Geothermal reservoir potential of volcaniclastic settings: the Valley of Mexico, Central Mexico. Renew. Energy 77, 423–429. https://doi.org/10.1016/j.renene.2014.12.034.
Lesparre, N., Boyle, A., Grychtol, B., Cabrera, J., Marteau, J., Adler, A., 2016. Electrical resistivity imaging in transmission between surface and underground tunnel for fault characterization. J. Appl. Geophys. 128, 163–178. https://doi.org/10.1016/j.jappgeo.2016.03.004.
Lopez, S., Lakhssassi, M., Giuglaris, E., 2011. Modeling of Bouillante Geothermal Field (Guadeloupe, French Lesser Antilles). Presented at the 19ème Conférence Géologique de la Caraïbe.
Manga, M., Hornbach, M.J., Le Friant, A., Ishizuka, O., Stroncik, N., Adachi, T., Aljahdali, M., Boudon, G., Breitkreuz, C., Fraass, A., Fujinawa, A., Hatfield, R., Jutzeler, M., Kataoka, K., Lafuerza, S., Maeno, F., Martinez-Colon, M., McCanta, M., Morgan, S., Palmer, M.R., Saito, T., Slagle, A., Stinton, A.J., Subramanyam, K.S.V., Tamura, Y., Talling, P.J., Villemant, B., Wall-Palmer, D., Wang, F., 2012. Heat flow in the Lesser Antilles island arc and adjacent back arc Grenada basin. Geochem. Geophys. Geosyst. 13, Q08007. https://doi.org/10.1029/2012GC004260.
Mas, A., Guisseau, D., Patrier Mas, P., Beaufort, D., Genter, A., Sanjuan, B., Girard, J.P., 2006. Clay minerals related to the hydrothermal activity of the Bouillante geothermal field (Guadeloupe). J. Volcanol. Geotherm. Res. 158, 380–400. https://doi.org/10.1016/j.jvolgeores.2006.07.010.
Massiot, C., Nicol, A., Townend, J., McNamara, D.D., Garcia-Sellés, D., Conway, C.E., Archibald, G., 2017. Quantitative geometric description of fracture systems in an andesite lava flow using terrestrial laser scanner data. J. Volcanol. Geotherm. Res. 341, 315–331. https://doi.org/10.1016/j.jvolgeores.2017.05.036.
Mathieu, L., 2010. The Structure of Guadeloupe, Maderas and Mt Cameroon Volcanoes and the Impact of Strike-slip Movements. Université Blaise Pascal - Clermont Ferrand II; Trinity College Dublin.
McNamara, D.D., Sewell, S., Buscarlet, E., Wallis, I.C., 2016. A review of the Rotokawa Geothermal Field, New Zealand. Geothermics, Taupo Volcanic Zone Geothermal Systems, New Zealand: Exploration, Science and Development. 59, pp. 281–293. https://doi.org/10.1016/j.geothermics.2015.07.007.
Micklethwaite, S., Ford, A., Witt, W., Sheldon, H.A., 2015. The where and how of faults, fluids and permeability – insights from fault stepovers, scaling properties and gold mineralisation. Geofluids 15, 240–251. https://doi.org/10.1111/gfl.12102.
Mielke, P., Nehler, M., Bignall, G., Sass, I., 2015. Thermo-physical rock properties and the impact of advancing hydrothermal alteration — a case study from the Tauhara geothermal field, New Zealand. J. Volcanol. Geotherm. Res. 301, 14–28. https://doi.org/10.1016/j.jvolgeores.2015.04.007.
Mielke, P., Weinert, S., Bignall, G., Sass, I., 2016. Thermo-physical rock properties of greywacke basement rock and intrusive lavas from the Taupo Volcanic Zone, New Zealand. J. Volcanol. Geotherm. Res. 324, 179–189. https://doi.org/10.1016/j.jvolgeores.2016.06.002.
Mielke, P., Bär, K., Sass, I., 2017. Determining the relationship of thermal conductivity and compressional wave velocity of common rock types as a basis for reservoir characterization. J. Appl. Geophys. 140, 135–144. https://doi.org/10.1016/j.jappgeo.2017.04.002.
Millot, R., Scaillet, B., Sanjuan, B., 2010. Lithium isotopes in island arc geothermal systems: Guadeloupe, Martinique (French West Indies) and experimental approach. Geochim. Cosmochim. Acta 74, 1852–1871. https://doi.org/10.1016/j.gca.2009.12.007.
Moeck, I.S., 2014. Catalog of geothermal play types based on geologic controls. Renew. Sust. Energ. Rev. 37, 867–882. https://doi.org/10.1016/j.rser.2014.05.032.
Morgan, S., Jones, R., Conner, J., Student, J., Schaner, M., Horsman, E., Blanquat, M. de S., 2017. Magma sheets defined with magnetic susceptibility in the Maiden Creek sill, Henry Mountains, Utah, USA. Geology 45, 599–602. https://doi.org/10.1130/G38932.1.
Munch, P., Cornee, J.-J., Lebrun, J.-F., Quillevere, F., Verati, C., Melinte-Dobrinescu, M., Demory, F., Smith, B., Jourdan, F., Lardeaux, J.-M., De Min, L., Leticee, J.-L., Randrianasolo, A., 2014. Pliocene to Pleistocene vertical movements in the forearc of the Lesser Antilles subduction: insights from chronostratigraphy of shallow-water carbonate platforms (Guadeloupe archipelago). J. Geol. Soc. 171, 329–341. https://doi.org/10.1144/jgs2013-005.
Murphy, H., Huang, C., Dash, Z., Zyvoloski, G., White, A., 2004. Semianalytical solutions for fluid flow in rock joints with pressure-dependent openings. Water Resour. Res. 40. https://doi.org/10.1029/2004WR003005.
Ólavsdóttir, J., Andersen, M.S., Boldreel, L.O., 2015. Reservoir quality of intrabasalt volcaniclastic units onshore Faroe Islands, North Atlantic Igneous Province, northeast Atlantic. AAPG Bull. 99, 467–497. https://doi.org/10.1306/08061412084.
Panaiotu, C., Necula, C., Merezeanu, T., Panaiotu, A., Corban, C., 2011. Anisotropy of magnetic susceptibility of quaternary lava flows from the east Carpathians. Romanian Rep. Phys. 63, 526–534.
Pape, H., Clauser, C., Iffland, J., 1999. Permeability prediction based on fractal pore-space geometry. Geophysics 64, 1447–1460. https://doi.org/10.1190/1.1444649.
Patrier, P., Beaufort, D., Mas, A., Traineau, H., 2003. Surficial clay assemblage associated with the hydrothermal activity of Bouillante (Guadeloupe, French West Indies). J. Volcanol. Geotherm. Res. 126, 143–156. https://doi.org/10.1016/S0377-0273(03)00133-1.
Patrier, P., Bruzac, S., Pays, R., Beaufort, D., Bouchot, V., Verati, C., Gadalia, A., 2013. Occurrence of K-feldspar-bearing hydrothermal breccias in the Bouillante geothermal field (Basse Terre – Guadeloupe). Bull. Soc. Geol. Fr. 184, 119–128. https://doi.org/10.2113/gssgfbull.184.1-2.119.

Peccerillo, A., Taylor, S.R., 1976. Geochemistry of eocene calc-alkaline volcanic rocks from the Kastamonu area, northern Turkey. Contrib. Mineral. Petrol. 58, 63–81. https://doi.org/10.1007/BF00384745.

Pinti, D.L., Castro, M.C., Lopez-Hernandez, A., Han, G., Shouakar- Stash, O., Hall, C.M., Ramirez-Montes, M., 2017. Fluid circulation and reservoir conditions of the Los Humeros Geothermal Field (LHGF), Mexico, as revealed by a noble gas survey. J. Volcanol. Geotherm. Res. 333–334, 104–115. https://doi.org/10.1016/j.jvolgeores.2017.01.015.

Pola, A., Crosta, G., Fusi, N., Barberini, V., Norini, G., 2012. Influence of alteration on physical properties of volcanic rocks. Tectonophysics 566–567, 67–86. https://doi.org/10.1016/j.tecto.2012.07.017.

Pola, A., Crosta, G.B., Fusi, N., Castellanza, R., 2014. General characterization of the mechanical behaviour of different volcanic rocks with respect to alteration. Eng. Geol. 169, 1–13. https://doi.org/10.1016/j.enggeo.2013.11.011.

Popov, Y.A., Pribnow, D.F.C., Sass, J.H., Williams, C.F., Burkhardt, H., 1999. Characterization of rock thermal conductivity by high-resolution optical scanning. Geothermics 28, 253–276. https://doi.org/10.1016/S0375-6505(99)00007-3.

Popov, Y.A., Beardsmore, G., Clauser, C., Roy, S., 2016. ISRM Suggested Methods for Determining Thermal Properties of Rocks From Laboratory Tests at Atmospheric Pressure. https://doi.org/10.1007/s00603-016-1070-5.

Pozzi, J.-P., Le Mouel, J.-L., Rossignol, J.C., Zlotnicki, J., 1979. Magnetic observations made on la Soufriere volcano (Guadeloupe) during the 1976–1977 crisis. J. Volcanol. Geotherm. Res. 5, 217–237. https://doi.org/10.1016/0377-0273(79)90017-9.

Ratouis, T.M.P., Zarrouk, S.J., 2016. Factors controlling large-scale hydrodynamic convection in the Taupo Volcanic Zone (TVZ), New Zealand. Geothermics 59, 236–251. https://doi.org/10.1016/j.geothermics.2015.09.003 (Taupo Volcanic Zone Geothermal Systems, New Zealand: Exploration, Science and Development).

Rejeki, S., Hadi, J., Suhayati, I., 2005. Porosity study for detail reservoir characterization in Darajat Geothermal Field, West Java, Indonesia. Proceedings, World Geothermal Congress, Antalya, Turkey.

Ricci, J., Lahitte, P., Quidelleur, X., 2015a. Construction and destruction rates of volcanoes within tropical environment: examples from the Basse-Terre Island (Guadeloupe, Lesser Antilles). Geomorphology 228, 597–607. https://doi.org/10.1016/j.geomorph.2014.10.002.

Ricci, J., Quidelleur, X., Lahitte, P., 2015b. Volcanic evolution of central Basse-Terre Island revisited on the basis of new geochronology and geomorphology data. Bull. Volcanol. 77 (84). https://doi.org/10.1007/s00445-015-0970-7.

Ricci, J., Quidelleur, X., Pallares, C., Lahitte, P., 2017. High-resolution K-Ar dating of a complex magmatic system: the example of Basse-Terre Island (French West Indies). J. Volcanol. Geotherm. Res. https://doi.org/10.1016/j.jvolgeores.2017.07.013.

Roduit, N., 2007. JMicroVision: un logiciel d'analyse d'images pétrographiques polyvalent. University of Geneva.

Rosas-Carbajal, M., Komorowski, J.-C., Nicollin, F., Gibert, D., 2016. Volcano electrical tomography unveils edifice collapse hazard linked to hydrothermal system structure and dynamics. Sci. Rep. 6, 29899. https://doi.org/10.1038/srep29899.

Rosener, M., 2007. Etude pétrophysique et modélisation des effets des transferts thermiques entre roche et fluide dans le contexte géothermique de Soultz-sous-Forêts. Strasbourg. 1.

Rowland, J.V., Sibson, R.H., 2004. Structural controls on hydrothermal flow in a segmented rift system, Taupo Volcanic Zone, New Zealand. Geofluids 4, 259–283. https://doi.org/10.1111/j.1468-8123.2004.00091.x.

Rowland, J.V., Simmons, S.F., 2012. Hydrologic, magmatic, and tectonic controls on hydrothermal flow, Taupo Volcanic Zone, New Zealand: implications for the formation of epithermal vein deposits. Econ. Geol. 107, 427–457. https://doi.org/10.2113/econgeo.107.3.427.

Sak, P.B., Navarre-Sitchler, A.K., Miller, C.E., Daniel, C.C., Gaillardet, J., Buss, H.L., Lebedeva, M.I., Brantley, S.L., 2010. Controls on rind thickness on basaltic andesite clasts weathering in Guadeloupe. Chem. Geol. 276, 129–143. https://doi.org/10.1016/j.chemgeo.2010.05.002.

Samper, A., 2007. Etude géochronologique, aspects géomorphologiques et géochimiques du volcanisme de l'île de Basse Terre (Guadeloupe), et datation des structures d'effondrement de flanc majeures de l'arc des Petites Antilles. Université de Paris-Sud. Faculté des Sciences d'Orsay (Essonne).

Samper, A., Quidelleur, X., Lahitte, P., Mollex, D., 2007. Timing of effusive volcanism and collapse events within an oceanic arc island: Basse-Terre, Guadeloupe archipelago (Lesser Antilles Arc). Earth Planet. Sci. Lett. 258, 175–191. https://doi.org/10.1016/j.epsl.2007.03.030.

Samper, A., Quidelleur, X., Komorowski, J.-C., Lahitte, P., Boudon, G., 2009. Effusive history of the Grande Découverte Volcanic Complex, southern Basse-Terre (Guadeloupe, French West Indies) from new K–Ar Cassignol–Gillot ages. J. Volcanol. Geotherm. Res. 187, 117–130. https://doi.org/10.1016/j.jvolgeores.2009.08.016.

Sanjuan, B., Brach, M., 1998. Etude hydrogéochimique du champ géothermique de Bouillante (Guadeloupe) (Rapport BRGM No. 39880). BRGM.

Sanjuan, B., Brach, M., 2015. Geochemical monitoring of the thermal manifestations located near the Bouillante geothermal power plant. Guadeloupe (FWI). Procedia Earth and Planetary Science, 11th Applied Isotope Geochemistery Conference AIG-11. 13, pp. 25–29. https://doi.org/10.1016/j.proeps.2015.07.006.

Sanjuan, B., Traineau, H., 2008. Development of the Bouillante geothermal field (Guadeloupe, French West Indies). IGA News Quaterly n°73, pp. 5–9.

Sanjuan, B., Lasne, E., Brach, M., 2000. Bouillante Geothermal Field (Guadeloupe, West Indies): Geochemical Monitoring During a Thermal Simulation Operation. Presented at the Workshop on Geothermal Reservoir Engineering, Stanford. p. 8.

Sanjuan, B., Brach, M., Lasne, E., 2001. Bouillante geothermal field: mixing and water/rock interaction processes at 250 °C. In: Cidu, R. (Ed.), Water Rock Interaction, WRI-10, International Symposium on Water Rock Interaction. A.A. Balkema Publishers, Villasimius, Italy, pp. 911–914.

Sanjuan, B., Le Nindre, Y.-M., Menjoz, A., Sbai, A., Brach, M., Lasne, E., 2004. Travaux de recherche liés au développement du champ géothermique de Bouillante (Guadeloupe) (Rapport BRGM No. RP-53136-FR). BRGM.

Sanjuan, B., Jousset, P., Pajot, G., Debeglia, N., Michele, M.D., Brach, M., Dupont, F., Braibant, G., Lasne, E., Duré, F., 2010. Monitoring of the Bouillante Geothermal Exploitation (Guadeloupe, French West Indies) and the Impact on Its Immediate Environment. Presented at the World Geothermal Congress 2010 (11 pp.).

Schön, Juergen H., 2015. Physical Properties of Rocks: Fundamentals and Principles of Petrophysics. Elsevier.

Scibek, J., Gleeson, T., McKenzie, J.M., 2016. The Biases and Trends in Fault Zone Hydrogeology Conceptual Models: Global Compilation and Categorical Data Analysis. https://doi.org/10.1111/gfl.12188.

Sibson, R.H., 1994. Crustal stress, faulting and fluid flow. Geol. Soc. Lond., Spec. Publ. 78, 69–84. https://doi.org/10.1144/GSL.SP.1994.078.01.07.

Sibson, R.H., 1996. Structural permeability of fluid-driven fault-fracture meshes. J. Struct. Geol. 18, 1031–1042. https://doi.org/10.1016/0191-8141(96)00032-6.

Sibson, R.H., Rowland, J.V., 2003. Stress, fluid pressure and structural permeability in seismogenic crust, North Island, New Zealand. Geophys. J. Int. 154, 584–594. https://doi.org/10.1046/j.1365-246X.2003.01965.x.

Simpson, M.P., Bignall, G., 2016. Undeveloped high-enthalpy geothermal fields of the Taupo Volcanic Zone, New Zealand. Geothermics 59, 325–346. https://doi.org/10.1016/j.geothermics.2015.08.006 (Taupo Volcanic Zone Geothermal Systems, New Zealand: Exploration, Science and Development).

Siratovich, P., Heap, M.J., Villeneuve, M., W Cole, J., Reuschlé, T., 2014. Physical property relationships of the Rotokawa Andesite, a significant geothermal reservoir rock in the Taupo Volcanic Zone, New Zealand. Geotherm. Energy 1 (10). https://doi.org/10.1186/s40517-014-0010-4.

Sizun, J.-P., 1995. Modifications des structures de porosite de gres lors de transformations petrographiques dans la diagenese et l'hydrothermalisme: application au trias de la marge ardechoise et du fosse rhenan. 1 (Strasbourg).

Stanek, M., 2013. Structural and Petrophysical Characterisation of Granite: Intended for Radioactive Waste Stocking (Strasbourg).

Stimac, J.A., Powell, T.S., Golla, G.U., 2004. Porosity and permeability of the Tiwi geothermal field, Philippines, based on continuous and spot core measurements. Geothermics 33, 87–107. https://doi.org/10.1016/j.geothermics.2003.03.002 (Philippine Geothermal Systems Response to Production).

Surma, F., Geraud, Y., 2003. Porosity and thermal conductivity of the Soultz-sous-Forêts granite. Pure Appl. Geophys. 160, 1125–1136. https://doi.org/10.1007/PL00012564.

Symithe, S., Calais, E., de Chabalier, J.B., Robertson, R., Higgins, M., 2015. Current block motions and strain accumulation on active faults in the Caribbean. J. Geophys. Res. Solid Earth 120, 2014JB011779. https://doi.org/10.1002/2014JB011779.

Tardani, D., Reich, M., Roulleau, E., Takahata, N., Sano, Y., Pérez-Flores, P., Sánchez-Alfaro, P., Cembrano, J., Arancibia, G., 2016. Exploring the structural controls on helium, nitrogen and carbon isotope signatures in hydrothermal fluids along an intra-arc fault system. Geochim. Cosmochim. Acta 184, 193–211. https://doi.org/10.1016/j.gca.2016.04.031.

Thinon, I., Guennoc, P., Bitri, A., Truffert, C., 2010. Study of the Bouillante Bay (West Basse-Terre Island shelf): contribution of geophysical surveys to the understanding of the structural context of Guadeloupe (French West Indies-Lesser Antilles). Bull. Soc. Geol. Fr. 181, 51–65.

Traineau, H., Sanjuan, B., Lasne, E., 2014. Main Results of a Long-term Monitoring of the Bouillante Geothermal Reservoir During Its Exploitation. Presented at the Deep Geothermal Days.

Vallance, J.W., Iverson, R.M., 2015. Chapter 37 - lahars and their deposits. The Encyclopedia of Volcanoes, pp. 649–664.

Verati, C., Patrier-Mas, P., Lardeaux, J.M., Bouchot, V., 2013. Timing of Geothermal Activity in an Active Island-arc Volcanic Setting; First (Super 40) Ar/(Super 39) Ar Dating From Bouillante Geothermal Field (Guadeloupe, French West Indies). Special Publication - Geological Society of London. 378. https://doi.org/10.1144/SP378.19.

Verati, C., Mazabraud, Y., Lardeaux, J.-M., Corsini, M., Schneider, D., Voitus, E., Zami, F., 2016. Tectonic evolution of Les Saintes Archipelago (Guadeloupe, French West Indies); relation with the Lesser Antilles arc system. Bull. Soc. Geol. Fr. 187, 3–10. https://doi.org/10.2113/gssgfbull.187.1.3.

Wang, P., Chen, S., 2015. Cretaceous volcanic reservoirs and their exploration in the Songliao Basin, Northeast China. AAPG Bull. 99, 499–523. https://doi.org/10.1306/09041413095.

Washburn, E.W., 1921. The dynamics of capillary flow. Phys. Rev. 17, 273–283. https://doi.org/10.1103/PhysRev.17.273.

Wilmarth, M., Stimac, J., 2015. Power density in geothermal fields. Proceedings. Presented at the World Geothermal Congress, Melbourne, Australia, p. 7.

Wilson, C.J.N., Rowland, J.V., 2016. The volcanic, magmatic and tectonic setting of the Taupo Volcanic Zone, New Zealand, reviewed from a geothermal perspective. Geothermics 59, 168–187. https://doi.org/10.1016/j.geothermics.2015.06.013.

Wyering, L.D., Villeneuve, M., Wallis, I., Siratovich, P., Kennedy, B., Gravley, D.M., Cant, J.L., 2014. Mechanical and physical properties of hydrothermally altered rocks, Taupo Volcanic Zone, New Zealand. J. Volcanol. Geotherm. Res. 288. https://doi.org/10.1016/j.jvolgeores.2014.10.008.

Yi, J., Wang, P., Gao, Y., Yao, R., Zhao, R., Chen, C., 2015. Vesicle distribution in basalt lava flow units in the Mesozoic rift basins of Northeast China and its application in gas reservoir prediction. Can. J. Earth Sci. 53, 59–70. https://doi.org/10.1139/cjes-2015-0004.

Zami, F., Quidelleur, X., Ricci, J., Lebrun, J.-F., Samper, A., 2014. Initial sub-aerial volcanic activity along the central Lesser Antilles inner arc: new K–Ar ages from Les Saintes volcanoes. J. Volcanol. Geotherm. Res. 287, 12–21. https://doi.org/10.1016/j.jvolgeores.2014.09.011.

## X.7. Article 6 – The characterisation of an exhumed high-temperature paleo-geothermal system on Terre-de-Haut Island (the Les Saintes archipelago, Guadeloupe) in terms of clay minerals and petrophysics

Beauchamps *et al. Geotherm Energy* (2019) 7:6
https://doi.org/10.1186/s40517-019-0122-y

Geothermal Energy

RESEARCH Open Access

# The characterisation of an exhumed high-temperature paleo-geothermal system on Terre-de-Haut Island (the Les Saintes archipelago, Guadeloupe) in terms of clay minerals and petrophysics

Gildas Beauchamps[1*], Béatrice Ledésert[1], Ronan Hébert[1], Vivien Navelot[2] and Alexiane Favier[3,4]

*Correspondence:
gildas.beauchamps@u-cergy.fr
[1] Laboratoire Géosciences et Environnement Cergy, Université de Cergy Pontoise, 1 Rue Descartes, 95000 Neuville-sur-Oise, France
Full list of author information is available at the end of the article

**Abstract**

The volcanic island of Terre-de-Haut (in the Les Saintes archipelago, Lesser Antilles arc) is described in the literature as an exhumed paleo-geothermal system. Outcropping conditions provide a good, nearly horizontal 2D view of the system. This present study focuses on clay minerals, as they are known to be good markers of hydrothermal alterations worldwide, and on flow pathways. At Terre-de-Haut, the distribution of the clay minerals has a 'concentric' zonation with smectite, illite and chlorite comprising the outer part to the inner part of the altered zone, respectively. In the active Bouillante geothermal system, located on Basse-Terre island, 35 km NNW of Terre-de-Haut, drillings have revealed a vertical succession of the same clay minerals: from bottom to top, chlorite above 240 °C, illite above 180 °C and smectite at lower temperatures. Both sites have the same clay minerals and can, therefore, be compared. Within those geothermal systems, pathways for the fluids are encountered at all scales, from the micrometre-scale (µm-scale; through microcracks within phenocrysts and at grain joints) to the metre- and kilometre-scale (m- and km-scale) due to fractures and faults. Petrophysical measurements indicate that fresh rock samples are porous and permeable, allowing hydrothermal alteration on a km-scale. The combination of 1D vertical data at Bouillante and this new 2D horizontal distribution of clay minerals and fractures on Terre-de-Haut allows for a 3D schematic representation of the geothermal systems of the Guadeloupe archipelago and suggests that they are of hectometre-size (hm-size).

**Keywords:** Geothermal systems, Hydrothermal alteration, Clay minerals, Petrophysics, Lesser Antilles, Guadeloupe, Les Saintes

### Introduction

Searching for new geothermal energy resources in the Lesser Antilles and particularly in Guadeloupe (Fig. 1a), it is important to better characterise geothermal systems in this tectonic- and volcanic-active environment. The Bouillante geothermal power plant (Basse-Terre of Guadeloupe) has been producing electricity since 1986 and provides 1D drilling information of the system. Terre-de-Haut (4.5 $km^2$, the Les Saintes

Springer Open

© The Author(s) 2019. This article is distributed under the terms of the Creative Commons Attribution 4.0 International License (http://creativecommons.org/licenses/by/4.0/), which permits unrestricted use, distribution, and reproduction in any medium, provided you give appropriate credit to the original author(s) and the source, provide a link to the Creative Commons license, and indicate if changes were made.

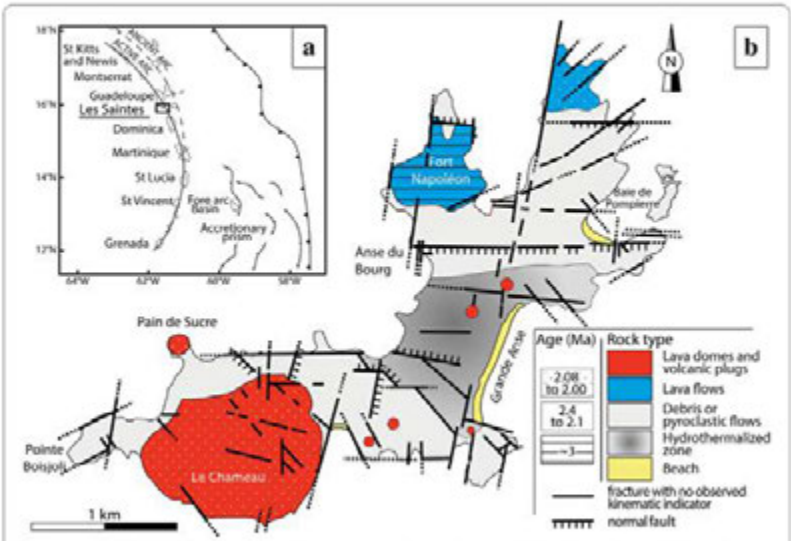


**Fig. 1** **a** Simplified geodynamic map of the Lesser Antilles Arc. **b** Simplified geological map of Terre-de-Haut (Les Saintes archipelago) indicating structural data, volcanic rock types and their ages (modified after Verati et al. 2016; Zami et al. 2014; Jacques and Maury 1988a, b; Jacques et al. 1984). Symbols refer to age of the rock formation, whereas colours refer to rock type. Note the orientation of the faults and fractures

archipelago), located 12 km south of Basse-Terre, is described in the literature as exhibiting an exhumed paleo-geothermal system (Jacques and Maury 1988a, b; Verati et al. 2016), giving access to a sub-horizontal 2D cross-section into the system. The combination of the geology of both sites might provide a 3D view of a geothermal system to better understand its fluid pathways. The mineralogy of a hydrothermally altered area on Terre-de-Haut has already been investigated (Jacques and Maury 1988a, b; Verati et al. 2016), but the authors did not focus on clay minerals, which are well known for being good indicators of hydrothermal alterations (Patrier et al. 2003; Mas et al. 2006; Bouchot et al. 2010). This present study focuses on the nature and distribution of clay minerals on Terre-de-Haut to propose a 3D conceptual model of geothermal systems of the Guadeloupe archipelago.

## Geological setting

The Guadeloupe archipelago, located in the Lesser Antilles arc (Fig. 1a), is the result of the subduction of the North American plate under the Caribbean plate at a velocity of approximately 2 cm year$^{-1}$ (Hawkesworth and Powell 1980; DeMets et al. 2000; Symithe et al. 2015). Two volcanic arcs result from this subduction (Bouysse 1983): the eastern one corresponds to the outer ancient arc, which was active from the Eocene to Early Miocene; and the western one corresponds to the inner arc, active from the Pliocene. Grande-Terre of Guadeloupe is located on the ancient arc; whereas, Basse-Terre and the Les Saintes archipelago are located on the active arc (Fig. 1a).

Little literature is available about the geology of Terre-de-Haut (Javey et al. 1974; Jacques et al. 1984; Jacques and Maury 1988a, b; Zami et al. 2014; Verati et al. 2016).

Regarding structural data, Verati et al. (2016) recognise four families of fault systems, active from 3 to 2 Ma. They establish a relative chronology, from the oldest to the most recent: (1) N050–N070, (2) N130–N140, (3) N090–N110 and (4) N000–N020 trending fault systems. Kinematic indicators and morphostructural observations demonstrate that the four families of fault systems display normal-slip movements, and three of them have a strike-slip movement (sinistral or dextral) also. The N090–N110 trending fault system is the only one without any evidence for strike-slip movement. Kinematic indicators revealing both dextral and sinistral strike-slips suggest that the N000–N020 and N050–N070 systems were active and reactivated at different stages during the tectonic evolution of the Les Saintes archipelago (Verati et al. 2016). These four families of fault systems affecting the Les Saintes archipelago are compatible with the global tectonic framework of the entire Guadeloupe archipelago (Verati et al. 2016). The 2004 Mw 6.3 Les Saintes earthquake (Beauducel et al. 2005) was correlated with a pure, normal faulting with NW–SE trending nodal planes, which are compatible with the identified onshore N130–N140 faults, indicating that the inherited faults' networks are likely to be reactivated during the present-day plate convergence (Verati et al. 2016).

Regarding the geochronological data, the most recent study (Zami et al. 2014) revealed the presence of three main subaerial volcanic phases on Terre-de-Haut (Fig. 1). The first phase, $2.98 \pm 0.04$ Ma old, consists of dacitic lava flows and explosive breccia and is located at Fort Napoléon. The second phase, dated at $2.40 \pm 0.04$ Ma, is widespread across the island, with basic andesitic lava and phreatomagmatic flows associated with two-pyroxene andesite. The third phase, between $2.08 \pm 0.03$ Ma and $2.00 \pm 0.03$ Ma, was expressed by the formation of the 'Le Chameau' dacitic dome ($2.00 \pm 0.03$ Ma) and is associated with some dykes.

The occurrence of a hydrothermal zone has been identified and described (Jacques et al. 1984; Jacques and Maury 1988a, b; Verati et al. 2016). This zone displays a succession of parageneses that are characteristic of high-temperature hydrothermal alteration in epithermal settings and its retrogression during cooling (Verati et al. 2016). Verati et al. (2016) observed a first high-temperature mineral assemblage composed of (i) aggregates of chlorite and epidote developed as pseudomorphs after primary plagioclase and clinopyroxene, or (ii) chlorite, serpentine and oxide aggregates formed at the expense of orthopyroxene. The pseudomorphosed minerals are crosscut by millimetric veinlets filled by quartz ± chalcedony ± pyrite ± chlorite ± smectite ± goethite aggregates. Sometimes, the veinlets connect vesicles filled with chalcedony and zeolites. A final advanced argillic alteration stage generated kaolinite, illite, smectite, and, in the most altered samples, gypsum and jasper are found (Verati et al. 2016). However, no thorough study of the clay minerals exists to date.

According to Verati et al. (2016), the age of hydrothermalism is constrained within a time span because the oldest volcanic rocks affected by the hydrothermal activity are dated at $2.40 \pm 0.04$ Ma (Zami et al. 2014), and none of the most recent volcanic plugs dated at $1.94 \pm 0.10$ Ma by Jacques et al. (1984) is hydrothermally altered, even when located in the hydrothermally altered zone (Fig. 1b, red spots). Hence, Verati et al. (2016) propose that the maximal timescale activity of the Les Saintes paleo-geothermal system is about 400 ky. However, for Zami et al. (2014), the hydrothermal activity lasted around 80 ky between $2.08 \pm 0.03$ and $2.00 \pm 0.03$ Ma.

## Materials and methods

The sampling was mainly conducted on outcrops of the second volcanic phase, as hydrothermal activity is restricted to these volcanic rocks (Verati et al. 2016). Additionally three samples from Le Chameau (i.e., late lava dome, Fig. 1) were collected as references. A set of 47 samples was collected in the field (see Fig. 2 and Table 1 for their location), in the apparently most intensely altered zone and its surroundings, either as fracture infillings or in the host rock to better understand how fluids flow through the rocks.

In the following discussion, we call samples in which the volcanic texture is preserved (phenocrysts in a microcrystalline groundmass including plagioclase microlites) as well as the phenocrysts themselves (preservation of main optical property such as morphology, twinning, and birefringence) 'fresh rocks' (see Fig. 3a). Fresh rocks are opposed to 'altered rocks', which have been submitted to strong hydrothermal alteration, sometimes together with strong fracturing. In altered rocks, the primary volcanic minerals have been completely replaced by newly formed minerals, and the original volcanic texture has been highly or completely overprinted (Fig. 3b).

X-ray Diffraction (XRD) analyses were performed at GeoRessources laboratory (University of Lorraine, France) and at the Institut de Recherche Criminelle de la Gendarmerie Nationale de Cergy-Pontoise (IRCGN, France), both on whole rock and on the < 2 µm fraction, using a method described by Holtzapffel (1985). The XRD was carried out using a Bruker D2 diffractometer (CuKα radiation, 30 kV, 10 mA, GéoRessources) and a Panalytical X'Pert3 Powder (CuKα radiation, 45 kV, 40 mA, IRCGN). The analytical conditions used for the acquisition of x-ray diffractograms were as follows: angular domain: $2\theta =$ between 2.5° and 30° for < 2 µm fraction, and between 3°

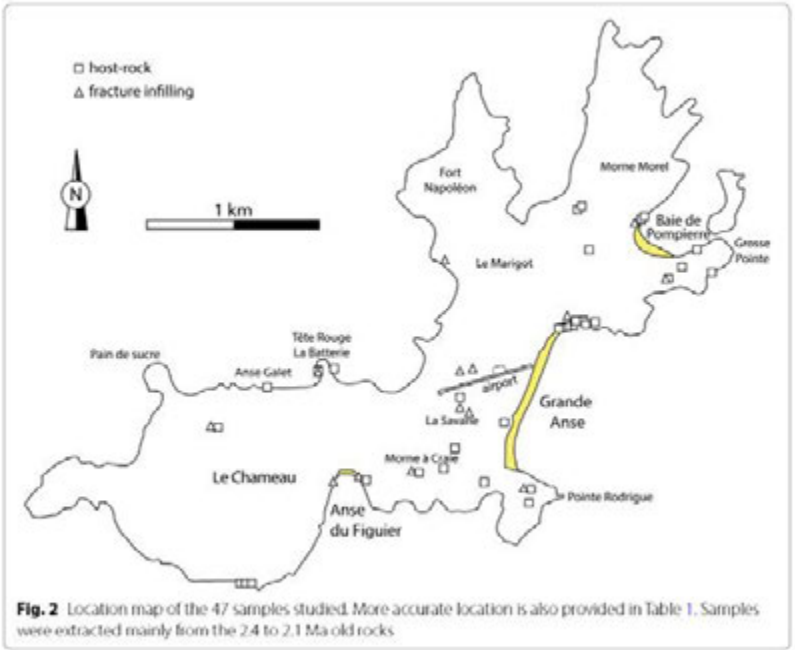


**Fig. 2** Location map of the 47 samples studied. More accurate location is also provided in Table 1. Samples were extracted mainly from the 2.4 to 2.1 Ma old rocks

**Table 1 List of samples collected on the field with their occurrence (fracture infillings (F.I.) or host rock (H. R.), locality, with their GPS coordinates when available, clay mineralogy, and petrophysical parameters [ρb: bulk density (g cm$^{-3}$), Φw: water porosity (%), *K*: permeability (m$^2$, measurement limits $10^{-19}$–$10^{-11}$ m$^2$)]**

| Sample | Occurrence | Locality | GPS coordinates | | Clay mineralogy | | | | Petrophysical properties | | |
|---|---|---|---|---|---|---|---|---|---|---|---|
| | | | Latitude | Longitude | Sme | Ilt | Chl | Kln(±Hall) | ph [g cm$^{-3}$] | ΦW [%] | *K* [m$^2$] |
| 15.142 | F. I. | Airfied (North) | N15°51′51.7″ | W061°34′57.8″ | ✓ | ✓ | | ✓ | 1.90 | 28.00 | |
| 15.144 | F. I. | Airfied (North) | | | ✓ | | | ✓ | | | |
| GEC 341 | F. I. | Anse du Figuier (East) | N15°51′30.5″ | W061°35′13.9″ | ✓ | | | | | | |
| GEC 342 | H-R | Anse du Figuier (East) | | | ✓ | | | | | | |
| GD15.136 | F. I. | Anse du Figuier (West) | N15°51′30.5″ | W061°35′20.8″ | ✓ | | | | 1.60 | 32.19 | |
| GEC 348 | H-R | Anse Galet | N15°51′50.1″ | W061°35′36.5″ | ✓ | ✓ | | | | | |
| 16.10 | H-R | Grosse Pointe | N15°52′13.2″ | W061°34′08′6″ | ✓ | | | | | | |
| GEC 213 | H-R | Grosse Pointe | | | ✓ | | | | | | |
| GEC 217 | F. I. | Grosse Pointe | N15°52′13.2″ | W061°34′14′6″ | ✓ | | | | | | |
| GEC 219 | H-R | Grosse Pointe | | | ✓ | | | | | | |
| 15.147 | H-R | La Savane | N15°51′46.9″ | W061°34′55.6″ | ✓ | ✓ | | ✓ | | | |
| GEC 308 | F. I. | La Savane | | | ✓ | ✓ | | ✓ | | | |
| GEC 317 | H-R | La Savane | | | ✓ | ✓ | | ✓ | | | |
| GEC 335 | F. I. | La Savane | | | ✓ | ✓ | | | | | |
| GEC 337 | F. I. | North of Le Chameau | N15°51′43.0″ | W061°35′46.3″ | ✓ | | | | | | |
| GEC 338 | H-R | North of Le Chameau | | | ✓ | | | | | | |
| GD15.139 | H-R | Le Chameau (South) | N15°51′11.7″ | W061°35′39.5″ | ✓ | | | | 2.33 | 12.94 | $2.94 \times 10^{-14}$ |
| GD15.140 | H-R | Le Chameau (South) | | | | | | | 2.24 | 15.64 | |
| GD15.141 | H-R | Le Chameau (South) | | | ✓ | | | | 2.45 | 8.06 | $1.08 \times 10^{-18}$ |
| GEC 220 | H-R | Le Marigot (East) | N15°52′14.6″ | W061°34′58.1″ | ✓ | | | | | | |
| GEC 221 | F. I | Le Marigot (West) | N15°52′18.4″ | W061°34′24.9″ | ✓ | | | | | | |
| GEC 328 | H-R | Morne a Craie | N15°51′32.3″ | W061°35′02.3″ | ✓ | | | | | | |
| GEC 330 | F. I. | Morne a Craie | | | ✓ | | | | | | |

**Table 1 (continued)**

| Sample | Occurrence | Locality | GPS coordinates | | Clay mineralogy | | | | Petrophysical properties | | |
|---|---|---|---|---|---|---|---|---|---|---|---|
| | | | Latitude | Longitude | Sme | Ilt | Chl | Kln(±Hall) | ph [g cm$^{-3}$] | ΦW [%] | $K$ [m$^2$] |
| GEC 331 | H-R | Morne a Craie | | | ✓ | | | ✓ | | | |
| GEC 332 | H-R | Morne a Craie | | | ✓ | | | ✓ | | | |
| GEC 333 | H-R | Morne a Craie | | | ✓ | | | ✓ | | | |
| 16.08 | H-R | Morne Morel | N15°52′26.9″ | W061°34′30.7″ | ✓ | | | | 2.25 | 17.47 | $1.06 \times 10^{-15}$ |
| 16.09 | H-R | Morne Morel | | | ✓ | | | | 2.04 | 22.95 | $1.31 \times 10^{-15}$ |
| GEC 236 | H-R | Grande Anse (North) | N15°52′04.1″ | W061°34′31.1″ | ✓ | | ✓ | | | | |
| GD16.01 | H-R | Grande Anse (North) | | | ✓ | ✓ | ✓ | | | | |
| GD16.02 | H-R | Grande Anse (North) | | | ✓ | ✓ | | | 2.07 | 17.11 | |
| GD16.03 | H-R | Grande Anse (North) | | | ✓ | ✓ | ✓ | | 2.02 | 26.05 | |
| GD16.05 | H-R | Grande Anse (North) | N15°52′02.0″ | W061°34′34.8″ | ✓ | ✓ | | | 2.08 | 22.88 | $1.16 \times 10^{-17}$ |
| GD16.06 | H-R | Grande Anse (North) | | | ✓ | ✓ | | | 1.97 | 23.55 | $5.26 \times 10^{-13}$ |
| GEC 238 | F. I. | Grande Anse (North) | | | ✓ | | | | | | |
| GEC 265 | H-R | Grande Anse (North) | N15°52′03.9″ | W061°34′32.4″ | ✓ | ✓ | ✓ | | | | |
| GEC 270 | H-R | Grande Anse (North) | | | ✓ | ✓ | ✓ | | | | |
| GEC 355 | H-R | Pointe Batterie (East) | N15°51′52.8″ | W061°35′24.0″ | ✓ | ✓ | | | | | |
| GEC 352 | H-R | Pointe Batterie (West) | N15°51′53.6″ | W061°35′22.1″ | ✓ | ✓ | | ✓ | | | |
| GEC 353 | F. I. | Pointe Batterie (West) | | | ✓ | ✓ | | ✓ | | | |
| GEC 321 | F. I. | Pointe Rodrigue | N15°51′29.2″ | W061°34′40.2″ | ✓ | | | ✓ | | | |
| GEC 322 | H-R | Pointe Rodrigue | | | ✓ | | | ✓ | | | |
| GEC 325 | H-R | Pointe Rodrigue | | | ✓ | | | ✓ | | | |
| 17TH27a | H-R | Pompierre (NE) | N15°52′22.9″ | W061°34′18.6″ | ✓ | | | | | | |
| GD15.137 | F. I. | Pompierre (NE) | | | ✓ | | | | | | |
| GD15.138 | H-R | Pompierre (NE) | | | | | | | 2.11 | | $1.45 \times 10^{-15}$ |
| GEC 207 | H-R | Pompierre (SE) | N15°52′17.8″ | W061°34′07.9″ | ✓ | | | | | | |

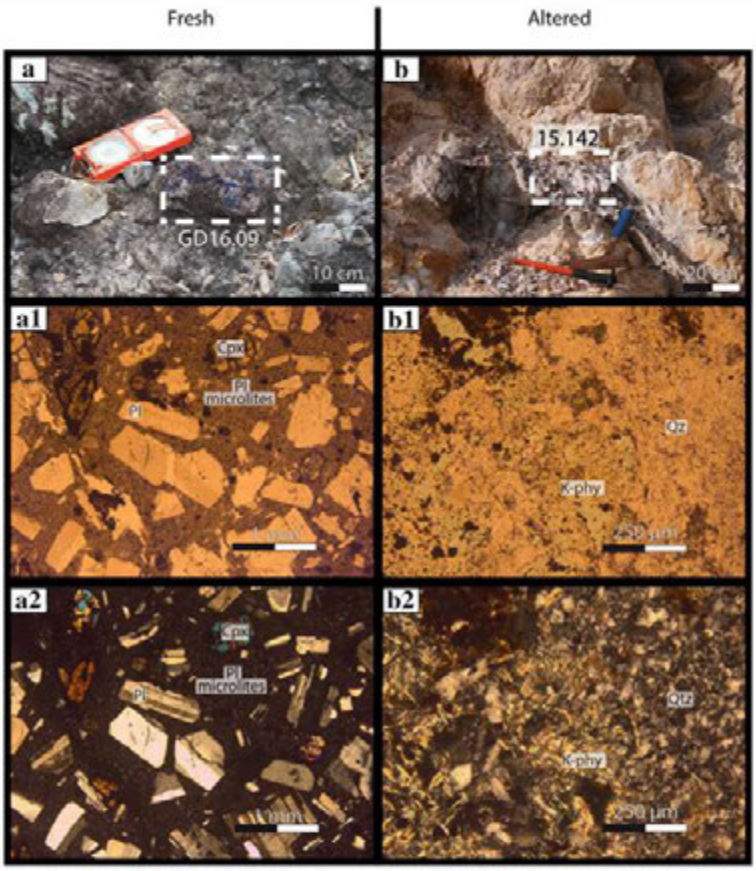


**Fig. 3** Examples of dark fresh (**a**) and yellowish hydrothermally altered (**b**) samples as found on the outcrops and corresponding thin sections seen by optical microscopy with plane polarized light (**a1** and **b1**) and crossed polarized light (**a2** and **b2**). Sample A corresponds to a clast in a debris flow while B sample was extracted from a fracture. Thin section of fresh sample A shows a rock in which the primary volcanic minerals and texture are preserved. Phenocrysts are euhedral but fractured (see also Fig. 4). Plagioclase (Pl) displays clear twins and clinopyroxene (Cpx) shows its normal birefringence. The groundmass is composed of µm-sized plagioclase microlites. Sample B seen in thin section shows a strongly transformed texture in which volcanic primary minerals cannot be distinguished anymore as they are replaced by newly formed minerals. Extensive crystallization of K-phyllosilicates (K-phy) and quartz (Qz) is observed. Mineral abbreviations (except for 'K-phy') according to Whitney and Evans (2010)

and 70° for whole-rock fraction, step increment: $2\theta = 0.01°$, counting time per step: 0.6 s. Each < 2 µm fraction sample was spread on a glass slide to stack clay minerals on their basal planes. Each sample was analysed in three states: (i) air-dried (natural state); (ii) glycolated for one night to allow swelling of specific clay minerals; and (iii) after heating at 490 °C for 2 h because kaolinite is sensitive to heat (16 selected samples). Furthermore, a formamide test was used to differentiate halloysite from kaolinite (Churchman et al. 1984) on six samples.

Microscopic observations have been done on thin sections using both optical microscopy and scanning electron microscopy (Zeiss Gemini 300).

Petrophysical properties, in particular porosity and density (14 samples) and nitrogen gas permeability (7 samples), were analysed on 25 mm diameter and 21 mm long plugs, under low confining pressure (20 bars). The samples were dried prior to measurements in an oven until a constant weight was reached. The drying temperature was set at 60 °C to avoid any change in mineralogy. Sample preparation is similar to that in Navelot et al. (2018). The measurements were done at Ecole Nationale Supérieure de Géologie (Nancy) (see Table 1). According to Navelot et al. (2018), the permeability measurements did not exhibit Klinkenberg effect (Klinkenberg 1941) and, therefore, no correction was required.

Helium, mercury porosity, and water (triple weight) porosity were measured. Helium porosity was measured using Micromeritics® model AccuPyc II 1340 gas pycnometer. Triple weight porosity measurements were done with distilled water. The porosity data were consistent for each method. In this study, only water porosity data are presented.

Whatever the porosity measurement method employed, the data being consistent ($\Delta = 1.4\%$ in average between water porosity and Helium porosity; $\Delta = 2.6\%$ in average between water porosity and mercury porosity) only triple weight porosity data are presented in the following.

## Results

In the field, rocks have different appearances depending on their alteration state—either fresh or altered. Fresh andesite is darker than the same altered rock, which has a yellowish colour (Fig. 3a, b).

Optical microscopy observations of thin sections from fresh and altered samples display different textures. A 'fresh' sample (Fig. 3a) was taken from a clast in a fresh debris flow, while the 'altered' sample (Fig. 3b) was taken from a fracture intersecting a completely transformed andesite, where no primary minerals are visible because of strong deformation and alteration.

In the fresh andesitic rock sample (Fig. 3a1 and a2), one can clearly observe a microlitic groundmass, which represents about 60% of the rock, as estimated by optical observation. Ninety percent of the phenocrysts are made of plagioclase of millimetric size with a euhedral shape frequently displaying a growth zonation. The other phenocrysts are mostly clinopyroxene and orthopyroxene. Opaque minerals are present, as well as amphiboles in some samples. The groundmass is fully microcrystalline and mainly composed of very fine plagioclase crystals. No volcanic glass was observed in our samples, and consistent with previous observations (Navelot 2018; Navelot et al. 2018). Phenocrysts of plagioclase and pyroxenes are strongly microcracked in the fresh sample (Fig. 4a), providing potential pathways for fluid circulation. The porosity of fresh andesite in our samples is related to micropores in the groudmass, as well as microcracks cross-cutting both groundmass and phenocrysts (Fig. 4a), which is in line with Navelot et al. (2018).

In the hydrothermally altered sample (15.142, Fig. 3b, b1, b2), the primary minerals are completely transformed into secondary minerals, such as microcrystalline quartz associated with well-developed K-phyllosilicates (illite or white mica). The Scanning Electron

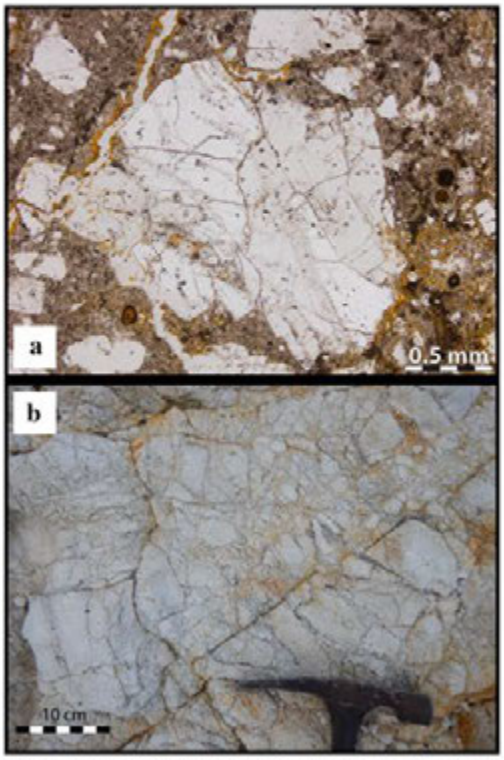


**Fig. 4** Micro- and meso-scale fracture networks seen in thin section (**a**) and on the outcrop (**b**). **a** Shows an intensely microfractured plagioclase in fresh sample. **b** Shows a strongly fractured zone north of Grande Anse

Microscopy (SEM) observations of this sample (Fig. 5) reveal two types of porosity: microcrack porosity and inter-mineral porosity between K-phyllosilicate crystals. In Fig. 5, K-phyllosilicate crystals are made of thin crystallites with a fibrous morphology and seem to fill this fracture and bridge it, indicating that they are post-fracturing. In addition, at the outcrop scale, numerous fractures were observed in altered zones, allowing the fluids to flow through the rock (Fig. 4b).

X-ray diffraction analyses performed on whole rock clearly reveal the mineralogical transformation induced by the hydrothermal alteration by comparing the data for a fresh andesite with a hydrothermally altered andesite. The alteration implies the transformation of primary minerals such as plagioclases and pyroxenes, their replacement by clay minerals, and an increase in the relative abundance of quartz (Fig. 6).

Regarding the < 2 µm fraction, the 43 diffractograms acquired can be classified into three main clay assemblages (Fig. 7). Figure 7a contains only smectite (14 Å at natural state, 17 Å when glycolated and 10 Å after heating). Figure 7b contains illite (peak at 10 Å whatever the state of the sample) together with smectite and kaolinite (7 Å peak at natural and glycolated states, no peak when heated). Figure 7c illustrates the presence of chlorite (14 Å peak whatever the state of the sample), illite and smectite.

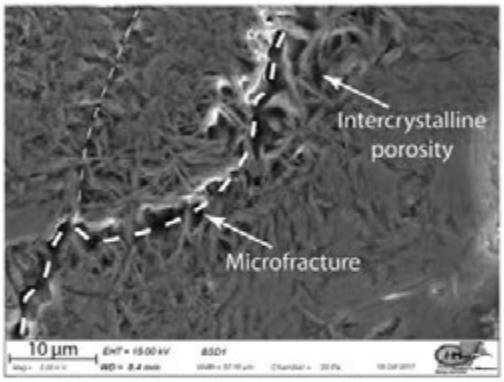


**Fig. 5** Scanning Electron Microscopy (SEM) image of a small zone of altered sample 15.142 showing a total replacement of primary volcanic minerals and groundmass by K-phyllosilicates. Crystallization of K-phyllosilicates is posterior to the development of microfractures as they partially bond them. Intercrystalline porosity is also encountered between K-phyllosilicate crystallites

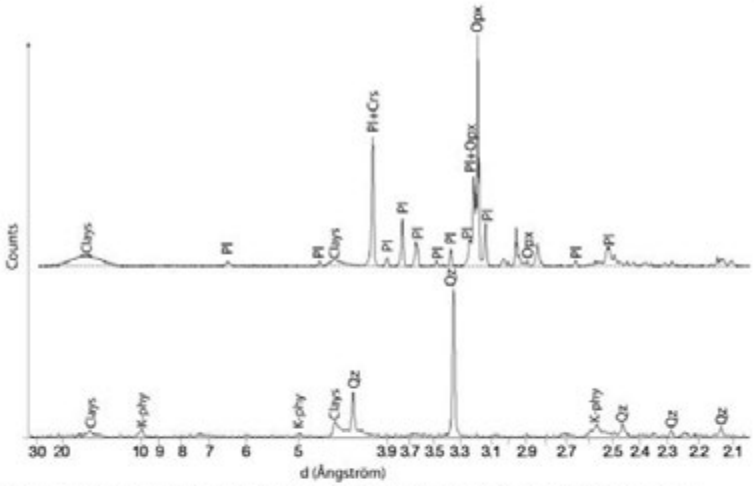


**Fig. 6** X-ray diffractograms performed on whole rock. Comparison of fresh (above) and altered facies (below). *Pl* plagioclase, *Opx* orthopyroxene, *Qz* quartz, *Crs* cristobalite, *K-phy* K-phyllosilicates

Figure 8 provides the location of each sample with its clay mineral assemblage, and the names of the minerals are provided in decreasing order of abundance. The most widespread assemblage on the island (Fig. 8), which occurs in host rock and in fracture infillings, consists of smectite ± kaolinite ± halloysite (Fig. 7a). This assemblage is called the 'smectite zone' in the following discussion. The second assemblage consists of smectite + illite ± kaolinite ± halloysite (Fig. 7b), and is called the 'illite zone'. This second zone's extension is more restricted; it crops out along a band that is hundreds of metres wide, orientated east–west, and cuts across the centre of the island (Fig. 8).

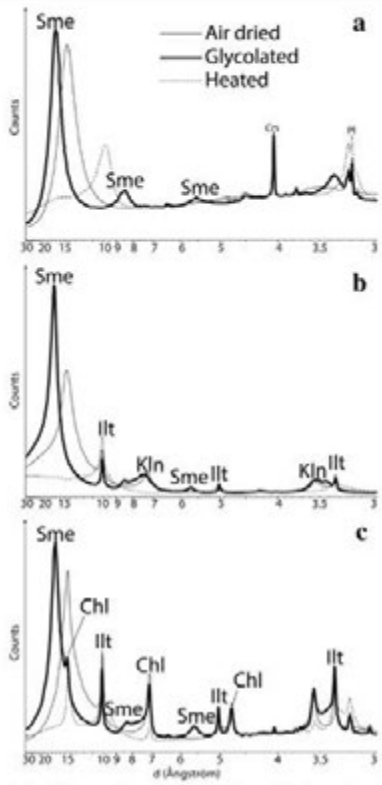


**Fig. 7** X-ray diffractogram of the different clay assemblages found in the analyzed samples 16.09 (**a**), 15.142 (**b**), 16.01 (**c**). For their location, see Table 1. (*d*(001), *d*(002) and *d*(003) are indexed, except for Kaolinite (= Kaol) where only *d*(001) and *d*(002) are indexed). Smectite (= Sme), Illite(= Ill), Chlorite (= Chl). A (from sample 16.09, Morne Motel): Smectite only; B (from sample 15.142, central part of Terre-de-Haut, airfield): Smectite + illite + Kaolinite ± Halloysite; C (from sample 16.01, north of Grande Anse): Smectite + Illite + Chlorite ± Kaolinite ± Halloysite

The third assemblage, which consists of smectite + chlorite + illite ± kaolinite ± halloysite (Fig. 7c), is only observed on the east side of the island, north of Grande Anse (Fig. 8), and is called the 'chlorite zone'. According to this study, this assemblage has the narrowest geographical distribution. The distribution of clay minerals allows us to distinguish the three different zones (Fig. 8).

No difference is apparent in the mineralogy between samples from fracture infillings and the surrounding rocks.

The effective porosity measured on 14 samples from Terre-de-Haut ranges from 6% for the fresh andesite, up to 36% for the most altered sample. The porosity values range is as follows: (i) for smectite bearing samples, 8% to 32%; (ii) for smectite + illite bearing samples, 23% to 28%; (iii) for smectite + chlorite + illite bearing samples, 17% to 26%. Reference samples collected at Le Chameau have 8% to 15% porosity.

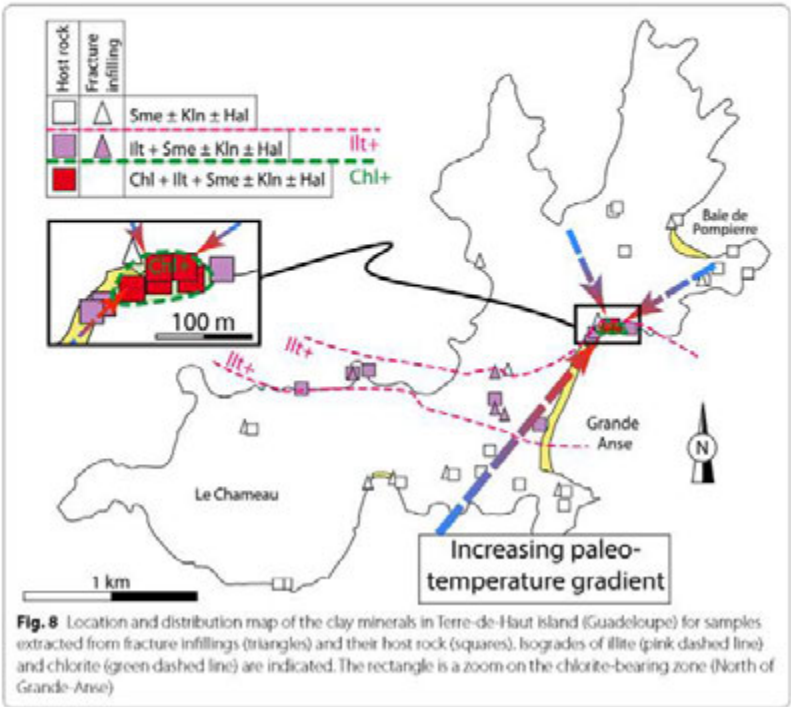


**Fig. 8** Location and distribution map of the clay minerals in Terre-de-Haut island (Guadeloupe) for samples extracted from fracture infillings (triangles) and their host rock (squares). Isograde of illite (pink dashed line) and chlorite (green dashed line) are indicated. The rectangle is a zoom on the chlorite-bearing zone (North of Grande-Anse)

Dry bulk density values range from 2.45 g $cm^{-3}$ for the fresh sample, to 1.60 g $cm^{-3}$ for the most altered sample. The highest densities measured belong to andesite that did not experience strong weathering or hydrothermal alteration. Regarding the samples located in the hydrothermal zone, three are composed of smectite + illite, and their density is between 1.90 and 2.08 g $cm^{-3}$; two have a mineralogical assemblage of smectite + illite + chlorite and are 2.02 g $cm^{-3}$ and 2.07 g $cm^{-3}$ of density. The lowest density (1.60 g $cm^{-3}$) was measured in a sample located in Anse Figuier, which is outside the central hydrothermally altered zone, where the rock could have experienced a low-temperature alteration.

Nitrogen gas permeability measurements performed on seven samples, either fresh or altered, reveal six orders of magnitude, from $10^{-18}$ to $10^{-13}$ $m^2$, between the least and the most permeable samples (Table 1). The sample with the lowest permeability ($10^{-18}$ $m^2$) (collected at Le Chameau) shows the lowest porosity (8%). However, for the other samples, no relationship between connected porosity and permeability appears. For example, for the three samples with a porosity around 23%, their permeability ranges on four order of magnitudes, from $10^{-13}$ to $10^{-17}$ $m^2$.

## Discussion

According to optical microscopy observations and whole-rock XRD analyses, hydrothermal alteration associated with an intense deformation implies a complete transformation of the texture of the rock. Fluids transformed the primary minerals, but may no longer be present in the case of intense hydrothermal circulation. The same process has

also been observed in samples from Bouillante drillings (Mas et al. 2006). In Terre-de-Haut, this whole-rock transformation is generally associated with strong fracturing and the formation of clay minerals.

By comparison with the data from Bouillante geothermal field, and according to Bouchot et al. (2010), the presence of chlorite corresponds to a temperature of crystallization above 240 °C, illite to temperatures higher than 180°, and smectite to temperatures lower than 180 °C.

The distribution of the clay assemblages and the estimated temperatures for each zone suggests a lateral paleo-temperature gradient increasing from the smectite zone to the chlorite zone through the illite zone. Thus, isograds of mineral appearance can be proposed for illite and chlorite (Fig. 8).

As stated in Patrier et al. (2003) and Opfergelt et al. (2012), kaolinite and halloysite result from meteoric weathering in Basse-Terre, and, therefore, they are not considered in this study.

According to Verati et al. (2016), the hydrothermally altered zone is controlled by the intersection of two normal fault families orientated N090–N110 and N130–N140, north of Grande Anse. These two faults are responsible for the collapse of this zone and are associated with hydrothermal fluid circulation. By comparison of Fig. 1 with Fig. 8, we can now add that this specific area corresponds to the highest temperature recorded and is preserved by clay minerals within the paleo-hydrothermal system.

In Fig. 9, the petrophysical properties of our rocks are compared with data from geothermal fields in similar geological contexts.

Figure 9 displays the relationship between porosity and bulk density from Terre-de-Haut, the Taupo volcanic zone (New-Zealand, Wyering et al. 2014; Siratovich et al. 2014), Kuril-Kamchatka island (Russia, Frolova et al. 2014) and Guadeloupe (Navelot et al. 2018).

In the Taupo volcanic zone (Wyering et al. 2014), Kuril-Kamchatka island (Frolova et al. 2010, 2014) and in the Darajat geothermal field (West Java, Indonesia, Rejeki et al. 2005), the alteration mineral assemblage and clay type play an important role in enhancing or reducing the primary porosity and density of the rocks.

Low to moderate temperature alteration increases the porosity and decreases the density of the rock; whereas, a high-temperature alteration hardens the rock, leading to a decrease in porosity and an increase in density (Frolova et al. 2010, 2014).

Data from Terre-de-Haut are distributed along the general trend describing a porosity-density linear relationship similar to the one observed in the other locations: the higher the density, the lower the porosity, and vice versa.

The more porous and less dense rock contains only smectite, confirming observations of Wyering et al. (2014). However, samples collected at Le Chameau, also containing smectite, have high density and low porosity. The Le Chameau formation, being more recent than hydrothermal alteration (Zami et al. 2014), means that we can conclude that smectite originates from weathering. In contrast to Wyering et al. (2014), who suggest that chlorite-silica alteration decreases porosity and increases density compared with illite alteration, our illite- and chlorite-bearing samples display similar values of porosity and density and cannot be distinguished. In the Rotokawa geothermal field (New-Zealand), the behaviour of petrophysical properties is mainly

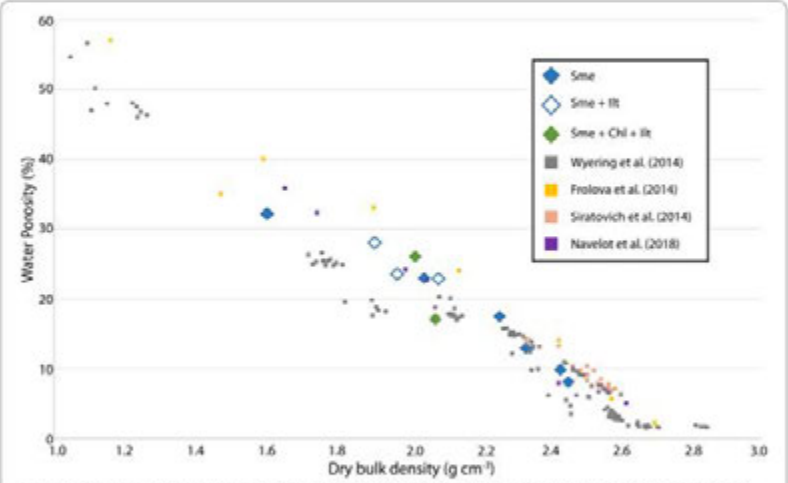


**Fig. 9** Graph representing the water porosity (triple weighing) versus bulk density, comparing data of this study differentiated by their specific clay assemblage with data from Taupo Volcanic Zone (New-Zealand, Siratovich et al. 2014; Wyering et al. 2014), Kuril-Kamchatka island (Russia, Frolova et al. 2014) and Guadeloupe (Navelot et al. 2018)

determined by the presence and intensity of microfracturing and seems to be largely independent of the alteration mineralogy, as Siratovich et al. (2014) observed similar alteration intensities (dominated by chlorite/epidote) in the different samples they analysed. The same behaviour might be observed on Terre-de-Haut.

Regarding the nitrogen gas permeability data, no relationship between clay mineralogy and permeability can be deduced from our measurements. The low permeability of the sample presenting the lowest porosity can be explained by its poorly connected and tortuous network of pores and narrow microcracks (Farquharson et al. 2015; Heap and Kennedy 2016; Kushnir et al. 2016; Heap et al. 2017). On the opposite, the two samples with the highest permeabilities ($10^{-14}$ $m^2$ and $10^{-13}$ $m^2$) indeed show the highest porosities (24% and 26%).

However, connected porosity is not correlated with permeability for the other samples, as volcanic rocks present microstructurally complex porosity networks (Farquharson et al. 2015; Heap et al. 2017). This microstructural complexity has not been deeply developed in this study.

From the results presented in this current study, no difference was found in the mineralogy of clays sampled in fracture infillings and in the surrounding rock, indicating that the entire area underwent widespread alteration, both through fractures and in the host rock, which can be explained by the connectivity of the network of multi-scale fractures (µm- to km-scale). These results do not allow the distinguishing of several hydrothermal events.

Our fracture data (Figs. 4 and 5) suggest that both fresh and hydrothermally altered rocks provide pathways for fluid flow (at µm-scale to m-scale)., which is an important point for geothermal projects (Grant et al. 1982). Unfortunately, our data do not

show striking evidence of correlation between permeability, porosity and degree of alteration.

Combining structural (Verati et al. 2016) and mineralogical data (this study), we propose a schematic representation of geothermal systems in the Guadeloupe archipelago (Fig. 10) based on investigations on land at Terre-de-Haut (outcrops) and drillings from Bouillante (Basse-Terre, Fig. 10a). The Bouillante drillings provide a 1D vertical insight into an active geothermal system (Fig. 10b), revealing a vertical zonation of clay minerals (Mas et al. 2006; Bouchot et al. 2010). This partial view is completed by the 2D planar view of Terre-de-Haut, which has been subjected to erosion and in which a lateral paleo-geothermal gradient was observed (Fig. 10c). Both these sites are consistent with a pluri-hm scale of geothermal systems in the Guadeloupe archipelago (Fig. 10d).

## Conclusion

The island of Terre-de-Haut exhibits a strongly hydrothermally altered east–west trending zone in the central part of the island. This area is characterised by the occurrence of several clay minerals that allow us to distinguish three different hydrothermal zones organised in a general concentric pattern. From the core to the rim of the area, one can

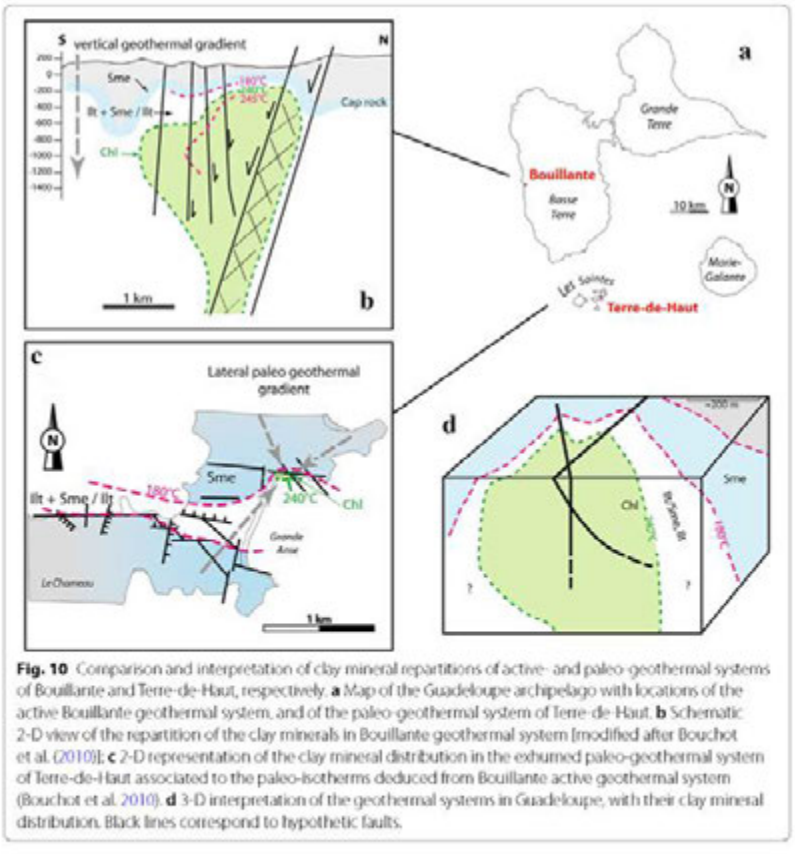


**Fig. 10** Comparison and interpretation of clay mineral repartitions of active- and paleo-geothermal systems of Bouillante and Terre-de-Haut, respectively. **a** Map of the Guadeloupe archipelago with locations of the active Bouillante geothermal system, and of the paleo-geothermal system of Terre-de-Haut. **b** Schematic 2-D view of the repartition of the clay minerals in Bouillante geothermal system [modified after Bouchot et al. (2010)]; **c** 2-D representation of the clay mineral distribution in the exhumed paleo-geothermal system of Terre-de-Haut associated to the paleo-isotherms deduced from Bouillante active geothermal system (Bouchot et al. 2010). **d** 3-D interpretation of the geothermal systems in Guadeloupe, with their clay mineral distribution. Black lines correspond to hypothetic faults.

observe the following: (i) a narrow chlorite zone located north of Grande Anse; (ii) an illite zone elongated in an east–west trend in the central part of Terre-de-Haut (La Batterie, airfield and Savane); and (iii) a large smectite zone that encompasses the two other zones. These clay minerals and their zonation are typical of altered zones in a geothermal context (Stimac et al. 2008; Pola et al. 2012; Frolova et al. 2010, 2014; Wyering et al. 2014). At Bouillante, 35 km NNW of Terre-de-Haut, a similar clay mineral zonation was observed vertically along the boreholes. Since Bouillante is an active geothermal site, the clay mineral zonation observed at Terre-de-Haut can indeed be considered as belonging to an exhumed paleo-geothermal system. The distribution of the clay minerals at Terre-de-Haut describes a paleo-geothermal gradient from the cooler smectite zone to the hotter chlorite zone, with the chlorite zone representing the central part of the reservoir, or at least the hotter preserved hydrothermal alteration zone.

The hydrothermal alteration on Terre-de-Haut appears to be fracture-controlled at all scales, from the km-scale to the µm-scale. At the km-scale, the extension of the illite zone is controlled to the south (from Anse Galet to La Savane) by N90° and N140° striking faults (Figs. 1 and 10), and to the north of Grand Anse by a N100° striking fault. As at Bouillante, the hydrothermally altered area of Terre-de-Haut is found at the intersection between N90°–N100° and N140° striking faults. At the mesoscale, numerous fractures intersecting each other are observed on the outcrops in the most altered area. At the mm- to the µm-scale, fresh phenocrysts are strongly microfractured and grain joints in the groundmass also provide pathways for the fluids. In the hydrothermally altered samples, in which primary volcanic minerals have been replaced by newly formed clay minerals, microfractures remain visible, and a porous network appears between the clay crystallites. When one considers the permeability of samples, even fresh samples display relatively intermediate to low values (between $10^{-14}$ and $10^{-18}$ $m^2$) because of microfractures and grain joints. The values of altered samples are even higher (up to $10^{-13}$ $m^2$) because of the porous network between clay mineral crystallites in addition to preserved microfractures. According to Heap and Kennedy (2016), these permeability values likely underestimate the permeability of a volcanic rock-mass, that is crosscut by discontinuities at the outcrop and km-scale such as contacts between volcano-sedimentary units and lava flow, cooling joints, fractures and faults (Navelot et al. 2018).

The combination of Bouillante and Terre-de-Haut petrological data (vertical by drilling and horizontal thanks to outcrops) allows for a 3D representation of geothermal systems in the Guadeloupe archipelago and enables us to estimate their pluri-hectometre size.

Finally, even though the hydrothermally altered zones at Terre-de-Haut and Bouillante are said to be controlled by fractures and their intersections (Calcagno et al. 2012; Verati et al. 2016; this study), no difference has yet been noted in the mineralogy of clays when one compares those found in fracture infillings with those sampled in their host rock. This observation suggests that fluids not only flow through fractures, but also pervasively through rock-effective porosity due to micro- and meso-fractures as well as grain joints. When the rocks are hydrothermally altered, high porosities and permeabilities are measured, indicating that the altered zones might behave as good geothermal reservoirs that can be exploited, such as at Bouillante.

**Authors' contributions**
This study is part of the PhD of GB supervised by BL, RH. VN made petrophysical measurements. VN and AF contributed to field work and interesting discussions. All authors read and approved the final manuscript.

**Author details**
[1] Laboratoire Géosciences et Environnement Cergy, Université de Cergy Pontoise, 1 Rue Descartes, 95000 Neuville-sur-Oise, France. [2] UMR 7359 GeoRessources, Ecole Nationale Supérieure de Géologie, Université de Lorraine, 2 Rue du Doyen Marcel Roubault, Vandoeuvre-lès-Nancy 54500, France. [3] UMR 5243 Géosciences Montpellier, Université des Antilles, Campus de Fouillole, 97159 Pointe-à-Pitre Cedex, Guadeloupe. [4] CNRS, Observatoire de la Côte d'Azur, IRD, UMR 7329 Géoazur, Université Côte d'Azur, 250 rue Albert Einstein, 06560 Valbonne, France.

**Acknowledgements**
Access to XRD both at Université de Nancy and at Institut de la Recherche Criminelle de la Gendarmerie Nationale (IRCGN) is greatly acknowledged. The authors are grateful to unknown reviewers for their helpful comments and suggestions. All the participants of GEOTREF project are thanked for their numerous interactions both in the field and in scientific meetings (GéoAzur, GeoRessources, Teranov, KIDOVA, Mines ParisTech, ENS Paris, IMFT, IPGS, LHyGes, UAG, UCP-GEC).

**Competing interests**
The authors declare that they have no competing interests.

**Funding**
Financial support for this study is provided by the GEOTREF project (http://www.geotref.com), and G.B. is grateful for his PhD grant, which is also funded by ADEME in the frame of "Les Investissements d'Avenir" program.

## Publisher's Note
Springer Nature remains neutral with regard to jurisdictional claims in published maps and institutional affiliations.

Received: 28 August 2018 Accepted: 13 February 2019
Published online: 28 February 2019

**References**
Beauducel F, Antenor-Habazac C, Bazin S, De Chabalier J-B, Nercessian A, Feuillet N, Jacques E, Bertil D, Boudon G, Lefriant A, Tapponnier P, Hirn A, Lepine J-C, Bernard P, Komorovski J-C, King GCP. The Mw 6.3 earthquake of Les Saintes (Guadeloupe) on November 21, 2004. IAVCEI European Seismological Commission Annual Workshop, Saint-Claude Guadeloupe, 2005; 2005.

Bouchot V, Traineau H, Guillou-Frottier L, Thinon I, Baltassat JM, Fabriol H, Bourgeois B, Lasne E. Assessment of the Bouillante Geothermal Field (Guadeloupe, French West Indies): Toward a Conceptual Model of the High Temperature Geothermal System. World Geotherm. Congr. 2010, Bali, Indonesia; 2010. p. 8.

Bouysse P (1983) The Lesser Antilles Island Arc: Structure and Geodynamic Evolution. (Service Géologique National), Bureau de Recherches Géologiques et Minières.

Calcagno P, Bouchot V, Thinon I, Bourgine B. A new 3D fault model of the Bouillante geothermal province combining onshore and offshore structural knowledge (French West Indies). Tectonophysics. 2012;526–529:185–95.

Churchman GJ, Whitton JS, Claridge GGC, Theng BKG. Intercalation method using formamide for differentiating halloysite from kaolinite. Clays Clay Miner. 1984;32:241–8.

DeMets C, Jansma PE, Mattioli GS, Dixon TH, Farina F, Bilham R, Calais E, Mann P. GPS geodetic constraints on Caribbean-North America Plate Motion. Geophys Res Lett. 2000;27:437–40.

Farquharson J, Heap MJ, Varley NR, Baud P, Reuschlé T. Permeability and porosity relationships of edifice-forming andesites: a combined field and laboratory study. J Volcanol Geotherm Res. 2015;297:52–68.

Frolova JV, Ladygin VM, Rychagov SN. Petrophysical alteration of volcanic rocks in hydrothermal systems of the Kuril-Kamchatka Island Arc. In: Proceedings, World Geothermal Congress 2010, Bali, Indonesia; 2010. p. 25–29.

Frolova J, Ladygin V, Rychagov S, Zukhubaya D. Effects of hydrothermal alterations on physical and mechanical properties of rocks in the Kuril-Kamchatka island arc. Eng Geol. 2014;183:80–95.

Grant A, Donaldson IG, Bixley PF. Geothermal reservoir engineering. London: Academic Press; 1982.

Hawkesworth CJ, Powell M. Magma genesis in the lesser Antilles island arc. Earth Planet Sci Lett. 1980;51:297–308.

Heap MJ, Kennedy BM. Exploring the scale-dependent permeability of fractured andesite. Earth Planet Sci Lett. 2016;447:139–50.

Heap MJ, Kennedy BM, Farquharson JI, Ashworth J, Mayer K, Letham-Brake M, Reuschlé T, Gilg HA, Scheu B, Lavallée Y, Siratovich P, Cole J, Jolly AD, Baud P, Dingwell DB. A multidisciplinary approach to quantify the permeability of the Whakaari/White Island volcanic hydrothermal system (Taupo Volcanic Zone, New Zealand). J Volcanol Geotherm Res. 2017;332:88–108.

Holtzapffel T. Les Minéraux Argileux: Préparation, Analyse Diffractométrique et Détermination, vol. 12. Lille: Soc. Géol. Nord Publ.; 1985. p. 136.

Jacques D, Maury R. L'archipel des Saintes (Guadeloupe, Petites Antilles): géologie et pétrologie. Géologie la Fr. 1988a;2–3:88–99.

Jacques D, Maury R. Carte géologique au 1/20 000e, département de la Guadeloupe, Les Saintes. BRGM, Service Géologique National: Orléans; 1988b.

Jacques D, Maury RC, Bellon H. Géologie et géochronologie des îles des Saintes, Guadeloupe. CR Acad Sci, Paris, serie II. 1984; 299, 11, 721–6.

Javey C, Alsac C, collaboration Mervoyer B. Excursion A6, livret-guide des excursions dans les F.W.I. In: VIIIe Conf. of Géol. des Caraïbes; 1974. p. 65–72.
Klinkenberg LJ. The permeability of porous media to liquids and gases. New York: Drilling and Production Practice; 1941. p. 200–13.
Kushnir AR, Martel C, Bourdier JL, Heap MJ, Reuschlé T, Erdmann S, Komorowski JC, Cholik N. Probing permeability and microstructure: unravelling the role of a low-permeability dome on the explosivity of Merapi (Indonesia). J Volcanol Geotherm Res. 2016;316:56–71.
Mas A, Guisseau D, Patrier Mas P, Beaufort D, Genter A, Sanjuan B, Girard JP. Clay minerals related to the hydrothermal activity of the Bouillante geothermal field (Guadeloupe). J Volcanol Geotherm Res. 2006;158:380–400.
Navelot V. Caractérisations structurale et pétrophysique d'un système géothermique en contexte volcanique d'arc de subduction. Exemple de l'archipel de Guadeloupe. Thesis, University of Lorraine; 2018.
Navelot V, Géraud Y, Favier A, Diraison M, Corsini M, Lardeaux JM, Mercier de Lépinay J, Legendre L, Beauchamps G. Petrophysical properties of volcanic rocks and impacts of hydrothermal alteration in the Guadeloupe Archipelago (West Indies). J Volcanol Geotherm Res. 2018;360:1–21.
Opfergelt S, Georg RB, Delvaux B, Cabidoche YM, Burton KW, Halliday AN. Mechanisms of magnesium isotope fractionation in volcanic soil weathering sequences, Guadeloupe. Earth Planet Sci Lett. 2012;341–344:176–85.
Patrier P, Beaufort D, Mas A, Traineau H. Surficial clay assemblage associated with the hydrothermal activity of Bouillante (Guadeloupe, French West Indies). J Volcanol Geotherm Res. 2003;126:143–56.
Pola A, Crosta G, Fusi N, Barberini V, Norini G. Influence of alteration on physical properties of volcanic rocks. Tectonophysics. 2012;566:67–86.
Rejeki S, Hadi J, Suhayati I. Porosity study for detail reservoir characterization in Darajat Geothermal Field,West Java, Indonesia. In: Proceedings, World Geothermal Congress, Antalya, Turkey; 2005.
Siratovich PA, Heap MJ, Villeneuve MC, Cole JW, Reuschlé T. Physical property relationships of the Rotokawa Andesite, a significant geothermal reservoir rock in the Taupo Volcanic Zone, New Zealand. Geotherm Energy. 2014;2:10.
Stimac J, Nordquist G, Suminar A, Sirad-Azwar L. An overview of the Awibengkok geothermal system, Indonesia. Geothermics. 2008;37:300–31.
Symithe S, Calais E, de Chabalier JB, Robertson R, Higgins M. Current blockmotions and strain accumulation on active faults in the Caribbean. J Geophys Res Solid Earth. 2015;120:2014.
Verati C, Mazabraud Y, Lardeaux J-M, Corsini M, Schneider D, Voitus E, Zami F. Tectonic evolution of Les Saintes archipelago (Guadeloupe, French West Indies): relation with the Lesser Antilles arc system. Bull Soc Géol Fr. 2016;187:3–10.
Whitney DL, Evans BW. Abbreviations for names of rock-forming minerals. Am Miner. 2010;95:185–7.
Wyering LD, Villeneuve MC, Wallis IC, Siratovich PA, Kennedy BM, Gravley DM, Cant JL. Mechanical and physical properties of hydrothermally altered rocks, Taupo Volcanic Zone, New Zealand. J Volcanol Geotherm Res. 2014;288:76–93.
Zami F, Quidelleur X, Ricci J, Lebrun JF, Samper A. Initial sub-aerial volcanic activity along the central Lesser Antilles inner arc: new K-Ar ages from Les Saintes volcanoes. J Volcanol Geotherm Res. 2014;287:12–21.

**Submit your manuscript to a SpringerOpen journal and benefit from:**

- ► Convenient online submission
- ► Rigorous peer review
- ► Open access: articles freely available online
- ► High visibility within the field
- ► Retaining the copyright to your article

**Submit your next manuscript at ► springeropen.com**